Report documentation page

Form approved omb no. 074-0188

Public reporting burden for this collection of information is estimated to average 1 hour per response, including the time for reviewing instructions, searching existing data sources, gathering and maintaining the data needed, and completing and reviewing this collection of information. Send comments regarding this burden estimate or any other aspect of this collection of information, including suggestions for reducing this burden to washington headquarters services, directorate for information operations and reports, 1215 jefferson davis highway, suite 1204, arlington, va 22202-4302, and to the office of management and budget, paperwork reduction project (0704-0188), washington, dc 20503

1. Agency use only (leave blank)

2. Report date 8 February 2000

3. Report type and dates covered

4. Title 2nd International Workshop on Adaptive Optics for Industry and Medicine.

5. Funding numbers
F61775-99-WF012

Author Conference Committee

7. Performing organization name(s) and address(es)

University of Durham
South Road
Durham DH1 3LE
United Kingdom

8. Performing organization report number

9. Sponsoring / monitoring agency name(s) and address(es)

EOARD
PSC802 Box 14
FPO 09499-0200

10. Sponsoring / monitoring agency report number
CSP-99-5012

11. Supplementary notes

12a. Distribution / availability statement Approved for public release; distribution is unlimited.

12b. Distribution code
A

13. Abstract ***(Maximum 200 words)*** The Final Proceedings for Int'l Workshop on Adaptive Optics, 12 July 1999 - 16 July 1999. This is an interdisciplinary conference. Topics include adaptive mirror technology, liquid crystal technology, wavefront sensing technology, static aberration correction, low-cost system integration, and applications.

14. Subject terms EOARD, Adaptive optics, active control, imaging telescopes, laser beam control, aberration control

Number of pages 398

16. Price code

17. Security classification of report unclassified

18. Security classification of this page unclassified

19. Security classification of abstract unclassified

20. Limitation of abstract
ul

CSP 99-5012
F61775-99-WF012

PROCEEDINGS OF

THE 2ND INTERNATIONAL

WORKSHOP ON

Adaptive Optics for Industry and Medicine

University of Durham, England
12 – 16 July 1999

EDITED BY

GORDON D. LOVE
University of Durham, England

World Scientific
Singapore • New Jersey • London • Hong Kong

AQF00-07-1713

Published by

World Scientific Publishing Co. Pte. Ltd.

P O Box 128, Farrer Road, Singapore 912805

USA office: Suite 1B, 1060 Main Street, River Edge, NJ 07661

UK office: 57 Shelton Street, Covent Garden, London WC2H 9HE

British Library Cataloguing-in-Publication Data
A catalogue record for this book is available from the British Library.

Proceedings of the 2nd International Workshop on
ADAPTIVE OPTICS FOR INDUSTRY AND MEDICINE

Copyright © 2000 by World Scientific Publishing Co. Pte. Ltd.

All rights reserved. This book, or parts thereof, may not be reproduced in any form or by any means, electronic or mechanical, including photocopying, recording or any information storage and retrieval system now known or to be invented, without written permission from the Publisher.

For photocopying of material in this volume, please pay a copying fee through the Copyright Clearance Center, Inc., 222 Rosewood Drive, Danvers, MA 01923, USA. In this case permission to photocopy is not required from the publisher.

ISBN 981-02-4115-1

Printed in Singapore by Regal Press (S) Pte. Ltd.

Sponsors

We wish to thank the following for their contribution to the success of this conference.

Adaptive Optics Associates, Inc.

European Office of Aerospace Research and Development, Air Force Office of Scientific Research, United States Air Force Research Laboratory

The Institute of Physics

The Optical Society of America

The University of Durham

DTIC QUALITY INSPECTED 1

20000406 120

Acknowledgements

The support of our sponsors (previous section) made this Workshop possible. Thanks to the International Programme Committee for their support and for chairing the sessions.

Pablo Artal	University of Murcia, Spain
Chris Dainty	Imperial College, UK
Janet Fender	USAF Research Labs, USA
Alan Greenaway	DERA Malvern, UK
Wenhan Jiang	Chinese Academy of Sciences, China
Alexei Kudryashov	Russian Academy of Sciences, Russia
Martin Levine	Adaptive Optics Associates, Inc. USA
Gordon Love	University of Durham, UK (Chair)
Fritz Merkle	Carl Zeiss, Germany
John O'Byrne	University of Sydney, Australia
Gerard Rousset	ONERA, France
Ken-Ichi Ueda	University of Electro-Communications, Japan
David Williams	University of Rochester, USA
H. John Wood	NASA Goddard, USA

Many people at the University of Durham helped arrange this workshop Thanks to the following people for their efforts. Sally Hewlett and the staff of Collingwood College hosted the event. Claire Davies, Angela Healer, and Kath Fall organised the finances. Judith Cooper and Rebecca Siddle dealt with the registrations. Pippa Love was the social secretary.

Finally thanks to Sunil Nair and the staff at World Scientific for their help in preparing these proceedings.

Local Organising Committee:
David Buscher, Judith Cooper, Thu-Lan Kelly,
Gordon Love (Chair), Richard Myers.

Introduction

This meeting was the Second International Workshop on Adaptive Optics for Industry and Medicine. The first was held in Shatura, Moscow Region, June 1997. The meeting provided an international forum on non-astronomical adaptive optics for scientists, engineers, and industrialists. The conference consisted of predominantly oral presentations, with a small number of posters.

The Workshop took place at Collingwood College, which is one of the 16 colleges of the University of Durham. The University is home to the UK's main centres for astronomical adaptive optics.

The programme of talks and posters was very varied, and brought together end users of adaptive optics who specialise in other disciplines, and adaptive optics system and component specialists. These proceedings contain 61 papers. There were 5 papers presented at the conference which do not appear here, and there are 3 papers here which were not presented at the conference due to various difficulties.

The papers are grouped together into 7 topics. These are...

- Extra-Cavity Adaptive Optics for Lasers
- Ophthalmic Adaptive Optics
- Microscopy
- Wavefront Correctors
- Intra-Cavity Adaptive Optics for Lasers
- Wavefront Sensors
- Adaptive Systems

The final number of people who attending the conference was over 100. This is virtually double the number of delegates who attended the 1st International Workshop on Adaptive Optics for Industry and Medicine, in 1997. It has been proposed that the 3rd International Workshop will take place in 2001 in New Mexico, USA. I look forward to another doubling of the numbers of delegates in two years time.

Gordon D. Love, Conference Chair

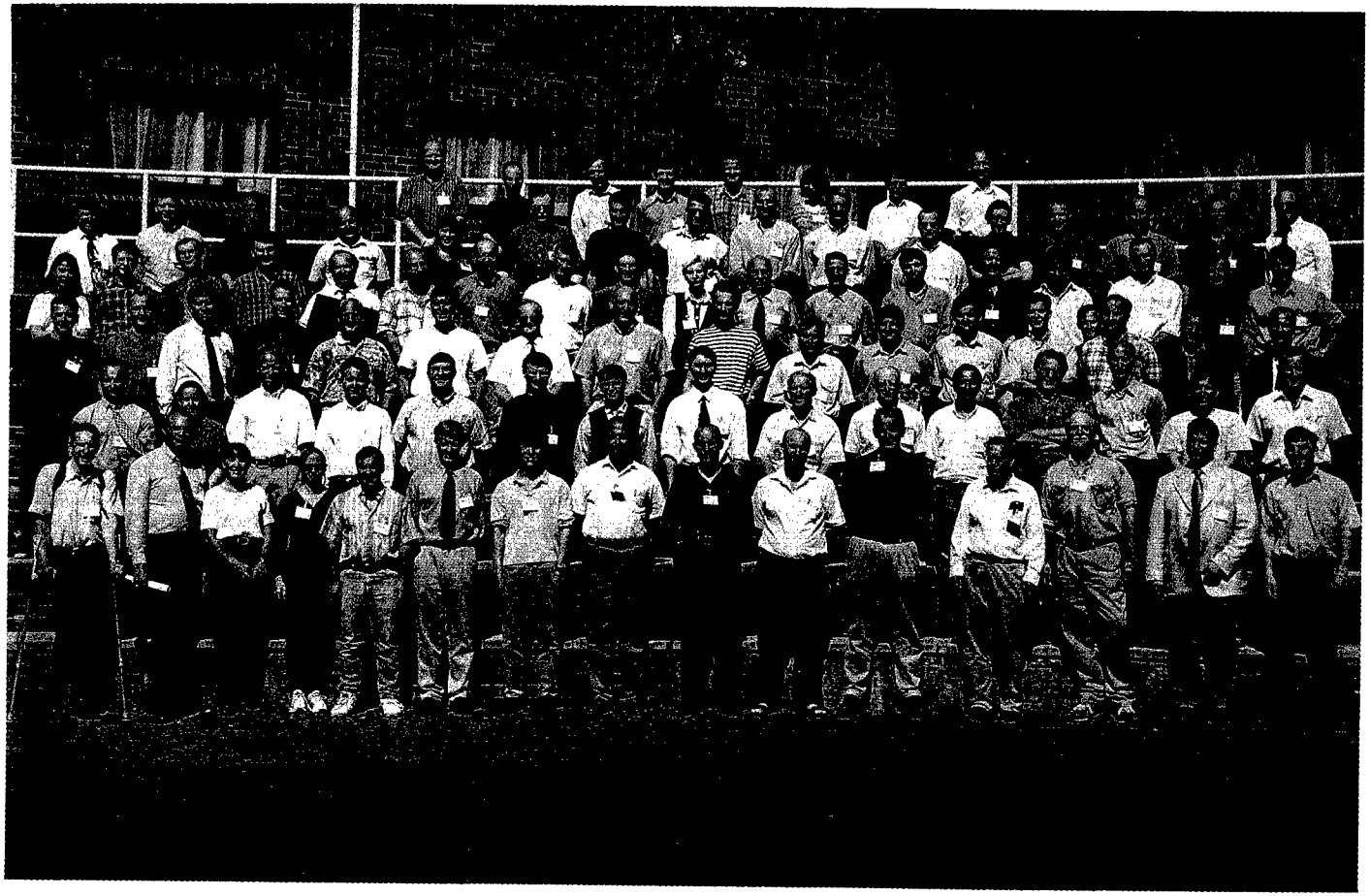

Contents

Sponsors v

Acknowledgments vi

Introduction vii

Extra-Cavity Adaptive Optics for Lasers 1

A Low-Cost Adaptive Optical System for Laser Wavefront Control 3
C.J. Hooker, E.J. Divall, W.J. Lester, K. Moutzouris,
C.J. Reason, I.N. Ross
Rutherford Appleton Laboratory, UK

A Wavefront Correction System for Inertial Confinement Fusion 8
W. Jiang, Y. Zhang, H. Xian, C. Guan, N. Ling
Institute of Optics & Electronics, China

High-Resolution Wavefront Control of High-Power Laser Systems 16
M.W. Kartz, S.S. Olivier, K. Avicola, J. Brase,
C. Carrano, D. Silva, D. Pennington, C. Brown
Lawrence Livermore National Laboratory, USA

Industrial Applications with Adaptive Optics 22
M. Negendanck, R. Schmidt, P. Hoffman
ERLAS GmbH, Germany
H.C. Manfred Geiger
University Erlangen-Nuremberg, Germany

Use of Deformable Mirrors in the 8-TW TiS-Laser ATLAS 28
H. Baumhacker, K.J. Witte, H. Stehbeck
Max-Planck-Institut für Quantenoptik, Germany
A. Kudryashov, V. Samarkin
Institute on Lasers and Information Technologies, Russia

Adaptive Optics for CO_2 Laser Material Processing 32
R. Schmiedl
Diehl Stiftung & Co., Germany

Ophthalmic Adaptive Optics **37**

Hartmann-Shack Wavefront Sensor in the Eye: Accuracy and Performance Limits 39
P. Artal, J.L. Aragon, P.M. Prieto, F. Vargas-Martin, E. Berrio
Universidad de Murcia, Spain

Single vs. Symmetric and Asymmetric Double-Pass Measurement of the Wavefront Aberration of the Human Eye 45
L. Diaz Santano Haro and J.C. Dainty
Imperial College of Science, Technology & Medicine, UK

3-D Cataract Imaging System 51
L.J. Otten, P. Soliz, I. McMakin,
Kestrel Corporation, USA
A.H. Greenaway, P.M. Blanchard
DERA, UK
G. Ogawa
New Mexico Eye Associates, USA

Vision Through a Liquid-Crystal Spatial Light-Modulator 57
L.N. Thibos, X. Qi, D.T. Miller
Indiana University, USA

Requirements for Segmented, Spatial Light Modulators for Diffraction-Limited Imaging Through Aberrated Eyes 63
D.T. Miller, X. Hong, L.N. Thibos
Indiana University, USA

Measurement of the Eye's Aberrations *in vivo* 69
M. Glanc, H. Gardette, K. Naoun, B. Bianchi, J.F. Gargasson,
Laboratorie de Biophysique de la Bision, France
E. Gendron, P. Lena
Obervatoire de Paris, France

Microscopy 77

Adaptive Aberration Correction in Ultrafast Scanning Multiphoton Confocal Microscopy 79
O. Albert, L. Sherman, M.H. Meunier, G. Mourou, T. Norris,
University of Michegan, USA
G. Vdovin
Technical University of Delft, Netherlands

Adaptive Optics in Confocal Microscopy 85
J.W. O'Byrne, P.W. Fekete, M.R. Arnison, M. Serrano,
H. Zhao, D. Philp, W. Sudiarta, C.J. Cogswell
University of Sydney, Australia

Wavefront Correctors 91

Performance Assessment and Applications of MEMS Adaptive Optics 93
R.K. Tyson
University of North Carolina, USA

The Active Micro Mirror: A New Adaptive Optical Micro-Component 99
G. Robert, L. Babadjian, S. Spirkovitch
ESIEE, France,
A. Coville
SFIM, France

Innovative Deformable Mirror Designs for Custom Applications 105
D.G. Bruns, D.G. Sandler
Trex Enterprises, USA

Modelling the Deformation of Adaptive Aspheric Optical Surfaces in the Bend and Polish Method of Manufacture 111
R.S. Chen, J. Maxwell
Imperial College of Science,
Technology & Medicine, UK

Current Performance Limits of Micromachined Membrane Deformable Mirrors 118
G. Vdovin
Technical University of Delft, The Netherlands

Modal Liquid Crystal Wavefront Correctors 123
G.D. Love, A.F. Naumov
University of Durham, UK
M. Yu. Loktev
P.N. Lebedev Institute, Russia
Igor Grualnik
Samara State University, Russia
Gleb Vdovin
Technical University of Delft, Netherlands

Characteristic of a Novel Small PZT Deformable Mirror 129
N. Ling, X. Rao, L. Wang, S. Jiao
Institute of Optics and Electronics, China

Large Adaptive Metal Mirrors 136
J.H. Lee, A.P. Doel, D.D. Walker
University College London, UK

Adaptive Optics for Testing Aspheric Surfaces 141
M. Daffner, St. Reichelt, H. Tiziani
Institut für Technische Optik, Universität Stuttgart

Intra-Cavity Adaptive Optics for Lasers 147

High-Power Solid-State Laser with Birefringence Compensation and Adaptive Resonator Mirror 149
N. Kugler, A. Vazquez
Laser-und Medizin-Technologie GmbH, Germany
H. Laabs, H. Weber
Optisches Institut der TU-Berlin, Germany

Simulation of Optical Resonators with Aberrations 155
I. Buske, U. Wittrock
FH-Muenster, Germany

Development of Adaptive Resonator Techniques for High-Power Lasers 163
L. Flath, J. An, J. Brase, C. Carrano, C.B. Dane, S. Fochs, R. Hurd, M. Kartz, R. Sawvel
Lawrence Livermore National Laboratory, USA

Some Methods of Intracavity Control of Spatial and Temporal Parameters of Industrial CO_2 Laser Beam 169
V.V. Samarkin
Institute on Laser and Information Technologies, Russia

Reduction of the Thermal Lens in Solid-State Lasers with Compensating Optical Materials 175
T. Graf, R. Weber, M. Schmid, H.P. Weber
University of Berne, Switzerland

Enhanced Correction of Thermo-Optical Aberrations in Laser Oscillators 181
I. Moshe, S. Jackel
Soreq NRC, Israel

Active Correctors as the Alternative to Graded Phase Mirrors — CO_2 and YAG Laser Beam Formation 187
T.Y. Cherezova, S.S. Chesnokov, L.N. Kaptsov
Moscow State University, Russia
A.V. Kudryashov, V.V. Samarkin
Institute on Laser Information Technologies, Russia

Bimorph Mirrors for Correction and Formation of Laser Beams 193
A.V. Kudryashov, V.V. Samarkin
Institute on Laser Information Technologies, Russia

Wavefront Sensors **201**

Apodized Micro-Lenses for Hartmann Wavefront Sensing 203
J.D Mansell, R.L. Byer
Stanford University, USA
D.R. Neal
Wavefront Sciences Inc. USA

Linear Wavefront Sensor: A New Method for Wavefront Sensing 209
X. Levecq, S. Bucourt
Imagine Optic, France

Integration of a Hartmann-Shack Wavefront Sensor 215
D.W. de Lima Monteiro, G. Vdovin, P.M. Sarro
Technical University of Delft, Netherlands

Flexible Configuration of Wavefront Sensor and Reconstructors for Adaptive Optics Systems 221
B.M. Levine, A. Wirth, C. Standley
Adaptive Optics Associates, USA

Sub-Lens Spatial Resolution Shack-Hartmann Wavefront Sensing 227
J.D. Mansell, R.L. Byer
Stanford University, USA

Application of Shack-Hartmann Wavefront Sensors to Optical System Calibration and Alignment 234
D.R. Neal
Wavefront Sciences Inc. USA
J.D. Mansell
Stanford University, USA

Analysis of Wavefront Sensing Using a Common Path Interferometer Architecture 241
J. Glückstad, P.C. Mogensen
Risø National Laboratory, Denmark

An All Optical Wavefront Sensor for UV Lasers Applications 247
S.R. Restaino
USAF Research Laboratory USA
A.C. Bernestein
University of New Mexico, USA

Wavefront Sensing and Intensity Transport 254
E.N. Ribak, S. Vinikman
Technion-Israel Institute of Technology, Israel

Laser Wavefront Sensing Using the Intensity Transport Equation 260
S. Woods, P.M. Blanchard, A.H. Greenaway
DERA, UK

Correction of Non-Common Path Errors in an Adaptive Optics System 266
N.P. Doble, D.F. Buscher, G.D. Love, R. Myers
University of Durham UK

Field of View Widening in Non-Astronomical Adaptive Systems 272
A.V. Larichev, N.A. Iaitskova, V.I. Shmalhausen
Moscow State University, Russia

Adaptive Compensation for Time-Dependent Thermal Blooming with Local Extrema in the Space of Control Coordinates 278
F. Yu. Kanev, L.N. Lavrinova V.P. Lukin
Institute of Atmospheric Optics, Russia

Influence of Local Extrema on the Efficiency of Gradient Algorithms for Laser Beam Control 284
F. Yu. Kanev, V.P. Lukin, L.N. Lavrinova
Institute of Atmospheric Optics, Russia

Radial Shear White Light Phase Stepping Interferometry for Wavefront Sensing in Adaptive Optics 290
A.R.D. Somervell, G.T. Bold, T.H. Barnes
University of Auckland, New Zealand

Multi-Plane Imaging with a Distorted Diffraction Grating 296
P.M. Blanchard, A.H. Greenaway
DERA, UK

Adaptive Systems **303**

A Low Cost Adaptive Optical System 305
C. Paterson, I. Munro, J.C. Dainty
Imperial College of Science, Technology & Medicine, UK

Analogue Correction for Distortions using Dynamic Holograms in Optically Addressed Liquid Crystal Modulators 311
V.A. Berenberg, A.A. Leshchev, M.V. Vasil'ev, V. Yu Venediktov
Research Institute for Laser Physics, Russia

Two-Wavelength Dynamic Holography and its Application in Adaptive Optics 317
V. Yu Venediktov, V.A. Berenberg, A.A. Leshchev, M.V. Vasil'ev
Research Institute for Laser Physics, Russia
M. Gruneisen
Air Force Research Laboratory, USA

Review of Wavefront Modulators and Sensors for Adaptive Optics 323
N. Collings
University of Cambridge, UK

Liquid Crystal Active Optics Correction Using Evolutionary Algorithms 328
P. Birch, C. Chatwin, R. Young, M. Farsari
University of Sussex, UK

The ELECTRA Astronomical Adaptive Optics Instrument 334
R.M. Myers, J. Allington-Smith, D. Buscher, P. Clark, N. Dipper, S. Juhos, C. Dunlop, R. Haynes, G.D. Love, G. Murray, R. Sharples, A. Zadronzny
University of Durham, UK

Blind Optimization of Optical Power into a Single Mode Optical Fiber Using a MEMS Deformable Membrane Mirror 340
M.L. Plett, D.W. Rush, P.R. Barbier, P. Polak-Dingels
Laboratory for Physical Sciences, USA

High Power Laser Diode to Fibre Coupling Using a Membrane Mirror 346
F. Gonté, A. Courteville, E. Rochat, K. Haroud, N. Collings, R. Dändliker
Institute of Microtechnology, Switzerland
G. Vdovin, S. Sakarya
Technical University of Delft, Netherlands

Improvement of a Laser Communication Beam Using Adaptive Optics 352
P.R. Barbier, D.W. Rush, P. Polak-Dingels, M.L. Plett
Laboratory for Physical Sciences, USA

Preliminary Results of Horizontal Path Length Propagation Experiments 358
G.R.G. Erry, P. Harrison, P.M. Blanchard, A.H. Greenaway
DERA, UK

Low-Order Adaptive Optics System for Free-Space Lasercom: Design and Performance Analysis 364
K.H. Kudielka, Y. Hayano, W. Klaus, K. Araki,
Communication Rescarch Laboratory, Japan
Y. Arimoto, J. Uchida
National Space Development Agency, Japan

A High Precision System for Wavefront Control 370
P. Jagourel, J.C. Sinquin, D. Waflard
CILAS, France
X. Levecq, G. Dovillaire
Imagine Optic, France

Development of a Curvature Adaptive Optics System for a Michelson Stellar Interferometer 378
C. Verinaud, A. Blazit, A. De Bonnevie
Observatoire de la Côte d'Azur, France

Blazed Holographic Optical Aberration Compensation 384
I. Percheron, J.T. Baker
Boeing North American Inc. USA
M. Gruneisen, T.Y. Martinez, D. Wick
USAF Research Labs, AFRL/DEBS, USA

Adaptive Optics in Laser Scanner Systems 389
E. Ellis, J.C. Dainty
Imperial College of Science, Technology & Medicine, UK

List of Delegates 395

Extra-Cavity Adaptive Optics for Lasers

A LOW-COST ADAPTIVE OPTICAL SYSTEM FOR LASER WAVEFRONT CONTROL

C J HOOKER, E J DIVALL, W J LESTER, K MOUTZOURIS, C J REASON, I N ROSS

Central Laser Facility, Rutherford Appleton Laboratory, Chilton, Didcot, Oxon OX11 0QX, U.K.

We have developed a closed-loop adaptive optics system based largely on off-the-shelf components. A bimorph-type mirror using low-voltage PZT material is controlled from a 200MHz Pentium PC, using locally written software. The Shack-Hartmann wavefront sensor uses an array of computer-generated zone plates rather than a lenslet array, to allow flexibility in the layout of the sensing apertures. The system currently operates at a frequency of 11 Hz in closed-loop mode, achieving full correction in two cycles. Strehl ratios as high as 0.8 have been measured for the output beam.

Introduction

The Central Laser Facility operates several high-power lasers as research facilities for university user groups. There is a continual programme of enhancement of these facilities in order to extend the range of science that can be carried out. One of the areas with potential for improvement is the beam quality, since a reduction in focal spot diameter by a factor of 1.4 is at present easier and cheaper than doubling the laser output energy to produce the same increase in intensity. Adaptive optics offers a means of achieving such improvements, so in the last few years we have developed a prototype adaptive mirror and control system, with a view to understanding how to build affordable systems that can be incorporated into our large lasers.

The Prototype Adaptive Mirror

The mirror is of conventional bimorph construction, with a 0.2 mm sheet of PZT (Morgan Matroc type PC5) glued to the back of the substrate. The substrate is 100 mm in diameter and 1.5 mm thick, and made of Pyrex to obtain the best possible match of its thermal expansion coefficient to that of PZT. The epoxy glue layer incorporates a 0.1 mm thick copper mesh to serve as a common ground plane for all the control electrodes. To overcome the problem of glue shrinkage noted with an earlier mirror, the PZT was bonded to the substrate before final polishing so that any curvature induced by glue shrinkage could be polished out, and the mirror would be flat when no voltages were applied. Polishing proved a rather tricky operation, which was performed with the PZT shorted out, so that static charges could not build up and distort the mirror. A peak-to-valley error of $\lambda/4$ was the best that could be achieved.

The PZT plate is 70 mm square, and the electrodes were printed onto the back using conducting ink. For the prototype mirror it was decided to use 60 electrodes in a square grid pattern, in fact an 8 x 8 square array with the 4 corner squares missing. Each electrode is a little less than 1 cm square. Fine wires are attached to the ink electrodes using silver-loaded conducting paint. The mirror was mounted in its holder using three foam rubber pads at the edges, and the mirror holder is mounted in a standard optical mount, which provides the only tip-tilt control. The control software specifically removes errors in pointing before calculating the required correction, so independent tip-tilt adjustment is not needed.

64-Channel Voltage Driver

The maximum drive voltage was the main choice that had to be made when considering the driver. It is useful to avoid high voltages for safety reasons, as well as to reduce the problems of tracking, dust accumulation etc. Another good reason for using low voltage is that the cost of a large number of driver channels varies quite strongly with voltage, as more space, thicker insulation and specialised components need to be provided. By using very thin (200μm) PZT plates, we were able to reduce the maximum drive voltage to – 64 volts and still obtain sufficient deflection for our purposes.

The driver is addressed from the computer digital I/O bus. Each channel has a 10°bit D/A converter which is followed by a push-pull transistor amplifier giving –°64°volts output with a 10°mA peak current. The set voltage on the 2°nF control electrodes is achieved in about 100°μs, which is well within the mechanical response time of the mirror. The component cost (including power supplies and rack) amounts to about £30 per channel.

Shack-Hartmann Wavefront Sensor

In our experimental set-up, the beam reflected from the adaptive mirror is monitored using the reflection from the front surface of a wedged plate. The sensor is a Shack-Hartmann type, in which an array of computer-generated Fresnel zone plates is used instead of the conventional lenslet array. The zone plate array was made using techniques developed for the fabrication of random phase plates for focal spot shaping on the Vulcan laser at the Central Laser Facility. Computer-generated masks are used to expose photoresist-coated plates which are placed in the beam to control the size and shape of the focal spot. For our application the amplitude masks themselves are adequate, since in combination with a normal lens they form good-quality foci. The zone plates in the present sensor have a principal focal length of 7 metres, and their centres lie on a 5 mm square grid; in consequence, each individual plate has only two complete zones: a clear central zone and an opaque second zone. The main lens has a focal length of about 1 metre. The pattern of foci formed by the combination fits within the CCD chip, and consists of spots with

FWHM diameters of 8-10 pixels, which is a good size for accurate centroiding. The spots are well-separated, and there are only very weak interference peaks between adjacent spots, so identification of the spots is easy and the background level is low. The accuracy of centroiding was checked by measuring the position of a spot before and after making a small, calibrated, displacement. A glass plate in the beam just in front of the camera was tilted through a measured angle, moving the spots by a calculated distance on the CCD. Displacements as small as 1/50 of a pixel could be made by this technique, and the accuracy of determining the centroid of a spot was found to be typically ~1/10 of a pixel. A check was also made on the mirror relaxation routine, which is designed to restore the mirror to a standard condition after it has been deformed in any way. An oscillating voltage with an exponentially-decaying envelope is applied simultaneously to all actuators, so the mirror is taken repeatedly around its hysteresis cycle at ever-decreasing amplitude, the entire process taking a few seconds. After deformation and subsequent relaxation, the Hartmann spots return reproducibly to within 1/10 pixel of their original positions, i.e. within the limits of measurement accuracy.

Control Program

The software to control the mirror was written in-house using the Delphi package. This provides a ready-made user interface, allowing us to concentrate on the control functions. The interface gives the operator control of all the functions of the mirror: there are commands to allow the generation of a new response matrix, to create, save or restore a reference Hartmann image, to apply voltages to all the actuators either individually or in selected groups, to relax the mirror, to switch into or out of closed-loop operation and to perform single passes of the correction cycle. Several diagnostic routines are included to display the slopes at different points on the mirror, the voltage levels applied to all the actuators and the closed-loop cycle frequency. Options to save the voltages, slopes and other quantities to files for later examination can be switched on if desired.

Closed-loop Operation of the Adaptive Mirror

Our first attempts to operate the mirror in a closed loop made use of curvature measurements, but these were unsuccessful mainly because the curvature produced by each actuator is highly localised. This makes measurement of the effect of actuators lying outside the beam area very difficult, and hence the entries for those actuators in the response matrix are dominated by noise. The pseudo-inverse matrix calculated from the curvature data did provide some control of the mirror in the central regions where the curvatures can be measured, but the edges became severely distorted. We therefore decided to switch from curvature to slope as the measured quantity, since the slope produced by an actuator extends several centimetres from the actuator itself. As a result, every actuator contributed real data to the response matrix, and the resulting control matrix was able to provide reasonably good

closed-loop control of the mirror for the first time. A further refinement added recently is to average the centroid positions measured from ten image to obtain better-quality slope data. This change produced much cleaner data for the response matrix, and has reduced the number of cycles required to reach the full correction.

In its most basic form, the control matrix is calculated by applying the PseudoInverse function in *Mathematica* to the measured response matrix, but the result is not satisfactory. A more sophisticated approach involves decomposing the response matrix into the product of three square matrices, one of which is diagonal and contains the singular values (SVs) of the original matrix. After inverting these matrices individually, they are multiplied together in reverse order to generate the control matrix. The singular values reflect the sensitivity of the mirror to different possible modes: those at the top left correspond to the lowest, and those at the bottom right to the highest spatial frequencies. By modifying the singular values before the final multiplication is carried out, it is possible to suppress any tendency the mirror may have to try and generate large amplitudes at high spatial frequency. With no modification, the mirror rapidly becomes severely deformed, with adjacent elements driven to the maximum voltages of opposite sign; the control program then halts because many of the Hartmann spots have moved too far from their original positions to be located correctly. The simplest approach to modifying the SVs is to set some number of them to zero, beginning on the lower right of the diagonal so as to suppress the highest frequencies first: the modifying function is then a simple step. Using the peak intensity in the far-field spot as a diagnostic, we found that the control matrices generated with between twenty and forty non-zero SVs all gave fairly good results, whereas those with either fewer or more failed to reach maximum intensity in the focal spot. A $1/10^{th}$-wave flat mirror was substituted for the adaptive mirror to record an ideal far-field spot using the same imaging system; the ratio of peak intensities in this spot and in the corrected spot from the adaptive mirror is a good approximation to the Strehl ratio. The same mirror is used to generate a reference wave front which is the target of the closed-loop control algorithm. The FWHM of the focal spot was also measured in each instance, but the variations were too small for it to be a useful diagnostic of the degree of correction. We found that the most basic level of correction would produce a reasonably good focal spot; subsequent refinements merely caused a redistribution of intensity within the focal pattern without greatly affecting the overall structure.

A variety of other modifying functions has been applied to the SVs, to investigate the effects of a gradual smooth or stepwise reduction in their values over some range. Modifying functions that have been tried include linear scaling from 1 to 0 between selected values and smoother gradations using a $\cos^2$ function. In each case the modifying function is calculated in *Mathematica* as a table of 60 values between 1 and 0, and the Nth SV is then multiplied by the Nth entry in the modifying table. The results from this investigation are not very conclusive: the peak intensity achieved appears relatively insensitive to the details of the modifying function

provided the first 10 SVs are included and the last 10 are reduced to some extent. Only minor differences were observed between linear and $\cos^2$ scalings.

Enhancement of the Closed-Loop Response

When closed-loop operation of the mirror was first achieved, the cycle time was close to 700 milliseconds. The most time-consuming steps were found to be the centroiding of the Hartmann spots, which took 500 ms, grabbing the frame from the camera (160 to 200 ms) and the voltage output to the driver box (90 ms). The first effort at reducing the cycle time was aimed at speeding up the centroiding, a part of the code not originally written with efficiency as a priority. Some very simple changes reduced the centroiding time to 90 ms, of which half involved the finding of the brightest grouping of pixels in each cell of the Hartmann pattern. Once the initial correction has been applied to the mirror, the spots should move very little, so the previous positions of the centroids can be used as a starting point for the next cycle, instead of locating all the spots afresh. Some further modifications reduced the cycle time to 130 ms, of which the calculation of the centroids now accounts for 6.5 ms: the image analysis and voltage calculation sequence takes 24 ms in total. With the screen display of the Hartmann pattern turned off, the cycle time is reduced to 93 ms, corresponding to a frequency of 10.7 Hz. The cycle time is now dominated by the hardware, in particular the voltage output stage, so attention has been switched to ways of reducing that part of the cycle. At a frequency of 11 Hz, however, the mirror can already correct for slowly-varying components of atmospheric turbulence.

Future Developments

We are constructing a 150 mm diameter mirror, incorporating a few developments in technology. The electrodes will be formed in nickel, plated onto the PZT, rather than printed; this should solve the problem of electrodes becoming detached under slight stress. New layouts of the electrodes and of the Hartmann array will match the response of the mirror to the residual aberrations known to be present on the laser beam. Some slight modifications to the electronics are planned, which will reduce the cycle time and may allow us to reach 25 Hz.

A WAVEFRONT CORRECTION SYSTEM FOR INERTIAL CONFINEMENT FUSION

WENHAN JIANG, YUDONG ZHANG, HAO XIAN, CHUNLIN GUAN, NING LING
Institute of Optics and Electronics, Chinese Academy of Sciences
P. O. Box 350, Shuangliu, Chengdu, 610209, China, Phone: +86-28-5196256
Fax: +86-28-5180070, E-mail: whjiang@mail.sc.cninfo.net

The basic arrangement and simulation results of a wavefront correction system for correcting static and dynamic wavefront errors in a new inertial confinement fusion system are reported.

1 Introduction

In inertial confinement fusion (ICF) system, a high power laser pulse is generated, amplified, frequency converted and focused on a target to initiate nuclear fusion reaction. In these systems two kinds of adaptive optics are demanded. (1) The wavefront correction system. In the processes of generating and amplifying, wavefront errors are induced. The sources of wavefront errors are static error due to figuring errors of optical components and inhomogeneity of optical material and dynamic error due to thermal distortion induced by pump light and high power laser, and turbulence in the optical path. This wavefront error at the front of frequency converter results in angle mismatch of frequency converting (FC). An adaptive optical system is needed to correct the wavefront of laser beam before entering the frequency converter. (2) Focus spot re-shaping system. The different shapes of focus spot are demanded in the physical experiments, such as the different size of round or square spots with uniform intensity distribution and very low intensity outside the spot or focus line with uniform width and intensity. An active mirror at the front of focus lens can be used for adjusting the shape of focus spots.

A new laser fusion system is planning to be built in China. Both wavefront correction system and beam shaping system are being considered for this new facility. In the Shatura Meeting held in June 1997 in Moscow we reported some preliminary researches on beam shaping[1]. In this paper we will present some considerations of the wavefront correction system.

2 Wavefront correction system

In 1985 we built an adaptive optical system[2] for the "Shenguang I" laser fusion system in the Shanghai Institute of Optics and Fine Mechanics, China. In this system a 19 elements deformable mirror and serial dithering control electronics are used for correcting the static wavefront error. Several years ago, some adaptive

optics systems were built in the Beamlet system[3, 4] and National Ignition Facility (NIF) laser system at the Lawrence Livermore National Laboratory, USA. Like the system for the Beamlet, the purpose of our new system is to correct the static and dynamic wavefront error in the laser generating and amplifying process. A deformable mirror, two Hartmann-Shack wavefront sensors and a parallel control electronics are used in this new system.

Figure 1 is the schema of the adaptive optical system. The pulsed Nd: glass laser is generated and preamplified in the front-end laser system, then amplified by the multi-pass slab main amplifier. The deformable mirror and the Hartmann-Shack (H-S) sensor 1 are located at the output end of the front-end system. Between the end of main amplifier and frequency converting device, the H-S sensor 2 is used to measure the wavefront of the laser beam output from the main amplifier. The static wavefront of the front-end laser system can be corrected by closing the loop of deformable mirror and H-S sensor 1 with a CW alignment laser. The dynamic wavefront of preamplifier and main amplifier cannot be corrected in the laser pulse duration but can be recorded by H-S sensor 2. After analyzing the wavefront record, the pre-correction is set in the H-S sensor 1 as a changed amount of calibrated original coordinate of Hartmann spots. By closing the loop between deformable mirror and H-S sensor 1 the dynamic wavefront can be compensated by the pre-correction of the deformable mirror and a flat wavefront of output laser beam can be obtained. The beam apertures (FWHM) of the front-end system and main amplifier are 70×70 mm and 220×220 mm^2 respectively.

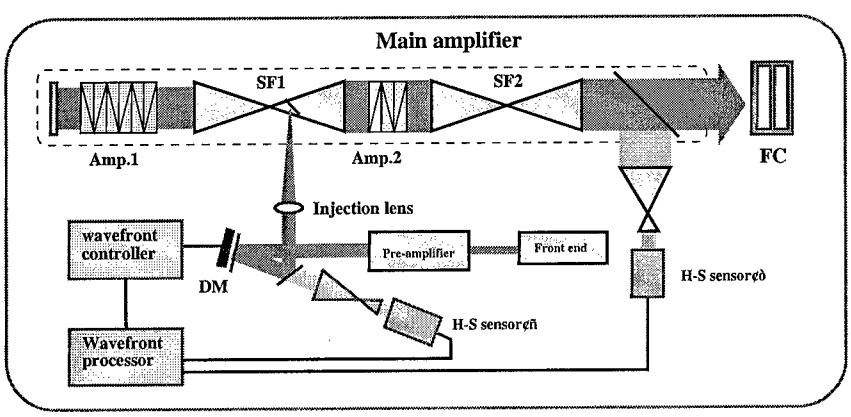

Figure 1. Schematic diagram of the wave-front correction system

3 Arrangement of actuators and subapertures

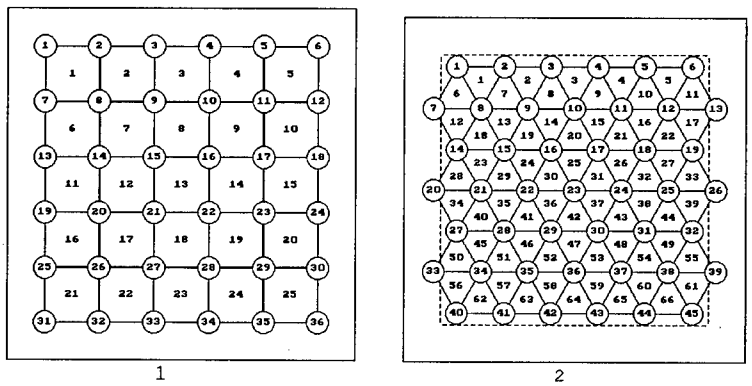

Figure 2. Two examples of arrangement of the actuators of deformable mirror and sub-aperture of H-S sensor.

The arrangement of actuators of deformable mirror and subapertures of H-S sensor operated in this square aperture beam is studied. Several kinds of arrangements are compared, as examples, two of them are shown in Fig. 2. The direct slope algorithm of wavefront reconstruction[7] is used and the criteria for comparing are: (1) conditional number of reconstruction matrix, which is the measure of stability of close loop correction, and (2) trace of matrix divided by the number of actuator N, $Tr\left[D^{+}\left(D^{+}\right)^{T}\right]\Big/N$, which is the measure of noise propagation. Where D^{+} is the reconstruction matrix. The conditional numbers of these two arrangement are 4.727 and 3.860, and the traces are 0.1073 and 0.0229 respectively. Different Zernike wavefront modes of 1λ RMS are corrected by these arrangements. Fig. 3 shows the residual RMS error after correction. A random wavefront consist of 65 Zernike modes (Fig. 4b) is corrected by these arrangements. The amplitudes of each modes are shown in Fig. 4a. The original wave-front is shown in Fig.4b. The residual errors after corrected by two arrangements are shown in Fig. 4c,d respectively. These results show us that arrangement 2 is better choice.

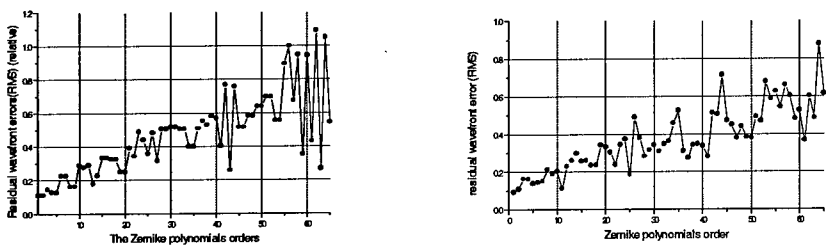

(a) (b)

Figure 3. The residual errors(RMS) of the first 65 Zernike modes with amplitude 1λ rms.

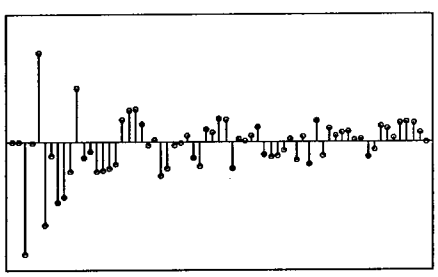

(a)The weight of the first 65 Zernike modes

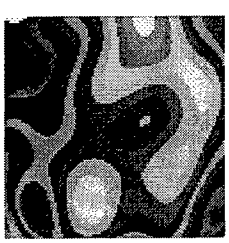

RMS:1.360

(b)The original wave-front

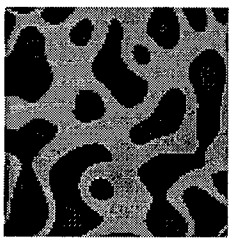

RMS:0.414

(c)After corrected by the arrangement 1;

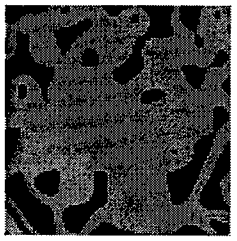

RMS:0.298

(d)After corrected by the arrangement2;

Figure 4. A wavefront compounded of 65 Zernike modes and residual error after correction.

Our previous research results showed that the triangle arrangement of actuators possesses better wave-front correction ability compared with other arrangements[8]. For a given actuators arrangement, such as the arrangement 2, we simulated the correction ability of different kinds of arrangements of the H-S sensor sub-apertures. As shown in figure 5, (a) is the triangle arrangement of actuators with hexagon arrangement of the H-S sensor and (b) is the triangle arrangement of actuators with rectangle arrangement of the H-S sensor.

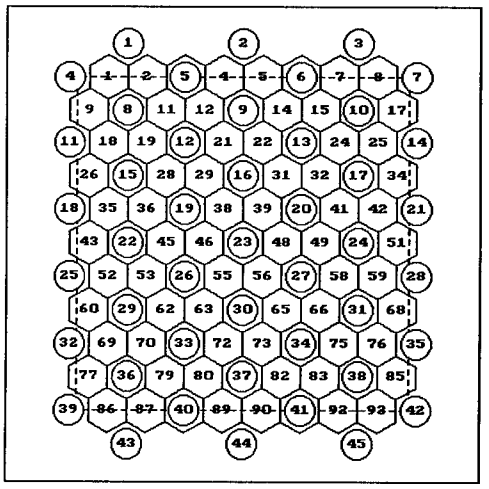

(a) the hexagon arrangement of sub-apertures

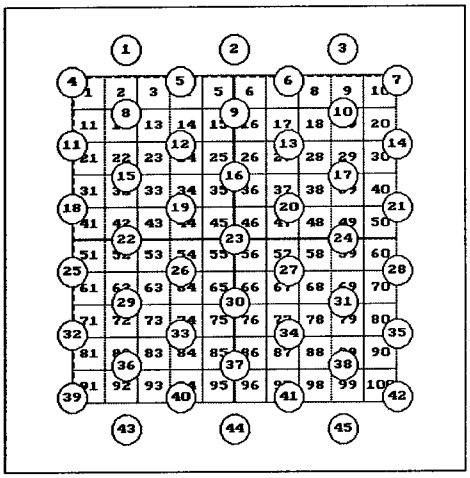

(b) the rectangle arrangement of sub-apertures

Figure 5, the triangle arrangement of actuators with different kinds of sub-apertures arrangements of the H-S sensor.

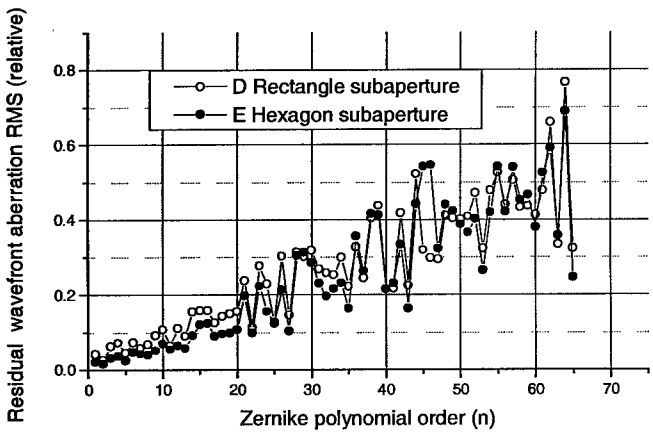

Fig.6(a), the correction residual wave-front error RMS of the Zernike polynomials.

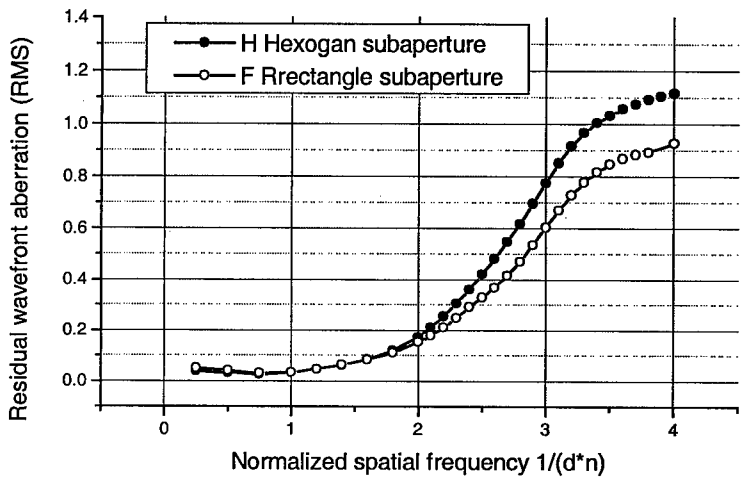

Fig.6(b) the correction residual wave-front error RMS of the different spatial frequency error.

Figure 6(a) and (b) show the correction residual wave-front error (RMS) of these arrangements of H-S sensor sub-apertures. Compared figure 3(b) and figure 6(a), both the hexagon and rectangle arrangements of H-S sensor sub-apertures have the better correction ability than that of triangle arrangement. We can not find apparent differences between the hexagon and rectangle arrangements in figure 6(a) but in figure 6(b). The condition number of hexogan arrangement is 3.84. Its trace is 0.021. The condition number of rectangle arrangement is 3.11 and its trace is 0.019 So the arrangement of actuators and sub-apertures shown in figure 5(b) is the best choice.

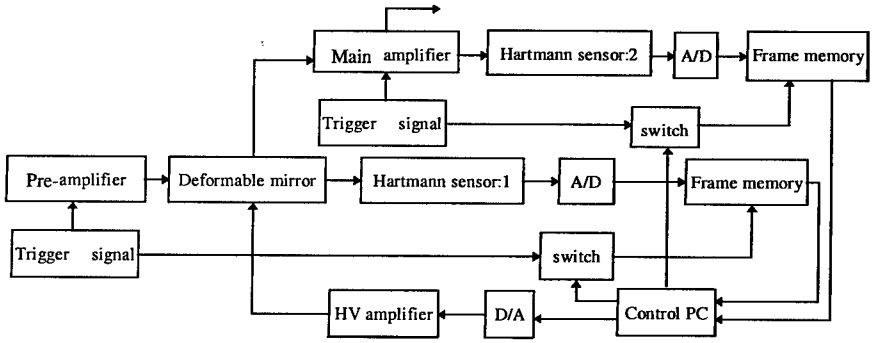

Figure 7. The Schema of control electronics.

The schema of control electronics is shown in Fig. 7. Both of the H-S sensors have a lenslet array made by binary optics technology and a progressive scanning CCD camera. The cameras are exposured by the laser pulse. The Hartmann spots are acquired and analyzed by a computer, the output is used to control the deformable mirror through high voltage amplifiers.

Other important issues such as light intensity adjustment for the CCD camera, aperture matching optics and calibration of H-S sensors are considered. This system is being constructed.

4 Acknowledgement

This work was supported by the Chinese National High-Technology R&D Project.

References

1. Zhige Zeng, et. al., Laser beam shaping by deformable mirror, International Workshop on Adaptive Optics for Industry and Medicine, June 9-13, 1997, Shatura, Moscow, Russia.
2. Wenhan Jiang, et. al., Hill-climbing wavefront correcting system for large laser engineering, SPIE Proc. vol. 965, pp. 266-272, 1988.
3. J. T. Salmon, et.al., An adaptive optics system for solid-state laser system used in inertial confinement fusion, UCRL-JC-122033, 1995.
4. B.M. Van Wonterghem, J. T. Salmon, R.W. Wilcox, "Beamlet Pulse-Generation and Wavefront-Control System", UCRL-LR-105821-95-1.
5. R. Sacks, et. al., "Application of Adaptive Optics for Controllong the NIF Laser Performance and Spot Size", UCRL-JC-130028, Aug. 17, 1998.
6. E. Bliss, "National Ignition Facility Subsystem Design Requirements Beam Control & Laser Diagnostics" UCRL-ID-126988, Rev. B, Nov. 1, 1996
7. Wenhan Jiang, et. al., Hartmann-Shack wavefront sensing and wavefront control algorithm, SPIE Proc. vol. 1230, pp. 608-611, 1991.
8. Hu Zhaohui, Jiang Wenhan, "Optimum matching of wavefront sensor and wavefront corrector," SPIE Proc. 2534, pp.318-326, 1995.

HIGH RESOLUTION WAVEFRONT CONTROL OF HIGH-POWER LASER SYSTEMS

MICHAEL W. KARTZ, SCOT S. OLIVIER, KEN AVICOLA, JAMES BRASE, CARMEN CARRANO, DENNIS SILVA, DEANNA PENNINGTON, AND CURTIS BROWN

Lawrence Livermore National Laboratory, 7000 East Ave. Livermore, Ca. 94550
email: kartz1@llnl.gov

Most large laser systems at Lawrence Livermore National Laboratory require adaptive optics to correct for internal aberrations in these high-power systems. Many of these systems, including those being developed for Inertial Confinement Fusion and Laser Isotope Separation, already contain adaptive optics based on conventional deformable mirror technology. Increasing requirements for laser system applications are currently driving wavefront control technology toward increased spatial frequency capacity, as well as reduced system costs. We will present recent progress in the utilization of liquid crystal spatial light modulator technology appropriate for high-resolution wavefront control of high-power laser systems.

1 Introduction

Nearly every new large-scale laser system application at LLNL has requirements for beam control which exceed the current level of available technology. For applications such as inertial confinement fusion, laser isotope separation, laser machining, and laser the ability to transport significant power to a target while maintaining good beam quality is critical.

There are many ways that laser wavefront quality can be degraded. Thermal effects due to the interaction of high-power laser or pump light with the internal optical components or with the ambient gas are common causes of wavefront degradation. For many years, adaptive optics based on thing deformable glass mirrors with piezoelectric or electrostrictive actuators have been used to remove the low-order wavefront errors from high-power laser systems. These adaptive optics systems have successfully improved laser beam quality, but have also generally revealed additional high-spatial-frequency errors, both because the low-order errors have been reduced and because deformable mirrors have often introduced some high-spatial-frequency components due to manufacturing errors. Many current and emerging laser applications fall into the high-resolution category where there is an increased need for the correction of high spatial frequency aberrations which requires correctors with thousands of degrees of freedom.

The largest Deformable Mirrors currently available have less than one thousand degrees of freedom at a cost of approximately $1M. A deformable mirror capable of meeting these high spatial resolution requirements would be cost prohibitive. Therefore a new approach using a different wavefront control technology is needed. One new wavefront control approach is the use of liquid-crystal (LC) spatial light modulator (SLM) technology for the controlling the phase of linearly polarized light. Current LC SLM technology provides high-spatial-resolution wavefront

control, with hundreds of thousands of degrees of freedom, more than two orders of magnitude greater than the best Deformable Mirrors currently made. Even with the increased spatial resolution, the cost of these devices is nearly two orders of magnitude less than the cost of the largest deformable mirror.

2 SLM Technology

The LC SLM devices utilized in the investigations described in this paper are a type of optically-addressed (OA) nematic LC SLM currently available from both Jenoptik and Hammamatsu. These devices are capable of phase correction of greater than one wave at visible and near-infra-red wavelengths. An OA_LC_SLM consists of a thin-film sandwich structure, shown in figure 1, with an amorphous silicon photo-semiconductor Amorphous Silicon (α-Si), a parallel aligned nematic liquid crystal, a dielectric mirror, and a pair of transparent electrodes on glass substrates. The voltage applied to the electrodes is divided between photo-semiconductor and liquid crystal layers, depending on the illumination intensity, thereby enabling 2D-image modulation of the refractive index of the LC.

To activate the OA_LC_SLM the amorphous silicon (α-Si) layer must be exposed to an image pattern. The resolution of control of the SLM is directly proportional to the resolution of the image pattern generated onto the α-Si layer up to some limit. In the state where no pattern is incident on the device, the impedance of the α-Si layer is very high, with or without the voltage applied across the electrodes. When an image pattern is projected onto the α-Si layer, the impedance of the α-Si reduces in proportion to the light intensity in that region and the voltage applied to the liquid crystal increases, causing electro-optic modulations in the liquid crystal layer due to the movement of liquid crystal molecules.

The resolution of the image projection system (which in this case is based on a liquid crystal display or LCD) determines at the resolution at which the SLM will effect the read beam. The currently available devices have the capability of providing control of up to 50 line-pairs/mm. The device from Jenoptik comes with a 832 x 624 LCD and Hamamatsu provides a 640 x 480 LCD. The operational configuration is shown in Figure 2.

These devices work with polarized light. The maximum phase shift is obtained when the polarization of readout light is parallel to the axis of the liquid crystal molecules. When the polarization of readout light is perpendicular to the axis of the liquid crystal molecules the phase shift is negligible.

3 Phase Reconstruction Methods

Accurately controlling wavefront phase with a high-spatial-resolution wavefront correction device requires a high-spatial-resolution wavefront measurement capability. This can be provided with a standard Shack-Hartmann wavefront sensor using available high-density lenslet arrays. However, computational requirements for traditional matrix-vector multiply wavefront reconstruction algorithms using slope data from a Shack-Hartmann (or other wavefront slope) sensor scale as N^2

where N is the number of phase points. For large N, greater than 10^3 this begins to become impractical. Since the slope measurement of the Shack-Hartmann sensor can be represented by a spatial filtering operation, an inverse filter can be designed to directly recover the wavefront from the slope data. This allows the reconstruction process can then be implemented as a 2D convolution operation using FFT's which scale as $N\log_2 N$. We have used computer simulations to demonstrate that for 4096 phase points the FFT-based algorithm is ~30 times faster than a matrix multiply (Figure 3). A similar approach has been utilized by Chanteloup et al[3] with a shearing interferometer as the wavefront slope sensor.

We have used the FFT-based reconstruction method in lab experiments using the test-bed described in Figure 3 with a Shack-Hartmann sensor of 1Kx1K pixels containing a lenslet array with greater than 2500 lenslets. To verify that the algorithm would accurately represent the pattern generated, a checkered phase pattern was produced on the LC SLM and Shack-Hartmann image data was recorded (figure 4a). The wavefront phase was then reconstructed using the FFT-based method (figure 4b). The resulting phase reconstruction accurately depicted the applied checkered phase pattern. Additional tests were performed using different phase patterns with each reconstruction accurately representing the applied pattern.

4 SLM Experimental Test Bed

A test-bed, shown schematically in Figure 5, has been assembled to allow the evaluation of SLM devices for high-spatial-resolution spatial wavefront control. This test-bed provides the capability to place both low-order and high-order aberrations onto a beam, to detect these aberrations with a high-spatial-resolution Shack-Hartmann sensor, and to correct these phase aberrations using the OA_LC SLM. This process is currently implemented using multiple computer systems in a human-in-the-loop closed-loop operation.

5 Experimental Results

An initial set of experiments has been completed using the Jenoptik OA_LC SLM. In these experiments, an aberration was placed into the main beam path (Figure 6a) and the resulting high-resolution Shack-Hartmann image was processed using the FFT-based method to reconstruct the phase (Figure 6b). From the reconstructed phase an appropriate correction image was generated and applied via the SLM. The applied correction produced a significantly improved far field spot, Figure 6c. The corrected wavefront was reanalyzed with the same methods (Figure 6d) and a significant improvement was observed in the reconstructed phase image.

Similar experiments utilizing the Hamamatsu AO_LC SLM are currently underway in the SLM test-bed with some modifications to improve the collimation of the write-beam from the back-light diode and thereby improve the correlation between the image pattern generated on the LCD and the phase correction produced by the SLM.

Design for the introduction of an OA_LC_SLM into a high-powered short-pulse laser is also currently in progress. The OA_LC_SLM will be used to correct high-spatial-frequency phase errors in the front end of the Petawatt Short-Pulsed Laser[4,5]. In this experiment we will be testing the ability of the SLM to correct for high-spatial-frequency errors and the effects on transport of the correction through the spatial filters of the system. The OA_LC_SLM will also be inserted into the system in two additional locations that have a higher beam fluence to evaluate the performance in high-power conditions and to determine the damage threshold.

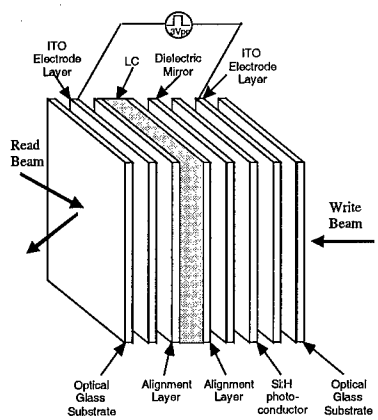

Figure 1 Anatomy of SLM

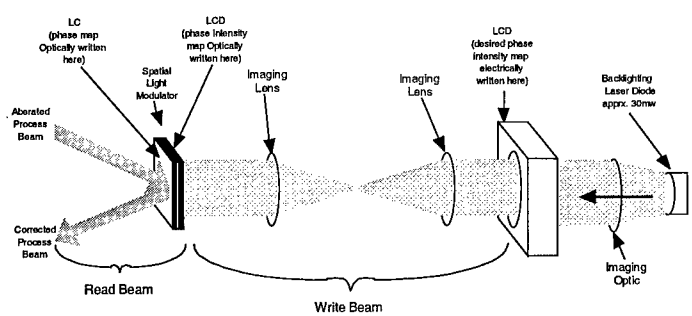

Figure 2 SLM Operation

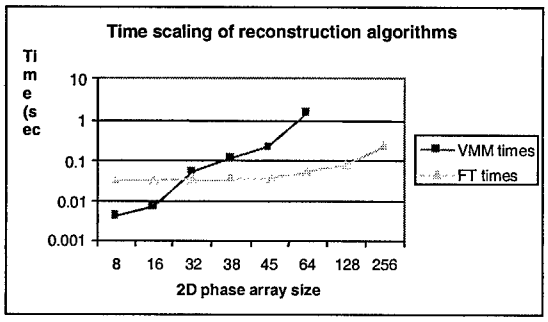

Times for single R10000 CPU in View

Figure 3 Phase Array Size versus Computation Requirements

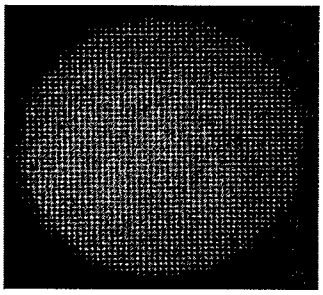

Figure 4a High-Resolution Hartmann Sensor

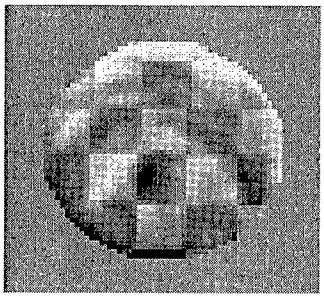

Figure 4b Reconstructed Wavefront using FFT's

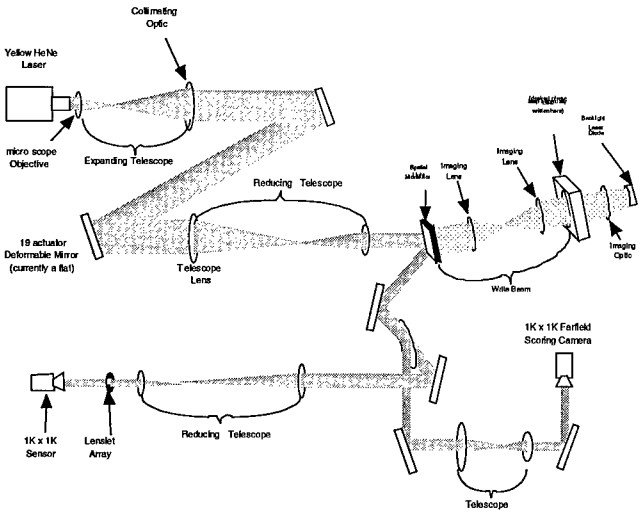

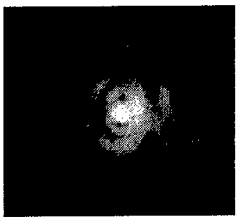

Figure 6a Aberrated far-field

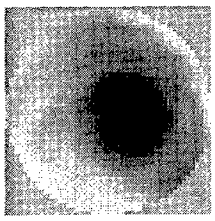

Figure 6b Aberrated Wavefront

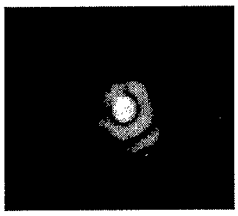

Figure 6c Corrected far-field

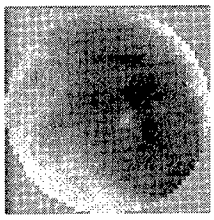

Figure 6d Corrected Wavefront

Figure 5 SLM Test Bed

6 Acknowledgements

The authors would like to acknowledge the technical assistance of B.J. Bauman, R. Sawvel, R. Hurd, J. An.

References

1. Klaus Freischland and Chris L. Koliopoulos Wavefront Reconstruction from Noisy Slope or Difference Data Using the Discrete Fourier Transform. SPIE Adaptive Optics Vol. 551 (1985)
2. Dennis C. Ghiglia and Louis A. Romero Robust two-dimensional weighted and unweighted phase unwrapping that uses fast transforms and iterative methods. Optical Society of America Vol. 11, No.1 (Jan. 1994).
3. B. Loiseaux, J.P. Huignard, J.C. Chanteloup, B. Wattelier, A. Migus, C. Dorrer, Laser Beam Shaping using Optically Addressed Spatial Light Modulators, Optical Society of America, Snowmass, CO, April 12-14, 1999
4. Pennington, D;Brown, C G;Cowan, T E;Ditmire, T;Fountain, W;Hatchett, S;Hunt, A;Johnson, J;Kartz, M;Key, M;Moody, J;Moran, M;Parnell, T;Perry, M D;Sangster, Petawatt class lasers and applications to laser-matter interaction experiments, Women's Technical and Professional Symposium, San Ramon, CA, October 15-16, 1998
5. Pennington, D.M.;Brown, C.G.;Kartz, M.;Landon, M;Perry, M.D.;Tietbohl,G; "Production of high intesity laser pulses with adaptive optics", International Workshop on Adaptive Optics for Industry and Medicine, Durham, England, July 12-16, 1999

INDUSTRIAL APPLICATIONS WITH ADAPTIVE OPTICS

MATTHIAS NEGENDANCK, RALF SCHMIDT, DR.-ING. PETER HOFFMANN
ERLAS GmbH, Germany

PROF. (UNIV.) DR.-ING. DR. H.C. MANFRED GEIGER
Head of the chair for manufacturing technology, University Erlangen-Nuremberg, Germany

The CO_2 laser has an increasing influence on small and middle-scale companies in the producing industry as well as on large companies like the car industry as a versatile tool, which is free of wear. It is mainly used for two manufacturing processes: Laser beam welding and laser beam cutting. In the following we want to introduce the capability of the adaptive optics of the Diehl's company integrated in laser machines in order to realise a high quality laser beam processing. As a first example a system technique for the compensation of beam path differences in laser beam cutting machines is described, secondly a processing head for laser beam welding combined with a novel sensor for a focus position control is introduced.

1 Adaptive optic for material processing

For all applications presented in this paper we use an adaptive optic, consisting of an deformable copper mirror, which is driven by a piezoelectric ceramic as an actuator. For detailed information on the adaptive optic please refer to Reinhold Schmiedls presentation, Diehl Stiftung, "Adaptive Optics for CO_2-Laser Material Processing".

2 Compensation of beam path differences at CO_2 laser beam cutting

2.1 Laser beam cutting

During laser beam cutting the beam melts or sublimates the material and a flow of gas expulses the liquefied or gaseous metal as it is shown in figure 1. Inert gases for a physical impulse transmission or oxidising gases to support a exothermal reaction are used. With this technique metals with a thickness up to several centimetres can be cut.
The main process parameters concerning the

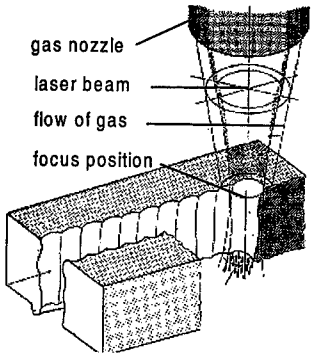

Figure 1: model of laser beam cutting

properties of the laser beam are as well as the temporal evolution of the beam power, the focus radius, the axial focus position and the K-number. The cutting quality and the cutting speed depends strongly on those three parameters.

2.2 *Laser machine for cutting*

The beam compensation system was integrated in a cutting machine – the CB 3000 produced by the the Behrens AG – with a Rofin Sinar RS 6000 CO_2-laser. The laser can be run in two different states: TEM 10* and TEM 20. The main parameters of the raw beam are shown in table 1.

	TEM 10*	TEM 20
Waist radius	6.2 mm	9.79 mm
Waist position / mm	-2900 mm	-1400 mm
K-number	0.48	0.23

Table 1: measured beam parameters

A typical design of the cutting machine is equipped with "flying optics", which means, that the processing head, including the focussing element is moved over the workpiece. The optical path length in the working room of laser machines is several meters long. Due to the diffraction of the light with a wavelength of $\lambda = 10.6\ \mu m$, the phase front curvature and the beam diameter of the unfocussed laser beam is not constant over the working room. This leads to a change of focus position and focus radius of the beam at the working piece, as it is shown in figure 2.

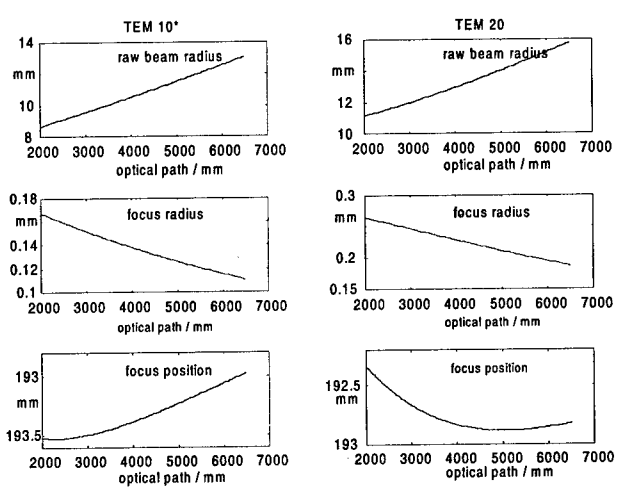

Figure 2: Raw beam diameter, focus radius and focus position in the working room of a laser cutting machine with a focussing lens of f = 190 mm

The variation in focus position over the whole working room is up to 0.5 mm, but the difference of the focus radii along the optical path is even worse (table 2):

	Minimum: focus radius	Maximum: focus radius	Increase
TEM 10*:	0.11 mm	0.16 mm	45 %
TEM 20	0.185 mm	0.25 mm	38 %

table 2: Variations in focus radii

These characteristics must lead to a non-uniform cutting quality along the working room.

2.3 Integration of adaptive optics

The problems discussed above can be solved by the integration of adaptive optics in the laser machine. To control focus radius and focus position, two adaptive optics have to be used. The first one is mounted in an adaptive telescope near the laser. It can change the illumination level on the focussing element and therefore the focus radius. The second one is near the processing head in a delta-housing, in order to correct the focus position. The mechanical set-up is shown in figure 3.

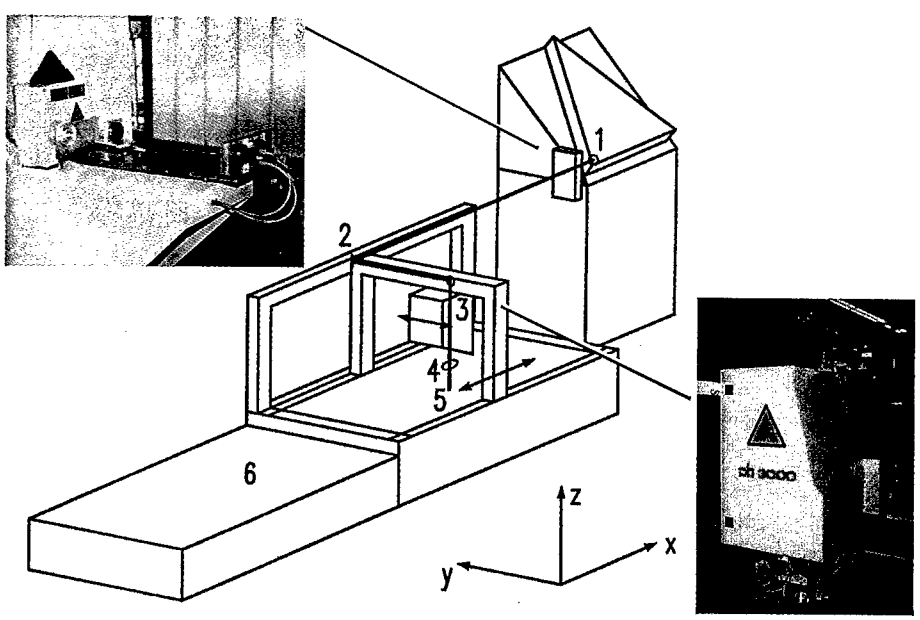

Figure 3: upper left corner: adaptive telescope; lower right corner: delta housing for the second adaptive optic; 1 Laser, 2 x-axis, 3 y-axis, 4 z-axis, 5 upper working table, 6 lower working table

2.4 *Experimental results*

The beam characteristics of the laser machine described above could be improved and enhanced, as it is shown by measurement results in figure 4. The upper diagram shows the behaviour of the axial focus position for three pre-set values. In the lower diagram the corresponding focus radii are shown.
The axial position can be varied in a range of about 7 mm, the focus radii have an average value of 0.131 mm and a standard deviation of 0.05 mm.

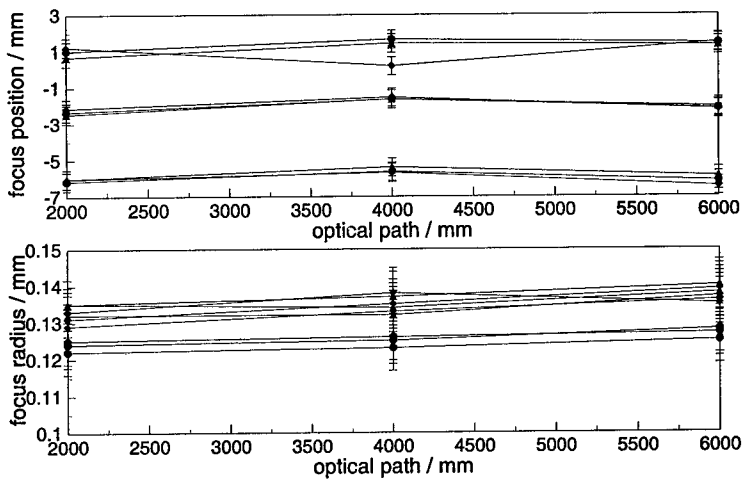

Figure 4: Upper diagram: controllable focus position for the values +1 mm, -2.5 mm, -6 mm; lower diagram: focus radius

With the integration of the adaptive optics in conjunction with the on-line computation the user has several advantages in laser beam cutting:

- Controllable focus position
- Controllable focus radius
- Identical beam parameters along the whole working room
- Optical switch for different laser modes

3 Laser Processing head for laser beam welding with focus position control

During laser beam welding processes the quality of the welding seam depends to high extend on the position of the focus point. The welding of parts of complicated shape formerly was accompanied by extensive time consumption or low quality results. To minimize the time used for preparing the welding track by teach in and to assure a high quality level of the welding seams, a sensor / actuator system using adaptive optics and a Distance-Control-Sensor (DisCo) has been developed.. The

whole system is easily connectable to all standard processing heads, so that it can easily be adapted to standard laser machines.

3.1 Processing head with integrated focus point controlling unit using adaptive optics

Similar to the application of the compensation of the beam path difference, an adaptive optic is integrated directly into the processing head, in order to act as an actuator for controlling the axial focus position (figure 5). The focus position can be shifted up to18 mm with a minimum influence on the beam quality due to effects like astigmatism etc.. Using the principle of active triangulation the detector system, determines the relative position of the focus to the work piece surface. Controlled by a PC this continuos position signal is transferred into the actuator signal, that maintains the focus point in ideal position by adapting the stroke of the adaptive optic. Both the sensor signal and the control signal are transmitted using a sample rate of 1000 Hz. Considering a typical path feed rate of the processing head as 4m/min the focus gets controlled each 0,067mm, this enables to weld even very small parts with high accuracy.

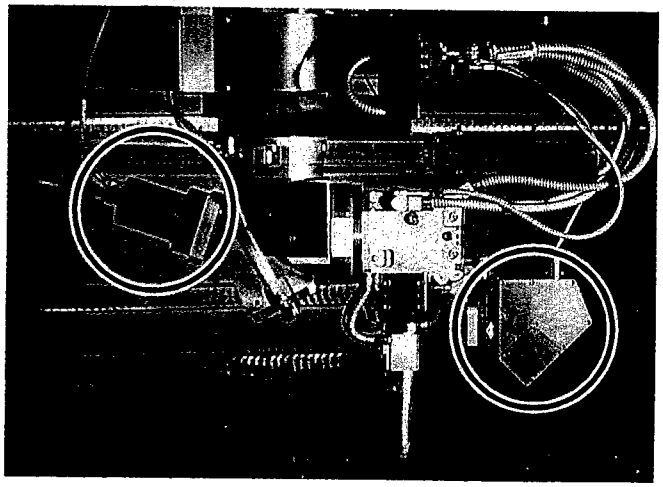

Figure 5: Processing head for CO2-Laser beam welding with integrated adaptive optics (left) and DisCo (Distance Control) Sensor (right)

During the experiments the processing head with the sensor / actuator system was adapted on a CO2-laser machine TLC 1005 of the company Trumpf. The laser integrated in the machine is a TLF 4000 Turbo with a maximum power output of 4 kW. The beam parameters measured with a focussing mirror with f = 270 mm and a power of 3800 W are: beam radius 0.242 mm (86 %), K-number =0.55 (86%).

3.2 *Experimental results*

To demonstrate the power of the sensor-actuator system an irregular steel plate with a thickness of 1 mm was welded with only a line track having been programmed. The sensor-actuator system compensates the irregularities and provides a high quality welding seam, as it can be seen in figure 6.

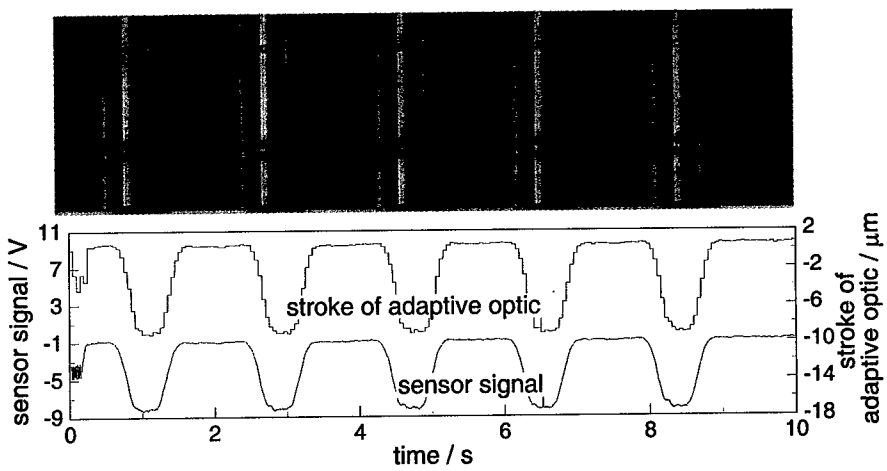

Figure 6: Upper welding without focus position control; lower welding with focus position control; upper graph stroke of the piezoelectric of the adaptive optic, lower graph sensor signal

Acknowledgements
The authors thank Dr. Norber Neubauer for his basic research work on the adaptive optic. The results of this report are based on projects supported by the BMBF (code number: 13N6786/2) and the Bayern Innovativ GmbH. The authors would like to thank for their sponsorship.

References

1. Neubauer, Norbert: Adaptive Strahlführungen für CO_2-Laseranlagen; Reihe Fertigungstechnik – Erlangen Nr. 70. Bamberg: Meisenbach 1997
2. Negendanck, M; Norbert Neubauer: Sensor / Actuator Systems for High Quality 3D - Laser Beam Welding; Proceedings of the 30th International Cirp Seminar on Manufacturing systems – LANE 97; Edited by M. Geiger, F. Vollertsen. Bamberg: Meisenbach
3. Geiger, M, Neubauer, Hoffmann, P.: Intelligent processing head for CO_2 laser material processing. Production engineering / Annals of the German academic society for production engineering / I (1994)2, 91-98
4. Hoffmann, P., Geiger, M.: Recent developments in Laser System Technology for welding applications. CIRP Annals 44 (1995) 1, 151-156

USE OF DEFORMABLE MIRRORS IN THE 8-TW TIS-LASER ATLAS

H. BAUMHACKER, K.J. WITTE AND H. STEHBECK
Max-Planck-Institut für Quantenoptik, Hans-Kopfermann-Str. 1, D-85748 Garching, Germany
E-mail: Baumhacker@mpq.mpg.de

A. KUDRYASHOV AND V. SAMARKIN
Institute on Laser and Information Technologies, Svyatoozerskaya Str. 1, Shatura, Moscow Region, 140700 Russia
E-mail: adopt@laser.nictl.msk.su

A 17-electrode bimorph piezoelectric deformable mirror is used to compensate for the thermal lensing and serious growth defects of a 40-mm diameter Ti:sapphire-crystal, which is used as amplifying medium in the 8-TW TiS-laser ATLAS 10. It was demonstrated that the peak fluence in the near and far field could be reduced by a factor of 3 and at the same time the focusability was enhanced from 3.5 to 2 times diffraction limited.

1 Introduction

Chirped pulse amplification Ti:sapphire lasers [1,2] are well suited to deliver extreme high power densities of up to 10^{21} W/cm^2 which, e.g. are required for experiments studying light-matter interaction in the relativistic regime [3,4]. Besides laser pulse energies in the 1 to 5 J region at pulse durations of 100 fs or less, a nearly diffraction limited focusability is required. The beam quality – evaluated in terms of a fluence distribution modulated as small as possible and a wavefront distortion as minimal as possible – is strongly affected by the optical quality of the TiS-crystals which are used as the amplifying medium.

In the 8-TW TiS-laser system ATLAS 10 (see Fig. 1), a 40-mm diameter TiS-crystal is used as a four-pass amplifier delivering 1.2 J in 150-fs pulses at 10 Hz. The crystal has serious growth defects and shows inhomogeneous thermal lensing when pumped by up to 5 J of a frequency-doubled Nd-YAG laser. The near-field fluence distribution in the plane of the first compressor grating is rather inhomogeneous, showing two main peaks with a fluence of up to 300 mJ/cm^2 (Fig. 2), which is beyond the damage threshold of the gratings. To flatten the profile, a 17-electrode bimorph piezoelectric deformable mirror [5] is used. This procedure differs from the usual application of adaptive optics in lasers, which only aims at the correction of the deformed wavefront so that the Strehl ratio gets close to unit [6,7]. In ATLAS 10, this will be done in a further step using a second DM which will be mounted further downstream from the compressor.

2 Deformable mirrors in ATLAS 10

The setup of the final amplifier of ATLAS 10 is shown in figure 1. Coming from the preceding part of the amplifier chain, the stretched pulses with 200-ps duration and 300-mJ energy pass the TiS-crystal disk four times. The crystal is pumped from both sides by frequency-doubled Nd-YAG laser pulses with up to 2.5 J. After amplification, the pulses are recompressed to about 150 fs in a grating compressor and

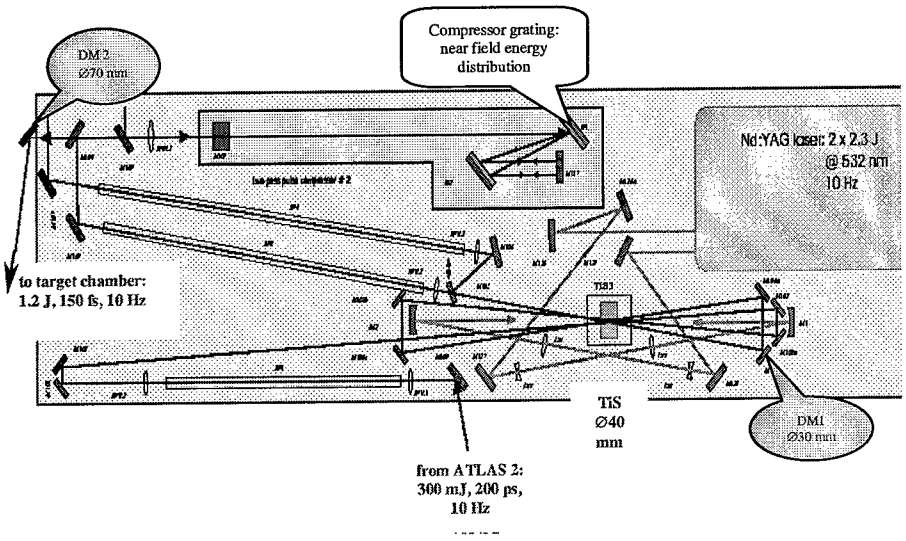

Figure 1. Setup of ATLAS 10 amplifier with 2 deformable mirrors.

the laser beam is guided via the DM 2 (not yet in operation) to the target chamber, where it is focused on different targets by an off-axis parabola. The DM 1 is in a position as close as possible to the pumped TiS-crystal, the component which contributes most to the wavefront deformation of the pulse. The fluence distribution in the near field is monitored in a plane corresponding to the plane of the first most heavily loaded compressor grating.

3 Experimental results

In several measuring campaigns, the fluence distributions were measured both in the near field at the grating site and at a distance about 30 m beyond downstream with and without DM 1 in operation. In addition, the pulse focusability was determined. The voltages applied to the 17 electrodes of the bimorph mirror were set such that

the near-field fluence distribution was homogenized (Fig. 2). Using this voltage pattern, the voltages of the outer zone electrodes were slightly changed in order to minimize the focal spot diameter of the beam when focused with a lens of 4-m focal length. The relative good shot-to-shot stability of the TiS laser allows the voltage pattern of the DM 1 to be adjusted only once a day without using a closed loop.

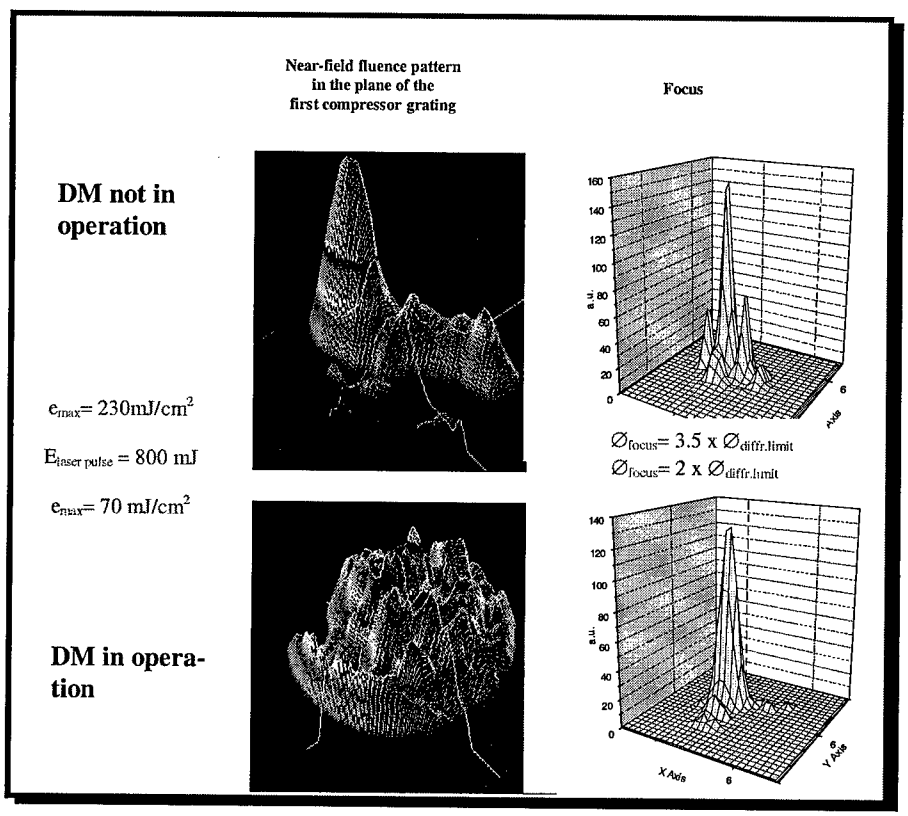

Figure 2. Near field distribution and focusability of the TiS-laser beam with and without DM 1 in operation.

As can be seen from figure 2 with the DM 1 in operation, the peak loading in the grating plane was reduced by a factor of 3, and, as a consequence, the laser pulse energy could be correspondingly enhanced. Despite the residual fluence modulation, it was possible to handle pulse energies of up to 1.5 J without any indication of damage on the compressor gratings. Although the focusability has been improved, too, from typically 3.5 to 2 times diffraction limited, corresponding to an enhancement of the Strehl ratio from $S \leq 0.1$ to $S = 0.4$, it turned out that with only one de-

formable mirror it is not possible to simultaneously optimize both the near-field and far-field fluence distribution.

4 Outlook

After the near-field fluence distribution could be significantly improved with a standard deformable bimorph mirror working simply without a closed loop, we will concentrate on minimizing the phase front aberrations and thereby enhancing the Strehl ratio. It is expected that the TiS laser beam can then be focused to near diffraction-limited diameters. The DM 2, which must handle a beam diameter of 70 mm, is under construction and will be implemented in ATLAS 10 in the next weeks. It is intended to operate it in a closed loop in combination with a Shack-Hartmann sensor. For the first time, one can then study the behaviour of two DMs operating in the same laser.

The improved focus quality and the enhanced pulse energy should lead to higher on-target intensities than achieved hitherto. The light-matter interaction should hence become more relativistic. This expectation will be examined in two experiments. The first concerns the production of fusion neutrons from deuterated plastics and the second the generation of high harmonics from solid surfaces. The neutron yield and the number of harmonics should significantly increase.

References

1. Strickland D. and Mourou G., Compression of amplified optical pulses. *Opt. Commun.*, **56** (1985) pp.219-221.
2. Maine P., Strickland D., Bado P., Pessot M. and Mourou G., Generation of ultrahigh peak power pulses by chirped pulse amplification. *IEEE Journal of Quantum Electronics* **24** (1988) pp.398-403.
3. Mourou G. and Umstadter D., Development and applications of compact high-intensity lasers. *Phys. Fluids B* **7** (1992) pp. 2315-2325.
4. Mourou G. A., Barty Ch. P. J. and Perry M. D., Ultrahigh-intensity lasers: Physics of the extreme on a tabletop. *Physics Today* (1998) pp.22-28.
5. The deformable mirror was produced in the mainframe of a collaboration with the Institute on Laser and Information Technologies of the Russian Academy of Sciences.
6. Akaoka K., Harayama S., Tei K., Maruyama Y. and Arisawa T., Closed loop wavefront correction of Ti:sapphire chirped pulse amplification laser beam. *SPIE* **3265** pp.219-225.
7. Druon F., Chériaux G., Faure J., Nees J., Nantel M., Maksimchuk A., Mourou G., Chanteloup J.C. and Vdovin G., Wave-front correction of femtosecond terawatt lasers by deformable mirrors. *Opt. Lett.* **23** (1998) pp.1043-1045.

ADAPTIVE OPTICS FOR CO_2 LASER MATERIAL PROCESSING

REINHARD SCHMIEDL

Diehl Stiftung & Co., Fischbachstr. 16, 90552 Roethenbach, FRG E-mail: Reinhard.Schmiedl@diehl-mun.de

The Diehl Stiftung & Co. develops and manufactures adaptive mirrors which are used in the beam delivery system of CO_2 laser machines to improve the processing results. With help of two adaptive mirrors the focus diameter and the focus position of the laser beam can be controlled independently. This offers a method to compensate the varying beam path lengths in laser machines with flying optics, as well as a capability to adapt the focus parameters to the processing demands in laser cutting, welding, and scanning systems.

1 Introduction

In CO_2 laser processing machines with flying optics the beam path length between laser source and focusing optic depends on the position of the working head within the processing space. Especially with increasing working areas these path length variations lead to varying processing qualities which may exceed the tolerance limits.

The reason is the widening of the laser beam, which is related to the beam path, will cause varying illumination and beam divergence at the focusing optic and therefore varying focus parameters (focus diameter, focus position) at the work piece. As conventional passive beam forming components like beam expanders reach their limits, adaptive optics may be used to compensate these path dependencies. They may keep the focus parameters constant or even control them in-line with work piece or process requirements.

Due to enlarging working areas of modern CO_2 laser machines, equipping of laser machines with adaptive optics is becoming a standard in Europe.

2 The Adaptive Mirror

Because of the wide power range of CO_2 lasers and the high absorption of CO_2 laser radiation (10,6µm) in glass, in CO_2 beam guidance systems commonly reflective optical components (mirrors) are used. Therefore an adaptive optic primarily designed for CO_2 applications is based on an adaptive mirror with adjustable spherical deflectable mirror plate, in order to generate optical surfaces with variable focal length.

Diehl Stiftung & Co. at Nuremberg develops and manufactures such adaptive mirrors. The adaptive mirrors made by Diehl are metal mirrors with deflectable surface, which may replace conventional passive mirrors in beam guidance systems of CO_2 laser machines with the aim to compensate the distance-relating variations of the focus parameters.

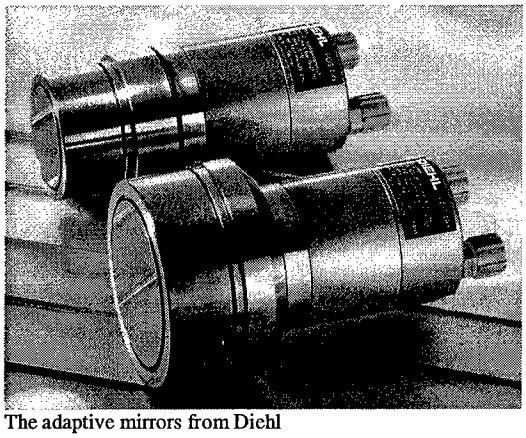
The adaptive mirrors from Diehl

The spherical deflection is approximately achieved by means of a circular metal mirror plate, which is restrained on its circumference, while an actuator is pressing from behind against it's centre. In this way approximately spherical mirror surfaces with a height up to 40µm in the centre of the plate can be realised. Even a surface change-over from concave to convex are adjustable using mirror plates with plane surface at a predefined actuator stroke.

The actuator deflecting the mirror plate is made up of a stack of piezo ceramic plates which expand with high force due to an applied electrical voltage. Unfortunately for exact expansion adjustment the intrinsic hysteresis of the piezo actuator has to be compensated. For this reason a wire strain gauge sensor is fixed to the ceramics stack enabling a precise measurement of the actuator elongation. The measuring signal is used in a closed control loop to adjust the stroke of the mirror centre with an accuracy of ±0,5µm at frequencies up to 50Hz and more.

During design of the adaptive mirror special care had to be taken in reaching reproducible optical properties under conditions of long term operations. Therefore the mirror plates are made of a special copper alloy and the actuator stroke is limited to about 40µm. Thus the mirror design enables good axial flexibility allied to extremely high rigidity in radial direction. For heat protection a scratch resistant surface coating with 99,8% reflectivity to CO_2 laser radiation and a connection to an external cooling system is provided. The cooling of the mirror is dimensioned to support sustained laser beam operations at a max. power of 3,5kW (40mm mirror) and 6kW (60mm mirror) without significant thermal influencing of the mirror's shape. Even pressure and temperature of the cooling water may vary over a wide range.

As with all optical mirrors their reflecting surface is the most sensitive part. With respect to this fact the adaptive mirror was designed such, that replacing of the mirror plate is possible with a minimum of time and costs.

To enable retrofitting of existing installations particular attention was placed on the compatibility of the adaptive mirror as a stand-alone device with established

beam guidance components. The outer dimensions of the adaptive mirror are chosen such, that it can be used instead of passive plane mirrors. In doing so the replacing of existing installations is possible with little expenditure.

Feature	Medium Power Optics	High Power Optics
Free aperture	40mm	60mm
Max. laser power at 10.6µm	3,5kW (cw)	6kW (cw)
Max. oscillating frequency	> 20Hz	> 20Hz
Type of water cooling system	Cu, Al	Cu, Al
Temperature of the cooling water	20°C ±5°C	20°C ±5°C
Piezo control voltage	-20V ... +120V DC	-20V ... +120V DC
Weight	1.35kg	1.85kg
Max. size (diameter x length)	72mm x 180mm	97mm x 180mm
Stroke of the piezo actuator: Standard Option	-20µm ... 0µm ... +20µm (concave/flat/convex) other ranges on request	-20µm ... 0µm ... +20µm (concave/flat/convex) other ranges on request
Vertical focus shift at f=180mm	-5mm ... +5mm	-5mm ... +5mm
Pressure of the cooling water	1bar...5bar	1bar...5bar
Operating temperature	+5°C... +40°C	+5°C... +40°C
Storage temperature	+5°C... +60°C	+5°C... +60°C
Relative air humidity	40% ... 80%	40% ... 80%
HR coating Standard Option	CO2 Laser (10.6µm) NdYAG Laser (1.06µm)	CO2 Laser (10.6µm) NdYAG Laser (1.06µm)

Technical data of the adaptive mirrors

3 The Control Unit of the Adaptive Mirror

To run the adaptive mirror an analogue control unit is necessary supplying the piezo actuator with expansion relating voltages from –20V to 120V. For precise elongation adjustment of the piezo actuator it's strain gauge sensor signals are fed-back to the control unit in order to adjust the piezo control voltage by means of a closed loop.

The adaptive mirrors should be integrated meticulously into the laser processing machine, as all information about position of working head, work piece geometry and material, process parameters is there available. It is up to the CNC programmer to calculate and to command the appropriate elongation of the piezo actuator. Commanding an elongation is possible via an analogue signal applied to the control unit. The signal magnitude, which may vary between 0V and 10V, is linear transformed into an actuator stroke from 0µm to 40µm. Particular care has to be taken in the system installation as an analogue interface is very sensitive to electromagnetic distortion. For higher resistance to jamming differential analogue inputs are available.

The analogue control unit may also be upgraded with a digital control unit which provides a digital serial interface with software handshake to the machine's

CNC. Optoelectronic couplers are used to completely isolate the adaptive optic system from the CNC so that an optimal processing reliability can be guaranteed. Nevertheless, controlling of the adaptive optic system must happen by the CNC, even if subtasks e.g. controlling the adaptive optic with help of a lookup table, system checks, processing of additional sensor inputs will be done by the digital control unit.

4 Physical Basics of Adaptive Optics

Two physical effects have to be considered in controlling the focus parameters e.g. in CO_2 laser processing machines:

- The focus diameter is indirect proportional to the illumination of the focusing optic.
- The axial focus position is influenced by the curvature of the laser beam's wave front (divergent / convergent beam) at the focusing optic.

Controlling the focus parameters is optimised if focus radius and focus position can be adjusted nearly independently. This is achieved by using two adaptive optics, the one located nearby the laser source the other one nearby the focusing head (adaptive telescope).

An adaptive optic located nearby the laser source can hold the illumination at the focusing optic and therefore the focus diameter constant. Due to the long distance (several meters) between the adaptive optic and the focusing optic, holding the illumination of the focusing optic constant has no noteworthy influence on the beam divergence which would lead to variations of the focal length.

Variations of the focal length are controlled by an adaptive optic installed nearby the processing head. Because of a short distance between the adaptive optic and the focusing optic divergence changes of the laser beam will not result in a significant change of illumination at the focusing optic. Thus the focus diameter remains approximately constant while the axial focus position is shifted.

If only one focus parameter has to be controlled actively, only a single adaptive optic is necessary. It's installation position depends on the focus parameter which has to be adjusted.

5 Applications

As described above, the main application of adaptive optics in CO_2 laser material processing is the assurance of beam path independent focus parameters. Thus processing speed and quality can be held on a constant high level within the complete working space, saving time and money.

Further applications of adaptive optics are in the sector of 3-dimensional laser material processing, where work piece and process relating focus shifts are desirable. With the adaptive optic installed in the focusing head, axial focus shifts

up to 10mm (20mm) are achievable in combination with a focusing optic of 5,, (7,5,,) focal length. Especially the rapid inertia-less focus positioning of the adaptive optic in comparison to the limited kinematics of the machine axes may be an advantage in applications, e.g. in the case of rapid changes for appropriate focus tracking along the work piece surface, or when there is a risk of collision between the working head and the work piece.

6 Future Prospect

For new products on the subject ,,Intelligent Beam Guidance and Forming Systems,, the German companies Diehl Stiftung & Co. and ERLAS GmbH in Erlangen agreed to work together. ERLAS is a new company with much experience in laser material processing. At present both companies are about to develop an "intelligent" processing head for laser welding, where an adaptive mirror is governed on-line by an optical sensor which supervises the processing quality. For further information see references 4 below.

References

1. Datasheet, Adaptive Mirror, Diehl Stiftung & Co., Roethenbach, FRG, 1999
2. Norbert Neubauer, Adaptive Strahlführungen für CO_2 Laseranlagen, Bamberg: Meisenbach 1997, Fertigungstechnik-Erlangen Vol. 70, Erlangen, University, Dissertation 1997
3. P. Hoffmann, S. Schuberth, M. Geiger, C. Kozlik, Process Optimising Optics for Beam Delivery of High Power CO_2 Lasers, in Laser Energy Distribution Profiles; Measurements and Applications, Proc. SPIE Vol. 1834, 1992.
4. M. Negendanck, "Industrial Applications with Adaptive Optics" these proceedings, Durham, 1999.

Ophthalmic Adaptive Optics

HARTMANN-SHACK WAVEFRONT SENSOR IN THE EYE: ACCURACY AND PERFORMANCE LIMITS

PABLO ARTAL, JUAN L. ARAGON, PEDRO M. PRIETO, FERNANDO VARGAS-MARTIN AND ESTHER BERRIO
Laboratorio de Optica, Universidad de Murcia,
Campus de Espinardo (Edificio C), 30071 Murcia, Spain.
E-mail: pablo@fcu.um.es

A general description of a Hartmann-Shack sensor to measure the aberrations of the human eye is presented. Different factors affecting its performance are reviewed: the size of the microlenses, the number Zernike modes required to describe the ocular aberrations, the statistical accuracy and the exposure time.

1 Introduction

Adaptive Optics (AO) promises important benefits in Visual Optics and Ophthalmology. For instance, by correcting the ocular aberrations, high resolution ophthalmoscopes may provide new diagnosis tools. Liang et al. [1] obtained images of the cone mosaic by using a deformable mirror as wavefront corrector. As an alternative, the use of liquid crystal spatial light modulators to correct the aberrations in the eye was also demonstrated [2]. In a different application, customized contact lenses designed to correct aberrations may ultimately improve spatial vision.

The initial step in AO involves the detection of the wavefront aberration (WA). Measuring the aberrations in the human eye is a difficult task where a mere translation of techniques from other applications usually fails. Although researchers were interested for centuries in measuring the degradation of the retinal image, further than the refractive errors, was not until the early 60's when Smirnov [3] measured the first WA in the eye. Techniques to measure the WA in artificial systems usually involve a single pass through the optics from a test source to the detector. In the case of the eye, a single-pass would require to place either the detector or the light source within the retina. Subjective methods can be considered to make use of the former solution since the retina itself acts as a detector. On the opposite, objective methods use the light reflected back in the retina. For example, from double-pass retinal images, the WA was calculated using phase retrieval techniques [4]. Other alternative, more appropriate for AO is revised here, the Hartmann-Shack (HS) sensor [5,6].

2 HS sensor theory and operation

In the HS sensor, a wavefront is sampled in a number of locations by a microlens array placed in the propagation path. The displacement of each spot is proportional to the average of the wavefront derivative across the microlens. Typical procedures to reconstruct the WA from the averaged derivatives are modal approaches, consisting in fitting the coefficients for the expansion of the wavefront on a certain functional basis; i.e., the Zernike circle polynomials [7]. The wavefront mean derivative can also be expressed as combination of the mode derivatives with the same coefficients. Two systems of N equations relates the measured x and y direction displacements of the N available spots and the mean x and y derivatives of each mode inside each microlens, through the mode coefficients. These two systems can be mixed since they have the same unknowns. In matrix notation can be expressed as:

$$\boldsymbol{d} = \mathbf{B}\,\boldsymbol{c}$$

where $\boldsymbol{d}$ and $\boldsymbol{c}$ are column vectors, representing the 2N spot displacements in x and y direction, and the unknown n coefficients respectively, and $\mathbf{B}$ is the nx2N matrix of microlens averaged x and y derivatives of the modes. If the number of microlenses is enough, the system is redundant, although in general inconsistent due to noise and aberration terms of order higher than the truncation mode.

2.1 Centroiding: pyramidal iterative search and sub-pixel resolution

The centroid location of each HS spot is iteratively evaluated in windows of decreasing size, each centered on the previous estimate. The first window is the whole area associated to the j-th pixel and the last one is the theoretical size of the diffraction pattern. The last window should be centered very close to the actual spot center, almost unaffected by tail asymmetries (see figure 1). Both window size and position are expressed with floating point numbers of pixels. This sub-pixel precision makes the method more robust since rounding to integer pixel number lead in some cases to incorrect and/or non-converging centroid estimates due to the asymmetries in the window positioning.

2.2 WA reconstruction

A matrix inversion method was used to reconstruct the WA. An expansion of the Zernike polynomials in rectangular coordinates for the square geometry of the microlens array, allows the elements of matrix **B** be expressed as a simple analytic function of the microlens edge positions. Each element of **B** represents the mean slope of a single

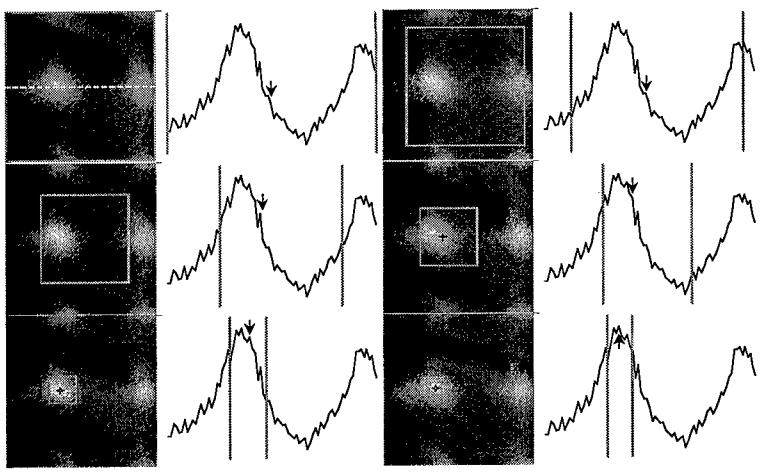

Figure 1. Example of centroid detection (arrows indicate the centroid location in each iteration).

Zernike polynomial (by columns) across one microlens in x or y direction (by rows). We have ordered the microlenses from top to bottom and from left to right, and placed all the x direction derivatives in rows 1 to N and the y direction derivatives in rows N+1 to 2N. However, it is important to note that the solution of the system is independent to changes in this ordering (except for noise artifacts) or to elimination of some rows, provided that the vector $\boldsymbol{c}$ was constructed consistent with the number and ordering of the elements considered. This permits to obtain an accurate estimation of the WA for variable number of modes and with incomplete centroiding data, which can be a common situation when measuring the eye.

The complete calculations takes less than 40 msec for each image in a Pentium-II PC, rendering the algorithm appropriate for real-time analysis.

3 Requirements for a HS sensor in the eye

Prior to decide the specifications of a HS sensor for use in the eye, it is important to know the characteristics and amount of the typical aberrations to be measured. The ocular aberrations depend largely on different conditions. There are individual variability, dependence on the pupil diameter, the age of the subject and the accommodative state. Moreover, it is also known that refractive surgery produces large amount of aberrations. However, despite the variability, in young subjects at best focus and for a medium pupil diameter, the *rms* of the WA typically ranges from 0.2 to 0.4 □m (figure 2). As an example of the change of the amount of aberrations with the pupil diameter, the *rms* in one of the subjects of figure 2

evolves from 0.25 □m to 0.7 □m, for 3.5 to 7 mm pupil diameter. Another relevant parameter is the number of modes required to describe, or to correct, the aberrations of the eye. Liang and Williams [6] showed that for a 3 and 7.3 mm pupil diameter, 4th and 8th order respectively were required.

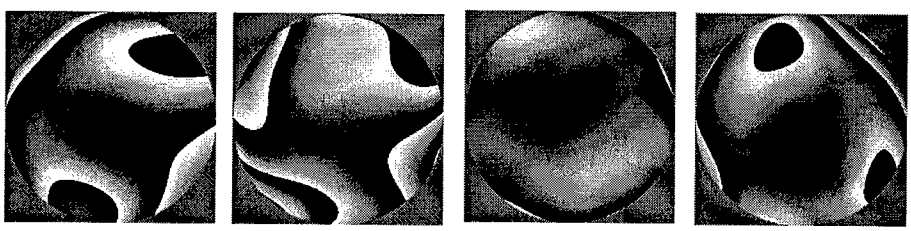

Figure 2. Example of WAs in four normal young subjects for a 4.5 mm pupil diameter.

Although it would depend on the particular conditions of the experiment, it maybe useful to indicate some desired general characteristics for a HS sensor in the eye. As a general feature, a robust, fast and automatic software analysis, with some of the capabilities previously presented is required. Other considerations are:

Temporal rate. The system should be able to operate either in static or dynamic temporal regimes. While a few second exposure measurements will be relatively free of speckle, HS spots will present high contrast speckle patterns for exposure times below 500 msec. Closed loop AO applications would require to measure the aberrations at a higher speed, at least around 30 Hz [8]. A HS sensor operating at this temporal rate with enough accuracy was recently demonstrated [8]. It uses a short coherence source and fast scanning of the image on the retina to reduce speckle.

Precision and range. The required accuracy of a HS sensor depends on the particular conditions and the range of aberrations desired to be measured. A general purpose sensor should be able to track defocus changes of around 3 diopters, without changing the geometrical configuration. Automatic search of the spots would overcome the problem of crossover for large aberrations. Although a precision of 0.01 □m maybe adequate, typical systems will present better performance.

4 Some factors limiting HS sensor performance

4.1 Statistical accuracy

To estimate the statistical accuracy of the HS sensor, we simulated in the computer an experiment in which a flat wavefront is detected with random errors in the centroid detection. Random fluctuations in the range [-1,1] pixels produces in the WA a statistical error hardly exceeding 0.05 □m. For individual Zernike modes the error is less than 0.015 □m. Although it is difficult to quantify the positioning error in a real sensor, a range of [-1,1] pixel is a highest limit when using a sub-pixel centroiding algorithm.

4.2 Spatial resolution

Two different, although related aspects, limit the spatial resolution of the WA estimates obtained from the HS data: the microlens size and the number of modes used to express the WA. Each lens of the array acts as a spatial integrator and, therefore, details smaller than its size are not captured. On the other hand, the number of modes is ultimately limited by the available data for fitting, and this truncation also results in a loss of higher order details. To evaluate the effect of the microlens size, the spot decentering data corresponding to a known WA were evaluated with the same rectangular geometry and pupil diameter, but different microlens sizes. The fitting results were quite stable for sensor configurations with 8 or more microlenses within the pupil diameter. This suggests that the spatial resolution of the HS sensor is not mainly affected by the lens size, provided that the total number of lenses was enough to fit the desired number of coefficients. As an example, to measure the aberrations in a typical eye with 6 mm pupil diameter, a microlens size smaller than 0.75 mm in diameter and 35 modes (7th order) should be used. In this case, around 50 HS spots will assure enough degree of redundancy for WA reconstruction.

4.3 Temporal fluctuations and exposure time

The effects of time averaging on the HS sensor performance were also evaluated by recording simultaneously double-pass (DP) images of a point source and HS images for different exposure times. Discrepancies found between the HS and DP estimates of the ocular MTF becomes smaller, and even negligible, for short exposure times. This suggests that the HS sensor may overestimate the retinal image quality for long exposure times, due to the temporal fluctuations of the eye's aberrations (see reference [9] for additional details).

5 Acknowledgments

Supported by Spain-DGES, grant PB97-1056, and EU, grant BR97-4608 CLAAS. Part of this research was carried out when one of the authors (PA) was on sabbatical at the University of Rochester, USA. He thanks comments and discussions with David Williams and other members of his group. JLA acknowledges a fellowship from Fundacion Seneca (Murcia, Spain).

References

1. Liang, J., Williams D.R., Miller D.T., Supernormal vision and high-resolution retinal imaging through adaptive optics, J. Opt. Soc. Am. A, 14, (1997) pp.2884-2892.
2. Vargas-Martin F., Prieto P. and Artal P., Correction of the aberrations in the human eye with liquid crystal spatial light modulators: limits to the performance. J. Opt. Soc. Am. A 15, (1998) pp.2552-2562.
3. Smirnov, M.S. Measurement of the wave aberration of the human eye. Biophysics 6, (1961) pp.776-794.
4. Iglesias I., Berrio E., and Artal P., Estimates of the ocular wave aberration from pairs of double-pass retinal images. J. Opt. Soc. Am. A. 15, (1998) pp.2466-2476.
5. Liang J., Grimm B., Goelz S., and Bille J.F. Objective measurement of WAs of the human eye with the use of a Hartmann-Shack wave-front sensor. J. Opt. Soc. Am. A. 11, (1994) pp.1949-1957.
6. Liang J., and Williams D.R., Aberrations and retinal image quality of the normal human eye, J. Opt. Soc. Am. A 14, (1997) pp. 2873-2883.
7. Noll R.J., Zernike polynomials and atmospheric turbulence, J. Opt. Soc. Am., 66, (1976) pp.207-211.
8. Hofer H.J., Artal P., Aragón J.L., Williams D.R., Temporal Characteristics of the eye's aberrations, Inves. Ophthal. Vis. Sci., Suppl. 40, (1999) pp. S365.
9. Prieto P.M., Vargas-Martin F., Goelz S., and Artal P. Analysis of the performance of the Hartmann-Shack sensor in the human eye, J. Opt. Soc. Am. A (submitted).

SINGLE VS SYMMETRIC AND ASYMMETRIC DOUBLE-PASS MEASUREMENT OF THE WAVEFRONT ABERRATION OF THE HUMAN EYE

L. DIAZ SANTANA HARO AND J.C. DAINTY
Blackett Laboratory, Imperial College, London SW7 2BZ, England
E-mail: l.diazsantana@ic.ac.uk and c.dainty@ic.ac.uk

1 Introduction

In measuring the wavefront aberrations of the eye objectively it is necessary to illuminate the eye and use the reflected and scattered light. Phase information loss due to the double-pass process in optics is a well-known problem[1, 2]. It is present when trying to estimate the optical quality of the eye, and this case has been described by Artal *et.al.*[3, 4]. The basic problem is that the odd aberrations may be incorrectly estimated and this is minimised in the double passage case by breaking or reducing the symmetry between the input and output, for example by having different numerical apertures for the entering and exiting light. The region where information is lost corresponds with that of the overlap between the entrance and exit paths. The eye is diffraction limited for pupil diameters smaller than 2mm once correction is made for focus and astigmatism. This means that, for the eye, only redundant information is lost if one of the system pupils is 2mm or less, while the other one is bigger. In this case, single and asymmetric double pass wavefront aberration measurements should provide the same data.

The basic problem of many double-pass methods of determining the wavefront aberration, such as those based on the Shack-Hartmann sensor, shearing interferometry and the curvature sensor, is that the reflection and scattering at the retina retains the coherence of the light to some extent. This means that in the double-pass the phase information accumulated in the first pass is retained in the second pass. To solve this problem we suggested generating a non-coherent light source at the retina by using lipofuscin, a naturally occurring fluorophore[5] in the same fashion as in astronomical laser guide star adaptive optics using the emission of light from atmospheric mesospheric layer[6]. This method provides us with a way of comparing double-pass with single-pass wavefront measurements. In addition, scattering properties of the retina are being studied by using light with different polarization states to illuminate the eye. Analysis of its polarization state after the double-pass in

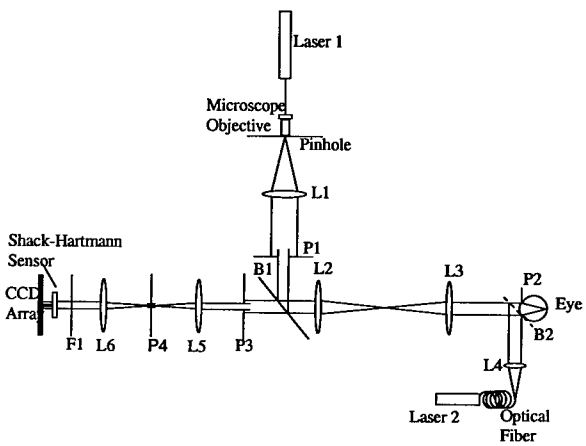

Figure 1. Experimental setup used to measure the wavefront aberration of the human eye

conjunction with the wavefront reconstruction is used for this purpose.

2 Experimental set-up

Fig. 1 shows the experimental setup used. Laser (1) is either a green He-Ne laser emitting at 543nm, or a red laser diode emitting at 635nm. Green light is used to excite lipofuscin and get a single-pass measurement, while red light is used to generate an asymmetric double-pass process. Red or green light is chosen by means of a mirror. The green beam is spatially filtered with a pinhole (PH) of 15μm and collimated by means of doublet (L1). The red laser diode is connected to an optical fiber; its tip is used as a point-like light source. It is collimated by the same doublet (L1). Beamsplitter (B1) is a either a dichroic filter which reflects light at $543nm$ and transmits all longer frequencies in the visible and near infrared, and is used when the green He-Ne is selected, or a polarising beam cube splitter is used when the other laser is selected. In between doublet L3 and the eye a quarter waveplate can be introduced. This plate in combination with the polarizing beamsplitter send into the eye circularly polarized light and transmit to the sensor only that light that does not change its polarization state after interacting with the ocular media. Entrance and exit pupils (P1) and (P3) are conjugated with the eye pupil (P2). The lens of the eye forms an image of the source at the retina, (exciting lipofuscin when using green light). Reflected (and fluorescent) light

propagate back through the system. Doublet (L4) is used to form a Fourier image at the pupil plane (P4); spatial filtering at this plane filters out most of the reflections from the system and cornea, and also autofluorescence light from ocular tissues other than the retina. Doublet (L5) recollimates the beam. Filter (F1) is an edge filter, used only when detecting fluorescence, which rejects virtually all the light below 550nm not reflected by dichroic (B1). Note that all the doublets in the system are used with a low numerical aperture to minimise any additional aberration introduced by the optics.

A Shack-Hartmann (S-H) sensor is conjugated with pupils (P2) and (P3). A reference beam is introduced via a removable beamspliter (B2). A collimated beam from a laser diode ($\approx$630nm) is used for this purpose. The lenslets of the Shack-Hartmann sensor were 0.8×0.8mm square (in the eye pupil plane). The Shack-Hartmann sensor casts an array of spots on the CCD array. The CCD camera is a Princeton Instruments model TE512 with a quantum efficency of 40% and a read out noise of approximately 10 electrons. By comparing the array of spots produced by the reference beam with that produced by the beam outgoing from the eye it is possible to reconstruct the wavefront of the latter. Its operation principle is described by Tyson[7].

Three different sets of measurements had been taken in a group of 10 subjects and comparison between them have been achieved. Ethical approval has been granted for measurement in a total of 20 normal subjects. The sets are the following:

1. Single-pass measurements using lipofuscin fluorescence.
2. Double-pass measurements using p linearly polarized light and collecting s polarized light.
3. Double-pass measurements using circularly polarized light and collecting light that did not change its polarization state.

Measurements from set 1 are single-pass measurements; set number 2 is expected to collect mainly scattered light, *i.e.* decohered light; this means that the size of the entrance pupil should not affect aberration measurements. Set number 3 is expected to collect backscattered light *i.e.* non-decohered light, or double-pass light; in this case it is expected to observe a variation in the aberrations when using different entrance pupils due to double-pass information loses. Because retinal lipofuscin is behind the layer of cones, by comparing set 1 against set 2 a difference only in defocus (apart from changes introduced by differences in tilting) is expected to be observed between both of them.

For each subject the data from every set were compared against each other and against the data within the same set for different pupil sizes. All

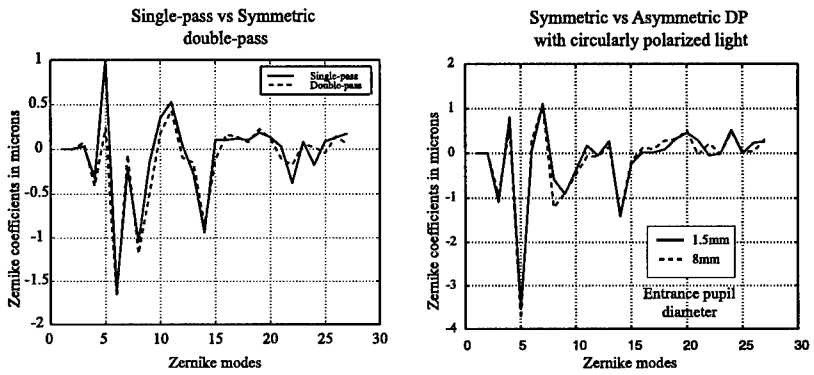

(a) (b)

Figure 2. (a) Single-pass vs symmetric double-pass using linearly polarized light. (b) Asymmetric double-pass vs Symmetric double-pass; both using circularly polarized light

three sets were taken varying the diameter of the entrance pupil from 1.5mm to 8mm. Due to the length of the session only 2 sets of data were taken from each subject. The subject's head was fixated by means of a bite bar and accommodation was paralysed and the pupil dilated using Phenliephrine 2.5% and Tropicamide 1%.

3 Results

The measured aberrations of the eye vary dynamically[8]. When accommodation is paralysed changes are due mainly to changes in eye tilting; however defocus and spherical aberrations (Zernike terms 5 and 14 in figure 2) are not expected to change with tilting, so this two terms are usually our reference "pivot" for comparison if variability of other Zernike terms is big. Additionally, comparison between two sets of data was always performed between the data where variability was a minimum.

Figure 2 shows the experimental results for 2 different subjects; the horizontal axis are Zernike modes and the vertical axis are the amplitude of these modes in microns. Figure 2a shows single-pass data using lipofuscin autofluorescence (set 1) against double-pass data using linearly polarized light (set 2) with a big entrance pupil. A change in defocus is observed (5th Zernike

mode), this corresponds with a depth of between 44 and 56 microns for the normal eye with a focal length between 16mm and 18mm. The layer of cones at the fovea is around 60 microns depth.

Figure 2b shows asymmetric double-pass data compared against symmetric double-pass data using circularly polarized light. Contrary to what we expected variability of aberrations is very small when changing the size of the entrance pupil. Three subjects were tested using this technique and this result was repeated in all of them.

4 Discussion

Unexpected results may be due to the presence of birefringent structures in the eye, such as cornea, lens and retinal fibre nerves. Haidinger brushes have been attributed to birefringence and selective absorption of light at Henle's nerve layer [9]. Similar patterns of light can be observed when photographing the macula with crossed polarizers[10]. Some of the Shack-Hartmann arrays of spots saved when taken data for set 2 present a light distribution characteristic of Haidinger brushes (See Fig. 3). This means that light used to sense the wavefront in sets 2 and 3 has been affected by several birefringent structures at the retina and cornea; and that the light selected to sense the wavefront may not be exactly the one we wanted to choose. The birefringence of the cornea may be playing a very important role. Varying the angle of polarization may provide us with very helpful information about the scattering process at the retina. Future experiments are to be carried to understand this process better.

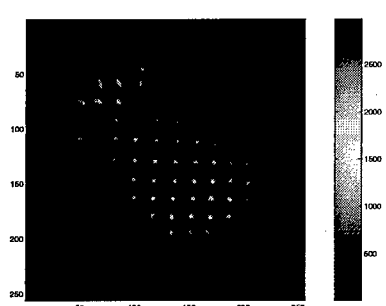

Figure 3. Array of SH spots with a light distribution characteristic of Haidinger brushes

5 Acknowledgements

L. Diaz Santana Haro is supported by CONACyT, Mexico and this project is funded by the UK Science and Engineering Research Council under Grant GR/M27043.

References

1. R.L. Fante. Imaging of an object behind a random phase screen using light of arbitrary coherence. *J. Opt. Soc. Am. A*, 2:2318–2328, 1985.
2. C.J. Solomon and J.C. Dainty. Imaging a coherently illuminated object through a random screen using a dilute aperture. *J. Opt. Soc. Am. A.*, 9:1385–1390, 1992.
3. P. Artal, I. Iglesias, N. López-Gil, and D.G. Green. Double-pass measurements of the retinal-image quality with unequal entrance and exit pupil sizes and the reversibility of the eye's optical system. *J. Opt. Soc. Am. A.*, 12:2358–2366, 1995.
4. P. Artal, S. Marcos, R. Navarro, and D.R. Williams. Odd aberrations and double pass measurements of retinal image quality. *J. Opt. Soc. Am. A.*, 12:195–201, 1995.
5. L. Diaz Santana Haro and J.C. Dainty. Single-pass measurements of the wave-front aberrations of the human eye by use of retinal lipofuscin autofluorescence. *Optics Letters*, 24:61–63, 1999.
6. B.J. Carter, J.R.P. Angel E.J. Kibblewhite, W.J. Wild, D.M. Wittman M. Lloyd-Hart, B.P. Jacobsen, and J.W. Beletic. Sodium beacons for adaptive optics on the multiple mirror telescope. In D.M. Alloin and J.M Mariotti, editors, *Adaptive Optics for Astronomy*, pages 205–210. Kluwer Academic Publishers, 1993.
7. R.K. Tyson. *Principles of Adaptive Optics.* Academic Press, 1991.
8. H.J. Hofer, P. Artal, J.L. Aragón, J. Porter, and D.R. Williams. Temporal characteristics of the eye's aberrations. In *Invest. Ophthalmol. Vis. Res.*, volume 40, No. 4, page S365, 1999. Suplement.
9. D.M. Snodderly, J.D. Auran, and F.C. Delori. The macular pigment, II. spatial distribution in primate retinas. *Invest. Ophthalmol. Vis. Res.*, 25:674, 1984.
10. B.F. Hochheimer and H.A. Kues. Retinal polarization effects. *App. Op.*, 21:3811–3818, 1982.

3-D CATARACT IMAGING SYSTEM

L. J. OTTEN, P. SOLIZ, AND I. MCMAKIN
Kestrel Corporation, 6624 Gulton Ct, Albuquerque, NM, 87109, (505) 345-2327

A. GREENAWAY, P. BLANCHARD
DERA Malvern, Malvern, UK, 01684 895390

G. OGAWA
New Mexico Eye Associates, Albuquerque, NM

This paper describes a new adaptive optics instrument and associated diagnostic system for volumetric, *in vivo* imaging of the human lens and visual acuity characterization. The system is designed to allow one to capture simultaneous, in-focus images of the human lens at multiple "image planes." Based on the adaptation of a deformable grating originally developed for atmospheric turbulence measurements, the instrument will demonstrate an improvement over current techniques for imaging cortical, nuclear and posterior subcapsular cataracts. The system will characterize the human lens optically and will automatically produce an estimate of visual function as affected by the measured abnormalities in the lens. The process that Kestrel and DERA Malvern will use to demonstrate the key techniques for simultaneously acquiring *in vivo* lens imagery at multiple focus planes employs a surrogate lens. Eventually the camera could be considered as a replacement for most standard slit lamp instruments allowing them to be converted into a 3-D imaging system.

1 Introduction

One of the underlying problems which limits the ability to characterize cataracts accurately or to grade them quantitatively for clinical or research settings is the limited capability of today's instrumentation for imaging the human lens. At present there is no commercial system that can image simultaneously at multiple focus planes within the lens. If one is to conduct research into cataractogenesis, an important capability is a means of classifying and measuring cataractous change *in vivo*. This would allow one to use baseline measurements to assess the effect of treatment or placebo and to quantify precisely the longitudinal changes in large populations used in epidemiological studies [1, 2, 3, 4].

Currently cortical cataracts are imaged in low light, using retroillumination. Low illumination levels demand fast optics with limited depth of field. This means that when one focuses, for example, on the posterior surface of the lens to image a posterior subcapsular opacification, cortical and nuclear cataracts 0.5 mm or more anterior to the posterior lens surface will not be in focus and are not easily detected. To overcome this problem it is necessary to capture several images focused at different levels within the lens. With existing slit lamps, including Scheimpflug cameras, it is not possible to measure precisely the distance along the

optical axis. The precise location of the lens opacities is important for predicting their effect on visual function and for calculating longitudinal changes. With the 3-D imager, one can focus at a known site along the optical axis, such as the pupil or posterior lens surface, and the location of the other image planes can be calculated deterministically.

Averaging about 4mm, the thickness of the human lens along the optical axis is between 3.5mm and 5.0mm. Using the proposed design, we capture simultaneously 3 to 5 in-focus images perpendicular to the optical axis at the center of the lens and at $\pm n$ mm, where n will vary from ±0.75mm to ±2.5mm.

2 Laboratory experiments

The technical breakthrough that makes the 3-D Cataract Imaging System possible is the use of a distorted amplitude grating that can focus an optical sensing system at several different planes simultaneously [5]. Light from a white light source illuminates an object volume. The light then passes through a focusing lens onto a distorted grating where the grating is stressed to produce a parabolic shape with the level of distortion being used to determine the distance between the focusing planes and to correct for non-uniformities within the focus media. The orders generated by the grating are then reimaged onto a 2-D detector where each order represents the image at a different plane (Figure 1).

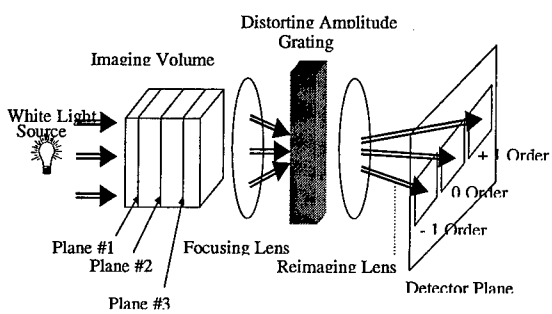

Figure 1. Distorted grating multiple imaging concept. The – 1, 0, and + 1 orders on the detector represent images of planes 1, 2 and 3.

2.1 Distorted Grating Theory

A standard one-dimensional diffraction grating consists of alternate regularly spaced strips of different transmissivity, reflectivity or optical thickness. Each diffraction order contains the same spatial information about the object as the zero order, though the non-zero orders are dispersed in wavelength.

If the grating geometry is locally distorted by a displacement of the strips in a direction perpendicular to their long axis, a phase shift is introduced in the wavefront scattered from the distorted region. The degree of phase shift is dependent on the amount of local distortion of the grating relative to its undistorted form. The level of local phase shift is related to the distortion of the grating through,

$$\phi = \frac{2\pi m \Delta}{d} \tag{1}$$

where d is the grating period, m is the diffraction order into which the wavefront is scattered and Δ is the distortion of the grating strips relative to their undistorted position, as shown in Table 1.

Table 1. Grating displacement, Δ, for phase shift, ϕ for m ± 1 and ± 2.

Phase Shift (ϕ) in +1 order	$-\pi$	$-\pi/2$	0	$\pi/2$	π
Grating Displacement (Δ)	-d/2	-d/4	0	d/4	d/2

Such a distortion of the grating produces phase shifts of equal magnitude but opposite sign in the wavefronts scattered into +1 and –1 diffraction orders and leaves the unscattered wavefront in the zero order unaltered. This 'detour-phase' principle has been used for many years for encoding computer-generated holograms [6].

In our applications the diffraction grating is designed specifically to introduce defocusing effects into the diffracted orders. A defocused optical system has a phase shift which can be represented by a quadratic function of the distance from the optical axis relative to the Gaussian reference sphere. The grating is therefore distorted as a quadratic function of distance from the optical axis of the system according to,

$$\Delta(x,y) = \frac{{}_0W_{20} d}{\lambda r^2}(x^2 + y^2) \tag{2}$$

where $\Delta(x,y)$ is a distortion in a direction perpendicular to the grating lines, x and y are Cartesian co-ordinates, d is the grating period, λ is the optical wavelength, ${}_0W_{20}$ is the degree of defocus introduced into the image formed in the +1 diffraction order (${}_0W_{20} \geq 0$) and r is the radius of the grating aperture which is centered on the optical axis. ${}_0W_{20}$ is the wavefront coefficient of defocus of the grating, equivalent to the pathlength difference introduced at the edge of the aperture between, in this case, the wavefront scattered into the +1 diffraction order and the Gaussian reference surface for that diffraction order.

The phase change imposed on the wavefronts scattered into the various diffraction orders can be calculated by combining the above equations to give,

$$\phi(x,y) = m\frac{2\pi\ {}_0W_{20}}{\lambda r^2}(x^2 + y^2) \tag{3}$$

This quadratic phase shift, introduced by the grating, leads to a different degree of defocus in all diffraction orders. Thus a series of images of the object with different defocus conditions is produced simultaneously and side-by-side on the detector in the different diffraction orders, or more usefully, in-focus images of different object planes are produced. The location and separation of the object planes that are imaged depend on the details of the optical system employed and the degree of grating distortion ($_0W_{20}$).

2.2 *Demonstrated Capability*

The technology has been validated in laboratory measurements and has shown the ability to image simultaneous three object planes separated by 2.6 cm onto one detector. A sample of these tests is shown in Figure 2. In this demonstration, three different objects at different image planes were imaged simultaneously onto one detector. The objects were a pinhole 400μm in diameter, a sheet of lens tissue, and a 175μm diameter wire. For this test an amplitude grating with two waves of quadratic distortion was used.

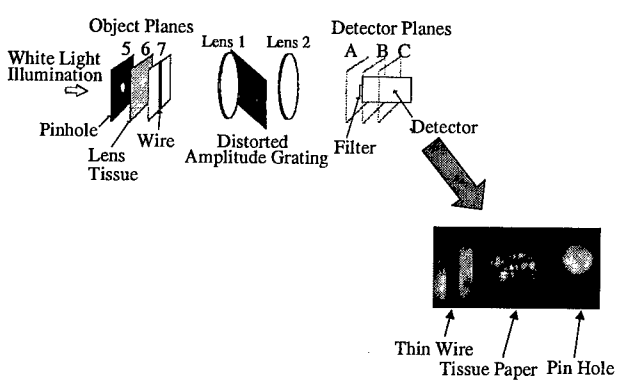

Figure 2. Laboratory demonstration of the ability of a distorted grating to image multiple object planes at one time. Note that although the objects were small, the recovered image retains all the relevant features.

2.3 *Laboratory Proof of Principle Experiment*

In the first laboratory experiments the test article will be a simulated human lens using two optical configurations. The first configuration validates the ability of the distorted grating to image multiple planes with separations similar to those found in the lens using a setup similar to that shown in Figure 3.

The imaging detector is a 1024 X 1024 pixel, 12-bit CCD camera, (SMD 1M60). The test demonstrates the application in simulated human lenses to produce volumetric images of lens opacities. Measurements will be performed to document the performance of the grating technology as illustrated in Figure 3. The test articles will have spatial resolution etchings that will allow one to calculate the spatial resolution of the system at each focus plane. Contrast sensitivity measurements will quantify the limits of the system to measure the earlier stages of lens opacities.

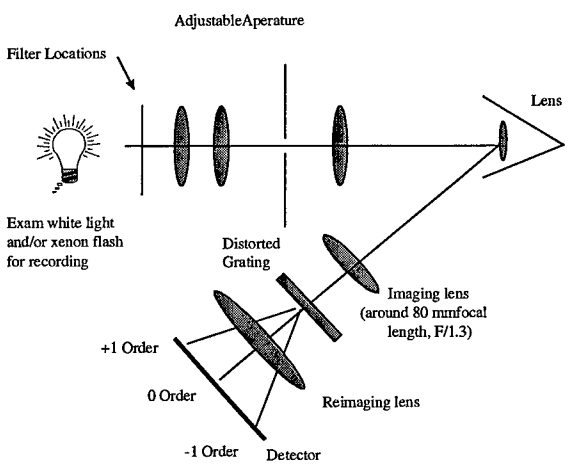

Figure 3. Simulated slit lamp optical layout.

2.4 *Simulated Lenses*

A set of simulated lens is fabricated to have different fiducial markings at the center and $\pm n$ mm from the center, n being the distance along the optical axis where a defect is introduced. Typical values for n are between ±0.75 mm and ±1.25 mm. For convenience, the test article is made using three off-the-shelf lenses with a combined magnifying power similar to the human lens. The lenses is appropriately cut, ground, marked, polished, and reassembled into a single lens, Figure 4. As noted in Figure 4, each of the object planes have a different fiducial orientation. The line thickness and spacing allows the resolution of the system to be verified for each image plane within the lens.

2.5 *Slit Lamp System Tests*

The second measurements use an optical configuration which is consistent with *in vivo* measurements of the human lens uisng a slit lamp instrument. The major difference is in the way the object planes are imaged. In this arrangement, the imaging will be accomplished using an off axis observation, Figure 3, similar to a slit lamp.

3 Conclusions

In this paper a new instrument and associated diagnostic system for volumetric, *in vivo* imaging of the human lens and visual acuity characterization are described. The system allows one to capture simultaneous, in-focus images of the human lens at multiple planes. The intent of the instrument is to improve current techniques for imaging cortical, nuclear and posterior subcapsular cataracts. The system characterizes the human lens optically and offers the opportunity to automatically produce an estimate of visual function as affected by the measured abnormalities in the lens.

4 References

1. Hockwin, O., Ahrend, M. H. J. and Bours, J., "Correlation of Scheimpflug photography of the anterior segment with biochemical analysis of the lens", *Graefes Arch Clin Exp Ophthalmol* 224:165, 1986.
2. Leske, M. C., and Sperduto, R. D., "The epidemiology of senile cataracts: A review", *Am Jour. Epidemiol*, 118:152, 1983.
3. Hiller, R. Sperduto, R. D., and Ederer, F., "Epidemiologic associations with nuclear, cortical and posterior subcapsular cataracts", *Am J Epidemiol* 124:916, 1986.
4. Hockwin, O., Eckerskorn, U., Schmidtmann, W., Dragomirescu, V., Korte, I., and Laser, H., "Epidemiological study of the association between lens cataract and case history, blood composition, and enzymes involved in lens carbohydrate metabolism", *Lens Res* 2:23, 1984.
5. Blanchard, P.M., and Greenaway, A. H. "Multiple-plane imaging with a distorted diffraction grating." In these proceedings.
6. Brown, B. R., Lohmann, A. W., 'Complex spatial filtering with binary masks', *Appl. Opt.* 5, 967-969, 1966.

VISION THROUGH A LIQUID-CRYSTAL SPATIAL LIGHT MODULATOR

LARRY N. THIBOS, XIAOFENG QI AND DONALD T. MILLER

Vision Science Group, Indiana University School of Optometry, Bloomington IN 47405, USA,

E-mail: thibos@indiana.edu

We evaluated the potential of using a liquid crystal spatial light modulator with 127 elements in an hexagonal array to correct focussing errors of the human eye. Refractive errors were induced by placing ophthalmic lenses of known power in front of the eye. A HEX-127 (Meadowlark, Inc.) spatial light modulator (SLM) was imaged in the entrance pupil of the eye and programmed to generate refractive power of the same magnitude as the ophthalmic lens but of the opposite sign. When the induced error was no greater than 1.5 diopters, the SLM satisfactorily corrected the induced error and the measured visual acuity was comparable to that when no refractive errors were present. Computations indicated that the SLM failed to correct refractive errors greater than 1.5 diopters because insufficient density of control cells under-sampled the desired wavefront. Consequently, the SLM diffracted significant amounts of energy into the higher orders, resulting in a multi-modal point spread function. The net effect was multiple duplication of the visual target in the retinal image with the overlapping of the duplicates leading to deterioration of visual acuity.

1 Introduction

Spatial light modulators (SLMs) fabricated from liquid crystals have the potential to correct defocus, astigmatism, and higher order aberrations of human eyes. The advantages of liquid crystal SLMs for ophthalmic applications include low cost, reliability, compactness, low power consumption, ease of control, and the ability to function in transmission mode.[5] The disadvantages of currently available devices include low spatial density of control cells and the need for polarized monochromatic light, although reflection-mode devices are less hampered by these factors.[2, 4] Previous experiments have demonstrated that a liquid-crystal SLM may be used successfully to correct small amounts of prismatic, focus and astigmatic errors of the eye[6] as well as higher order aberrations.[7] The emphasis of those experiments was on optical assessment of the SLM when used in conjunction with an eye. Here we evaluate the effectiveness of those corrections for improving visual performance.

2 Methods

The SLM used in this study is the Hex-127 model by Meadowlark, Inc. which contains 127 cells in an hexagonal array. The edge-to-edge distance of each cell is 1mm, with a gap of 0.036mm in between cells, which results in a fill factor of 93%. The cells are confined to a circular area 12mm in diameter. The manufacturer's calibration of retardance as a function of applied voltage, obtained at 650 nm, was assumed to apply at our test wavelength of 580 nm. At this test wavelength the maximum change of retardance was 1 wavelength, which allowed us to utilize phase wrapping to implement modulo 2π wavefront shaping.[3] The purpose of wavefront shaping was to mimic the focusing behavior of ophthalmic lenses. In ophthalmic optics the diopter is the traditional unit of refractive power, which is defined the inverse of focal length in meters. Dioptric power is related to wavefront error by the formula[6]

$$W(r) = \frac{D}{2} r^2 \tag{1}$$

where D is the power of the lens in diopters, r is the radius of the aperture delineating the wavefront in mm, and W is the retardance in μm. For example, to mimic a +1 diopter lens across a 3 mm pupil would require 1.125 μm of wavefront retardance at the pupil center compared to pupil margin.

The experimental apparatus is shown in Fig. 1. The observer viewed a Bailey Lovie eye chart[1] that was projected on a screen with a high-intensity projection monitor (Proxima 5900). A lens collimated light from the screen for transmission through an interference filter, a polarizing filter, the SLM, and a 12 mm diameter aperture to mask the active area in the SLM. A pair of relay lenses imaged the SLM in the eye's pupil plane with a magnification factor of 0.25. This reduced the image of the SLM formed in the eye's entrance pupil to 3mm in diameter.

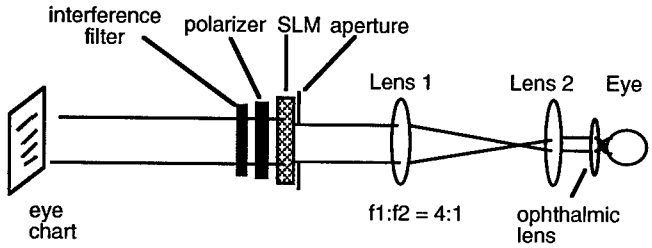

Figure 1. Schematic diagram of experimental apparatus.

Ophthalmic lenses were placed immediately in front of the eye to optimally correct focus and astigmatic refractive errors. In Experiment #1, the same refractive error was induced with either the SLM or an additional ophthalmic lens so their effects on visual acuity could be compared. In Experiment #2 the power of the SLM was of equal magnitude but opposite sign to that of the added ophthalmic lens. The observer's task was to read the letters of the eye chart, which were calibrated in terms of their angular subtense measured from the center of the eye's pupil. Target luminance as seen by the observer was 20 cd/m^2.

3 Results

The results of Experiment #1, shown in Fig. 2, indicate that visual acuity declines as a result of induced refractive error by about the same amount regardless of the source of the error. Although the absolute levels of acuity achieved by the two observers were slightly different, the level of visual performance that could be achieved when viewing through a blurring lens was nearly the same as when viewing through an SLM programmed to deliver the same amount of defocus.

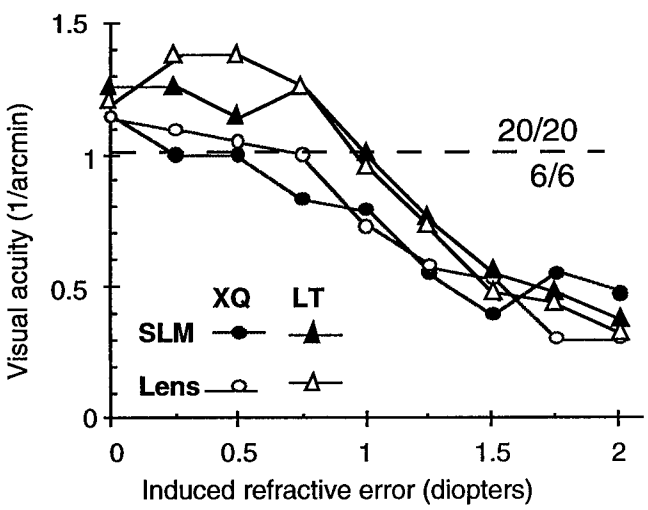

Figure 2. Effect on visual acuity of refractive error induced by SLM or lens.

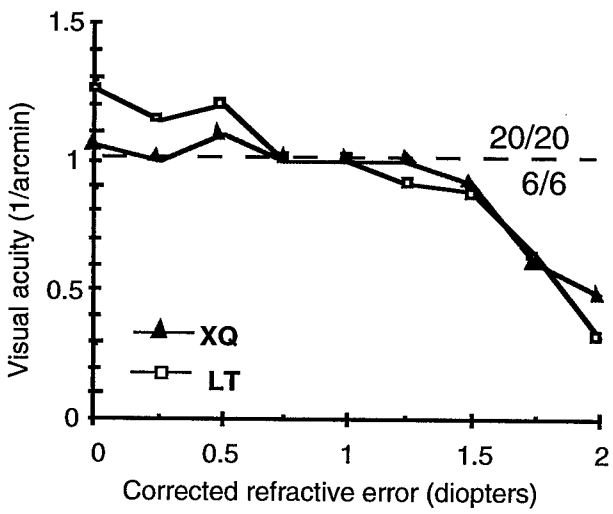

Figure 3. Effect on visual acuity of residual refractive error following correction by SLM.

The results of Experiment #2, shown in Fig. 3, indicate that the SLM effectively neutralizes the refractive error induced by the ophthalmic lens provided that the lens power is no larger than 1.5 diopters. For both subjects acuity remained near the normal level of 20/20 (6/6 metric) when the refractive error induced by the ophthalmic lens was corrected by the SLM. However, when the induced refractive error exceeded 1.5 diopters, acuity fell rapidly.

4 Discussion

To investigate the probable cause of the decline in visual acuity that occurs for larger refractive errors, we measured the point spread function (PSF) of the system by replacing the observer's eye with a model eye consisting of a video camera with a high quality photographic lens. The eye chart was replaced by a point source of light placed at the focal point of a collimating lens. This point source was the 25 μm pinhole of a conventional spatial filter illuminated by 580 nm light from a monochromator. As in the previous experiments, an ophthalmic lens was used to induce a refractive error in the model eye and this error was corrected by the SLM. The recorded image of the pinhole for a series of induced refractive errors is shown in Fig. 4. Also shown are computer simulations of the SLM when programmed to

correct the induced error. These results show that when the SLM is programmed to produce larger amounts of focusing power the PSF becomes multi-modal as more energy is diffracted into the higher orders. These effects may be traced to undersampling of the desired wavefront due to the low spatial density of the SLM.

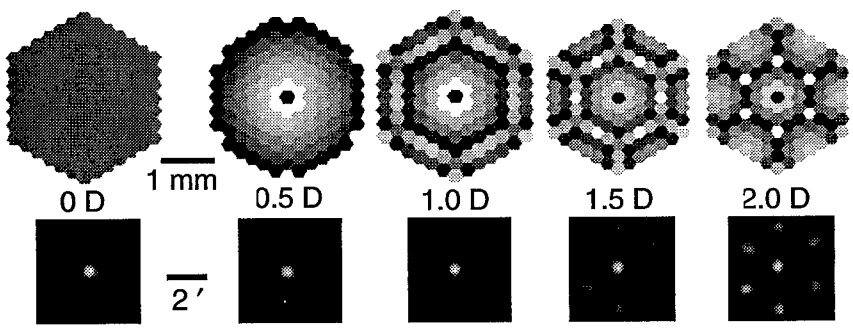

Figure 4. Point spread functions of model eye (bottom row) when refractive error is corrected by the SLM (upper row).

The effect of a multimodal PSF on the retinal image of the eye chart is shown in Fig. 5. Multiple copies of the image are present, each displaced slightly according to the hexagonal pattern of spots in the PSF. For low power conditions the secondary images are of low contrast and do not interfere greatly with the visibility of the primary image. However, as the SLM power increases so does the contrast of the secondary images and eventually these overlapping secondary images have a strong masking effect which severely limits visual performance.

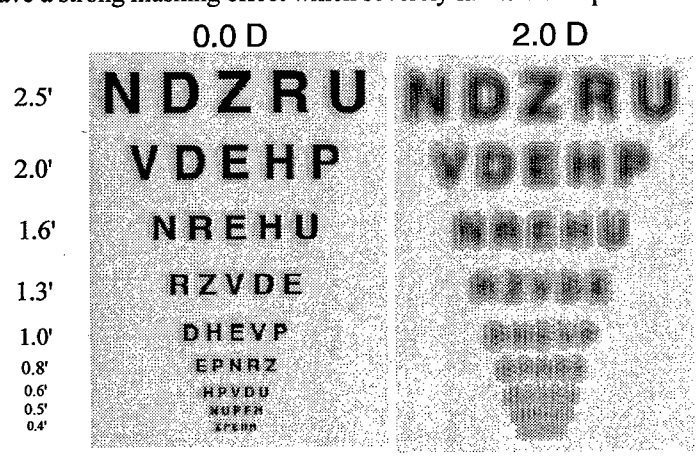

Figure 5. Simulated retinal image of eye chart.

5 References

1. I. Bailey and J. Lovie, (1976). New design principles for visual acuity letter charts. *Am. J. Optom. & Physiol Opt.*, **53**, 740-745.

2. D.J. Cho, S.T. Thurman, J.T. Donner and G.M. Morris, (1998). Characteristics of a 128x128 liquid-crystal spatial light modulator for wave-front generation. *Opt. Lett.*, **23**, 969-971.

3. A. Glindemann, (1994). Improved performance of adaptive optics in the visible. *J. Opt. Soc. Am. A*, **11**, 1370-1375.

4. G.D. Love, (1993). Liquid-crystal phase modulator for unpolarized light. *Appl. Opt.*, **32**, 2222-2223.

5. G.D. Love, J.V. Major and A. Purvis, (1994). Liquid-crystal prisms for tip-tilt adaptive optics. *Opt. Lett.*, **19**, 1170-1172.

6. L.N. Thibos and A. Bradley, (1997). Use of liquid-crystal adaptive-optics to alter the refractive state of the eye. *Optom. Vis. Sci.*, **74**, 581-587.

7. F. Vargas-Martin, P.M. Prieto and P. Artal, (1998). Correction of the aberrations in the human eye with a liquid-crystal spatial light modulator: limits to performance. *J. Opt. Soc. Am. A*, **15**, 2552-2562.

REQUIREMENTS FOR SEGMENTED SPATIAL LIGHT MODULATORS FOR DIFFRACTION-LIMITED IMAGING THROUGH ABERRATED EYES

DONALD T. MILLER, XIN HONG AND LARRY N. THIBOS

Vision Science Group, Indiana University School of Optometry, Bloomington IN 47405, USA, E-mail: dtmiller@indiana.edu

Spatial light modulators (SLMs) have not yet provided diffraction-limited imaging through the human eye's ocular media. To guide future improvements in SLM designs that might enable such imaging, we have modeled the performance of hexagonally- and square-packed configurations of segmented SLMs in conjunction with measured wave aberration data of normal human eyes. The model included the effects of pupil size, number and arrangement of actuators, and mono- and poly-chromatic light. Results indicate that diffraction-limited performance should be attainable for medium sized pupils with existing, commercial SLMs. The required segment density was found to be substantially higher at the pupil's edge than at its center. In polychromatic light, SLM performance at large pupil sizes was found to be limited more by phase wrapping than material dispersion of the corrector. Both, however, were substantially less degrading than the naturally occurring longitudinal chromatic aberration of the human eye.

1 Introduction

Recently, adaptive optics[1] has been used to correct the wave aberrations of the living human eye. The first attempt employed a 13-actuator segmented mirror[2]. Correction was limited to the astigmatism in one subject's eye, based on a conventional prescription. Correction to higher-order aberrations was first realized with a 37-actuator deformable mirror coupled to a Hartmann-Shack wavefront sensor[3]. Liquid crystal spatial light modulators (LC-SLMs) have also been investigated for correction of prism, defocus and astigmatism[4], as well as the full wave aberrations of the eye[5]. Membrane mirrors are just beginning to be explored[6]. None of these corrector devices, however, have yet to provide diffraction-limited imaging in the human eye for large pupils. More over, the characteristics of the correcting device, such as actuator number, that are required to achieve diffraction-limited imaging have not been determined. This precludes optimally matching corrector performance and cost to that required of a particular imaging task in the eye. In addition, lack of corrector requirements has stymied improvements in corrector design that could enable diffraction-limited imaging. To address this problem for segmented SLMs, we have modeled the SLMs' performance in conjunction with measured wave aberration data of normal human eyes.

2 Methods

At present, no analytic model exists for characterizing the impact of ocular aberrations on image quality. This is unlike the situation for imaging through atmospheric turbulence, which has well developed theoretical models that are rooted in the fundamental mechanisms of turbulence. Without such models available, our approach was to simulate the imaging process through the eye and SLM using measured wave aberration data of normal human eyes in conjunction with an optical model for segmented SLMs. The simulation included the effects of pupil size D (0 to 8 mm); facet number (0 to 72 facets across pupil diameter); actuator arrangement (hexagonally- and square-packing); and mono- and polychromatic light (0.4 to 1.0 μm). The test object for the simulation was taken to be a point source, and the Strehl ratio was used as the figure of merit. The Strehl ratio is defined as the ratio of the light intensity at the peak of the diffraction pattern of an aberrated image to that at the peak of an aberration-free image. Generally, an optical system is considered to be diffraction-limited if it has a Strehl ratio > 0.8.

A Hartmann-Shack wavefront sensor using a 632.8 nm HeNe laser measured the local wavefront slopes at 177 locations across a 6 mm pupil in 12 subjects with spectacle correction in place. The lowest 66 Zernike modes of the wave aberration were reconstructed from the slope measurements. All subjects had normal corrected vision and ranged from 12 to 50 years of age. The subjects' line of sight was centered along the optical axis of the sensor with the aid of a dental impression attached to an x-y-z translation stage, which held the subject's head fixed. The subject fixated on a white-light target. No topical drugs were administered. Measurements typically consisted of illuminating the eye for 0.2 seconds with a total exposure energy of 2 μjoules, which is about 200 times below the ANSI maximum permissible exposure[7].

The SLM model was designed to be representative of both reflective and transmissive devices, such as segmented micromirrors and LC arrays, respectively. The model consisted of a two-dimensional array of segmented facets with each facet restricted to modulating only the piston component of the local wavefront. Facet inter-spacing was r_s. The facets completely covered the circular pupil of the imaging system and provided a 100% fill factor (i.e. no gaps between adjacent facets). Facet number was specified by the number of facets across the pupil diameter, D/r_s. The phase profile of the SLM, for correcting a specific aberrated wavefront, was determined by setting the phase of each facet to minus the average wavefront phase incident on the facet[8].

To evaluate SLM performance in polychromatic light, the simulation included the effects of material dispersion and phase wrapping in the SLM, and the longitudinal chromatic aberration (LCA) of the eye. Transverse chromatic aberration was assumed negligible as alignment was taken to be along the eye's visual axis.

3 Aberration correction in monochromatic light

Figure 2 shows the corrected Strehl for hexagonally- and square-packed SLM arrays as a function of D/r_s for a 6 mm pupil and 0.6 μm wavelength. All four curves are of similar shape. The Strehl rises sharply at low facet numbers ($D/r_s < 12$) followed by a gradual rise converging to one at larger values. The figure shows the pronounced debilitating effect of the residual astigmatism and defocus, left uncorrected by trial lenses. Average values for defocus and astigmatism across the 12 subjects were 0.09 and 0.15 diopters, respectively. A corrected Strehl of 0.8 required four times more facets with astigmatism and defocus present than without. For a Strehl of 0.8, D/r_s is predicted to be slightly higher for the square configuration (21.7 and 49.2 square facets versus 20.1 and 45.0 hexagonal facets for the two astigmatic and defocus cases). This is not unexpected as facet density is lower for the square array for the same D/r_s value. The total number of facets across the whole pupil, however, is found to be essentially the same for the two configurations (440 and 1,860 hex facets compared to 460 and 1,890 square facets). This is in agreement with the general rule that wavefront correction is primarily determined by the total degrees of freedom of the SLM with other factors, such as facet arrangement, playing a secondary role.

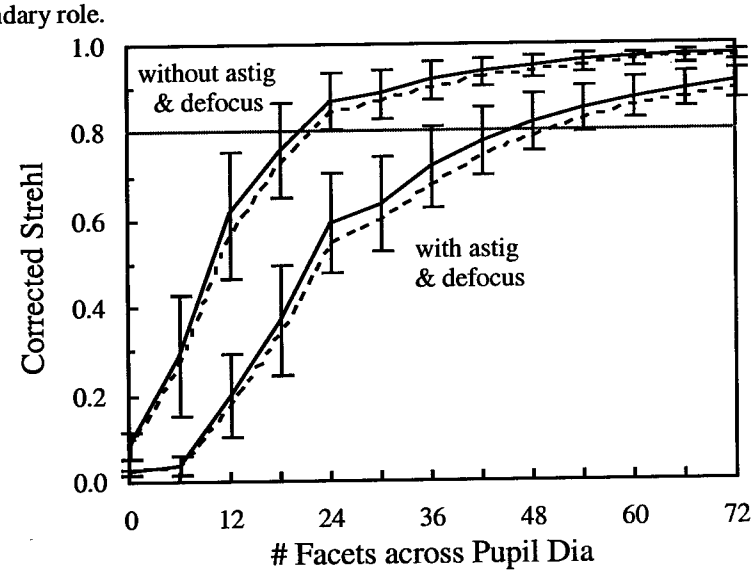

Figure 2. Corrected Strehl ratio for (solid) hexagonally- and (dashed) square-packed SLM configurations as a function of facet number. Pupil diameter and λ were set to 6 mm and 0.6 μm, respectively. Top two curves have defocus and astigmatism removed. Bottom two curves contain the residual amount of defocus and astigmatism uncorrected by trial lenses. Error bars represent ±1 standard deviation across the 12 subjects.

Pupil size and wavelength are two key parameters that can strongly influence SLM performance. To guide the design of SLMs for use with the eye at various pupil sizes and wavelengths, simulations were conducted to predict SLM performance along two orthogonal axes in D-λ space. The two axes chosen were $\lambda = 0.6$ μm and $D = 6$ mm. Figure 3 shows the number of facets needed to achieve a corrected Strehl of 0.8 along these two axes. At small to medium pupil diameters (< 4 mm), D/r_s need not be larger than 15, which can be realized with existing, commercial devices. Fitting the simulation results to a third-order polynomial, allows D/r_s to be calculated at any pupil diameter ranging from zero to the

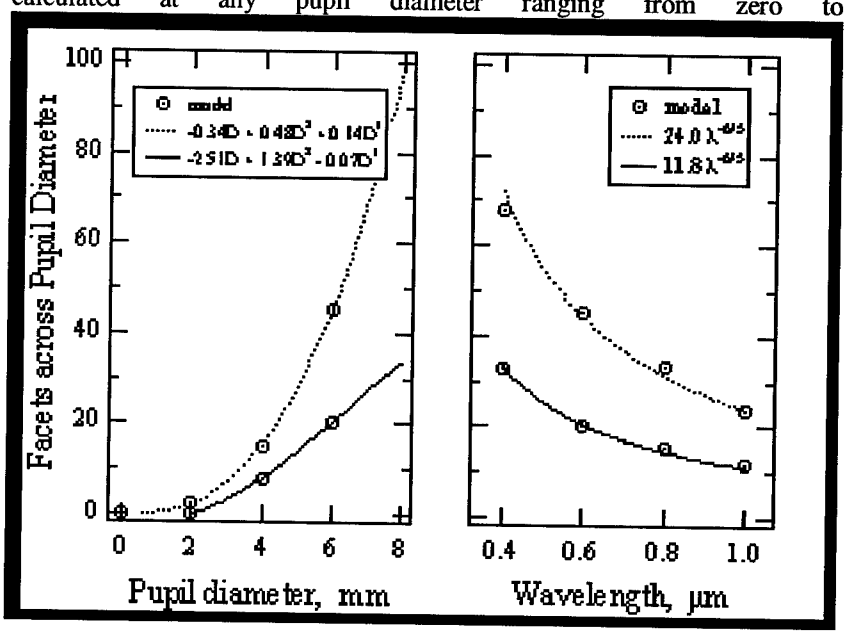

Figure 3. Number of facets required to achieve diffraction-limited imaging (Strehl = 0.8) along two orthogonal axes in D–λ space. The two axes are (left plot) $\lambda = 0.6$ μm and (right plot) $D = 6$ mm. Simulation results were fit to $\lambda^{-6/5}$ and third-order polynomial functions.

maximum physiological size of 8 mm. Interestingly, the polynomial curve is not linear, which it would be for the case of Kolmogorov turbulence. This implies that if a Fried's parameter could be developed for the human eye, it would be dependent on pupil position with a larger Fried's parameter near the pupil center and progressively smaller values at increasingly larger pupil eccentricities. This suggests non-uniform facet dimensions with larger facets in the middle and smaller at the edge. The second plot of Figure 3 shows the dependence of D/r_s with wavelength. As expected, wavefront correction at shorter wavelengths requires more facets than at longer wavelengths to achieve the same imaging performance. Unexpected was the close fit of the required correction to a $\lambda^{-6/5}$ curve, which is the wavelength

dependence of D/r_s for Kolmogorov turbulence. A slightly better fit was achieved with an exponential function.

It is not known if D/r_s for the eye can be mathematically expressed as separate D and λ functions, i.e. $D/r_s = F_1(D)*F_2(\lambda)$, as is the case for Kolmogorov turbulence. If true, the fitted curves along the two orthogonal axes in Figure 3 could be combined to determine D/r_s for any D and λ combination. As an initial attempt to assess the legitimacy of $F_1(D)*F_2(\lambda)$, we obtained estimates of D/r_s using both the simulation and $F_1(D)*F_2(\lambda)$ expression for several D and λ combinations. None of the D-λ combinations coincided with the D = 6 mm or λ = 0.6 mm axes. The percent difference between estimates was found to be no greater than 20%, lending support for separate D and λ functions for at least the D–λ combinations considered here.

4 Aberration correction in polychromatic light

Material dispersion and phase wrapping are the two primary characteristics of SLMs that reduce SLM performance in polychromatic light. The induced dispersion in liquid crystal arrays is that of the liquid crystal material itself. The most commonly used liquid crystal material in LC-SLMs is E-7 and was therefore chosen as the representative material in the simulation. Mirror correctors have no dispersion – an advantage of these devices. Phase wrapping was restricted to modulo 2π as it is often required in commercial SLMs. It also provides the worst-case scenario as 2π wrapping represents the smallest phase retardation that still allows full correction at the design wavelength.

Figure 4 shows the performance of four types of SLMs used to correct the wave aberrations of the 12 subjects. The corrector types correspond to the four possible combinations of dispersion and phase wrapping. The effect of facet number was eliminated by reducing facet size to a single pixel. As shown in Figure 4, perfect correction occurred for the SLM type having no phase wrapping and no dispersion. An example would be a segmented mirror with actuator stroke greater than the peak-to-valley of all 12 aberrated wavefronts. Introducing the liquid crystal material E-7 caused the corrected Strehl to fall sharply at wavelengths below 0.55 microns. A gradual monotonic decrease occurred at longer wavelengths. 2π phase wrapping present in the final two corrector types was found to be the clear limiting factor that restricted spectral range, reducing the full width at half height (FWHH) of the corrected Strehl to about 125 nm. However, this restriction is only important if the spectral performance of the human eye is wider. The solid curve in Figure 7 reflects the performance of the diffraction-limited eye corrupted only by the typical amount of LCA. The FWHH of this curve is only 20 nm, five times less than that of a phase-wrapped SLM.

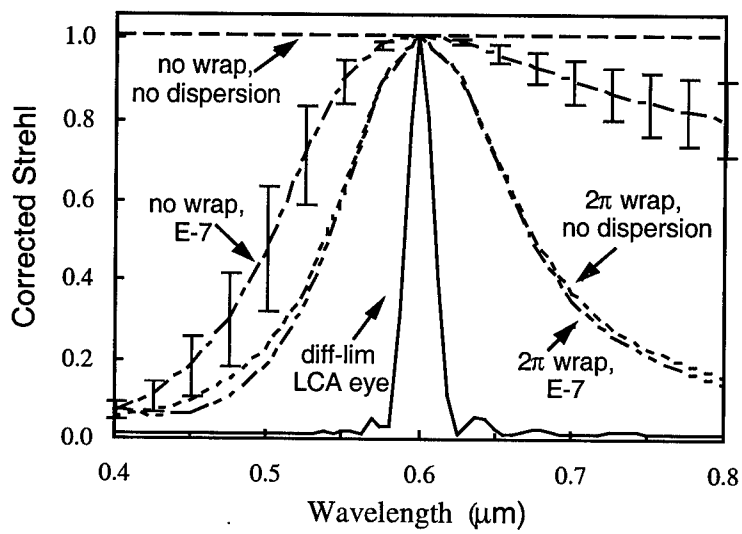

Figure 4. SLM performance in polychromatic light. The dashed curves represent the performance of SLM types that correspond to the four possible combinations of dispersion and phase wrapping. Dispersion was that of the liquid crystal material E-7. Phase wrapping was modulo 2π. The design wavelength was 0.6 μm and the pupil size 6 mm. The solid curve is the performance of the diffraction-limited eye corrupted only by longitudinal chromatic aberration.

References

1. R. K. Tyson, *Principles of Adaptive Optics* (Academic Press, New York, 1998).
2. A. W. Dreher, J. F. Bille, and R. N. Weinreb, "Active optical depth resolution improvement of the laser tomographic scanner," *Appl. Opt.* **24**, 804-808 (1989).
3. J. Liang, D. R. Williams, and D. T. Miller, "Supernormal vision and high resolution retinal imaging through adaptive optics," *J. Opt. Soc. Am. A* **14**, 2884-2892 (1997).
4. L. N. Thibos and A. Bradley, "Use of liquid-crystal adaptive optics to alter the refractive state of the eye," *Optom. Vision Sci.* **74**, 581-587 (1997).
5. F. Vargas-Martin, P. M. Prieto, and P. Artal, "Correction of the aberrations in the human eye with a liquid-crystal spatial light modulator: limits to performance," *J. Opt. Soc. Am. A* **15**, 2552-2562 (1998).
6. L. Zhu, P-C Sun, D-U Bartsch, W. R. Freeman, and Y. Fainman, "Adaptive control of a micromachined continuous membrane deformable mirror for aberration compensation," *Appl. Opt.* **38**, 168-176 (1999).
7. ANSI, *American National Standard for the Safe Use of Lasers, ANSI Z136.1-1993* (Laser Institute of America, Orlando, FL, 1993).
8. G. D. Love, "Wave-front correction and production of Zernike modes with a liquid-crystal spatial light modulator," *Appl. Opt.* **36**, 1517-1534 (1997).

MEASUREMENT OF THE EYE'S ABERRATIONS IN VIVO

M. GLANC, H. GARDETTE, K. NAOUN, B. BIANCHI, J.F. LE GARGASSON
Laboratoire de Biophysique de la Bision–Université Paris 7-France

E. GENDRON, P. LENA.
Département de Recherche Spatiale–Observatoire de Paris/Meudon-Université Paris7-France

An optical system used to measure aberrations in human eyes is proposed. A monochromatic light spot illuminates the retina and a Shack-Hartmann wave-front sensor analyses the backscattered light. The wave-front analysis is based on a modal wavefront estimation, using the Zernike polynomials. An adjustable diaphragm allows to change the diameter of the incoming probe-beam. With this experiment, it is shown that one can obtain in vivo a relatively repeatable measurement of the astigmatism and defocus of the eye.

1 Introduction

The possibility of measuring the eye's aberrations opens up many ways in physiological optics: for instance, the study of the objective improvement of vision after refractive surgery. However, our work is in keeping with a more general plan: high-resolution imaging of the retina by using adaptive optics. Before correcting the eye's aberrations, it seems to be interesting, if not necessary, to measure them correctly, which is the aim of the present paper. An autorefracto-keratometer is used to validate Shack-Hartmann (SH) measurements with two different sizes of beam.

2 Experimental setup

We illuminate the retina with a monochromatic light spot, and analyse the backscattered light with a SH wavefront sensor using a Zernike polynomial decomposition, in order to derive the overall aberrations of the eye. The following figure shows the experimental setup. The exit pupil of the eye is conjugated with the array of microlenses. The laser beam (632.8 nm) is spatially filtered and expanded into a plane wave. An iris is used to control the size of the illuminated pupil. The parallel beam is brought to focus on the retina. To stabilize both the eye orientation and accommodation, a target at infinity can be provided to the patient through a point source at lens L2 focus. The backscattered light forms a distorted wavefront at

the eye's exit. The incoming light is linearly polarized and a beamsplitter cube keeps only the backscattered perpendicular polarization. A final analyser rejects any additional scattered light. The SH pattern is received by a high-sensitivity CCD camera (Hi-SIS22) with 12 electrons rms read-out-noise.

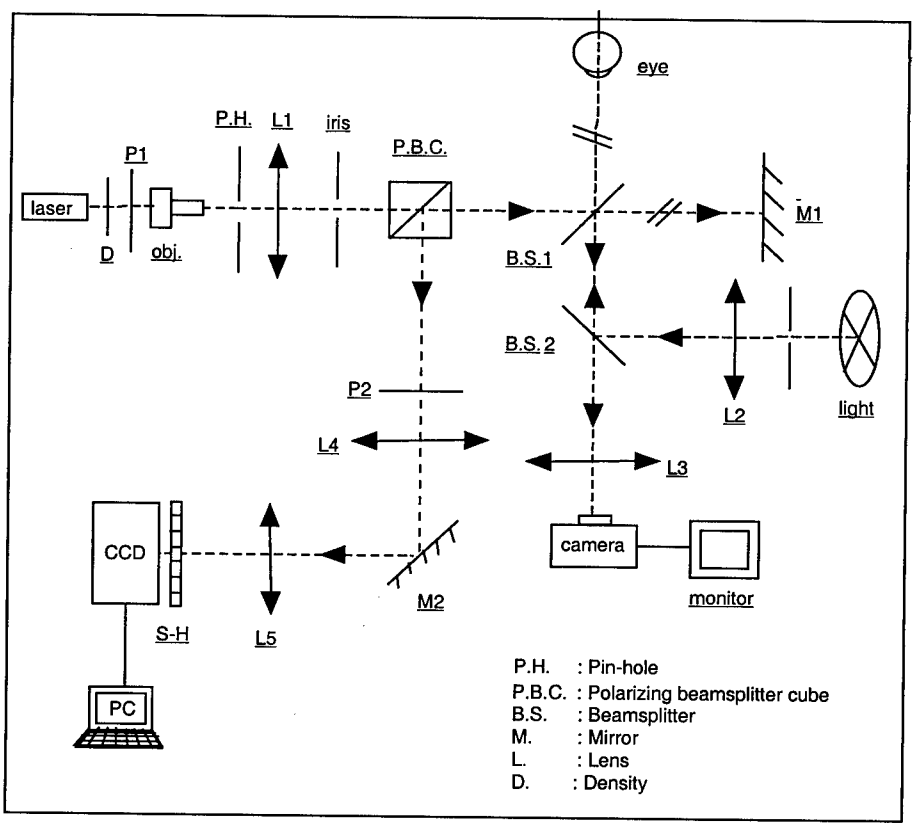

OPTICAL DESIGN

The wave front analysis is based on a modal wave front estimation. The normal difference to the perfect wave is assumed to be expressed by : $\Delta h = \sum_i a_i \cdot Z_i$ (1),

where Z_i is the ith Zernike polynomial, a_i is the ith Zernike coefficient. The variation of Δh along x and y gives us the local angles θ_x and θ_y :

$$\tan(\theta_x) \approx \theta_x = \frac{\Delta h(x+dx,y) - \Delta h(x,y)}{dx} = \frac{\partial(\Delta h)}{\partial x}$$

In the focal plane of each microlens m, we observe a mean shift of the light spots center of gravity:

$$\delta x_m = f \cdot \langle \theta_x \rangle_m = f \cdot \left\langle \sum_i a_i \cdot \frac{\partial Z_i}{\partial x} \right\rangle_m \text{ and } \delta y_m = f \cdot \langle \theta_y \rangle_m = f \cdot \left\langle \sum_i a_i \cdot \frac{\partial Z_i}{\partial y} \right\rangle_m$$

f is the micro-lenses' focal length.
After some mathematical developments, we obtain :

$$[\delta] = f \cdot [\Delta Z] \cdot [a] \quad (1)$$

with

$$[\delta] = \begin{bmatrix} \delta x_1 \\ \delta y_1 \\ \delta x_2 \\ \delta y_2 \\ \vdots \\ \delta y_m \end{bmatrix} \text{ and } [\Delta Z] = \begin{bmatrix} \langle \partial Z_1 / \partial x \rangle & \langle \partial Z_2 / \partial x \rangle & \cdots & \cdots \\ \langle \partial Z_1 / \partial y \rangle & \langle \partial Z_2 / \partial y \rangle & & \\ \langle \partial Z_1 / \partial x \rangle & \langle \partial Z_2 / \partial x \rangle & & \\ \vdots & & & \\ \langle \partial Z_1 / \partial y \rangle & \cdots & \cdots & \langle \partial Z_k / \partial y \rangle \end{bmatrix} \text{ and } [a] = \begin{bmatrix} a_1 \\ a_2 \\ \vdots \\ a_k \end{bmatrix}$$

By inversion of the relation (1) (svd method), we get the Zernike a_i coefficients which characterize the different aberrations :

$$[a] = \frac{1}{f} \cdot [\Delta Z] \cdot [\delta] \quad (2)$$

The software we developed calculates the matrix [ΔZ], and from the measurements of the spots shifts on the CCD (matrix $[\delta]$), we obtain $[a]$.
In order to recover exclusively the Zernike coefficients corresponding to the eye's aberrations, we have to subtract the aberrations introduced by the optical components of the setup : to do so, we put a flat mirror in the eye's place and evaluate the Zernike coefficients derived from the so acquired Shack-Hartmann picture.
Three almost emmetropic eyes were assessed: K.N. 31 years old, D. F. 31 years old, I.N. 28 years old.
We did the experiments in a dark room. The pupils of the subjects were dilated with Tropicanamide® (2 drops in each eye), so their accomodation was partially inhibited and the resulting pupil diameter was about 8 mm. The maximum power reaching the eye was 1 μW.

In the first series of experiments, the diameter of the laser beam entering the eye was 8 mm (so called double pass procedure, DP). The acquisition time of the picture on the CCD was about 400 ms.
In the second series, the diameter of the beam was 1 mm (so called simple pass, SP), and the acquisition time was 1 s.

3 Results

We obtained the 8 first Zernike coefficients for each eye. Since the coefficients a_1 and a_2 represent the overall tilt of the wavefront, they are of no importance to the optical performance and can be ignored. We further derived the values of defocus and astigmatism in diopters (dt) and compared them with the clinical refraction correction determined on the same subject for small pupil size with an autorefracto-keratometer (A.R.K.). The results are shown in the following tables :

Table 1. Comparison of defocus and astigmatism (SH and A.R.K.)

	K.N.					
	SH				**A.R.K.**	
	RE (Right eye)		LE (Left eye)		RE	LE
	DP	SP	DP	SP		
Def(dt)	0	-0.3	-0.5	-0.3	-0.25	0.5
Cyl(dt)	0.3	0.15	0.3	<0.1	0.5	0
Axis(°)	68	100	94	96	90	0
	D.F.					
	SH				**A.R.K.**	
	RE		LE		RE	LE
	DP	SP	DP	SP		
Defocus	0.8	0.4	0.8	0.6	0.75	1
Cylinder	<0.1	<0.15	<0.1	0.15	0	0
Axis	60	100	90	65	0	0
	I.N.					
	SH				**A.R.K.**	
	RE		LE		RE	LE
	DP	SP	DP	SP		
Defoc	0.50	0.35	0.40	<0.10	0.75	0.25

us						
Cylinder	0.20	0.15	0.25	0.20	0	0.25
Axis	88	86	100	55	0	165

Table 2. The 8 first Zernike polynomials (ρ and ϕ are the normalized polar coordinates of a point in the plane of the exit pupil)

Z	Polynomials	names
3	$2\rho^2 - 1$	Focus
4	$\rho^2 \cos 2\phi$	Astigmatism
5	$\rho^2 \sin 2\phi$	Astigmatism
6	$(3\rho^2 - 2)\rho \cos\phi$	Coma
7	$(3\rho^2 - 2)\rho \sin\phi$	Coma
8	$6\rho^4 - 6\rho^2 + 1$	3rd order spherical aberration

Table 3. Higher order aberration (SH derivation)

Zernike (μm)	K.N.			
	DP		SP	
	RE	LE	RE	LE
Z_3	0.02	-0.66	-1.11	-1.11
Z_4	-1.14	-0.88	-0.34	-0.12
Z_5	0.25	-0.66	-0.45	-0.11
Z_6	0.05	varying	varying	varying
Z_7	-0.21	varying	0.09	varying
Z_8	-0.21	-1.01	-0.21	-0.50
	D.F.			
	DP		SP	
	RE	LE	RE	LE
Z_3	2.92	3.01	1.53	2.20
Z_4	varying	0.13	-0.12	-1.06
Z_5	0.92	-0.25	-0.30	0.44
Z_6	0.37	0.55	varying	0.07
Z_7	0.32	-0.32	-0.09	0.44
Z_8	0.46	0.57	0	0.02
	I.N.			
	DP		SP	

	RE	LE	RE	LE
Z_3	1.76	1.32	1.41	0.21
Z_4	0.80	0.76	-0.55	0.76
Z_5	0.41	0.94	-0.23	0.74
Z_6	varying	varying	varying	varying
Z_7	0.20	varying	0.18	varying
Z_8	0.28	-0.02	0.32	-0.32

NB : each value is the average of results derived from 4 samples.

Two typical Shack-Hartmann patterns obtained:

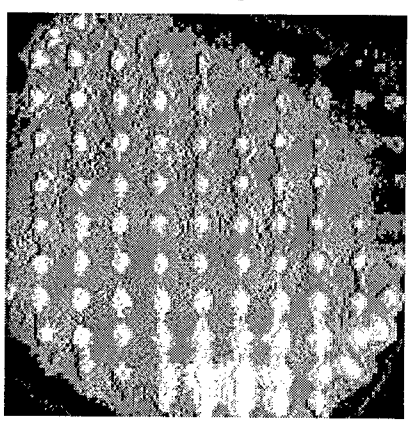

Right eye in DP
for subject D.F.

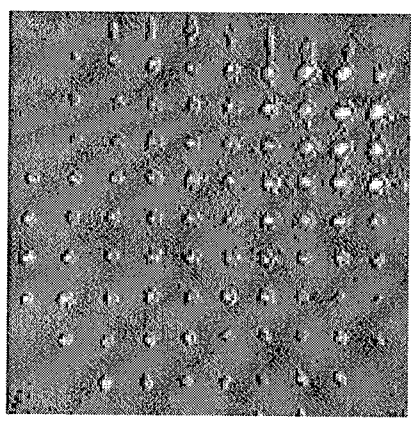

Right eye in SP
for subject D.F.

4 Discussion

In the first table, the good agreement between the three sets of values for astigmatism seems to demonstrate a satisfactory behavior for the whole procedure. Our results are in accordance with those of Liang [1] with the following exceptions :
-The repeatability in our experiments is worse. It is probably due to the fact that their images were preprocessed before being analysed.
-Liang and al used 5 Zernike polynomials to split the wave aberration, whereas we use 8.
The autorefractokeratometer seems to be less sensitive than the Shack-Hartmann wavefront sensor in the evaluation of astigmatism. The values of defocus are similar with both instruments but are always a bit smaller for the Shack-Hartmann. An

offset of about 0,3 diopters exists between the derived defocus and the clinical one. It could be due to a slight misfit between the physical size of the lenslet array and the size assumed in the software (which requires an integer truncation).

In the third table, we note that the differences between simple and double pass are the lowest for defocus. For this aberration (Z_3), the ratio SP coefficient /DP coefficient is between 0.15 to 1.68 (with a bad value of –55.5). This fact shows that the difference between simple and double pass procedure for the estimation of the defocus coefficient is quite small.

If the retina were behaving like a mirror, most of the 8 first Zernike coefficients would be cancelled in the two passes (as mentioned by Liang). In practice, it is not true: the coma coefficient especially is even varying a lot. This is probably due to difficulties in properly centering the eye (centering problems generate coma), and to the irregular and granular structure of the fundus of the eye (a phase structure information could add up to the phase aberration information).

The similar diameter of the spots in both series of experiments (SP and DP) proves that the limiting constraint is not the diffraction but the statical aberrations and the inhomogeneities of the eye. J.C. He and al introduce their article by mentioning the same remark [2].

The correct display of the signal (spots) shows that the power entering the eyes is high enough for good signal-to-noise ratio and all lenslets are illuminated (9x9 pattern). However, some characteristics of the SH pictures restrict the conclusions that can be drawn from those first series of experiments. From now on, we have to determine which elements can be improved and which represent an intrinsic limit of the method.

- Individual sub-pupils images present a significant uniform background, probably due to incomplete rejection of cornea reflection and/or scattered light.
- The illumination of the sub-pupils is clearly inhomogeneous. This phenomenon appears clearly on the pictures obtained by the double pass method. It could be related to the retina polarizing properties (Haidinger's brushes), or to the surface state at the focusing point (anisotropic scattering pattern), or be a manifestation of the Stiles Crawford effect.

The pupil's outline seems to be very irregular and bright, especially in a zone corresponding to the pupil's lower part ; this could be due to the lachrymal river as it is located at the same place.

5 Future development

This experiment is a first step in the development of a closed-loop adaptive system to image the retina, using a CILAS 13-actuators correcting mirror. But we have to find a way to improve the repeatability of the measurements, otherwise it will be difficult to integrate the closed-loop in the current design.

6 Acknowledgments

We thank Françoise GEX and all her team at the Observatoire de Paris for the design and the setting up of the micro-lenses.
We express a deep gratitude to the company CILAS and particularly to David WAFLARD, Pascal JAGOUREL and Jean-Louis LOUREAU for their technical supports, helps and their motivating contribution to this research.

This work is supported by CILAS, by the Région Paris Ile de France, and by the French Ministère de l'Education nationale, de la recherche et de la technologie through the Observatoire de Paris. M. GLANC (also at Observatoire de Paris, DESPA) is supported by a CNRS-BDI grant.

References

1. J.Liang, B.Grimm, S.Goelz and J.F. Bille, "Objective measurement of wave aberrations of the human eye with the use of a Hartmann-Shack wave-front sensor" , J.Opt.Soc.Am.A, Vol.11, No.7, July 1994.
2. J.C. He, S. Marcos, R.H. Webb, S.A. Burns, "Measurement of the wave-front aberration of the eye by a fast psychophysical procedure", J.Opt.Soc.Am.A, Vol.15, No.9, September 1998

Microscopy

ADAPTIVE ABERRATION CORRECTION IN ULTRAFAST SCANNING MULTIPHOTON CONFOCAL MICROSCOPY

O.ALBERT, L.SHERMAN, M.H.MEUNIER, G.MOUROU, AND T.NORRIS
NSF Center for Ultrafast Optical Science, University of Michigan, 1006 IST Building, 2200 Bonisteel Bd, Ann Arbor MI 48109, USA
E-mail: aolivier@eecs.umich.edu, tnorris@eecs.umich.edu

G.VDOVIN
Departement of Electronic Instrumentation, Technical University of Delf, P.O. box 5031, 2600 GA Delf, Netherland
E-mail: gleb@guernsey.et.tudelft.nl

Multi-photon scanning confocal microscopy with extremely short optical pulses (10fs) requires reflective optics, and ultimately requires control of the spatial wavefront in order to achieve diffraction-limited performance. We have demonstrated the use of a deformable mirror to adaptively optimize the focusing of a 10fs pulse in a scanning confocal microscope. We optimize the second harmonic generation or the two photon fluorescence signal from our sample using a feedback loop based on a genetic algorithm. To improve the speed of the convergence of our algorithm we use a Zernike orthogonal basis to control the deformable mirror.

1 Introduction

Two-photon fluorescence microscope has improved the resolution of confocal microscopy [1,2]. 2D and 3D imaging with these systems are extensively used for biological and medical research. Important issues for those systems include the time needed to get an image, and whether or not it is possible to scan the sample in front of the microscope. Laser scanning, instead of sample scanning, allows a faster scanning speed and avoids moving the sample. The laser scanning imaging area is also limited by off-axis aberrations induced by the objective. A conventional way to correct for aberrations is the use of plan objectives that are specially designed for this application.

We propose a setup that uses an uncorrected objective coupled with an adaptive optic system to correct for off-axis aberrations. Taking advantage of the latest development in adaptive optical materials, we use a computer controlled deformable mirror as a wavefront shaper for our system.

As a demonstration system, our objective is a large aperture f:1 parabolic mirror allowing a $1\mu m$ pixel resolution and no chromatic aberration. We have experimentally demonstrated an increase of the scanning area of about 10 times allowing an image area of 150×150 $1\mu m$ pixels.

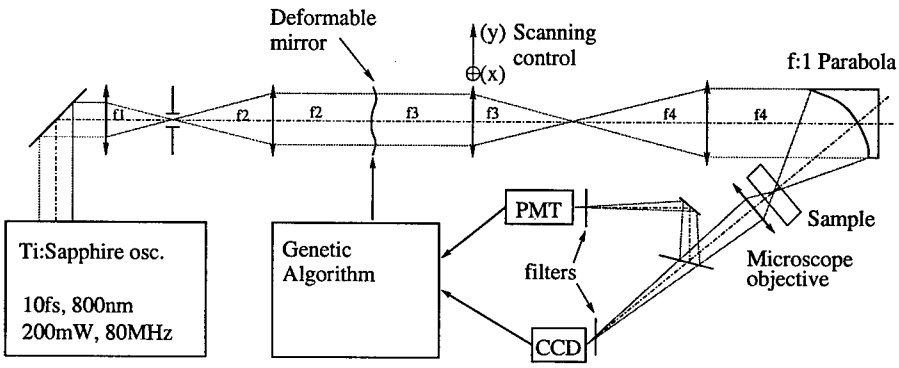

Figure 1. The experimental setup.

2 Experimental setup

The experimental setup is sketched in Fig. 1. The two-photon excitation wavelength is 800nm. It is provided by a Ti:Sapphire laser oscillator of 10fs duration and a repetition rate of 80MHz. The beam is expanded, using a telescope (f_1,f_2), to match the size of the deformable mirror. It is then expanded again to match the 25.4mm diameter of the f:1 parabola. The second telescope (f_3,f_4) is also used for the scanning.

For this demonstration we have chosen a large aperture f:1 parabola for the objective. Being a mirror, the parabola is free of chromatic aberration. The parabola is also well suited for femtosecond pulses as it does not affect the chirp of the pulse.

The deformable mirror is a micromachined silicon membrane mirror with 37 electrostatic actuators [3].The shape of the mirror is computer driven, using a home-made Labview code. The deformable mirror is imaged on the parabola by the (f_3,f_4) telescope, so that the wavefront change introduce by the deformation of the mirror will correspond to a wavefront change on the parabola, without amplitude modulation. Then, the parabola focuses the pulses with corrected wavefront in the sample, allowing a diffraction limited spot size.

3 Adaptive aberration correction

Most aberration correction systems first measure the wavefront with a wavefront sensor, then calculate the correction to apply on the adaptive optic. Our system can find the right correction to apply on the mirror without knowing

anything about the wavefront of the laser on the parabola.

The correction signal we are using is the two-photon fluorescence intensity or the second harmonic intensity (depending on the sample) generated by the sample at the focus spot of the objective. We assume that this signal will increase with the square of the power density of the laser, and that the maximum power density is achieved for a diffraction limited spot size.

For finding the appropriate mirror shape out of the two-photon intensity signal we use an evolutionary algorithm (EA). These algorithms are often used for optimization of non-linear systems with a large number of variables [4,5,6]. The EA used for our system is a genetic algorithm. A genetic algorithm is a model of *machine learning* which derives its behavior from a metaphor of some of the mechanisms of evolution in nature [6]. This is done by the creation within a system of a population of individuals represented by chromosomes. The population then goes through a process of evolution. Considering our aberrations correction problem, our individuals correspond to mirror shapes. And the chromosomes of each individual are coding the position of each actuator of the mirror. Each individual is then composed of 37 chromosomes. The trial population for our system is composed of one hundred individuals (or mirror shape).

This population of mirror shapes corresponds to generation zero of the evolution of the system. To start the evolution process, we test each individual on the system. The mirror shape corresponding to each individual is applied to the deformable mirror and we then measure the second harmonic intensity from the sample. This signal gives the fitness of each individual of the population. We then select the ten best individuals of this population according to there fitness. Those chosen ones become the *parents* of the next generation.

The next generation is obtained by randomly crossing the chromosomes of the parents to create a new population of one hundred individuals. Every individual in this generation looks like its parents and allows the convergence to the optimum individual or mirror shape that will correct all aberrations in the system. To introduce some diversity in the system, all children have a small probability to mutate. A mutation is a random chromosome change. This is a way, for the population, to avoid local solution to the problem by randomly exploring the space of the system. This generation is then tested on the system, ten best individuals are selected, that will become the parents of the next generation.

This algorithm allows our system to find a wavefront correction that will give a diffraction limited spot size for each scanning position. It takes a maximum of fifteen generations for the algorithm to converge to a solution,

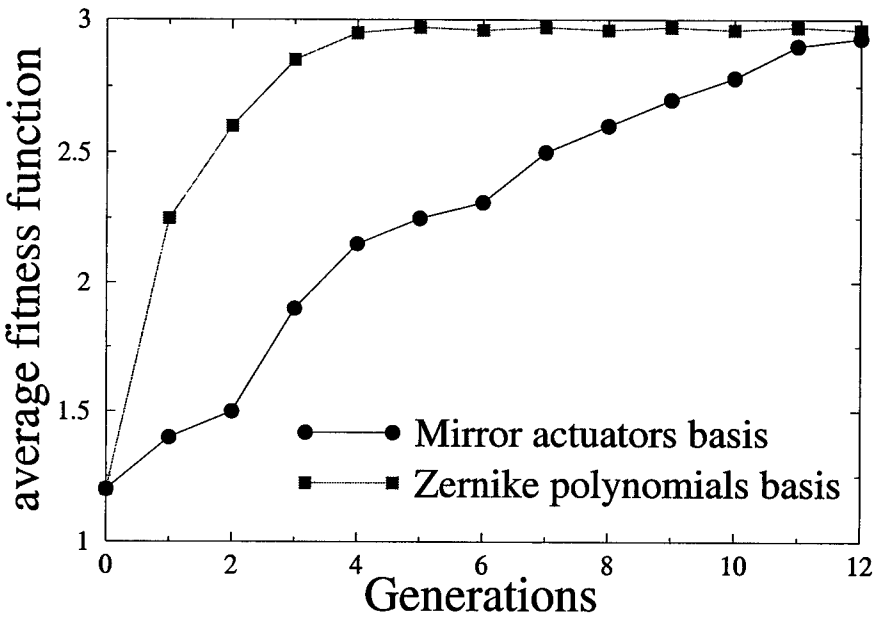

Figure 2. Genetic algorithm improvement of the average fitness function with generations for two different populations. The first population is composed of 100 individuals with deformable mirror actuators chromosomes. The second is composed of the same number of individuals with Zernike polynomials amplitude chromosomes.

and it takes three minutes for the system to go through those generations; this time is determined by the $1\mu s$ response time of the deformable mirror.

To speed-up the process, we have reduced the size of the chromosome basis. Even if the 37–actuators basis seems logical for our system, we still have to remember that the system is dealing with wavefront aberrations, and that an optimized basis exist to describe those aberrations. The *Zernike polynomials* are the most reliable way to describe wavefront aberrations and there properties are well suited to our problem [7]. The Zernike polynomials describes aberrations in a disk surface that can be the one of the deformable mirror or the aperture of the parabola. The Zernike polynomials define an orthogonal basis for aberrations within that disk. This orthogonality property means that each polynomial of the basis is not coupled with the other, ' and when one use N polynomials it defines a true N dimension basis.

We now consider that the chromosomes of each individual in our system represent a Zernike polynomial amplitude, instead of an actuator position. According to the maximum spatial frequency that can be reproduced on the mirror, we have limited our Zernike polynomial basis to the four first orders of polynomials (except the zero order corresponding to the piston). Consequently, the corresponding basis is a true fourteen dimensional basis. The chromosome basis has changed from a non-orthogonal thirty seven dimension basis to an orthogonal fourteen dimension basis. Having fewer chromosomes to deal with, and having no coupling between them, makes the job easier for the genetic algorithm and we have speeded-up the correction time to less than a minute, or five generations as shown on Fig. 2.

4 Experimental results

With the microscope setup presented above, we are able to correct aberration introduced by the parabola during the scanning process. The diffraction limited spot achievable with the top hat pulse mode and the f:1 parabola has a $1.1\mu m$ diameter. The measured spot diameter is $1.0 \pm 0.5\mu m$ on axis and in the corrected scanning area.

Each correction of the wavefront is stored in a database and can be recalled during scanning of samples. Each element of the database contains information on the location of the corrected points, and the corresponding voltages to apply to the deformable mirror. The database allows a fast scanning rate, that can ultimately match the standard video rate if the scanning machinery is fast enough.

The adaptive part of the system is versatile enough so that the parabola can be replaced by any objective. Changing the objective will just imply that the learning system will have to find a new database before being able to record images.

References

1. W. Denk, J. Strickler, and W. Webb,"Two-photon laser scanning fluorescence microscopy," *Science*, vol. 248, pp. 73–76, april 1990.
2. C. Sheppard and D. Shotton, *Confocal laser scanning microscopy.* Springer, 1997.
3. g. Vdovin, S. Middelhoek, and P. Sarro, "Technology and applications of micromachined silicon adaptive mirrors," *Opt. Eng.*, vol. 35, pp. 1382–1390, 1997.

4. D. Goldberg, *Genetic Algorithms in search, optimisation, and machine learning.* Addison-Wesley, 1989.
5. T. Baeck and H.-P. Schwefel, "An overview of evolutionary algorithms for parameter optimisation," *Evolutionary computation*, vol. 1, no. 1, pp. 1–23, 1993.
6. J. Heitkoetter and D. Beasley, "The hitch-hiker's guide to evolutionary computation: a list of frequently asked questions." USENET: comp.ai.genetic. Available via anonymous FTP from rtfm.mit.edu/pub/usenet/news.answers/ai-faq/genetic/.
7. Born and Wolf, *Principles of optics.* Pergamon Press, 6 ed., 1997.

ADAPTIVE OPTICS IN CONFOCAL MICROSCOPY

J.W. O'BYRNE, P. W. FEKETE, M. R. ARNISON, H. ZHAO, M. SERRANO, D. PHILP, W. SUDIARTA AND C. J. COGSWELL

School of Physics A28, University of Sydney, 2006, Australia
email: j.obyrne@physics.usyd.edu.au

A confocal microscope offers superior imaging compared to a conventional optical microscope. However most confocal microscopes operate in reflection because of the imaging difficulties caused by aberrations induced by the specimen itself. Work at the University of Sydney has focussed recently on overcoming these problems and constructing a practical confocal transmission microscope. We have demonstrated image improvement by removing image motion in real time using a tip-tilt mirror, and in post-processing of CCD images. Other low order aberration correction requires a wavefront sensing technique appropriate to the confocal situation and a device to provide the correction, both of which are also being investigated.

1 Introduction

A confocal microscope delivers superior imaging over a conventional microscope in both resolution and the ability to optically section specimens (i.e. to image a single plane within the specimen). These capabilities stem from the strong rejection of multiply scattered light even in thick, highly scattering media. This sectioning ability makes it possible to record a collection of adjacent planes of focus and process them into a full 3D image.

The confocal optical design delivers a focussed spot of light into the specimen and relays that spot to a pinhole aperture in front of a detector. The confocal image then consists of point-by-point measurements of the transmitted (or reflected) light as the specimen is raster scanned under the fixed illumination path. The fixed light path in our system eliminates variable off-axis aberrations such as field curvature and coma that are characteristic of beam-scanning confocal designs.

When specimens thicker than about ~5 μm are imaged in *transmission*, the focussed image spot is often deflected off-axis by refractive index structures within the specimen, causing it to miss the detector pinhole. Thus the information conveyed by the signal amplitude (e.g. absorption or phase change in the specimen, depending on the imaging mode) is lost. This produces erroneous dark regions in the image and makes it virtually impossible to use a fixed pinhole arrangement. This effect does not arise in *reflection* because tilt effects introduced when the light enters the specimen tend to be cancelled out when the beam reflects back along essentially the same path. Apart from image motion, further aberrations may also be introduced which deform the ideal Airy pattern on the detector pinhole and

thereby alter the detected signal. Of course, each of these aberrations itself carries information about structure within the specimen if it can be interpreted.

Because of these difficulties, there are currently no commercial confocal *transmission* microscopes. However operation in transmission offers several advantages, such as the ability to provide phase information, not available in reflection. Conventional optical microscopes are more often used in transmission and it is clearly desirable to do the same for confocal microscopes.

Over the last few years we have developed a confocal microscope system to explore confocal imaging in both reflection and transmission [1,2]. We have obtained confocal transmission images, including differential interference contrast (DIC), from thin samples. The images exhibit improved imaging performance compared with non-confocal imaging. Ultimately our interest lies in imaging thick objects in three dimensions under multiple scattering conditions. However, as the imaging is moved deeper into the specimen, the image quality is reduced for each successive plane. In order to obtain high-resolution transmission images of a thick specimen it is essential to use Adaptive Optics (AO) techniques to compensate for the aberrations introduced by the specimen itself [3,4].

2 Tip/tilt correction of image motion

The first and simplest step in most AO systems is the elimination of image motion. In confocal transmission imaging, this motion can be tens of microns in a highly structured part of the specimen, much larger than the detector pinhole.

In order to correct image motion we have implemented a closed loop tip-tilt

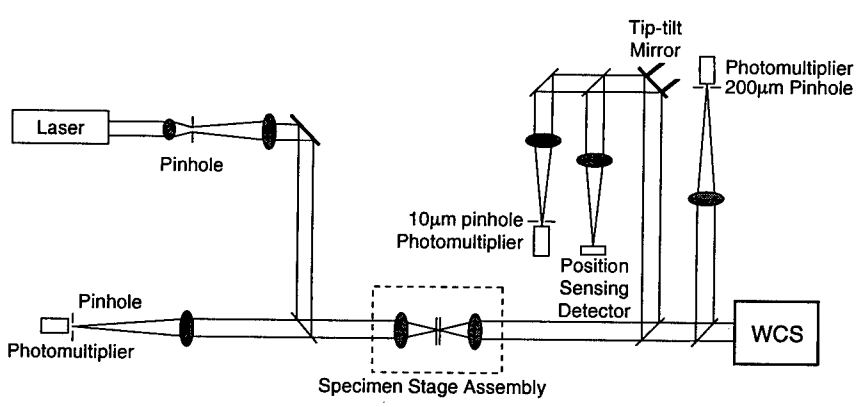

Figure 1. Confocal microscope incorporating tip-tilt AO components.

servo in our confocal system, as illustrated in Figure 1. The tip-tilt system consists of a Position Sensing Detector (PSD) whose output drives a fast piezoelectrically mounted mirror. Any displacement of the image centroid as determined by the PSD produces a control voltage which causes the piezo to deflect the beam back on axis.

This layout permits simultaneous acquisition of tilt-corrected and uncorrected images. Use of a large pinhole in either arm results in conventional rather than confocal imaging. Figure 2 shows one resulting transmission image set. The first image was taken using a 200 μm pinhole, which simulates the acquisition of a conventional image. The second image is confocal, without tilt correction. It shows dark regions at refractive index boundaries, indicating loss of signal due to aberrations. The third image is a tilt corrected confocal image showing fine detail in these same regions. It generally has significantly finer lateral resolution than either the uncorrected or conventional images. These images are 512 x 512 pixels and took 25 seconds to acquire at a rate of 20 lines per second. This frame rate is set by the pixel rate which is itself determined by the bandwidth of the tip-tilt servo - currently up to 1.5 kHz. This highlights the speed limitations of any real-time AO system.

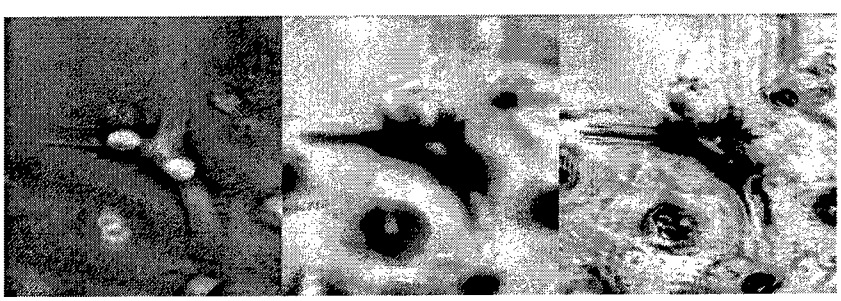

Figure 2. Conventional, uncorrected confocal and tilt corrected confocal images of a kangaroo rat kidney cell. Each image is 75 microns across.

3 Using a CCD to create a 'virtual pinhole'

In 1992 [1,3] we first proposed the idea of replacing the physical pinhole found in all confocal systems with a 'virtual pinhole' formed from selected pixels of a CCD array. Although not really an AO technique, this approach has an obvious application in replacing the more complex tip-tilt correction. For each image, a 'virtual pinhole' of any desired size can be defined and moved from frame to frame as the focussed spot moves. Experiments to date have been limited to single pixel 'virtual pinholes' selected to be the maximum value within each CCD

frame. Figure 3 illustrates the ability to eliminate loss of confocal signal caused by motion of the focussed spot. It was taken with a Dalsa 64x64 CCD camera, operating at up to 400 Hz frame rate. The benefit of maximum detection is very similar to that from tip-tilt correction, although it is not strictly equivalent to the centroiding employed in the PSD. Centroiding could, of course, be performed using an appropriate algorithm, with an arbitrary size 'virtual pinhole' defined around the centroid.

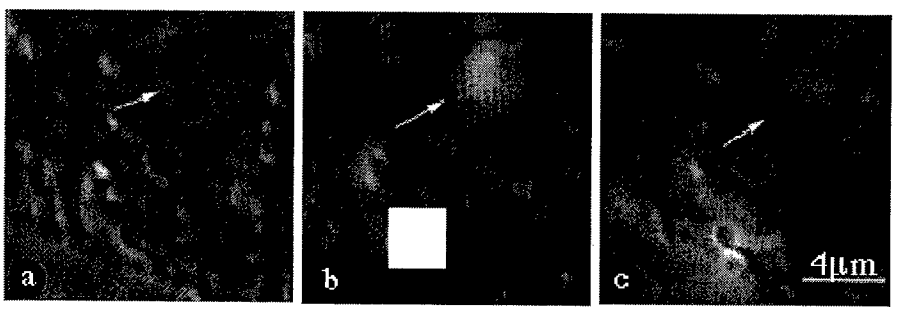

Figure 3. Algae seen in transmission differential interference contrast (DIC) imaging. (a) conventional, (b) on-axis single pixel, (c) maximum value pixel. The white square in (b) blocks a region of extreme brightness. Arrows highlight a region where the images show significant differences.

Apart from simply displacing the focussed spot, other aberrations introduced by the specimen will deform the ideal Airy disk. In a fixed pinhole system this is ignored and light from the diffraction maximum is assumed to be a reliable measure of structure within the specimen at the focal plane. With a CCD, deformation of the Airy disk is recorded and the information it contains can be used to understand the aberration and the structures which produced it.

For example, defocus of the spot in the CCD image indicates variation in the optical path length through different parts of the specimen. If this occurs on the transmitted (output) side of the specimen it can be simply corrected by refocussing the output microscope objective. If it occurs on the illumination (input) side of the specimen it indicates movement of the focal plane within the specimen and will lead to incorrect placement of features in depth in the confocal data set. Monitoring in both reflection and transmission or in double-pass through the specimen may be required to discern between these two possibilities.

Of the other low order aberrations, spherical aberration is the most important. It increases as the focal plane is moved deeper into the specimen because of the overlying material in the optical path. Quite small amounts of spherical aberration will clearly degrade image performance, more so in depth than in the transverse direction [5]. We have partially corrected this effect using available meniscus lenses, but it could clearly be monitored and corrected in real-time with a suitable AO wavefront sensor and phase modulator.

4 Low order correction

Most AO systems employ a Shack-Hartmann wavefront sensor which allows reconstruction of the wavefront from tilt measurements across individual sub-apertures. These individual measurements are made using centroiding detectors like the PSD described earlier. An alternative is the curvature sensor [6] which measures wavefront curvature across sub-apertures. This is achieved by making intensity measurements of extra-focal images, symmetrically either side of a focal point. Curvature sensing works well in astronomical AO, but our experiments indicate that the strong diffraction effects in confocal microscopy defeat this approach.

More recently we have begun to test a related technique based on the Transport of Intensity Equation (TIE) [7]. This involves taking images at focus and symmetrically on either side. It assumes the paraxial approximation but makes no geometrical optics approximations. Most of the computation is done in Fourier space where the technique fast and easy. Initial results using a CCD are promising and testing in the confocal system is now proceeding.

The other critical element of an AO system is the phase modulator. Typically this is a deformable mirror with >20 sub-apertures driven by peizoelectric actuators. These mirrors work successfully in astronomical applications, but they are very costly - more than the confocal microscope itself. We have been exploring a lower cost option - a bimorph mirror featuring a small number of controlled sub-apertures which is more appropriate to the level of correction likely in a confocal system.

The bimorph mirror is made from two piezoelectic wafers and is controlled by a pattern of electrodes on one of the wafers [8]. This has recently been tested in the confocal microscope in an arrangement similar to that illustrated for the tip-tilt mirror in Figure 1. The beam was expanded to match the 35 mm beam diameter of the bimorph mirror. A fast wavefront sensor was not available and so wavefront aberrations were measured using a conventional phase-shifting interferometry technique (which is itself a challenge in the presence of strong diffraction). Figure 4 illustrates the improvement in the focussed spot delivered to the pinhole.

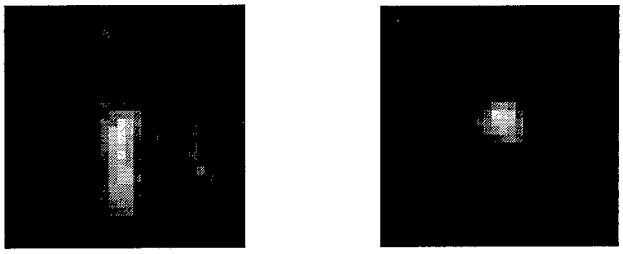

Figure 4. The aberrated focussed confocal spot (left) was corrected (right) using a bimorph mirror.

The Strehl ratio, which measures the power in the diffraction peak of the Airy pattern, was improved from 0.1 to 0.8 in this experiment.

The bimorph mirror represents just one approach to AO phase modulation. Non-mechanical devices using liquid crystal phase screens or micro-machined solid state optical devices are exciting possibilities for the future.

5 Conclusion

Our investigations have shown that it is essential to implement AO if a confocal microscope is to be operated in transmission. A tip/tilt system on our microscope has demonstrated improved imaging over an uncorrected system. A preliminary demonstration of further correction has been achieved using a bimorph mirror. We are currently investigating alternative approaches to wavefront sensing in the confocal context.

There remain larger questions to answer such as how to decide where the aberrations arise within the specimen (before or after the focal plane) and thus what impact they have on the confocal imaging plane? Also, how do we extract further information about the specimen from the aberrations themselves?

6 References

1. Cogswell, CJ and O'Byrne, JW, 1992, A high resolution confocal transmission microscope: I. System design, *SPIE*, **1660**, 503-511.
2. Cogswell CJ, Larkin, KG, O'Byrne, JW and Arnison, MR, 1994, High-resolution, multiple optical mode confocal microscope: I. System design, image acquisition and 3D visualisation. *SPIE*, **2184**, 48-54.
3. O'Byrne, JW and Cogswell, CJ, 1992, A high resolution confocal transmission microscope: II. Determining image position and correcting aberrations, *SPIE*, **1660**, 512-520.
4. Dixon, AE and Cogswell, CJ, 1995, Confocal microscopy with transmitted light, in *Handbook of Biological Confocal Microscopy*, 2nd edition, J. B. Pawley, ed., Plenum, NY, 479-487.
5. Sheppard, C.J.R, 1998, Aberrations in high aperture conventional and confocal imaging systems, *Appl. Opt.*, **27**, 4782-4786.
6. Roddier, F, 1988, Curvature sensing and compensation: a new concept in adaptive optics, *Appl. Opt.*, **27**, 1223-1225.
7. Paganin, D. And Nugent, K.A., 1998, Non-interferometric phase imaging with partially coherent light, *Phys. Rev. Lett.*, **80**, 2586-2589.
8. Zhao, H., Fekete, P.W. and O'Byrne, J.W. 1997, Prototype bimorph mirror for the AAT adaptive optics system, *SPIE*, **3126**, 384-390.

Wavefront Correctors

PERFORMANCE ASSESSMENT AND APPLICATIONS OF MEMS ADAPTIVE OPTICS

ROBERT K. TYSON
Department of Physics, University of North Carolina at Charlotte, 9201 University City Blvd., Charlotte, NC 28223 USA

Tactical airborne electro-optical systems are severely constrained by weight, volume, power, and cost. Micro-electrical-mechanical (MEM) adaptive optics provide a solution that addresses the engineering realities without compromising spatial and temporal compensation requirements. Through modeling and analysis, we determined that substantial benefits could be gained for laser designators, ladar, countermeasures, and missile seekers. The development potential exists for improving seeker imagery, extending countermeasures keepout range, improving the range for ladar detection and identification, and compensating for supersonic and hypersonic aircraft boundary layers. Innovative concepts are required for atmospheric path and boundary layer compensation. We have developed designs that perform these tasks using high speed scene-based wavefront sensing, IR aerosol laser guide stars, and extended-object wavefront beacons.

1 Introduction

Electro-optical tactical weapon systems, including infrared imaging seekers, laser designators, laser radars, and active infrared countermeasures have limitations dictated by severe combat thermal and vibrational environments. The weapon performance may be degraded by the constraints on its ability to detect and specify targets or its ability to accurately aim and project a laser to a target. Fig. 1 shows a series of image frames taken from a video stream from a seeker, like that used on the current generation cruise missile. The imagery is transmitted to flight crew for aimpoint designation and terminal guidance. Atmospheric turbulence, in the flight path between the missile seeker and the target, and through the aero-optical boundary layer near the seeker window, can reduce the spatial resolution and degrade the performance of the system. Improving the imagery or laser propagation in situations of severe optical distortion can make the difference between a successful mission and a failure.

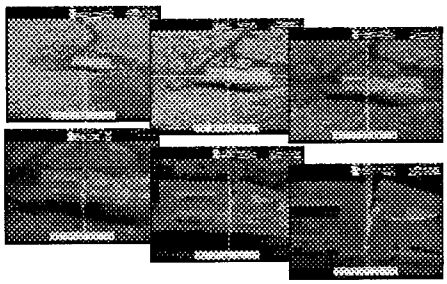

Figure 1. Detailed analysis of imagery was used to define the levels of atmospheric turbulence and missile vibration in terms of its effect on image quality.

Conventional adaptive optics systems[1] provide possible solutions for compensating the atmospheric propagation path used in tactical systems. The telescope and the aperture is usually defined by the operational envelope and packaging constraints. The sensors are often predetermined for specific missions. The addition of a wavefront sensor, a deformable mirror, and a control computer complicates the system. So, the tradeoff is fairly straightforward. If the adaptive optics system can be integrated into a tactical system, and its weight and power penalty is offset by the system's improved performance, it is a viable option for development. The recent advances in low-cost MEMS deformable mirrors make it possible to develop electro-optical enhancements with a few hundred channels, which can improve image resolution with complete system production costs in the range of $1500 per unit.

2 Missile seeker system analysis

We investigated MEMS optical systems to determine how much image improvement was possible while remaining low-weight, low-volume, low-power consumption, and low production cost. We use the resolved scene for wavefront sensing. Using digital signal deconvolution of the image and phase error linearization, we can achieve significant image improvement.

For the analysis, we use knowledge of the environment surrounding the imagery. We back-calculate that the spatial coherence length of the atmospheric turbulence and a characteristic (Greenwood) frequency. In the 8-12 micron band, we determined that r_0 =18cm and f_G=24Hz were reasonable assumptions for later bandwidth calculations. This leads to a scaling law calculation of the benefits of low-cost adaptive optics on the seeker.

A conventional adaptive optics system contains a specific wavefront sensor. When the light entering the optical system is assumed to be a plane wave with only correctable aberrations, we assume that the intensity distribution is uniform. That is, we assume that the system is looking at a point-like source. Conventional wavefront sensors have corrupted signals if they observe an extended or resolved source. When a resolved scene is all that is available for sensing the distorted wavefront, other techniques must be used. With no *a priori* knowledge of the scene, the object, nor the aberrations, determining phase is a tedious and time consuming process because multiple samples of the image must be used.[2] (The imaging process is not directly invertable to extract the phase.) Multiple samples require precious time. For a closed-loop system to work, the sampling must be faster than the disturbances. This stresses the speed of signal processing or, conversely, limits the control bandwidth and therefore the level of aberration compensation.

Because of the tactical scenario where a cruise missile will be used, we will make use of the assumption that an approximation of the target scene will be available. That is, "the target is known." We recognize that the specific object/scene information will most likely be slightly different than a projection[3] and we account for the differences as unknown parameters relating to magnification of the target scene (due mostly to range) and slight rotation of the scene (due to the attitude of the incoming missile with respect to the target). With this information, we constructed an adaptive optics wavefront sensor scheme (Fig. 2) that makes use of the known object information to generate the system point spread function (PSF). This is followed by recently-developed processing algorithms that generate the wavefront phase estimate from multiple PSFs without an iterative procedure like that used in phase diversity.

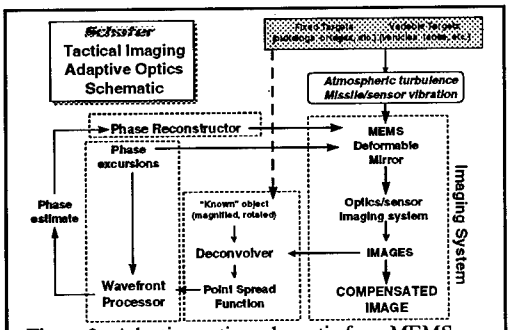

Figure 2. Adaptive optics schematic for a MEMS-based missile seeker compensation system.

We improve the imagery by making use of linear systems theory in the formation of images. Each bit of detail in the object is transferred to the image with some distortion, or loss of information. Even a perfect "diffraction-limited" (finite aperture) system loses information. The image formation process is limited by diffraction which, except for an infinite aperture with no aberrations, spreads out the light and masks some of the information transfer. Aberrations add to the distortion and "blurring" of the image. The image is formed by convolving the blur that would occur from a point source (the point spread function, PSF, $P(x,y)$), weighted by the light distribution of a perfect object, $O(x,y)$.

The first step in the wavefront sensing process is deconvolving the image by dividing the Fourier spectrum of the image, which we sense, by the spectrum of the object, which we get from external data. The inverse transform of this is the PSF.

$$P(x,y) = F^{-1}[F[P(x,y)]] = F^{-1}\{F[I(x,y)] \,/\, F[O(x,y)]\} \quad . \qquad (1)$$

The second step is a wavefront processor that computes the phase estimate from a series of PSFs, effectively inverting the diffraction equation

$$P(x,y) = \left| \iint A(x',y') \exp(-i2\pi\phi(x',y')) \exp(-i2\pi(xx'+yy') / \lambda f) dx'dy \right|^2 \qquad (2)$$

Both processes can be exactly calculated with some assumptions: (1) The deconvolver will work exactly *if* the object is known exactly. In a tactical imaging situation, we know the object (target) will be known, but its range, aspect angle, and

our direction of flight and attitude may be varying; and, (2) The phase can be reconstructed from the PSF if the amount of phase aberration is small enough so that the exponential $\exp[-i2\pi\phi(x', y')]$ in Eq. 2 can be represented by its first terms $1-i2\pi\phi(x', y')$. When this occurs, the PSF can be inverted to find the phase without an iterative method. This is preferred for a real-time adaptive optics control system. We have determined that the phase error over a 10 cm aperture at the 8-12μm band, can be linearized with only a few percent phase estimate error.

An algorithm developed by Wild,[4] calculates a closed-form exact solution for the unknown wavefront phase, shown in Fig. 2 as the phase estimate. The accuracy of the phase estimate depends upon a number of factors: First, the accuracy goes up as the number of phase excursions increase. Secondly, because the algorithm linearizes the phase errors, the accuracy goes up as the amount of unknown phase is reduced.

Simulations show that the algorithm works quite well for phase error variances less than 0.5 rad^2. For larger errors, the accuracy is reduced and the number of excursions must be increased, translating into lower control bandwidth. For atmospheric turbulence, this implies that the coherence length r_0 must be greater than 0.45 D where D is the aperture diameter. This condition is met quite easily at IR wavelengths and the ranges of tactical missiles. We conclude that our algorithm is limited by the processor speed and not the strength of the turbulence. Simulations show that we can retain a 70Hz closed-loop bandwidth with two phase excursions per frame on a limited scene.

The goal of this study was to determine how much image quality can be improved with adaptive optics. For the analysis, we assumed that we had a 10 cm aperture imaging seeker in the 8-12 micron band that was up to 10 km from the target in severe turbulence conditions. The uncompensated atmospheric turbulence Strehl ratio was about 0.69. Strehl ratio is roughly equal to the inverse of the resolution size in the target plane. With a coherence length of 18 cm and a Greenwood frequency of 24Hz, Fig. 3 shows that the Strehl ratio can be improved by 20% with an 11 channel adaptive optics system with a closed-loop

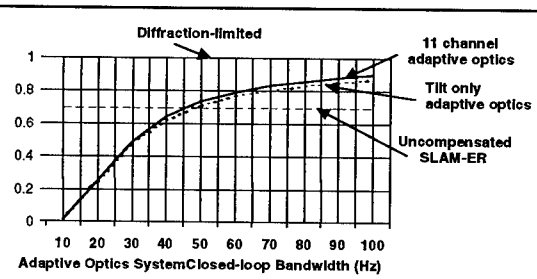

Figure 3. Analysis shows that image improvement is possible for an IR seeker with low-cost MEMS adaptive optics operating at a closed-loop bandwidth of 70Hz.

bandwidth of 70 Hz. This 20% improvement in image resolution is feasible with prototype MEMS deformable mirrors if the sensing algorithms can operate at the near 1kHz frame rate. (To achieve a closed-loop bandwidth of 70 Hz, we require wavefront sensor signals to be about 5 times the bandwidth, or 350 Hz. Our wavefront sensing concept, as it is currently designed, requires three separate images per wavefront sensing cycle. Thus, the camera frame rate and integration time must be compatible with 1kHz.)

The imagery does not have to be fully compensated over the entire missile engagement time. Blurring is removed at longer ranges, but absolute accuracy for aimpoint selection is improved at shorter distances. With a few frames in a 70 Hz closed-loop bandwidth, we can improve the resolution. In the final seconds of flight, when the optical propagation path is short, the aero-boundary turbulence layer dominates. Since the aero-boundary is somewhat constant (at a constant velocity), we can correct for it at a much lower bandwidth, possibly 10 Hz, which greatly relaxes the requirement for high speed imagery and processing.

3 MEMS technology

The state-of-the-art of MEMS adaptive optics technology is represented by the most recent developments of MEMS Optical, Inc. They have produced prototype multichannel micromirrors with a process that promises to reduce the production level costs to a small fraction of conventional macro-adaptive optics The mirror employs electrostatic forces to move each actuator in a piston motion. In order to achieve a large fill factor, while allowing room for the supporting springs and electronic traces, a lens-let array is used. The segmented micromirror array has a total of 325 actuators with a 500 μm pitch. With 21 actuators across the diameter, this results in an effective diameter of 10.5 mm. Figure 4 shows the current generation mirror.

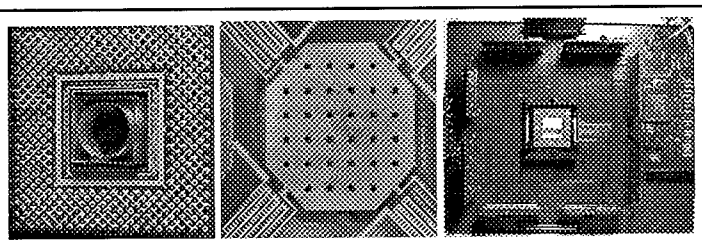

Figure 4. Photos of a prototype MEMS deformable mirror. The mirror is overlayed with a lenslet array to establish a fill factor of 100%. The left picture shows the 1 cm diameter lenslet array over the front surface of a segmented MEMS deformable mirror. The middle picture is a photomicrograph of a single mirror segment of the array. The right picture shows the back of the mirror mounted into its driver card.

4 Future plans

The ultimate objective of this research is to produce MEMS adaptive optics systems suitable for deployment. Based upon these analytical results, we will be performing a number of demonstrations and analytical studies.

The first laboratory demonstration will show how an integrated phase compensation system with MEMS adaptive optics can meet the spatial resolution requirements of tactical missions. The second experiment will show how the tactical mission requirements for high-speed adaptive optics are met by using a general purpose computer with sensing algorithms scaled to missile engagement bandwidths. The third laboratory experiment will show that a varying view of a target object, as expected during the terminal phase of engagement, can be compensated. In conjunction with the laboratory demonstrations, we will continue theoretical analysis of the tactical missions and their impact on the system configuration.

5 Acknowledgements

This work was perfomed while the author was with Schafer Corporation, 321 Billerica Road, Chelmsford, MA 01824 USA. The research was supported by the U.S. Navy Small Business Innovative Research (SBIR) Program under NAVAIR contract N68335-97-C-0114 and NAWCWPNS contract N68936-98-C-1042. MEMS deformable mirror data was supplied by MEMS Optical, Inc., Huntsville, AL.

6 References

1. Tyson, Robert K., *Principles of Adaptive Optics*, 2nd Ed., Academic Press Boston, 1997.
2. Paxman, R. G., Fienup, J. R., "Optical misalignment sensing and image reconstruction using phase diversity," *J. Opt. Soc. Am.* **5**, p. 914, 1988.
3. Hebert, Thomas J., Henneberger, Bernard E., "Optical filtering approach to regularized tracking of an object's position and orientation," *Appl. Opt.* **37**, p. 7577, 1998.
4. Wild, Walter J., "Linear phase retrieval for wave-front sensing," *Opt. Lett.* **23**, p. 573, 1998.

THE ACTIVE MICRO MIRROR: A NEW ADAPTIVE OPTICAL MICRO-COMPONENT

G. ROBERT, L. BABADJIAN, S. SPIRKOVITCH

ESIEE, Cité Descartes, 93162 Noisy-le-Grand, France email: robertg@esiee.fr, babadjil@esiee.fr, spirkovs@esiee.fr

A.COVILLE

Sfim Industries, av R.Garnier, 91344, Massy, France, email: acoville@sfim.fr

The Active Micro Mirror (AMM) is a new kind of micromachined deformable mirror. It is a silicon mirror which can be electrostatically actuated by electrodes located on each side of the mirror. In this article we describe the characteristics and the results of modelisation and testing of our deformable micro mirror.

1 Introduction

The aim of the Adaptive Micro Mirror project (AMM) is to study the technical feasability of a silicon micromachined deformable mirror, to evaluate its performances and applications, and to experiment some of its potentialities.

The choice of micromachining technologies increases the field of appplications of the AMM compared to standard deformable mirrors: great flexibility of fabrication (size, shape,...), small size and light weight (easy to integrate in a system), possible mass production (decrease the cost of the mirror).

We will first describe the main specifications of the AMM and its basic principles. Then, we will talk about the technology of fabrication. Then, we will talk about the modelisation and the command of the mirror and give some results of simulation. At the end, we will validate this technological and theoretical study by a comparaison between simulations and experimentations.

2 Basic principles

Micromachined deformable mirrors are actually an active field of research [1,2]. Based on theses studies and on our personal needs, we identify a lot of new potential applications for this new active component: optical aberration correction, optical alignment, medical imagery...

In order to satisfy most of theses applications, we defined typical specifications to be met by the AMM:

Parameters	Values
Surface	>4 cm^2
Shape	Square, round,...
Amplitude of deformations	Max +/- 10 µm
Kind of deformations	First optical aberrations: focus, tilt, piston, astigmatism,...
Bandwith	300 hz

Table 1: typical specifications of the AMM

The AMM is composed by a thin silicon membrane fully built-in between two conductive electrodes. Applying voltage on theses electrodes will electrostatically deforme the mirror in the both directions.

We show a schematic view of the device in *figure 1*:

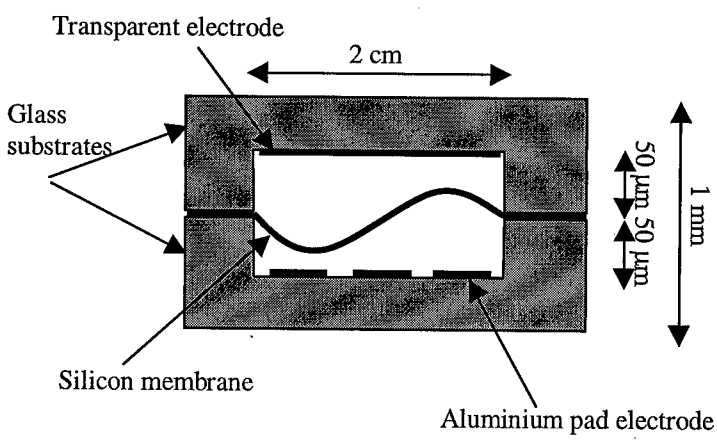

Figure 1: Scheme of the AMM

3 Fabrication process

The process of fabrication uses standard materials and technologies of micromachining: silicon and glass wafers, photolithography, thermal processes (oxidation, doping,...), chemical etching of silicon and glass (EDP, HF,...), assembly (anodic bonding), metallisations (aluminium,...).

The advantages of this kind of fabrication is a precise and reproducible control of critical dimensions (thickness of the membrane, space of the gap,...), the flexibility of fabrication (with the same process we can vary most of the technical parameters), and the mass production (which made the AMM affordable for any laboratory or industry).
Figure 2, shows a photograph of a micromachined AMM.

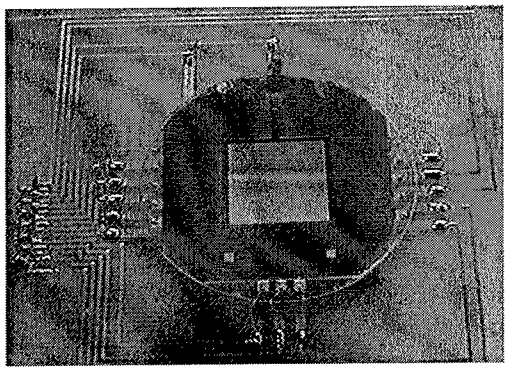

Figure 2: photograph of the AMM

4 Modelisation and command

The AMM can be deformed in virtually any shapes. The spatial frequency of the deformation is mostly limited by the number and the size of the pad eletrodes. One possible way for determining the command is to choose a large matricial pattern of electrodes and to simulate or experiment the deformations generated by this pattern. It usually gives a complex command with many different voltage channels and is not optimized for the deformations of interest.

We choose the reciprocal approach of this method. We fixed at first some important parameters: kind of deformation to be generate, number of electrodes, maximal command voltages. We determine a unique pattern of electrode which agrees with this parameters. Then, we calculate with this pattern a first repartition of voltages for each deformation, and iterate this step to optimize this voltage values.

We applied this method for a particular case defined by: generation of the most common optical deformations (focus, piston, astigmatism, coma) with an amplitude up to 5 μm, a mean-square error lower than few percent of the amplitude of the deformation for a defined surface, less than 20 electrodes, command voltages below 200V. Our modelisation gives us a unique pattern of 13 electrodes (plus one continuous electrode on the other side of the mirror), with the corresponding voltage commands for each deformation. We give some modelisation results on the *figure 3*.

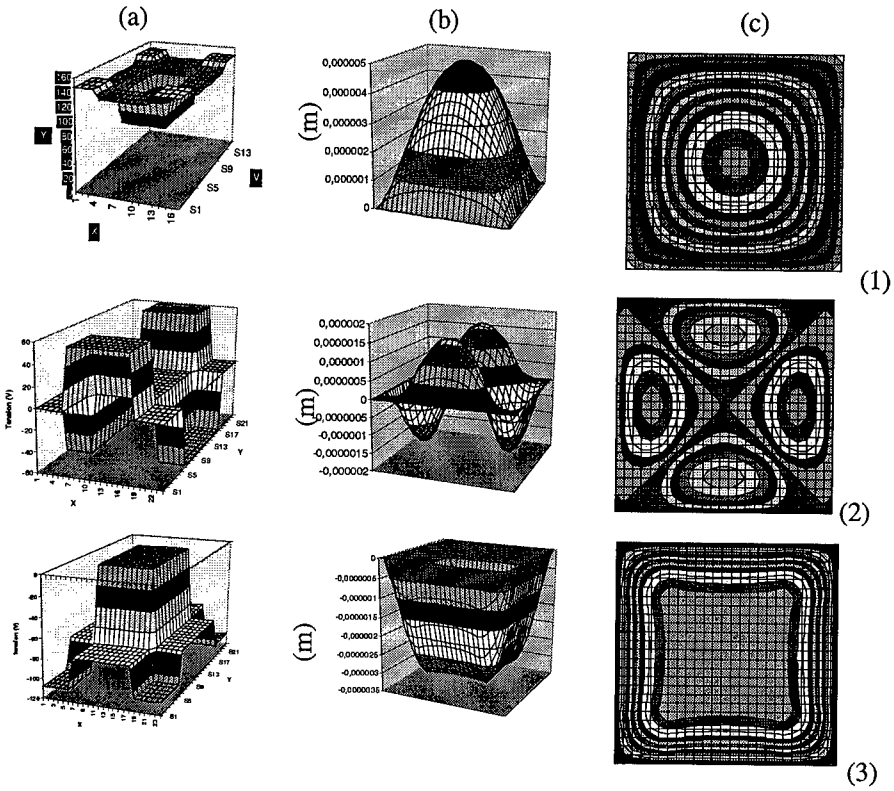

Figure 3: a) repartition of voltage on the 13 electrodes; b) simulation in 3d view; c) simulation in contour lines view. 1) focus; 2) astigmatism; 3) piston

5 Experimentation / Validation

In order to validate this modelisation, we developed a Labview interface to generate easily the voltage commands and an electronic circuit to amplify them to the different electrodes. We fabricated some AMM with the corresponding pattern of 13 electrodes too, and compared the interferometric results with the numerical computation. We resume theses results for the 3 previous deformations for different amplitude of deformation on *figure 4*.

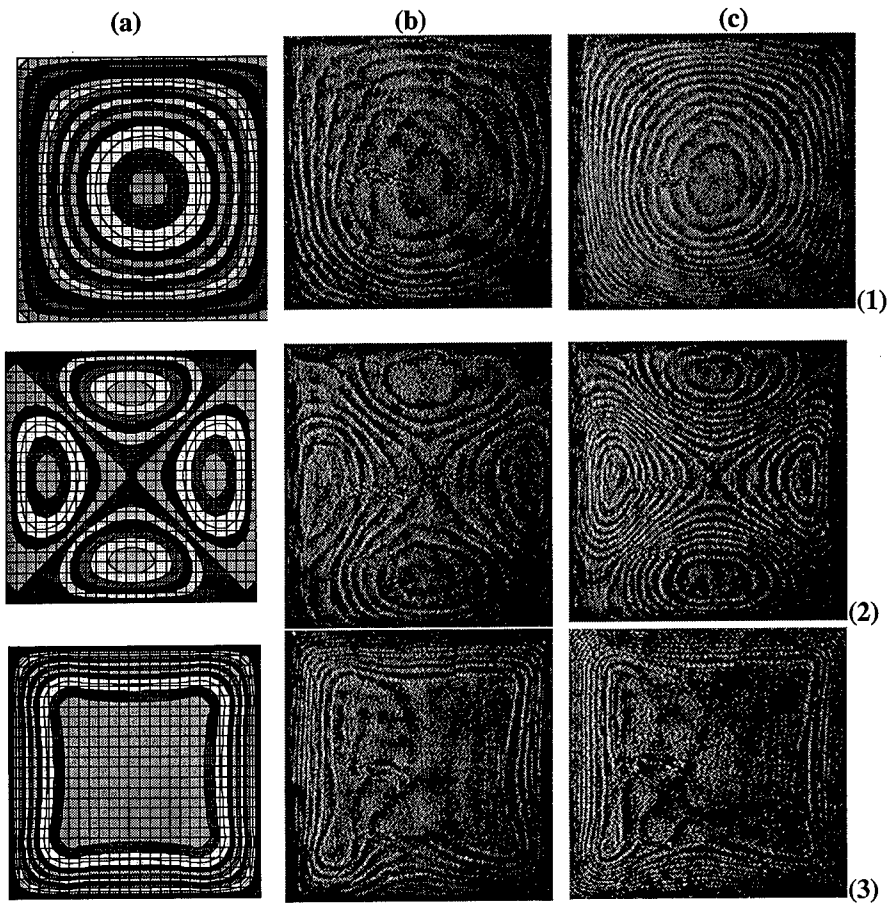

Figure 4: a) modelisation in contour lines view; b) c) interferometric measurement. 1) focus; 2) astigmatism; 3) piston

This first part of the AMM project made the proof of the technological feasibility of a silicon micromachined deformable mirror, developed an optimised method for the determination of the command (optimized pattern and control voltages), and validated the choice of the theoretical models with a good adequation between the results of numerical simulations and experimentations.

References

1. [1] "Technology, characterization and applications of adaptive mirrors fabricated with IC compatible micromachining", G.Vdovin, S.Middelhoek, SPIE Vol 2534, pp116, 1995.
2. [2] "Fabrication and characterization of a micromachined deformable mirror for adaptive optics applications", L.M.Miller, M.L.Agronin, R.K.Bartman, SPIE Vol 1945, pp421, 1993.
3. [3] "Preliminary Results on a Silicon Gyrometer Based on Acoustic Mode Coupling in Small Cavities", T.Bourouina, A.Exertier, S.Spirkovitch, B.Chaumet, E.Pleska, Journal of Microelectromechanical Systems, vol 6, N°4, pp347, Dec. 1997.

INNOVATIVE DEFORMABLE MIRROR DESIGNS FOR CUSTOM APPLICATIONS

DONALD G. BRUNS AND DAVID G. SANDLER

Trex Enterprises 10455 Pacific Center Court, San Diego, CA, USA

E-mail: dbruns@thermotrex.com or dsandler@thermotrex.com

New deformable mirror components and designs developed at Trex Enterprises (formerly ThermoTrex) are reviewed. These include long stroke actuators, zero holding-power actuators, wide operating temperature actuators, and simply replaceable facesheets. Systems built with each of these features are shown.

1. Introduction

ThermoTrex designed and built its first adaptive optics system for US military programs over 15 years ago. These deformable mirrors were made from individual segmented silicon substrates actuated with custom tubular PZTs. Each actuator tube supplies three control modes; piston, tip, and tilt. The largest of these mirrors is shown in Figure 1. These segments had a damped step response time of less than 100 microseconds and actuator strokes of 8 microns.

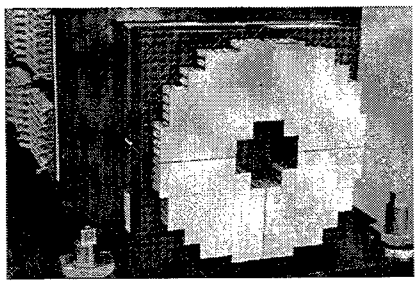

Figure 1. This 1500 degree-of-freedom segmented mirror, built in 1985, is still the world's highest-order deformable mirror to be tested at 1 kHz operation.

Trex's original DM design was motivated by the need to scale AO components for atmospheric correction to extremely large numbers of actuators, for use on large telescopes at sites with relatively poor seeing. Designed for use in the UV and visible spectrum, the segmented mirrors were designed for laser weaponry with narrowband laser pulses, so the presence of wavelength step discontinuities in the residual error map did not degrade far-field spot characteristics. Thus, the segmented design was an efficient and relatively low-cost solution for this mission. For the remainder of the 1980's, Trex remained focused on military applications, building several more segmented DM's for the US Navy and Air Force, including white-light versions and mirrors with water cooling attached directly to the back of the mirror.

However, in the 1990's our focus shifted to astronomical and commercial applications. We now offer a baseline commercial and astronomical system for low-order correction, using a Xinetics DM and proven Trex design for low-cost, high-speed wavefront processor. As an example, Figure 2 shows testing in our AO laboratory of this control system for the Italian TNG telescope. In the last several years we have designed and built entirely new DM designs aimed at providing new capabilities for a variety of customers. In the remainder of this paper, we briefly review some of these innovative designs.

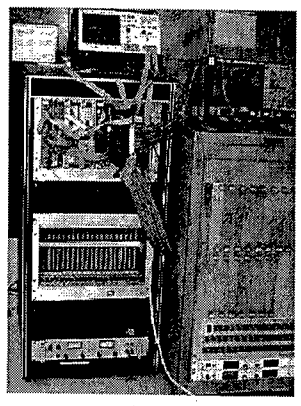

Figure 2. TREX reconstructor next to Xinetics driver rack.

2. High-speed electromagnetic actuators

Electromagnetic actuators are preferred when extra-long strokes or reliably long lifetimes exceed the importance of high bandwidth or compactness normally found in piezoelectric actuators.

Our first deformable mirror based on this new technology was the 25 actuator deformable mirror built for the University of Arizona in 1995, shown in Figure 3. This DM used voice coil actuators connected via magnets to a 2 mm thick glass mirror substrate. Capacitor position sensors surrounding each actuator, formed by the back surface of the substrate and the front surface of the reaction body, were used in the closed loop control of the mirror's shape. This mirror was successfully operated in our lab and at the Starfire Optical Range in Albuquerque, NM, where ThermoTrex has installed a 10 kHz fast figure sensor. This mirror was designed to be a prototype for an adaptive secondary mirror for the MMT.[1] A subsequent 60 element, concave mirror prototype was built and tested.[2]

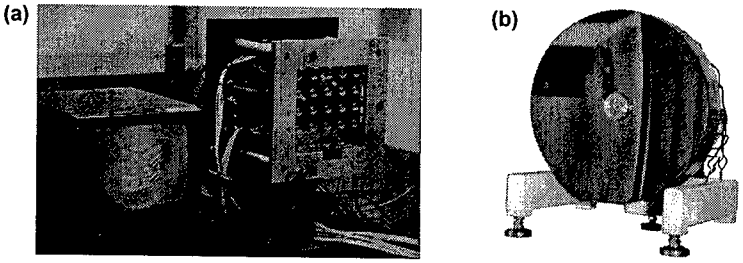

Figure 3. Continuous face sheet mirrors, actuated with voice coils. (a) 25 actuator flat DM operated at a 10 kHz update rate; (b) 60 actuator concave DM.

3. Electromagnetically-actuated, large aperture deformable mirror

The National Ignition Facility (NIF) at Lawrence Livermore National Laboratory is building a system of 192 high energy lasers which operate in parallel with the goal of demonstrating nuclear fusion.[3] These lasers are flashlamp-pumped, which contributes to significant thermally-induced wavefront distortion. To correct the distortion, NIF will use 192 deformable mirrors, each with 39 actuators operating at 10 Hz. The NIF is designed with a 30 year lifetime goal, so this requires over 7000 actuators to operate for nearly 10^{10} cycles. In addition, the deformable mirrors are exposed to damaging levels of ultraviolet radiation, so the normal epoxy actuator-to-substrate attachment techniques were not allowed.

ThermoTrex built a prototype DM for the NIF program, shown in Figure 4. The mirror was successfully flattened via closed loop commands to a 33 nm RMS figure, and could apply a defocus deformation of more than 9 microns on the surface.

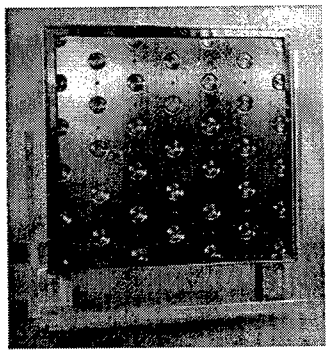

Figure 4. The NIF prototype deformable mirror uses 39 long-stroke electromagnetic actuators to control the thermal distortion in a 400 mm diameter laser beam.

The mirror substrate uses a 10 mm thick piece of BK-7 glass, flat on both sides. To attach the mirror to the actuators without using epoxy, atmospheric pressure was used. A very weakly formed vacuum, equal to 99% of atmospheric pressure, was all that was required to keep the glass in contact with the actuators as their lengths were changed to deform the mirror. Use of this technique offered the additional advantage that the mirror could be easily replaced; demounting the mirror, then remounting it, took only a few minutes in the laboratory.

Electromagnetic actuators were required to complete the design. Since the glass was relatively thick, simple voice coils were not strong enough to generate the necessary forces. Instead, a solenoid design was utilized. Since the air gap is relatively small, the actuator efficiency is relatively high. The raw actuator stroke is limited by the air gap, but this was easily set at 100 microns. Internal springs were used to generate the bias pushing force, while the atmospheric pressure provided the pulling force.

Since the electromagnetic force, and thus the actuator length, is not linear, a capacitor sensor surrounding each actuator was used with an analog control loop to maintain the actuator length. This internal closed loop system also compensated for the different glass forces resulting from different mirror shapes.

Two samples of this actuator type have been undergoing a life test since last year. We are operating them with long strokes at about 200 Hz, and so far have

seen no degradation in performance for 5 x 10^9 cycles. This test will run until we see a failure.

The mirror's static performance is shown in Figure 5. These interferograms were taken using the NIF wavefront control test station at LLNL. The first figure shows the surface with an applied deformation of 4.5 microns on the mirror, while the second figure shows the best flattened surface. The surface was flattened to yield a 33 nm RMS wavefront over a 400 mm square aperture, using a control loop designed for DM. The wide range of the actuators are evident in the amount of figure correction. This is the first demonstration of electromagnetic actuators operating a DM in a closed-loop system.

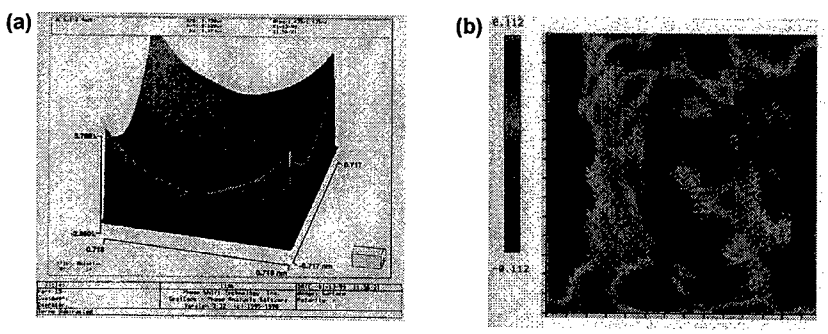

Figure 5. The NIF prototype DM shows it large stroke capability. a) mirror surface producing 9 microns of defocus; b) mirror flattened to 33 nm RMS

4. Lightweight, all-temperature deformable mirror

A third type of deformable mirror uses commercial New Focus, Inc., Picomotor actuators acting on magnets attached to a thin glass membrane, as shown in Figure 6. This type of system has an enormous stroke, useful for compensating for a very weak reaction structure, but also has a bandwidth only fast enough to compensate for thermal drift. A larger version of this type of deformable mirror, still under construction, is also shown in the figure.

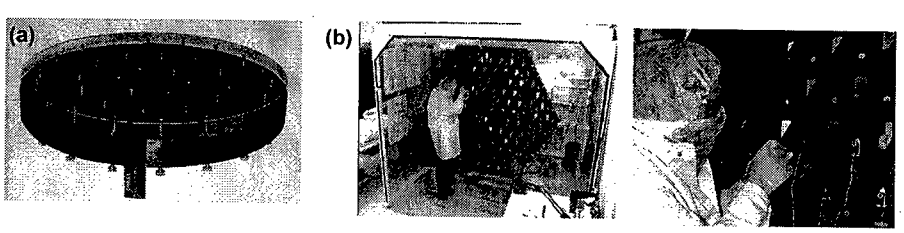

Figure 6. Thin membrane mirrors supported by Picomotor actuators can compensate for a weak reaction structure. (a) 36 actuator system, with attached glass; (b) 166 actuator system with closed-loop capability.

Another lower bandwidth actuator was developed to support NASA's research for the Next Generation Space Telescope. This actuator has the task of controlling the shape of a thin glass mirror supported on a very lightweight support structure. Glass is used as the mirror substrate because it polishes well and even at a 2 mm thickness, has adequate stiffness over small (100 mm) regions. The support structure must include lightweight actuators with high resolution and long stroke, to compensate for thermal or gravitational changes in its figure. Since the mirror shape will be figured with an on-board interferometer or similar technique, the requirements on the raw support structure include some degree of stability, but not precision.

The actuator requirements are summarized in the following table:

Specification	***Requirement***	***Reason for specification***
Mass	< 50 gm	Reduces the total system mass
Holding power	Zero watts	Telescope must operate with passive cooling
Operating temperature	Cryogenic and room temperatures	Lab tests at all temperatures
Resolution	< 30 nm	Enables diffraction-limited imaging at visible wavelengths
Stroke	> 2 mm	Corrects for large-scale support structure drift
Dimensions	< 50 mm	Fits into cells in the support structure
Operation	Compatible with "go-to"	Closed-loop control

Trex Enterprises designed and built the prototype actuator we named the WormScrew, shown along with its cryogenic performance in Figure 7.

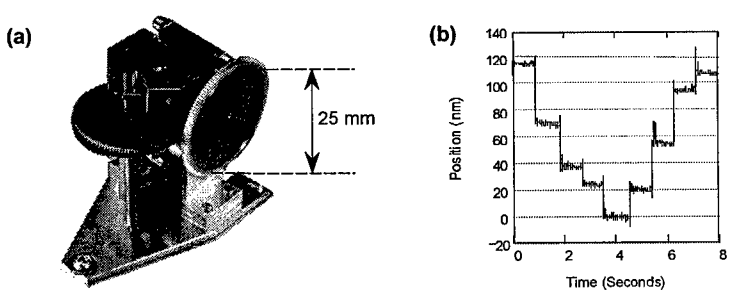

Figure 7. The WormScrew actuator operates from cryogenic to room temperature. a) the actuator stroke is applied through a worm gear driving a lead screw; b) at 77 K, the step size is identical in both directions with little backlash.

The WormScrew actuator uses a small stepping motor to drive a spur gear. A stepping motor does not require power to hold its position, due to the magnetic detents at each step. The first spur gear drives a worm gear which drives another spur gear connected to the lead screw. Since a conventional gear train is not used to

generate the small step size, light spring loading on this single interface reduces backlash to a negligible level. The actuator resolution is determined by the gear ratios, so it can vary from typically 20 nm per step to 200 nm per step while still meeting the NGST mass and size requirements.

The prototype actuator weighs about 65 grams, but it was made using off-the-shelf gears. The next iteration, still using standard gears, weighs only 25 grams. The energy to move each step is only a few millijoules, and can operate at one hundred steps per second. This bandwidth is adequate to control thermal drift in conventional systems. The mirror shown in Figure 6 is compatible with this type of actuator.

5. Conclusions

New deformable mirror designs have been developed to correct optical aberrations in applications outside of conventional atmospheric-induced turbulence correction. These novel DMs use specially designed actuators to meet requirements beyond the performance of existing PZT technology. These system designs can be applied to correcting beams from industrial lasers used in manufacturing processes, or in active optics in remote sites. Since the mirrors are not bonded to the actuators, they are easily replaced in the event of damaged coatings. Ultra-lightweight, high-performance optics can also be produced at low cost and within short schedules, since new types of extremely accurate lightweight actuator can be relied on to produce and maintain the final precision optical figure.

References

1. D.G. Bruns, *et al*, "Adaptive Secondary Development", in *Adaptive Optics*, July 8-12, 1996, Maui. OSA 1996 Technical Digest Series Volume 13.

2. D.G. Bruns, *et al*, "Final Prototype design for the adaptive secondary mirror of the 6.5-m MMT", in *Adaptive Optics and Applications*, July 30 - August 1, 1997, San Diego, CA. SPIE Volume 3126.

3. R. Zacharias, *et al*, "The National Ignition Facility (NIF) Wavefront Control System", in *Third International Conference on Solid State Lasers for Application to Inertial Confinement Fusion*, cosponsored by the U.S. DOE and the French CEA, June -10, 1998, Monterey, California.

MODELLING THE DEFORMATION OF ADAPTIVE ASPHERIC OPTICAL SURFACES IN THE BEND AND POLISH METHOD OF MANUFACTURE

RUNG-SHENG CHEN and J. MAXWELL

Applied Optics, Blackett Laboratory, Imperial College of Science,Technology & Medicine,London SW7 2AZ, UK
E-mail: rschen@op.ph.ic.ac.uk, j.maxwell@ic.ac.uk

The bend and polish method of manufacture for aspheric optical surfaces, as originally proposed and used by Bernhard Schmidt [1] for the "adaptive" correction of the low order spherical aberration of a spherical mirror in his astrographic camera, and more recently used to manufacture the facets of the Keck 10m telescope primary mirror [2] and other astronomical components [3], has the advantage of producing smoothly continuous aspheric surfaces with fine surface texture. In the classical application, when the method is used to manufacture Schmidt corrector plates, the assumption is that a simply supported circular plate deformed by atmospheric pressure will assume a paraboloic shape. This is an approximation which is adequate for some applications, but needs refinement if it is to be of more general use. This paper describes the precise modelling of the classical case and gives the general requirements and results of rigorous modelling where the aberration correction requirements are more subtle.

1 Introduction

By bending an optical component and by then grinding and polishing it spherical or flat using conventional optical surface working methods allows us to manufacture optical surfaces with a smooth aspheric profile and with a high quality of surface texture.

This method was originally proposed and used by Bernhard Schmidt for the manufacture of the apparently awkwardly shaped aspheric plate which is required for his outstanding successful astrographic camera [1]. In the Schmidt's camera the corrector plate is required to introduce a wavefront aberration which is opposite to and twice the magnitude of difference between the spherical mirror used in this system and the equivalent aberration-free paraboloid, as shown in fig.1.

Schmidt exploited the fact that a thin parallel plate sitting on the edge of a vacuum cup-chuck deforms to a paraboloid-like catenary shape when the cup is partially evacuated; by working this concave surface with a spherical grinding tool and polishing it, the process (illustrated in fig.2) generates the required shape,

which is by definition the difference between the paraboloid and the sphere which are on the catenary and on the grinding and polishing tools respectively. By choosing the correct partial vacuum for the deformation of the plate and by using grinding and polishing tools of the precisely the correct radius, the corrector plate may be matched to the spherical mirror that is to be corrected.

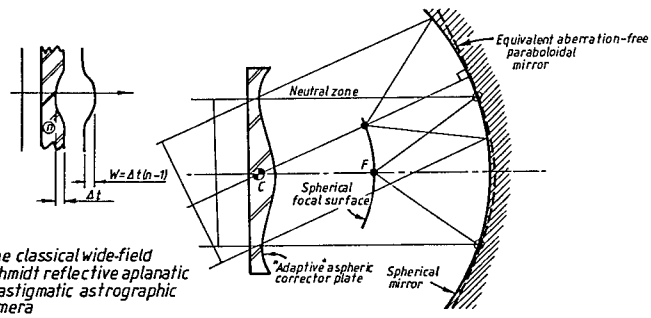

Fig 1 The classical wide-field Schmidt reflective aplanatic anastigmatic astrographic camera

For the efficient application of this method in the classical context, and more importantly, for its application in a wider range of contexts, the precise modelling of the elastic deformation of a glass corrector plate during the manufacturing process is important, and it is this that is the subject of this paper.

The aspheric profile that is generated by the manufacturing process shown in fig.2 is critically dependent on the zonal radius of the initial contact between the paraboloid-like catenary and the spherical grinding and polishing tools, which, in turn, is critically dependent on the radius of these tools. By bending the grinding and polishing tools to the correct curvature using a brace like the one in fig.2, it is possible to select the required curvature. In this case the deformation is achieved not by partial vacuum but by the application of a mechanical force through a pushing member with an appropriately selected contact diameter.

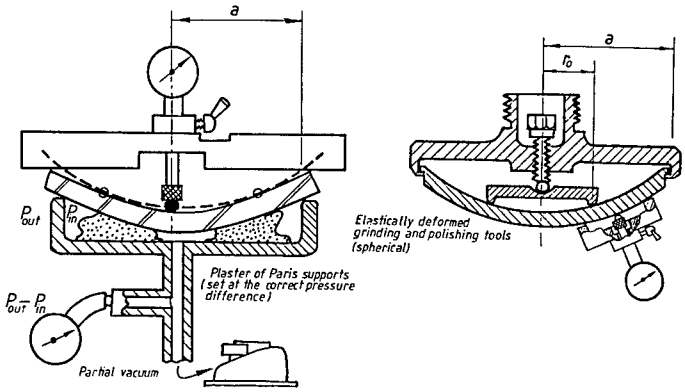

Fig 2 A proposed manufacturing procedure for a classical Schmidt plate based on references [4] and [8], but with elastically deformed tooling

The foundation for the required numerical solution for the mechanical deformation of the grinding and polishing tools shown in fig.2 are given as case 3 in Table X of reference [6] p.194-195, and are repeated here for convenience

$r < r_0$,

$$y = -\frac{3W(m^2-1)}{2\pi E m^2 t^3}\left[\frac{(3m+1)(a^2-r^2)}{2(m+1)} - (r^2+r_0^2)\log\frac{a}{r_0} + \right.$$

$$\left. + (r^2 - r_0^2) - \frac{(m-1)r_0^2(a^2-r^2)}{2(m+1)a^2}\right] \qquad (1a)$$

$r > r_0$,

$$y = -\frac{3W(m^2-1)}{2\pi E m^2 t^3}\left[\frac{(3m+1)(a^2-r^2)}{2(m+1)} - (r^2+r_0^2)\log\frac{a}{r} - \right.$$

$$\left. - \frac{(m-1)r_0^2(a^2-r^2)}{2(m+1)a^2}\right] \qquad (1b)$$

Where the quantities are defined as follows

W=total loading	t=thickness	m=1/Poisson's ratio
a=radius	E=elasticity modulous	r=radius variable

The formulae given here for the part of the tool outside and the part of the tool inside the diameter of the pushing member have to be solved for constant curvature and for equality of curvature, and this requires an aspheric profiling of the tool plate prior to deformation.

For stability during the grinding and polishing process Frank Cooke [4] recommends the use of a plaster-of-Paris support in the partial vacuum cup-chuck, which is allowed to set and hold the substrate when it is deformed to the correct curvature.

2 More general applications for the bend and polish method

The Schmidt system and Schmidt corrector plate bend and polish manufacturing process have both been successful in the astronomical field each in their own way. Ironically, the most prominent application of Schmidt systems has been in large

sizes above 1 meter aperture, where the bend and polish method has not found favour, unlike for smaller systems. On the other hand, for the facets of the Keck 10m primary mirror the initial optical working was done using an adaptation of the Schmidt method [2] and completed by using ionic figuring.

Fig.3 shows a refracting system which is exactly equivalent to the classical catadioptric Schmidt system. In this case the corrector plate does not have the same profile as in the reflecting case, and, for the same focal ratio, the corrector plate shown in fig.3 requires a stronger aspheric profile than the classical system shown in fig.1, because the spherical aberration of a single lens is greater than that of a single mirror of the same focal length.

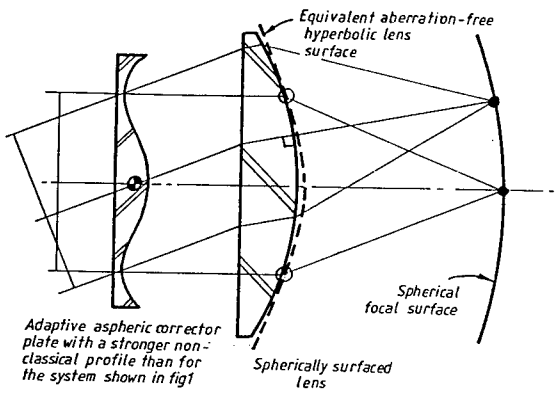

Fig3 The lens version of the system shown in fig1

In the more commercial business of manufacturing compact, catadioptic flat-field Schmidt-Cassegrain systems for smaller scale astronomical telescopes, the Schmidt method of aspheric manufacture has been adapted by using a vacuum bed of the opposite aspheric profile to that required on the final corrector plate [3].

For the development of wide field high resolution microlithographic reduction objectives, the current situation is that if the cost of manufacture of these systems is to be held within reasonable bounds [5] it looks as though the way forward is to reduce the number of components required by the use of aspheric optical surfaces. The bend and polish method of manufacture is likely to have a role to play in this new development in this technology, because it is potentially the most reliable manufacturing method for aspheric surfaces.

More directly, the bend and polish method of aspheric manufacture is of potential importance for the correction of the residual aberrations of conventional spherically surfaced optical systems. A typical application, where the residual zonal spherical aberration of (for example) a simple cemented achromat may be

corrected using a double sided bend-and-polish manufactured corrector plate is in hand with us, as a practical demonstration of the method.

Further examples for the potential application of the bend and polish technique are doublet corrector plates that can be used to correct the residual chromatic aberration of the normal conventional corrector plate and, more subtly, for the correction of the typical chromatic variation of the spherical aberration of most achromats, however complex.

All these applications for the bend and polish process rely on an accurate model for the elastic deformation of a plate under various loading conditions, and it is this that has stimulated this work.

3 The error in the assumed paraboloic-catenary deformation of a circular plate when deformed by partial vacuum on a simply supporting vacuum cup-chuck

Fig.4 shows the difference between a true paraboloid and the parabolic-catenary that is predicted by a standard closed-form analytical expression for a simply supported circular glass plate (reference [6], case 1, Table X, p194-195).

$$y = -\frac{3W(m^2-1)}{8\pi m^2 t^3}\left[\frac{(5m+1)a^2}{2(m+1)} + \frac{r^4}{2a^2} - \frac{(3m+1)r^2}{m+1}\right] \qquad (2)$$

As can be seen in fig.4, the error in the parabolic assumption in this case is approximately 1 wavelength of (visible light) on the deformed surface (approximately 0.5 wavelength on the transmitted wavefront). This of course is a result that can be directly scaled for any diameter or thickness of the plate using all the terms in equation (2).

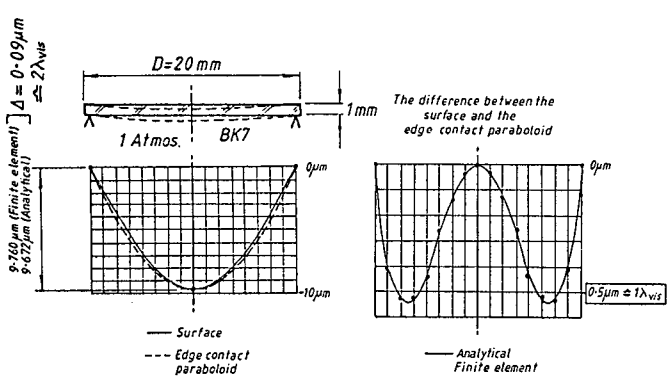

Fig4 The difference between the catenary sag of a partial vacuum deformation of a circular plate and a paraboloid

The significance of fig.4 lies in the form and the magnitude of the difference between a paraboloid and the surface generated by the elastic deformation. Because the form of this difference curve varies as r^4, just as the spherical aberration of a spherical concave mirror or a simple spherical convex lens does, it represents a direct addition to the magnitude of the aberration correction that is required in the Schmidt case.

4 An example of the application of finite element methods to predict the elastic deformation of circulary symmetric glass plates

For the case of a circular glass plate, whether it is initially flat and parallel or whether it is aspheric, the best way to compute the deformation under vacuum loading, or under the influence of a circularly symmetric mechanical brace loading, is to use a closed analytical solution for the surface deformation. As we shall see the numerical result are, by definition, smooth, and apparently correct (as judged in comparison with finite-element computed surface deformations and by the circumstantial agreement between different sources [7]). They have a respectable analytical pedigree (see ref [6] , preface) and they are of course rapid in computation.

For the purpose of non rotationally symmetric geometries, and for checking flat and aspheric circularly symmetric geometries, the alternative method of finite element computation is, at least in principal, readily to hand in off-the-shelf software, and fig.5 shows a comparison between a closed analytical solution and a finite element computation of the partial vacuum deformation of a circular plate of uniform thickness made from Schott BK7 glass (the most frequently encountered borosilicate crown optical glass).

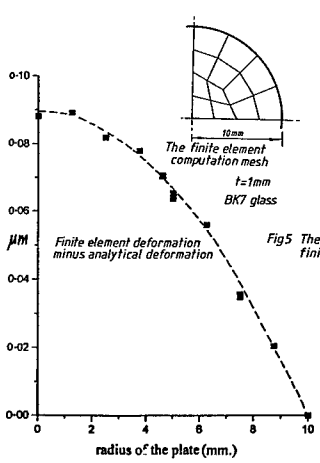

Fig5 The detail of the difference between the finite element and the analytical computation

What we see in fig.5 is (a) a small difference in the maximum deformation (of approximately $\lambda/5$ of visible light) and (b) an essentially parabolic error curve which is computed as the difference between the finite element computed curve and the closed-form analytical computation.

5 Acknowledgement

Thanks are given to Yen-Chiang Optical Instrument Factory (Taiwan, R.O.C.) for the financial support to this research. Also we would like to thank Prof. D. R. J. Owen of Dept. of Civil Engineering, University of Swansea for his help in supplying the finite elenment method computer program; Dr. Hitchings and Dr. L. Iannucci of Dept. of Aeronauties at Imperial College are also thanked for their help with the understanding the finite element method.

References

1. (a) Bernhard Schmidt: "Rapid Coma-Free Mirror System" Originally published in the Central Zeitung Fur Optik und Mechanik, 52 Jahrgang, Heft 21.
   (b) Schmidt's paper is reprinted in translation in S. Marx and W. Pfau "Astrophotography With the Schmidt Telescope" CUP 1992.
2. J.Lublinear and J.E.Nelson: "Stressed Mirror Polishing 1: A Technique for producing Nonaxisymmetric Mirrors", *Applied Optics,* **19** (1980) pp. 2332–2340 and J.E.Nelson et al " Stressed Mirror Polishing 2: Fabrication of an Off-Axis section of a Paraboloid", ibid pp2341-2352.
3. (a) T.J.Johnson and J.F.O'Rourke (Celestron Pacific Inc): US Patents 3,837,124(1974); 3,837,125(1974); 3,889,431(1975). (b) J.J.Krewark (Criteron Manufacturing Company Inc.): US Patent 3,932,148 (1976).
4. Frank Cooke, "Making a Schmidt by Vacuum Deformation", *Applied Optics,* **11** (1972) pp. 222–225.
5. See for example: Hwan J. Jeong, David A. Markle, Garaint Owen, Fabian Pease, Andrew Grenville and Rudolph von Bunau: "The Future of Optical Lithography", *Solid State Technology,* **37** (1994) pp. 39–47.
6. (a) Raymond J. Roark:"Formulas for Stress and Strain", third edition, McGraw-hill book company, Inc. 1954. (b) W. Grckeler: "Handbuch der Physik (Julius Springer-Verlag, Berlin), **6** (1928) pp. 214, Eq.(5). (c) R. T. Fenner: "Engineering Elasticity", Ellis Horwood Limited, London 1986.
7. Edgar Everhart, "Making a Corrector Plate by Schmidt's Vacuum Method", *Applied Optics,* **5** (1966) pp. 713–715.

CURRENT PERFORMANCE LIMITS FOR MICROMACHINED MEMBRANE DEFORMABLE MIRRORS

GLEB VDOVIN

Electronic Instrumentation, ITS
Delft University of Technology
Mekelweg 4, 2628 CD Delft The Netherlands

We describe the recent progress and intrinsic limitations of the technology of micromachined membrane deformable mirrors (MMDM).

1 Technology and environmental limits

Micromachined membrane deformable mirrors (MMDM)[1,2] represent an attractive alternative to the conventional deformable mirror technology because they are cheap, small, consume little power and can be operated with in a kilohertz frequency range. MMDM feature high actuator density, in some sense filling the niche between thin-plate and bimorph deformable mirrors (actuator spacing of the order of centimeters) on one side and surface micromachined SLM (TI DMD) on the other.

A typical MMDM is formed by a flexible tensed membrane suspended on a silicon frame over a structure of electrostatic actuators -see Fig. 1.

The mirror membrane should satisfy the following requirements:

- good mechanical strength;
- combination of lateral tension, membrane surface density and membrane size, securing the first resonance frequency of the membrane to be higher than the its typical working frequency, typically in the range 1Hz to 5kHz;
- high mechanical polish and high reflectivity.

If the membrane area is not larger than $5cm^2$, the best results can be obtained with LPCVD-deposited silicon nitride films, released using bulk silicon micromachining[3]. The thickness of the membrane can reach $0.8\mu m$, with a typical value in the range 500..600nm. The reflective coating, deposited on such a thin substrate can dramatically change its mechanical properties, for instance aluminum coatings evaporated from tungsten boat are compressively stressed and can therefore reduce the tension of the membrane mirror improving its voltage sensitivity and reducing its speed of response. Too thick coating can result in overall compressive stress in the membrane leading to its catastrophic failure.

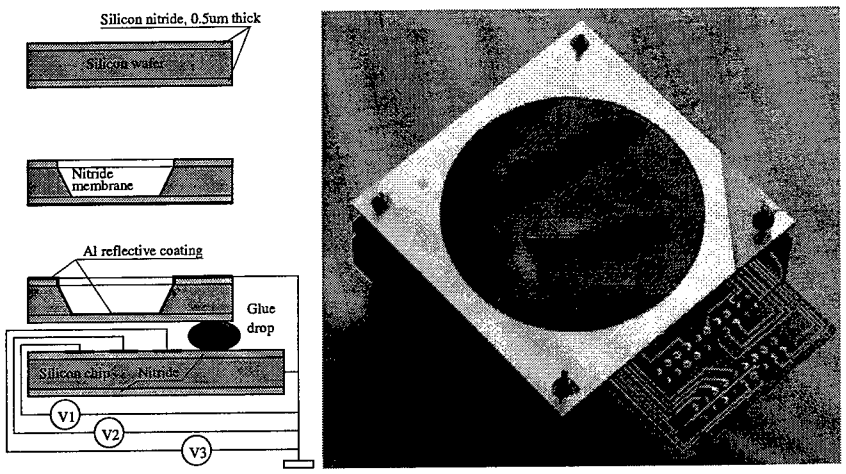

Figure 1: Fabrication technology for a small silicon-mounted MMDM used for fabrication of MMDM up to 15mm in diameter (left), a custom made MMDM with membrane diameter of 50mm (right).

Large mirrors (up to 5cm in diameter) can be fabricated using composite nitride-polysilicon-nitride membranes with a thickness up to 20μm. The tension of a composite membrane is defined by the nitride layer as polysilicon can be fabricated with near-zero stress. These mirrors have lower resonance frequency and slower response than the mirrors with a nitride membrane. Although no tests were conducted, they should have higher resistance to pulsed laser load as they have much higher thermal capacity.

The thermal behavior of membrane mirror under low and high temperature depends on the ratio of thermal expansion coefficients of the silicon frame and the membrane material. Thermal expansion of nitride is lower than that of silicon, therefore the tension of the membrane will be reduced at low temperatures – silicon frame will contract stronger than the membrane. At higher temperatures the tension of the membrane will increase due to stronger expansion of the silicon frame. This analysis is valid only for the case when the mirror temperature changes as a whole. For the case of CW laser load, the temperature of loaded membrane will be lower than the temperature of silicon frame, reducing the membrane tension locally.

Environmental limits of MMDM depend mainly on the package design.In the case of "standard" PCB package with PGA connector on the back side, the mirror is operational in the temperature range -70 ... 150C. This range can be extended to its low side by using a cryogenic-certified connectors for electric contacts. For operation at temperatures higher than 150C the package should be implemented using ceramic printed substrata.

With respect to the ambient humidity, MMDM has properties similar to any other reflective optical component. A special attention should be paid to the situations when MMDM is introduced to warm ambient as this may cause vapor condensation on the mirror surface, temporarily affecting the performance.

2 Correction precision, range and the number of actuators

The mirror membrane is fixed along its edges. To eliminate the influence of fixed boundary conditions, the light aperture should occupy approximately the central 50% of the mirror surface. For example, if a membrane mirror has an aperture of 15mm, only the central area of 10mm in diameter can be used for functional correction of wavefront aberrations. To ensure best spatial resolution, the array of electrostatic actuators is also placed under the central area of the membrane, occupying only about 60% of the membrane area.

The design of a micromachined deformable mirror allows deflection of the mirror surface only in the direction of the control electrodes, corresponding to a positive curvature of the mirror surface. To be able to correct an aberration that has both positive and negative curvature, the mirror surface should be pre-deformed to a concave spherical shape, having a weak positive optical power in the biased "zero" position - see Fig. 2. The surface displacement of the biased mirror surface limits the amplitude of the corrected aberration, moreover the correction amplitude and precision depends on the characteristic size of the aberration to be corrected.

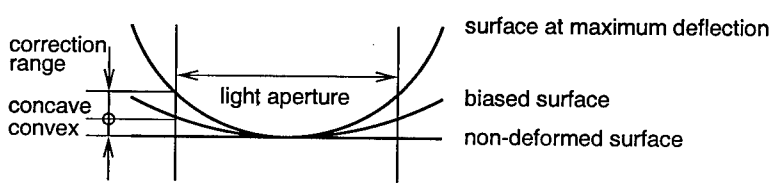

Figure 2: Biased operation of micromachined adaptive mirror. All possible mirror deflections are limited by the initial flat surface and the surface of maximum deflection. The biased surface between these two surfaces provides an approximately equal amount of convex and concave deflection. The light aperture should always be inside the clear aperture to eliminate the influence of the fixed membrane boundary.

The bias curvature $C_b = 1/R_b$, where R_b is the radius of biased surface, should be equal to the half of the maximum achievable curvature $C_{max} = 1/R_{max} = 2/(R_b)$. The range of curvature control is limited by the curvature of the biased membrane. The shape of the membrane $s(x)$ – that is needed to correct for a hypothetic harmonic aberration – can be described by a harmonic function with a period T and amplitude A: $s(x) = A\sin(2\pi x/T)$ - for simplicity we consider a one-dimensional case. The curvature of the membrane $C(x) = 4\pi^2 A/T^2 \sin(2\pi x/T)$ is limited by the value of $4\pi^2 A/T^2$. This value (positive or negative) can not exceed the absolute value of the bias curvature given by

$|1/R_b|$. The amplitude of achievable harmonic deformation of the membrane mirror is given by:

$$A_m = \frac{T^2}{4\pi^2 R_b} \tag{1}$$

where T defines the characteristic size of the aberration to be corrected. Finally the achievable P-V correction amplitude in terms of wavefront deformation will be four times larger (P-V amplitude of a harmonic function is two times larger than its amplitude, further the phase deformation equals to doubled mirror surface deformation), yielding for P-V amplitude of wavefront correction:

$$A_{wf} = \frac{T^2}{\pi^2 R_b} = \frac{1}{\pi^2 f R_b} \tag{2}$$

where f is the spatial frequency of the surface deformation. For aberrations with a spatial period smaller than the mirror aperture, the membrane corrector represents a low-frequency filter, with a maximum amplitude of corrected aberration decreasing with aberration spatial frequency by 40dB per decade or 12dB per octave. For the typical values of our system $T = 1$cm and $R_b = 4$m – aberration over the whole aperture – the maximum amplitude of correction equals 2μm while for a local aberration with $T = 5$mm the maximum amplitude of correction is almost an order of magnitude lower and equals only 0.5μm.

Equation 2 defines the maximum amplitude of the wavefront that can be corrected as a function of the aberration period T. *A is the maximum amplitude of a wavefront with a spatial period of T_{min}, that still can be corrected by the mirror. Wavefronts with larger amplitude and/or smaller periods can not be corrected.*

$$T_{min} = \pi\sqrt{R_b A} \tag{3}$$

Assuming the mirror diameter is D and we need at least 4 actuators to correct an aberration with a spatial period T, the total number of actuators providing correction with amplitude precision A and period T_{min}

$$N = \frac{16D^2}{\pi^2 R_b A} \tag{4}$$

For a deformable mirror with light aperture of $D = 10$mm, $R_b = 5$m and $A = 10^{-7}$m we have $T_{min} \sim 2$mm and $N \sim 400$. For comparison, the real device has only $N = 37$ actuators. For a mirror with $D = 35$mm, $R_b = 20$m and $A = 10^{-7}$m we obtain $T_{min} \sim 4.5$mm and $N \sim 800$. As we made no assumption about the nature of the deformable mirror response, this analysis is valid in general for any curvature-limited deformable mirror device.

Discussion

Technological limitations define the parametric area in which the performance of MMDM is optimal. At present the following technical parameters are feasible:

	Nitride MMDM	**Composite MMDM**
Membrane dimension	1mm to 25mm	1mm to 50mm
Membrane shape	rectangular circular elliptical	rectangular circular elliptical
Membrane thickness	400nm to 800nm	1μm to 10μm
Coating	metals, dielectrics	metals, dielectrics
Coating thickness	up to 2μm	up to 2μm
Response time		
80% amplitude	200μs to 5ms	1ms to 20ms
Maximum reflectivity	98.8%	89% Al-coated no data for multilayer
Surface deflection	10μm for a 15mm mirror	33μm for a 50mm mirror
Initial flatness	0.5μm P-V over 15mm 150nm RMS over 15mm	5μm P-V over 35mm 450nm RMS over 35mm
Bias curvature (ROC)	5m for a 15mm aperture	20m for a 50mm aperture
Maximum control voltage (typical)	200V	330V
CW power load	80W in a 5mm beam	no data available
Packaging	printed board	printed board with mechanical adjustments

Table 1: Performance limits for nitride and nitride-polysilicon MMDM (as of July 1999).

Acknowledgments

This work was supported by LTR ESPRIT project on Micro-Optical SIlicon Systems (MOSIS) and ESA project on Adaptive Optics Technology.

References

1. G.V. Vdovin, P.M. Sarro, Flexible mirror micromachined in silicon, Applied Optics **34**, 2968–2972 (1995)
2. G.V. Vdovin, Simon Middelhoek, Pasqualina M. Sarro, Technology and applications of micromachined silicon adaptive mirrors, Optical Engineering **36**, 1382–1390 (1997)
3. M. Bartek, G.V. Vdovin, R.F. Wolfenbuttel, Selective and non-selective deposition of thick polysilicon layers for adaptive mirror device, J. Micr omech. Microeng **7**, 133-136 (1997)

MODAL LIQUID CRYSTAL WAVEFRONT CORRECTORS

GORDON D. LOVE AND ALEXANDER F. NAUMOV

Dept. of Physics and School of Engineering, University of Durham, DH1 3LE U.K.
E-mail: g.d.love@durham.ac.uk

MICHAEL Yu. LOKTEV

P.N. Lebedev Physical Institute Samara Branch, Russian Academy of Sciences,
Novo-Sadovaya Street 221, Samara 443011, Russia

IGOR R. GURALNIK,

Samara State University, Acad. Pavlov Street 1, Samara 443011, Russia

GLEB V. VDOVIN

Electronic Instrumentation, TU Delft, P.O. Box 5031, 2600 GA Delft, The Netherlands

Liquid crystal wavefront correctors have traditionally been used as zonal wavefront correctors, whereby the influence function is usually piston-only over the area defined by the device pixels. By applying a distributed voltage across the device, a continuous LC cell may produce modal wavefront deformations. In this paper we will describe the concept of modal liquid crystal wavefront correctors, review some of the current results.

1 Introduction

Liquid crystal spatial light modulators (LC-SLMs) are an alternative to the deformable mirror in an adaptive optics system. They are particularly attractive for non-astronomical applications where low cost, compactness, and low power consumption may be more important. Their main drawback is their slew rate, which is much slower than that for a deformable mirror. There are several papers in these proceedings describing work using LC-SLMs. They modulate optical path length by refractive index control, instead of real path length adjustment.

Most LC-SLMs are zonal wavefront correctors. In other words, the device is addressed via electrodes leading to an actuator (or pixel), and the refractive index is modulated over an area localised to the size of the pixel. The desired wavefront shape is built up in a series of steps. These devices are analogous to a segmented mirror, except that in a mirror the influence function is generally tip-tilt-piston, and in a LC-SLM the influence function is piston-only. See, for example, references [2,3] for papers on zonal LC-SLMs. Some authors [1] have noted that these pixelated structures can give rise to diffraction at the pixel boundaries. This is true for any zonal wavefront corrector, but the fact that the influence function is

piston-only means that the fitting error is larger for a LC-SLM than for a deformable mirror for a given number of actuators.

In this paper we describe how to produce a LC-SLM with a non-local influence function. Such devices do not have a pixelated electrode structure, and are analogous to continuous facesheet mirrors. We proceed by describing the simplest devices, prisms and lenses, and then describe a full modal LC-SLM wavefront corrector.

2 Liquid crystal prisms

The simplest type of LC device is a LC prism [4]. An approximately linear phase ramp is produced by using a single LC cell, and applying a voltage ramp along one of the electrodes, as shown in the following figure 1.

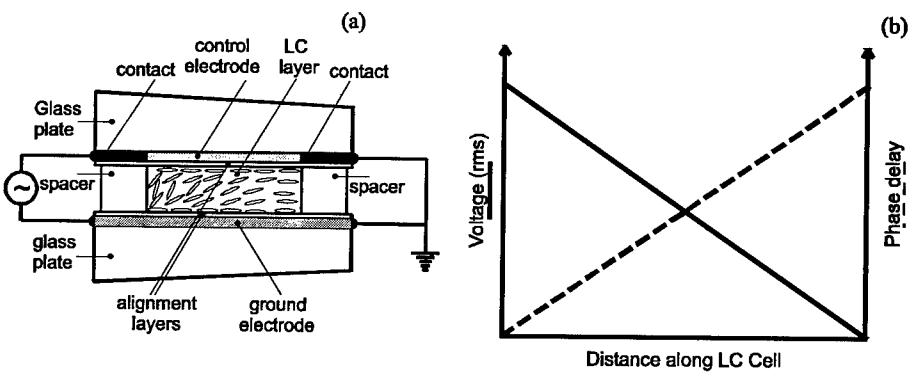

Figure 1. A liquid crystal prism (or beam deflector) produced using a single LC cell. (a) A voltage ramp is applied along the top electrode so that there is a maximum voltage (typically 10V rms AC) across the left hand side of the cell, which linearly decreases to 0V across the right hand side. The corresponding voltage and phase profiles are shown in (b). The phase profile assumes that the phase shift is a linear function of voltage, which is only approximately true over a limited range of the LC dynamic range.

In the LC prism, the electrical properties of the actual device have been ignored. This is acceptable, assuming that the applied frequency is relatively small and the top electrode resistance is relatively small. In this case the voltage simply falls linearly across the cell.

3 LC lens

It is possible to use the actual electrical properties of the LC cell produce more complicated voltage profiles across the device [5]. In this case it is necessary to use a high resistance top electrode, and higher frequency control voltages, as shown in figures 2 and 3. The LC cell can be modeled similarly to a transmission line,

whereby there is a distributed resistance (the top electrode), and a distributed capacitance and conductance (produced by the LC layer). The resulting phase and voltage profile is shown in figure 4.

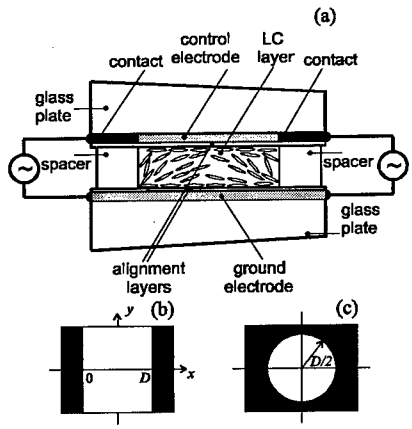

Figure 2. A LC lens. This is similar to a LC prism, except that the top electrode needs to be have much higher resistance (~MΩ), and a AC voltage is applied to both ends of the top electrode. (b) and (c) show the geometries necessary to produce a cylindrical and circular lens respectively

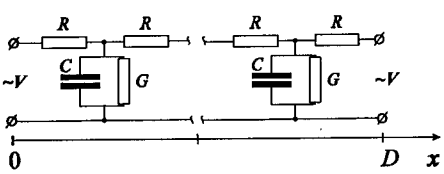

Figure 3. The electrical equivalent of the LC lens shown in figure 2. Voltage V is applied to either end. The series of resistors, R, correspond to the top electrode, and the series of capacitors and conductances, C and G, correspond to the LC layer. Note the similarities with a transmission line.

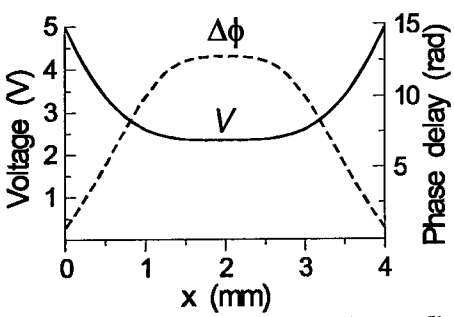

Figure 4. Corresponding voltage a phase profile across a LC lens, using the circuit shown in figure 3. In this case a realistic voltage-phase relationship was used in the calculation.

The voltage profile across the device is described by the following second order partial differential equation,

$$\frac{\partial^2 V}{\partial x^2} = RC\frac{\partial V}{\partial t} + RGV ,$$

where V, is the voltage, R is the sheet resistance of the top electrode, and C and G are the capacitance and conductance per unit length of the LC layer. The above equation is for a 1-d (cylindrical lens). A similar equation applies for the 2-d (circular) lens. A full solution of the equation is complicated by the fact that both R and G are functions of the voltage, V. The control of a LC lens is described in more detail in reference [6].

The following analogy can be used to further understand the principle of a modal LC lens. Imagine a thin rubber membrane on metal ring. If this membrane is placed in a liquid and the ring vibrates perpendicularly to the membrane surface, then the resulting membrane oscillations will be larger at the edge than at the centre. The amplitude and frequency of the forced oscillations determine the profile

of the membrane. The amplitude of the AC voltage across the lens aperture behaves in a similar fashion.

Figure 5 shows a LC lens placed with its optical axis at 45^0 between crossed polarizers (equivalent to an interferometric arrangement). The focal length, f, can be calculated using the following equation,

$$f = \frac{\pi D^2}{4\Delta\phi\lambda},$$

where D is the lens diameter, $\Delta\phi$ is the variation in phase from the centre to the edge of the lens, and λ is the wavelength. The focal lengths produced long due to the finite stroke of the LC cell. Currently achievable f-ratios are from ~ 100 to ∞. Figure 6 shows an example of a LC lens producing an image.

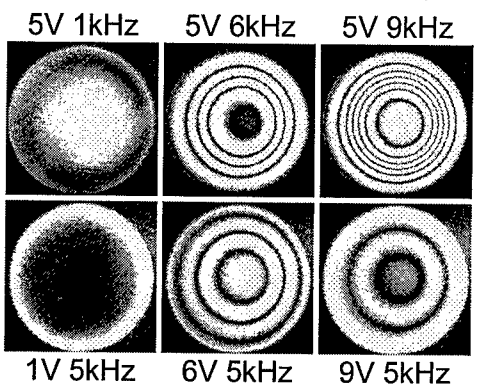

Figure 5. Interferograms (produced by placing the device between crossed polarizers) from a spherical LC lens, for different values of applied voltage (rms) and frequency.

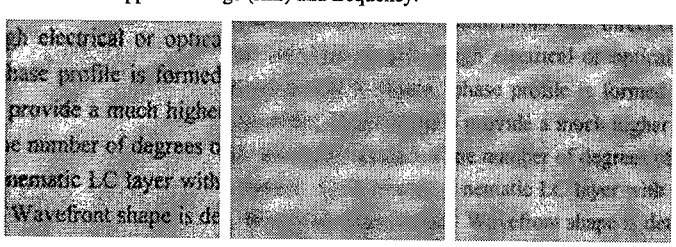

Figure 6. Example of a LC lens producing an image. (Left) lens off, system adjusted to give a good focus. (Middle) System mechanically adjusted to induced defocus. (Right) LC Lens turn on to correct for induced defocus.

Figure 7 shows the PSF from a LC lens compared to an ordinary lens.

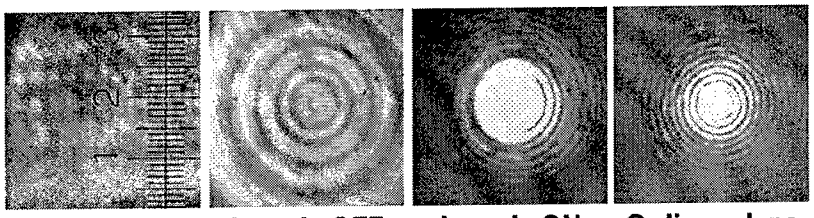

Figure 7. PSFs produced by a LC lens by passing a beam of laser light through a lens, followed by a CCD camera. The left image shows the scale, where each major unit is 1mm, and the sub-units are 100 μm.

A LC lens can obviously be used as a variable focal length lens. It can also be used as a defocus corrector in an adaptive optics system. By carefully controlling the applied voltages to a modal LC lens it is possible to produce non-parabolic phase profiles. For example, we have demonstrated the production of controlled spherical aberration from $+3\lambda$ up to -4λ for $\lambda = 632.6$ nm. Such a device would be useful for the correction of spherical aberration.

4 A modal LC wavefront corrector

How can a modal LC device be used to produce more complicated wavefront shapes? Figure 8 shows a modal LC wavefront corrector [7]. Individual leads are inserted through holes in the glass substrate, and make contact with a high resistance continuous electrode. The dielectric mirror reflects light and means the device works in reflection mode. Each lead corresponds to an actuator. The impulse function around each actuator can be controlled by adjusting the applied voltage and frequency. Figure 9 shows an interferogram from the central area of a 16x16 actuator modal LC device.

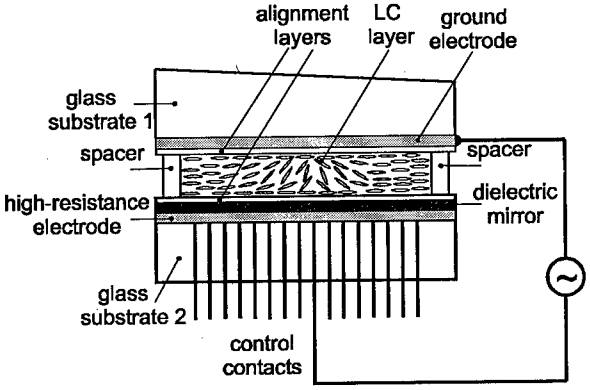

Figure 8. A modal LC wavefront corrector. Each of the addressing leads leading from the bottom of the device makes contact with the continuous high resistance electrode, through the dielectric mirror. The impulse function around each lead can be controlled by altering the applied voltage and frequency.

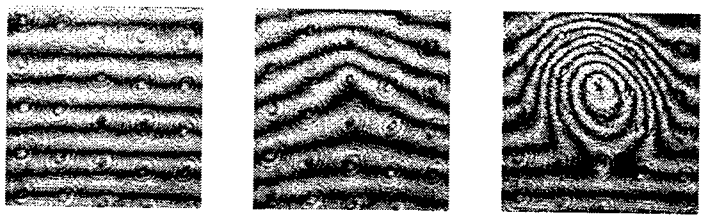

Figure 9. Interferogram from the central area of a 16x16 actuator modal LC wavefront corrector. The applied voltage was 5V rms, at frequencies of 1KHz, 10KHz, and 100KHz, respectively.

5 Conclusion

Modal addressing of LC devices allow a continuous phase profile to be produced. They have the advantage that the fitting error will be less than a pixelated device for a given number of actuators. This may mean that LC wavefront correctors can be produced with a very large number of actuators, and with a very high fill factor (unity), which is difficult to achieve currently.

References

1. Dayton D.C., Browne S.L., Sandven S.P., Gonglewski, J.D., and Kudryashov, A.V. Theory and laboratory demonstration on the use of a nematic liquid-crystal phase modulator for controlled turbulence generation and adaptive optics. *Appl. Opt.* **37** (1998) pp.5579-5589.
2. Dou R., and Giles M.K. Closed-loop adaptive optics system with a liquid crystal television as a phase retarder. *Opt. Lett.* **20** (1995) pp.1583-1585.
3. Love G.D., Wavefront correction and production of Zernike modes with a liquid crystal SLM. *Appl. Opt.,* **36** (1997) pp. 1517-1524.
4. Love G.D. Major J.V., and Purvis, A., Liquid crystal prisms for tip—tilt adaptive optics, *Opt. Lett.* **19** (1994) pp.1170-1172.
5. Naumov A.F., Loktev M.Yu., Guralnik I.R., Vdovin, G., Liquid-crystal adaptive lenses with modal control, *Opt. Lett.*, **23** (1998) pp. 992-994.
6. Naumov A.F., Love G.D., Loktev M.Yu., Vladimirov F.L., Control optimization of spherical modal liquid crystal lenses, *Opt.Express*, **4** (1999), pp.344-352.
7. Naumov A.F. Vdovin G.V., Multichannel LC-based wavefront corrector with modal influence functions. *Opt.Lett.,* **23** (1998) pp. 1550-1552.

CHARACTERISTIC OF A NOVEL SMALL PZT DEFORMABLE MIRROR

NING LING, XUEJUN RAO, LAN WANG, SHILONG JIAO

Institute of Optics and Electronics, Chinese Academy of Sciences, P. O. Box 350, Shuangliu, Chengdu 610209, China. E-mail: whjiang@mail.sc.cninfo.net

A 19-element small PZT deformable mirror with outer diameter 24mm has been developed. In this paper, the characteristics of this DM such as influence function, hysteresis and non-linearity of deformation, resonance frequency are reported. The fitting capability of the DM to the lower order Zernike aberrations is investigated experimentally. The results are reported.

1 Introduction

Deformable mirror (DM) is the key element of adaptive optics (AO) system. The size, volume and cost of DM decide that of the adaptive optical system to a certain extent. Several types of DMs were developed in our Lab[1]. The main specifications of these DMs are listed in Table 1. There are two kinds of DMs, monolithic PZT and integrated by discrete PZT stacks. The voltage sensitivity of deformation of the monolithic DM is small and the diameters of the DMs with PZT stacks are rather large (>70mm). In order to reduce the size and cost of AO systems for some applications, a novel small DM made by PZT has been developed. In this paper, the specifications of this small DM as well as the experimental results of fitting capability to the low order Zernike aberrations will be reported.

Table 1. Deformable mirrors developed in IOE, CAS

Type	Monolithic	PZT stack actuator			
Number of actuators	21	19	21	37/55	61
Aperture mm	Φ50	Φ70	Φ50	Φ100	Φ120
Max. deformation μm	±0.8	±1.5	±2.5	±1.5	±2.0
Max. voltage V	±1000	±700	±650	±400	±300
Resonance frequency Hz	19K	10K	8K	7K	5K

2 Description

The specifications of the small DM are as follows:

1. Diameter of mirror: 24mm,

2. Clear aperture: 20mm,
3. Number of actuators: 19,
4. Maximum deformation: ±1μm,
5. Maximum voltage: ±700V,
6. Hysteresis and non-linearity:< ±4%,
7. Resonance frequency: >30kHz.

Figure 1 is the photo of the DM. Figure 2 shows the configuration of its actuators. The curve of deformation versus voltage is shown in Figure 3, from which one can see that the hysteresis and non-linearity are very small. Figure 4 shows the surface deformation of the mirror when voltages are applied at actuators of different positions separately. From these influence function curves, the couplings of the central actuator, which is the deformation at the center of neighboring actuator, is 7.5%. The couplings of the edge actuator and actuator at the second ring are 15% and 10% respectively. From the amplitude and phase response shown in Figure 5, there is no resonance between 0~30kHz. The mirror has very fast response speed.

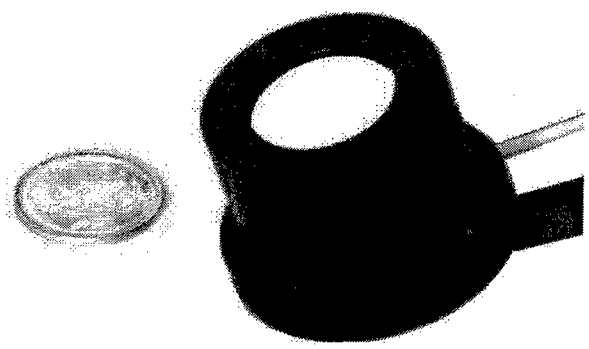

Figure 1. Photo of the DM

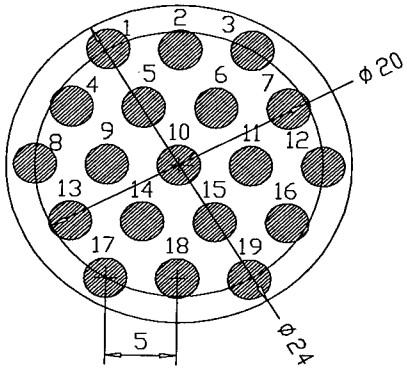

Figure 2. Configuration of actuators.

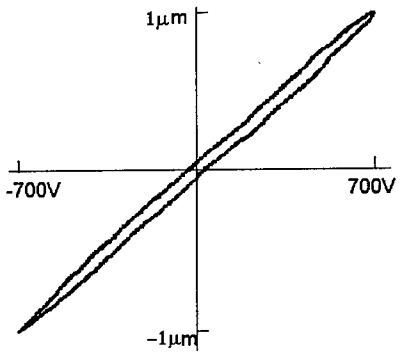

Figure 3. Deformation versus voltage.

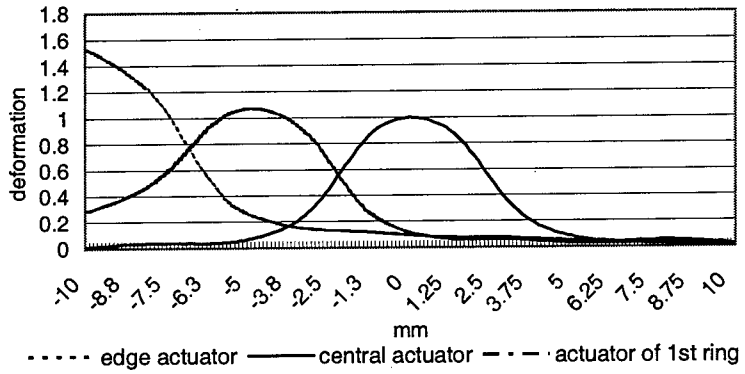

Figure 4. Influence function of actuators at different position.

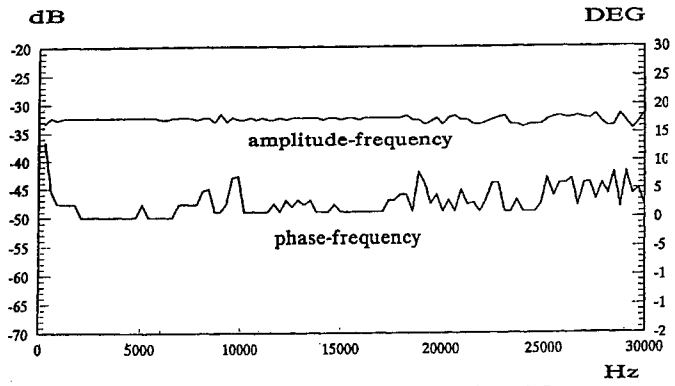

Figure 5. Frequency response of the DM.

3 Fitting capability to low order Zernike aberrations

The fitting capability of the DM to different low order Zernike modes were investigated. The expression of Zernike modes is

$$Z_i = \sqrt{n+1}R_n^m(r)\sqrt{2}\begin{cases}\cos(m\theta) & m \neq 0, i = even \\ \sin(m\theta) & m \neq 0, i = odd \\ 1 & m = 0\end{cases}$$

where

$$R_n^m(r) = \sum_{s=0}^{(n-m)/2} \frac{(-1)^s (n-s)!}{s![(n+m)/2-s]![(n-m)/2-s]!} r^{(n-2s)}$$

n is the radial degree, m is the azimuthal frequency, m≤n, n-m=even. In the experiments, the Zernike modes of n=2,3,4 are fitted by the DM. These aberrations are listed in Table 2.

Table 2. Aberrations fitted by the DM in experiments

n	m: 0	1	2	3	4
2	$\sqrt{3}(2r^2-1)$ defocus		$\sqrt{6}r^2\sin 2\theta$		
			$\sqrt{6}r^2\cos 2\theta$ astigmatism		
3		$\sqrt{8}(3r^3-2r)\sin\theta$		$\sqrt{8}r^3\sin 3\theta$	
		$\sqrt{8}(3r^3-2r)\cos\theta$ Coma(3rd order)		$\sqrt{8}r^3\cos 3\theta$	
4	$\sqrt{5}(6r^4-6r^2+1)$ spherical		$\sqrt{10}(4r^4-3r^2)\cos 2\theta$		$\sqrt{10}r^4\cos 4\theta$
			$\sqrt{10}(4r^4-3r^2)\sin 2\theta$		$\sqrt{10}r^4\sin 4\theta$

Voltages are applied to the actuators of DM[2]. The surface figures are measured by a Zygo interferometer. From the residual wavefront, which is the differences between a given Zernike aberration and the measured wavefront produced by the DM, the increments of the voltages at actuators for reducing residual wavefront are computed by wavefront reconstruction algorithm. By adjusting the voltages at actuators, the rms of residual wavefront is minimized. After several iterations, the residual wavefront comes to its minimum, which is mainly of higher spatial frequency and cannot be corrected by the DM.

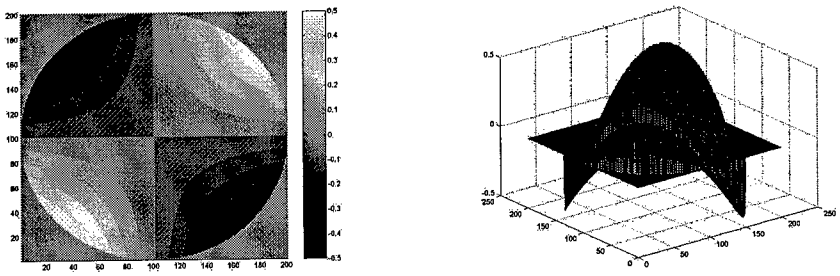

6a. Zernike mode n=2, m=2

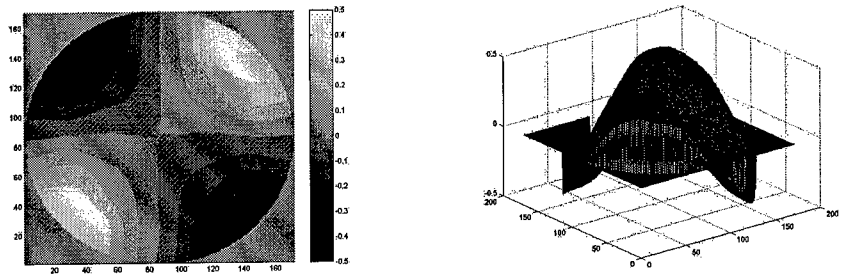

6b. Wavefront produced by DM

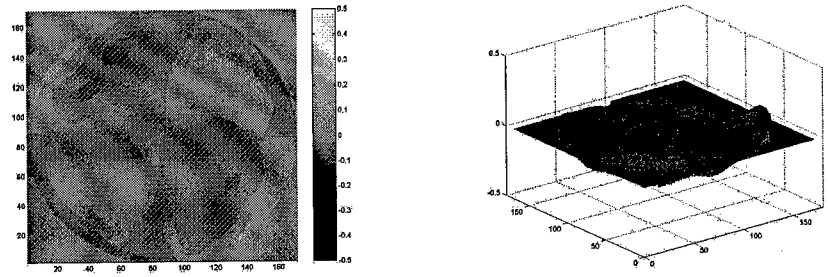

6c. Residual wavefront.

Figure 6. Fitting experiment for Zernike mode n=2, m=2.

Figure 6 is an example. Figure 6a is the given Zernike aberration of astigmatism (n=2, m=2). Figure 6b is the wavefront produced by the DM. Figure 6c is the residual wavefront. Figure 7 summarizes the experimental results, which shows the rms of the Zernike wavefronts of different orders and the rms of the minimized residual wavefront corrected by the DM.

From Figure 7, we can see that the fitting capability of DM decreases with higher mode order. It is obvious that the spatial frequency of wavefront is higher for higher order and the DM can only correct the aberration of low spatial frequency due to limited number of actuators. For the same radial order n, the fitting capability of DM is better for higher azimuthal frequency m. From the radial term of Zernike expression, we can see that the derivative of R_n^m has n-m-1 roots along the radius. It means that there are n-m-1 vertexes along a radius and the radial frequency is about $(n-m-1)/2$. The radial frequency is lower for higher azimuthal order m of a given n, hence the fitting error is smaller.

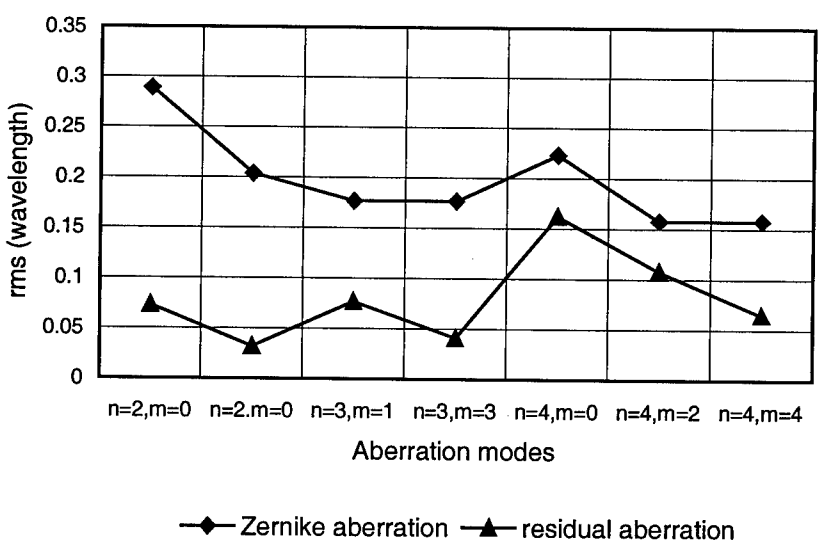

Figure 7. Fitting capability of the DM to low order Zernike aberrations.

4 Conclusion

The novel small DM has low hysteresis and non-linearity, very high resonance frequency and appropriate coupling between neighboring actuators. These specifications make it suitable for high-speed adaptive optical systems. The fitting

capability to low order Zernike modes are investigated experimentally. Results shows that it can correct aberrations up to n=4 and m=4. Fitting error is smaller for larger azimuthal frequency m with the same radial order n.

5 Acknowledgement

This work was supported by the National High-Technology R&D Project of China.

References

1. Ning Ling, Chunlin Guan, Deformable mirrors and fast steering mirrors developed in the Institute of Optics and Electronics, Chinese Academy of Sciences, *SPIE Proc.* **2828**, (1996) pp. 472-478.
2. Wenhan Jiang, Ning Ling, Xuejun Rao, Fan Shi, Fitting capability of deformable mirror, *SPIE Proc.*, **1542,** (1991) pp. 130-137.

LARGE ADAPTIVE METAL MIRRORS

J.H. LEE, A.P. DOEL, D.D. WALKER

Optical Science Laboratory, Dept Physics & Astronomy, UCL Gower Street, WC1E 6BT E-mail: apd@star.ucl.ac.uk

1 Introduction

OSL has been at the forefront of the development of large adaptive mirror technology. Though the original focus for this work was the development of adaptive secondary mirrors for large telescopes, the technology developed is directly applicable to other fields such as high power laser beam forming. OSL has undertaken a series of commissioned studies [1, 2, 3], that have demonstrated the optical efficiency, and mechanical feasibility of performing adaptive correction with large deformable metal mirrors.

OSL has built and tested a prototype adaptive metal mirror (see figures 1,2,3). The approach is innovative in its combination of modern aluminium mirror technology (formed as a thin meniscus) with the adaptive function. The prototype consists of a 270mm diameter mirror faceplate to the back of which are interfaced 7 magnetostrictive actuators via flexure couplings. These in turn are connected to a rigid aluminium backing (or reaction) plate against which the forces react. The faceplate is manufactured from a 10mm thick aluminium alloy sheet and has a concave spherical surface with a radius of curvature of 2955mm.

The magnetostrictive actuators used in the demonstrator contain a strain gauge position feedback system, which can be used in a control loop to compensate for the hysteresis properties of the actuators, thus linearizing the mirror response. The flexure couplings used to interface the actuators to the faceplate have been designed to satisfy the conflicting requirements of flexibility for accommodating mirror motion and stiffness for maintaining radial support and high resonant frequency. The couplings have also been designed to allow quick and easy removal and replacement of broken or damaged actuators.

The use of aluminium alloy as a faceplate material provides several advantages over the conventional glass-ceramic materials. These are:-

Ten times the yield strength of polished glass, and fifty times that of ground or damaged glass, so aluminium mirrors are robust. They are therefore ideally suited to surviving the many stress-cycles suffered by deformable (active and especially adaptive) mirrors, particularly at a location above a primary mirror where stress-failure could be catastrophic.

Unlike glass, large aluminium substrates can be machined to a few microns precision using standard low-cost industrial engineering facilities. This impacts favourably on schedule as well as cost.

Aluminium mirrors and associated aluminium structural components can be machined by normal metal working shops, can be light-weighted by standard milling, and can take tapped holes etc for fixtures. This again can reduce production costs.

High thermal diffusivity, which leads to temperature differences across the mirror being rapidly equalised. This means the mirror figure is not distorted despite the high thermal expansion coefficient. The mirror will also follow the ambient temperature closely eliminating mirror seeing effects. The mirrors can also be easily cooled if required.

A similar glass-ceramic faceplate would be highly vulnerable to damage when removed from the application environment (e.g. for cleaning, aluminising, or maintenance of the actuators or control electronics). A minor or even possibly microscopic defect could act as a stress-concentration that could lead to catastrophic failure in service at an indeterminate time in the future.

In producing the aluminium faceplate the machining and grinding process introduces residual stresses in the material that can effect the final figure. These stresses are removed by thermally cycling the substrate. The aluminium substrate is then coated with a 100-200μm layer of nickel for final polishing. If necessary the final polished optical surface can then be further coated with conventional coatings (aluminium, silver, etc) to obtain a high reflectance.

The demonstrator has been successfully used to validate important technological aspects of the OSL approach to adaptive mirrors. The manufacturing, assembly, disassembly, reassembly and calibration techniques for an adaptive secondary system have been developed and it has given insight into the replacement of actuators and confirmed the previous finite element analysis of the actuator influence functions. The measured influence functions for the central and an edge actuator are shown in figure 4. The ability of the mirror to fit various zernike deformations has also been measured and the fitting for the four zernike terms are shown in figure 5. The system has been extensively statically tested and the results presented in recent papers [4,5,6].

Recently initial tip/tilt testing of the current system has been performed with the demonstrator operated in closed loop with a quad-cell sensor. Tip/tilt aberrations were generated with a rotating glass plate and figure 7 shows the resulting quad-cell sensor

signal for the demonstrator in open and closed loop. As can be seen the tip/tilt aberration was suppressed by a factor of ~10 in this preliminary experiment. With refurbishment of the actuators, residual hysteresis and thermal effects will be reduced which should improve the tip/tilt result.

2 Current and Future Developments

Aluminium adaptive mirror technology offers a potentially inexpensive and reliable way of producing large or mid-sized adaptive mirrors. Currently at OSL the 270mm demonstrator is being tested to investigate its dynamic performance. The next planned stage is to build a 60cm prototype mirror with 19 actuators. Preliminary FEA analysis of such a system has already been undertaken to investigate horizontal and zenith deformation

The aluminium mirror technology itself has been demonstrated at the large scale at OSL by producing a 1.8m diameter mirror (non adaptive) under contract to the Birr foundation (see figure 6)

References

1. B.C. Bigalow, D.D. Walker, R.G.Bingham, P. D'Arrigo, Feasibility of Deformable Secondary Mirrors for Adaptive optics and IR chopping, Report to the Gemini-UK project, 1993
2. B.C. Bigalow, D.D. Walker, R.G.Bingham, Design of an Adaptive Secondary Mirror, Phase II: Zernike polynomial fitting to Mirror FEA Model and design of a 270mm demonstrator mirror. Report to the Gemini-UK project, 1994.
3. B.C. Bigalow, R.W.Wilson, C.R.Jenkins, D.D.Walker, Analysis, simulation and Performance Comparison of Adaptive Optical Correction with Deformable Secondary Mirrors, Report to the Gemini-UK project, 1994.
4. D.D. Walker, J.H. Lee, R.G. Bingham, D. Brooks, M.Dryborough, G.Nixon, H.Jamshidi, S.W.Kim, B. Bigalow, Rugged adaptive telescope secondaries: experience with a demonstrator mirror, The SPIE International Symposium on Astronomical Telescopes and Instrumentation, Kona, 1998.
5. J.H. Lee, A.P. Doel, D.D. Walker, Adaptive Secondary Mirror: Demonstrator: Design and Simulation, To appear in Opt. Eng., 1999.
6. J.H. Lee, A.P. Doel, D.D. Walker, Adaptive Secondary Mirror: Demonstrator: Construction and Evaluation, Submitted to Opt. Eng.,1999.

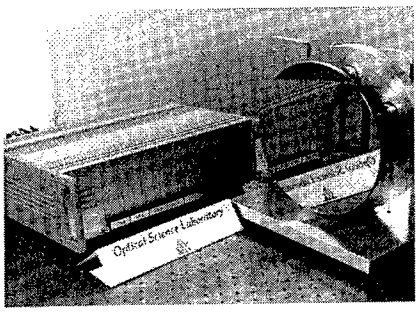

Figure 1. The Adaptive Secondary Demonstrator along with its associated drive Electronics

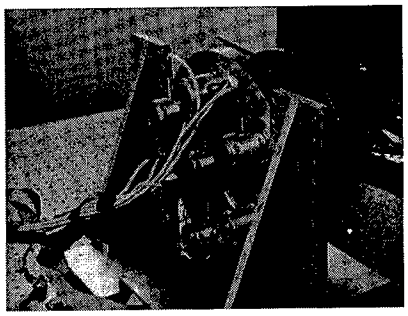

Figure 2. A close up view of the mirror actuators and flexure couplings

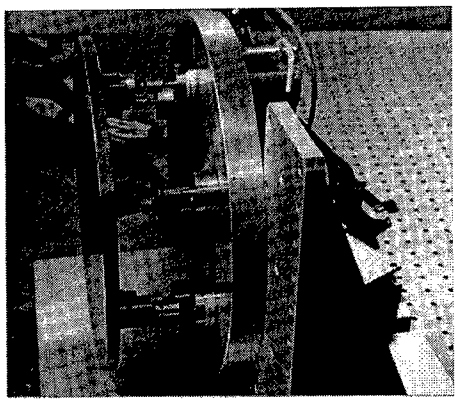

Figure 3. A view of the back of the demonstrator showing connections to actuators

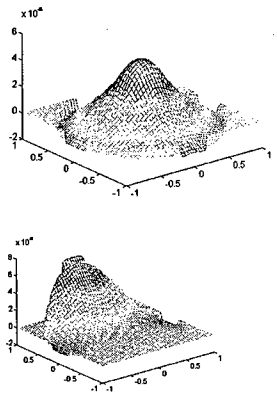

Figure 4. Measured influence functions for the central (top) and an edge actuator (bottom)

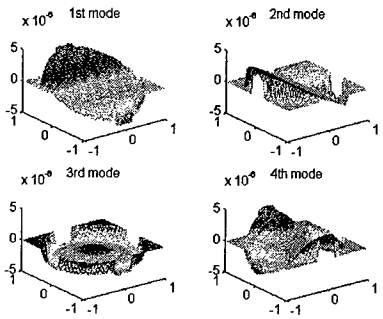

Figure 5. Zernike terms Z2-Z5 reproduced by the demonstrator

Figure 6 The Birr 1.8m aluminium mirror on the OSL polishing machine

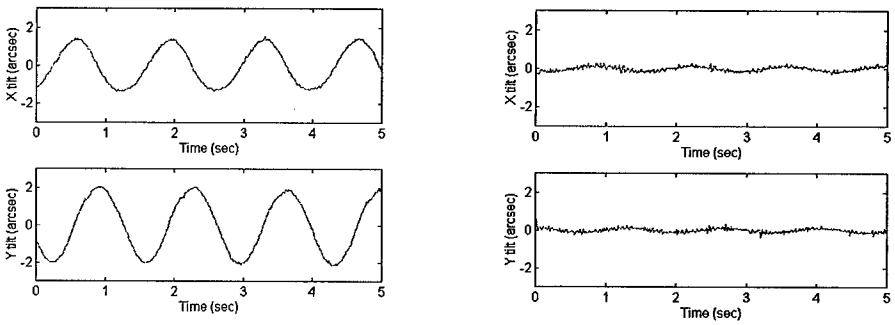

Figure 7 Open (left) and closed (tight) loop quad-cell signals

ADAPTIVE OPTICS FOR TESTING ASPHERIC SURFACES

M. DAFFNER, ST. REICHELT, H. TIZIANI
Institut für Technische Optik, Universität Stuttgart

e-mail: daffner@ito.uni-stuttgart.de

Aspherical surfaces will be widely used in future. Due to high fringe densities interferometrical evaluation is difficult. Adapted reference surfaces or appropriate compensating optics, refractive or CGHs can be used to reduce the fringe density.
By implementing an adaptive mirror in a Twyman Green type Interferometer it is possible to reduce the fringe density in order to allow numerical evaluation. As an example an aspherical surface was analysed where an adapted mirror was used. For the evaluation of the aspherical coefficients ray tracing is needed. A known surface was used for the calibration.

Our main activity was to study the potential of an adaptive mirror device in measuring aspherical surfaces. This was one part of our activities in the **ESPRIT Project MOSIS**. The used membrane mirrors were supplied by Gleb Vdovin, TU Delft, project partner in **MOSIS.**

1 Measurement of aspherical surfaces

The problem are steep aspherical surfaces. In interferometrical evaluations of these surfaces this results in high fringe densities. Therefore it is necessary to use adapted reference surfaces or additional compensating optics, refractive or CGHs.
By implementing an adaptive mirror in a Twyman Green type interferometer we have already shown that it is possible to reduce this fringe density down to numerically evaluable densities. An example of an asphere was characterised using this setup. We introduce our actual measuring scheme, the scheme of evaluating the aspherical coefficients by ray tracing as well as the calibration. We mention actual problems of the measurements and propose solutions.

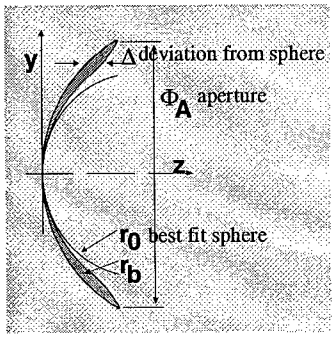

Fig.1: Scheme of an aspherical surface

Symmetrical aspherical surfaces are described as follows in equation (1).

$$z(y) = \frac{\rho y^2}{1+\sqrt{1-\varepsilon\rho^2 y^2}} + b_4 y^4 + b_6 y^6 + ... + b_{2N} y^{2N} \quad (1)$$

Where ρ is the curvature at the pole of the surface, ε is the conic coefficient and z the sag of the surface parallel to the z-axis. The b_i are the aspheric coefficients.

The main problems in measurement of aspheres are:

- High local slope of the aspherical surfaces.
- Vignetting, even by high local slopes.
- Costly and time consuming designing, fabrication, testing and calibrating of compensators. Production of conventional refractive compensators take couples of months.
- Low flexibility.
- Aligning procedures for master or reference and test surface are difficult.

2 Recent results, improvement by using an adaptive micro mirror

Normally in aspheric metrology it is necessary to use refractive compensators or additional CGHs. By implementing the adaptive mirror in a Twyman Green type interferometer it is shown that it is possible to reduce this fringe density in order to allow numerical evaluation.
Our first set up worked with an adaptive reference surface after passing the asphere in transmission. The disadvantage was the reduced sensitivity. The first generation adaptive mirror was used.

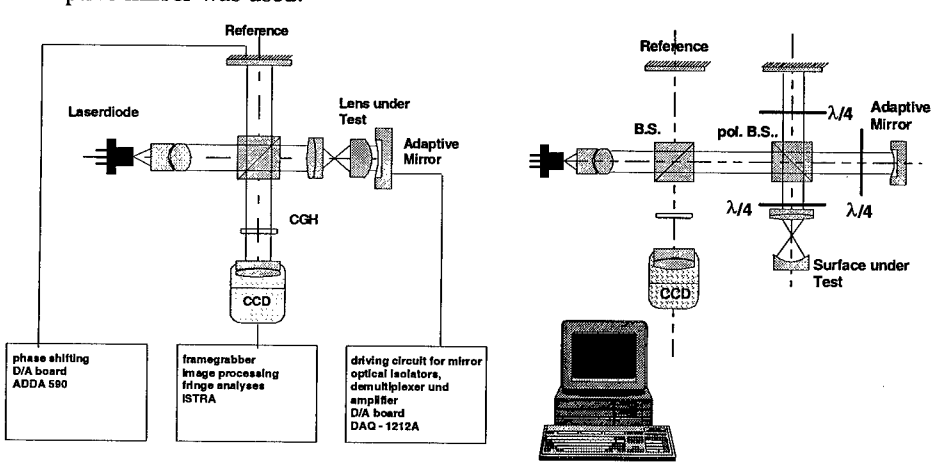

Fig.2: Examples of set-ups for measuring aspheric lens surfaces in reflection or transmission.

Further it was necessary to calibrate the mirror shape for several given voltage distributions. For the evaluation of the shape of the aspheres ray - tracing of the compensating optics in the interferometrical set-up is needed. The characterisation of the optical set-up was done by ray-tracing with CODEV.
For the first measurements of reflective aspherical surfaces we investigated aspheric moulds.

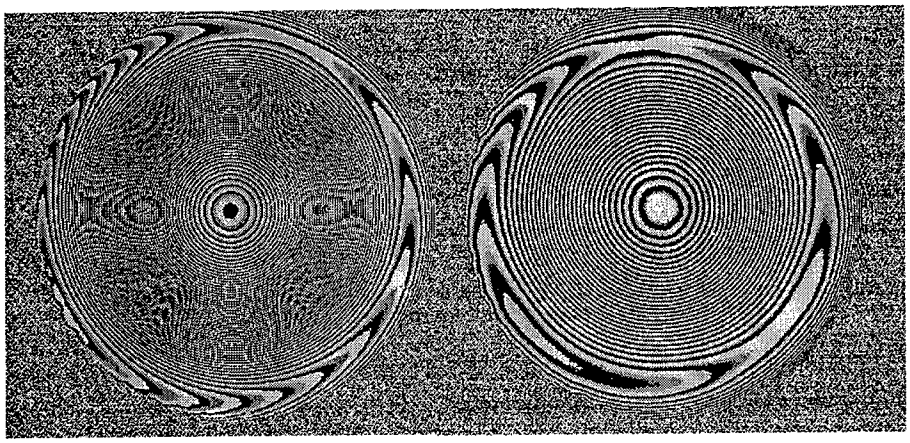

Fig.4: Interferogram without compensation

Fig.5: Interferogram after adapting the reference by the adaptive mirror device

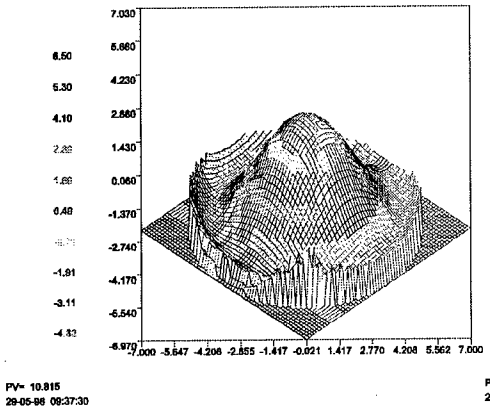

Fig.6: Measured aspherical wavefront

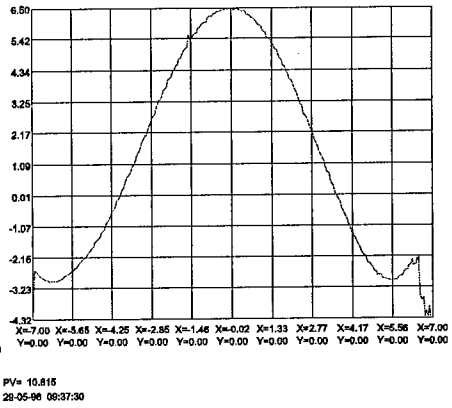

Fig.7: Section of the measurement

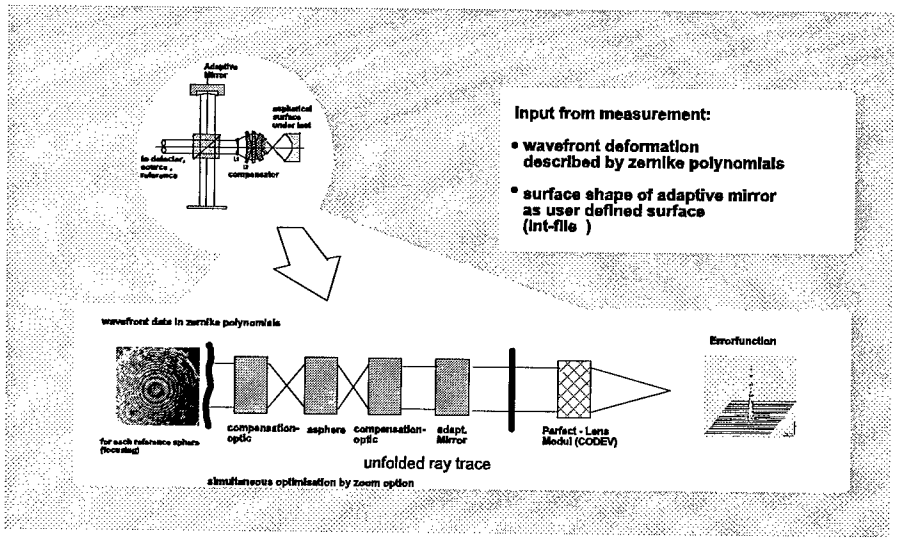

Fig.8: Scheme of ray tracing. Aberrations introduced by the optical set up are also considered.

This method is also especially suitable for the measurement of toroidal surfaces – aspheres with different curvatures in meridional and sagittal plane and cylindrical aspheres.

3 Scheme of the measurement

1. Adjusting the best fit reference surface. That leads to an optimized voltage pattern at the mirrors electrodes. The membrane is deformed in a way that we receive minimised fringe density in the interferogramm. The optimal arrangement of the electrodes utilizing the symmetry is to group them in concentric rings.

2. Measurement with ISTRA using 5 step phase shifting algorithm.

3. Calibration of membran mirror deformation. At first these deformations are measured using a known reference surface. For mirrors with a higher amount of deflection a Shack Hartmann Sensor may be used.

4. By ray tracing with CODEV we obtain the aspheric coefficients of our test surface. Aberrations introduced by the optical set up are also considered.

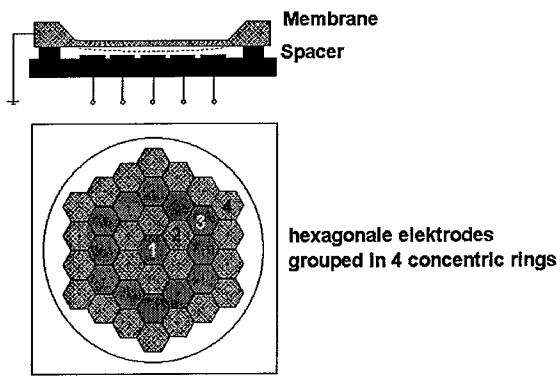

Fig.9: Grouping of electrodes

Table 1: Example of evaluating the aspherical coefficients

Measured aspheric coefficients	Real (known) coefficients
a_4=0,602x10^{-3}	a_4=0.60x10^{-3}
a_6=-0,38x10e^{-4}	a_6=-0,34x10^{-4}
a_8=-0,2x10^{-7}	a_8=-0.29x10^{-7}

(r_0=3,5103)

Some small discrepancies occurred. The deviation of the aspheric coefficient can be due to two reasons. First a reduced aperture of the asphere was used. A deviation of the higher orders will result. The second was due to an numerical inaccuracy of the polynomial fitting of zernike polynomials.
Using the adaptive mirror we have realised a flexible, easy to align set up. In the future adaptation of the reference, calibration, and alignement of the set up will be further improved.

4 Further development

The dynamic range of the mirror is limited to about 15µm maximum deflection. In future the deflection should be improved, but it seems that it will be limited by 20 µm.
The asymmetry of the former devices has been overcome by the new electrode structure. Instead of using hexagonal electrodes the new design utilises concentric rings. This is more suitable to our task.

Combining the adaptive mirror device with other compensating elements may be needed for some aspheric surfaces. The wavefront can be adapted with a micro mirror together with a static element such as:

- Refractive compensators (eg masters)
- CGHs as single elements or in combination with refractive elements
- Aspherical zoom

Using the mirror in reflection whereas the test object is been used in transmission would lead to an improvement of the aspherical range we can test. It will be a compromise of a reduced sensitivity.

5 References

1. Vdovin, G., Adaptive mirror micromachined in silicon,
2. Development and application of novel optoelectromechanical systems micromachined in silicon. First Year Report. LTR Open Scheme Project No. 31063,
3. Development and application of novel optoelectromechanical systems micromachined in silicon. Final Report. LTR Open Scheme First Phase Project No. 21063,
4. Tiziani, H. J., Prospects of testing aspheric surfaces with computer-generated holograms, Proceedings of the SPIE - The International Society for Optical Engineering Vol: 235 p. 72-79. 1980,
5. Dörband, B.; Tiziani, H. J., Testing aspheric surfaces with computer generated holograms: analysis of ad-justment and shape errors, Applied Optics, Vol: 24 Iss: 16 p. 2604-11. Aug. 1985,
6. Pfeifer, T.; Tutsch, R., Anwendung synthetischer Hologramme zur hochgenauen Formprüfung asphärischer Oberflächen, Technisches Messen tm, Vol: 56 Iss: 1 p. 9-16,
7. T. Haist, M. Schönleber, H.J. Tiziani, Computer-generated holograms from 3D-objects written on twisted-nematic liquid crystal displays, Optics Communication, 140(1997) p. 299-308.

Intra-Cavity Adaptive Optics for Lasers

HIGH-POWER SOLID-STATE LASER WITH BIREFRINGENCE COMPENSATION AND ADAPTIVE RESONATOR MIRROR

N. KUGLER AND A. VAZQUEZ

Laser- und Medizin-Technologie Berlin gGmbH, Schwarzschildstraße 8, D-12489 Berlin, Germany, n.kugler@lmtb.de

H. LAABS AND H. WEBER

Optisches Institut der TU-Berlin, Straße des 17. Juni 135, D-10623 Berlin, Germany

In this article an efficient and straightforward method for the compensation of thermally induced birefringence in high power Nd:YAG rod lasers is discussed. The scalar aberrations of a birefringence compensated two rod system are analyzed. Resonators with a small stability range and therefore beam quality near the diffraction limit are introduced. To improve the brightness of such resonators a multi-channel deformable high reflecting mirror is investigated with the aim of using it as a resonator mirror. As the damage threshold of the multi-channel mirror is still too low, results with an adaptive resonator were obtained using a single actuator mirror as HR-mirror. The maximum average output power of the adaptive resonator is 145 W at a beam quality of $M^2 \cong 2$.

1 Introduction

A key interest in the development of laser sources is to gain high output power with high beam quality ($M^2 \leq 2$), i.e. a high brightness laser. As the beam propagation factor of laser resonators is in general proportional to the width of the stability range, high power lasers (>100 W) with a beam quality near the diffraction limit require a dynamically stable resonator with a small range of stability [1-6].

In the case of Nd:YAG rod lasers the thermally induced stress birefringence must be compensated if the width of the stability range (in terms of refractive power of the rod) is less than 20 % of the absolute refractive power, otherwise the losses of the resonator increase dramatically [6,7]. In the next section our method of birefringence compensation in Nd:YAG rod lasers is described [8-10]. In section 3 the scalar aberrations measured in a birefringence compensated diode-pumped laser are analyzed [11]. In section 4 different deformable mirrors are compared and in section 5 a dynamically stable resonator with adaptive HR-mirror is discussed.

2 Stress birefringence

As it is well known the parabolic temperature profile in a pumped Nd:YAG rod causes radial and tangential stress within the rod. The birefringence induced by the stress leads to depolarization of linearly polarized modes and to bifocusing of the thermal lens [6-8]. Both effects reduce the brightness of a high power laser as the fundamental mode volume within the rod is limited and the stability is decreased [1-4]. For Nd:YAG the difference in the refractive power for radially and tangentially polarized light is approximately 20%. This results in limitations with regard to the design of stable resonators, because both refractive powers have to be in the limit of stability of the resonator to keep losses small.

As discussed in Ref. 8 and Ref. 9 in detail the stress induced birefringence in Nd:YAG can be compensated to a great extent when two rods with equal refractive powers are imaged onto each other by a telescope. The distance between the rods and the focal length of the lenses have to be chosen in a way that the principal planes of the thermal lenses are imaged onto each other (Fig. 1). A 90° quartz rotator between the rods swaps amplitude and phase of the radial and the tangential polarization state. Therefore the polarization dependent phase retardation in the first rod will be compensated in the second rod.

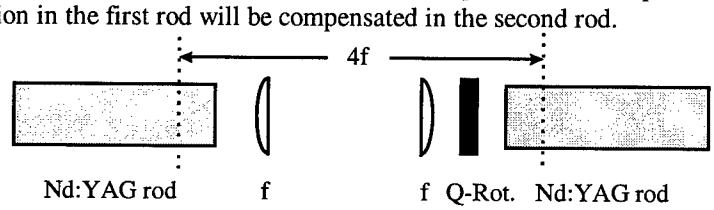

Figure 1. Birefringence compensation scheme with a telescope imaging the principal planes of the thermal lenses onto each other.

For a comparison with the uncompensated situation the quartz rotator was substituted by a quartz glass to preserve the optical path length of the system. Experimental results show that the depolarization of 25% can be reduced to less than 4% [8] which indicates that the thermally induced stress birefringence is compensated to a high degree.

3 Aberrations

Due to inhomogeneous pumping light distribution and due to the temperature dependence of the heat conductivity and other material constants of the YAG crystal, the radial temperature profile in the rod will differ from the ideal parabolic temperature profile, leading to aberrations [11]. These aberrations can be measured

with a Shack-Hartmann wavefront sensor (Fig. 2). An expanded HeNe-laser beam propagates through the aberrated thermal lens and is imaged onto the 16x16 lens array of the Shack-Hartmann sensor. A wavefront of the unpumped system is recorded as reference. Due to the 'laser-cooling' effect, the thermal lens of a laser rod is approximately 10% weaker when the laser is running at sufficiently high power. For our measurement we recorded the aberrations under lasing conditions.

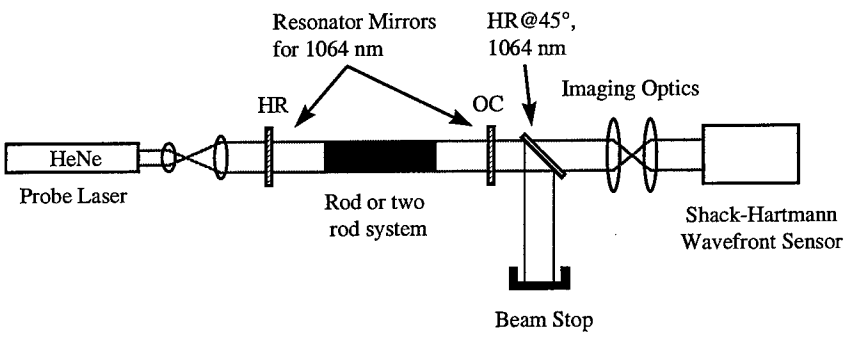

Figure 2. Set-up for the measurement of aberrations in a high power diode-pumped Nd:YAG rod laser.

The aberrations can be expressed in term of Zernike functions. In table 1 the terms with the highest peak-to-valley phase shifts are summarized. The phase shifts are normalized to the HeNe-wavelength (λ=633nm).

Table 1. Measured peak-to-valley phase differences of the thermal lens and its dominant aberrations (λ=633nm).

Name	Zernike function	peak to valley phase shift / λ
- all - (first 37)	Σ(first 37)	18.7
Defocus	r^2	18.5
Astigmatism	$r^2 \cos(2\phi)$	1.04
Coma	$(3r^3-2r) \cos(\phi)$	0.35
Spherical Aberration	r^4	0.30

4 Deformable mirror

A major goal of the investigations is to correct the aberrations of the thermal lens by introducing additional aberrations with the opposite sign with a deformable resonator mirror (Fig. 3). This requires not only detailed knowledge of the aberrations of the thermal lens and how they propagate to the deformable resonator mirror but also a deformable mirror which is capable of high power and power densities.

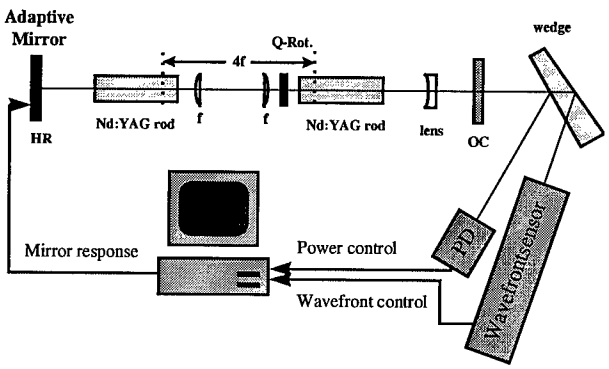

Figure 3. Scheme of a resonator with an adaptive mirror controlled by a PC. The computer reads the beam parameters of the laser and calculates a response function for the mirror.

The deformable mirror investigated is based on SiN and it is fitted with up to 37 actuators. Fig. 4 (left) shows the sketch of the deformable membrane mirror with metal and dielectrical coating for high reflectivity.

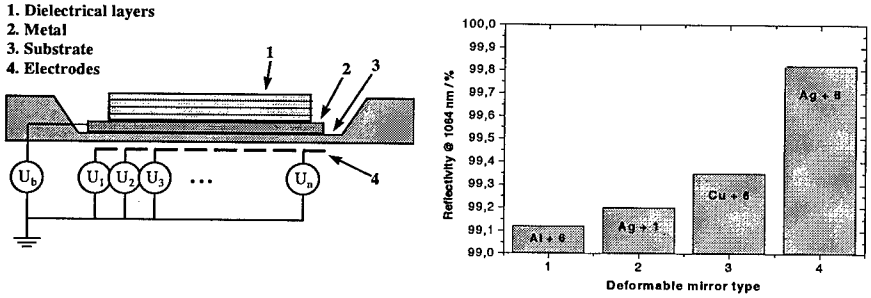

Figure 4. Left: Sketch of the multi-channel deformable membrane mirror with metal coating and dielectrical enhancement. Right: Comparison of the reflectivity of mirrors with different coatings.

The mirror will be controlled by a PC which reads the laser parameters, evaluates them and sets the actuators of the mirror accordingly. In Fig. 4 (right) different types of deformable mirrors are compared. A maximum reflectivity of more than 99.8 % can be obtained with a silver coated mirror with 6 layers of dielectrical coating (*Ag+6*). In table 2 the results of a damage threshold measurement for the *Ag+6* mirror are listed. The mirror is suitable for resonator external use, but as the resonator internal power of cw-lasers is usually much higher, the mirror is not yet capable of resonator internal usage.

Table 2. Damage threshold measurement of mirror Ag6. The last row was recorded during resonator internal use of the deformable mirror.

Beam diameter	Exposure time	Power	Power density	Status
4 mm	30 s	80 W	637 W/cm^2	OK
8 mm	15 min	70 W	139 W/cm^2	OK
4 mm	15 min	68 W	541 W/cm^2	OK
2 mm	15 min	67 W	2133 W/cm^2	OK
≈ 3 mm	< 10 s	160 W	2264 W/cm^2	Damage

Alternatively an adaptive mirror consisting of a high reflection coated glass plate with a diameter of 40 mm is used for resonator internal usage. The glass plate is fixed at the edge. In the centre of the mirror a piezo-electric actuator bends the plate by an elevation of 40 μm maximum. In the central area of the mirror (diameter of approximately 10 mm) the aberrations are small and the mirror can be regarded as spherical mirror. Therefore this mirror can not be used for aberration correction but it is still proper for the variation of the stability range of the adaptive resonator. The radius of curvature of the mirror can be varied from infinite to ρ=2 m convex.

5 High brightness laser with deformable mirror

With an adaptive resonator as sketched in Fig. 5 an average output power of 145 W at a beam parameter product of 0.6 mm mrad ($M^2 \cong 1.8$) can be achieved.

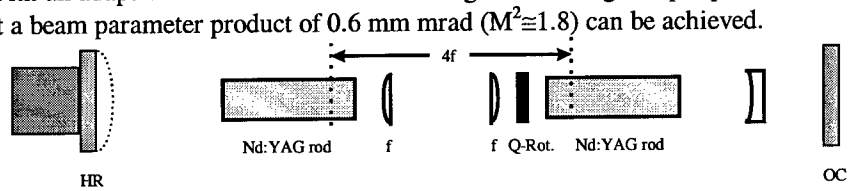

Figure 5. Set-up of the dynamically stable resonator with birefringence compensation and adaptive high reflecting mirror.

6 Conclusion

A two rod system as described in section 2 is an efficient method for the compensation of stress birefringence in rod lasers and a first step to increase the maximum brightness extractable of a high power Nd:YAG laser. For a reduction of the remaining scalar aberrations a deformable resonator mirror can be used provided the aberrations of the thermal lens are known and their propagation to the deformable mirror can be calculated. For high power operation a membrane mirror with a reflectivity of more than 99.8% is required.

7 Acknowledgements

This work was partly supported by the European Community within the project LTR 31063 - MOSIS. The coating of the membrane mirrors was provided by LaserComponents GmbH.

References

1. Steffen J., Lörtscher J. and Herziger G., Fundamental Mode Radiation With Solid-State Lasers, *IEEE J. Quantum Electron.*, **QE-8** (1972) pp. 239-245
2. Hanna D. C., Sawyers C. G. and Yuratich M. A., Telescopic resonators for large-volume TEM_{00}-mode operation, *Opt. Quant. Electron.*, **13** (1981) pp. 493-507
3. Magni V., Resonators for solid-state lasers with large-volume fundamental mode and high alignment stability, *Appl. Opt.*, **25** (1986) pp. 107-117
4. Cerullo G., De Silvestri S., Magni V. and Svelto O., Output power limitations in CW single transverse mode Nd:YAG lasers with a rod of large cross-section, *Opt. Quant. Electron.*, **25** (1993) pp. 489-500
5. Bostanjoglo G., Dommaschk R., Beck Th. and Weber H., Stable resonators with variable reflectivity mirrors for multi-kW Nd:YAG lasers, in *XI International Symposium on Gas Flow and Chemical Lasers and High-Power Laser Conference*, H. J. Baker, ed., *Proc. SPIE* **3092** (1997) pp. 44-47
6. Kugler N., Seidel S. and Weber H., High-power Nd:YAG laser with birefringence compensation and adaptive HR mirror, in *Laser Optics '98: Solid State Lasers*, Vladimir I. Ustyugov, ed., *Proc. SPIE* **3682** (1998) pp.145-154
7. Koechner W., *Solid-State Laser Engineering*, 3rd ed., Springer-Verlag Berlin (1992) pp.381-400
8. Lü Q., Kugler N., Weber H., Dong S., Müller N. and Wittrock U., A novel approach for compensation of birefringence in cylindrical Nd:YAG rods, *Opt. Quant. Electron*, **28** (1996) pp. 57-69
9. Kugler N., Dong S., Lü Q. and Weber H., Investigation of the misalignment sensitivity of a birefringence-compensated two-rod Nd:YAG laser system, *Appl. Opt.*, **36** (1997) pp. 9359-9366
10. Seidel S. and Kugler N., Nd:YAG 200-W average-power oscillator-amplifier system with stimulated-Brillouin-scattering phase conjugation and depolarization compensation, *J. Opt. Soc. Am. B*, **14** (1997) pp. 1885-1888
11. Hodgson N. and Weber H., Influence of Spherical Aberrations of the active Medium on the Performance of Nd:YAG Lasers, *IEEE J. Quantum. Electron.*, **QE-29** (1993) pp. 2497-2507

SIMULATION OF OPTICAL RESONATORS WITH ABERRATIONS

IVO BUSKE, ULRICH WITTROCK

Fachhochschule Münster, Stegerwaldstrasse 39, 48565 Steinfurt
Germany
E-mail: buske@fh-muenster.de, wittrock@fh-muenster.de

We present numerical calculations of the eigenmodes of laser resonators with aberrations. Due to the aberrations the diffraction losses of the resonator increase drastically if the resonator is at the boundary of the stable region. This means that is impossible to obtain near diffraction-limited beam quality if aberrations are present. A resonator with an adaptive mirror could greatly improve the beam quality of high-power solid state lasers.

1 Introduction

Since the advent of the laser great efforts have been undertaken to develop lasers that have both high beam quality and high power. This is a very difficult goal because of the optical aberrations of the active medium that occur at high power. The aberrations are due to the heat generation that is inevitable in the laser process. The heat has to be extracted from the laser medium, leading to temperature gradients. These temperature gradients in turn produce refractive index gradients and stress birefringence in the active medium. In solid state lasers, various shapes of the laser crystal as well as various pumping and cooling schemes have been devised to minimize the aberrations. Despite some success with new schemes, the standard rod laser is still the most prevalent type. In this paper we present a numerical analysis of diffraction losses, beam quality and output power of an Nd:YAG rod laser with aberrations.

2 Thermo-Optical Aberrations of Pumped Laser Rods

In a high-power rod laser the cylindrical rod is transverse-pumped through its barrel surface and the barrel surface itself is water-cooled. In the case of ideal homogeneous pumping of the rod, the heat source density is constant throughout the rod. If the surface heat transfer coefficient is also constant everywhere at the barrel surface, the resulting temperature profile in the rod is a rotationally symmetric parabola centered on the rod axis. Since the refractive index is a function of temperature, the temperature profile leads to a refractive index profile of the same shape. A parabolic index profile presents an ideal lens, the so-called thermal lens of a solid state laser [1].

In practice, many more effects come into play and produce aberrations of the thermal lens. The temperature profile causes stresses in the crystal that in turn cause birefringence. This thermal birefringence has the same rotational symmetry as the temperature profile. If cylindrical coordinates are introduced for the laser rod, the principle axes of the refractive index ellipsoid are oriented in the radial and azimuthal directions. The stress distribution is such that a laser beam with purely azimuthal polarization would still see an exact parabolic index profile. A beam that is radially polarized everywhere would also see an exact parabolic index profile, albeit with a different curvature of the parabola. Both radially and azimuthally polarized laser beams would have a singularity on their axis, where neither of the two polarization states is defined. Thus, the eigenmode of a laser rod with thermal birefringence must have zero intensity on its axis. However, the gain at the rod center is very high and additional modes will be oscillating. These modes with high on-axis intensity are subject to strong aberrations. Generally, thermal birefringence is the strongest aberration in solid state rod lasers. Fortunately, a solution to this problem has been devised a few years ago that can eliminate the effects of thermal birefringence in laser rods [3, 4]. The scheme is based on relay-imaging of two identical rods with a 90°-rotation of the polarization between the rods. The complete system of the two rods behaves just like one birefringence-free rod. It is for this reason that in our studies we neglected thermally induced birefringence.

Another source of aberration is due to the fact that the thermal conductivity of YAG is actually a function of temperature. Strongly pumped rods have a large temperature difference between their center and their barrel so that the thermal conductivity varies significantly across the rod and the temperature profile is no longer parabolic [2]. This leads to spherical aberration.

In practice, further aberrations arise because pumping of the laser crystal is always to a certain extend non-uniform, resulting in a non-uniform heat source density in the crystal. Finally, distortion of the rod end faces due to thermal stress presents additional aberrations.

Figure 1 shows the wavefront aberration of a rod from a commercial high-power lamp-pumped continuous-wave Nd:YAG laser. The rod has a diameter of 5 mm and a length of 130 mm. The wavefront was measured with a Shack-Hartmann wavefront sensor at an electrical pumping power of 4.9 kW [7]. This pumping power would produce a laser output power of approximately 150 W with a stable, highly-multimode resonator.

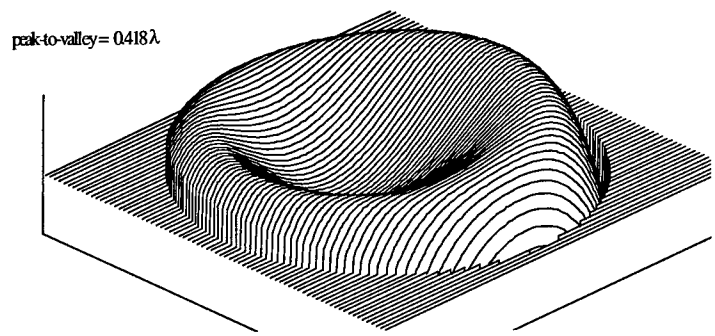

Figure 1:Wavefront aberration of a laser rod at pumping power 4.9kW without the focus-term, tip- and tilt-term and astigmatism. The diameter of the circular aperture is 4 mm, the wavelength is λ=1.064μm. This aberration was used in our numerical simulations.

3 Spherical Resonators

The eigenmodes of stable spherical resonators are Gauss-Laguerre- and Gauss-Hermite-modes for resonators with circular and rectangular apertures, respectively [5]. (This is strictly true only for a bare cavity without a gain element. For resonators with gain, the complex Gauss-Laguerre- and Gauss-Hermite-modes are the eigenmodes [5].) Nevertheless, a good estimate for the beam quality of spherical resonators can be obtained from the simple model of the "embedded Gaussian mode" that is based on the real Gauss-Laguerre- and Gauss-Hermite-modes [6]. Let $w_{00}(z)$ be the radius of the fundamental mode of the resonator, defined by the second moment of the intensity distribution. The fundamental mode of a resonator is determined by the g-parameters and the length of the resonator. The g-parameters are defined as:

$$g_i = 1 - L / R_i,$$

where L is the resonator length and R_i are the radii of curvature of the mirrors 1 and 2 with i =1, 2. A resonator is stable if $0 < g_1 \cdot g_2 < 1$. The second-moment diameter of a certain higher-order Gauss-Laguerre- and Gauss-Hermite-eigenmode of the resonator has a diameter $M \cdot w_{00}(z)$ that is larger than the diameter of the fundamental mode by the constant factor M everywhere along the z-axis. For a Gauss-Laguerre-mode this factor M is given by

$$M = \sqrt{(2P + L + 1)}$$

where P is the number of radial nodes and L is the number of azimuthal nodes. The beam quality of this mode in terms of Siegman's beam quality number "M^2" is simply M^2 because both the beam waist and the far-field divergence angle are M-times larger for the higher-order mode than for the fundamental mode. The beam

quality of a multi-mode resonator is determined by the highest-order mode that can pass through the apertures of the resonator. Almost all of the energy of a Gauss-Laguerre mode is contained within its second-moment diameter [2]. We can thus assume that the second-moment diameter of the highest-order mode is equal to the radius of the limiting aperture of the resonator. If the limiting aperture is at position z in the resonator and has the radius a_z, we obtain for the factor M

$$M = \frac{a_z}{w_{00}(z)}$$

and the beam quality number of the resonator is

$$M^2 = \left(\frac{a_z}{w_{00}(z)} \right)^2 .$$

Experiments have shown that this equation predicts the beam quality of stable multi-mode resonators very well. However, the equation fails for strongly-pumped solid state lasers close to the limits of stability of the g-diagram, i. e. if $0 = g_1 \cdot g_2$ or if $g_1 \cdot g_2 = 1$. The equation predicts almost diffraction-limited beam quality but in experiments this is never observed. Instead the beam quality number is much larger than unity and the laser output power drops to very low levels and fluctuates strongly. The obvious explanation for this is the influence of the aberrations of the thermally loaded laser crystal. Apparently, a laser with a resonator that is close to the limits of stability of the g-diagram is more sensitive to aberrations than a highly multi-mode resonator. In order to test this assumption we calculated the eigenmodes of resonators with and without aberrations and compared the diffraction losses, output powers, and M^2-values.

4 Simulation of Non-Spherical Resonators

Very few theoretical studies of non-spherical resonators have been performed. There is of course an infinite number of non-spherical resonators, each of which has its own set of eigenmodes. In order to study the influence of aberrations in a real high power solid state laser we used the measured aberrations from figure 1 in our numerical calculations of the resonator eigenmodes.

Term	Polynomial	Denotation	measured coefficient [waves]	coefficient used in simulation [waves]
1	1	piston	0	0
2	$\rho \cos(\varphi)$	tilt x	1.3	0
3	$\rho \sin(\varphi)$	tilt y	0.2	0
4	$2\rho^2 - 1$	defocus ρ^2	12.0	0
5	$\rho^2 \cos(2\varphi)$	astigmatism x	0.176	0
6	$\rho^2 \sin(2\varphi)$	astigmatism y	-0.52	0
7	$(3\rho^3 - 2\rho) \cos(\varphi)$	coma x	0.05	**0.05**

8	$(3\rho^3 - 2\rho)\sin(\varphi)$	coma y	-0.135	**-0.135**
9	$6\rho^4 - 6\rho^2 + 1$	spherical ρ^4	-0.13	**-0.13**
10	$\rho^3\cos(3\varphi)$	trifoil x	0.023	**0**
11	$\rho^3\sin(3\varphi)$	trifoil y	0.044	**0**
16	$20\rho^6 - 30\rho^4 + 12\rho^2 - 1$	spherical ρ^6	-0.02	**-0.02**

Table 1: Fringe set of Zernike polynomials with coefficients of a measured thermal lens (λ =1064 nm) and the coefficients used in our simulation.

Table 1 shows the Zernike polynomials of the wavefront aberration. Column 4 of the table shows the Zernike coefficients, column 5 shows the coefficients that were used in our calculations. The coefficients of the piston term, the tip- and tilt-terms, the focus term and the astigmatism terms were set to zero. This allows us to study the sole influence of higher-order aberrations. These higher-order aberrations can not be compensated by adjusting the resonator mirrors or by using cylindrical optics. They are also the reason that the Gauss-Laguerre modes and Gauss-Hermite modes are no longer eigenmodes of the resonator. The calculations were performed with the program GLAD [8] according to the Fox- and Li-algorithm [9].

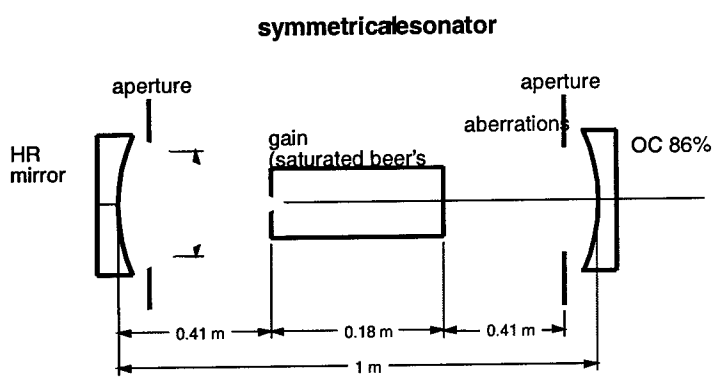

Figure 2: Set up and distance of the optical elements in the resonator model to calculate the eigenmodes.

Figure 2 shows a schematic diagram of the resonator that was used in the calculations. The resonator is symmetric with both mirrors having the same radii of curvature and the same distance from the laser rod. No thermal lensing was introduced into the resonator, however, the effect of an ideal thermal lens could be taken into account by a change of the radius of curvature of the mirrors. The aberrations were introduced as a thin phase sheet at the output coupling mirror. The reflectivity of the output coupler is 86%. The gain medium is a 180 mm long Nd:YAG-crystal with a saturation intensity of 2 kW/cm^2. The gain saturation in the active medium leads to high-order multimode oscillation. Apertures of 4 mm radius are placed in front of both mirrors. From the power loss V_1 and V_2 at

aperture 1 and 2 we calculate the relative round-trip power loss v that is defined as

$$v = 1 - V_1 \cdot V_2 .$$

5 Results

We have calculated resonators with g-parameters between $g = -0.9999$ and $g = -0.30$. Figure 3 shows the results for resonators without aberrations. For $g > -0.92$ the M^2-values obtained from the simple model based on Laguerre-Gaussian-modes that was presented in section 3 and the diffraction calculation are similar with relative deviations of less than 25%. Figure 4 shows the corresponding relative round-trip power loss v. The losses increase as g approaches -1 and the boundary of the stable region is reached. This can be understood if one considers a decomposition of the laser beam into Laguerre-Gaussian-modes. Some higher-order modes are oscillating even though they have a larger diameter than the aperture and experience considerable losses. But only these modes can deplete the gain in the annular region of the laser rod where the fundamental mode has low intensity and doesn't saturate the gain.

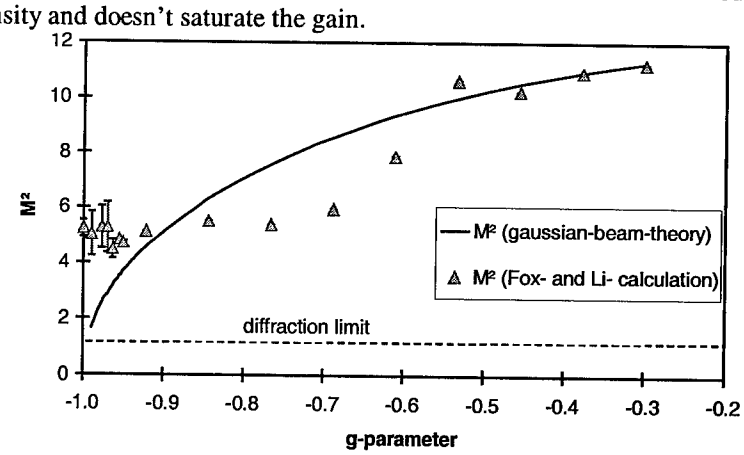

Figure 3: M^2 values of the diffraction and the M^2 values obtained from the gaussian-beam theory.

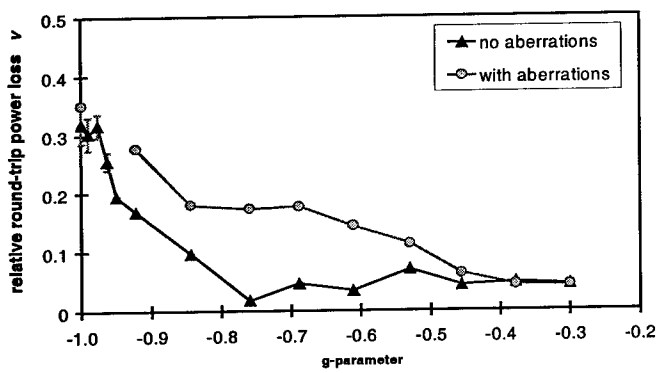

Figure 4: Diffraction losses of a resonator with and without aberrations including the standard deviation. The diffraction losses of a resonator with aberrations increase for g < -0.4 in comparison to the resonator without aberrations.

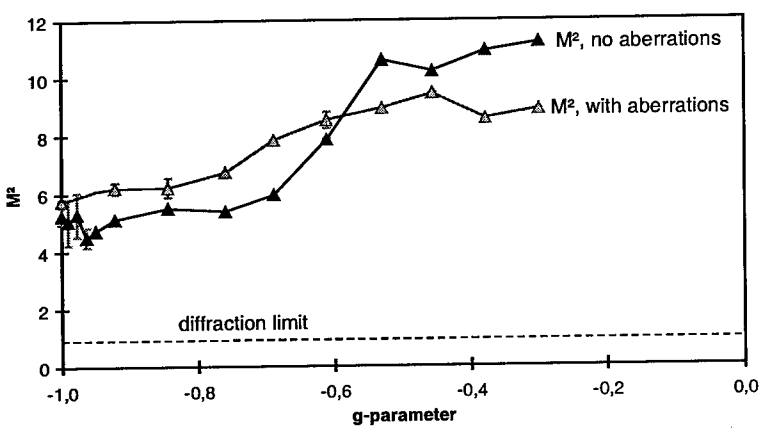

Figure 5: Comparison of beam quality with and without aberrations for g = –1 .. –0.3.

Figure 5 shows a comparison between the M^2-values with and without aberrations. The losses, shown in figure 4, also increase dramatically. This leads to reduced output power.

The Fox- and Li-algorithm does not converge for near-diffraction-limited resonators. Therefor M^2-values vary slightly at each round trip. The error bars in Figure 3-5 indicate the standard deviation of the M^2-values of the last 100 round trips. For g > –0.95 the standard deviation is so small that it is invisible in this graph.

6 Conclusion

We numerically calculated the eigenmodes of stable resonators with aberrations. The wavefront aberration used for the calculation is realistic since it steams from a measurement carried out by another group at a high-power solid state laser. Our calculations show that the aberrations lead to increased losses if the resonator is close to the boundary of the stable region of the g-diagram. This proves that aberration control is essential in order to obtain high output power and good beam quality. We will continue our numerical analysis to obtain more quantitative data on the influence of aberrations on losses, output power and beam quality of solid state lasers. This information is necessary in order to assess the accuracy of wavefront correction that is required in resonators with adaptive mirrors.

References

1. W. Koechner, Solid State Laser Engineering, Springer Verlag (1976).
2. N. Hodgson and H. Weber: Optical Resonators, Springer Verlag (1997).
3. Q. Lü and U. Wittrock, German Patent Application, Anordnung zur Kompensation der Doppelbrechung und Bifokussierung in Lasermedien, P 44 15 511.5 (1994)
4. Q. Lü, N. Kugler, H. Weber, S. Dong, N. Müller, and U. Wittrock, A novel approach for compensation of birefringence in cylindrical Nd:YAG rods, Optical and Quantum Electronics **28**, 57 (1996).
5. A. E. Siegman, Lasers, University Science Books (1986).
6. A. E. Siegman, SPIE vol. **1224** (1990).
7. Private Communication, Laser- und Medizin-Technologie Berlin gGmbH (1999).
8. Applied Optics Research, Escondido, CA.
9. A. G. Fox, T. Li, Resonant modes of a maser interferometer, Bell Syst. Tech. J. **40**, 453 (1961).

DEVELOPMENT OF ADAPTIVE RESONATOR TECHNIQUES FOR HIGH-POWER LASERS

LAURENCE FLATH, JONG AN, JAMES BRASE, CARMEN CARRANO, C. BRENT DANE, SCOTT FOCHS, RANDALL HURD, MICHAEL KARTZ, AND ROBERT SAWVEL

Lawrence Livermore National Laboratory, P.O. Box 808, L-258, Livermore, CA 94551, USA

E-mail: flath1@llnl.gov

The design of an adaptive wavefront control system for a high-power Nd:Glass laser will be presented. Features of this system include: an unstable resonator in confocal configuration, a multi-module slab amplifier, and real-time intracavity adaptive phase control using deformable mirrors and high-speed wavefront sensors. Experimental results demonstrate the adaptive correction of an aberrated passive resonator (no gain).

1 Introduction

Solid-state amplifiers present obstacles to the objective of high average power lasers; they provide a low gain per pass and suffer from wavefront distortions due to thermal gradients in the lasing material. The low amplifier gain requires a low magnification resonator, which increases the sensitivity of wavefront quality to aberrations and alignment errors [1]. When operated in a heat-capacity mode [2], the thermal aberrations are time-varying, thus preventing the use of a static corrector optic.

An adaptive optics system provides a means to control the wavefront evolution in laser cavities [3-10]. Intracavity wavefront sensing allows real-time adaptive control of the resonator's mode structure and vastly improves the output beam quality. In this paper we present the successful implementation of high-spatial resolution intracavity adaptive phase control in a confocal unstable resonator with a sub-threshold Nd:Glass disk amplifier. This work lays the foundation for extentions to high average power heat-capacity laser systems.

2 Adaptive Unstable Resonators

Using intracavity wavefront correction in unstable resonators has several advantages compared to extracavity sensing [8-10]. Using a high-spatial resolution wavefront sensor and adaptive optics (Figure 1), it is possible to directly control the mode shape. Alignment sensitivity is reduced because individual components of the wavefront (e.g. tip/tilt) may be extracted and acted upon by dedicated active components. And because the field propagated through multiple passes in the cavity, the corrector's dynamic range requirements are reduced.

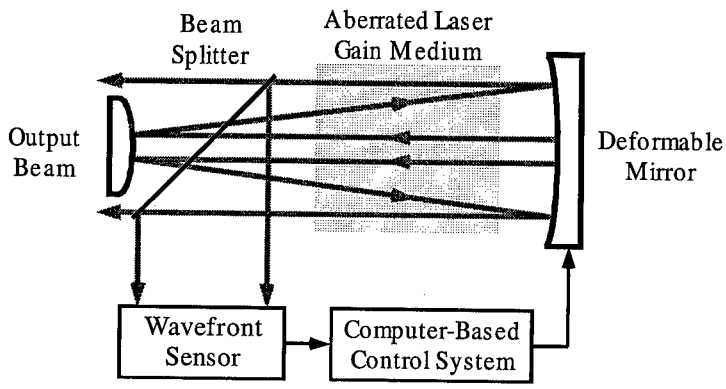

Figure 1. Adaptive wavefront correction in a positive-branch unstable resonator.

Of course, there are also difficulties with this type of arrangement. Aberrations in the laser medium are magnified in each round-trip pass through the cavity, and thus lower the output wavefront quality and far-field Strehl ratio. The correction calculations are more complex than a simple phase mapping; the aberration mode amplification is dependent on mode order and cavity position [10].

Intracavity control of an unstable resonator was first demonstrated to correct misalignments in a CO_2 laser by Stephens and Lind [9]. In these and subsequent experiments, the deformable mirror was controlled using a multi-dither approach based on feedback from the far-field peak intensity [6, 7]. In the work described in this paper, we use high order intracavity wavefront sensing to measure the spatially resolved field at the laser output. The full wavefront information is then used to directly control the deformable mirror. The experiments described here demonstrate correction of an aberrated passive resonator (no gain) – future experiments will use the system to correct an amplified beam. The experiment consists of a positive branch unstable resonator with magnification M = 1.31 and equivalent Fresnel number N_{eq} = 20.4. The aberration is provided by a prototype flashlamp-pumped Nd:Glass heat capacity amplifier, which can be pumped to a temperature which provides approximately 2.0 waves of low-order aberration in one pass. In the experiment, the amplifier is heated by flashlamp pumping, then the adaptive resonator control loop is closed to correct an injected probe beam.

The heart of our system is a negative feedback loop that adaptively controls the surface of a deformable mirror (DM), using difference between the time-varying wavefront gradient and the desired wavefront slope (flat) to form an error signal. The relation between the error signal and the surface profile of the DM is described by a control law:

$$\vec{\beta} = \mathbf{S}\vec{\alpha} \;\rightarrow\; \vec{\alpha} = \mathbf{A}\vec{\beta}\,,$$

where $\vec{\alpha}$ and $\vec{\beta}$ are vectors describing the intra-cavity wavefront slope and the surface function of the DM, respectively. **S** is a matrix describing the feedback system. The matrix **S** is calculated as the pseudoinverse of the system matrix **A** [11].

The system matrix is measured by a calibration procedure where the influence of each individual DM actuator on the wavefront slope is recorded, the combined result (the forward matrix **A**) is inverted using singular-value decomposition [12], and the eigenmodes of the system are weighted according to the desired system response. In this manner modes by which the DM has no or little influence may be rejected, analogous to the action of a spatial filter. Note that for an intracavity DM, the wavefront sensor response is more complex than in a single-pass system. For the passive case described here, the wavefront sensor measures the weighted sum of multiple passes through the resonator.

3 Passive Resonator Testbed System

As a first step toward a high-average power laser, we constructed a testbed system, with the objective of verifying the general approach for wavefront sensing and control . The experimental setup (schematic shown in Figure 2) consists of a probe laser, an unstable resonant cavity (URC), a deformable mirror (DM), a solid-state laser amplifier module, a wavefront sensor (WFS), and a far-field sensor (FFS).

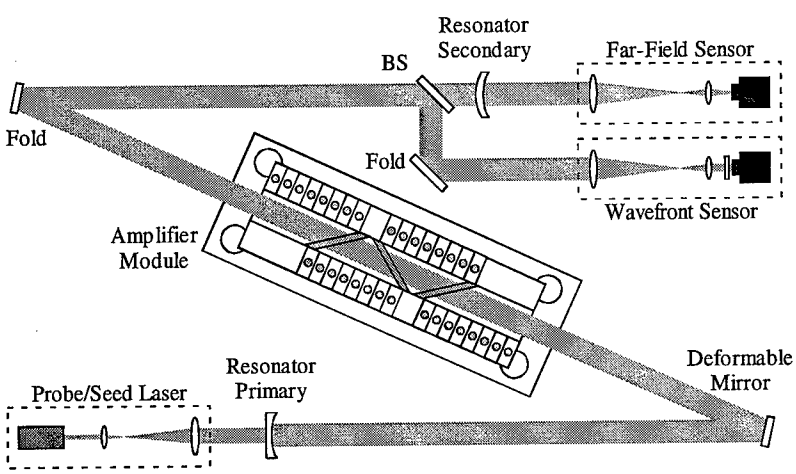

Figure 2. Schematic layout of the adaptive unstable passive resonator testbed.

The URC consists of a 97% reflective primary of radius 39.5 m, and a -30.1 m radius secondary mirror with a 51 mm diameter 97% reflective central coating. The geometry of the secondary optic couples the laser output energy into an annular

cross-section. The mirrors are aligned confocally, resulting in a cavity length of 4.7 m and a resonator magnification $M = 1.31$. The URC is seeded with a solid-state probe-laser emitting CW radiation at 1053 nm, and is expanded to a diameter of 51 mm to match the central reflective zone of the secondary mirror. The beam is injected through the primary mirror and collimated at the cavity-side of the primary. Thus, one round-trip pass of the probe beam results in an output annulus outer diameter of $M \cdot 51$ mm = 67 mm. The deformable mirror has 109 PZT actuators in a hexagonal-close-pack arrangement, with spacing of 7 mm and stroke of $\pm$ 2.7 μm, and a surface roughness of 19 nm RMS (165 nm P-V, mostly edges). The laser amplifier consists of three flashlamp-pumped Nd:Glass slabs alternately oriented at Brewster's angle of 56.6°. For the current pump/resonator configuration, the laser runs just below threshold. During operation the amplifier is pumped at a rate of 10 Hz for 15 seconds. The intracavity wavefront is sampled at the plane of the DM by a Shack-Hartmann sensor consisting of a reducing telescope and a lenslet array (750 μm-spaced lenslets, $f = 20.1$ mm). The spot pattern is imaged directly onto the focal plane of a 12-bit digital camera, which uses a 1024 x 1024 pixel frame transfer CCD. Images are acquired at the camera's full frame rate of 8.4 Hz. A far field sensor consisting of a magnifying telescope and an identical digital camera are used to monitor the annular output of the cavity. Figure 3 shows the relationship between the beam profile, the DM actuator positions, and the wavefront sampling of the WFS.

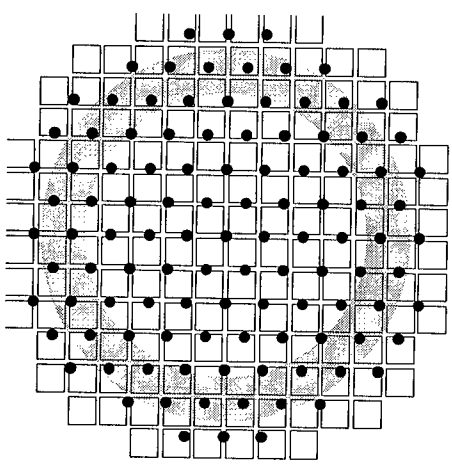

Figure 3. Relative position of deformable mirror actuators (dots) and wavefront sensor lenslets (squares) with respect to the output beam (annulus).

The system controller is a UNIX workstation with two digital camera inputs and the DM output interface. Control loop operation consists of determining the wavefront slopes from the spot positions on the WFS camera, multiplying by the system matrix **S**, and sending the result to the DM.

4 Experimental Results

The results of closed-loop operation of the adaptive optical system are shown in Figure 4. The system was calibrated by measuring the intracavity wavefront before pumping the amplifier, yielding a control loop reference wavefront. To generate the worst-case aberrations, the Nd:Glass slabs were heated by pulsing the laser amplifier flashlamps 150 times. The uncorrected far-field image in Figure 4a has a residual wavefront error of 1.96 λ rms, and a calculated Strehl ratio of 0.04. With this as the starting point for the controller, the output in Figure 4b resulted after 19 control loop iterations - a residual wavefront error of 0.16 λ rms, and a Strehl ratio of 0.31 (an eight-fold improvement).

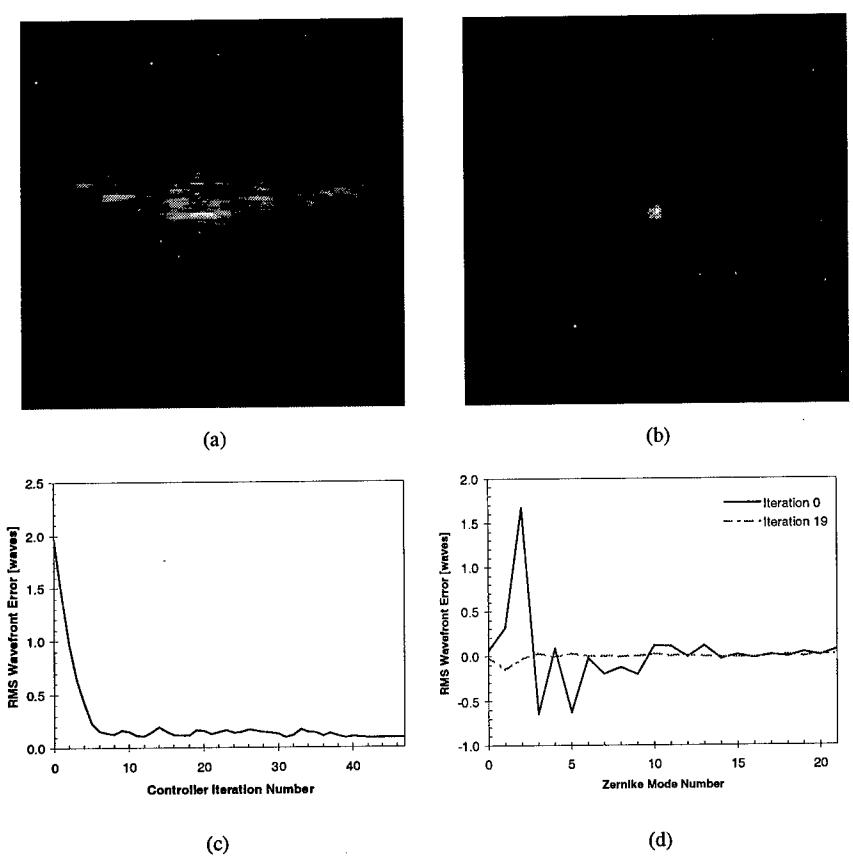

Figure 4. Testbed system far-field images (a) immediately after 150 pulses induce intracavity aberrations, and (b) after nineteen iterations of adaptive loop control. Controller performance (c) over time in terms of control loop iteration number, and (d) Zernike mode decomposition of the wavefront error.

To evaluate the performance of the controller we decompose the wavefront into its constituent Zernike modes (Figure 4c). It is clear that most of the initial wavefront error is of low order, as we expect for this type of laser amplifier [1]. Figure 4d shows that the algorithm converges in less than 10 iterations.

5 Acknowledgements

This work was performed under the auspices of the U. S. Department of Energy by the Lawrence Livermore National Laboratory under contract number W-7405-ENG-48. The authors would like to acknowledge the support and technical assistance of G. Albrecht, B. Bauman, B. Bhachu, R. Buff, D. Gavel, L. Lindberg, W. Manning, E. Stappaerts, and J. Wintemute. This research was funded by the U.S. Army High-Energy Laser Test Facility under WFO Proposal No. L7378.

References

1. Koechner W. Solid-State Laser Engineering, Fourth Edition, (Springer-Verlag, Berlin, 1996) pp. 262-278.
2. Albrecht G. F., Sutton S. B., George E. V., Sooy W. R., and Krupke W. F. Solid state heat capacity disk laser, *Laser and Particle Beams* **16-4** (1998) pp. 605-625.
3. Siegman A. E. Unstable optical resonators, *Applied Optics* **13-2** (1974) pp. 353-367.
4. Freeman R. H., Freiberg R. J., and Garcia H. R. Adaptive laser resonator, *Optics Letters* **2-3** (1978) pp. 61-63.
5. Oughstun K. E. Intracavity adaptive optic compensation of phase aberrations. I: Analysis, *Journal of the OSA* **71-7** (1981) pp. 862-872.
6. Spinhirne J. M., Anafi D., Freeman R. H., and Garcia H. R. Intracavity adaptive optics. I. Astigmatism correction performance. *Applied Optics* **20-6** (1981) pp. 976-984.
7. Anafi D., Spinhirne J. M., Freeman R. H., and Oughstun K. E. Intracavity adaptive optics. II. Tilt correction performance. *Applied Optics* **20-11** (1981) pp. 1926-1932.
8. Kudryashov A. V. Intracavity laser beam control, *Proceedings of the SPIE* **3611** (1999) pp. 32-41.
9. Stephens R. R. and Lind R. C. Experimental study of an adaptive-laser resonator, *Optics Letters* **3-3** (1978) pp. 79-81.
10. Oughstun K. E. Theory of intracavity adaptive optic mode control, *Proceedings of the SPIE* **365** (1982) pp. 54-65.
11. Tyson R. K. Principles of Adaptive Optics, Second Edition, (Academic Press, San Diego, 1998).
12. Press W. H., Teukolsky S. A., Vetterling W. T., and Flannery B. P. Numerical Recipes in C: The Art of Scientific Computing, Second Ed. (Cambridge University Press, Cambridge, 1992) pp. 59-70.

SOME METHODS OF INTRACAVITY CONTROL OF SPATIAL AND TEMPORAL PARAMETERS OF INDUSTRIAL CO_2 LASER BEAM

VADIM V. SAMARKIN

Group of Adaptive Optics for Industrial & Medical Applications. Institute on Laser and Information Technologies -IPLIT RAN. Russian Academy of Sciences.Svyatoozerskaya Str.1, Shatura, 140700 Russia

Variable reflectivity mirror in the unstable resonator was used to improve the quality of multimode beam of the multi-kW cw CO_2 laser. Eight-fold increasing of the axial brightness of radiation and angular divergence of 1 mrad were achieved. Characteristics of the industrial 1.5 kW cw CO_2 laser beam with a temporal reflectivity controlled mirror as a output mirror of the resonator were investigated. The pulse-periodical regime of the beam generation in the range of pulse repetition up to 2 kHz was realised.

1 INTRODUCTION

Improvement of quality and possibility of alteration of temporal parameters of the laser beam at laser treatment of materials significantly expand the sphere of application of industrial lasers. It means increasing of quality and speed of treatment, increasing the thickness of the material under treatment, possibility of treatment of non-traditional materials such as glass, ceramics, ferrites and others.

2 IMPROVEMENT OF THE AXIAL BRIGHTNESS OF THE LASER BEAM

It is usually desirable for laser technology to have a laser device operating in a single mode for a good quality output beam and providing an efficient power extraction at the same time. For industrial CO_2 lasers the problem of achieving high-quality beam is closely related to the generated beam power.[1] In the lasers of power range $P_{out} \approx 1.5 - 4$ kW the interelectrode distance of gas-discharge chamber (GDC) exceeds the diameter of the stable resonator (SR) principal mode, but it is not large enough to provide the effective use of the unstable resonator (UR) due to small Fresnel number at $h/L \ll 1$, where h is the interelectrode distance, L is the amplification length. So a complex problem occurs which calls for matching the single-mode optical resonator with GDC in order to take full advantage of its active volume, i.e. to achieve high-quality beam without essential reduction of generation efficiency.

The conventional ways of increasing the volume of the SR principal mode do not give the wished result due to limitations placed by aberrations of the wavefront in the optical elements and in the active medium itself. Exponential field

distribution profile with the order more than 2 is expected to provide better energy extraction (in comparison with the more standard gaussian profile) while being less affected by aperturing since it has a large beam size and a fast decreasing of intensity near the edges. There is well known method proposed by Prof. Belanger for formation of super-gaussian beam distribution of the CO_2 laser by using a graded-phase mirror resonator.[2] But this method has a serious drawback: since the mirror surface profile is rigid, every change of laser parameters needs its own special mirror. In paper [3] authors suggested to overcome this problem by use of intracavity flexible bimorph mirror inside laser cavity for the given intensity distribution formation. Special intensity distributions (super-gaussian) can be formed also by intracavity variable reflectivity mirror [4-6]. The main disadvantage of these methods is that all of them are optimal only for the single mode regime of laser generation (for example – TEM_{00}-gaussian)

To improve the beam quality and optimal match of resonator with GDC the telescopic UR with convex output variable reflectivity mirror (VRM) was used for the industrial cw CO_2 laser with self-sustained dc discharge and fast-transverse gas flowing. When this laser is operated in multimode regime with the SR, its rated power is 2.8 kW and divergence is about 3 mrad. It does not fully comply with the requirements to laser beam quality for laser technology, e.g. precise cutting of material. Different VRMs were manufactured with the typical features ρ_{max} (VRM

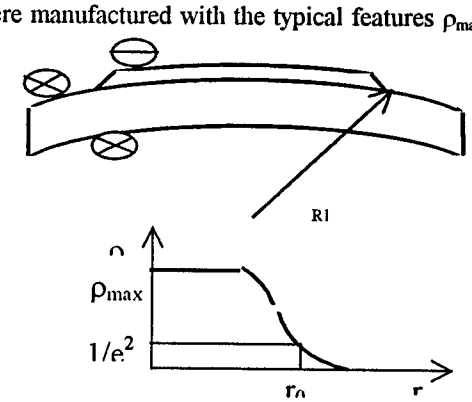

Fig. 1. VRM design

reflectivity) varied from 40 % to 85 % and r_0 (radius of reflecting coating at $1/e^2$ level of ρ_{max}) varied from 9.0 to 12.5 mm (see Table 1 and Fig. 1).

The radial distribution of VRM reflectivity is described by the high-level supergaussian function

$$\rho \approx \rho_{max} \exp\left\{-2(r/r_0)^n\right\} \qquad \text{where n=14 – 32.}$$

Table 1. Parameters of the output mirrors of CO_2 laser resonator:

ρ_{max} - mirror reflectivity; r_0 - radius of reflecting area.

Designation of resonator	Resonator configuration	ρ_{max}, %	r_0, mm
A	SR (R_1=R_2=30 m)	45	25
B	UR (R_1=-20 m, R_2=36 m)	68.6	10.35
C	—"—	47	10.75
D	—"—	40	9.7

This VRM with the radius of curvature of R_1=-20 m was placed into five-pass UR as a output mirror of the resonator. So UR included VRM, rear mirror with R_2=36 m, 2 folding mirrors, 6 diaphragms limiting laser beam size. In the case of SR both output and rear mirrors were of curvature radii of R_1=R_2=30 m, and the reflectivity of output mirror was 45%. The main investigations were performed at magnification

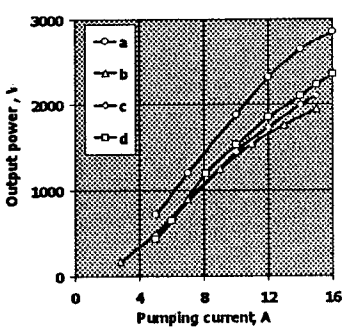

Fig. 2. Laser beam power for different configurations of resonator (see Table 1) vs pumping current.

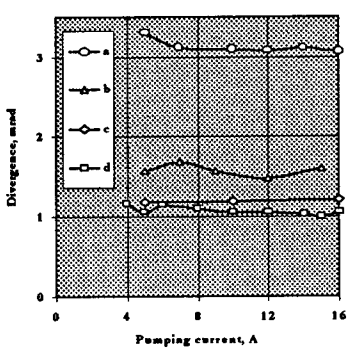

Fig. 3. Laser beam divergence for different configurations of resonator (see Table 1) vs pumping current

value of UR M=1.8. Diameters of diaphragms were varied from 36 to 41 mm. In experiments the output beam power and its stability, near and far fields beam distributions at different discharge currents were measured. The beam divergence by 84% level of energy concentration was calculated.

The dependencies of power and divergence on the discharge current for various parameters of UR with VRM are shown in Figs. 2 and 3. For comparison there are given results of the beam investigations with SR. The diaphragms of 41 to 43 mm diameters for beam size limiting were installed in the SR. In this case maximal multimode radiation power was 2.85 kW and divergence was 3.2 mrad.
As can be seen from Figs. 2 and 3, the use of UR with VRM gives substantial reduction of the laser beam angular divergence for 2 – 3 times at average power fall from 15 % to 30 %. At the reflectivity of VRM ρ_{max}=40 % (r_0=9.7mm) and diaphragms diameters of 38 mm eight-fold increasing of the axial brightness of radiation and angular divergence of 1 mrad were achieved. The average power fall was only 15 % lower than the beam power at the same discharge current in the multimode regime with the SR. Fig. 4 illustrates beam intensity distributions in the far field for multimode generation with SR and generation with VRM in UR..

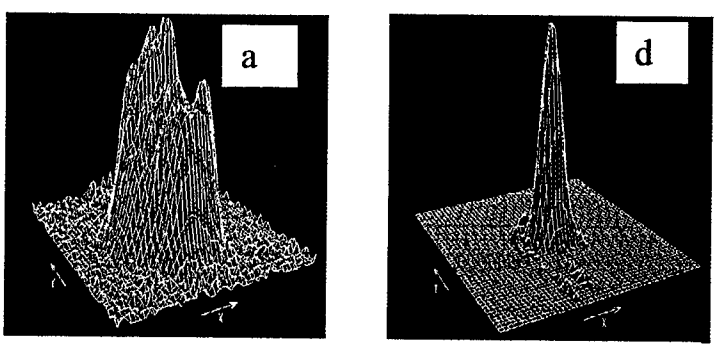

Fig. 4. Far field distributions of the laser beam at pumping current I=15 A for SR (a) and UR (d) (see Table 1).

3 CONTROL OF TEMPORAL PARAMETERS OF THE CO_2 LASER BEAM

One of the major characteristics of CO_2 laser beam that can influence the technological process results is the temporal beam modulation. The use of pulse periodical beam in the 0.5-1 kHz range of pulse repetition rate with pulse duration from 50 to 2500 μs increases of metal melting depth value up to 2-4 times [7]. The pulse periodical regime improves the quality and productivity of the laser welding process and provides the possibility of greater thickness materials treatment without increasing of average laser power [8]. Moreover, the pulse periodical regime of continuous pumped industrial CO_2 laser operation expands the sphere of its

application for treatment of materials with low thermoconductivity and fragility such as glass, ceramics, ferrites etc.[9]

The beam modulation is usually performed by electrical excitation method that has some frequency limitation. This paper presents the results of investigating the characteristics of the industrial cw CO_2 laser beam with 1.5 kW average output power, where the resonator output mirror was substituted for a temporal reflectivity controlled mirror. The mirror was kind of a Fabry-Perrot interferometer (FPI) consisting of 2 parallel positioned wedge-shaped plates of ZnSe with antireflection coating for the wavelength λ=10.6 mm on the outside faces. The change of distance between the plates by $\lambda/4$ resulted in mirror transmission (or reflection) variation from minimum value to maximum one. The distance was approximated to the wavelength λ for CO_2 laser beam and changed by using of block of piezostacks. Fig. 5 shows the photo of FPI mirror used in experiments.

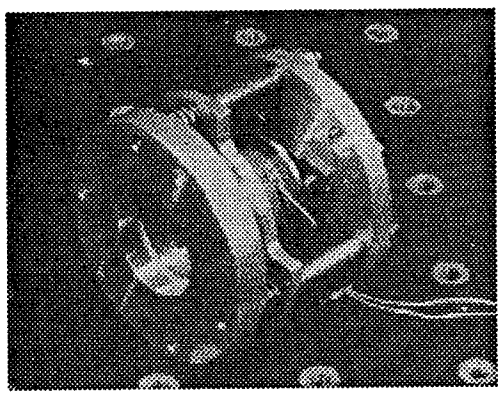

Fig. 5. Photo of the FPI mirror.

The pulse-periodical regime of generation of CO_2 laser beam with the 100% modulation depth in the range of pulse repetition up to 2 kHz was realized. Therewith, the 2.5 times excess of peak pulse power was achieved over the average power level. Output laser beam pulses at 2 kHz frequency of mirror transmittance modulation are shown in Fig. 6. The obtained results show that application of controlled FPI-based mirrors in resonators of industrial CO_2 lasers with continuous or quasicontinuous pumping is promising in realization of pulse-periodical generation regime.

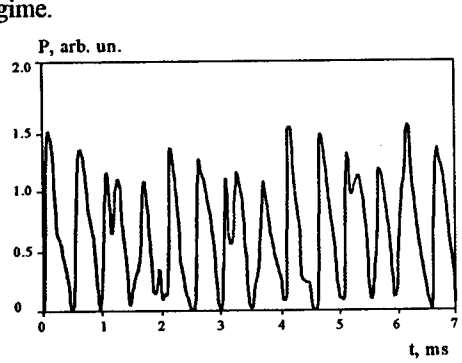

Fig. 6. Laser beam pulses at 2 kHz frequency of FPI mirror reflectivity modulation.

4 CONCLUSIONS

Divergence of the beam of industrial CO_2 laser was reduced by factor 3 (1.0 mrad against 3.0-3.5 mrad for multimode beam) with an average beam power downfall only for 13% (2.4 kW against 2.75 kW for multimode regime) by use of VRM in UR. Total modulation of the laser beam in the 0.1-2 kHz range of pulse repetition rate with pulse duration 0.05 - 10 ms was realised by use of FPI mirror in the SR. Q-switch regime with 2.5 times excess of peak pulse power over the average power level was achieved.

5 ACKNOWLEDGMENTS

The author would like to thank V.P.Yakunin and M.G. Galushkin.

REFERENCES

1. M.G.Galushkin, V.S.Golubev, A.M.Zabelin, "The physical and technical factors, determining beam quality of high-power industrial CO_2 lasers", *Proc. SPIE*, v. 3092, pp. 134-137, 1996.
2. P.A.Bélanger, R.L.Lachance and C.Paré, "Super-Gaussian output from a CO_2 laser by using a graded-phase mirror resonator," *Opt. Lett.* **17**, 739-741 (1992).
3. T.Y.Cherezova, S.S.Chesnokov, L.N.Kaptsov, A.V.Kudryashov, V.V.Samarkin, "Intracavity active mirror for the formation of the specified laser output", *Conf. Adaptive Optics Systems and Technology,* 21-22 July 1999, Denver, USA.
4. Y.Takenaka, M.Kuzumoto, K.Yasui, S.Yagi, M.Tagashira, "High power and high focusing cw CO_2 laser using an unstable resonator with a phase unifying output coupler", *IEEE J. Quantum Electron.* **27**, pp. 2482-2487, 1991.
5. S. De Silvestri, V.Magni, O.Svelto, G. Valentini, "Lasers with super-gaussian mirrors", *IEEE J. Quantum Electron.* **26**, pp. 1500-1509, 1990.
6. N.A.Generalov, V.P.Zimakov, N.G.Solov'ev, M.Yu.Yakimov, "Beam quality improvement of transverse flow multi-kilowatt industrial lasers by means of special optical resonator schemes", *Izvestiya Akademii Nauk, Seriya Fizicheskaya* **58**, pp. 270-275, 1994 (in Russian).
7. A.G.Grigoriants, Principles of Laser Treatment of Materials, Moscow, Mashinostroenie, 1989 (in Russian).
8. V.A.Lopota, S.G.Gorny, I,N.Ivanova, L.I.Shternin, "Efficiency of material treatment under various conditions of CO_2 laser beam interaction with surface", *Poverkhnost,* no. 11, pp. 123-130, 1983 (in Russian).
9. V.S.Kovalenko, O.V.Lavrinovich, "Laser machining of ceramic materials", *Proc.VI Intern. Conf. on Production Engineering*, Osaka, Japan, Nov. 10 -13, 1987.

REDUCTION OF THE THERMAL LENS IN SOLID-STATE LASERS WITH COMPENSATING OPTICAL MATERIALS

Th. GRAF, R. WEBER, M. SCHMID, H.P. WEBER

University of Berne, Institute of Applied Physics
Sidlerstrasse 5, CH-3012 Berne, Switzerland
E-mail: thomas.graf@iap.unibe.ch

The thermally induced lens is a critical issue in high-power diode-pumped solid-state lasers. A self-adaptive scheme for the compensation of the thermal lens is presented. The requirements for such an element and its influence on the resonator are discussed. With an appropriate compensating element and the correct resonator design, constant beam parameters are expected to be achieved over a pump range of several kilowatts.

1 Introduction

The power-dependent thermally induced lens is a major problem that has to be considered in the development of high-power solid-state lasers. The thermal lens is caused by inhomogeneous temperature distributions inside optical materials. The heating of the material results from absorption of either the pump power (gain medium) or the laser power itself (other optical elements). In general, three different effects contribute to the thermal lens: Firstly, the temperature dependence of the refractive index, in this paper referred to as dn/dT-part. Secondly, the axial expansion of the optical material leading to curved end faces, referred to as end-effect. Thirdly, the local strain of the material due to thermally induced stress leading to birefringence, which is not considered in this article. While birefringence reduction schemes were demonstrated successfully [1,2], compensation of the phase front distortions resulting from the temperature dependence of the refractive index and the expansion of the material are addressed in alternative active medium designs [3] but have not been solved yet for lasers with rods as gain elements. Moreover, it would be desirable to maintain constant beam parameters over a wide range of pump powers. This can be reached by adapting the resonator parameters to the respective pump power level. Although active mirrors [4] or resonator length adjustments [5] are possible means, they require sophisticated mechanical set-ups and/or electronic control. In addition, they usually do not allow to compensate for the aberrations.

Another possibility to compensate for the thermally induced lens is to take advantage of the effect itself by using a heated optical element. In the case of longitudinally pumped lasers, the absorption of the pump light in an end mirror or a lens was proposed to heat the compensating element [6]. For high-power lasers, trans-

versal pumping is preferred due to its simpler scalability and since it is less expensive. In this case a compensating element, which is placed inside the resonator and absorbs part of the laser radiation, is more promising since there is no simple way to use part of the pump power to heat the compensating element unless a separate pumping unit is used (Figure 1). Fortunately, optical glasses with a strong negative dn/dT, with an absolute value comparable to that of Nd:YAG, such as the phosphate laser glasses Schott LG-760 or Hoya LHG-8 [6, 7], are readily commercially available. A compensating element, which is heated by the intra cavity power, shows many advantages. On the one hand, no additional pump source is required. On the other hand, the thermal lens is directly correlated to the output power and aberrations will be inherently and passively compensated. In addition, if the compensating element is doped with the same active laser ion as the gain medium, the amount of absorption (from the lower laser level) can be temperature controlled.

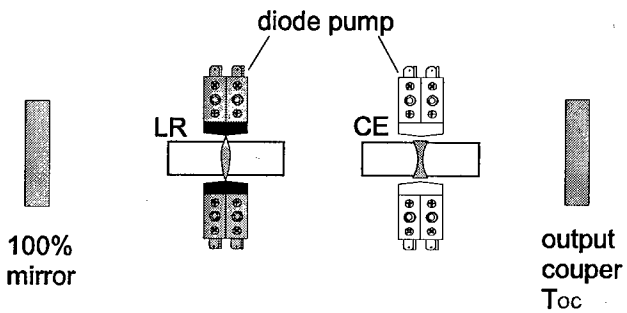

Figure 1. A laser resonator with an intra-cavity compensation scheme. LR: laser rod, CE: compensating element. The diode-pump for the CE is optional and is only needed if the CE does not absorb the laser radiation.

2 Thermal considerations

A good insight into the basic thermal behaviour of heated optical materials is achieved with a simplifying analytical approach that describes the thermally induced lens as presented in the references [7-9]. With this, the values of the relevant quantities involved can be estimated in a first approach. In this first step, we assume homogeneously heated rods with closely spaced thin lenses for the different contributions (dn/dT, end-effect) in both the active medium and the compensating element.

Under these conditions the dioptric power of the total thermal lens in a heated optical element is given by the sum of the dioptric powers of the different contributions with $D_{therm} = D_{dn/dT} + D_{end}$, where $D_{dn/dT}$ is the contribution due to the temperature dependence of the refractive index, and D_{end} results from the bending of the end surfaces of the rod.

Homogeneous heating of a rod produces a temperature difference between the centre the circumference which is independent of the cooling given by [7]

$$\Delta T = \frac{1}{4 \cdot \pi \cdot k} \cdot \frac{P_{heat}}{\ell_{heat}} \tag{1}$$

where k is the heat conductivity, ℓ_{heat} the length over which the element is heated, and P_{heat} is the total heating power. Together with the coefficient for the temperature dependence of the refractive index dn/dT and the expansion coefficient a_{exp} this temperature gradient is responsible for the thermal lens. With the above approximations the two contributions to the dioptric power D of the thermal lens in a heated rod of radius R_{Rod} are given by [7]

$$D_{dn/dT} = \Delta T \cdot \frac{2 \cdot dn/dT \cdot \ell_{heat}}{R_{Rod}^2} = \frac{dn/dT}{2 \cdot \pi \cdot k} \cdot \frac{P_{heat}}{R_{Rod}^2} \tag{2}$$

$$D_{end} = \Delta T \cdot \frac{4 \cdot a_{\exp} \cdot (n_0 - 1)}{R_{Rod}} = \frac{a_{\exp} \cdot (n_0 - 1)}{\pi \cdot k} \cdot \frac{P_{heat}}{\ell_{heat} \cdot R_{Rod}} \tag{3}$$

where n_0 is the undisturbed refractive index.

Apart from material and geometrical parameters equations (2) and (3) depend on the heat source P_{heat}. In the case of the laser rod, the heating power is given by the fraction of the pump power P_{pump} which is absorbed and converted to heat:

$$P_{heat,LaserRod} = \eta_{transf} \cdot \eta_{abs} \cdot \eta_{heat} \cdot P_{pump} = \eta_h \cdot P_{pump} \cdot \tag{4}$$

For Nd:YAG, the heat conversion factor η_{heat} is about 35% under lasing conditions [10] and the transfer η_{transf} and absorption η_{abs} efficiencies are typically about 80%.

If an external pump heats the compensating element, the heating is described by the same formula as the heating of the laser rod. In the scheme proposed in this paper, the heating of the compensating element is assumed to result from weak absorption of the intra-cavity circulating power. Therefore, the heated volume is given by the mode size at the location of the compensating element. For the following analytical approach, the multimode-beam in the compensating element is assumed to have about the same size as the rods (laser and compensating element). Furthermore, heating takes place over the whole length of the compensating element given by

$$P_{heat,compEl} = \alpha_{abs} \cdot \ell_{compEl} \cdot P_{cir} = \alpha_{abs} \cdot \ell_{compEl} \cdot \frac{P_{out}}{T_{OC}} \tag{5}$$

where α_{abs} is the absorption coefficient at the laser wavelength in the compensating element, ℓ_{compEl} is its length, P_{cir} is the intra cavity circulating power, P_{out} is the output power and T_{OC} is the transmission of the output coupler. The output power is related to the pump power, the laser threshold P_{th}, and the slope efficiency η_{slope} by

$$P_{out} = \eta_{slope} \cdot (P_{pump} - P_{th}) \tag{6}$$

With this and the eqs. (1-3), the dioptric powers of the thermally induced lenses in the laser rod (subscript *LaserRod*) and the compensating element (subscript *compEl*) are found to be

$$D_{LaserRod} = \frac{dn/dT_{LaserRod}}{2 \cdot \pi \cdot k_{LaserRod}} \cdot \frac{\eta_h \cdot P_{pump}}{R^2_{LaserRod}} \tag{7}$$

$$D_{compEl} = \left(\frac{dn/dT_{compEl}}{2 \cdot R_{compEl}} + \frac{a_{\exp} \cdot (n_0 - 1)}{\ell_{compEl}} \right) \cdot \frac{L_{compEl} \cdot \eta_{slope} \cdot (P_{pump} - P_{th})}{\pi \cdot k_{compEl} \cdot R_{compEl} \cdot T_{OC}} \tag{8}$$

where $L_{compEl}=\alpha_{abs} \cdot \ell_{compEl}$ is the loss introduced by the compensating element. These are the two lenses which are produced inside the cavity, and which should compensate each other. We note that the end effect in the laser rod is neglected. This is allowed when the unpumped length at the ends of the rod is longer than the rod diameter, which is usually fulfilled for transversal pumping. The end effect in the compensating element can also be avoided if a composite rod with non-absorbing (e.g. undoped) ends is used.

The aim of the compensation is that the sum of the dioptric powers of the two lenses vanishes, i.e. $D_{LaserRod} + D_{compEl} = 0$. This condition can be combined with the equations (10) and (11) and solved for L_{compEl} in order to find out the required absorption for the compensating element. For this estimation the laser is assumed to operate well above threshold, i.e. the threshold power is set to $P_{th} \doteq 0$. Furthermore η_{slope} is set to be independent of L_{compEl}, which is allowed if this additional loss is small. With a length of the compensating element of a few centimetres, the end effect is about ten times weaker than the dn/dT-part and can be neglected. Finally, with additional realistic assumptions for the quantities involved ($dn/dT_{LaserRod} \approx -dn/dT_{compEl}$, $\eta_{heat} \approx \eta_{slope}$ for Nd:YAG, and $R_{compEl} \approx R_{LaserRod}$) the required absorption loss inside the compensating element is found to be

$$L_{compEl} \approx T_{OC} \frac{k_{compEl}}{k_{LaserRod}} \tag{9}$$

As the heat conductivity of technical glass is typically ten times smaller than that of Nd:YAG, and typical output coupler transmissions are about 10%, one gets a required overall absorption in the compensating element of 1%. This number is very encouraging and shows that the principle of passive intra-cavity compensation with optical materials with a negative *dn/dT* is possible without significant influence on the laser performance.

3 Resonator considerations

Obviously the performance of a thermally compensated resonator significantly depends on where the compensating element is placed. Ideally, for an optimised compensation the negative thermal lens should be placed exactly at the same loca-

tion as the positive thermal lens. Since this is not possible physically, one has to superimpose the two lenses optically such that the beam parameter (q-parameter) at the location of the positive lens is the same as at the location of the negative lens. This is achieved with an optical system that has a total ray transfer matrix given by the identity matrix (with positive or negative sign). For heated rods this optical system has to be inserted between the principal planes of the two elements. Equivalently, the thermal lenses can be treated as thin lenses sandwitched between two unperturbed rod peaces of length $L_{Rod}/2$ [11]. For the sake of simplicity only the thin thermal lenses without the rods are shown in figure 2. The dashed line in the graph of figure 2 shows the fundamental-mode radius at the location of the thermal lens in the laser rod as a function of the pump power for a typical, transversally pumped Nd:YAG laser with the uncompensated cavity labelled A. In the cavity B the compensating element is optically superimposed to the laser rod with two lenses F. As soon as the laser threshold is reached (at 100 W) the lens in the compensating element sets in (absorbing about 1% of the circulating power) and the mode radius does not change any more with increasing power. If this is combined with a telescope to get a large fundamental-mode radius in the laser rod, this setup can lead to a diffraction limited beam over the whole pump power range.

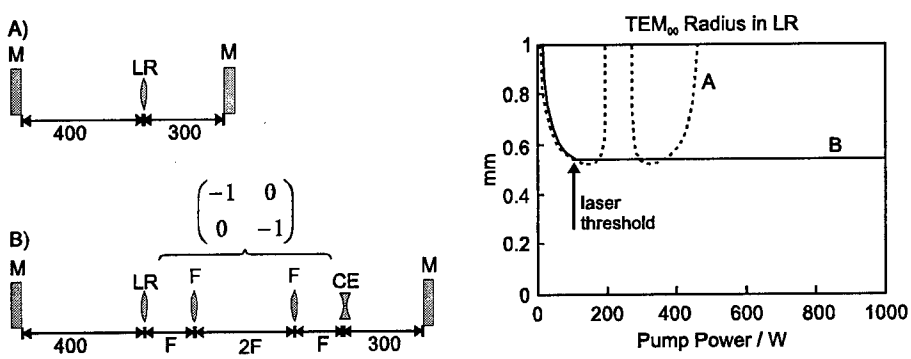

Figrue 2. Influence of the compensating element (CE) on the mode radius in the laser rod (LR). M: mirror, F: focal length of lenses. Distances in mm.

4 Conclusions and outlook

By discussing the thermal effects in optical rods we have shown, that a self adaptive scheme to compensate for the thermally induced lens in a laser rod is realistic. Optical materials with the required properties are available and will soon be tested.

References

1. Q. Lü, N. Kugler, H. Weber, S. Dong, N. Müller, U. Wittrock, "A novel approach for compensation of birefringence in cylindrical Nd:YAG rods", Optical and Quantum Electronics, 28 (1996), 57-69.
2. N. Kugler, S. Dong, Q. Lü, H. Weber, "Invesatigation of the misaglingement sensitivity of a birefringence-compensated two-rod Nd:YAG laser systen", Applied Optics 36 (36), (1997), 9359-9366.
3. A. Giesen, H. Hügel, A. Voss, K. Witting, U. Brauch, H. Opower, "Scaleable concept for diode-pumped high-power solid-state lasers", Appl. Phys. B58, (1994), 365-372.
4. U. J. Greiner, H.H. Klingenberg, "Thermal lens correction of a diode-pumped Nd:YAG laser of high TEMoo power by an adjustable-curvature mirror", Optics Letters 19 (16), (1994), 1207-1209.
5. D.C.Hanna, C.G. Sawyers, M.A.Yuratich, "Telescopic resonators for large-volume TEMoo-mode operation", Optical and Quantum Electronics 13, (1981), 493-507.
6. R. Koch, "Self-adaptive elements for compensation of thermal lensing effects in diode end-pumped solid-state lasers - proposals and preliminary experiments", Optics Communications 140, (1997), 158-164.
7. W. Koechner, "Solid-State Laser Engineering", Springer Series in Optical Sciences.
8. W. Koechner, "Absorbed pump power, thermal profile and stresses in a cw pumped Nd:YAG crystal", Applied Optics 9 (6), (1770), 1429-1434.
9. R. Weber, B. Neuenschwander, H.P. Weber, "Thermal effects in solid-state laser materials", Optical Materials 11, (1999), 245-254.
10. T.Y. Fan, "Heat Generation in Nd:YAG and Yb:YAG", IEEE J. Quantum Electron., vol. 26, no. 6, June 1993, pp. 1457-1459.
11. Vittorio Magni, "Resonators for solid-state lasers with large-volume fundamental mode and high alignment stability", Applied Optics 25, January 1986, pp. 107-117.

ENHANCED CORRECTION OF THERMO-OPTICAL ABERATIONS IN LASER OSCILLATORS

I. MOSHE AND S. JACKEL

Non-linear optics group, Soreq NRC, 81800 Yavne, Israel

E-mail: inon@ndc.soreq.gov.il

A method is presented for dynamic compensation of thermally induced birefringence and thermal focusing effects in heated laser rods, using an imaging variable radius mirror (IVRM). This compensation method performs imaging together with retracing that dynamically adapts to the pump power load. The IVRM is comprised of discrete elements, where the distance between the elements determines the amount of optical correction. The unique feature of this method is its simplicity and efficiency in correction of birefringence effects together with radial thermal lensing. The IVRM was successfully implemented in stable resonators, based on Nd:Cr:GSGG laser material, to optimally compensate for thermal lensing and thermal induced birefringence under dynamic thermal conditions.

1 Introduction

Power oscillator are an attractive means to efficiently obtain near diffraction limited laser beams, independent on the pumping power conditions. While solid state laser materials have excellent lasing properties, they also have optical properties that are very sensitive to thermal conditions. High pump power causes thermo-optical aberrations in the transmitted beam that reduce the beam quality and the lasing efficiency. In some situations, the pump power changes, thus causing the optical aberrations to dynamically change. In order to overcome these problems, dynamic thero-optical solid-state laser systems should be designed to adaptively compensate for the specific optical aberrations.

Thermal focusing and astigmatism can be statically compensated in laser resonators, by proper selection of the cavity mirrors, polishing the laser rod with concave faces[1], or adding compensating optical elements inside the cavity [1,2]. Dynamic correction of these aberrations can be done by dynamically changing the radius of curvature of the cavity's mirrors or by moving optical elements inside the resonator. In previous work, a Variable Radius of curvature Mirror – VRM and a cylindrically zoom lens were implemented in stable and unstable resonators to achieve optimal lasing performance at variable pump conditions (changing repetition-rate, zero warm-up time) [3,4].

Thermally induced birefringence causes two main problems[5]. The first problem is polarization distortion, where a linear polarized beam passing through the birefringent laser rod, accumulates different phase delay on its radial and

tangential axes, and becomes elliptically polarized. This distortion is not uniform for the whole beam, but is angularly and radially dependent. The second problem is bi-focality, which causes the radial and the tangential polarization components of the input beam to focus differently. In the case of a linearly polarized input beam, the birefringent rod behaves as an cylindrical lens.

A standard technique to minimize polarization distortion in single rod oscillators/amplifiers uses a Faraday Rotator (FR) which rotates the polarization direction by 90 degrees between rod passes [6]. Implicit with this method is ray retracing on the second pass through the distorting medium. Unfortunately, this condition cannot be met in the presence of bifocal lensing, which causes the optical path of the first pass to be different from that of the second pass [7]. Enhanced birefringence compensation, insensitive to birefringence induced bifocality, was achieved in double rods oscillators [8,9]. This technique used an image relay telescope between the laser rods in addition to a 90^0 quartz rotator. The disadvantage of this method is its inability to dynamically compensate for thermal lensing between the laser rods.

In this work, we describe an Imaging Variable Radius Mirror – IVRM that achieved reimaging of the laser rod principal plane upon itself together with beam retracing through the rod. The IVRM was found to provide substantially enhanced performance in resonators that lacked double-pass ray retracing.

2 Theory

The IVRM is basically based on an imaging lens and a reflecting mirror (fig. 1). The lens focal length f, the laser rod principal plane to lens separation d, and the lens to mirror separation d_2 are set so as to 1:1 reimage the rod principal plane. Equation 1 represent the d_2 value, which needed to obtains 1:1 reimaging. Using this value of d_2, the rod principal plane is 1:m relayed upon the mirror, where m is given by equation 2. In our case, we used m = (-)1 and thus d1=d2=2f.

$$d_2 = \frac{d_1 f^2 - d_1^2 f}{2 d_1 f - d_1^2 - f^2} \quad , \; m = f / (f - d_1) \qquad (1),(2)$$

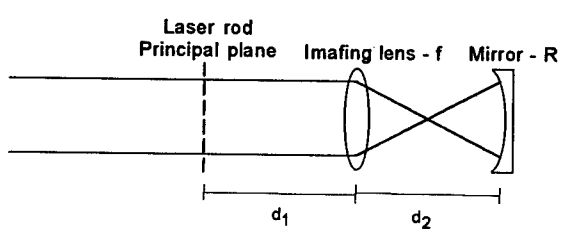

Figure 1: Basic scheme of the IVRM

The mirror radius of curvature needed for beam retrace in the presence of thermal lensing with focal length of f_T is:

$$R = f / (1 - f/f_T) \qquad (2)$$

Dynamic adjustment of the rear mirror radius could be implemented with a flexible membrane mirror or with VRM composed of discrete optical elements[3,4]. The IVRM was implemented in this work using the second option, which, for our application, was more cost effective, robust, and simpler to use. The VRM consisted of a stationary negative lens and a concave mirror mounted on a translation stage aligned parallel to the optical axis. The concave mirror was moved relative to the negative lens in order to control the beam's effective radius of curvature. The distance between the mirror and the negative lens, as function of the pump power, is shown in figure 3. At higher thermal load(>15KW), the IVRM operation becomes very sensitive to Δ variations. One can solve these problems by adding a negative lens near the laser rod or by polishing a concave surface onto the rod itself.

Figure 4 demonstrates necessity of reimaging with the IVRM in laser systems. This graph presents a calculation of the beam diameter ratio for radial and tangential polarizations, of a collimated incoming beam, after double pass the laser rod and the FR and recollimation by the VRM or the IVRM. The VRM enlarges the ratio while recollimating the beam because of the non-reciprocal laser rod and FR combination. The IVRM, by contrast, is insensitive to bi-focal lensing. A unity ratio is maintained while recollimating the laser beam. This means that good ray retracing was achieved insensitive to the beam polarizetion.

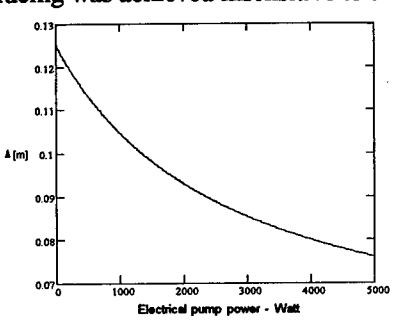

Figure 3. Distance between the IVRM negative lens (f_{lens}=(-)10cm) and mirror (R_{mirror}=(-)20cm), needed for retracing, as function of electrical pump power. Thermal focusing of the 10x0.635cm Nd:Cr:GSGG laser rod was 5 Diopted/KW.

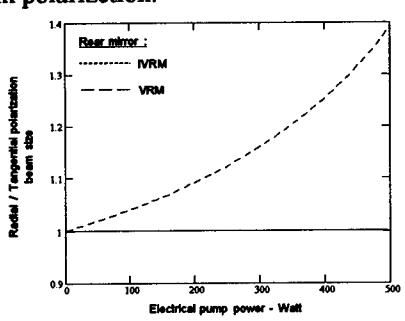

Figure 4. Radial polarization beam size divided by tangential polarization beam size after double passing the laser rod and FR, using a VRM or an IVRM.

3 Experiments

The experiment systems were based on a 0.635x10cm Nd:Cr:GSGG single flashlamp pumped laser rod. This laser material was used due to its enhanced absorption of flashlamp light (two to tree times better than Nd:YAG), and its smaller cross section for stimulated emission (twice smaller than Nd:YAG) which results in enhanced ability to store energy in Q-switched systems [6]. Unfortunately, strong thermal aberrations accompany these advantages and necessitate the use of advanced compensation techniques even at moderate pump power. Thermal lensing and thermal astigmatism (induced by pump inhomogeneity) were measured, after one pass through the rod, to be 5 and 0.8 Diopter/KW, respectively. These values are about eight times worse than those of a Nd:YAG rod placed in the same laser head.

The Faraday Rotators (FR), purchased from Electro-Optics Technology, used to rotate the beam polarization by 45 degrees, were made of terbium gallium garnet crystals inside a permanent magnets.

The IVRM as a resonator rear mirror was tested, and compared to a performance of such VRM, in stable two mirror resonators containing a polarizer.

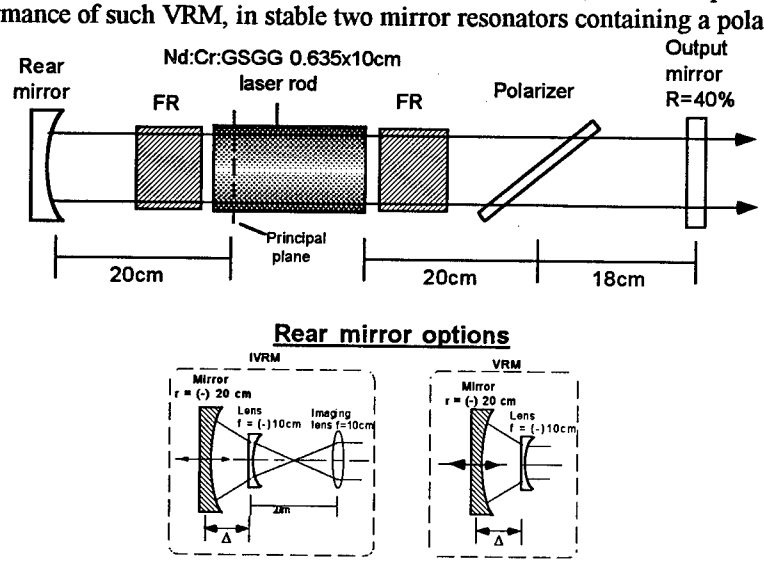

Figure 5 : Stable resonator scheme with either an IVRM or a VRM as the rear mirror.

The stable mode oscillator (fig. 5) was built as a concave-flat resonator, where the IVRM/VRM was the rear concave mirror and the front mirror was a plano, 40% reflectivity, static mirror. A FR was placed between the laser rod and the IVRM/VRM for birefringence compensation, and another FR was placed on the other side of the laser rod in order to maintain polarizer axes in a single plane. A

cylindrical zoom was added to the system in order to dynamically compensate for thermal astigmatism and to eliminate beam quality reduction [3].

The laser rod was pumped with 28J electrical pump energy, and the output power was measured as function of repetition rate. Figure 6 show the output energy normalized to the "cold operation" (0.2Hz) output energy, using the IVRM and the VRM. For these measurements, the adaptive mirrors were aligned to achieve maximum output power. Addition measurements were performed without the polarizer and thus, without birefringence loss. The same results were achieved while using the VRM and the IVRM. The output power in this case is the maximum one can extract from the oscillator. The output energy at cold operation with and without a polarizer and FRs was 1.02 J and 1.4J, respectively. Figure 6 depicts good birefringence compensation while using the IVRM, in contrast to the relative inefficiency of a simple VRM in eliminating birefringence loss.

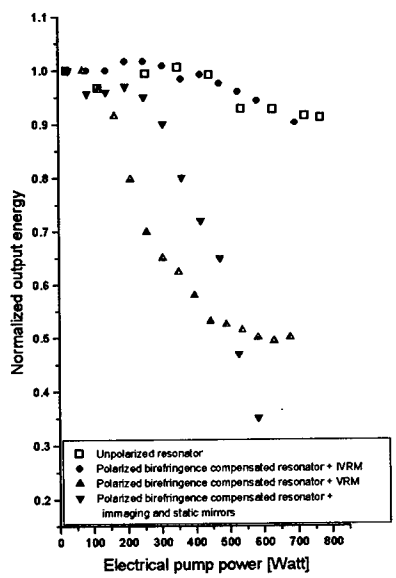

Figure 6 : Comparison of birefringence efficiency in the stable resonator aligned to maximum output power, while using IVRM and VRM. A reference measurement was made without the polarizer and FRs.

Even though an imaging lens plus static mirror could compensate for birefringence loss as well, it could not compensate for dynamic thermal focusing, and thus would not keep on the resonator in an optimal state. The static configuration failed to maintain constant output energy, because the thermal lensing caused differing amounts of diffraction losses at the rod aperture. Thus, the IVRM is an excellent method for simultaneous compensation of birefringence and variable amount of

thermal lensing. The beam quality measurements showed the same behavior with either the IVRM or the VRM, and remained around $M^2 \approx 2.2$.

4 Conclusions

An advanced Variable Radius Mirror (VRM), the Imaging VRM (IVRM), was theoretically designed and experimentally implemented in stable flashlamp pumped Nd:Cr:GSGG resonators. The IVRM has superior performance over the "first generation" VRM, when thermal birefringence induced bi-focal lensing is present. The IVRM, which produces reimaging of the laser rod principal plane back onto itself as well as dynamic focusing control, enables efficient compensation for both, birefringence (with the aid of a Faraday-Rotator), and dynamic thermal lensing. The IVRM was used to maintain optimal lasing efficiency and output beam quality from the oscillators, under variable heat conditions. As the VRM, the IVRM is also simple, robust, and cost effective.

5 References

1. S. P. Barnes and S. J. Scalise, Distributed aperture effect in laser rods with negative lenses, Appl. Opt. 17 1537 (1978).
2. D. C. Hanna, C. G. Swayers, M. A Yaratich, Telescopic resonator for large volume TEM_{00} – mode operation, Opt. Q. Elect. 13 493 (1981).
3. Working beyond the static limits of laser stability by use of adaptive and polarization-conjugation optics, I. Moshe, S. Jackel, and R. Lallouz, Appl. Opt. 37 6415 (1998).
4. I. Moshe, S. Jackel, and R. Lallouz, Dynamic correction of thermal focusing in Nd:YAG confocal unstable resonators using a Variable Radius Mirror, Appl. Opt. 37 7044 (1998).
5. W. Koechner, D. K. Rice, Effect of birefringence on the performance of linearly YAG:Nd lasers, IEEE J. Q. Elect., QE-6 557 (1970).
6. W. Koechner *Solid-State Laser Engineering* , 4rd ed., (New York: Springer-Varlag,1996).
7. S. Jackel, I. Moshe, A. Kaufman, R. Lavi, R. Lallouz, High-Energy Nd:Cr:GSGG lasers based on phase and polarization conjugated multiple-pass, Opt. Eng. 36 2031 (1997).
8. Q. Lü, N. Kugler, H. Weber, S. Dong, N. Müller, U.Wittrock, A novel approach for compensation of birefringence in cylindrical laser Nd:YAG rods, Opt. Q. Elect. 28 57 (1996).
9. J. Sherman, Thermal compensation of a cw-pumped Nd:YAG laser, Appl. Opt. 37 7789 (1998).

ACTIVE CORRECTORS AS THE ALTERNATIVE TO GRADED PHASE MIRRORS — CO_2 AND YAG LASER BEAM FORMATION

T.Y.CHEREZOVA, S.S.CHESNOKOV, L.N.KAPTSOV,

Department of Physics, Moscow State University, Vorobyovy Gory, Moscow, 119899, Russia

A.V.KUDRYASHOV, V.V.SAMARKIN

Institute of Laser Information Technologies, Russian Academy of Sciences, Gubkina 3, B-333, Moscow, 117971, Russia

Theoretical and experimental formation of a super-gaussian fundamental modes of the 4th and 6th orders of CW CO_2-laser with stable resonator with the help of an intracavity flexible controlled mirror is shown. We used semi-passive bimorph deformable mirror with four controlling electrodes. The increase of power of fundamental modes up to 12% and the enlarging of the peak intensity in the far-field in 1.6 times in the comparison with the gaussian TEM_{00} mode of the same resonator are observed. The theoretical calculations has shown the possibility of the formation of the super-gaussian fundamental modes at the output of $YAG:Nd^{3+}$ laser resonator by means of intracavity flexible mirror.

1 INTRODUCTION

The idea of formation of the given laser output by using Graded-Phase Mirrors (GPM) belongs to Prof. P.A.Bélanger et. al. [1-2]: the experimental results with GPM used in pulsed TEA and CW CO_2 lasers have shown an increase of monomode energy output as compared to the output of a conventional semiconfocal resonator [2].

But the GPM can only serve for the specific application they were design for: every change of laser parameters needs its own unique mirror. On the other hand with the help of just one flexible controlled mirror it is possible to form a number of the given laser outputs [3]. It is also possible to compensate for different phase distortions caused, for example, by thermal deformations of laser mirrors or by aberrations of active medium. Such phase distortions could destroy the given laser output intensity distribution and predict them completely is not possible because some of them depends, for example, on the pumping power, the inhomogeneity of active medium and so on. That is why for solving different tasks it is more universal and perspective to use flexible controlled mirrors.

2 ALGORITHM OF THE GIVEN LASER OUTPUT FORMATION BY MEANS OF THE DEFORMABLE MIRROR AND THEORETICAL RESULTS

Let's consider the laser with the geometry of stable resonator shown in Fig.1 consisting of plane output coupler 7, CO_2 tube 6, convex 5, concave 4 mirrors and bimorph flexible one 2. The laser resonator was based on the industrial fast axial flow continuos discharge CO_2 laser TLA-600 produced by ILIT, Russian Academy of Sciencies [4].

Azimutal symmetry can be assumed which allows us to use the one dimensional Huygens-Fresnel integral equations [5] and to calculate the propagation of the desired laser beam $\Psi_1(r_1)$ from output mirror through all resonator's elements to the deformable one:

$$\gamma_2\Psi_2(r_2) = \int_0^b K_1(r_1, r_2)\Psi_1(r_1)r_1 dr_1 \tag{1}$$

$$\gamma_1\Psi_1(r_1) = \int_0^a K_2(r_2, r_1)\Psi_2(r_2)r_2 dr_2 \tag{2}$$

where γ_i is the eigenvalue and $\Psi_i(r_i)$ is the eigenmode of the resonator, r_i, are radial coordinates, i=1 is related to plane output mirror of the diameter 2b, i=2 - to the active one of the diameter 2a,

$$K_1(r_1, r_2) = \frac{j}{B} J_0\left(k\frac{r_1 r_2}{B}\right)\exp\left(-\frac{jk}{2B}\left(Ar_1^2 + Dr_2^2\right)\right) \tag{3}$$

$$K_2(r_2, r_1) = \frac{j}{B} J_0\left(k\frac{r_1 r_2}{B}\right)\exp\left(-\frac{jk}{2B}\left(Ar_1^2 + Dr_2^2\right)\right)\exp\left(jk\varphi_{mirror}(r_2)\right). \tag{4}$$

Here J_0 is the Bessel function of zero order, A, B, D are the constants determined by the ABCD ray matrix of the laser resonator. We consider empty resonator, so A=1, B=L, C=0, D=1.

In the plane of active mirror the wave front of the desired laser beam was extracted and served to determine the appropriate shape of the bimorph flexible mirror. Such surface profile was reconstructed with minimal RMS error by combining with appropriate weights the experimentally measured response functions of the mirror. The weights correspond to the voltages applied to each mirror electrode. Convergence to the given initial field distribution was calculated by the Fox and Li iterative method of successive approximations [5].

Fig.2(a) shows the main results of such calculations: gaussian TEM_{00} mode intensity distribution on plane output coupler and super-gaussian one of the 4th order, formed by intracavity controlled mirror. In Fig.3(a) it is shown calculated super-gaussian beam of the 6th order. Far-field pattern of the formed super-gaussian beam of 4th order is given in Fig.4(c). As one may see it is possible to increase the peak value of intensity in the far-field in 1.6 times in the

comparison with the gaussian TEM_{00} mode of the resonator. The side-lobes of the formed beam are not very sufficient so that the beam quality factor of the super-gaussian mode is very close to 1 (M^2=1.06).

3 EXPERIMENTAL RESULTS OF THE FORMATION OF THE SUPER-GAUSSIAN FUNDAMENTAL MODES

The scheme of experimental setup is shown in Fig.1. For enlarging laser beam inside resonator we added (see Fig.1) the convex mirror 5 (R=-700 mm, reflectivity 100%) and concave mirror 4 (R=2020 mm, reflectivity 100%). The resonator contains also the bimorph flexible corrector 2 (R=69 m). The size of the diaphragm 3 (≈46 mm) had been chosen to have a pure fundamental gaussian TEM_{00} mode output. To apply voltages to the electrodes of flexible mirror we used block of control 1. The main parameters of the resonator are: Fresnel numbers $N_1=b^2/\lambda B=0.6$, $N_2=a^2/\lambda B=6.5$, stability factor G=0.5. (Here b=8 mm - the radius of the plane output coupler, a=25 mm - the radius of active bimorph mirror, λ=10.6 μ - the wavelength, B=9100 mm - the effective length of the resonator).

The near-field intensity distribution was observed with the help of 8 - LBA-2A ("Laser Beam Analyzer"), the far-field pattern (in the focal plane of lens 11, f=275 mm) was analyzed by 12 - MAC-2 ("Mode Analyze Computer").

For the experiment we used the semi-passive bimorph flexible mirror produced in ILIT [6]. The construction of the mirror is shown in Fig.5. It consists of copper plate firmly glued to a plane actuator disc. The last one is made of two piezoceramic discs, soldered together and polarized normally to their surfaces. The thickness of each piezoceramic disc is 0.35 mm while the thickness of the copper plate is 2.5 mm. The interface between the two piezoceramic discs contains a continuous conducting "ground" electrode. Another continuous conducting electrode between the piezodisc and the copper plate "e1" is used to control the curvature of the whole mirror. The controlling electrodes "e2", having a round form, "e3" and 'e4', having a ring form were attached to the outer surface of the piezodisc.

Applying voltages to the electrodes of the controlled mirror which we have calculated before for the formation of the 4th order of super-gaussian beam we were able to form the intensity distribution in the near-field shown by dashed curve in Fig.2(b). Solid curve represents the gaussian TEM_{00} mode generating without applying voltages to the mirror electrodes. The power of the formed super-gaussian beam was on 10% higher then the gaussian one and the waist was widened in 1.26±0.05 times (according to our calculations in 1.29 times).

In the focal plane of lens 11, Fig.1, (far-field) the peak value of intensity increases in 1.6 times (Fig.4 (b)) in the comparison with the gaussian mode (Fig.4(a)). This fact is in good agreement with the theory (see Fig.4(c)). The shape

of the far-field pattern becomes more narrow, but the side lobes which should exist are not distinguished at noise level.

Experimental formation of the 6th order of super-gaussian beam is shown in Fig.3(b). In this case we had 12% of power increase in the comparison with gaussian TEM_{00} mode. The far-field pattern of formed mode is very similar to the one of the 4th order of super-gaussian beam.

4 CONCLUSION

The experimental results of the formation of super-gaussian fundamental modes have shown the possibility to increase power on 10-12% and to enlarge the peak value of the intensity in the far-field zone in 1.6 times in the comparison with gaussian TEM_{00} mode. The experimental results are in good agreement with the theoretical calculations of the formation of the given super-gaussian modes by means of intracavity controlled flexible mirror in stable resonator of industrial CW CO_2-laser. Similar theoretical results were got also for the solid-state YAG:Nd^{3+} laser.

References

1. P.A.Bélanger and C.Paré, "Optical resonators using graded phase mirrors," *Opt.Lett.* **16,** 1057-1059 (1991).
2. R. van Neste, C.Paré, R.L.Lachance, and P.A.Bélanger, "Graded-phase mirror resonator with a super-gaussian output in a CW-CO_2 laser," *IEEE J.Quantum Electron.* **30**, 2663-2669, (1994).
3. T.Yu.Cherezova, S.S.Chesnokov, L.N.Kaptsov, A.V.Kudryashov. "Super-Gaussian laser intensity output formation by means of adaptive optics". *Optics Communications*, v155, pp.99-106, (1998).
4. M.G.Galushkin, V.S.Golubev, Yu.N.Zavalov, V.Ye.Zavalova, V.Ya.Panchenko. "Enhancement of small-scale optical nonuniformities in active medium of high-power CW FAF CO_2 laser". In Optical Resonators - Science and Engineering, R.Kossowsky et.al., Editors, Kluwer Academic Publishers, 289-300, (1998).
5. A.G.Fox, T.Li, "Resonant modes in a maser interferometer," *The Bell Syst.Tech.J.* **40**, March, 453-488 (1961).
6. Kudryashov A.V., Shmalhausen V.I. "Semipassive bimproph flexible mirrors for atmospheric adaptive optics applications.", *Opt. Eng.*, V. 35, N11, 3064-3073, (1996).

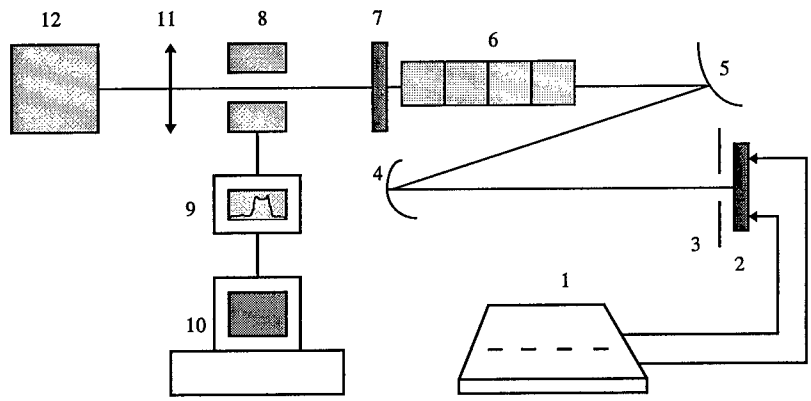

Fig.1. Scheme of experimental set-up to form super-gaussian TEM_{00} mode: 1 - block of mirror's electrodes control, 2 - semi-passive bimorph mirror, 3 - diaphragm, 4 -concave mirror R=2020 mm, 5 - convex mirror R=-700 mm, 6 - active medium of CO_2, 7 - output ZnSe coupler with coefficient of reflectivity 69%, 8 - LBA-2A (Laser Beam Analyzer), 9 - oscilloscope, 10 - computer, 11 - lens f=275 mm, 12 - MAC-2 (Mode Analyze Computer).

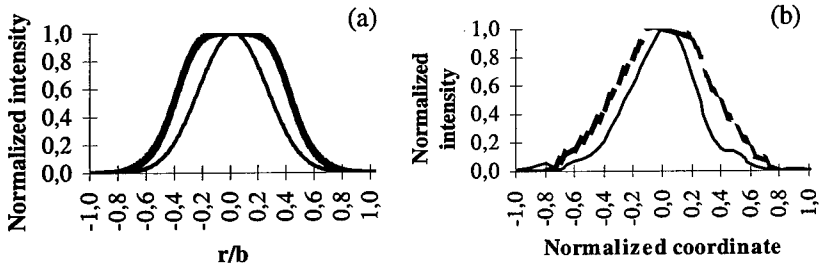

Fig.2. Formation of the 4th order of the super-gaussian fundamental mode: (a) – theory, (b) – experiment.

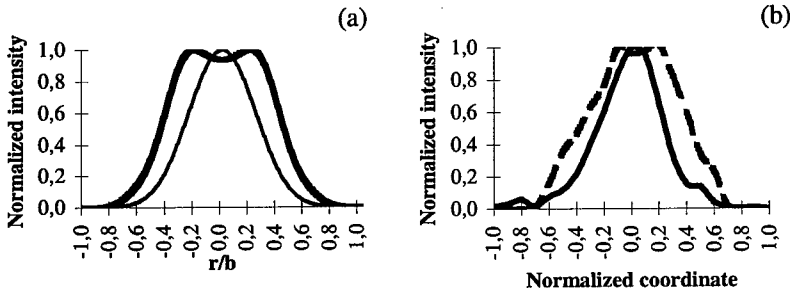

Fig.3. Formation of the 6th order of the super-gaussian fundamental mode: (a) – theory, (b) – experiment.

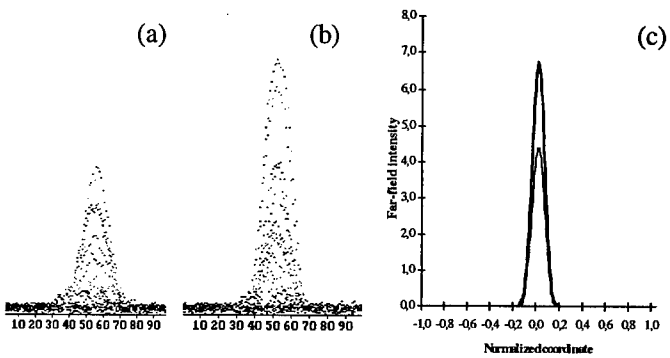

Fig.4. Far-field pattern of laser beam: (a) – experiment – gaussian TEM_{00} mode, (b) – experiment – super-gaussian TEM_{00} mode, (c) – theory – gaussian and super-gaussian modes.

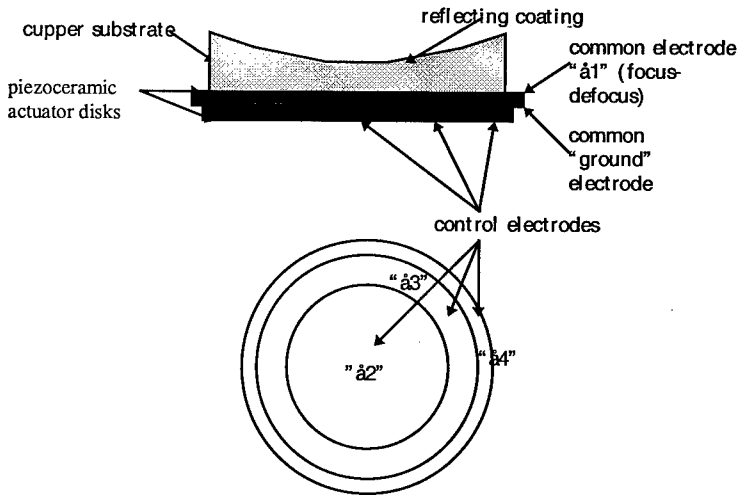

Fig.5. The construction of the bimorph deformable mirror and scheme of it's electrodes

BIMORPH MIRRORS FOR CORRECTION AND FORMATION OF LASER BEAMS

ALEXIS KUDRYASHOV AND VADIM SAMARKIN

Adaptive Optics for Industry and Medicine Group, Institute on Laser and Information Technologies, Russian Academy of Sciences, Svyatoozerskaya Str.1, Shatura 140700 Russia

The results of the research activities of the Group of Adaptive Optics from IPLIT RAN are presented. The design of the different types of the bimorph correctors for the low-order aberrations compensation is discussed. The 20 channel compact and low-cost control system capable of interfacing with personal computer is presented.

1 INTRODUCTION

Adaptive optics is known to be invented as a tool for compensation of different wavefront distortions of the light beam penetrated through some turbulent media and usually is used for various astronomical applications[1]. But starting from late 70th several types of experiments showing the efficiency of the use of adaptive systems to improve the laser beam quality were carried out[2]. Almost all these experiments were made on the CO_2 high power lasers and the obtained results were really promising. Here we should mention the works of Oughuston[3,4] (theoretical calculations), and R.Freeman et. al.[5,6,7] (mostly experiments). But then there was some sort of a gap in the interest towards the application of active optical elements in laser resonators. The main reason for this probably was the cost of the key elements of any adaptive system – deformable mirrors, wavefront sensors and systems of electronic control with the high speed computers. But later the situation changed together with the progress in laser technology and new problems were to be solved with the help of lasers. The interest in active laser beam control appeared again as well as the price of the elements of adaptive systems significantly dropped.

The main tasks that could be resolved by methods and technique of adaptive optics are:

1. Stabilisation and optimisation of different laser radiation parameters.
2. Formation and maintenance of the given intensity distribution of laser beam on the given surface.

Possible new fields of application of adaptive systems are laser microtechnology, laser etching, laser heating technology as well as laser ophthalmosurgery and laser dermatology.

2 ACTIVE MIRRORS FOR LASER BEAM CONTROL

2.1 Bimorph active correctors

While designing the adaptive system the main problem is to choose the appropriate corrector – the key element of any adaptive system, that might be used to control the laser beam. So, when deciding what kind of active corrector would be most suitable for the intracavity laser beam control we should first of all keep in mind the necessity to compensate for these low-order aberrations and to use the less number channels to correct them. In fact that means that we have to use the corrector with the so called modal response functions of actuators. And among these type of deformable mirrors the most appropriate ones are the bimorph semipassive correctors[8, 9, 10].

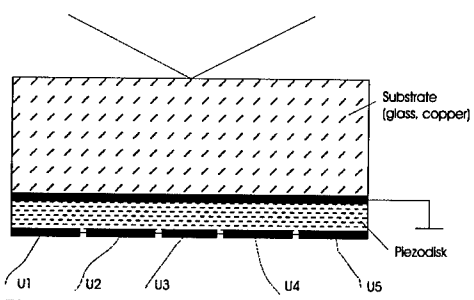

Fig. 1. Scheme of a semipassive bimorph corrector.

The traditional semipassive bimorph mirror consists of a glass, copper or quartz substrate firmly glued to a plate actuator disk made from piezoelectric ceramic (see Fig. 1). Applying the electrical signal to the electrodes of the piezoceramic plate causes, for example, tension of the piezodisc. Glued substrate prevents this tension, and this results in the deformation of the reflective surface. To reproduce different types of aberrations with the help of such

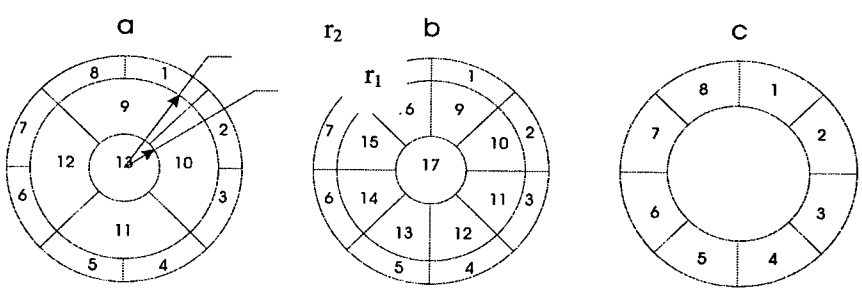

Fig. 2. Schemes of the control electrodes on the surface of the piezodisk.

corrector the outer electrode is divided in several controlling electrodes, that have the shape of a part of a sector. The size as well as the number of such electrodes depends upon the number and the type of the aberrations to be corrected. In our work we usually used the geometry of the electrodes given on Fig. 2. The behavior of the bimorph corrector (deformation of the surface when the voltage is applied to the particular electrode) is well described by the following equation[11]:

$$D'\nabla^2\nabla^2 W + (\rho_1 h_1 + \rho_2 h_2)\frac{d^2W}{dt^2} = \frac{d_{31}\nabla^2\tilde{E}(x,y)E_1(2\Delta_1 h_1 - h_1^2)}{2(1-\nu)}$$

$$\Delta_2 = \frac{E_2 h_2^2 + E_1(h^2 - h_1^2)}{2(E_2 h_2 + E_1 h_1)}; \quad \Delta_1 = h - \Delta_2$$

$$D' = \frac{E_2}{1-\nu^2}\left(\frac{\Delta_1^3}{3} + \frac{\Delta_2^3}{3} - \Delta_1^2 h_1 + \Delta_1 h_1^2 - \frac{h_1^3}{3}\right) + \frac{E_1}{1-\nu^2}\left(\Delta_1^2 h_1 - \Delta_1 h_1^2 + \frac{h_1^3}{3}\right)$$

Here, h_1, h_2 – the thickness of a piezodisk, and substrate, E_1, E_2 – Young's modulus of a piezodisk and substrate, h – total thickness of the mirror, ν - the Poisson ratios, d_{31} – transverse piezo modulus, $\tilde{E}(x,y)$ - the strength of the electric field applied uniformly to the given electrode. This equation was used to optimise radii r_1 and r_2 (Fig. 2) for the best correction of the low order aberrations such as coma, astigmatism, spherical aberration.

Several types of the bimorph correctors were produced in the Group of the Adaptive Optics. The main features of a bimorph corrector are shown in Table 1.

Working aperture	40, 50 mm
Thickness of the mirror	3 – 5 mm
Number of actuators	8, 13, 18
Mirror quality	0.2 μ (P-V)
Stroke	7 – 15 μ
First resonance	2 – 7 kHz
Substrate material	Glass, quartz, copper, silicon

Table 1. Main features of a semipassive bimorph mirrors.

The static and dynamic characteristics of the mirrors were studied by an interference method. The sensitivity of correctors was estimated from the displacement of the interference fringes at the center of the pattern when the voltage of 100 V was

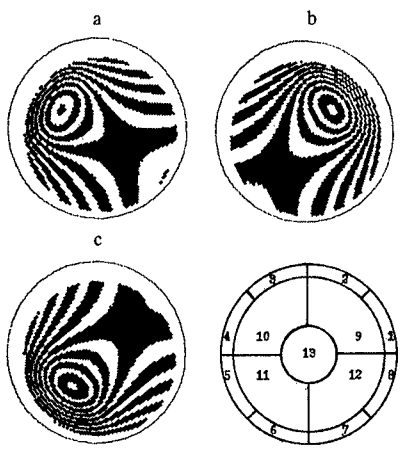

Fig. 3. Level map (step 0.2 μ) of the response functions of the middle ring of the electrodes. a – electrode number 10 (P-V=1.414 μ); b – electrode number 9 (P-V=1.579 μ); c – electrode number 11 (P-V=1.574 μ). Applied voltage was +100 V.

applied to all electrodes. It amounted to 1.7 μ. The frequency of the first resonance of our correctors was in the range of 3 - 5 kHz. The response functions of the middle ring of electrodes of the 13-element corrector are presented in Fig. 3.

It should be pointed out that the response functions of every electrode of this corrector is the modal one, meaning that by applying voltage to a given element we get the deformation of the whole mirror surface. This result on the one hand complicates the process of mirror control but at the same time reduces the number of elements that need to be used to correct for the low-order aberrations. Analyzing the level map given in Fig. 3 we can point out that the shape of the response functions of different electrodes looks very close, and the amplitude of the surface deformation is also very close.

Type of aberration	RMS error
Defocus	0.1 %
Astigmatism	0.2 %
Coma	3.0 %
Spherical aberration	5.3 %

Table 2. RMS errors of several aberrations approximation by 17-electrode bimorph corrector.

Table 2 presents the measured RMS errors of approximation of some low-order aberrations by 17-electrode bimorph corrector.

2.2 *Water-cooled bimorph corrector*

For high average power CO_2 lasers there is the problem of constructing controllable cooled mirrors, production of which is rather complicated. A corrector of this kind should satisfy a number of technical requirements: it should have the necessary optical strength, its service life should be long (~ 1000 hours), and it should be easy to construct and use. The mirror surface should be continuously deformable and the amplitude of displacement of the corrector surface should be ~$\lambda/2$ (λ=10.6 μ - is the wavelength of the corrected radiation).

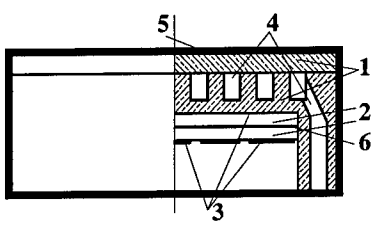

Fig. 4. Copper water cooled bimorph mirror. 1 - copper substrate; 2 - piezoceramic disks; 3 - control electrodes; 4 - canals for cooling water; 5 - reflecting surface; 6 - common electrode.

We have developed water cooled mirrors based on semi-passive bimorph piezoelement. They consisted of a copper (or molybdenum) plate 2.5 mm thick and 100 mm in diameter. One side of the plate was polished and used as a mirror, whereas two piezoelectric ceramic disks 0.3 mm thick and 50 and 46 mm in diameter were glued on the other side (Fig. 4). First piezodisk was used to control for the curvature of the mirror surface and 17 electrodes (Fig. 2) were evaporated on the outer side of the second piezodisk to compensate for different aberrations of the wavefront. The cooling system of the corrector was of the waffle type. A copper plate consisted of two solded disks in which channels of 0.5 mm deep were formed for the circulation of the cooling liquid. The size of the contact areas between the plates was 3x3 mm. Fig. 5 shows the sample of such a corrector.

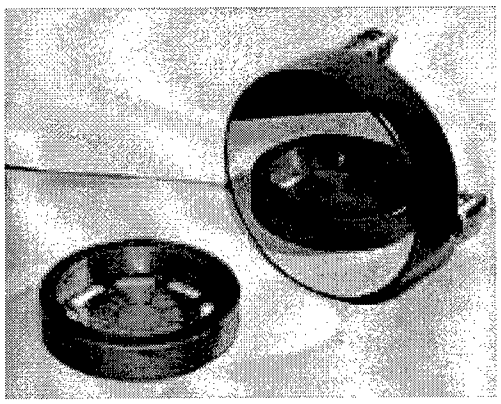

The sensitivity of correctors was estimated from the displacement of the interference fringes at the center of the pattern when the voltage of 100 V was applied to all electrodes. It amounted to 1,7

μ. The frequency of first resonance of our correctors was in the range of 3 - 4 kHz. An active mirror was tested under an optical load of CO_2 laser radiation with an average power density of 2.5 kW/cm^2 [12]. The corrector surface profile was determined using a shearing interferometer. This optical load produced practically no deformation of the mirror surface, indicating that the cooling system was effective. There were no distortions of corrector response function under the action of this load. A similar test of an uncooled adaptive mirror resulted in considerable thermal deformation of the surface.

This types of the bimorph correctors were successfully used as an intracavity mirrors to control for the radiation of a CO_2 [13], YAG [14], copper-vapor [15] and eximer[16] industrial lasers.

3 CONTROL SYSTEM FOR ADAPTIVE MIRROR

The up-to-date adaptive mirrors require high-power compact and low-cost control system capable of interfacing with personal computer. The capacitive load and a great many channels pose specific difficulties in realization of these characteristics. The suggested control system presents a variant of solving these problems. The amplifier unit ensures the adjustment of control voltages in the range ± 300 V in 20 channels by the orders from the IBM PC (the parallel data channel). The frequency range of operation from 0 to 500 Hz is therewith attained in all the channels at 0.2 μF load per channel. Fig. 6 shows the sample of this control block.

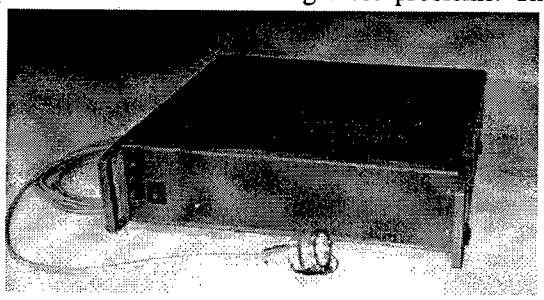

Fig. 6. Photo of the control block for adaptive mirror.

4 CONCLUSION

Bimorph mirrors, control system and required software was developed and manufactured at IPLIT RAN. Low cost and multipurpose application are the distinctive peculiarities of this device. They can be suggested for compensation of large-scale low-order aberrations in the adaptive imaging systems, laser beam formation and correction in the tasks of material processing technologies, image correction in retinoscopy and endoscopy, etc.

REFERENCES

1. *Topical Meeting on Adaptive Optics*, Proceedings ed. M.Cullum, ESO, Garching, 1996.
2. R.R.Stephens, R.C.Lind, "Experimental study of an adaptive-laser resonator", *Opt. Lett.* **3**, 79-80 (1978).
3. K.E.Oughstun, "Intracavity adaptive optic compensation of phase aberrations. I: Analysis", *J. Opt. Soc. Amer.* **71,** 862-872 (1981).
4. K.E.Oughstun, "Intracavity adaptive optic compensation of phase aberrations. II: Passive cavity study for a small N_{eq} resonator", *J. Opt. Soc. Amer.* **71,** 1180-1192 (1981).
5. J.M.Spinhirne, D.Anafi, R.H.Freeman, H.R.Garcia, "Intracavity adaptive optics. 1: Astigmatism correction performance", *Appl. Opt.* **20,** 976-983 (1981).
6. D.Anafi, J.M.Spinhirne, R.H.Freeman, K.E.Oughstun, "Intracavity adaptive optics. 2: Tilt correction performance", *Appl. Opt.* **20,** 1926-1932 (1981).
7. J.M.Spinhirne, D.Anafi, R.H.Freeman, "Intracavity adaptive optics. 3: Hsuria performance", *Appl. Opt.* **21,** 3969-3983 (1982).
8. S.A.Kokorowsky, "Analysis of adaptive optical elements made from piezoelectric bimorphs", *J. Opt. Soc. Am.* **69**, 181-187 (1979).
9. M.A.Vorontsov, A.V.Kudryashov, S.I.Nazarkin and V.I.Shmalgauzen, "Flexible mirror for adaptive light-beam formation systems", *Sov. J. of Quantum Electron.* **14**, 839-841 (1984).
10. S.G.Lipson, E.Steinhaus, "Bimorph piezoelectric flexible mirror", *J. Opt. Soc. Am.* **69**, 478-481 (1979).
11. A.V.Kudryashov, V.I.Shaml'hausen, "Semipassive bimorph flexible mirrors for atmospheric adaptive optics applications", *Opt. Eng.* **35**(11), 3064-3073 (1996).
12. M.A.Vorontsov, G.M.Izakson, A.V.Kudryashov, G.A.Kosheleva, S.I.Nazarkin, Yu.F.Suslov, and V.I.Shmalgauzen, "Adaptive cooled mirror for the resonator of an industrial laser", *Sov. J. of Quantum Electron.* **15**, 888 (1985).
13. A.V.Kudryashov, V.V.Samarkin, "Control of high power CO2 laser beam by adaptive optical elements", *Opt. Comm.* **118**, 317-322 (1995).
14. T.Yu.Cherezova, L.N.Kaptsov, A.V.Kudryashov, "CW industrial rod YAG:Nd^{3+} laser with an intracavity active bimorph mirror", *Appl. Opt.* **35**(15), 2554-2561 (1996).
15. S.A.Gnedoi, A.V.Kudryashov, V.V.Samarkin, V.P.Yakunin, "The use of an intracavity adaptive mirror in control of the radiation emmitted from a copper-vapor laser", *Sov. J. of Quantum Electr.* **19**, 1182-1183 (1989).
16. A.S.Akhmanov, M.A.Vorontsov, A.V.Kudryashov, V.Ya.Panchenko, V.K.Popov, A.Yu.Poroikov, V.I.Shmal'gauzen, "Control of spatial characteristics of excimer laser radiation by an intracavity controllyed mirror", *Sov. J. of Quantum. Electr.* **18**(8), 955-956 (1988).

Wavefront Sensors

APODIZED MICRO-LENSES FOR HARTMANN WAVEFRONT SENSING

JUSTIN D. MANSELL AND ROBERT L. BYER
Stanford University, USA. jmansell@stanford.edu

DANIEL R. NEAL
Wavefront Sciences, Inc. USA.

One of the fundamental sensitivity limits of Hartmann-type wavefront sensors, especially for coherent light, is the crosstalk between adjacent lenses caused by the hard-edge diffraction from the lens apertures. In this paper we describe the use of lens apodization to reduce the hard-edge diffraction and thus reduce the crosstalk between lenses. First, diffraction modeling of the crosstalk reduction between classic square aperture diffraction and gaussian diffraction is presented. We present a new technique for apodization of micro-lenses based upon evaporation of a metal through a micromachined array of apertures. A one-dimensional trace through the apodization aperture was shown to fit well to a 3rd order super-gaussian profile. Finally, the intensity profiles from unapodized and apodized lenses are presented showing no hard-edge ringing with apodization when observed on a CCD.

1 Introduction

All Hartmann-type wavefront sensors measure the spot positions of light diffracted from an array of apertures to determine the shape of an optical wavefront impinging on the aperture array. Hartmann's original invention of the sensor used diffraction from hard apertures put into an opaque screen or plate.[1] Astronomical adaptive optics adopted the Hartmann sensor, but the need for high photon efficiency precluded the use of such a screen. To address this need, Roland Shack and Ben Platt introduced the use of arrays of lenses in place of the opaque screen.[2] The development of micro-optics, specifically using binary optics, allowed the fabrication of high-quality small arrays of lenses to be realized.

Today the Hartmann-type wavefront sensor is being used for optical metrology and laser beam characterization. Lenses used for Shack-Hartmann wavefront sensing have fairly long focal length because this improves the sensitivity of the sensor to phase tilt by increasing the moment arm and spreading the focal spot over many pixels on a CCD which provides better centroid accuracy. These slow (large f/#) lenses create large diameter diffraction patterns and the diffraction pattern from an individual lens in the detection plane spreads into the area behind its neighboring lens and creates crosstalk. Coherent sources of radiation exacerbate the crosstalk through interference. We present a solution to this problem by applying a gaussian or super-gaussian intensity profile to each lens. For a gaussian intensity profile, the far-field diffraction pattern is a gaussian. Although with this intensity profile there is still light leaking from one lens to another, the amount of light is greatly reduced and the crosstalk is reduced because the intensity profile is smooth.

In this paper we present diffraction analysis of square lenses and lenses with a gaussian intensity profile. We discuss the possible use of super-gaussians to maximize transmitted intensity while maintaining the beneficial effects of apodization. Then we present the apodization technique for micro-lenses. Finally, we present measured intensity profiles at the focus of apodized and unapodized lenses.

2 Modeling of Crosstalk

To demonstrate the effect of crosstalk, we modeled an array of lenses with different far-field diffraction patterns. The focal plane was modeled by coherently adding an array of far-field diffraction patterns.[3] To model the CCD, the intensity measured by each pixel was determined by summing 100 intensity points evenly distributed over that pixel. The intensity was then digitized to a set number of bits. The spot position was determined using the centroid, which is the sum of the intensity times the position for a given pixel divided by the sum of the intensity. To eliminate the fluctuations in the intensity outside the main focal spot, the intensity was thresholded by subtracting a value from the intensity measured at each pixel and zeroing the intensities below zero. For square lenses, we define a unitless parameter to characterize the diffraction called the *lens order* that is the lens diameter (length of a square side) divided by the focal spot radius. This parameter is exactly four times the Fresnel number of a simple lens, which is given by the radius squared over the product of the focal length and the wavelength.[4]

To see the effects of crosstalk, we modeled a variety of square lens arrays with 100 lenses by evaluating the centroid of the focal spot in the fifth row and column and moving the position of the focal spot adjacent to it. Measuring the motion of the centroid, the crosstalk can be illustrated. Throughout this modeling, we assumed 100 pixels per square lens, a square pixel size of 10 microns, a threshold of 10%, 12 bits of digitization, and a wavelength of 633 nm.

We modeled lens arrays with a sinc and a gaussian electric field distribution. To get an idea of the optimum lens order for this case, the RMS crosstalk error was determined for a variety of lens orders for motion from the center to the point where the adjacent focal spot reaches the edge of its lens. The RMS error from the sinc electric field slowly dropped off from 1.4 microns at N=4 to 0.27 microns at N=8. Beyond a lens order of 6, no crosstalk could be measured on the gaussian aperture lenses because the shifts in the intensity profiles were less than the 12 bit digitization used.

3 Gaussian and Super-Gaussians

A super-gaussian is mathematically identical to a gaussian except that the argument of the exponential is raised to a higher power. The power of the super-gaussian will be refered to as its order. A normal gaussian is a 2nd order super-gaussian. By placing a super-gaussian intensity profile on a square lens such that the edge of the square has 1% transmission throws away quite a bit of the light through either reflection or absorption. A gaussian transmission profile rejects 90% of the

incoming light when compared to an equivalent unapodized aperture. Moving to a 5th order super-gaussian, only 65% of the light is rejected. The low transmission is not appropriate for astronomical applications, but for optical metrology and laser characterization where photons are plentiful, this loss is acceptable.

4 Fabrication of Intensity Profiles

The micro-lenses were fabricated in a standard clean room using integrated circuit technology from wafers of fused silica 4 inches in diameter and 400 microns thick. Before the lenses were fabricated, the apertures were deposited on the wafers. This was done by evaporating nickel through apertures made from thin silicon nitride on a silicon wafer held a distance from the glass substrate.

To fabricate the evaporation mask, silicon wafers were coated with 1.2 microns of silicon nitride. The silicon nitride was patterned on both sides of the wafer using photolithography and plasma etching to create the evaporation apertures on one side and release patterns on the opposite side. The release patterns were 1cm squares that allowed a silicon etchant, potassium hydroxide, to release the membrane on the opposite side with the appropriate patterns for evaporation. Then the wafers were placed into 20 wt% KOH at 80C to selectively remove the silicon and release the nitride membranes.

Several different evaporation aperture patterns, shown in Figure 1, were used to create the apodization. Initially it was thought that the best pattern would be a half-tone, but due to the 60 micron feature limit which resulted from using 2400 dpi laser-printed masks, the closest pattern to this was an array of 60 micron diameter holes on a 120 micron grid. These holes were placed only outside a circle of a given radius so that the center of the circle would have high transmission and the edges would have less transmission. This pattern will be referred to as the hole-array pattern. Another pattern that was used was an array of cross-type patterns at the edges of the lenses. The widths of the lines forming the cross were varied between 120 microns and 200 microns. This pattern will be referred to as the cross-pattern. Lenses were designed to be approximately 600, 800, and 1000 microns in diameter.

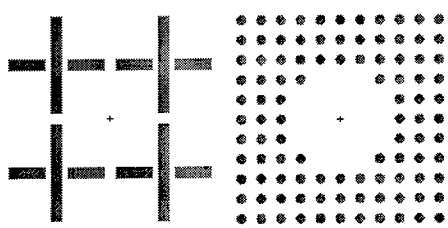

Figure 1 - Mask patterns used to create holes in the silicon nitride membrane for evaporation apodization.

The evaporation of nickel onto the substrates took place in a standard e-beam evaporator with a target to substrate separation of 10 inches. The behavior of this system was modeled like an extended optical source using ray optics. The modeling made clear that in order to have optimum control over the intensity profile, the distance between the mask and the substrate should be minimized to avoid

unnecessary spreading of the nickel. Due to the limited feature size in our masks, we were forced to use a distance of about 2.5 cm between the substrate and the mask to achieve enough spreading of the nickel that the individual apertures in the hole-array pattern could not be resolved in the transmitted intensity profile. Much below 2.5cm, the transmitted intensity profile of the hole-array pattern had visible bumps corresponding to the locations of the individual holes. Another feature of this process that became clear during the modeling was the image magnification and distortion printed onto the substrate. The spreading of the e-beam is radially dependent and thus produces magnification and a pincushion distortion in the intensity profile printed to the mask. This distortion can be compensated in the creation of the masks. (To perform our testing, we only compensated for the linear magnification term which limited our useable mask area, but greatly simplified the mask design.)

To achieve acceptable intensity profiles, the amount of nickel deposited and distance between the mask and the substrate were adjusted. The separation of the mask and the substrate allowed control of the spreading of the intensity pattern. The amount of nickel deposited allowed control of the maximum optical density. We found that 200nm of nickel created enough stress on the silicon nitride membranes to rupture them, so this defined our upper limit of the deposition thickness. The process that resulted in the intensity profiles presented here deposited 200nm of nickel onto the fused silica substrate with a separation of 0.75 inches.

5 Intensity Profile Results

The intensity profiles of the arrays were measured before the lenses were placed onto the wafers. To accomplish this, the wafer was scanned through the focus of a helium neon laser at 633nm using a motorized translation stage. A digitizing oscilloscope recorded the transmitted light as measured on a photodiode. The most successful run was for a separation of the wafer and mask of 0.75 inches and 200nm of nickel deposited onto the mask. One profile produced by the cross pattern was fit to a super-gaussian and determined to have an order equal to 3.08. The RMS fit error was only 0.126 volts out of a peak voltage of about 5.9V. The hole-array patterns produced similar smooth intensity profiles, but because of the reduced amount of nickel transmitted through these masks, they did not achieve sufficient optical density to eliminate the ringing associated with the edges of the lenses.

6 Apodized Lenses

After the intensity mask was created on the glass, 5 microns of AZ4620 photoresist were spun onto the front side to protect the nickel coating. It was then hard-baked for 10 minutes at 120C. AZ4620 was then spun onto the backside of the wafer to a thickness of 12 microns and baked for 15 minutes in an oven at 90C. The resist was exposed and developed to form cylindrical pillars. The pillars were transformed into lenses by placing the substrate on a small glass petrie dish lid that was sitting in a crystallization dish with 20mL of acetone in the bottom. Then a seal was made

over the top by placing a large plastic petrie dish lid over the crystallization dish and a full 1 gallon jug of acetone on top of the plastic petrie dish lid. This allowed the acetone vapor to begin to dissolve the pillars of resist and form lenses. After five minutes of exposure, the wafer was placed into an oven set at 120C for 10 minutes to drive off the solvents and solidify the lenses. Finally the lenses were transferred into the substrate using a CF_4 and O_2 plasma etch.

The intensity profile of the focal plane was determined by imaging the focal plane of the lens under test onto a Cohu 2122 CCD with a 30mm achromatic lens. A diode laser collimated with a shear plate was used as the light source. Because the important details of the intensity profiles were very low intensity, the dynamic range of the CCD had to be pushed using electronic shuttering of the camera. The CCD was adjusted to be in a linear regime by setting the shuttering to 1/10,000 s and using the current knob on the diode laser and the gain knob on the CCD. Images were then taken with the shutter set at 1/10,000s, 1/4000s, 1/1000s, and 1/250s. Although this procedure resulted in saturating the CCD in the focal spot, the diffracted wings remained unsatured. Slices through the intensity profile were taken of the focal spots normal to the scanning direction of the CCD to prevent any effects of CCD blooming.

Figure 2 shows the measured intensity profiles for 1/250s shuttering (40x amplification). The lenses without nickel profiles on them showed the classic circular-aperture diffraction profile. The apodized lenses exhibited no observable diffraction ringing.

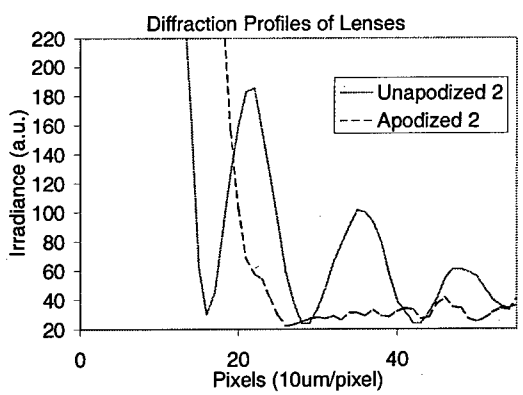

Figure 2 - Focal spot profiles with respect to readius for an apodized and an unapodized circular lens.

7 Conclusions

We have used modeling to demonstrate that apodizing lenses reduces the crosstalk for Shack-Hartmann wavefront sensing. Further we have demonstrated a technique for apodizing micro-lenses using evaporation of a metallic absorber through a mask. Application of this technique can thus be used to reduce the crosstalk in Shack-Hartmann wavefront sensing below its ability to be observed by standard CCDs.

8 Acknowledgements

We would like to acknowledge the NSF which funded this research under grant number 2WMF572. Special thanks go to Tom Carver for his assistance in the many evaporation runs that were necessary for calibration of the process and his technical advice in the process flow and Marty Fejer and Eric Gustafson for technical advice.

References

1. J. Hartmann. *Z. Instrumentenkd.* Vol. 24. p. 99-117. April 1904.
2. R.B Shack and B.C. Platt. Abstract only. JOSA vol. 61, p. 656, 1971.
3. J.K. Gruetzner, S.D Tucker, D.R. Neal, A.E. Bentley, and K Simmons-Potter. "Optical and control modeling for adaptive beam-combining experiments." SPIE Proc. vol. 2534, p. 99-104, 1996.
4. A.E. Siegman. Lasers. University Science Books, 1986.

LINEAR WAVEFRONT SENSOR : A NEW METHOD FOR WAVEFRONT SENSING

XAVIER LEVECQ AND SAMUEL BUCOURT

Imagine Optic, 2 rue Jean Rostand, 91893 Orsay cedex, France

E-mail: contact@imagine-optic.com

Shack Hartmann technology is classically presented in a matrix approach. We describe in this paper a new method for wavefront sensing with a linear Shack-Hartmann. The idea is based on the real need of the user : a « waveline » can provide a simple way and low cost system for tilt and focus control and also a very useful information for optical adjustment ; in the other hand, the same system can be used for a complete characterization of the wavefront after a radial scan of the beam. The line geometry and smart softwares are offering new powerful advantages for such sensors : speed, dynamic, accuracy...

1 Introduction

Linear Shack-Hartmann is not a classical way to measure and characterize wavefront. We will see, in this paper, the advantages to take a linear approach for wavefront measurement. We will present applications where a 2 dimensional (matrix) measurement is not required and where a linear wavefront sensor (with its advantages) is perfectly convenient and much more efficient than a 2 dimensional shack Hartmann sensor.

2 Waveline sensing principle

The H-LINE technology is based on classical Shack-Hartmann, but using a linear geometry which means a linear CCD ship and a linear array of cylindrical microlenses, as shown in fig. 1 ; the local slope are measured in the same way as the classical SH, by processing the centroid position of each spot. A slim slot can be placed in front in order to select the incoming light ; it is also a way to make a pre-tilt-adjustment of the sensor (in the x direction on fig.1) to work with the nearly normal incidence (± 3°).

Once the local slopes are processed, the wavefront has to be reconstructed. A zonal or a modal mode can be chosen. We have developed a modal reconstruction.

As the geometry is linear, we have taken the Legendre polynomial base which is an orthogonal base on a linear support.

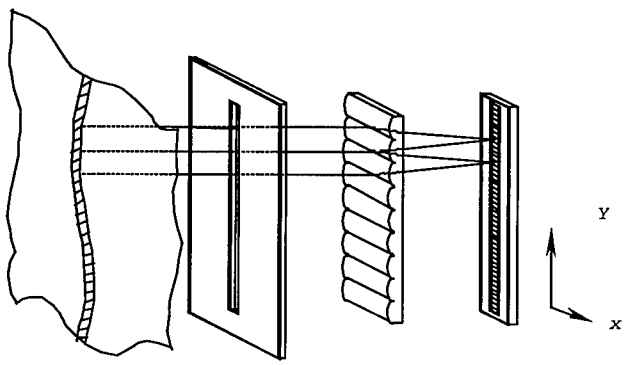

Figure 1.

The typical parameter of this wavefront sensor which is commercially available are the following : CCD with 2048 pixels, 50 to 200 microlenses in the measurement direction, and a physical aperture dimension of 28,7 mm.

3 Wavefront sensing principle

A radial sampling of the wavefront leads to a complete characterization of the wavefront with no loss of the useful information. The idea is that the user can choose an adapted "resolution" of the sampling to see more or less the classical aberration order.

Information contained in some wavefront meridian lines is widely sufficient to respond in most of cases to users demands. Indeed, one meridian line provides exact values of x tilt, of focus, of spherical aberrations (3rd and 5th order); two orthogonal wavefront lines drive to exact values of tilts (x and y), of focus, of comas, of spherical aberrations (3rd and 5th order) and of astigmatism. By extension, acquisition of four meridian lines provides 32 of 36 first Zernike polynomials; eight meridian lines give a still higher precision exceeding Zernike polynomial n° 66 (Fig 2).

The mathematics to achieve the link between the Legendre lines and the Zernike decomposition is a projection from the Legendre base to the Zernike base. To do that without any loss of information for the considered aberrations is to respect the orthogonality properties of the polynomials in the projection.

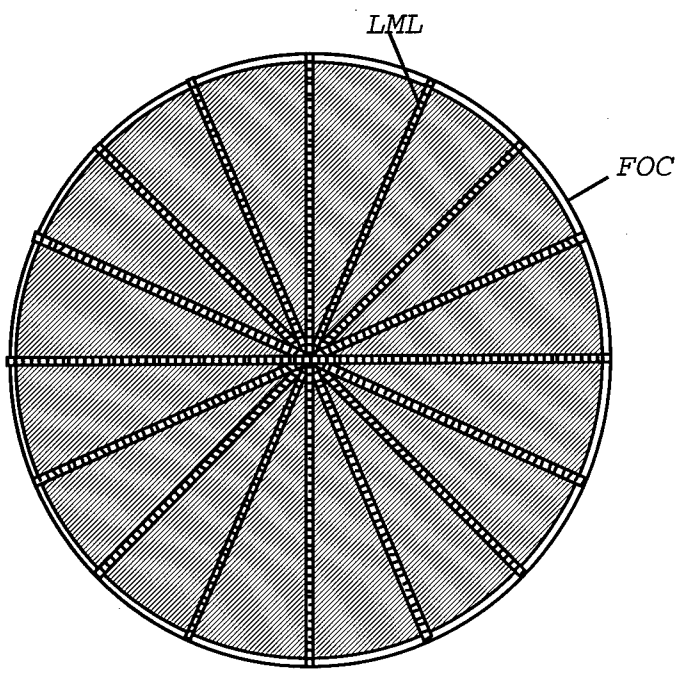

Figure 2.

4 Advantages and applications

This new concept offers some strong advantages compare to the classical approach and even compare to other technology. One of them is the very high dynamic of this sensor thank to the numerous pixels and to smart processing software (more than 10000 λ stroke). This leads to work with very divergent or convergent beam (till N = 2) as well as collimated beam (keeping the same accuracy : $\lambda/75$ rms). Moreover, the high aperture of the sensor (28,7 mm on the standard version) makes it easy to place in a beam without using any optical system (which introduced some distortion in the beam the user wants to check).

Another property of this sensor is the speed : because there is only one line to measure (and not a complete matrix), it is possible to work at a rate of 100 Hz in the standard version of the device. It is very convenient for the user who can adjust in real time his optical bench or system.

Thank to the above points, this sensor becomes the perfect tool to be used for optical adjustment ! Let's give a simple illustration of this (fig. 3). To align an

optical system, the user can process in four simple steps which are leading to a high accuracy and reproducible alignment :

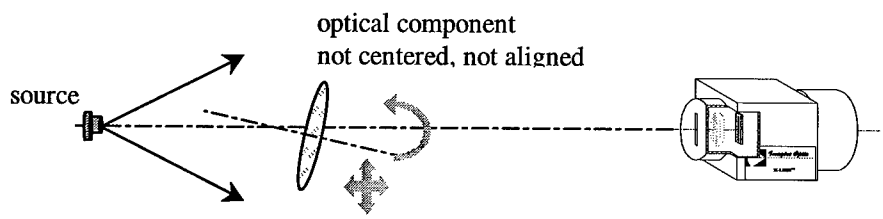

Figure 3.

- Control the source position and center the sensor
- Center lenses controlling image source position
- Focus control (collimated beam or other)
- Suppressing the tilt of the system, optimizing coma and astigmatism (fig. 4)

Once the optical bench is well aligned, it can be useful to control the quality of the wavefront. It is possible with the same sensor by a radial sampling with no change in the optical configuration, even if the beam is diverging or converging ! Moreover, the H-LINE technology offers a high resolution (till a few hundred of subapertures !)

Figure 4.

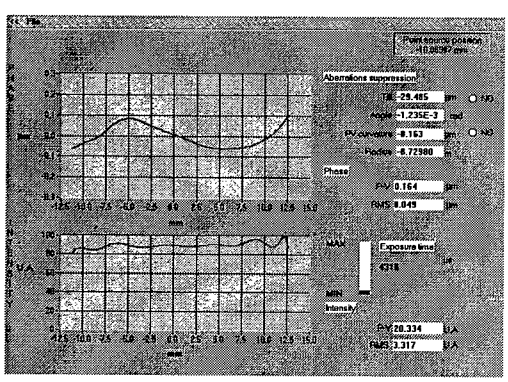

That means the operator can control an objective in its working configuration (with for instance a back focal lens of a few centimeters).

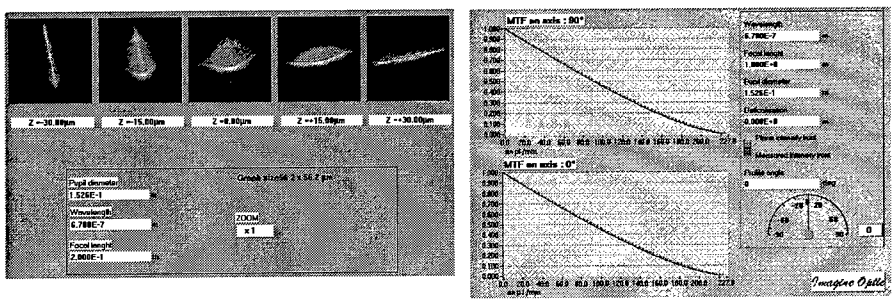

Figure 5.

To complete the quality control, the software provides the table of the Zernike, the point spread function and the MTF, a spot diagram, the Sthrel ratio, etc... all the tools needed to completely characterized the system (Fig 5).

5 Applications : focus control of industrial laser

The focus is an aberration which can be measured very easily with a H-LINE. Two applications are developed around the measurement of this parameter :

1. an optical probe to make 3D measurement
2. an adaptive probe to make a focusing control of a laser

3D measurement find applications in industry for distance control : thank to this probe, it is possible to operate surface mapping or process control (fig. 6).

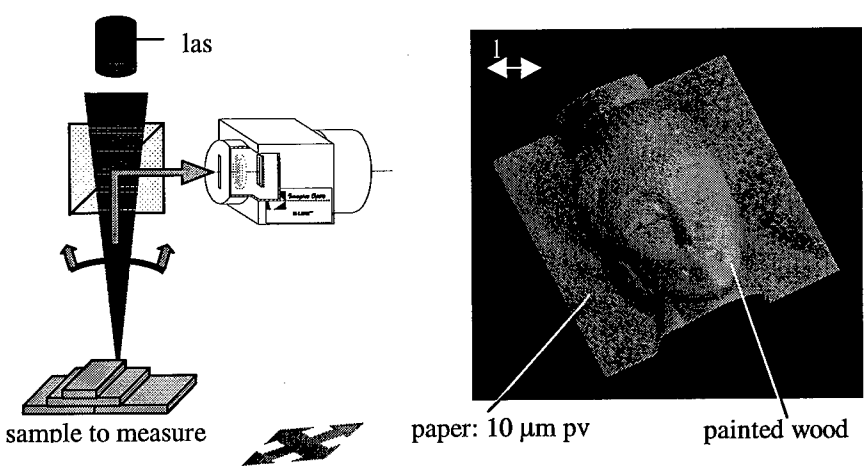

Figure 6.

Such a system can reach 1 μm accuracy on distance measurement with 20 mm stroke or 5 μm accuracy with 100 mm stroke. The bandwidth is over 500 Hz.

Using the same philosophy, it is possible to measure in the same time the focus of a laser and the real location of the target. Then, a direct comparison can lead to a close loop, in order to keep the focussed spot at the same distance of the target. This application can be used for laser welding or cutting (Fig 7).

6 Conclusion

This new generation of sensors is offering very large possibilities for a moderate cost (less than 20 k$). Because the waveline is a basic parameter of the wavefront, easy to manage and containing lots of information, this sensor can be used as well as for labs application (optical adjustment), for process control in industry or for many applications in adaptive control of beams (tilt and focus).

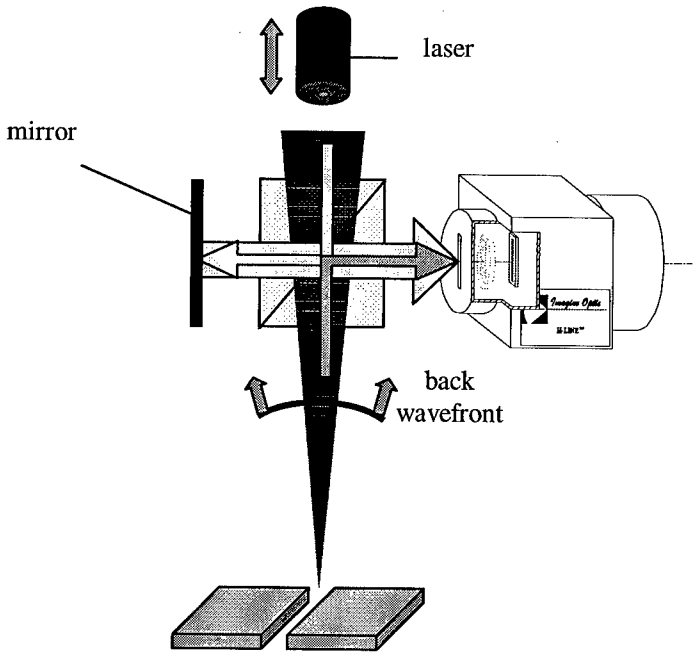

Figure 7.

INTEGRATION OF A HARTMANN-SHACK WAVEFRONT SENSOR

D. W. DE LIMA MONTEIRO, G. VDOVIN AND P. M. SARRO

Electronic Instrumentation Laboratory – Faculty of Information Technology and Systems
Delft University of Technology, Mekelweg 4, 2628 CD Delft, The Netherlands
E-mail: davies@ei.et.tudelft.nl

We report on the possibilities for a novel integration approach to Hartmann-Shack wavefront sensors, which combines two consolidated technologies, i.e., planar micro-optics and microelectronics standard CMOS process. Therefore, a compact low-cost device comprising micro-lenses and silicon photodetectors can be fabricated, taking full advantage of component optimization in both technologies. Currently, expensive CCD image sensors, a powerful computer and complicated data reduction algorithms are required to generate the wavefront profile. This hinders system miniaturization and real-time results. As an alternative, an array of optical position-sensitive detectors (PSD's) can be tailored to the aimed application and generates output voltages proportional to the spots positions, thus avoiding CCD's rather complex image analysis. This paper presents the initial step for an integrated H-S sensor based on a micro-lens array to be geometrically mounted on top of a PSD array fabricated in standard CMOS process line. To date, several PSD's featuring different photosensitive characteristics and two-dimensional layouts have been fabricated at our laboratory. Results on these devices are discussed.

1 Introduction

Among several types of wavefront sensors, the Hartmann-Shack is the one that is most widely employed, not only due to its practicality but also because it offers the possibility to have information about aberrations in real-time [1, 5]. Nevertheless, there is no integrated and cheap H-S sensor available yet and each time one needs it, one either has to assemble off-the-shelf components to make one, or buy a big and expensive system. An H-S wavefront sensor basically consists of a microlens array, a detector and a data processing unit. On the first step to the development of a low-cost integrated device, we investigate the possibilities of replacing the traditional CCD by an array of CMOS position-sensitive detectors (PSD's). This allows future integration of reliable low-cost low-power electronic circuitry to the sensor. There will be as many PSD's as microlenses, and each of them will output the position of a single light spot. The PSD is the building block of the detector part. This means that as soon as we make one PSD which offers acceptable performance, we must simply make an array of them to have the whole detector for the H-S sensor. We then tried different sorts of two-dimensional PSD's and analyzed their behavior. High accuracy (< 1 μm), 200 μm position range and independence on light intensity are the main specifications to be met at this stage.

2 Implementation

Two different geometrical structures, for 2D PSD's, based on a multi-pixel arrangement were fabricated using a standard 1.6μm double-metal n-well CMOS process line. The first one features 25 pixels arranged in a *chessboard-like* configuration (Fig. 1a) in which "white pixels" are responsible for measuring the X coordinate and the "black pixels" measure the Y coordinate, without interdependence of the coordinate signals [3]. The second structure consists of two complementary *spiral-shaped* sensing elements in each of the 25 pixels present (Fig. 1b). The current dividing method was used for the output currents and therefore linear chains of divider resistors were properly connected to "white" and "black" elements in both structures [4]. The dimensions of all PSD's have been made about 2000μm x 2000μm with individual cells about 400μm x 400μm large.

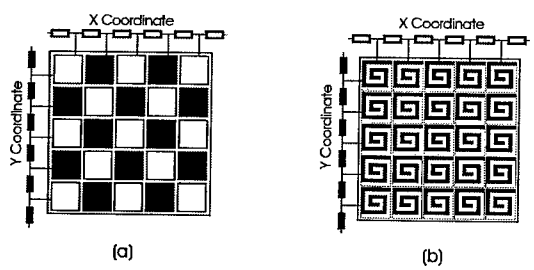

Figure 1. (a) chessboard-like structure, (b)spiral structure

We made three chessboard-like structures, two with photodiodes and one with phototransistors as the photo-sensing elements. The upper p^+/n-well junction was used for the photodiodes, and the vertical configuration with a very small emitter was employed for the p^+/n-well/p-substrate phototransistors. The peculiarity about the photodiode structures is that one was made with a single n-well for the whole device area with shallow p+ regions embedded in it, and the other with multiple n-wells, as can be seen in the cross-sections shown in Fig. 2. The pitches and fill factors for each structure are displayed in Table 1.

Table 1. Geometrical characteristics of the structures (5x5 pixels)

		Chessboard-like			Spiral
Photosensitive element		photodiode	photodiode	Phototransistor	photodiode
Architecture		single n-well	multiple n-wells	vertical pnp	single n-well
Pitch in x-direction (μm)		860	898	828	419
Pitch in y-direction (μm)		820	858	828	419
x array	# pixels	13	13	13	25
	Fill factor (%)	0.48	0.45	0.49	0.41
y array	# pixels	12	12	12	25
	fill factor (%)	0.44	0.41	0.45	0.41

Every cell of the spiral structure has, as the name implies, two juxtaposed spiral-shaped photodiodes so as to fill a 400μm x 400μm area. Each coordinate pixel is then 340μm x 340μm large. The upper p^+/n-well junction is used and a single n-well is common to all pixels. The photodiode with multiple n-wells as well as the phototransistor approaches were not considered due to the large gaps between spirals in a pixel that they would require due to technology limitations. The implemented structure is shown in Fig. 3.

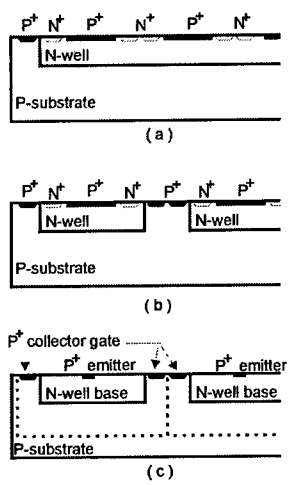

Figure 2. Cross-section of (a) single n-well, (b) multiple n-wells and (c) phototransistor PSD structures

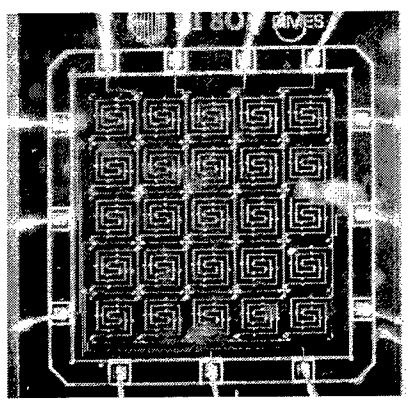

Figure 3. Photograph of implemented spiral-structure PSD

3 Experimental Results

A He-Ne laser was used for the measurements (λ = 633nm). The photodiodes operated with the n-wells (cathodes) and substrates grounded and the phototransistors had the substrate (collector) kept at –14V. The output corresponding to the position in each direction is normalized and proportional to the difference of the currents at both ends of the respective resistive chain. Amplification offset and dark currents were subtracted from each signal.

3.1 General results on the various structures

We measured the coordinate response to spot centroid displacements over 80% of each device surface. Spots with approximately gaussian intensity profile and

diameters ranging from 1 to 5 pixels swept the surface of each device. The incident light power was 5 μW for these measurements. Mismatch between X and Y coordinate outputs were found to be less than 10% and 4% for chessboard and spiral structures, respectively. Computer models were built to simulate the spatial response of the devices for different spot sizes and number of pixels.

It was found that the spiral structure featured close agreement to the simulation prediction for every spot size analyzed (Fig. 4 and Fig. 5), whereas the chessboard-like structures did not achieve the performance predicted and departed from the prediction for decreasing spot sizes [2]. Among these latter, the best results for 80% of the device area were exhibited by the phototransistor structure.

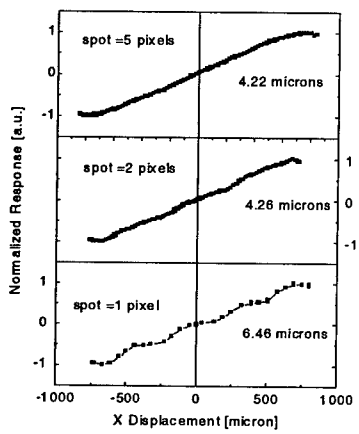

Figure 4. Spiral PSD response along the x-axis. Accuracy is indicated next to each curve.

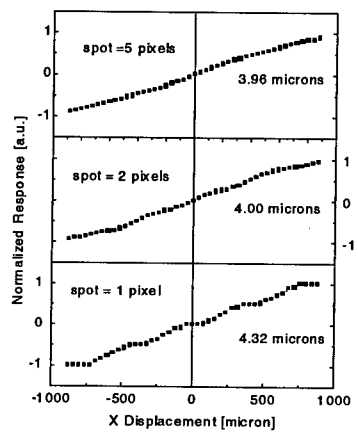

Figure 5. Simulation of the spiral PSD response along the x-axis. Accuracy is indicated.

The way the accuracy varies with spot size, for the spiral PSD, is presented in Fig.6. It is found that the accuracy variation with spot size is intimately dependent on the geometrical structure [2].

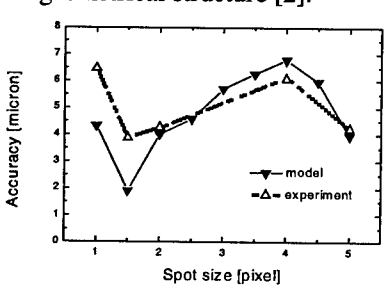

Figure 6. Comparison of accuracy variation versus spot size for the real and ideal spiral PSD's (5x5 pixels)

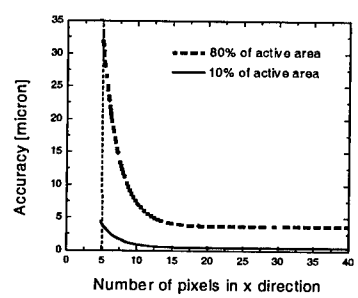

Figure 7. Comparison of accuracy variation versus number of pixels in one direction for 80% and 10% of the active area (5x5 pixels)

In Fig. 7 we plot the accuracy variation with number of pixels, for a spot diameter equal to 2 pixels, according to computer simulations. It is seen that the accuracy improves with increasing number of pixels and has a minimum value < 4μm and <0.5μm from about 25 pixels onwards in one direction, when respectively 80% and 10% of the device area is considered. This means that a 25x25-pixel PSD will perform as well as, say, a 100x100-pixel. The non-linearity was mainly observed at outermost pixel regions, i.e., the edges of the response curve, where the spot departed from the detector area. With a larger number of pixels the non-linearity, due to edge effects, is expected to decrease. When a large enough number of pixels is present, then the non-linearity is strictly dependent on the 'ripple' caused by the discrete structure of the sensor and finite size of the light beam.

3.2 Results on the spiral structure for a H-S wavefront sensor

Each individual spiral photodiode has responsivity equal to 0.09A/W and its dark current is 400nA. For the H-S wavefront sensor we need a position sensitive range of about 200μm centered at the middle of the PSD and position accuracy better than 1 μm. Besides, it should also allow for some intensity fluctuations of the light source. We therefore performed tests in the range ±100mm with reference to the device center. A rectangular 6x6 micro-lens array (focal length = 5mm, lens diameter = 1.5mm) was used. An aperture (F = 1.0mm) was used to select one single lens and screen the others. The detector was placed outside focus, so that a spot size equal to two pixels could be used.
The response of the spiral-structure PSD for various incident power levels is displayed in Fig. 8. Power levels below 1.5μW presented non-linearity > 25%.

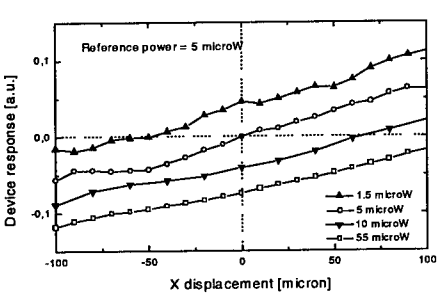

Figure 8. Spiral PSD response along x-axis over 10% of the device area for different incident power levels (spot = 2 pixels)

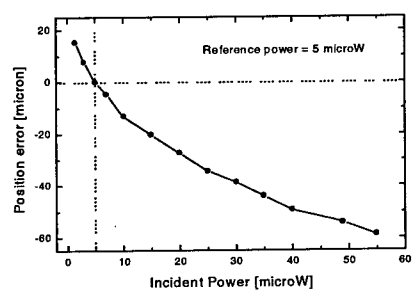

Figure 9. Spiral PSD position error due to zero value shift with variation of the incident power

We considered 5 μW as the reference incident power and observed that there is a shift from the zero position as the intensity changes. As Fig. 9 shows, for a calibrated curve at 5 μW, a position error of about 15 μm will be added to calibrated value if the power changes to 1.5 μW, and the same amount of error will be subtracted if the power changes to 10 μW. This means that for the position error to be smaller than the accuracy at 5 μW (error < 4.2 μm), the maximum allowed fluctuation in power should be ± 1 μW. If the reference power is taken at a higher value, then the allowed power fluctuation around that value is also higher. To achieve position accuracy better than 1 μm we would need to fabricate a device with at least ten pixels in one direction, as suggested by Fig. 7.

4 Conclusions

Our results are that the spiral structure reaches much better results than the chessboard-like one and allows spots comparable to the pixel size. But although a spiral PSD can be made with a larger number of pixels, so as to improve accuracy, there is a dependence on the light intensity. Therefore, the real center of the device is not well defined. These factors make this device unattractive for a wavefront sensor. Nevertheless, to ensure a defined center and avoid intensity dependence, CMOS PSD's with alternative layouts and different readout techniques can still be investigated for this purpose.

5 Acknowledgements

We acknowledge the funding from LTR ESPRIT project MOSIS.

References

1. Geary J. M., Introduction to Wavefront Sensors. (SPIE Optical Engineering Press, Bellingham – USA, 1995).
2. Lima Monteiro D. W. de, Vdovin G., Sarro P. M., Various layouts of analog CMOS optical position-sensitive detectors. To be published in *Proc. SPIE* (Denver – USA, July 18-23, 1999).
3. Mäkynen A., Ruotsalainen T., Kostamovaara J., High accuracy CMOS position-sensitive photodetector (PSD), *Electronics Lett.* **33** (2) (1997) pp. 128-130.
4. Tartagni M., Perona P., Computing centroids in current-mode technique. *Electronics Lett.* **29** (21) (1993) pp.1811-1813
5. Tyson R., Principles of Adaptive Optics. (Academic Press, San Diego – USA, 1991).

FLEXIBLE CONFIGURATION OF WAVEFRONT SENSOR AND RECONSTRUCTORS FOR ADAPTIVE OPTICS SYSTEMS

B. MARTIN LEVINE, ALLAN WIRTH, AND CLIVE STANDLEY

Adaptive Optics Associates, 54 CambridgePark Drive, Cambridge, MA 02140-2308 USA

Email: marty@aoainc.com

It is now possible to build low cost adaptive optics systems with commercial electronics and with no specialized computing coprocessors such as dedicated digital signal processing boards. The ability to change configuration of a wavefront sensor including its sensitivity, dynamic range, and also subsequent type of wavefront reconstructor have a variety of applications in adaptive optics, wavefront control, and deformable mirror calibration. We present our implementation of these methods as used in adaptive optics systems, metrology systems, and commercial wavefront sensors.

1 Overview

The paradigm for building adaptive optics (AO) systems has been heavily influenced by rapid advances in personal computer (PC) technology. It is now possible to base real time AO systems on a single processor PC and obtain data throughput rates of 1KHz for 37 actuators [1]. It is equally important for such systems to be easy to use, and a portion of this ease-of-use is the ability to reconfigure the wavefront reconstructor to suit the application. We will review the physical layout, the methods for deriving wavefront reconstructors, and the performance of a PC based AO system. As a result of this system, more flexible methods for deriving wavefront reconstructors are also shown. A graphical user interface (GUI) driven software package for these reconstructors shows how the user can select from zonal, modal, curvature, or even stochastically derived reconstructors. We briefly discuss each type of reconstructor and show how it is computed based on poking of actuators in a deformable mirror and subsequently measured by a wavefront sensor. Such a system has recently been used to compute the flat mirror state of a 241 actuator deformable mirror to 36nm rms flatness.

2 PC based adaptive optics

2.1 Adaptive optics components

The required functional components for a PC AO system show below as a top view. It was built to compensate horizontal path turbulence using modal control as will be explained. The major optical and electrical interface subsystems are the wavefront

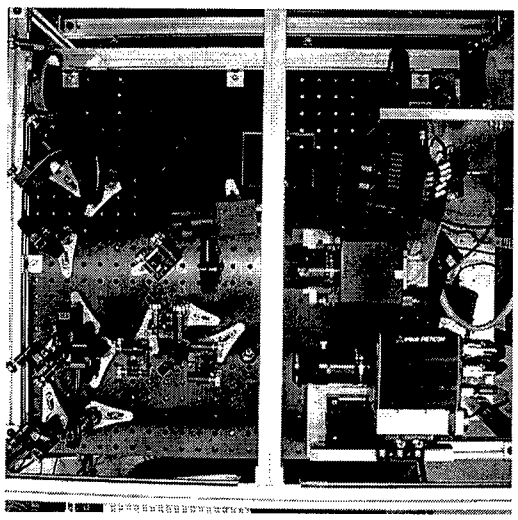

sensor, tip/tilt mirror, deformable mirror, and the coupling optics between the components. The wavefront sensor used is a Shack-Hartmann lenslet array in a hexagonal grid manufactured by AOA. The resulting spot images were recorded by a 128 x 128 pixel format DALSA CA-D1-0128 camera with measured rate of 780 frames per second. The camera output was digitized by a MuTech MV1000 PCI bus frame grabber. The tip/tilt mirror used was model S330.10 built by Polytec PI. Control voltage signals were sent to the amplifier via a Digital to Analog Converter board (DAC) connected through the computer's ISA bus. A Xinetics 37 actuator deformable mirror was used to correct the higher order wavefronts. An ISA interface card and software from Creative Design Solutions was used to send voltage signals to the deformable mirror high voltage electronics chassis where were then amplified and sent to the deformable mirror.

2.2 *Computing environment*

All real time operations were controlled by a Server personal computer (Server). This machine contained all the interface cards described above. Its function was to acquire and process all the data from the wavefront sensor camera, process the data into estimates of wavefront error, and send out correction signals to the tip/tilt mirror and the deformable mirror. A preliminary timing experiment showed that a PC running at 200 MHz CPU clock speed using the DOS operating system was capable of performing all these operations in real-time. It is noteworthy that the entire real time operation was designed to be run using no additional coprocessors or DSP boards, thus a truly inexpensive real-time system wasbe realized.

The Client PC was an IBM compatible 133Mhz Pentium running under the LINUX operating system. The existing data analysis software was written to include the AO calibration and control loop functions using the Tcl/Tk tool kit supplied using WaveLab, AOA's commercially available software data reduction software [2,3]. The Server and Client PC communicate with each other via an Ethernet connection .

2.3 *Wavefront control*

Limited by the number of actuators and the nature of the turbulence, we chose to correct the incident turbulence using modal control [4,5]. The rationale for this choice was as the turbulence would increase, the resulting corrections although suboptimal due to the limited number of actuators could still be significant. We have also had success with this approach in AOA's integration of the ALFA AO system built for the Max-Planck-Institutut für Astronomie, in Heidelberg, Germany [6]. Modal control also provides a flexible way to calibrate the wavefront sensor and to reconfigure wavefront reconstruction for desired correction. A simple mathematical model for modal estimation of wavefront control starts with the relation between the turbulent wavefront in each subaperture, $\vec{\Phi}$, and the measured wavefront gradient, $\vec{g}$ is:

$$\vec{g} = \vec{M}\vec{I}_f\vec{\Phi} \qquad (1)$$

where the matrix $\vec{M}$ denotes the geometric relationship between the positions of the subapertures of the wavefront sensor and the positions of the actuators on the deformable mirror. The matrix $\vec{I}_f$ stands of the spatial influence of each actuator for each of the measured gradients. Further, the wavefront can be modeled as a model decomposition e.g. as a sum of coefficients times each of the Zernike polynomials [7], hence (1) can be rewritten as:

$$\vec{g} = \vec{M}\vec{I}_f\vec{Z}\vec{a} = \left[\vec{M}\vec{I}_f\vec{Z}a_1\vec{M}\vec{I}_f\vec{Z}a_2 \ldots \vec{M}\vec{I}_f\vec{Z}a_k\right] \qquad (2)$$

The numerical values for the matrix product $\vec{M}\vec{I}_f\vec{Z}$ are found during calibration by setting a single mode of the deformable mirror and collecting the respective gradients in all of the subapertures. In this way each column of the matrix is determined, and then combined into one matrix. Because the modes are usually global and observable throughout the entire pupil of the wavefront sensor, this matrix is usually always full rank, with the corresponding reconstructor matrix is given by:

$$\left(\vec{M}\vec{I}_f\vec{Z}\right)^+ = \left[\left(\vec{M}\vec{I}_f\vec{Z}\right)^T\left(\vec{M}\vec{I}_f\vec{Z}\right)\right]^{-1}\left(\vec{M}\vec{I}_f\vec{Z}\right)^T \qquad (3)$$

The superscript T denotes matrix transpose, the -1 superscript a matrix inverse, and the + superscript a generalized inverse. The generalized inverse still exists in the case where there is no matrix inverse but requires special inversion methods such as those using a singular value decomposition [8]. In practice this reconstructor is determined from a time average (2 seconds) of gradients measured from a set of modal 'pokes' on the deformable mirror. Our AO system is tripod mounted can be

subject to frequent small movements which may change the alignment between the subapertures and the DM actuators. Thus an updated reconstructor can be quickly derived when a change in structure is expected. The modes are estimated from the matrix multiplication of the reconstructor with the measurement of wavefront gradient for each frame of data acquired as:

$$\hat{\vec{a}} = \left(\vec{M}\vec{I}_f\vec{Z}\right)^+ \vec{g} \qquad (4)$$

We will generalize on this flexible configuration for wavefront reconstruction in the next section.

2.4 *AO system performance*

We tested the system at field trials along a 1km near ground horizontal path. Shown in the figure below are the average open and closed loop power spectral densities (left) and magnitudes (right) for the average of the first 8 higher order modes (i.e. excluding tip and tilt). The shape of the responses closely match with the control model used [1]. We are still investigating effects of scintillation, and digitization in the wavefront sensing camera on the performance of the control system.

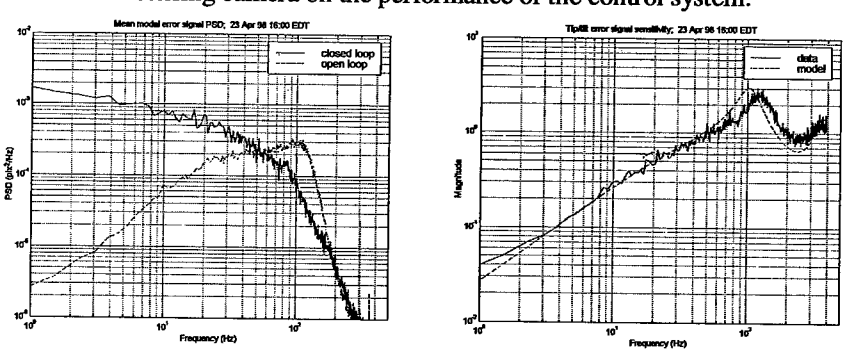

2.5 *Advanced flexible wavefront reconstruction*

The analysis shown in Section 2.3 can be extended using the signular value decomposition (SVD). Using Equation 2, the SVD takes the form:

$$\vec{g} = \vec{M}\vec{I}_f\vec{Z}\vec{a} = \vec{U}\vec{W}\vec{V}^T\vec{a} \qquad (5)$$

where instead of a Zernike polynomial basis, the matrix, V, is the vector of orthnormal modes, and the vector a is still the vecotr of modal weights. Similarly if desired, the zonal reconstructor can be derived by the generalized inverse:

$$\vec{R} = \vec{V}\vec{W}^{-1}\vec{U}^{T} \qquad (6)$$

with the resulting actuator voltages given by:

$$\hat{\vec{a}} = \vec{V}\vec{W}^{-1}\vec{U}^{T}\vec{g} \qquad (7)$$

Such a reconstructor was implemented in another project where it was desired to determine the null position of a 241 actuator deformable mirror. Usually such a project is done via interferometry with the actuators adjusted by hand. However, using the SVD based reconstruction approach, we were able to easily derive a reconstrutor by observing the performance of the mirror by poking each of its actuators and observing the result. With this reconstructor, we iteratively corrected a portion of the residual wavefront error until the resulting error was negligible which in our case corresponds to 36nm rms. This result is verified by the interferograms shown in the figure below. The irregularities in the fringes are due to turbulence in the path.

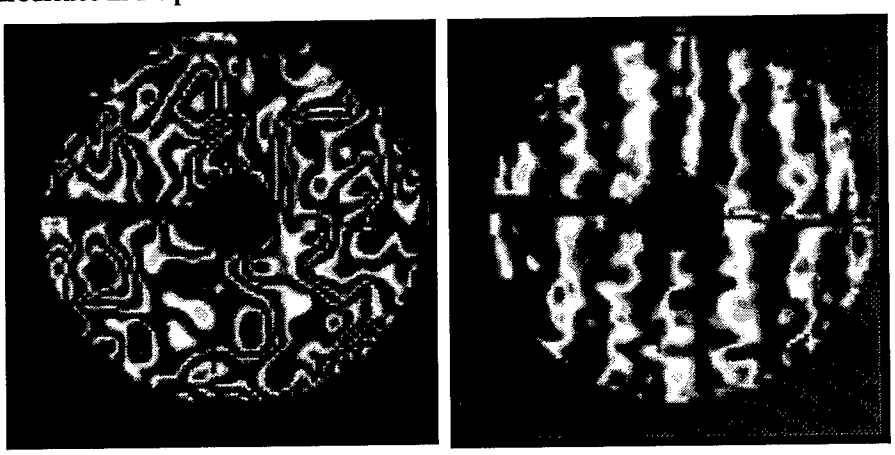

Zero Count State
(Fringes Before Flattening)

UDM Flattened to λ/25 rms
(Measured "Double-Pass")

3 Summary

Flexible wavefront reconstruction has been demonstrated in a PC based AO system used to correct for horizontal path near ground turbulence. These principles have been extended using SVD methods to derive flexible wavefront reconstructors which has been implemented for a mirror flattening procedure for a 241 actuator deformable mirror. Future configurations will be capable of performing real-time wavefront control at 100 actuators or more as well as using these techniques for 10,000 subapertures or more for metrology applications.

Acknowledgements

The authors would like to acknowledge the contributions of Pierre Barbier, David Rush, Penny Polack-Dingels, University of Maryland Laboratory for Physical Sciences, and Douglas Looze, Department of Electrical and Computer Engineering. University of Massachusetts.

References

1. B. Martin Levine, Allan Wirth, Herbert DaSilva, Franklin M. Landers, Stacy Kahalas, and Theresa L. Bruno, Pierre R.Barbier, David W. Rush, Penny Polack-Dingels, and Geoffrey Burdge, and Douglas Looze, 'Active compensation for horizontal line of sight turbulence over near ground paths', Proc. SPIE, v3324, (1998).
2. P. Alexander and L.F. Gladden, 'How to create an X-window interface to GNUplot and FORTRAN programs using the Tcl/Tk toolkit', Computers in Physics, v9, p57-64,(1995).
3. Both Tcl and Tk are freely available in the public domain. for further information, see B.B. Welsh, Practical Programming in Tcl and Tk', Prentice Hall PTR, Upper Saddle River, NJ, (1995).
4. F. Roddier, M Northcott, and J.E. Graves, 'A simple low-order adaptive optics system for near-infrared applications', Publ. Astron. Soc. Pac., v103, 131-149, (1991).
5. J. Anuskiewicz, J.E. Graves, M.J. Northcott, and C. Roddier, 'Adaptive optics at the University of Hawaii I: Current performance at the telescope', Proc. SPIE v2201, (1994).
6. A. Wirth, J. Navetta, D. Looze, S. Hippler, A. Glindemann, and D. Hamilton, "Real-time modal implementation for adaptive optics', Applied Optics, **37**, p4856-4597, (1998).
7. R.J. Noll, 'Zernike polynomials and atmospheric turbulence', J. Opt. Soc. Amer. v66,p207-211, (1976).
8. W.H.Press, B.P. Flannery, S.A. Teukolsky, and W.T. Vetterling, Numerical Recipes, The Art of Scientific Computing, Cambridge University Press, New York, Section 2.9, (1986).

SUB-LENS SPATIAL RESOLUTION SHACK-HARTMANN WAVEFRONT SENSING

JUSTIN D. MANSELL AND ROBERT L. BYER

Edward L. Ginzton Laboratory, Stanford University, USA. jmansell@stanford.edu

Traditionally the spatial resolution of Shack-Hartmann wavefront sensing has been limited by the size of the lenses used in the array. To see features smaller than a lens diameter the wavefront had to be magnified before entering the sensor with a lens or set of lenses. The disadvantage of this technique is that the magnifying lenses then impose their own aberrations and the field of view of the wavefront sensor is reduced. We present a technique for increasing spatial resolution using the hard aperture of the lens to limit the wavefront area being sensed. Diffraction modeling and experimental results using this technique are presented.

1 Introduction

Hartmann wavefront sensing began as a technique for optical metrology[1], but the adoption of the technique by the adaptive optics community changed its primary usage. Recently Hartmann sensors have been developed to address the needs of optical metrology again.[2] Improvements to the Shack-Hartmann wavefront sensor are making it competitive with interferometry for some applications. There are several companies selling Shack-Hartmann wavefront sensors at a fraction of the cost of commercial interferometers. Furthermore, Shack-Hartmann wavefront sensors offer vibration insensitivity and typically higher dynamic range in a single compact package. Even with these attractive features, Shack-Hartmann wavefront sensing, to date, has not been able to reach the spatial resolution of interferometry.

Our goal in this work was to show that the Shack-Hartmann wavefront sensor could be used to measure features smaller than the size of the micro-lenses that comprise the sensor. Our first idea was to do the inverse spatial Fourier transform of the intensity field at the focus of the each of the lenses, but we decided that the lack of intensity field resolution made this prohibitive, so we investigated an alternate technique that we call knife-edge wavefront sensing.

In this paper, we show that small aberrations can be seen by a Hartmann-type test when a special measurement technique is employed. The basic idea is to move the wavefront across the micro-lens array in steps that are a fraction of a micro-lens diameter. The hard edges of the lens aperture, like a knife-edge, adjust the section of the wavefront exposed to each lens. The centroid of the intensity distribution in the far-field is the average tilt seen by the micro-lens aperture.

Although this is the first time very small features have been seen with a Hartmann-type sensor, it is not the first time a Hartman-type sensor has been moved over a wavefront. Ghozeil[3] used a rotating Hartmann screen to test large telescope

optics in 1974. According to his paper, he rotated this screen to extract mirror surface aberrations from the measurement noise and to increase the number of samples on the mirror. This paper presents a study of the motion of the wavefront sensor relative to the wavefront has been used to extract features smaller than the micro-apertures used in the Hartmann test.

2 Theory of Knife-Edge Wavefront Sensing

Each lens in a Shack-Hartmann wavefront sensor measures the tilt seen by that lens by determining the position of the spot at the focus of the lens, typically with a centroid algorithm. This procedure works especially well at determining spatially large aberrations like the low-order Zernike aberrations. If the wavefront has features smaller than the lens, they are effectively averaged out when finding the position of the focal spot and cannot be seen with the Hartmann sensor in its classical implementation.

By moving the sensor a small distance normal to the optical axis (typically a fraction of a lens diameter), the limits over which the average tilt is performed are changed. For the purposes of this paper, the small section of the wavefront which enters the lens aperture after the small step will be called the new region and the section no longer seen by a given lens will be called the old region. The lateral motion of the sensor results in a shift in the centroid if there is a difference in tilt between the new region and the old region. This allows for wavefront features to be viewed that are on the order of the sensor displacement.

In this section we describe knife-edge wavefront sensing using ray optics and Fourier modeling. We use a sinusoidal phase grating as the test wavefront because we know from Fourier theory that any wavefront can be represented as a linear superposition of sinusoids. First we will present a ray optics theory to give the reader an intuitive feel for the sensitivity and spatial resolution of the measurement. We then discuss a modification we made to the aperture shape which is shown to smooth out the sensitivity of the measurement by breaking the resonance with the spatial frequency. Then the results of computer modeling done using Fourier propagation will be presented.

2.1 Ray Optics Theory

A theory of knife-edge wavefront sensing can be derived by applying ray optics. Assume that the wavefront shaped by a perfect two-order blazed grating and that that the lens aperture is designed perfectly for the wavefront such that the number of grating periods distributed over the lens aperture is exactly an integer plus one half. The amount of light in each order can be approximated by the amount of light covering the piece of the grating diffracting it in each direction. Using this knowledge to weight the intensity in the two diffracted orders and applying this to

the centroid formula, the center of this intensity pattern can be determined. To give an intuitive feel for the sensitivity of knife-edge wavefront sensing to a phase grating, we make a further approximations to reduce the centroid shift into a recognized form. Using the paraxial ray approximation ($\sin\theta = \tan\theta = \theta$) and assuming that Λ is much greater than d, the formula for the centroid is given by,

$$\overline{x} = \frac{f\lambda}{d}$$

where f is the focal length of the micro-lens, λ is the wavelength, and d is the diameter of the micro-lens. This formula is recognized as the spot radius of a square lens. The shift in the centroid is actually double this number because as the lens is scanned, the amount of light oscillates between the two diffracted orders. Therefore, the shift in the centroid is exactly the focal spot diameter of a square lens.

The minimum grating period is determined by crosstalk. Light diffracting into the adjacent lens field of view limits the grating period to be approximately given by, that the spot size is small compared to the lens diameter and using the paraxial ray approximation, the maximum grating period is found to be approximately,

$$\Lambda_{\min} = \frac{2f\lambda}{d}$$

which is equal to the square lens spot diameter.

2.2 *Breaking Spatial Frequency Resonance*

There are some wavefronts that will not produce a change in the average tilt though. Consider an integer number of sinusoidal periods. The average tilt induced by this aberration is zero for an averaging window of this size no matter where the start or stop of the averaging is located. Because of this case, a break in the spatial frequency of the lenses had to be created to accommodate viewing sinusoidal aberrations. Slanting two of the edges of the square aperture of typical Shack-Hartmann lenses accomplished this.

2.3 *Fourier Modeling*

Using the approximations presented above, the centroid motion and the minimum resolvable grating period are equal to the focal spot diameter. To verify this, Fourier transform modeling was performed on a variety of lenses and a variety of apertures with respect to spatial wavelength. The focal plane of a lens with a known hard aperture was modeled while moving the wavefront in the x direction in steps of one tenth of a period. The centroid was performed after pixelating the intensity to a 30 by 30 pixel array and digitizing to 8 bits. Then the maximum centroid shift was determined as the wavefront was moved.

Figure 1 shows a result of this modeling with the peak-to valley centroid response plotted against the spatial frequency of the sinusoidal grating. The square aperture lens shows the expected spatial frequency resonances, while the lenses with slanted edges break the spatial frequency enough to flatten out the peak-to-valley centroid shift. The focal spot diameter of this square micro-lens for 633nm light is 4.1 microns. This is approximately a factor of three higher than the focal spot diameter of this micro-lens. The discrepancy between the Fourier modeling and the ray optics theory can be accounted for by the numerous approximations in the theory. The behavior is well predicted by the linear optics theory. Once the appropriate aperture tilt was applied, the response is effectively constant with respect to the spatial wavelength of the diffraction grating.

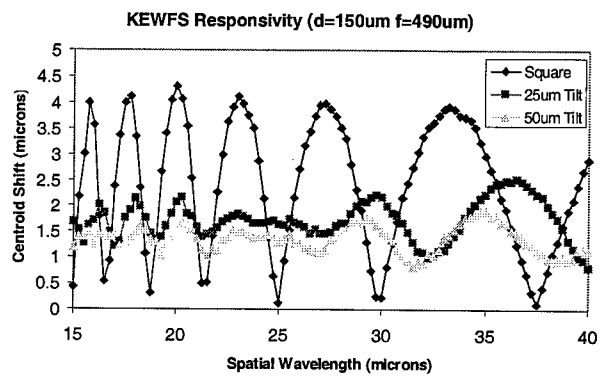

Figure 1 - **Fourier modeling results for knife-edge wavefront sensing for a wavelength of 633nm.**

3 Fabrication of the Lens Arrays

Microlens arrays were fabricated using standard integrated circuit techniques. Circular pillars of photoresist were generated on a glass substrate using photolithography. The photoresist pillars were then exposed to acetone vapor for five minutes in a small crystallizaton dish. The acetone began to dissolve the pillars and they reflowed into lenses. After 10 minutes in a 120 C oven, the wafers were placed for several hours in a plasma etch flowing CF_4 and O_2. The appropriate apertures imposed on the lenses by doing a lift-off of 200nm of aluminum. The apertures were designed to be squares with sides equal to the diameter times the square root of two such that they fit inside the circular lenses. Apertures were designed with no aperture slant, aperture slant on one side, and aperture slant on both sides. The aperture slant for each apertures was one eighth the circular lens diameter.

Several different lens arrays were fabricated. The lens diameters were 150 microns, 200 microns, 250 microns, and 300 microns. The sag on all the lenses

were approximately the same at 12.5 microns. The focal lengths were then calculated to be 0.49 mm, 0.87 mm, 1.36 mm and 1.96 mm respectively.

4 Experimental Results

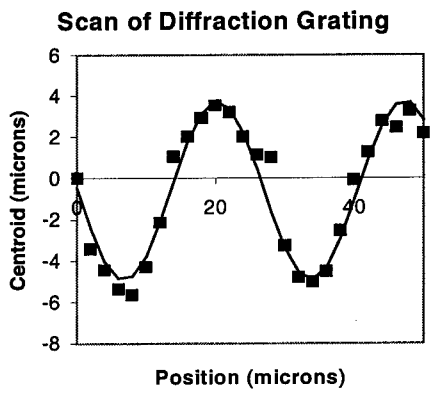

Figure 2 - Scan of a 28-micron period diffraction grating.

Two different test objects were measured using the knife-edge wavefront sensing technique: a 25mm focal length lens array and a 28 micron wavelength diffraction grating. To test the technique,a HeNe laser expanded to a 1cm waist to illuminate a test object. A 50mm focal length 1 inch diameter lens was then used to re-image the optic onto the array of lenses. The focal plane of the lens array was re-imaged onto a CCD array using a 1 inch diameter 75mm focal length lens with about 3.7 magnification. An iris was placed at the focus of the 50mm lens to limit the spatial frequency impinging on the lens array and to avoid stray scattered light causing crosstalk. The test object was placed on a three axis translation stage with motion parallel to the table and normal to the propagation controlled by a micrometer capable of one micron accuracy.

The first object scanned was a phase-only 28 micron period diffraction grating. Adjusting an iris at the focus of the 50mm focal length lens blocked the diffraction beyond the first order. The grating was then measured with the knife-edge wavefront sensing using two-micron step scan and a two-side slanted 150-micron diameter lens array to form the Shack-Hartmann wavefront sensor. The change in the position of the centroid of the focal spots, shown in Figure 2, was measured using the CLAS-2D[4] software by Wavefront Sciences, Inc. Fits to the centroid shift extracted a spatial wavelength of 27 microns, 1 micron different from the profilometer measurement.

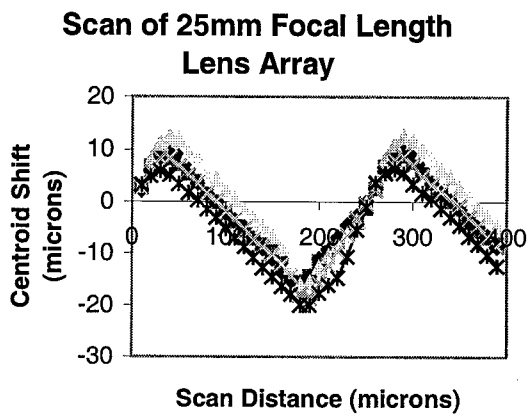

Figure 3 - Scan of a 25mm focal length lens array with a 100 micron diameter 870micron focal length knife-edge wavefront sensor lens array.

The next phase-only element measured with the knife-edge wavefront sensing technique was a lens array provided by Wavefront Sciences. The array was composed of 252micron diameter lenses with a focal length of 25mm. Figure 3 shows the results of knife-edge scanning it across a wavefront sensor comprised of 100micron diameter 870 micron focal length lenses. The portion of the centroid motion corresponding to the scan over the center of the lens was linear. Assuming the lens is exactly parabolic, the slope of the derivative is the reciprical of the wavefront radius of curvature. Fitting this data to a line, the measured lens array focal length was determined to be 23.2 mm. The 7% error is probably due to errors in measuring the distance between the knife-edge lens array and the CCD.

5 Conclusions

We have described and demonstrated a technique called knife-edge wavefront sensing which allows Shack-Hartmann wavefront sensors to resolve features smaller than the size of an individual lens by moving the sensor in small steps across the wavefront. This technique, while impractical for astronomical adaptive optics applications, allows for more spatial resolution for applications like optical metrology and laser beam characterization. The technique, while only demonstrated here in one dimension, is applicable to a two-dimensional scan as well.

6 Acknowledgements

We would like to thank the NSF for funding this research under grant number 2WMF572. We would like to thank Tom Carver, Marty Fejer, and Eric Gustafson for their help.

References

1. Hartmann, J. *Zeitschrift fur Instrumentenkunde*. April 1904. p. 99-117.
2. D.R. Neal, D.J. Armstrong, and W.T. Turner. "Wavefront sensors for control and process monitoring in optics manufacture" SPIE Vol. 2993-29, p. 1-10.
3. Ghozeil, I. "Use of a screen rotation in testing large mirrors." SPIE vol. 44, p. 247-52.
4. CLAS-2D is software written to do Shack-Hartmann Wavefront Sensing by Wavefront Sciences, Inc.

APPLICATION OF SHACK-HARTMANN WAVEFRONT SENSORS TO OPTICAL SYSTEM CALIBRATION AND ALIGNMENT

DANIEL R. NEAL ,

WaveFront Sciences, Inc.; 14810 Central SE; Albuquerque, NM 8712, USA
drneal@wavefrontsciences.com

JUSTIN MANSELL ,

Stanford University; Edward L. Ginzton Laboratory; Stanford, CA 94305, USA
jmansell@stanford.edu

Optical systems are normally aligned by centering the energy distribution in various apertures. However, the use of both irradiance and phase information can in many cases greatly simplify this process, and can provide information for closed-loop alignment and control of an optical system. This can be accomplished by using a Shack-Hartmann wavefront sensor for alignment and performance testing.

While Shack-Hartmann wavefront sensors are commonly used for adaptive optics, they have many other applications. The modern Shack-Hartmann wavefront sensor is compact, rugged, and insensitive to vibration, and has fully integrated data acquisition and analysis. Furthermore, even wavefronts of broad band sources that cannot normally be tested with interferometers can be measured with Shack-Hartmann wavefront sensors. The instrument also provides information about the optical system performance, including peak-to-valley (P-V) wavefront deviation, RMS wavefront error, the modulation transfer function (MTF), and the point spread function (PSF). Since the difference of two wavefronts is easily computed, the effect of individual optical elements on a complex optical system can be examined.

In this paper we will present an alignment methodology using the Shack-Hartmann wavefront sensor to setup even complex optical systems. An example of using the methodology to align a lens is presented. Alignment of the Shack-Hartmann wavefront sensor to a 24-inch telescope at Stanford University is presented. The higher-order static aberrations in the telescope are then measured with the Shack-Hartmann wavefront sensor.

1 Introduction

Alignment of optical systems comprised of even the simplest components can often be a tedious difficult task. It is often difficult to assess the final accuracy of the alignment task, other than overall performance measures of the total system. In many cases it is difficult to tell which element is misaligned, and how to fix it. The application of interferometry to this task is often difficult since this usually requires double-pass testing of the optical system and alignment to the interferometer beam. The use of an interferometer can be especially difficult if the total optical path is long. A shearing interferometer can sometimes be used for optical element positioning; however, complex analysis is required to provide a quantitative

interpretation of the aberrations and it requires the use of fairly narrow bandwidth sources. An autocollimating telescope provides a simple method for aligning an optical system, but, like the shearing interferometer, offers no easy way of extracting performance information. Clearly a means is needed for aligning and calibrating optical systems, especially with broadband sources.

The Shack-Hartmann wavefront sensor was invented in 1971 when Roland Shack modified the Hartmann optical test by substituting an array of lenses for the array of apertures generally used for the test.[1] It was primarily developed in the successive two decades for use in adaptive optics systems, but recently has been commercialized for optical metrology.[2] The commercially available Shack-Hartmann sensor can be built in a compact rigid assembly, which makes it ideal for aligning and testing optical systems. The Shack-Hartmann wavefront sensor (SHWFS), shown in Figure 1, relies on an array of small lenses to create focal spots on a CCD. The motion of the focal spots is dictated by the average gradient of the wavefront over each lens. Thus the grid of focal spots can be used to provide a measure of the wavefront gradients across the entire aperture. These gradients can then be integrated to provide the wavefront of the incident radiation. More detailed documentation is available on the operation of the sensor in various sources[3,4] and will not be discussed here, but for later discussion of the sensor, we will introduce some terms associated with the sensor. The lens array creates a pattern of focal spots on the CCD. The CCD image is broken into subapertures (called Areas Of Interest or AOIs) of N x N pixels (corresponding to the region behind each lens) in which the spot position is determined: The algorithm usually used to determine the position of the focal spots on the CCD is called the first moment or centroiding. The size of the irradiance distribution on the CCD can be characterized by the second moment of the distribution.

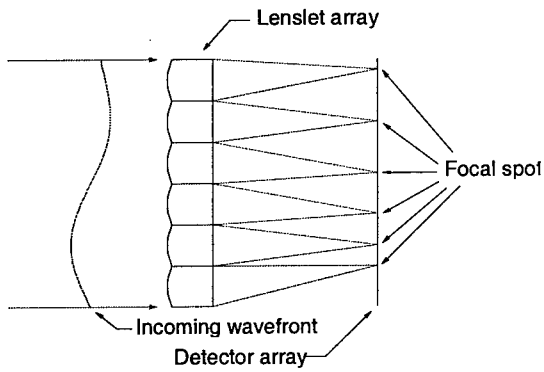

Figure 1 – Basic components of a Shack-Hartmann wavefront sensor.

There are several important advantages to using the Shack-Hartmann wavefront sensor for measuring the wavefront. Unlike many beam diagnostic systems, the instrument requires no moving parts. The incident radiation does not have to be coherent. The instrument provides a measure of both the irradiance and phase distributions of the incident light. The SHWFS acquires all of the information from

a single CCD image, so short exposure times can be used to reduce sensitivity to vibration and pulsed sources may be analyzed and aligned. The processing of the CCD image is straightforward, simple, and may readily be performed on PC computers at high speed. Furthermore, the point-spread-function (PSF)[5], modulation transfer function(MTF), Zernike wavefront decomposition[6], beam quality parameter[7] and other analysis parameters can also be performed. The SHWFS can be configured for a variety of aperture sizes, wavelengths, sensitivities and dynamic ranges. At WaveFront Sciences, Inc., we have integrated the SHWFS with the lenslet array, detector, electronics, data acquisition, control and analysis software into a single package which we call the Complete Light Analysis System (CLAS-2D)[8].

The key advantage of a SHWFS for optical alignment is that it provides a measurement of both irradiance and phase distributions. This information can be displayed in such a way as to make the alignment of optical systems quite easy. The body of this paper will describe the methodology of this process and will present some examples of the application of these methods to various optical systems.

2 Alignment of optical systems

For any optic in a system, there are various degrees of freedom commonly used to align an optical system. These include centering, tilt angle, and optical element rotation. Misalignments in any of these degrees of freedom will result in optical aberrations. Unfortunately, many of these aberrations are highly coupled, so it is difficult to adjust any one degree of freedom without adversely affecting other parameters.

As an example of this, consider the alignment of a simple lens used to collimated a point source. In this case there are five degrees of freedom: x-y centering of the intensity distribution, tip/tilt (or angle of arrival) of the distribution, and focus. However, errors in any of these parameters will result in aberrations that may be highly coupled. For example, de-centering of the lens results in both a translation of the intensity distribution and a tilt of the resulting wavefront. It also introduces an apparent rotation of the lens that can affect the collimation and astigmatism of the wavefront.

One of the convenient features of the CLAS-2D Shack-Hartmann wavefront sensor system is that important parameters for optical alignment are presented in a simple graphical form. A simplified example the graphic interface is shown in Figure 2. In this case, an ellipse represents the irradiance profile. The position of the ellipse represents the position of the centroid of the beam. The size of the ellipse represents the size of the beam on the sensor. The major and minor axes of the ellipse can also easily be calculated by computing the cross moment. The average tilt is shown as a vector whose center is the center of the ellipse, its end-point represented by the average tilt. An arbitrary scale factor is applied to the average tilt since it has different units in general from the position information.

These few parameters can be acquired, computed and displayed extremely fast. 5–10 Hz is routinely achievable, even for high-resolution sensors and slow computers. This allows adjustment of optical components in the optical train with near real-time feedback. This greatly speeds up the alignment process and makes possible an automatic alignment.

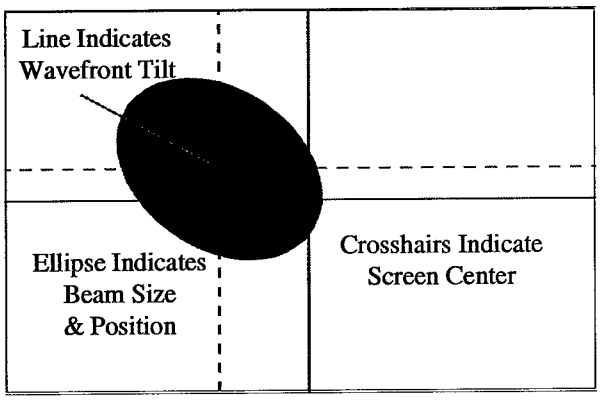

Figure 2 – Simple graphical representation of average tilt, beam position, and beam size, and beam ellipticity.

There is one drawback to the above representation. It is difficult for the user to tell from this display when the wavefront aberration has exceeded the dynamic range of the instrument. Usually the dynamic range is defined as the range of input angles for each AOI where the focal spot remains completely behind one lens. There are AOI tracking methods that may be applied to improve the dynamic range, but these are not usually applied to the initial alignment step. While this drawback may seem limiting, in practice it is fairly easy to identify and overcome. Adding sufficient tilt to exceed the dynamic range causes rapid, wild swings of the tilt vector.

We have found that the following sequence of steps is useful for achieving optical alignment with the SHWFS:

1. Position apertures or otherwise define the optical axis.
2. Position the SHWFS as the last element in the optical train. Align the sensor to be accurately centered (minimize (x,y)), and oriented orthogonal to the optical axis (minimize θ_x,θ_y).
3. Insert optical elements one at a time. Align each element to re-center the irradiance distribution and minimize the average tip/tilt.
4. Collimate the system as required by minimizing the RMS or P-V wavefront error. This requires the use of the full wavefront produced by the SHWFS.
5. Optimal element rotation can be achieved by adjusting the rotation iteratively, while assuring that the centering and tilt are maintained.

Note that this sequence has been described for multi-lens telescopes, where the final leg is designed for a collimated space. Where this assumption is invalid, it may be

necessary to use a recollimating lens. By pre-recording the appropriate reference, aberrations in this lens may be subtracted.

Step 5 in the above list relies on an additional property of real optics. Consider the case of a doublet that is significantly rotated, as shown in Figure 3. In this case, numerous aberrations are introduced. The chief aberrations are astigmatism and defocus, although tilt, coma, spherical aberration and other terms may be present. However, if the initial irradiance distribution was centered on the SHWFS before inserting the lens, this position records accurately the average values. All of the

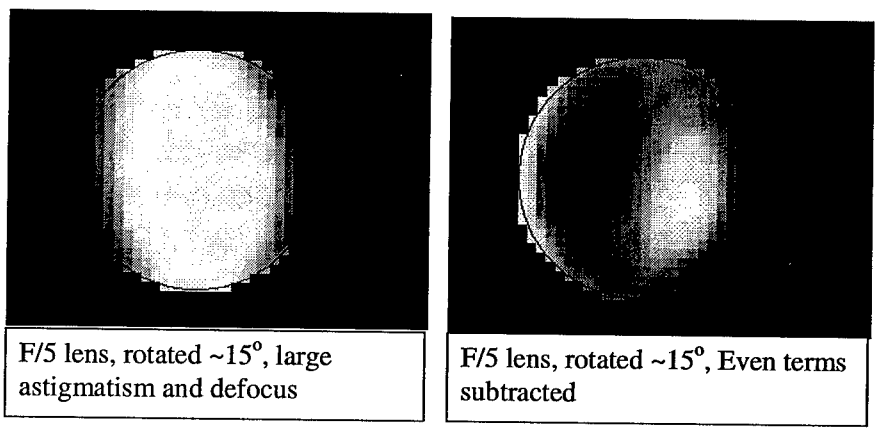

Figure 3 – Aberrations for an F/5 lens rotated 15°. Note that the odd terms will results in a net average tilt.

even terms will be exactly symmetric (by definition) about this location. Hence they will have an average net tip/tilt contribution of zero. Only the odd terms will have a value. The presence the coma term, however, is small for simply decentered lenses, and is only significant when the lens has rotation. Thus it is possible to identify the condition (i.e. decouple the degrees of freedom) where the lens has minimum rotation and is accurately centered. This will result in a well-centered intensity distribution and minimum tip/tilt. Any other condition (decentered plus compensating rotation) will not allow both conditions to be simultaneously met. The experimenter may align the lens by adjusting the rotation in small steps, recentering the irradiance distribution between each one. When both the minimum tip/tilt and centration have been achieved, the optic is correctly aligned.

Once the optical system has been aligned, the SHWFS can also be used to measure the residual higher-order aberrations. Many different analysis functions can be performed, including Zernike decomposition, fringe display, point spread function

and modulation transfer function. An example of using the wavefront sensor to characterize an existing optical system is presented in the following section.

3 Alignment and measurement of a 24" telescope

As an example of this process, this section presents the results of aligning and measuring the performance of a 24 inch diameter Cassegrain telescope at Stanford University. In this case, the SHWFS was mounted directly on the telescope with the addition of a single 50mm collimating lens. The SHWFS used was comparable in weight to the eyepieces used by the telescope, so did not appreciably affect the balance or weight load on the telescope. The process described above was used to align the system with a bright star (Arcturus) as a reference. Since this telescope operates almost at sea level, there was a significant amount of turbulence present during this process. Nevertheless, it was a straightforward matter to install, align and collimate the collimating lens and the wavefront sensor. Once installed, the sensor was used to record many images of different stars. Since the version of this sensor was not designed especially for low-light conditions, only a few bright stars were examined.

After the basic alignment was achieved, the telescope was characterized using the SHWFS. A plane-wave reference was pre-recorded in the laboratory using a well-collimated HeNe laser beam. Since we were interested in evaluating the telescope and not the atmospheric turbulence, 30 frames were taken at 1-second intervals and the images were averaged together. By comparing the plane-wave reference and the averaged image data, a measure of the telescope optics were made. Figure 4 shows one such measurement. Another measurement was preformed after rotating the SHWFS and the lens by 90 degrees to make sure that the aberrations measured were indeed in the telescope and not in the wavefront sensor or the collimating lens. The two measurements were almost identical.

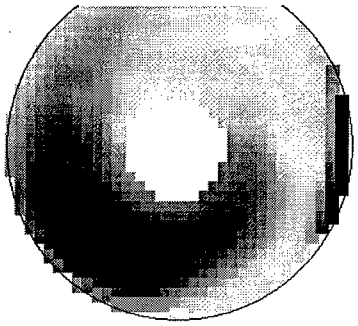

Figure 4 – Average aberrations of the 24-inch telescope. The P-V wavefront error is 3.6λ. The wavefront was computed using a plane wave reference.

4 Conclusions

In this paper we have argued that the Shack-Hartmann wavefront sensor is a good choice for measuring the alignment of optics because of its vibration insensitivity, broadband light performance, and ease of use. We introduced an iterative method for using the sensor to quickly achieve good alignment of an optic. We used this method to test a doublet in the laboratory and to align the Shack-Hartmann

wavefront sensor to a 24" telescope at Stanford Univeristy. Once properly aligned, we used the Shack-Hartmann wavefront sensor to determine the higher-order aberrations in the telescope. The Shack-Hartmann wavefront sensor determined to be a valuable tool for characterizing the alignment of optical elements and the performance of even a complex optical system.

5 Acknowledgements

Special thanks go to Helen Kung who provided assistance with the telescope measurements and the data analysis.

References

1. R.B. Shack and B.C. Platt,. "Production and use of a lenticular Hartmann screen.". J.Opt. Soc. Am. Vol. 61, p. 656. (1971)
2. CLAS-2D by Wavefront Sciences, Inc.
3. Masud Mansuripur. "The Shack-Hartmann Wavefront Sensor". Optics & Photonics News, April 1999. p. 48-51.
4. Daniel Malacara. Optical Shop Testing. Wiley, 1992. pp. 367-97.
5. D.R. Neal et al. "Shack-Hartmann Wavefornt Sensor Testing of Aero-optic Phenomena" American Institute of Aeronautics and Astronautics, 98-2701.
6. D.R. Neal, D.J. Armstrong, and W.T. Turner. "Wavefront sensors for control and process monitoring in optics manufacture". SPIE Vol. 2993-29. (1997).
7. D. R. Neal, W. J. Alford, and J. K. Gruetzner, "Amplitude and phase beam characterization using a two-dimensional wavefront sensor," SPIE Vol. **2870**, pp. 72–82 (1996).
8. CLAS-2D is available from WaveFront Sciences, Inc., 14810 Central S.E., Albuquerque, NM 87123.

ANALYSIS OF WAVEFRONT SENSING USING A COMMON PATH INTERFEROMETER ARCHITECTURE

JESPER GLÜCKSTAD AND PAUL C. MOGENSEN
Optics and Fluid Dynamics Department, Risø National Laboratory
DK-4000 Roskilde, Denmark
Email: jesper.gluckstad@risoe.dk

A common path interferometer (CPI) provides an attractive wavefront sensing scheme due to its inherent simplicity and robustness. The working principle is, that a part of the incoming wavefront is extracted and perturbed to generate a so-called synthetic reference beam for interference with the remainder of the wavefront. Many different CPI schemes have been proposed and independently analysed. We have developed a new general approach that can be applied to CPI analysis, which simplifies the treatment and understanding of the operation of the majority of CPIs that utilise spatial frequency filtering.

1 Introduction

Imaging and visualising phase objects, wavefront disturbances or aberrations has always been a subject of considerable interest in optics. One of the best known techniques is Zernike's phase contrast method [1] for which he received the 1953 Nobel Prize. The Zernike method assumes that the phase object or phase disturbance is limited to the so-called small scale phase approximation where a Taylor expansion to first order is sufficient for a mathematical description:

$$\exp(i\phi(x,y)) \approx 1 + i\phi(x,y) \tag{1}$$

The light corresponding to the two terms in this Zernike small scale phase approximation can be separated spatially by use of a Fourier transforming lens with the phase distribution located in the front focal plane of the lens and the spatial Fourier transformation generated in the back focal plane. In this first order approximation the constant term represents the amplitude of on-axis focused light and the second spatially varying term represents off-axis or scattered light in the back focal plane. Zernike realised that by using a small quarter wave phase shifting plate acting on the focused light it becomes possible to obtain a linear visualization of small phase structures by generating interference between the two phase quadrature terms in Eq. (1).:

$$I(x',y') \approx 1 + 2\phi(x',y') \tag{2}$$

In general we cannot assume that a series expansion to first order as in the Zernike approximation is a sufficient representation of a given phase perturbation. Higher order terms in the expansion:

$$\exp(i\phi(x,y)) = 1 + i\phi(x,y) - \phi^2(x,y) - i\phi^3(x,y) + \phi^4(x,y) + \ldots \tag{3}$$

need to be taken into account for phase perturbations breaking the small phase approximation. At first glance it may be surprising that spatially varying terms in Eq. (3) also can contribute (sometimes even significantly) to the strength of the on-axis focused light. There are however many examples in the literature where it is inherently and incorrectly assumed that only the first term in the Taylor series expansion contributes to the strength of the focused light [2-8]. The Fourier analysis approach taken in this paper includes the effect of all the terms in Eq. (3).

An equally important issue to consider when analysing the effect of spatial filtering on the light diffracted by phase perturbations is to define spatially what is meant respectively by the focused and the scattered light. In the previous description of Zernike phase contrast it was inherently assumed that the focused light is spatially confined to an unphysical delta function. As we know, any aperture truncation will inevitably lead to a corresponding spatial broadening of the focused light. Therefore it is very important that we explicitly define what is meant by "focused light" and "scattered light" before a precise spatial filtering operation can be applied. In this context it is necessary to look more carefully at the sequence of apertures confining the light wave propagation through the optical setup.

2 Generic model

A commonly applied architecture that provides an efficient platform for spatial filtering is illustrated in Fig. 1 and is based on the so-called *4-f* lens filtering configuration.

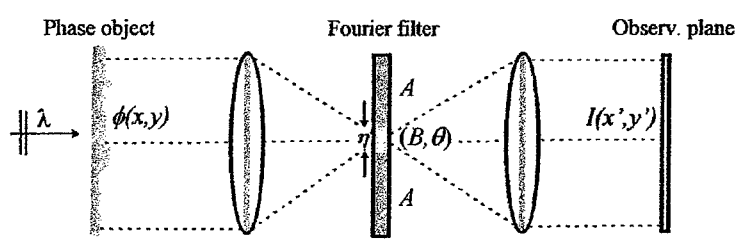

Fig. 1: Phase disturbance modeled as an aperture truncated phase object. Filter parameters are given by (A, B, θ) and η indicates the fraction of filter radius measured to the radius of the diffracted airy disk from a circular input object aperture.

An output interferogram of an unknown phase object or phase disturbance is obtained by applying a spatially circular truncated on-axis centered filtering operation in the spatial frequency domain between two Fourier transforming lenses. The first lens performs a spatial Fourier transform so that direct propagated light is focused onto this on-axis centered filtering region whereas spatially varying object information generates light scattered to locations outside this central region. Applying different phase and amplitude parameters, (A, B, θ), for the two filtering regions we can obtain

an interference pattern at the detector plane by use of the second Fourier lens. Effectively, the focused and filtered on-axis light acts as a synthetic reference beam for the scattered light thereby implementing a mechanically robust common path like interferometer. We will show later that depending on the choice of filtering parameters and radius of the on-axis centered filtering region, several interferometer schemes can be implemented by this *4-f* lens filtering configuration, i.e. phase contrast, dark central ground, point diffraction and field-absorption filtering.

3 Mathematics

Assuming a circular input aperture with radius, Δr, truncating the phase disturbance modulated onto a collimated, unit amplitude, monochromatic field of wavelength, λ, we can write for the incoming light amplitude:

$$a(x,y) = \mathrm{circ}(r/\Delta r)\exp(i\phi(x,y)) \tag{4}$$

at the entrance plane of the setup shown in Fig. 1.

Similarly, we assume a circular on-axis centered spatial filter of the form:

$$H(f_x,f_y) = A\left(1+\left(BA^{-1}\exp(i\theta)-1\right)\mathrm{circ}(f_r/\Delta f_r)\right) \tag{5}$$

where $B \in [0;1]$ is the chosen filter absorption of the focused light, $\theta \in [0;2\pi]$ is the applied phase shift to the focused light and $A \in [0;1]$ is a filter parameter describing field absorption for off-axis scattered light as indicated in Fig. 1. The spatial frequency coordinates are related to spatial coordinates in the filter plane as: $(f_x,f_y) = (\lambda f)^{-1}(x_f,y_f)$ and $f_r = \sqrt{f_x^2+f_y^2}$.

Performing an optical Fourier transform of the input field from Eq. (4) followed by a multiplication with the filter parameters in Eq. (5) and performing a second optical Fourier transform (corresponding to an inverse Fourier transform with inverted coordinates) we can obtain an expression for the intensity describing the interferogram at the image plane of the *4-f* setup:

$$I(x',y') = A^2\left|\exp(i\tilde{\phi}(x',y'))\mathrm{circ}(r'/\Delta r) + |\bar{\alpha}|\left(BA^{-1}\exp(i\theta)-1\right)g(r')\right|^2 \tag{6}$$

where

$$\begin{cases} \bar{\alpha} = \left(\pi(\Delta r)^2\right)^{-1}\iint\limits_{\pi(\Delta r)^2}\exp(i\phi(x,y))dxdy = |\bar{\alpha}|\exp(i\phi_{\bar{\alpha}}) \\ \tilde{\phi}(x',y') = \phi(x',y') - \phi_{\bar{\alpha}} \end{cases} \tag{7}$$

The generally complex and object dependent term, $\overline{\alpha}$, corresponding to the amplitude of the focused light clearly plays a significant role in the expression for the interference pattern described by Eq. (6). Referring to the discussion in the introduction we are now able to confirm that the frequently applied assumption that the amplitude of the focused light is approximately equal to the first term of the Taylor expansion in Eq. (1) generally results in misleading interpretations of the generated interferograms.

Of similar importance in the analysis of Eq. (6) is the term $g(r')$ describing the spatial profile of a so-called "synthetic reference wave" diffracted from the aperture of the on-axis centered filtering region. It is essentially the interference between this term, carrying all the information about the filtering parameters, and the imaged phase object that eventually generates an interferogram. To obtain an accurate description for the synthetic reference wave and thereby an accurate derivation for Eq. (6) the zero-order Hankel Transform followed by a series expansion in the spatial dimension, r', greatly simplifies the analysis. Despite the relative simplicity of this approach it has not previously been reported in the literature to the knowledge of the authors [9].

Having a circular input aperture with radius, Δr, and a filter-dot radius measured in the spatial frequency component, Δf_r, we can obtain the following expression for the "synthetic reference wave" $g(r')$ by use of the zero-order Hankel Transform:

$$g(r') = 2\pi\Delta r \int_0^{\Delta f_r} J_1(2\pi\Delta r f_r) J_0(2\pi r f_r) df_r \tag{8}$$

Using the substitution:

$$\eta = (0.61)^{-1} \Delta r \Delta f_r \tag{9}$$

where η is a factor describing the fraction of filter radius measured to the radius of the mainlobe of the Airy function shaped diffracted light from the circular input aperture (see Fig. 1) we finally obtain the following series expansion of Eq. (8):

$$\begin{aligned} g(r') = 1 - J_0(1.22\pi\cdot\eta) - \left[(0.61\pi\cdot\eta)^2 J_2(1.22\pi\cdot\eta)\right](r'/\Delta r)^2 + \\ \left[(0.61\pi\cdot\eta)^3 / 4\{2J_3(1.22\pi\cdot\eta) - 0.61\pi\cdot\eta\cdot J_4(1.22\pi\cdot\eta)\}\right](r'/\Delta r)^4 .... \end{aligned} \tag{10}$$

expressed in radial coordinates normalized to the radius of the imaged input aperture (with scaling factor included in case of magnification different from unity).

For the curvature of $g(r')$ to be kept small over a sufficiently large spatial region centered around $r'=0$, η should be chosen so that $g(r') \leq 1$, corresponding to the

first zero-crossing of the Bessel function, $J_0(1.22\pi\cdot\eta)$ where $\eta \cong 0.62$. Moreover, it is very important to keep η to the smallest possible value in order to make sure that the scattered object light is not propagated through the zero-order filtering region. Finding a minimum applicable η-value is less apparent, but obviously choosing a very small value will reduce the strength of the synthetic reference wave to an unacceptable low level compromising the fringe visibility in the interference with the diffracted light. In short, we have demonstrated the importance of including the influence of η and being aware that the choice of η can have a significant impact on the resulting interferometric performance (of equal importance to the choice of the filtering parameters A, B and θ). Depending on the accuracy needed for the description of the generated interferograms one can choose to include a number of spatial higher order terms from the expansion in Eq. (10). Clearly, the influence of the higher order terms has the largest impact along the boundaries of the imaged input aperture. For η-values smaller than 0.62 and operating within the central region of the image plane, spatial higher order terms are insignificant and we can approximate the synthetic reference wave with the first and space invariant term in Eq. (10):

$$g(r' \in central\ region) \approx 1 - J_0(1.22\pi\cdot\eta) \tag{11}$$

so that we can simplify Eq. (6) as:

$$I(x',y') \cong A^2\left|\exp\left(i\tilde{\phi}(x',y')\right) + K\left|\overline{\alpha}\right|\left(BA^{-1}\exp(i\theta) - 1\right)\right|^2 \tag{12}$$

where $K = 1 - J_0(1.22\pi\cdot\eta)$. The influence of the finite on-axis filtering radius on the focused light is hereby effectively reduced to act as an extra filtering parameter so that the four-parameter filter set $(A, B, \theta, K(\eta))$ together with the complex object dependent term, $\overline{\alpha}$, effectively defines the type of filtering scheme we are applying.

Some examples are given below:

- Zernike phase contrast filtering: $\left(A = 1, B \cong 0.1, \theta = \pm\pi/2, K \cong 1, \overline{\alpha} \cong 1\right)$, Ref. [1].
- Generalised phase contrast: $(A = B = 1, \theta = 2\sin^{-1}(|\overline{\alpha}|^{-1}/2), K \cong 1)$, Refs. [10,11].
- Dark central ground filtering: $\left(A = 1, B = \theta = 0, K \cong 1, \overline{\alpha} \neq 0\right)$, Ref. [4].
- Field-absorption filtering: $\left(A < 1, B = 1, \theta = 0, K \cong 1, \overline{\alpha} \neq 0\right)$, Ref. [12].
- Point diffraction interferometry: $\left(A \neq B, \theta = 0, K < 1, \overline{\alpha} \neq 0\right)$, Ref. [13].
- Phase-shifting point diffraction: $\left(A = B = 1, \theta \neq 0, K < 1, \overline{\alpha} \neq 0\right)$, Ref. [14].

The visibility and irradiance of the interferograms described by Eq. (12) can be optimized in many ways. Using a pure phase filtering approach, a greater than 90% energy efficient phase-intensity conversion can be achieved as was experimentally demonstrated in Refs. [10,11]. To have complete control over the visibility and the irradiance it is generally advantageous to apply amplitude filtering parameters other than unity. This optimisation process can be facilitated by the use of a recently demonstrated graphical method originally proposed in Ref. [15].

ACKNOWLEDGMENTS
This work is supported by the Danish Technical Scientific Research Council.

REFERENCES

1. F. Zernike, How I discovered phase contrast, Science **121** (1955) pp. 345-349.
2. H. H. Hopkins, " A note on the theory of phase-contrast images", Proc. Phys. Soc. B., **66**, (1953) pp. 331-333.
3. S. F. Paul, "Dark-ground illumination as a quantitative diagnostic for plasma density", Appl. Opt., **21**, 14, (1982) pp. 2531-2537.
4. R. C. Anderson and S. Lewis, "Flow visualization by dark central ground interferometry", Appl. Opt., **24**, 22, (1985) p. 3687.
5. M. P. Loomis, M. Holt, G. T. Chapman and M. Coon, Applications of dark central ground interferometry, Proc. of the 29th Aerospace Sciences Meeting, AIAA **91-0565**, (1991) pp. 1-8.
6. C. A. Mack, Phase contrast lithography, Proc. SPIE, **1927**, (1993) pp. 512-520.
7. Y. Arieli, N. Eisenberg and A. Lewis, Pattern generation by inverse phase contrast, Opt. Comm. **138,** (1997) pp. 284-286.
8. J. Glückstad, Pattern generation by inverse phase contrast – comment, Opt. Comm. **147**, (1998) pp. 16-19.
9. J. Glückstad, Image decrypting common path interferometer, Proc. SPIE, **3715** (1999) pp. 152-159.
10. J. Glückstad, Phase contrast image synthesis, Opt. Comm. **130**, (1996) pp. 225-230.
11. J. Glückstad, L. Lading, H. Toyoda and T. Hara, Lossless light projection, Optics Letters **22**, (1997) pp. 1373-1375.
12. C. S. Anderson, Fringe visibility, irradiance, and accuracy in common path interferometers for visualization of phase disturbances, Appl. Opt. **34** (1995) pp. 7474-7485.
13. R. N. Smartt, W. H. Steel, Theory and application of point-diffraction interferometers, Japan J. Appl. Phys. **14**, (1975) pp. 351-356.
14. C. R. Mercer, K. Creath, Liquid-crystal point-diffraction interferometer, Opt. Lett. **19**, 12, (1994) pp. 916-918.
15. J. Glückstad, Graphic method for analyzing common path interferomters, Appl. Opt. **37**, 34, (1998) pp. 8151-8152.

AN ALL OPTICAL WAVEFRONT SENSOR FOR UV LASER APPLICATIONS

SERGIO R. RESTAINO

USAF Research Laboratory, 3550 Aberdeen SE, Kirtland AFB, NM 87117 USA
E-mail: restaino@plk.af.mil

AARON C. BERNESTEIN

The University of New Mexico, Dept. of Physics and Astronomy, 800 Yale Albuquerque NM 87115 USA

Wavefront sensing for adaptive optics applications is nowadays a routine technique based primarily on two schemes: the Shack-Hartmann (SH) and the Curvature Sensing/Phase Diversity (PD) . While both these schemes are well suited for applications of ground-based observations of exo-atmospheric objects, this is not necessarily true for other type of applications. For laser with very short pulse duration the bandwidth problem associated with conventional wavefront sensing is a serious short coming. In this framework our group started the a program of investigation for an all optical wavefront sensor based on moiré techniques.

1 Introduction

Several applications of UV high power lasers need a better wavefront that avoids problems of self-focusing, or where the focal spot is too poor to concentrate a meaningful amount of energy for optimal industrial and military applications. We have considered applications of both a modified SH and PD techniques. In both cases serious problem arose before laboratory tests could be started. In both cases the main drawback was the temporal bandwidth of the sensor. Other considerations were the availability of good, inexpensive optics at the operating wavelength. Next we looked at a modified version of the basic moiré deflectometry (MD) with the intent of making this technique an all optical sensor. Moiré deflectometry is a well known and established technique to measure the contours of three-dimensional objects and a variety of other characteristics. The basic optical component is a Ronchi grating. Such gratings are inexpensive and readily available in fused silica as off-the-shelf items.

In the second section of this paper we will give a brief description of moiré deflectometry. The intuitive description of the sensor is given in the third section. In the fourth section we present some basic analysis. Finally some experimental results will be presented in the last section.

2 Moiré deflectometry

Moiré' interferometry can be regarded as a form of holographic interferometry. Although moiré' techniques have been used for many years, only in the past couple of decades has the full potential of moiré' interferometry been realized, see for example [1]. The basic set-up for moiré' deflectometry is shown in Fig.1

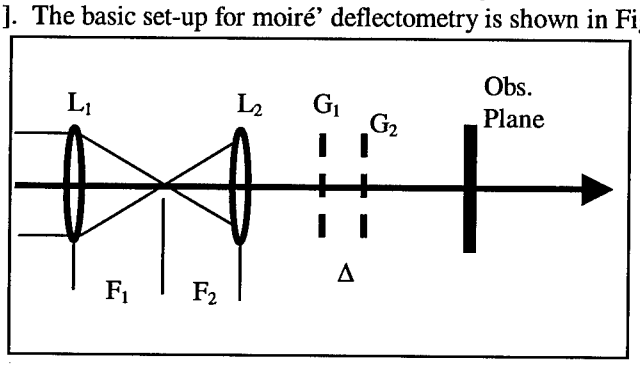

Figure 1: Set-up for MD

In all that follows we assume one-dimensional Ronchi grating generating one-dimensional fringe patterns. The analysis of the one-dimensional case will not lose generality and the extension to the two dimensional case is straightforward The two gratings, G_1 and G_2, are at a distance Δ from each other and rotate of an angle θ as shown in Fig. 2. With this arrangement on the observation plane one will obtain a series of fringes.

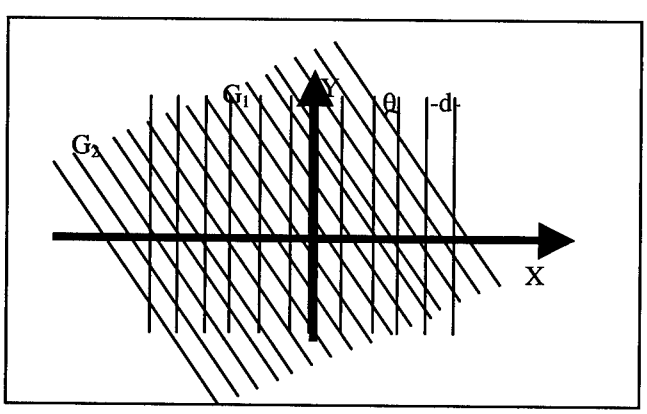

Figure 2: Geometry of the moiré' interferometry

With this type of set-up, and assuming that the wave-field with aberrations is described by

$$u(x,y) = \exp\left[i\frac{2\pi}{\lambda}\varphi(x,y) \right]$$

Where $\varphi(x,y)$ is the aberration function. If we assume that the grating G_1 lays perpendicularly to the x axis, then we can write the transmission coefficient of G_1, expressed as a Fourier series, as

$$t_1(x,y) = \sum_n C_n \exp(i2\pi\xi_n x)$$

Where $\xi_n = n/d$ and C_n are the Fourier coefficients. For a Ronchi grating only the first three coefficients of the expansion are significant. Furthermore, we the assumption that G_1 is symmetrical about the y axis ($C_1 = C_{-1}$) and assuming that the grating is sinusoidal, i.e. $C_0 = 1$ and $C_1 = C_{-1} = 1/2$, the intensity impinging on G_2 will be

$$\begin{aligned} I_{G2}(x,y) = \frac{3}{2} + \frac{1}{2}\cos\left\{ \frac{2\pi}{\lambda}\left[\frac{\lambda^2}{2d^2}\Delta - \frac{\lambda}{d}x + \varphi(x,y) - \varphi(x - \frac{\lambda\Delta}{d}, y) \right] \right\} + \\ + \frac{1}{2}\cos\left\{ \frac{2\pi}{\lambda}\left[-\frac{\lambda^2}{2d^2}\Delta - \frac{\lambda}{d}x + \varphi(x + \frac{\lambda\Delta}{d}, y) - \varphi(x,y) \right] \right\} + \\ + \frac{1}{2}\cos\left\{ \frac{2\pi}{\lambda}\left[-2\frac{\lambda}{d}x + \varphi(x + \frac{\lambda\Delta}{d}, y) - \varphi(x - \frac{\lambda\Delta}{d}, y) \right] \right\} \end{aligned}$$

Under the condition that $\lambda\Delta/d$ is smaller than unity, we can expand $\varphi(x,y)$ in Taylor-series, and take only the first three terms. Let the grating G_2 be sinusoidal too and the angle between G_2 and y axis be θ, the transmission function of the grating is

$$t_2(x,y) = 1 + \cos 2\pi \frac{x\cos\theta + y\sin\theta}{d}$$

Finally we can write the intensity after the grating G_2 as

$$I_2^+(x,y)=\cos\left\{2\pi\left[-\frac{\partial^2\varphi}{\partial x^2}\frac{\lambda\Delta^2}{2d^2}+\frac{\lambda\Delta}{2d^2}\right]\right\}\cos\left\{2\pi\left[-\frac{\partial\varphi}{\partial x}\frac{\Delta}{d}+\frac{x(1-\cos\theta)-y\sin\theta}{d}\right]\right\}+B$$

Where the term B includes constant terms and other terms that vary faster than the grating and that can be regarded as background. If we set the first cosine term equal to μ we can obtain the equation for the moiré' fringes

$$y=\frac{1-\cos\theta}{\sin\theta}x-\frac{\partial\varphi}{\partial x}\frac{\Delta}{\sin\theta}-\frac{Md}{\sin\theta}-\begin{cases}0(\mu>0)\\ \dfrac{d}{2\sin\theta}(\mu<0)\end{cases}M=0,\pm1,\pm2,\ldots$$

If we set φ=0, then the moiré' pattern is a set of parallel fringes, whose period in the y direction is

$$D=\frac{d}{\sin\theta}$$

In the presence of aberration the local shift of moiré' fringes in the y direction is

$$h=\frac{\partial\varphi}{\partial x}\frac{\Delta}{\sin\theta}$$

This shows that the measurement of the fringe displacement is directly proportional to the gradient of the aberration function. From the last two expressions, if we define the sensitivity as the number of shifted fringes, i.e. $s=h/D$ we can readily see that the sensitivity can be tuned by adjusting the distance Δ between the gratings and the period d of the gratings.

3 The Spatial filter

The use of MD by itself however, does not solve the problem of temporal bandwidth. In normal operations one has to acquire the fringes and process them. Usually this is done by using a CCD camera and a digital computer. Our basic idea consists of using a lens to produce the Fourier transform of the fringe pattern. The Fourier transform is then passed through a spatial filter that has a gradient of transmission such that can attenuate or enhance specific areas of the power spectrum of the fringes. At this point another lens form an intensity distribution on a CCD camera. This last intensity distribution is directly proportional to the gradient of the wavefront that we want to measure. A schematic of the optical layout is shown in Fig. 3. The gradient transmission spatial filter is a slit with a triangular transmission profile as shown in Fig.4

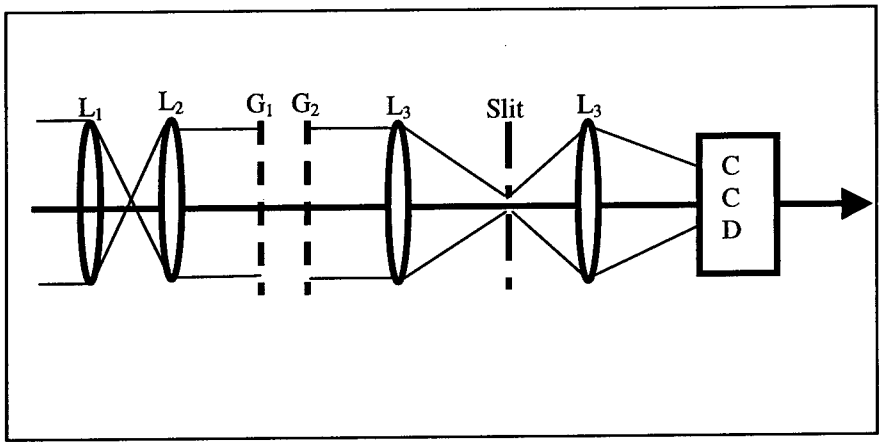

Figure 3. Schematic of the experimental set-up

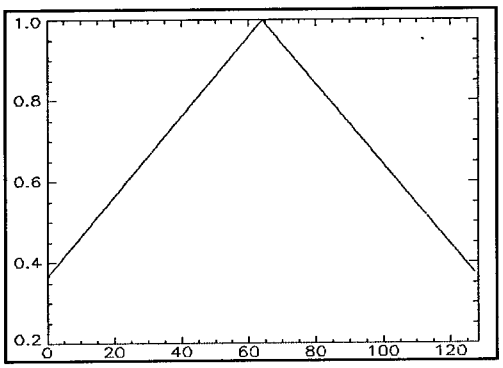

Figure 4: cross-cut of the transmission gradient slit

From the discussion in the previous section we can see that the Fourier transform of the fringe pattern is proportional to the Fourier transform of the wavefront function.

$$\Im(y) \;= \alpha - \beta\left|\Im(\varphi)\right| - \gamma$$

Where α, β and γ constants. The transmission profile of the slit in one-dimension is of the form

$$\Lambda(x) = \begin{cases} 1-|x| & |x| \leq 1 \\ 0 & otherwise \end{cases}$$

The intensity pattern after the second lens will be

$$I_{CCD} = \alpha \sin c^2 \xi - \frac{\partial \varphi}{\partial \xi} * \sin c^2 \xi - \gamma \sin c^2 \xi$$

Where * indicates a convolution. By choosing in an appropriate way the size of the slit and positioning it appropriately in the focal plane of lens L_3 one can obtain a modulation of intensity that is directly proportional to the gradient of the wavefront. By calibrating the sensor one can eliminate the unwanted terms.

4 Experimental results

Some preliminary experimental results were carried out. We used a one dimensional set up, i.e. two Ronchi gratings with a one dimensional slit with a transmission

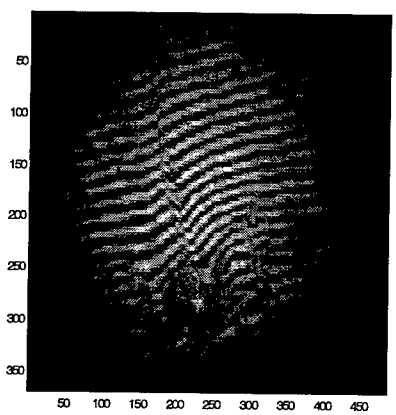

Figure 5: Moiré fringes in presence of aberrator

profile identical to the one shown in Fig. 4. Fig. 5 shows the moiré interferogram in the presence of an aberrator. In Fig. 7 is shown the intensity pattern after the spatial filter and the re-imaging lens. The two most distinctive characteristics of our aberrator, a plastic cover case, are a prominent 'hill' shape feature in the bottom part and a 'streak' running from the hill up. Both these features are 'visible' in the fringe pattern in Fig. 5. However, especially around the bright spot, a standard fringe analysis tool will have severe problems. The intensity encoding of the aberration, as shown in Fig. 6, offers an easier way not

only to visually infer the aberrations but to quantify them. The scheme and the set-up are very promising but more tests are needed in order to fully characterize such a technique. One of the main problems with the data presented in this paper has been the inability of measuring the amount of aberrations introduced by our aberrator in an independent way as form of confirmation of our results. This inability resides in the large amount aberrations that were above the capabilities of a standard Zygo interferometer. One of the next steps will be to reproduce these results using a well characterized aberrator.

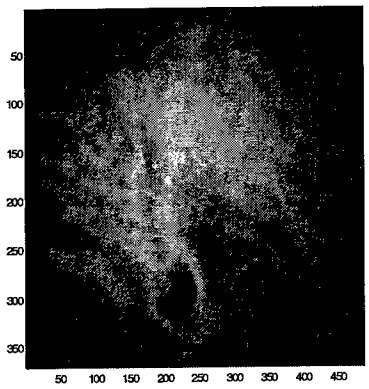

Figure 6: Intensity encoding of the aberrations

5 Conclusions

I have presented some preliminary results on the use of moiré deflectometry techniques in conjunction with a spatial filter to obtain an all-optical wavefront sensor. While more analysis and testing is required the preliminary results are very encouraging. The noise characteristics of such a sensor need to be addressed and the full dynamical range of sensitivity adjustment also require further study.

References

1. MacGovern, A.J., *App. Opt.* **11**, 2972 (1972)

WAVE FRONT SENSING AND INTENSITY TRANSPORT

EREZ N RIBAK AND SHIRLY VINIKMAN
Department of Physics, Technion – Israel Institute of Technology
Technion City, Haifa 32000, Israel

E Mail eribak@physics.technion.ac.il

The Transport of Intensity Equation is explored in various applications for sensing of wave fronts. Curvature sensing provides the phases in a plane where the intensity is well known, by solving partial differential equations. It is also possible to measure phases in two planes under simple assumptions. Solutions of differential equations depend strongly on boundary conditions that require accurate measurement. It is shown that scintillation can be corrected in such cases, even without the boundary conditions.

1 Beam propagation

We start with a wave propagating in the $+z$ direction:
$u(x,y,z,t) = \exp(-i2\pi ct/\lambda)u_z(\mathbf{r})$, $\mathbf{r} = (x,y)$.
We express u_z in terms of real intensity (or irradiance) and phase
$u_z(\mathbf{r}) = [I_z(\mathbf{r})]^{1/2}\exp[i\varphi(\mathbf{r})]$. The paraxial equation is

$$\Pi = \left(i\frac{\partial}{\partial z} + \frac{\nabla^2}{2k} + k\right)u_z(\mathbf{r}) = 0,$$

where $\nabla^2 = \partial^2/\partial x^2 + \partial^2/\partial y^2$; $k = 2\pi/\lambda$. If $\Pi = 0$ then also $\Pi u_z^* - u_z\Pi^* = 0$, and we get the Transport of Intensity Equation (TIE), also known as the Irradiance Transport Equation [7, 6]:

$$k\frac{\partial}{\partial z}I(\mathbf{r},z) = -\nabla\cdot[I(\mathbf{r},z)\nabla\varphi(\mathbf{r},z)].$$

This equation ties intensity and phase values along the optical propagation path. we will discuss three aspects of the equation:

- Curvature sensing in one plane
- Phase sensing in two planes
- Reduction of scintillation effects.

2 Curvature sensing in one plane

If $I(x,y,z=0)=I_0=\text{const}$, the ITE reduces to

$$-\frac{k}{I_0}\frac{\partial I}{\partial z}=\nabla^2\varphi+\delta(e)\frac{\partial\varphi}{\partial\vec{n}};\ e=edge\ ,$$

combined with Neumann boundary conditions $\partial\varphi/\partial\vec{n}$ measured through the ***intensity*** around $\delta(e)$. We approximate the longitudinal derivative as

$$\frac{1}{I_0}\frac{\partial I}{\partial z}\approx\frac{I(z-\Delta z)-I(z+\Delta z)}{I_0\cdot 2\Delta z}\approx\frac{1}{\Delta z}\frac{I(z-\Delta z)-I(z+\Delta z)}{I(z-\Delta z)+I(z+\Delta z)}.$$

We constructed an optical system that allows us to re-image different planes on the camera (Figure 1). By moving the lens in front of the camera, we can choose the two planes to overlap (before and after reflection from the sample), or at any two other locations.

In order to solve the TIE we use the Fourier relationship $FT\{\varphi\}=\omega^{-2}FT\{\nabla^2\varphi\}$, where ω is the spatial frequency [5, 2]. However, to apply that we also need to plug in the boundary conditions. This is done by defining a slightly larger domain. We rewrite the TIE with an additional term, whose value is equal to zero:

$$-\frac{k}{I_0}\frac{\partial I}{\partial z}=\nabla^2\varphi+\delta(e)\frac{\partial\varphi}{\partial\vec{n}}-\delta(e+\Delta)\frac{\partial\varphi}{\partial\vec{n}}\ .$$

The last two terms can now be absorbed into the laplacian:

$$-\frac{k}{I_0}\frac{\partial I}{\partial z}=\nabla^2\varphi\ ,$$

subject to the boundary conditions $\partial\varphi/\partial\vec{n}=0$ around $\delta(e+\Delta)$. The equation is solved by the method of Projection on Convex Sets, by repeatedly entering the measured intensity signals inside the boundary, finding the phase, applying the boundary conditions, and so on [2, 5].

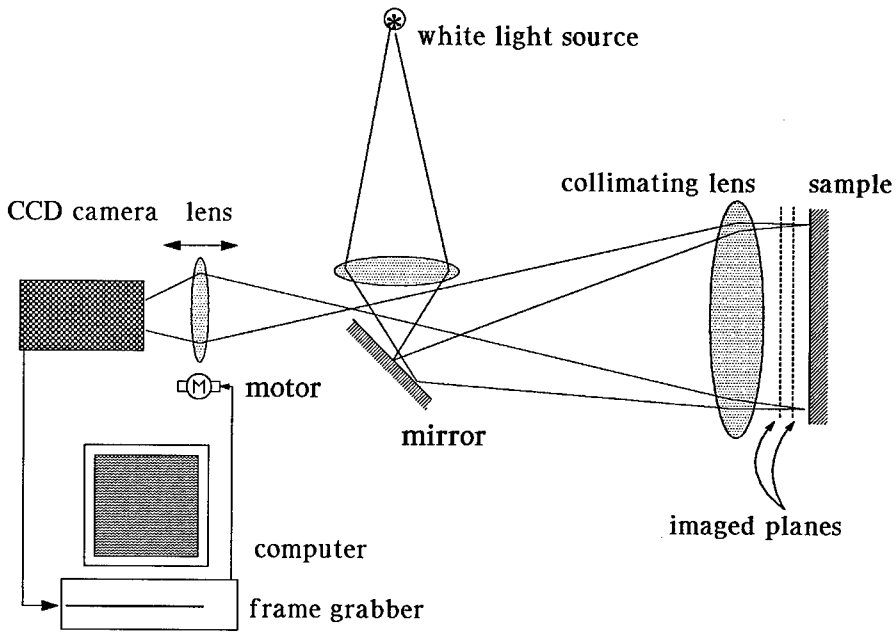

Figure 1: Optical system for measuring reflected wave fronts.

In our experimental setup, we are interested in local details. The wave front might be tilted, have global curvature, or other aberrations on a large scale. This is of low importance if one is looking for small-scale details. To get rid of global aberrations, we fit by least-squares the wave front to Zernike polynomials, and remove them [4]. In Figure 3, we show a cut through a deformable mirror under different voltages. Global tip and tilt have been removed, and the most obvious effect is the curvature change. While testing deformable mirrors, we were able to achieve repeatability of 5%, and local accuracy of few Ångstroms [1]. Our ability to improve this accuracy requires better optics, fine alignment of the measurement planes, and a better digitizing camera (we currently use standard, inexpensive optical and electronic equipment).

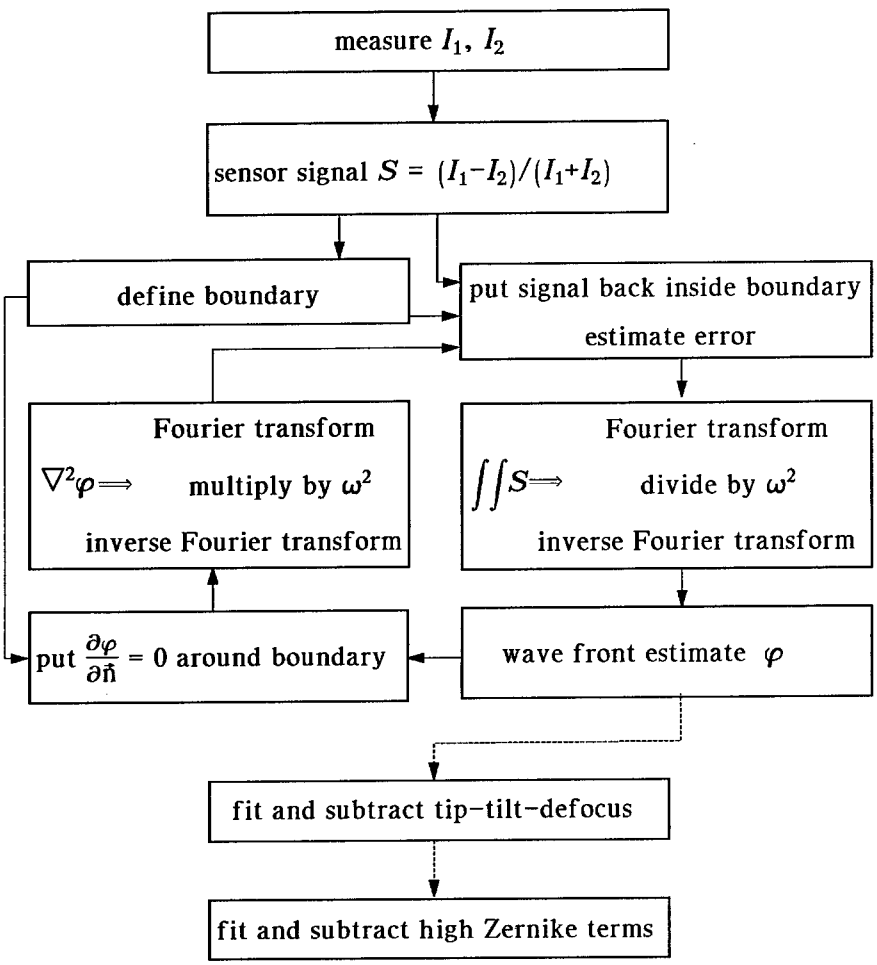

Figure 2: Processing of data: iterative enforcement of signal and of boundary conditions.

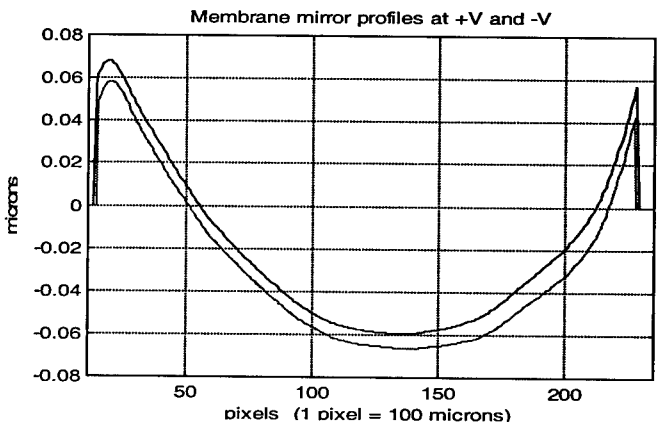

Figure 3: Cuts through a flexible mirror under electric field.

3 Phase sensing in two planes

We start again with the assumption that the intensity is constant before hitting the first distorting surface. The TIE can now be approximated (for small distortions) by

$$\frac{dI(\mathbf{r},z)}{I(\mathbf{r},z)} = d\ln I(\mathbf{r},z) \approx -\frac{1}{k} dz \nabla^2 \varphi(\mathbf{r},z).$$

On integration, we only consider distortions in two planes, say z_1 and z_2, and neglect them elsewhere. If I_0 is the initial intensity, then

$$-k\ln\frac{I(\mathbf{r})}{I_0} \approx z_1 \nabla^2 \varphi_1(\mathbf{r},z_1) + z_2 \nabla^2 \varphi_2(\mathbf{r},z_2).$$

If either one of the planes is close to the observation plane, we see that most of the intensity changes will be due to the other plane. This is exactly the case of astronomical scintillation, created by distant turbulent layers [3].

By judicious choice of the detection plane, one can be sensitive to either distorting plane. Imaging one of the planes on the detector, it has no effect on the intensity fluctuations. Only the distortions in the second plane are measured. The opposite is also true: focusing on the second plane, intensity scintillation will be a result of phase variations in the first.

The detector signal, to be fed into the phase recovery algorithm, is $I(z-\Delta z) - I(z+\Delta z)/I(z-\Delta z) + I(z+\Delta z)$. The denominator is actually the intensity (with scintillation imposed on it), which is being normalized away.

However, it would be more beneficial to use this intensity to estimate the phase fluctuations in the other plane [3]. Thus, four images are to be taken: two, just before and after the first plane, and two, just before and after the second plane. It might be possible to reduce the number of measurements in special cases.

4 Reduction of scintillation effects

In direct continuation of the previous sections, one can see that different phase values can lead to the same scintillation pattern. Any two wave fronts, whose laplacians are equal, will create the same scintillation. The boundary conditions might be different in this case. Alternatively, two wave fronts differing by a multiplicative factor, create the same pattern if coming from different distances:

$$-k \ln \frac{I(\mathbf{r})}{I_0} \approx z_1 \nabla^2 \varphi_1(\mathbf{r}) = z_1 \nabla^2 \tilde{\varphi}_1(\mathbf{r}) = z_2 \nabla^2 \varphi_2(\mathbf{r}) = z_1 \nabla^2 \left[\frac{z_2}{z_1} \varphi_2(\mathbf{r}) \right]$$

This allows one to correct for scintillation effects using adaptive optics, even if the phase is not properly measured. Correction is also possible if the deformable mirror cannot follow the phase (say because it is limited in stroke), or cannot be placed exactly at the plane conjugate to the distortions. All one has to do is find a phase distribution that does match the scintillation pattern and the mirror location, and apply it to the deformable mirror.

References

1. Barty, A, K A Nugent, D Paganin, and A Roberts, Quantitative optical phase microscopy, *Optics Letters* **23** (1998) pp 817-9.
2. Restaino, S R, Wave-front sensing and image deconvolution of solar data, *Applied Optics* **35** (1992) pp 7442-9.
3. Ribak, E N, E Gershnik, and M Cheselka, Atmospheric Scintillations as a Remote Wave-front Sensor, *Optics Letters* **21 (1996)** pp 435-7.
4. Roddier, C, and F Roddier, Wave Front Reconstruction from Defocused Images and the Testing of Ground-Based Optical Telescope, *J Opt Soc Am A* **10** (1993) pp 2277-87.
5. Roddier, F, and C Roddier, Wave Front Reconstruction Using Iterative Fourier Transforms, *Applied Optics* **30** (1991) pp 1325-27.
6. Streibl, N, Phase Imaging by the Transport Equation of Intensity, *Optics Communications* **49** (1984) pp 6-10.
7. Teague, M R, Deterministic Phase Retrieval: A Green's Function Solution, *J Opt Soc Am* **73** (1983) pp 1434-41.

LASER WAVEFRONT SENSING USING THE INTENSITY TRANSPORT EQUATION

SIMON WOODS, PAUL M. BLANCHARD and ALAN H. GREENAWAY
DERA Malvern, St. Andrews Rd., Malvern WR14 3PS, UK
Email: scwoods@taz.dera.gov.uk

A Green's function solution to the Intensity Transport Equation is used to determine the wavefront of a laser-beam from measurements of the intensity profile in two planes equally spaced about the wavefront measurement plane. This paper describes the algorithm, the experimental arrangement to make the measurements and presents some preliminary results.

1 Introduction

Laser-beam wavefront measurements may be required for a number of reasons. In industrial laser material processing applications, such as high precision cutting and drilling, aberrations of the laser wavefront have a detrimental effect on the quality of focus of the beam on the workpiece, which limits the precision that can be achieved. It is therefore advantageous to be able to make measurements of the wavefront, either for prior correction of fixed aberrations or for real-time adaptive beam-shaping.

Wavefront measurements may also be useful when setting up a laser, in order to achieve optimal alignment of the optics. Where a collimated beam is required, this could be obtained by adjusting the position of the collimating lens until the wavefront sensor indicates zero defocus component in the phase profile. Such an approach could be especially useful in situations where there is insufficient free space to propagate the beam far enough to confirm collimation by beam diameter measurements.

Various methods exist for wavefront sensing, including interference-based techniques such as shearing interferometry [1], sub-aperture wavefront slope-sensors (Shack-Hartmann) [1], phase diversity [2] and curvature sensing [3]. It is the latter approach which was chosen for this work, due to the recent development within this group of a system for simultaneous imaging of three different planes onto a single detector surface. This enables measurements of the intensity profile in two planes either side of the pupil to be made simultaneously. The Intensity Transport Equation is then solved using a Green's function approach, which expresses the solution as an integral and can be readily converted into a numerical algorithm.

In section 2 the Intensity Transport Equation is presented, with a description of its solution using a suitably chosen Green's function, and the practical implementation of the solution. Section 3 describes the experimental testing of the method's sensitivity to defocus in a HeNe beam.

© British Crown copyright 1999. Published with the permission of the Defence Evaluation and Research Agency on behalf of the Controller of HMSO.

2 Theory

2.1 *The Intensity Transport Equation (I.T.E.)*

The Intensity Transport Equation [4] describes the evolution of the intensity profile of a beam as it propagates along the z-axis, as a function of the local intensity, $I_z(\mathbf{r})$, and phase, $\phi_z(\mathbf{r})$:

$$\frac{\partial I_z(\mathbf{r})}{\partial z} = -\frac{\lambda}{2\pi}\nabla\cdot\left(I_z(\mathbf{r})\nabla\Phi_z(\mathbf{r})\right) \tag{1}$$

The physical meaning of this equation may be understood by considering a region in which $I_z(\mathbf{r})$ is constant; the I.T.E. then simplifies to

$$\frac{\partial I}{\partial z} = -I\frac{\lambda}{2\pi}\nabla^2\Phi_z(\mathbf{r}),$$

which relates the increase or decrease in the local intensity propagating along the optical axis to the local curvature of the wavefront, as indicated in Figure 1.

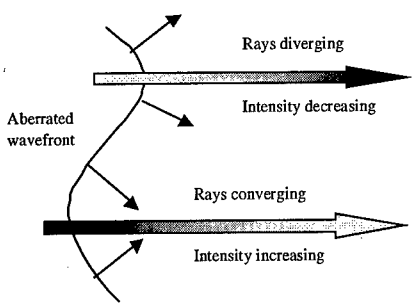

Figure 1. Local wavefront curvature leads to local focusing or defocusing and hence to a local increase or decrease in intensity as the wavefront propagates forward.

It is therefore possible to determine the phase profile by measuring the intensity derivative in the direction of propagation and solving the I.T.E. for $\phi_z(\mathbf{r})$.

2.2 *Green's function solution to the I.T.E.*

Green's second theorem [5] gives the solution for a function $f(\mathbf{r})$ within a two-dimensional region R bounded by perimeter P as

$$\begin{aligned} f(\mathbf{r}) = &\int_R G(\mathbf{r},\mathbf{r}')\nabla^2 f(\mathbf{r}')\,\mathrm{d}^2\mathbf{r}' \\ &+\oint_P f(\mathbf{r}')\nabla G(\mathbf{r},\mathbf{r}')\cdot\mathrm{d}\hat{\mathbf{n}}' - \oint_P G(\mathbf{r},\mathbf{r}')\nabla f(\mathbf{r}')\cdot\mathrm{d}\hat{\mathbf{n}}' \end{aligned} \tag{2}$$

where $G(\mathbf{r},\mathbf{r}')$ is a Green's function satisfying $\nabla^2 G(\mathbf{r},\mathbf{r}') = \delta(\mathbf{r}-\mathbf{r}')$.

If the pupil plane contains a circular aperture of radius a, within which the intensity distribution is uniform and outside which it is zero, the intensity function may be written as

$$I(\mathbf{r}) = I_0\left[1 - U(r-a)\right],$$

where U(r) is the unit step function. The I.T.E. then gives

$$-\frac{2\pi}{\lambda I_0}\frac{\partial I(\mathbf{r})}{\partial z} = \nabla\cdot\left(\left[1-U(r-a)\right]\nabla\phi(\mathbf{r})\right)$$

$$= -\delta(r-a)\hat{\mathbf{n}}\cdot\nabla\phi(\mathbf{r}) + \left[1-U(r-a)\right]\nabla^2\phi(\mathbf{r})$$

where $\hat{\mathbf{n}}$ is the unit vector normal to the aperture edge. Multiplying this equation by a Green's function $G(\mathbf{r},\mathbf{r}')$ and integrating over the entire plane gives

$$-\frac{2\pi}{\lambda I_0}\int\frac{\partial I(\mathbf{r})}{\partial z}G(\mathbf{r},\mathbf{r}')\,\mathrm{d}^2\mathbf{r}' =$$

$$-\oint_P G(\mathbf{r},\mathbf{r}')\nabla\phi(\mathbf{r}')\cdot\mathrm{d}\hat{\mathbf{n}}' + \int_R G(\mathbf{r},\mathbf{r}')\nabla^2\phi(\mathbf{r}')\,\mathrm{d}^2\mathbf{r}'$$

Substituting Eq(2) into the above gives

$$\phi(\mathbf{r}) = -\frac{2\pi}{\lambda I_0}\int\frac{\partial I(\mathbf{r})}{\partial z}G(\mathbf{r},\mathbf{r}')\,\mathrm{d}^2\mathbf{r}' + \oint_P \phi(\mathbf{r}')\nabla G(\mathbf{r},\mathbf{r}')\cdot\mathrm{d}\hat{\mathbf{n}}'. \qquad (3)$$

If the Greens function is chosen to satisfy Neumann boundary conditions, i.e.

$$\nabla G(\mathbf{r},\mathbf{r}')\cdot\hat{\mathbf{n}} = 0, \quad \forall\,\mathbf{r}\in P$$

then the second integral in Eq(3) vanishes, and the solution for the phase simplifies to

$$\phi(\mathbf{r}) = -\frac{2\pi}{\lambda I_0}\int\frac{\partial I(\mathbf{r})}{\partial z}G(\mathbf{r},\mathbf{r}')\,\mathrm{d}^2\mathbf{r}'. \qquad (4)$$

The same result is obtained for apertures that are not circular. In all cases, the differential of the aperture-edge intensity step in the I.T.E. provides the delta-function which accounts for the second perimeter integral in Eq(2). Provided the Green's function satisfies the Neumann boundary conditions on P, the first perimeter integral in Eq(2) vanishes, and the solution is reduced to the single integral of Eq(4).

2.3 *Implementation*

The intensity derivative in Eq(4) cannot be measured directly. Instead, it is approximated by the intensity difference between two planes equally spaced either side of the pupil:

$$\frac{\partial I(z)}{\partial z} \approx \frac{I(z+\delta z/2) - I(z-\delta z/2)}{\delta z}$$

The choice of δz is a compromise between having the planes far enough apart for the intensity difference to be measurable, and sufficiently close together that the approximation for the derivative remains valid. This is discussed by Teague [4].

The Green's function is determined only by the aperture around which its normal derivative is required to vanish. It therefore only needs to be calculated once for each pair of points **r** & **r'**, and the values can then be stored for lookup. The general problem of deriving a formula for the Green's function is well known [6] and will not be entered into here.

It should be mentioned that the wavefront could be expressed in terms of a sum over any orthogonal set of functions, such as the Zernike modes, by choosing the appropriate Green's function. The set of discrete points $\{\mathbf{r}_i\}$ is just one of the possible choices.

The integration is approximated by a simple sum. The Green's function has already been evaluated for each (**r**,**r'**) pair, and so the numerical integration can potentially be carried out very quickly (50μs per point, or per wavefront mode, on a 450MHz PC for a 40×40 matrix).

It has been assumed in the preceding analysis that the intensity in the pupil plane is uniform. Since laser-beams nominally have Gaussian intensity profiles, the validity of this approximation will depend on how much of the full beam width is used for wavefront sensing.

3 Experiment

3.1 The wavefront sensor

The basic experimental arrangement for simultaneous measurement of the beam intensity profile in two planes is shown in Figure 2. The quadratically distorted grating puts equal and opposite amounts of defocus into the +1 and –1 diffraction orders, so that the grating-lens combination forms images of the two planes indicated, at equal distances from the lens, as well as an image of the far-field.

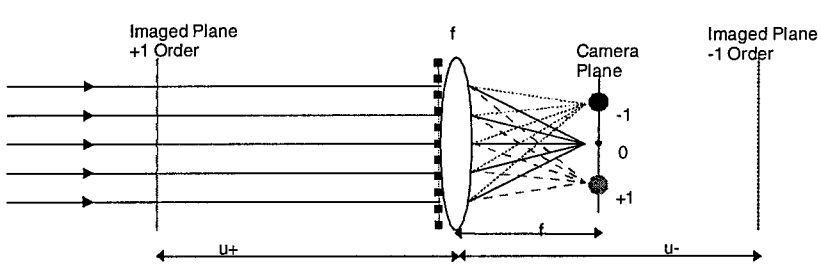

Figure 2. The basic experimental arrangement.

The Green's function had been previously calculated on a 40×40 grid of points and stored. The intensity profiles from the two planes were extracted from the camera image, the −1 order profile flipped in x and y to correct for its negative magnification relative to the +1 order, the difference taken, and the integral carried out to obtain the wavefront.

3.2 Defocus testing

An experiment to test the wavefront sensor for defocus sensitivity was carried out using a 5mW HeNe laser with a wavelength of 633nm. A collimated beam was formed by focussing the beam onto a 25μm pinhole placed one focal length away from the collimating lens. The wavefront sensor arrangement shown above was placed in the beam, using a grating-lens combination which gave a plane separation of 148cm.

Defocus was introduced into the pupil plane by moving the collimating lens on a translation stage. Figure 3 shows a graph of the theoretical number of waves of error introduced, and the number of waves of defocus in a Zernike analysis of the wavefront estimate.

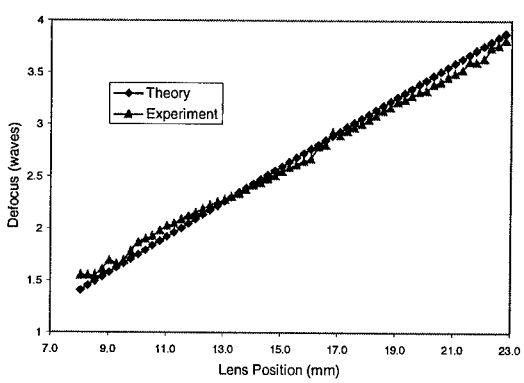

Figure 3. Applied and measured defocus.

It can be seen that there is good agreement between applied and measured defocus, with an RMS error of 0.07 waves.

4 Conclusions

We have demonstrated laser wavefront sensing using a Green's function solution to the Intensity Transport Equation. The method involves using a diffractive optical element to simultaneously image two planes onto the same camera. The intensity

difference is then integrated with a pre-calculated Green's function to give the wavefront.

The technique has been used successfully to measure defocus in the beam from a HeNe laser, to within an RMS error of 0.07 waves ($\lambda/14$).

Future work will include testing the technique using deliberately applied aberrations other than defocus and experiments to measure the wavefront on low beam-quality, high-power lasers.

Acknowledgements

This research is part of Technology Groups 8 (Visible and IR Technology) of the MOD Corporate Research Programme.

References

1. Roggemann and Welsh, "Imaging through turbulence", (CRC Press 1996), Chap. 5
2. R. A. Gonsalves, "Phase retrieval and diversity in adaptive optics", Opt. Eng., 1982, Vol. 21, No. 5, p. 829-32
3. F. Roddier, "Curvature sensing and compensation: a new concept in adaptive optics", Applied Optics, 1988, Vol. 27, No. 7, p. 1223-5
4. M. R. Teague, "Deterministic phase retrieval: a Green's function solution", J. Opt. Soc. Am., 1983, Vol. 73, No. 11, p. 1434-41
5. Boas, "Mathematical Methods in the Physical Sciences", (Wiley 1983), Chap. 6, p. 281
6. Duff and Naylor, "Differential Equations of Applied Mathematics", (Wiley 1966), Chap. 7

CORRECTION OF NON-COMMON PATH ERRORS IN AN ADAPTIVE OPTICS SYSTEM

NATHAN DOBLE, DAVID BUSCHER, GORDON LOVE AND RICHARD MYERS
School of Engineering and Dept. of Physics, University of Durham, South Road, Durham. DH1 3LE

E-mail: n.p.doble@durham.ac.uk

Optical aberrations in an actual adaptive optics system which occur after the wavefront sensing can be the limiting aberration in a system. We describe work on correcting these errors using dithering techniques in the ELECTRA adaptive optics system.

1 Introduction

All adaptive optics systems suffer from non-common path errors and such errors can have a substantial effect on the output image quality. Such errors arise due to mechanical stresses in the system, effects of gravity or thermal fluctuations. The errors that occur before the correction device are corrected for in the normal closed loop operation of the AO system. However, errors in the path to the output camera are not. We propose an easily applicable technique that only requires measurements from the image intensity profile at the output camera. When used in conjunction with a search algorithm the segmented mirror can be offset to account for these errors. This procedure is not restricted to astronomical systems; indeed any system where active correction is required can benefit from this technique. We present experimental results of image evaluation procedures and theoretical studies in segmented mirror alignment.

2 Non-common path errors and the ELECTRA system

The ELECTRA system [1] is designed for the William Herschel Telescope (WHT) at La Palma. The size and number of mirror segments was chosen to provide a 15-40% correction in median seeing conditions at 0.5μm If one imagines a 10 by 10 array with each of the 6 corner segments missing then that is the segment layout. Each can be driven individually in tip, tilt and piston with an overall throw of 6μm. The width of each is 7.54mm square with a separation of 0.08mm. Applying an offset to these segments allows for correction of the non-common path error.
The technique is summarized in Figure 1, an incident plane wave from the alignment source impinges of the mirror and the image recorded by the CCD camera contains the aberrations due to elements in the science arm (the non-

common path error) and the initial random state of the mirror. The final mirror will then be flattened and offset for the non-common path error. There are two main considerations in the dithering technique; one is the characterization of the image and the second is the search strategy. These are treated separately in the following two sections.

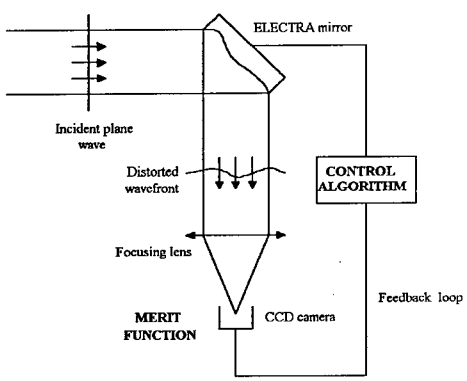

Figure 1 – Schematic of the output arm of the ELECTRA system

3 Image quality evaluation

In order to characterize the image we want a single number which is either maximized or minimized (depending on its exact form). The use of such image sharpening metrics was first proposed by Buffington *et al.* [2-4]. Ideally these functions should have only one extrenum corresponding to the case with zero aberration. Two such metrics are given below

$$J_1 = \int M(x,y) I(x,y) dxdy$$

$$J_2 = \int I^n(x,y) dxdy \quad \text{where } n = 2,3,4$$

Table 1 – Various image metrics. *I(x, y)* is the intensity at the point *(x, y)*

The first metric is used in conjunction with a mask, *M(x, y)*. The mask is chosen to mimic the PSF in the absence of any aberration, obviously this is only really applicable for point sources. The second metric has proved the best in experiment for point like sources. A simple experiment was preformed in which the

aberration was provided by a microscope slide and the correction device was a Meadowlark Hex 69 LC-SLM dithered using modal correction in the form of a Zernike expansion. The results are presented in Figure 2, metric function 2 was used with n=2.

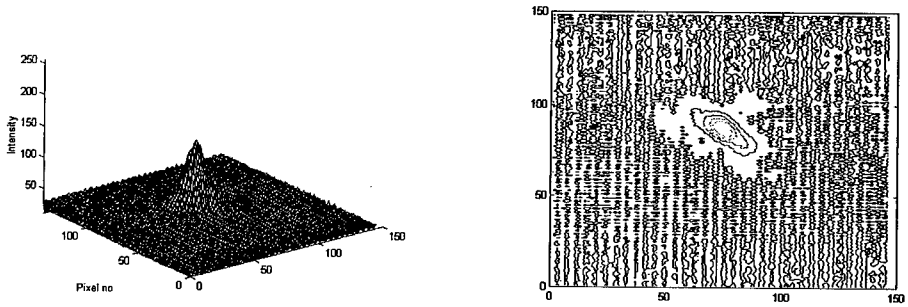

a) Initial PSF: MF = 0.49, RMS error = 0.171, SR = 0.3

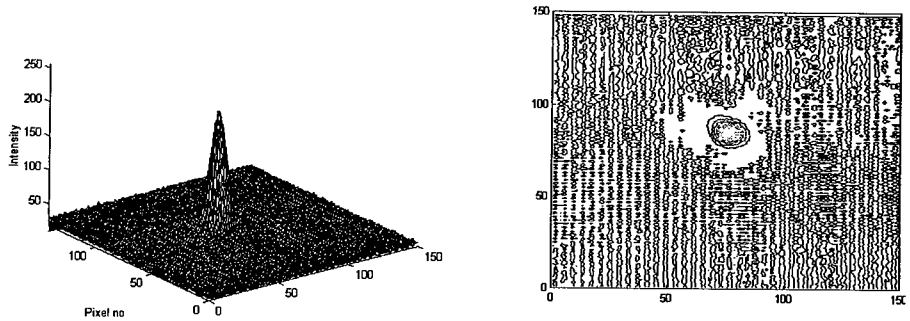

b) Corrected PSF: MF = 0.54, RMS error = 0.09, SR = 0.73

Figure 2 – Initial and final PSFs for static correction for the first 10 Zernike modes using a LC-SLM

4 Search strategies

Two algorithms were tried, the simplex [5] and simulated annealing approaches. The simplex algorithm proved to effective although tended to require more iterations than the simulated annealing approach. Only the simplex technique will

be detailed here. For the ELECTRA mirror having 76 segments each with 3 degrees of freedom the total number of parameters is $N = 228$. A simplex is an $N+1$

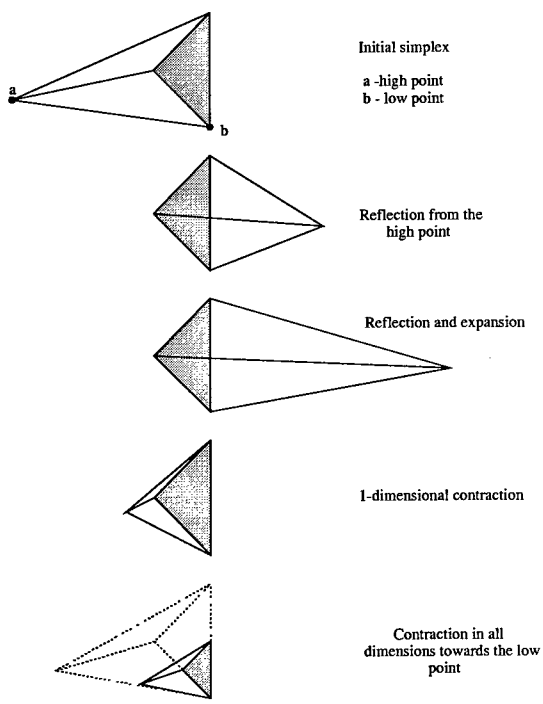

Figure 3 – Possible outcomes for a step in the simplex method

dimensional figure whose initial vertices are random mirror configurations, the simplex then performs a series of steps detailed in Figure 3 in order to proceed through the extremely complex topology.

The method was tried using a mirror found a highly misaligned state using the merit function I^2, results are shown in Figure 4. If the mirror has a high initial RMS error then the final surface may contain one of more segments with a half wavelength piston error, such a displacement is undetectable in the far field. The minimization wavelength was 1μm. Table 2 shows the achieved correction for varying initial conditions, the algorithm was nudged after it claimed to find the first minimum such 'nudges' are not costly but proved beneficial for the more highly misaligned states. Figure 5 shows the evolution of the correction with the nudge clearly visible.

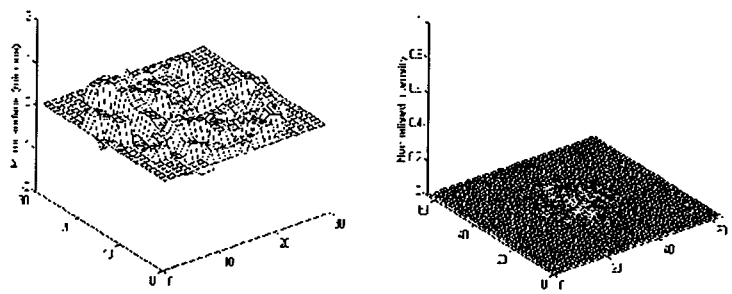

a) – Initial mirror surface RMS error = 0.24, SR ~5%

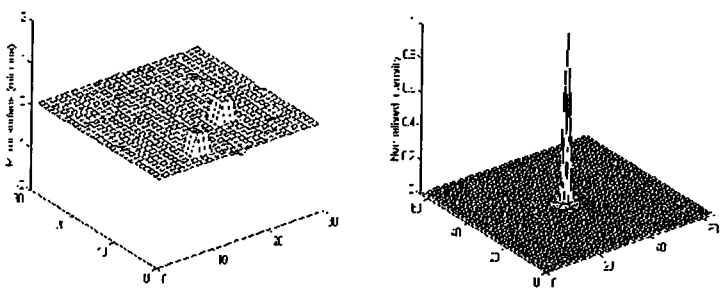

b) – Final mirror surface RMS error = 0.051, SR ~90%

Figure 4 – Initial and final mirror surfaces. Final state contains several segments with half integer piston error

Initial RMS error	Strehl ratio - before	Strehl ratio - after	Final RMS error	Iterations
0.07	0.98	0.98	0.018	3870
0.1	0.98	0.98	0.021	4973
0.14	0.97	0.98	0.023	6330
0.19	0.95	0.97	0.029	6371 *
0.24	0.885	0.90	0.051	9235 *
0.29	0.73	0.81	0.072	10729 *

Table 2 – Final correction for varying initial conditions. The * denotes the half wavelength ambiguity.

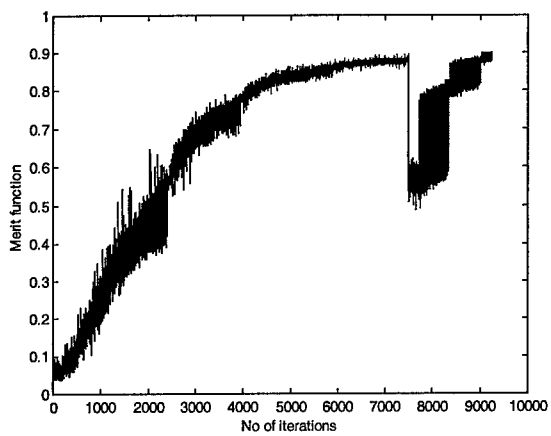

Figure 5 – Evolution of the correction. The nudge is clearly visible at around 7600 iterations

5 Conclusion

The simple alignment of a segmented mirror has been demonstrated in theory. Further work is required to investigate the effect of a change of merit function on nudging the simplex and whether a complete change of algorithm mid-search may be useful to reach a better state. To remove the half wavelength ambiguity minimization at several wavelengths is required These points and the actual implementation of the ELECTRA apparatus are the subject of ongoing research.

References

1. R. M. Myers, A. P. Doel, C. N. Dunlop, J. V. Major, R. M. Sharples and A. J. Vick, An. Astronomical AO system for use on a 4m-class telescope at optical wavelengths. Proc. SPIE, 2201, 1994.
2. R. A. Muller and A. Buffington. Real-time correction of atmospherically degraded telescope images through image sharpening. J. Opt. Soc. Am., 64(9): 1200, 1974.
3. A. Buffington, F. S. Crawford, R. A. Muller, A. J. Schwemin, and R. G. Smits. Correction of atmospheric distortion with an image-sharpening telescope. J. Opt. Soc. Am., 67(3): 297, 1977.
4. A. Buffington, F. S. Crawford, R. A. Muller, and C. D. Orth. First observatory results with an image-sharpening telescope. J. Opt. Soc. Am., 67(3): 304, 1977.
5. N. C. Mehta and C. W. Allen, Remote alignment of segmented mirrors with far-field optimization, Applied Optics, 31, 30, 1992.

FIELD OF VIEW WIDENING IN NON-ASTRONOMICAL ADAPTIVE SYSTEMS.

A. V. LARICHEV, N. A. IAITSKOVA AND V. I. SHMALHAUSEN

International Laser Center, Moscow State University
Vorobiovy gory, Moscow, 119899 Russia
E-mail: shm@lado3.ilc.msu.su

Fundamental limitation on field-of-view in a non-astronomical adaptive optical system due to its anisoplanatism is analyzed. Some possibilities of field-of view widening in adaptive optics are discussed. An estimation of possible isoplanatic patch of an adaptive system for retinoscopy is made using some heuristic approximation for irregular aberration structure function.

1 Introduction

Instrumental limitation in astronomical adaptive optics due to its anisoplanatism is well studied [1,2]. In most cases it restricts the angular size of the corrected zone up to a few arc seconds. The idea of enlarging the isoplanatic patch using a number of phase correctors [3] leads to complicated systems. If the distorting medium is stratified, the corrector location optimization and some modification of its control algorithm may give a good result [4]. These estimations are supposed to be useful especially for non-astronomical applications, when phase distortions are usually concentrated in one or a few layers. The main problem in such a case is that we usually have no reliable mathematical model of irregular aberrations, and the best thing one can do is to make up some heuristic model which does not contradict with experimental data.

2 The basic assumptions and block diagram of an adaptive system

The basic diagram of a system under discussion is shown in fig. 1.

The optical block contains a phase corrector, which image is located within the inhomogeneous layer. It is supposed that the rays passing through that virtual corrector are not restricted by the other optical elements. Thus, the virtual corrector is the input pupil of the adaptive system. Phase distortions for all the rays outgoing from each object point are summarized along the ray and with the phase shift, introduced by corrector. Then the result is averaged over the pupil area. Similar approach can be used in the case of two or more layers. To perform those calculations the structure function of phase distortion should be known. For atmospheric turbulence it is taken in a conventional form: $D(r)=6.88(r/r_o)$, where r_o

is the Fried's radius. For other applications we use "atmospheric-like" approximation $D(r)=(r/r_c)^{\gamma}$, where r_c is the correlation radius, and $1<\gamma<2$.

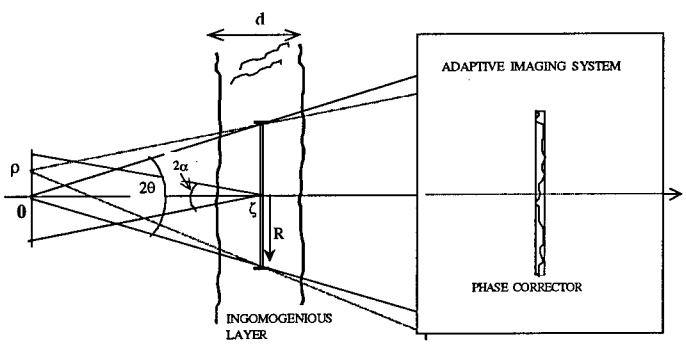

Figure 1.

3 Isoplanatic angle and residual mean square error estimation

3.1 Atmospheric layers

In fig. 2 the value of isoplanatic angle for a single turbulent layer is depicted versus the corrector image relative coordinate (L is the distance between the object and the input aperture). Relative coordinate of the layer center is taken 0.5. Relative thickness of the layer is the parameter. It can be seen from this figure that for thick layers (d>0.6L) optimization of the corrector position is not effective and its conventional location close to the input aperture does not decrease much the field-of-view. In the case of thin layers (d<0.2L), on the contrary, proper position of corrector is of great importance. The isoplanatic angle for such a thin layer is inverse proportional to its relative thickness. Residual error of adaptive compensation averaged over a certain area in the object plane for one, two and three thin layers is shown in fig. 3. Only for a single layer this error can be made zero by changing the corrector plane. For two or more thin layers and for a layer of a finite thickness only a minimum can be achieved. It is notable that the position of that minimum and its depth does not depend much on whether piston mode is removed or not. This result is in contrast with that known from astronomical application, when the corrector plane is located close to the input aperture.

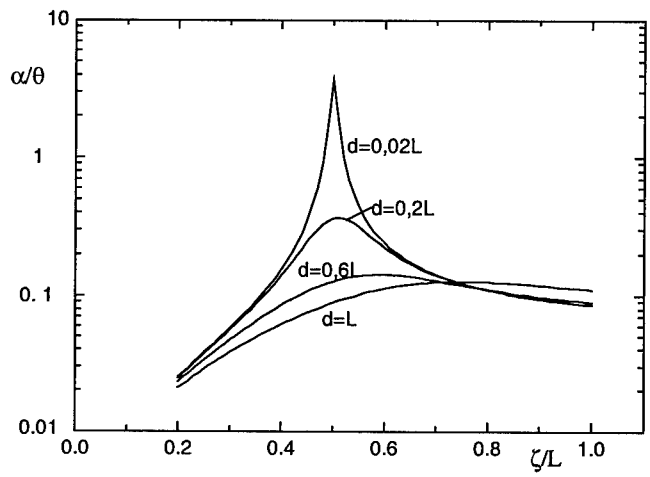

Figure 2. Isoplanatic angle dependence on the corrector location.

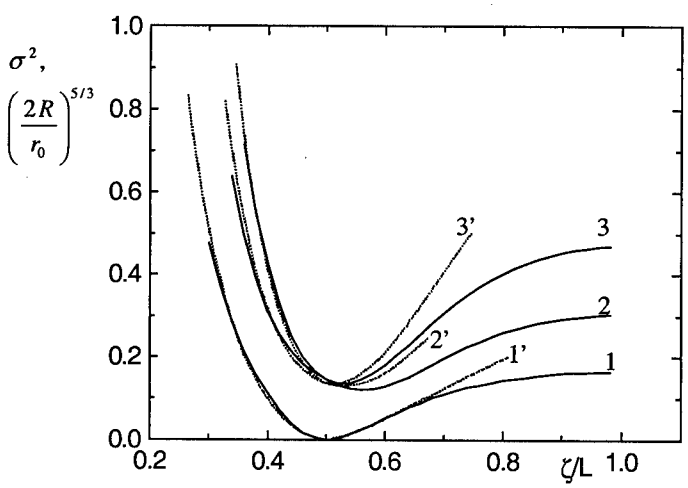

Figure 3. Mean square error dependence on the phase corrector location.
1 – one thin layer, y=0.5L; 2 - two layers, y_1=0.4L, y_2=0.6L; 3 – three layers, y_1=0.4L, y_2=0.5L, y_3=0.6L.
1, 2, 3 –piston removed. 1', 2', 3' – piston not removed.

3.2 *A multi-reference system*

Residual error of adaptive correction averaged over a certain area can be decreased if a multi-reference technique is used. In the algorithm proposed [4] the correcting phase shift is calculated as a weighted sum of the phases measured from different references. In fig. 4a the error distribution along the object is shown for a number of different angles between the references. The reference configuration (for 8 of them) is shown in fig. 4b. Zero distance between references means that a conventional single-reference system is analyzed. In a multi-reference system of that kind the residual error in the central region increases, while on the periphery it decreases. So a compromise for a given area can be found.

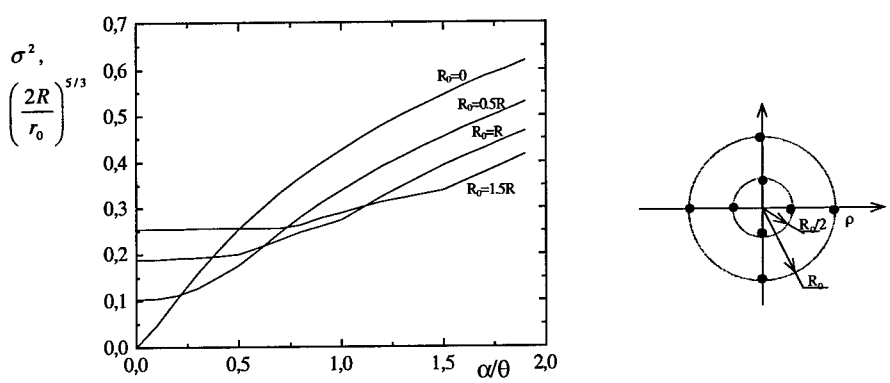

a) b) Reference configuration.

Figure 4. Mean square error in a multireference adaptive system. $R_0 = R\alpha/\theta$.

3.3 *Human Eye Aberrations*

Aberrations of human eye significantly reduce the quality of retinal image [5]. The contrast and resolution of retinal image can be improved by means of adaptive optics [6] within the isoplanatic angle of at least one degree. We try to estimate the isoplanatic zone of an adaptive system for retinal imaging and discuss some methods of its enlarging. This way of field-of-view widening is alternative to another one when only a small number of lower aberrations is compensated for by adaptive corrector and the others are reduced by a deconvolution algorithm [7].The main difficulty is that we do not have enough information to develop a reliable mathematical model for small-scale irregular aberrations, and only have to

speculate about it. Nevertheless, some plausible estimation can be done. Using available data [5] about the mean square aberration coefficients dependence on its number, we tried to approximate it by $\varepsilon^2 = N^{-b}$, where N is the aberration number and b is an empirical value. We have obtained $b \approx 1.4 \sim 1.5$, which is significantly less than for the atmospheric turbulence. It means that if we use an "atmospheric-like" structure function γ should be less than the common value of 5/3. Estimation gave $\gamma \approx 1.33 \sim 1.56$, but that result is not very reliable because of insufficient statistics. The basic block diagram of an eye inspection system and its equivalent scheme are presented in fig. 5a,b. As the phase corrector and the distorting layer are placed now in parallel rays, the analysis of the isoplanatic angle leads to an universal dependence on a parameter η as it is shown in fig. 6. Here the mean square aberration suppression factor is depicted versus the normalized angle. Knowing the suppression factor required one can estimate the size of the isoplanatic patch.

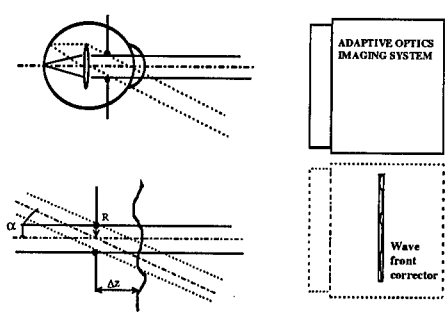

Figure 5. The basic block diagram of an eye inspection system.

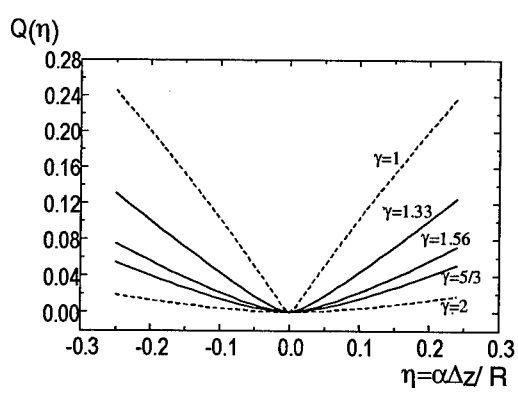

Figure 6. The mean square aberration suppression factor.

4 Discussion

Let us try to apply the results above to estimate the size of field-of-view of an adaptive device for retinoscopy. According to [5,6] mean square aberration cased by irregular distortions (N>4) is about ε^2 =2.5. The desired level of aberrations over the field-of-view for diffraction limited image is $\varepsilon^2 = 0.15$. So the suppression factor should be Q=0.06. This is an "optimistic" estimation. In the other case it may be supposed that all aberrations including the large scale ones are to be corrected. In that case we obtain a "pessimistic" estimation of the suppression factor of Q=0.005. To make use of these estimations we approximated the upper curve in fig.6 by an empiric formula $Q=0.78\eta^{1.2}$. That leads to an estimation of the isoplanatic patch angular size: $\alpha = (R/\Delta z)\ (Q/0.78)^{0.85}$, where R is the eye pupil radius (in our case it was 7.3/2 =3.65 mm) and Δz is the distance between the pupil and the distorting layer. We take here the worst possible situation when the most intensive distortions lay near the outer surface of the eye. In this case Δz is also about 3.5 mm. These values leads to an "optimistic" corrected field-of-view of 6 angular degrees, and "pessimistic" – of 0.85 degree. We believe that these estimations are in good accordance with experimental results [6].

References

1. Fried D. Anisoplanatism in adaptive optics *JOSA A* **72** N1 (1982) pp.52-61.
2. J. Hardy, Instrumentation limitation in adaptive optics for astronomy, *in Active Telescope System, F.Roddier ed., Proc. Photo-Opt. Instrum. Eng.***1114** (1989) pp. 2-13.
3. Johnston D. and .Welsh B. Analysis of multiconjugate adaptive optics *JOSA A* **11** (1994) pp. 394-408.
4. Shmalhausen V.I. and Iaitskova N.A. Adaptive corection of the image in anisoplanatic condition for stratified atmosphere. *Optika atmosferi i okeana (Rus. Journal)* **11** N4 (1998) pp.364-370.
5. Liang J.and Williams D. Aberration and retina image quality of the normal human eye *JOSA A* **14** N11 (1997) pp.2873-2883.
6. Liang J., Williams D., Miller D. Supernormal vision and high-resolution retinal imaging through adaptive optics *JOSA A* **14** (1997) pp. 2884-2892.
7. Larichev A. and Kudryashov A. Retinoscopy and Adaptive Optics. (to be published).

ADAPTIVE COMPENSATION FOR TIME-DEPENDENT THERMAL BLOOMING WITH LOCAL EXTREMA IN THE SPACE OF CONTROL COORDINATES

F.YU. KANEV, L.N. LAVRINOVA, AND V.P. LUKIN

Institute of Atmospheric Optics, Academicheskii Ave., 1, Tomsk, 634055, Russia, E-mail: lukin@iao.ru

Laser beam adaptive control with the use of a multidither algorithm is considered under the conditions of thermal blooming. It was shown that if the algorithm is applied before the termination of transient processes in a medium, an adaptive system finds the region of the extremum but leaves it in a short while. Time required to find the extremum is defined by the value of a gradient step, lesser is the step, greater is the time, but the time interval during which the system remains in the vicinity of the extremum is inversely proportional to the value of the step. The problem becomes even more complicated if local maxima appear in the space of control coordinates.

1 Mathematical description of a beam propagation. An algorithm of control

Analysis of the control in a homogeneous medium was performed in approximation of nonstationary wind refraction. The beam and medium interaction is defined by the following dimensionless parameter:

$$R_v = \frac{2ka_0^2\alpha I}{n_0\rho_0 C_p V}\frac{\partial n}{\partial T},$$

which is proportional to the intensity I, squared initial radius of the beam a_0, and also depends on other parameters of the beam and medium. The field of the laser beam in the observation plane is characterized by a criterion of focusing

$$J(t) = \frac{1}{P}\iint \exp(-(x^2+y^2)/r_a^2)I(x,y,z_0,t)dxdy,$$

actually $J(t)$ is the power of light within the aperture. In this equation r_a is the radius of the aperture, P is the total power of the beam. The diffraction length $z_d = 2ka_0$ of radiation was chosen as a spatial scale of the problem along the axis of the beam propagation (here k is the wave number). In the plane perpendicular to the beam propagation the scale was the initial radius a_0. The temporal scale of the problem was the wind clearing time $\tau_V = a_0/|\mathbf{V}|$ characterizing the development of transient processes associated with heating of the medium. Corresponding variables are normalized to these scales.

Corrections for nonlinear distortions are considered with the use of multidither[1] sensing according to which a change in the control coordinates of the adaptive corrector $\mathbf{F} = \{F_1, F_2, ..., F_N\}$ is performed by the following formula:

$$\mathbf{F}(t) = \mathbf{F}(t-\tau_d) + \alpha(t-\tau_d)\,\mathbf{grad}\,J(t-\tau_d).$$

The components of the vector $\mathbf{grad}\,J(t-\tau_d)$ are derivatives $\partial J(t)/\partial F_i$ calculated during the test soundings.

2 Estimation of the accuracy in seeking the extremum when performing control using non steady-state parameters

The possibility of performing control with the use of non steady-state parameters (before termination of the transient processes in the beam – medium system) has been considered by the authors of Refs. 2 and 3. In this article we present some results of a detailed investigation into this problem. The possibility is being assessed of not only determining the extremum during a finite time interval, but also of tracing the goal function's extremum location during the process of the medium heating by the beam.

The isolines in Fig. 1 show the distribution of the criterion $J(t)$ over the space of two control coordinates (tilt and defocusing) at different moments in time. Figure 2 illustrates the motion of the extremum (curve *1* in Figs. 2*a* and *b*). Obviously, positioning the adaptive system in the extremum at every moment in time would provide for the highest efficiency of control. The speed with which a corrector profile is changed is determined by an interval between two successive iteration steps and by the coefficient α (the step in tilt α_{Tilt} can differ from that in focusing α_{Foc}). Varying these two parameters, interval between the steps and the coefficient α, enabled us to reveal that three variants of the control are possible.

1. The coefficient α is small ($\alpha_{Tilt}=1.0, \alpha_{Foc}=0.5$). In this case the algorithm reaches maximum in $15\tau_V$ and remains in the extremum practically without any limitations on time. In this version the control is very slow.
2. Increasing the gradient step, that is α approaches optimal value. In Figs. 2*a* and *b* this variant is characterized by curves *2*. In the interval from 0 to $4\tau_V$ the system moves slower than the maximum, after $4\tau_V$ the tilt, defocusing, and the criterion J are approach optimal values, but the algorithm does not stop in the extremum, the focusing continues to increase that finally leads to defocusing ($t > 6.5\,\tau_V$).
3. Further increase of α (curves *3* in Figs. 2*a* and *b*). Although in this variant the tilt and defocusing differ, at the initial moments in time, from optimal values, those are nearer to optimum as compared to the above two examples. At $t > 2\tau_V$ the growth of tilt and defocusing continues and exceeds the optimal values.

If summarizing, one may arrive at a conclusion that it is impossible to find out the optimal value of the gradient step that would allow the adaptive system to

detect coordinates of the extremum at the initial moments in time and to hold the optimal focusing after termination of the medium heating.

When performing control, we assumed that multidither sounding provides for detecting the extremum of the function presented in Fig. 1. Every point determined by this function is a solution to the problem of nonstationary wind refraction given certain initial conditions. If the frequency is high (time between the test variations is much shorter than the characteristic time of thermal lens change), the function does not change during the time of the gradient step change. Thus, one may expect, within the framework of the assumption made, that, as a result of heating of the medium, at a gradient step larger than the optimal one (the gradient step is kept constant during the control) the control coordinates and criterion of focusing would oscillate in the vicinity of extremum and the larger is coefficient α, the larger is the amplitude of oscillations. However, this situation has never been observed in the numerical experiments.

Among the causes of inaccurate detection of the extremum coordinates may be the difference between the "frozen" hill and the function presented in Fig. 1. To confirm this hypothesis, the following numerical experiment has been conducted. We have simulated propagation of the beam under conditions of nonstationary wind refraction up to $3\tau_V$ time with control coordinates corresponding to the maximum in the goal function (tilt equals to 3.0, focusing to 1.0). Then, having fixed the thermal lens, we have varied the control coordinates and calculated the light field on the object (solution of the problem on beam propagation under conditions of a constant thermal lens). In that way we have simulated the distribution of the goal function as it is sensed by fast multidither sounding. Thus obtained distribution is presented in Fig. 3. As seen from this figure, it differs from the function shown in Fig. 1*b* (this function was calculated for time of $3\tau_V$). Since the goal function that has been introduced into the control algorithm is different than the function whose extremum is being sought, one can arrive at a conclusion that multidither sounding using non-steady-state parameters of the problem is inherently unstable. The algorithm does not always provide for accurately determining the extremum (one may expect only approaching the maximum neighborhood) while, in any case, the adaptive system leaves, in a while, the vicinity of the extremum and moves toward overfocusing. The time during which the adaptive system is in the vicinity of extremum depends on the gradient step value. If the choice of α is wrong, this time can be quite short (as, for example, that shown in Fig. 2 when the parameters correspond to curve *3*; the adaptive system was in the vicinity of the maximum only during $1\tau_V$ to $2\tau_V$).

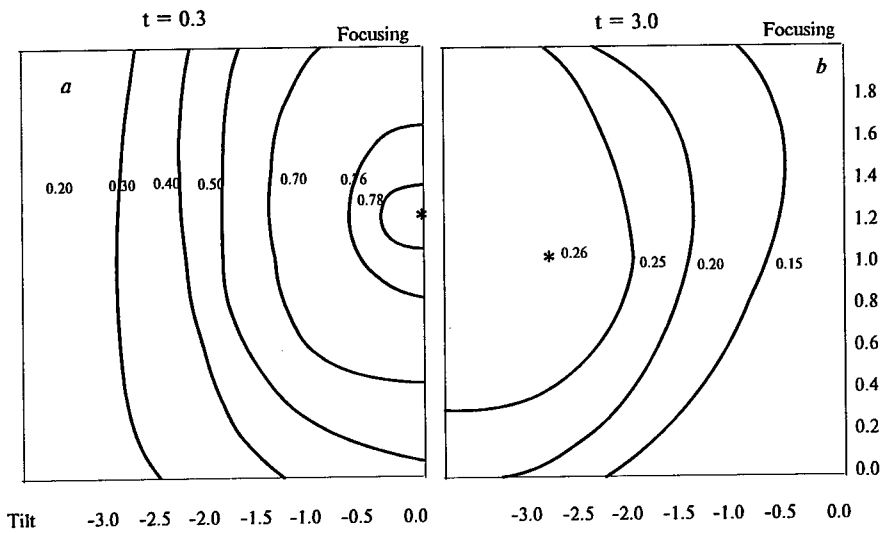

Figure 1. Distribution of the criterion $J(t)$ in the space of coordinates of tilt and focusing recorded at different moments in time. The initial conditions have been taken one and the same in all calculations, namely, $R_v = -100$; $z = 0.5$; $z_{nl} = 0.1$, $r_a = a_0$.

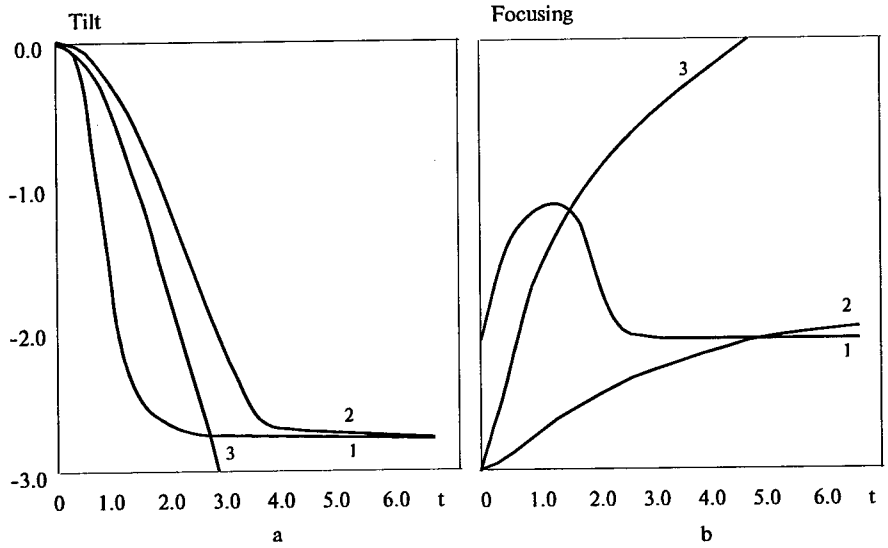

Figure 2. Changes of the extremum coordinates (tilt (a) and defocusing (b)) at heating of a medium by a beam (curve 1 in all the figures) and corresponding changes in those due to control (curve 2 corresponds to $\alpha_{Tilt} = 2.5$, $\alpha_{Foc} = 0.2$, curve 3 to $\alpha_{Tilt} = 2.5$, $\alpha_{Foc} = 0.5$).

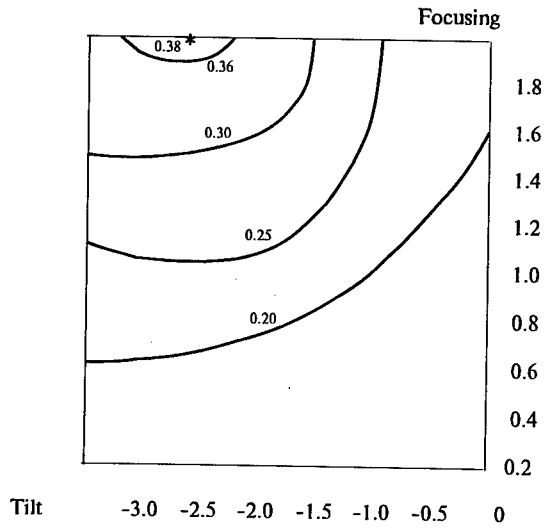

Figure 3. Distribution of $J(t)$ for a frozen thermal lens.

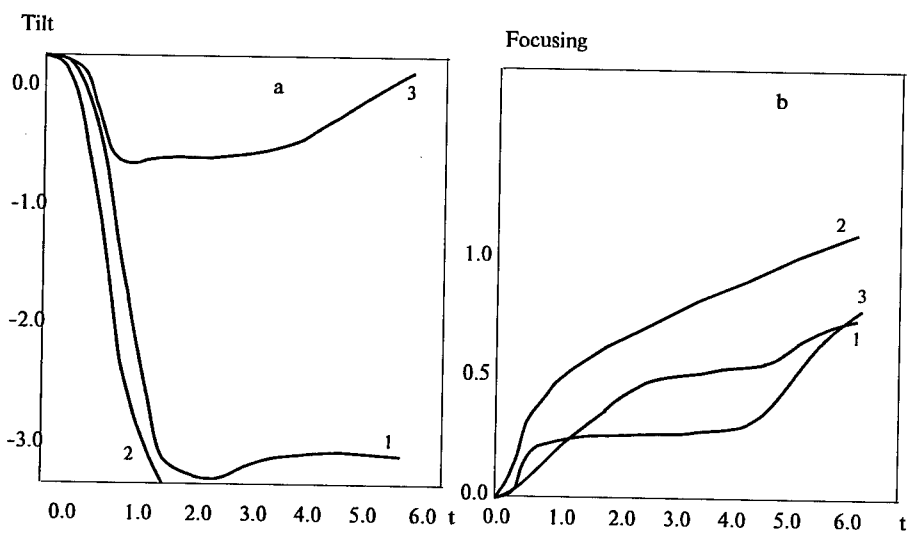

Figure 4. Changes of tilt (a) and defocusing (b) due to the control performed. Curve 1 corresponds to $\alpha_{Tilt} = 10$, $\alpha_{Foc} = 0.7$ (catching the global extremum), curve 2 to $\alpha_{Tilt} = 10$, $\alpha_{Foc} = 0.8$ (the gradient step has been increased and the control algorithm leaves the vicinity of maximum), and curve 3 to $\alpha_{Tilt} = 8$, $\alpha_{Foc} = 0.7$ (termination of the control in a local maximum).

3 Peculiarities of multidither sounding under the presence of local extrema

Solving the problem on propagation of laser beams under condition of time-dependent thermal blooming enables one to show that at the initial moments in time ($t < 3\tau_V$) only one extremum occurs, the second one taking place only at $t \geq 3\tau_V$. So, one may assume that if the algorithm is capable of accurately detecting the motion of the extremum in the space of control coordinates the local maxima would not influence the control efficiency.

To illustrate this situation, Fig. 4 presents the change of tilt (*a*) and defocusing (*b*) for the case of control when local extrema appear at different values of the gradient step α. As a result of thorough selection, we have managed to achieve the situation that algorithm identifies the global extremum ($\alpha_{Tilt} = 1.0$, $\alpha_{Foc} = 0.6$) and the adaptive system is being kept in its vicinity for quite a long time (curves *1* in Figs. 4*a* and *b*).

One of the possibilities to perform the control with the use of non steady-state parameters is in the control only over tilt at the very initial moments in time, with the focusing being fixed. Such a procedure allows the algorithm to reach the vicinity of a global extremum within a wide range of α_{Tilt} values and then to proceed to control over the tilt and focusing simultaneously.

On the whole one may conclude that the control algorithm is capable of tracing the tilt variations due to heating of the medium by a beam quite accurately what enables the adaptive system to reach the vicinity of the extremum. At the same time no exact determination of the global maximum coordinate over focusing is possible (it should be kept in mind that these conclusions are only true for the control over non steady-state parameters).

References

1. M.A. Vorontsov and V.I. Shmalgausen, *Principles of Adaptive Optics* (Nauka, Moscow, 1986), 453 pp.
2. I.V. Malafeeva and S.S. Chesnokov, Atmos. Oceanic Opt. **6**, No. 12, 861–863 (1993).
3. F.Yu. Kanev and S.S. Chesnokov, Atmos. Opt. **2**, No. 11, 1015–1019 (1989).

INFLUENCE OF LOCAL EXTREMA ON THE EFFICIENCY OF GRADIENT ALGORITHMS FOR LASER BEAM CONTROL

F.YU. KANEV, V.P. LUKIN, AND L.N. LAVRINOVA

Institute of Atmospheric Optics, Siberian Branch of the Russian Academy of Sciences, Akademicheskii Ave., Tomsk, 634055, Russia

The control over high-power laser beam based on the aperture sounding algorithm and its modification is considered in this paper using methods of numerical experiment. A domain of the problem parameters is shown to exist for which local extrema appear in the space of control coordinates. A decrease in the efficiency of correction for the beam thermal blooming due to these local extrema is estimated. The method for seeking the global (basic) maximum is proposed.

1 Introduction

A comparison of algorithms for phase control over laser beams in a nonlinear medium carried out by many authors[1–3] shows that none of the algorithms known at present is free of serious drawbacks. Thus, for example, it is characteristic of the phase conjugation method that the correction becomes unstable as the radiation power increases.[3,4] The aperture sounding[5] has a higher stability and, perhaps, a faster performance. At the same time decrease of the efficiency of this algorithm (and others based on the gradient method) is observed if local extrema are present in the space of the beam control coordinates.[1] So up to now this problem has been investigated less thoroughly than it is needed.

2 Numerical model and the software version of the model

Beam propagation was considered in the approximation of stationary wind refraction for the case of a homogeneous medium. Under such conditions the complex amplitude of a field, E, can be described by the following system of equations[2]:

$$2ik\frac{\partial E}{\partial z} = \Delta_{\perp}E + 2\frac{k^2}{n_0}\frac{\partial n}{\partial T}TE, \tag{1}$$

$$(\mathbf{V}\nabla)T = \frac{\alpha}{\rho_0 C_p} \tag{2}$$

where k is the wave number, n_0 is the undisturbed magnitude of the refractive index n, z is the coordinate axis along which the beam propagates, T is the temperature of

a medium, **V** is the wind velocity vector, α is the absorption coefficient; notations of other physical values are of common use.

The interaction between the beam and the medium is characterized by the dimensionless parameter

$$R_V = \frac{2ka_0^2 \alpha I}{n_0 \rho_0 C_p V}$$

that is proportional to the intensity I and to the initial radius of the beam a_0, and depends on other parameters of the medium and radiation. Nonlinear distortions in the observation plane $z = z_0$ can be described using the following criterion:

$$J(t) = \frac{1}{P} \iint \exp(-(x^2 + y^2)/r_a^2) I(x, y, z_0, t) dxdy \tag{3}$$

In formula (3) r_a is the radius of the receiving aperture and P is the total power of the beam.

We have considered the correction for nonlinear distortions based on two algorithms. The aperture sounding algorithm[1] according to which the change of adaptive corrector control coordinates $\mathbf{F} = \{F_1, F_2, \ldots, F_N\}$ is performed according to the following formula:

$$\mathbf{F}(t) = \mathbf{F}(t - \tau_d) + \beta(t - \tau_d)\, \mathbf{grad}\, J(t - \tau_d), \tag{4}$$

and a modified aperture sounding algorithm[6]

$$F_i(t) = F_i(t - \tau_d) + \beta(t - \tau_d) sign\left(\frac{\Delta I(t - \tau_d)}{\Delta F_i(t - \tau_d)}\right), \tag{5}$$

where F_i is the ith component of the vector of control coordinates, $\beta(t - \tau_d)$ is the coefficient whose value decreases at the iterations that had led to a decrease in the control efficiency function (in our problems it is the criterion $J(t)$, formula (3)), sign is the function of taking a sign. The algorithms (4) and (5) are differ by that, according to expression (4), in the process of test variations the value and direction of the iteration step are determined, while according to the algorithm (5) only the motion direction (direction to an extremum) is sought, and the step value is completely specified by the coefficient $\beta(t - \tau_d)$. The program that realizes the calculation scheme is developed using the methods of object-oriented programming (programming language C++). All data characterizing the variant of the calculation chosen are displayed on the main panel (Fig. 1). During the calculations the basic parameters of a beam in the observation plane are being displayed on the panel either. Those are the field distribution, criterion J, maximum intensity, energy radii of the beam along the axes that are perpendicular to the propagation direction. The input parameters and the control algorithm are specified by the interface panels that are accessible through the program menu.

3 Accuracy of detecting the principal maximum against the background of local extrema

The aperture sounding algorithm (and its modification) can be considered as a gradient method of seeking of the efficiency function extremum. The extremum is being sought in the space of control coordinates F_i. Therefore, to reveal the algorithm peculiarities, in order to simplify the problem, it is possible to consider the procedure of seeking the global extremum against a relatively simple analytical function that has local maxima. The basic relationships obtained from simplified analysis can also be correct for more complicated problems of the adaptive optics.

We have considered a function of one variable which has a global maximum and two local ones disposed symmetrically relative to its global maximum. Regardless of local extrema present the algorithm could, in certain cases, identify the main peak. The relative width and height of the local extrema (normalized to the corresponding parameters of the global extremum) have been varied. That allowed us to determine the boundary of the domain where the algorithm always isolates the global maximum. For the algorithm (4) the results are presented in Fig. 2*a*. The region of the parameters, for which a global maximum is determined, is above the curve. As to the algorithm (5) the corresponding data are presented in Fig. 2*b*. In the algorithm considered the step value is determined as $\beta \cdot \mathrm{sign}(\Delta J/\Delta F_i)$, i.e., it does not depend on the value of the derivative. On the whole a conclusion can be drawn, in a one-dimensional case, that a choice of the algorithm is determined by the characteristics of the function under study (by the shape of local extrema).

For the sake of clarity in describing the "hill" and peculiarities of seeking the maximum, let us consider the control, in the problem of compensation for nonlinear distortions, to be performed in the space of two coordinates (slope and focusing). In this case the "hill" of the efficiency function is a distribution of the criterion J (formula (3)), each value of which corresponds to fixed values of the slope and focusing.

When the extension of a nonlinear layer ($Z_{nl} = 0.25\, Z_d$) increases a secondary maximum appears in the space of control coordinates. The height of this maximum is approximately one sixth of the principal maximum height. That means that if the system stops at a local extremum, then the control efficiency will strongly decrease. With further increase of nonlinearity (modulus of the parameter R_v) there are two extrema in the criterion distribution (Fig. 3), with the height difference between these extrema being about 30%. The intensity distributions over the beam cross sections which correspond to the points of maxima and the intensity distribution in the control beginning (i.e., for zero values of the slope and focusing) are presented in the same figure. The local maximum corresponds to the situation when the intensity distribution has two extrema of practically equal heights.

At the global extremum the distribution of light field is Gaussian and the value of maximum intensity is close to the diffraction-limited one. Use of the algorithms (4) and (5) with the above chosen parameters yields the following results: the compensation for distortions stops at a local extremum (motion trajectories are shown in Fig. 3*a*). Further increase of focusing does not lead to the growth of the criterion J (overfocusing), increase of the slope (and thus approaching to the global extremum) is also impossible because of the peculiarities of the algorithms (4) and (5). An increase of the gradient step β does not allow one to approach to global maximum either.

A sufficiently simple method of "smoothing the hill" when local maxima disappear is to increase the receiving aperture radius r_a. The "hill" calculated for the same parameters used in the example considered above, but for $r_a = a_0$ is presented in Fig. 4. One can see from this figure that only one maximum with coordinates corresponding approximately to the coordinates of local extremum in Fig. 5*a* is observed in this case.

Thus, we can draw a conclusion that one of the possible methods to solve the problem of local maxima influence is to increase the receiver aperture. In this case the coordinates of an extremum are found a little bit less accurately than in the case of small receiving areas. But, after an approximate determination of the coordinates of a maximum a decrease of the aperture and more accurate localizing of the extremum are possible.

References

1. M.A. Vorontsov and V.I. Shmalgauzen, *Principles of Adaptive Optics* (Nauka, Moscow, 1986), 336 pp.
2. S.A. Akhmanov, M.A. Vorontsov, V.P. Kandidov, A.P. Sukhorukov, and S.S. Chesnokov, Izv. Vyssh. Ucheb. Zaved. Ser. Radiofiz. **23**, No. 1, 1–37. (1980).
3. F.Yu. Kanev and V.P. Lukin, Atm. Opt. **4**, No. 12, 856–863 (1991).
4. P.A. Konyaev, Atmos. Oceanic Opt. **5**., No. 12, 814–818 (1992).
5. F.Yu. Kanev and S.S. Chesnokov, Atm. Opt. **2**, No. 2, 1015–1019 (1989).
6. S.S. Chesnokov, Kvant. Elektron. **10**, No. 6, 1160–1165 (1983).

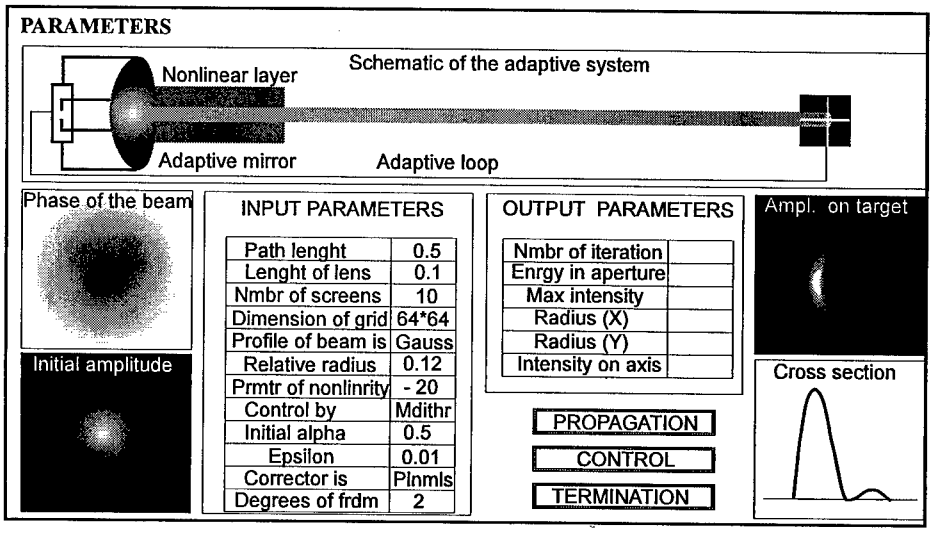

Figure 1. Interface of the program developed for the numerical model used.

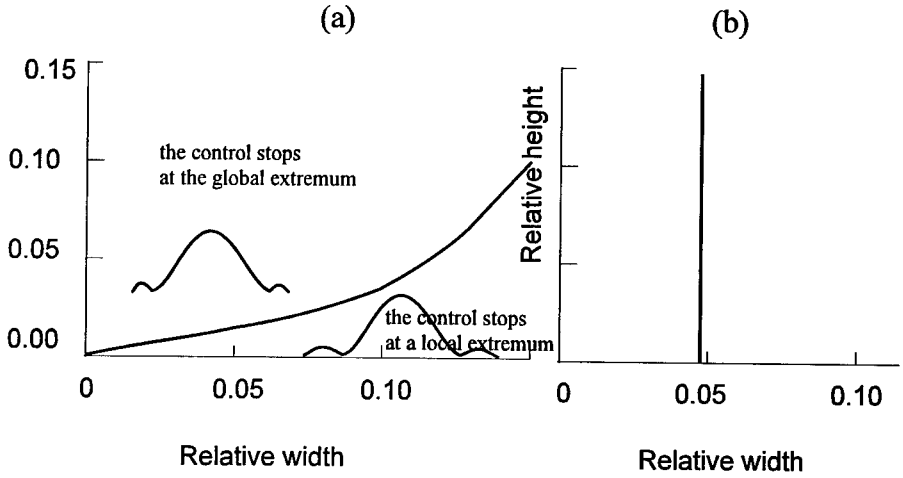

Figure 2. The boundaries of the region where the determination of the global maximum in the presence of local ones is possible (as found for the function specified analytically): the algorithm (4), above the curve the control stops at the global extremum, below the curve the control stops at a local extremum (a); the algorithm (5), to the left of the straight line is the global extremum, to the right of the straight line is a local extremum (b).

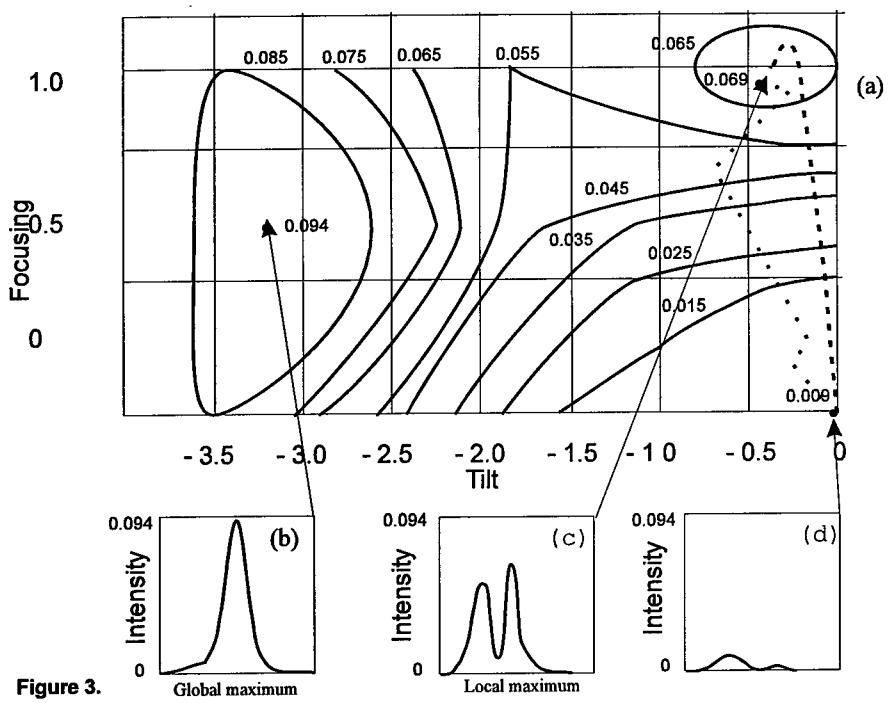

Figure 3.

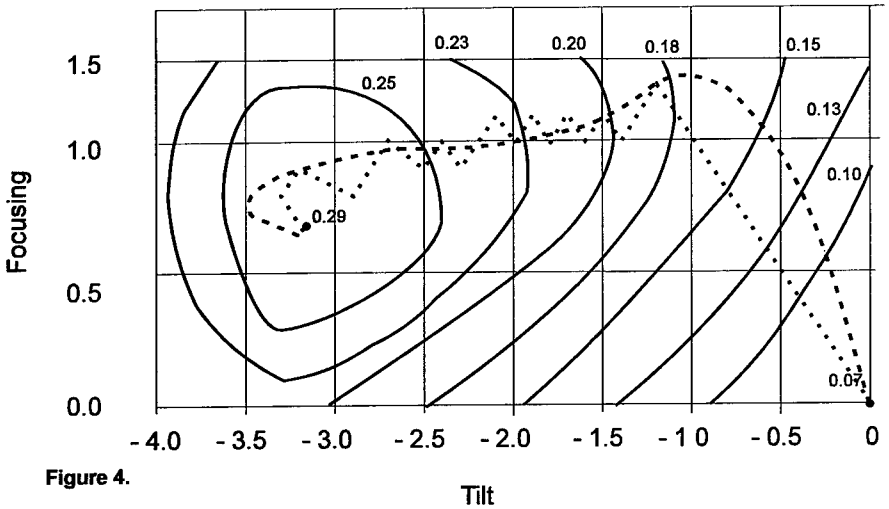

Figure 4.

RADIAL SHEAR WHITE LIGHT PHASE STEPPING INTERFEROMETRY FOR WAVEFRONT SENSING IN ADAPTIVE OPTICS

A.R.D.SOMERVELL, G.T.BOLD, AND T.H.BARNES

Physics Dept. University of Auckland Private Bag 92019, Auckland, New Zealand

We examine the fundamental limitations of a phase-stepping wavefront sensor for use with a thermal source in an adaptive optics system. We show that - in principle - it should be possible to measure wavefronts to sufficient accuracy at the required speed provided that white-light fringes are used and the aberrations are small. The errors caused by using phase-stepping with white light fringes are determined and error-compensation schemes suggested.

1 Introduction

Hartmann-Shack sensors are often used in adaptive optics[1] but interferometric sensors have also been applied[2]. Shearing interferometers - e.g. the cyclic radial shearing interferometer[3] - are often used because they are self-referenced. The phase ambiguity introduced by the co-sinusoidal fringe intensity profile has been overcome in other applications by phase-stepping[4] but the wavefront must be measured very rapidly in adaptive optics and the light gathered per step is small thus reducing phase accuracy. With a thermal source, the problem is compounded by spatial coherence requirements.

In this paper, we calculate the phase accuracy that might be expected from a phase-stepping radial shear interferometer operating with a thermal source at sampling rates required for adaptive optics. The accuracy depends on source temperature and detector noise but, for source temperatures ~3000K, we estimate the phase accuracy to be <0.5 radian for a 64 detector array operating on white light fringes. Phase stepping using white light fringes causes systematic phase errors but these can be compensated if the source spectrum is known.

2 Theory

Figure 1 shows our optical system. Wavefronts from a thermal source propagate through the turbulent medium and are collected by a telescope which feeds a cyclic radial shearing interferometer. The central circular region of the input beam passes through a phase modulator, which enables the system to be phase stepped. Phase measurements are made in the annulus surrounding this

central core in the output beam using n^2 detectors. The system makes phase measurements at twice the maximum atmospheric fluctuation frequency.

Assuming a four step algorithm, the phase at each output pixel is:

$$\phi = \tan^{-1}\left[\frac{I_4 - I_2}{I_1 - I_3}\right] \quad (1)$$

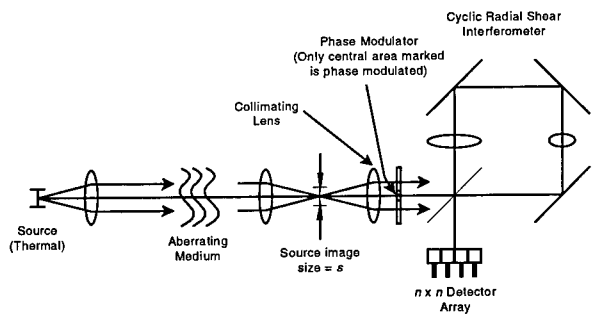

Aberration Measurement System

Figure 1

Where I_1, I_2, I_3, I_4 are the intensities in the four fringe images. We assume the photocurrent has the form: $I = I_A + I_B \cos\phi$, where I_A, I_B are constants for each phase measurement and it is then easy to show that the phase error is:

$$\Delta\phi = \Delta I / \sqrt{2} I_B \quad (2)$$

Where ΔI is the noise at each step.

The noise arises from three sources: Shot noise on I_A, shot noise on the detector dark current I_D, and detector and amplifier noise which we represent by an equivalent noise current I_N. The RMS shot noise on current i is: $\Delta i = \sqrt{2ie\Delta f}$ where e is the electronic charge and Δf is the system bandwidth which in our case is 8 times the nominal maximum atmospheric frequency f_a, so the phase measurement error is given by:

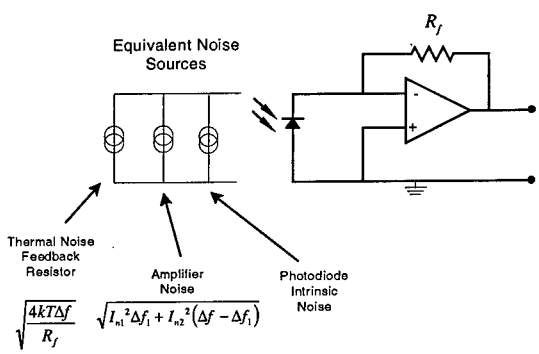

Photodiode Amplifier Input Stage

Figure 2

$$\Delta\phi = \frac{2\sqrt{f_a e(I_A + I_D + I_N)}}{I_B} \quad (3)$$

It now remains to determine I_A, I_B, I_D and I_N

In Figure 1, we assume that the beamsplitter has equal intensity transmission and reflection coefficients of value R, and the lateral magnification of the radial shearing telescope is M. If the total optical power entering the interferometer is

P_{in}, then the output beam powers are $M^2 P_{in} E R^2$ and $P_{in} E R^2 / M^2$, where E is the optical system efficiency. For a black body source, geometry gives P_{in} to be:

$$P_{in} = \frac{\pi}{32}\frac{s^2}{F^2}\int P(\lambda)d\lambda \qquad (4)$$

where s is the size of the source image, F is the F/No. of the collimating lens, and $P(\lambda)$ is the Planck radiation law.

If the interferometer were operating in monochromatic light, the interferometer equation: $Iout = I_1 + I_2 + 2\sqrt{I_1 I_2}\cos(\phi)$ would hold. However, our interferometer operates in white light, and temporal coherence reduces fringe contrast at large path differences. We therefore write the interferometer equation as: $Iout = I_1 + I_2 + 2\sqrt{I_1 I_2}\gamma(x)\cos(\phi)$ where $\gamma(x)$ is the coherence envelope and x is path difference[5]. Note that spatial coherence effects with radial shear reduce fringe contrast at the field edges. However, we initially assume that the interferometer is at zero path difference and consider a point at field centre so the interfering beams are fully coherent. With n^2 detectors, the constant part of each detector current is:

$$I_A = \left(M^2 + \frac{1}{M^2}\right)\frac{ER^2}{n^2}\frac{\pi}{32}\frac{s^2}{F^2}\int P(\lambda)S(\lambda)d\lambda \qquad (5)$$

and the varying part is:

$$I_B = \frac{2ER^2}{n^2}\frac{\pi}{32}\frac{s^2}{F^2}\int P(\lambda)S(\lambda)d\lambda \qquad (6)$$

where $S(\lambda)$ is the detector characteristic in A/W.

The allowable source image size, s, is set by coherence. We limit s so the spatial coherence between centre and edge at the input exceeds some value (>0.5). Assuming a square source and using the Citterte Van Zernike theorem, we write:

$$\gamma \approx \mathrm{sinc}\left(\frac{2\pi}{\lambda_m}\frac{s}{4F}\right) \geq 0.5 \qquad (7)$$

Where: $\gamma(x)$ is the degree of coherence between centre and edge-of-field

λ_m is the mean operating wavelength

Solving this, we find that: $\frac{s}{F} \leq \frac{7.6\lambda_m}{2\pi}$ and substituting into (6) and (7) we find:

$$I_A = \left(M^2 + \frac{1}{M^2}\right)\frac{ER^2}{n^2}\frac{57.76\lambda_m^2}{128\pi}\int P(\lambda)S(\lambda)d\lambda \qquad (8)$$

and:

$$I_B = \frac{2ER^2}{n^2}\frac{57.76\lambda_m^{\ 2}}{128\pi}\int P(\lambda)S(\lambda)d\lambda \qquad (9)$$

We note that as we move out from the centre of the field, spatial coherence effects from the finite source size cause the fringe contrast to decrease. As the path difference increases (large aberrations), temporal coherence causes further reduction in fringe contrast depending on the source spectrum. Both effects must be taken into account (see calculation results below).

The dark current I_D in Equ.3 is given by the manufacturer. We now find the equivalent noise current I_N from the detector amplifier first stage. Assuming a current-to-voltage converter (Figure 2), the total RMS input noise current is:

$$i_n = \sqrt{\frac{4kT}{R_f}\Delta f + I_{n1}^{\ 2}\Delta f_1 + I_{n2}^{\ 2}\left(\Delta f - \Delta f_1\right)} \qquad (10)$$

where k is Bolzmanns constant, T is the absolute temperature of the input amplifier, Δf $(= 8f_a)$ is the system bandwidth, and I_{n1}, I_{n2} are OP-Amp input noise currents per √Hz up to and above Δf_1.

We find the equivalent noise current I_N by equating to an equivalent shot noise:

$$\sqrt{2I_N e\Delta f} = \sqrt{\frac{4kT}{R_f}\Delta f + I_{n1}^{\ 2}\Delta f_1 + I_{n2}^{\ 2}\left(\Delta f - \Delta f_1\right)} \qquad (11)$$

Solving and substituting for Δf we find:

$$I_N = \frac{1}{2e}\left[\frac{4kT}{R_f} + \frac{I_{n1}^{\ 2}\Delta f_1}{8f_a} + \frac{I_{n2}^{\ 2}(8f_a - \Delta f_1}{8f_a}\right] \qquad (12)$$

In the calculations below, we found that the contribution of the third term in this expression (high frequency OP-Amp equivalent input noise current) always dominated the first two terms, and was also much greater than shot noise.

3 Calculation results - potential phase measurement accuracy

We can now estimate the phase accuracy as a function of source temperature. I_N is calculated from Equ. 12, I_D is estimated from photodiode data, and I_A, I_B are calculated from Equs. 8 and 9 respectively. In our calculations we assumed:

$T = 2000K - 4000K$, $R = 0.3$, $M = 2.5$, $f_a = 200Hz$, $n = 8$, $E = 1$, $F = 3$, $R_f = 100k\Omega$, $I_{n1} = 0.8\text{pA}/\sqrt{\text{Hz}}$ to $\Delta f_1 = 10Hz$,

$I_{n2} = 0.2\text{pA} / \sqrt{\text{Hz}}$ above $10Hz$ (OP07 Op-Amp), and $I_D = 10nA$.

Figure 3 shows the estimated phase error at the field centre (zero path difference, full coherence) as a function of source temperature. It is interesting to note that an error of <0.1 radian (~0.016λ) can be achieved at a source temperature of 3000K - possible with incandescent lamps. Further out in the field, the coherence falls and the phase error increases (Figure 4, phase error vs. position for a source temperature of 2700K). Even at the field edge (coherence is 0.5 here) the error is less than 0.25 radian.

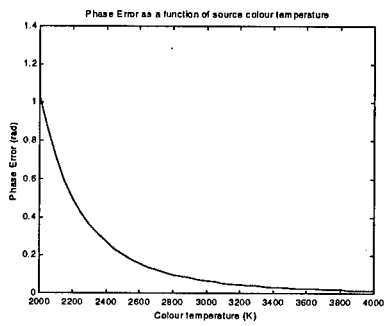

Figure 3

These figures are surprising given that the allowable source image size is only 3μm for the required coherence, and the system is making 400 phase calculations per second. We believe they are a reasonable estimate of limiting performance.

4 White light fringes

Phase stepping using white light fringes gives some interesting problems. White light phase stepping attempts to measure the fringe phase underneath white light coherence envelope[5]. Fringe contrast falls with increasing path difference and noise effects increase, causing larger phase errors. This is shown in Figure 5, where the error increases to ~π radians at 6μm path difference with source temperature =2700K. The system is best suited for correcting small aberrations. The varying coherence envelope also causes effective variation of I_B during stepping, and therefore an additional error. In our case this is small (<0.6 rad) and can be reduced further by stepping geometric phase in the interferometer[6].

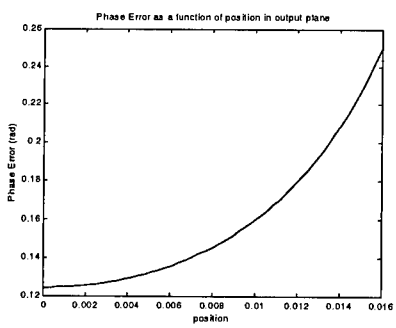

Figure 4

Finally, a systematic error arises from variation of effective fringe frequency with path difference. This only occurs when the source spectrum in wavenumber space is asymmetric (the case for nearly all broadband sources). Figure 6 shows the variation of measured phase with interferometer path difference in our system, and the error becomes larger than a wavelength at modest path differences. However, in a cyclic radial shearing interferometer the path difference is zero at the centre of

the field, and so a systematic correction can be applied working out from the centre of the field.

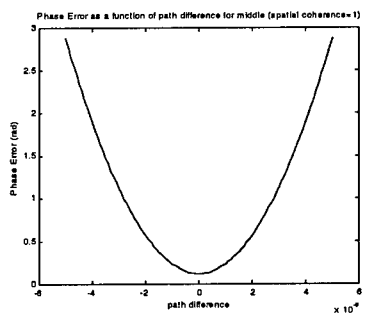

Figure 5

5 Conclusion

Surprisingly, it seems that phase stepping may be a viable technique for wavefront sensing in certain adaptive optics applications. It is clear that white-light phase-stepping must be used to achieve sufficient phase measurement accuracy if the source is thermal, but this should be possible with a cyclic radial shearing interferometer. The main limitations are set by spatial and temporal coherence effects, but calculations indicate that achievable phase measurement accuracy is still acceptable. Typical phase errors of order 0.6 rad should be achievable with source temperatures of 3000K or greater with an 8 x 8 detector array and system bandwidth up to 200Hz.

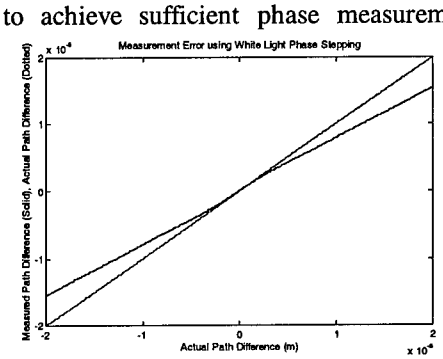

Figure 6

The use of white light phase stepping causes systematic errors in the phase measurement characteristic, which depend on the source spectrum. If a radial shearing interferometer is used, these errors can be compensated by working out from the zero path difference position at the centre of the fringe field.

The authors are grateful to the Marsden Fund of New Zealand for support during this work.

References

1. Hartmann J. 1900 *Instrumentenkunde* **20** 51 and: Hardy J.W. 1978, *Proc. Inst. Elect. Electron. Engrs.* **66** 651
2. Wyant J.C. 1976 *Appl. Opt.* **14** 2622
3. Barnes T.H., Eiju T., and Matsuda K. 1996 *Opt. Comm.* **132** 494
4. "Phase measurement interferometry techniques" K.Creath in *Progress in Optics* XXVI ed. E.Wolf 1988, 349
5. Hariharan P. and Roy M. 1994 *J. Mod. Opt.* **41** 2197
6. Hariharan P. and Roy M. 1995 *J. Mod. Opt.* **42** 2357

MULTI-PLANE IMAGING WITH A DISTORTED DIFFRACTION GRATING

P. M. BLANCHARD AND A. H. GREENAWAY

Electronics Sector, Defence Evaluation and Research Agency, St. Andrew's Road, Great Malvern, Worcs, WR14 3PS, UK

We describe a simple technique for imaging multiple layers within an object field simultaneously onto a single camera. The approach uses a binary diffraction grating in which the lines are distorted such that a different level of defocus is associated with each diffraction order. The design of the gratings is discussed and their ability to image multiple object planes is validated experimentally. The grating provides a simple and robust method of obtaining the multiple images required in a phase diversity wavefront sensing system. Incorporation of a grating into such a system is described.

1 Introduction

The imaging of multiple layers within an object field is useful in many applications including microscopy, medical imaging and data storage. The most common approach to recording such information is to re-focus physically the imaging system by moving a lens or the camera to generate a through-focal-series. However, in applications where the object or imaging conditions are rapidly changing a method for simultaneously capturing images from each layer is needed. One way of achieving this, whilst maintaining the full resolution and depth of field of the optics, is to use beamsplitters, however this leads to complex optical systems and the need for multiple and synchronised cameras. The use of a simple diffraction grating to divide the beam can simplify the optics, but multiple cameras are again needed to image the multiple layers in a snapshot.

This paper describes a technique in which the grating structure is distorted to allow its continued use as beamsplitter, whilst modifying its function to produce simultaneous images of multiple object planes on a single image plane camera. This leads to simple optics, reduced cost through the use of fewer cameras and automatic synchronisation of the multiple images.

2 The Principle

Local displacements of the lines in a diffraction grating can be used to introduce arbitrary phase shifts into the wavefronts diffracted into the non-zero orders. The basic principle (the 'detour phase effect') has been used to encode diffractive optics elements and computer generated holograms [1,2] and for phase calibration of an aperture synthesis array [3].

The local phase shift, $\phi_m(x,y)$, in light diffracted into the *m*th order is dependent on the amount of local grating shift through,

$$\phi_m(x,y) = \frac{2\pi m \Delta_x(x,y)}{d} \tag{1}$$

where d is the grating period and Δ_x is the displacement of the grating strips along the x-axis relative to their undistorted position (Figure 1b). All orders other than the zeroth undergo a phase shift which is linearly dependent on the grating displacement, and the phase shift is of equal magnitude but opposite sign in the positive and negative orders of the same coefficient.

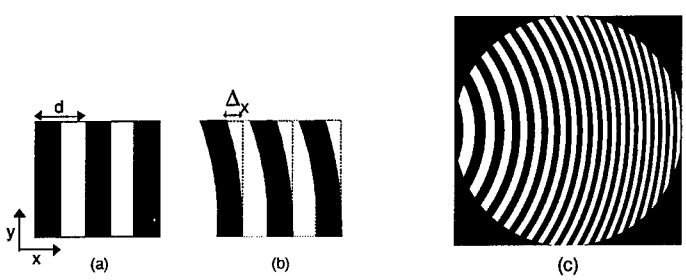

Figure 1 : a) Undistorted grating, (b)Grating displacement by Δ_x, (c) Grating distorted according to equation 2 with R=20d and W_{20}=3 λ

Our interest is in generating different levels of defocus in the wavefronts diffracted into each order. In the paraxial case, defocus is characterised by a phase shift, relative to the in-focus system, which varies as the square of the distance from the optical axis. A diffractive element combining the dual role of beamsplitter and defocus is achieved by encoding this quadratic phase shift into a grating by distorting its structure according to,

$$\Delta_x(x,y) = \frac{W_{20} d}{\lambda R^2}(x^2 + y^2) \tag{2}$$

where λ is the optical wavelength, x and y are Cartesian co-ordinates with an origin on the optical axis and R is the radius of the grating aperture. The parameter W_{20}, used here to define the defocusing power of the gratings, is the standard coefficient of defocus equivalent to the extra pathlength introduced at the edge of the aperture, in this case for the wavefront diffracted into the +1 order. Gratings distorted according to equation 2 consist of lines which are the arcs of circles (Figure 1c).

3 The Use of Distorted Gratings in Imaging Systems

The grating shown in Figure 1c has optical power in the non-zero orders. In practice it is convenient to use such gratings in close proximity to a lens, with the lens providing the majority of the focussing power and the grating effectively modifying the focal length of the lens. When such a grating is placed in contact with a lens of focal length f, the focal length of the combination in each diffraction order is given by,

$$f_m \approx \frac{f R^2}{R^2 + 2 f m W_{20}} \tag{3}$$

This multi-focal effect enables the imaging of multiple object planes into a single image plane, as illustrated in Figure 2. In this simple one lens system each image will have a slightly different magnification.

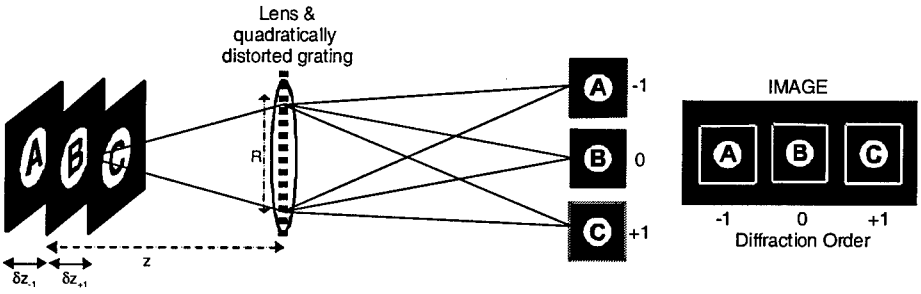

Figure 2 : Imaging of multiple object planes simultaneously unto a single image plane using a quadratically distorted diffraction grating.

The object plane spacings (δz_m) can be controlled by changing the grating power (W_{20}) according to,

$$\delta z_m = -\frac{2 m z^2 W_{20}}{R^2 + 2 m z W_{20}}, \tag{4}$$

where z is the distance from the central object plane to the primary principle plane of the optical system.

This distorted grating approach has the advantages that the full resolution and depth of focus of the optical system (without the grating) is maintained when the grating is added and that images of multiple planes can be measured on a single camera in a snapshot using a simple optical arrangement.

4 Experimental Verification

The simultaneous imaging of three object planes was demonstrated experimentally using the system shown schematically in Figure 2, with an object consisting of masks of the letters A B and C located along the optical axis and spaced by ~4.8mm. A simple distorted binary amplitude grating was fabricated by laser printing the grating structure onto a piece of A4 paper and photographically reducing it onto a 35mm transparent slide. The grating ($W_{20}=10\lambda$, R=1cm, d=100μm) was in contact with a lens of focal length 12cm. The objects were illuminated from behind using a white light source and a filter with a 10nm wide bandpass centred at 650nm was placed in front of the CCD camera. The experimental results (Figure 3) show that the letter A is imaged into the –1 order, B is imaged into the zero order and C is imaged into the +1 order. This simple demonstration illustrates the power of the technique described in this paper.

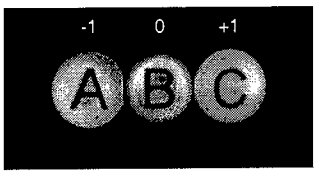

Figure 3 : Experimental image of 3 objects at different ranges. The images have been normalised by adjusting the grey level scaling in each diffraction order to equalise their peak intensities. The raw intensity in the three orders could be adjusted by using a phase rather than amplitude grating.

5 Application to Wavefront Sensing

Knowledge of the phase aberrations introduced by the atmosphere allows their correction using adaptive optics, whereby the conjugate of the measured wavefront is applied as a correction. We are interested in a wavefront sensing technique called phase diversity [4] which can be used with extended objects or scenes. The technique requires the collection of two or more images of the intensity distribution in two spatially separated planes in the vicinity of the entrance pupil of the instrument.

The two images used for phase diversity must be measured within a timescale in which the atmosphere is effectively stationary, hence a system that can image the two planes simultaneously is desirable. The technique described in the previous sections is therefore ideally suited to this application.

For phase diversity wavefront sensing using our 28cm diameter telescope the plane separation needs to be increased to the order of several hundred metres. This increase in plane separation leads to significant differences in magnification

between images, which can be overcome only by using an impractically long optical system. The optical system has therefore been modified and the distorted grating used in a different configuration, as shown in Figure 4.

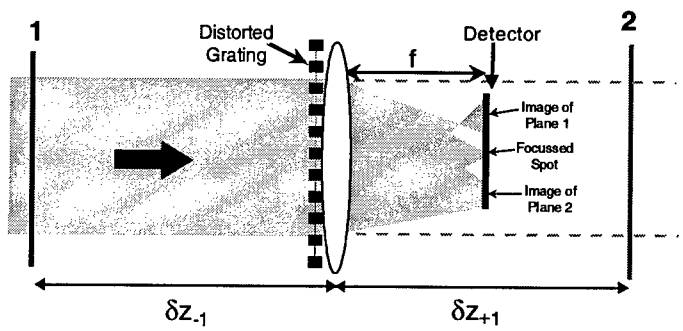

Figure 4 : Schematic of the optical system used for wavefront sensing

The camera is placed one focal length away from the lens, so as to record an image of an object at infinity. Addition of the defocus grating effectively decreases the focal length of the lens in the +1 diffraction order and increases its focal length in the –1 order. The object planes imaged into each non-zero diffraction order have locations (δz_m) and magnifications (M_m) given by,

$$\delta z_m = \frac{R^2}{2\,m\,W_{20}}, \qquad M_m = \frac{2\,m\,f\,W_{20}}{R^2} \tag{5}$$

This system therefore has the advantage that the images corresponding to the +1 and –1 diffraction orders correspond to object planes equal distances either side of the lens, and that the images have magnifications of equal magnitude (but opposite sign). In addition, the zero order can provide a direct image of the scene.

Such a system is currently being set up for the measurement of atmospheric turbulence over horizontal paths using a chrome-on-glass grating with $W_{20}=60\lambda$ and d=50μm. In this case, the grating/lens combination of Figure 4 is placed in a re-imaged telescope pupil plane and the +1 and –1 orders image planes approximately +/- 400m either side of the telescope pupil.

The ability of the system shown in Figure 4 to provide data suitable for the phase diversity algorithm has been tested in the laboratory by applying a variable amount of defocus to nominally collimated laser beam. A 1.5cm diameter laser beam was incident on a grating with $W_{20}=60\lambda$, R=7.5mm and d=30μm, adjacent to a 10cm focal length lens. With the laser beam accurately collimated the image in Figure 5b was recorded. This shows a focussed spot in the zero order and equal size

images of planes 74cm either side of the grating/lens. When a focus error is applied to the laser beam (or the camera is moved along the optical axis), the images in the non-zero orders change size in opposition, but do not change shape – as expected for pure defocus. The phase diversity calculation involves extracting and subtracting the +1 and –1 images, and multiplying the result by a pre-calculated matrix to generate the wavefront shape. The experiments have shown that defocus can be accurately measured in this way, and the ability to measure other aberrations has been demonstrated in simulations.

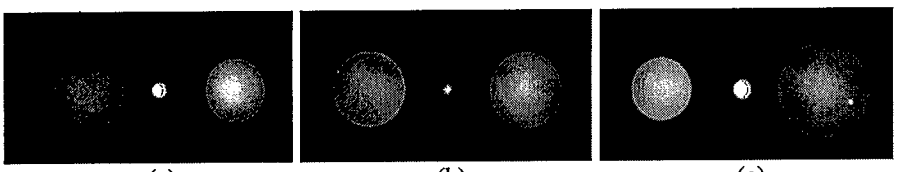

(a) (b) (c)

Figure 5 : Experimental images taken through the grating system of Figure 4 using a HeNe laser as teh source. Image (b) corresponds to a collimated input beam. Images (a) and (c) correspond to applied defocus of opposite sign.

6 Acknowledgements

This research is part of Technology Groups 1 (Acoustics, Magnetics & Hydrodynamics) of the MOD Corporate Research Programme. The authors would like to thank Simon Woods for his analysis of phase diversity data.

© British Crown copyright 1999. Published with the permission of the Defence Evaluation and Research Agency on behalf of the Controller of HMSO.

References

1. B. R. Brown and A. W. Lohmann, "Complex spatial filtering with binary masks," Appl. Opt. **5**, 967-969 (1966).
2. M. Li, A. Larsson, N. Eriksson, M. Hagberg and J Bengtsson, "Continuous-level phase-only computer-generated hologram realised by dislocated binary gratings," Opt. Lett. **21**, 1516-1518 (1996.)
3. P. M. Blanchard, A. H. Greenaway, R. N. Anderton and R Appleby, "Phase calibration of arrays at optical and millimeter wavelengths," J. Opt. Soc. Am. A **13**, 1593-1600 (1996).
4. R A Gonsalves, 'Phase retrieval and diversity in adaptive optics', Opt. Eng. **21**, 829-832 (1982).

Adaptive Systems

A LOW COST ADAPTIVE OPTICAL SYSTEM

C. PATERSON, I. MUNRO AND J. C. DAINTY
Applied Optics, The Blackett Laboratory, Imperial College of Science, Technology and Medicine, London, SW7 2BZ, UK
E-mail:carlp@ic.ac.uk

A low cost adaptive optics system with an open loop frame of several hundreds of frames per second, using a single processor is described. It is constructed almost entirely of commercially available components. The construction of the system, its control and performance are discussed.

1 Introduction

Until recently, all adaptive optics (AO) systems with reasonable spatial and temporal bandwidths (> few Hz and 10–100 spatial order correction) have been extremely expensive with component costs in excess of £10^5, and have consequently been limited to military and astronomical applications. If adaptive optics is to find applications in industry and medicine, the cost of the systems must be reduced by orders of magnitude. This can be achieved by using commercially available components.

2 Description of the system

Figure 1 shows a schematic of the system. The tip-tilt mirror, membrane mirror and Shack–Hartmann lenslet array all lie in planes conjugate to the input pupil. However, since these components are potentially all of different working diameters, $4f$ relay optics have been used to re-image the optical pupil. Although the beamsplitter near the entrance pupil adds to the complexity of the system and significantly reduces its light efficiency, it also adds flexibility. It is a simple matter to substitute different deformable mirrors just by replacing the mirror and one of the lenses in the relay arm.

The tip-tilt mirror (Physik Instrumente Model E610.00), for the purpose of the experiments described in this paper, was switched off and acted as a passive beam-steering mirror. Thus all correction was in fact carried out by the electrostatic membrane mirror. This was supplied by Delft TU (commercially available) and has a circular membrane of diameter 15 mm with 37 close-packed hexagonal electrodes. Conjugate to these two mirrors is the Shack–Hartmann lenslet array (CSEM Zurich) of the wavefront sensor, which consists of 0.2 mm square lenslets of focal length 25 mm. The detector cam-

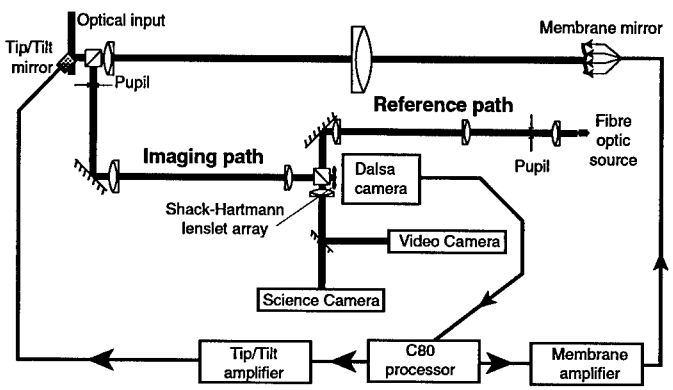

Figure 1. System setup

era is a high speed CCD (DALSA CA-D1-0128A) with 128x128 16 μm square pixels, which has a maximum frame rate of about 800 Hz. The reference path provides a near diffraction limited plane wave to calibrate the zero-offset positions of the Shack–Hartmann spots on the CCD camera.

The wavefront sensor data from the CCD camera are collected by a Bitflow RoadRunner framegrabber and transferred to the C80 digital signal processor board, which processes them to produce the required actuator signals to be applied to the deformable mirror(s), which are converted to voltages by a 40-channel D/A and low-current analogue amplifier system (Thomson-CSF). The output is recorded by video or the science camera (Starlight Xpress SX).

3 Spatial control of the membrane mirror

The ability of the AO system to correct a given static aberration is limited primarily by the deformable mirror. The membrane mirror is a modal device and the deformations are by no means orthogonal. A principle components analysis (singular value decomposition[1]) of the mirror's influence function gives quantitative information about its ability to correct static aberrations.

For a given set of actuator signals, represented by the vector $\mathbf{x}_m$, the effect of the resulting mirror deformation on the reflected wavefront is given by

$$\phi_{\mathrm{m}} = \mathbf{A}_{\mathrm{m}}\mathbf{x}_{\mathrm{m}} \tag{1}$$

where $\mathbf{A}_{\mathrm{m}}$ is the matrix representing the influence functions of the mirror [2]. Conversely, the actuator signals which produce a least-squares best fit to a

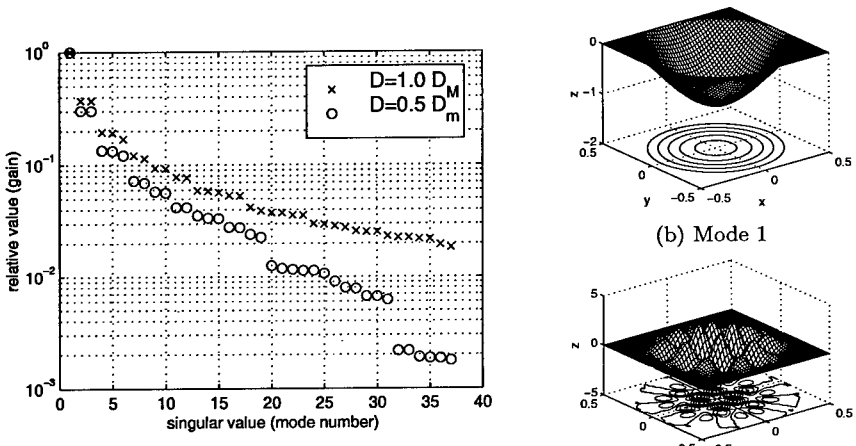

(a) Plot of relative singular values

(b) Mode 1

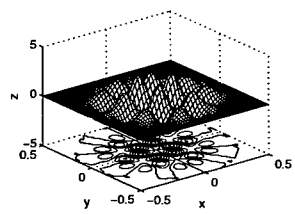

(c) Mode 37

Figure 2. The orthogonal modes of the membrane mirror

required wavefront change ϕ_0 is given by

$$\mathbf{x}_0 = \mathbf{A}_\mathrm{m}^{-1}\phi_0 \tag{2}$$

where $\mathbf{A}_\mathrm{m}^{-1} = \mathbf{V}\mathbf{S}^{-1}\mathbf{U}^\mathrm{T}$ is the pseudo-inverse of $\mathbf{A}_\mathrm{m} = \mathbf{U}\mathbf{S}\mathbf{V}^\mathrm{T}$. The columns of matrices $\mathbf{U}$ and $\mathbf{V}$ make up orthonormal sets of the possible mirror deformations and actuator signals respectively, which can be thought of as the spatial 'modes' of the mirror. The diagonals of $\mathbf{S}$ are the singular values and represent the 'gains' of the different modes, i.e., how much of each deformation mode results from unit of its corresponding actuator signal mode. These singular values, and in particular the range of values (the condition), give a measure of the controllability of the mirror: the larger the singular value the easier it is to produce that deformation mode.

Fig. 2 shows plots of the singular values for two different optical pupil sizes D and those modes corresponding to the largest (mode 1) and smallest (mode 37) singular values for $D = D_\mathrm{m}$, where D_m is the membrane diameter.

In a real system it is important to limit the range of these singular values, which can be done by discarding modes with the smallest gains. These modes not only swamp the control matrix resulting in large actuator signals which have to be clipped, but can also be very sensitive to noise in the wavefront sensor. Since the membrane deformation is zero at its edge, it is necessary to choose the optical pupil to be smaller than the membrane in order to correct for aberrations which are non-zero at the pupil boundary.

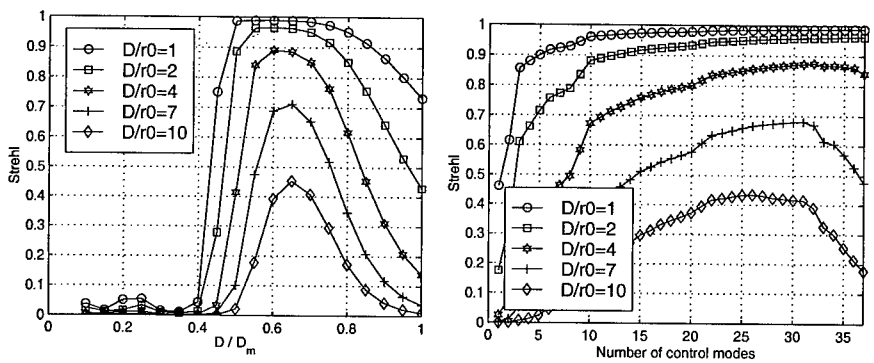

(a) Strehl v. optical pupil

(b) Strehl v. number of spatial modes (for $D = 0.55D_m$)

Figure 3. Mean Strehl ($S = e^{-<\phi^2>}$) correcting for Kolmogorov turbulence using the membrane mirror. (Monte Carlo with $\lambda = 633\,\text{nm}$, maximum actuator voltage $V_{\text{max}} = 200\,\text{V}$, maximum membrane deflection was $7.5\,\mu\text{m}$ with all electrodes set to V_{max})

Monte–Carlo simulations have been performed for phase aberrations produced by different strengths of Kolmogorov atmospheric turbulence using least-squares correction and clipping of the actuator signals. Fig. 3 shows the resulting mean Strehl (using the approximation to Strehl $S = e^{-<\phi^2>}$) for (a) different optical pupil diameters and (b) different numbers of spatial modes. The optimum choice of optical pupil diameter is $D \approx 0.65D_{\text{m}}$. Note that as the aberrations become stronger, better correction can be obtained by discarding more of the spatial control modes.

4 System control

The closed loop control of the system uses a simple integrator (the gain was set to -0.6 for the experimental results below). The spatial control matrix for the system was calculated online. Each mirror actuator was varied (poked) in turn and the effect on the output of the wavefront sensor recorded. In this way, the mirror–sensor response matrix was built up. The system control matrix was calculated by least-squares pseudo-inverting the response matrix as described above, discarding those modes necessary to reduce the condition factor of the system. Although this technique is is not optimal, it does avoid the need for a direct wavefront reconstructor, simplifying the system. The number of modes to discard was determined experimentally as described below.

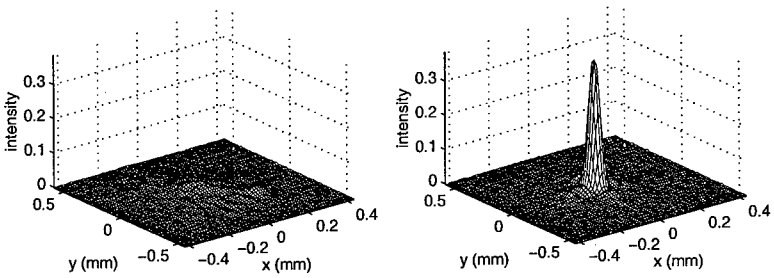

(a) AO system off (b) AO system on

Figure 4. Point source image through Kolmogorov turbulence ($D/r_0 = 5$, 4sec exposure)

5 Performance of the system

The dynamic performance of the system has been investigated using a wavefront generator based on the use of a ferroelectric 256x256 pixel spatial light modulator[3]. This was used to generate different time-varying wavefronts with quasi-Kolmogorov aberrations[4] simulating the effect of a single layer of 'frozen' turbulence travelling with an effective wind speed v. The ratio v/r_0, where r_0 is the Fried parameter gives a measure of the speed at which the aberrations are changing. Long exposures recorded with the science camera (fig. 4) were used to calculate the Strehl ratios of the corrected and uncorrected outputs.

Figs. 5(a-c) shows the resulting Strehl ratios for different strengths and speeds of Kolmogorov turbulence for both the system on and off. These results show that the system is capable of improving the Strehl ratio at wind speeds of up to about $v/r_0 \approx 100\,\mathrm{Hz}$ Fig. 5(d) shows the effect of discarding spatial modes from the system control matrix. Optimum performance in this case can be achieved by using 20–25 of the available 37 modes.

6 Conclusions

A low-cost, high-speed, reasonably high spatial order AO system based almost entirely on commercially available components has been demonstrated (total cost UK£20K). The dynamic performance of the system has been tested using Kolmogorov turbulence aberrations (generated using an SLM wavefront signal generator). It has been shown that discarding some of the spatial control modes of the system improves the performance of the system. The system is flexible to enable different deformable mirrors, wavefront sensors and control systems to be investigated. A number of improvements are currently being

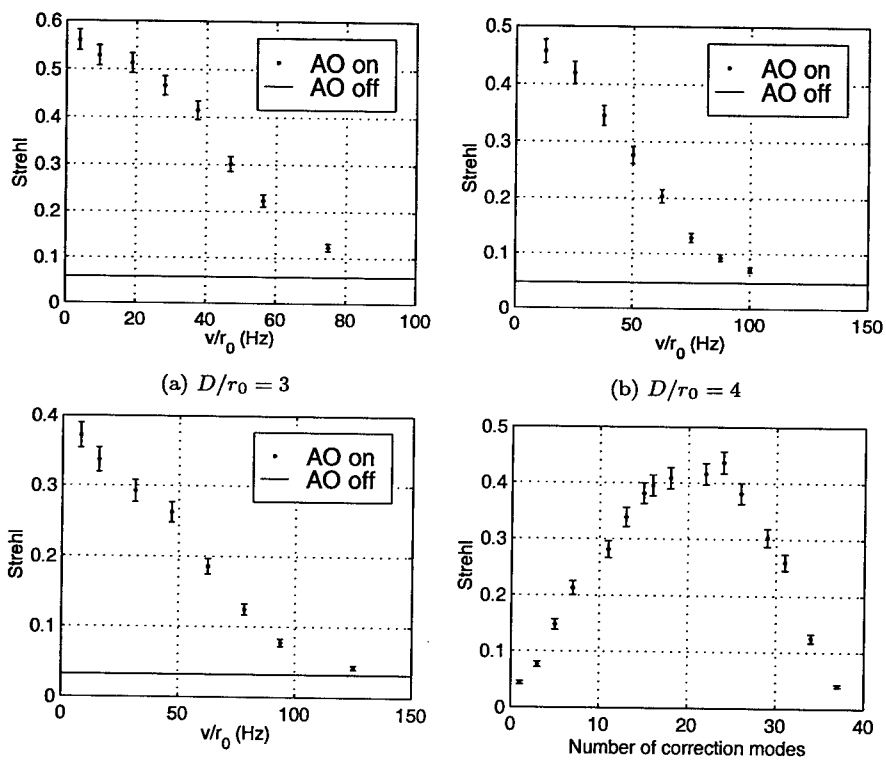

(a) $D/r_0 = 3$ (b) $D/r_0 = 4$

(c) $D/r_0 = 5$ (d) $D/r_0 = 4$, $v/r_0 = 50\,\mathrm{Hz}$

Figure 5. Experimental performance of the system (measured as Strehl) for Kolmogorov turbulence of different strengths and wind speeds

investigated—specifically increasing the open-loop frame rate of the system and trying more advanced spatial and temporal control.

References

1. B. P. Flannery et al, Numerical Recipes in C , CUP (1993).
2. R. K. Tyson, Principles of Adaptive Optics , Academic Press (1998)
3. M. A. A. Neil et al, Opt. Lett. **23**, 1849 (1998).
4. A. Glindemann et al, J. Mod. Opt. **40**, 2381 (1993)

This work was funded by the UK EPSCR with additional support from Spectron Laser Systems, Pilkington Technology Centre and the EU(MOSIS).

ANALOGUE CORRECTION FOR DISTORTIONS USING DYNAMIC HOLOGRAMS IN OPTICALLY ADDRESSED LIQUID CRYSTAL MODULATORS

VLADIMIR A.BERENBERG, ALEXEY A.LESHCHEV,
MICHAEL V.VASIL'EV, VLADIMIR YU.VENEDIKTOV,

199034, Research Institute for Laser Physics, Birzhevaya, 12, St.-Petersburg, Russia.
Phone: (812) 328-10-93. Fax: (812) 328-58-91. E-mail: vened@ilph.spb.su

We describe the results of series of experiments on the dynamic holographic correction for distortions in the wide spectral range of visible light. The hologram-corrector was recorded in optically addressed liquid crystal spatial light modulator by pulsed radiation and was read out in the scheme of one-way image correction by the incoherent wide spectral band radiation of the thermal source. The performance of the system with the holographic corrector was evaluated in standard optical terms of frequency\contrast characteristics.

1 One-way imaging

One-way image correction scheme (see Fig.1) employs the method of holography to high-quality imaging through some distorting media and (or) with the use of some poor-quality optical schemes [1,2]. Such an approach, which is also known as the method of phase subtraction, is based on recording the hologram of distortions as the pattern of interference of the probe wave, distorted by the said medium or system, with the non-distorted reference wave. Illuminated by the same distorted probe wave, this hologram reconstructs the non-distorted reference wave. If the probe wave was emitted by some point source, this reconstructed reference wave can be treated as an image of this point source, and the said hologram represents the phase corrector of distortions. Such an element can subtract not only the distortions of the image of this point source, but also the distortions of images of some other points or objects in the vicinity of this point source.

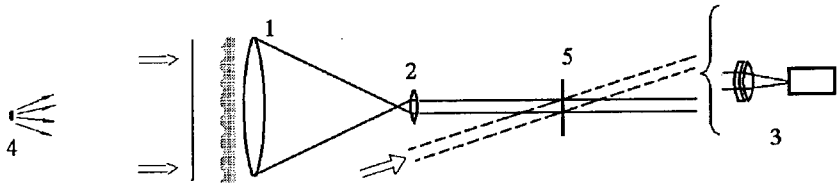

Figure 1. One-way holographic image correction. In the Figure: 1 – distorted optical system (lens) to be corrected, 2 – eye-piece, 3 – system of image registration, 4 – imaged object and source of coherent radiation for hologram record, 5 – hologram.

Such a holographic corrector can be used not only at the wavelength of the hologram record λ, but also within some finite spectral band ($\lambda \pm \Delta\lambda$). In this case, however, there are observed several kinds of chromatic effects. The first one is caused by the dependence of the angle of diffraction on the hologram-corrector upon the radiation wavelength. In other words, the hologram expands the radiation from the imaged object to its spectrum. This problem can be easily solved by the use of the auxiliary diffraction grating, which recombines all the spectral components into a collinear beam [3]. Next, if one uses the volume (thick) hologram as a corrector, there is observed the well-known effect of spectral selectivity [4] due to the violation of Bragg conditions. Thin (plain) holograms are free of this effect. One more chromatic effect is as following. If the hologram was recorded at one wavelength λ and reconstructed at the shifted wavelength $\lambda+\Delta\lambda$, the phase distortions φ are subtracted not completely, but only down to some residual level, equal to $(\Delta\lambda/\lambda)\varphi$ of the primary level of distortions.

2 Dynamic holographic correction

The progress in the field of the dynamic (real-time) holography made it possible to realise the similar schematics of phase subtraction in a real time regime. To this moment were published several experiments with the dynamic holographic correction of distortions in the schemes of one-way imaging with phase subtraction [5-10] and in the similar scheme of the telescopes with the proximal beacon [11-15]. The optically addressed liquid crystal spatial light modulators (OA LC SLMs) seem to be the most appropriate devices for the record of hologram-corrector [5]. These devices [16] have the sandwich-like structure, containing the layers of semiconductor (photoconductor - PC) and of liquid crystal (LC). The PC layer is exposed by some image; it can be the interference pattern of two waves, recording the hologram. The photoinduced charge carriers modify the electric field in the LC layer. This modification results in re-orientation of the LC molecules and thus in the modification of optical properties of LC, and thus the dynamic hologram is recorded. Its diffraction efficiency can be rather high – close to the theory limit; recently we have shown the OA LCSLM elements with the diffraction efficiency of ~20-30 % for the non-polarised radiation [17].

In the previous experiments [5,6,13] it was shown that the dynamic holograms, recorded in OA LC SLM, provide the efficient correction of distortions in the coherent or in the narrow band incoherent radiation. We report the first to our knowledge experiment with the wide-spectral band imaging in the scheme of phase subtraction in dynamic hologram, recorded in OA LC SLM. The quality of the corrected image of the standard test chart was evaluated in quantitative terms of dependence of the image contrast vs. spatial frequency.

3 Experimental results

Dynamic holograms in our experiments were recorded in LC SLM elements, using the polymer photoconductor [18]. Diameter of holograms in these experiments was equal 15 mm. S-effect [19] was used for the hologram record in SLM with the nematic LC (NLC), and in the case of ferroelectric LC (FLC) we have used the DHF-effect [20,21]. Holograms were recorded by pulsed radiation [22,23] of second harmonics of Nd:YAP laser (0.54 μm). After transient period the hologram revealed itself and could be read by incoherent radiation from the thermal source. The repetition rate of hologram renewal can be rather high (some 100-1000 Hz), but we have evaluated the optical performance in a single-shot mode of action. The diffraction efficiency of the holograms, recorded in NLC SLMs, was equal nearly 30% for the linearly polarised radiation. The holograms, recorded in FLC SLM, revealed slightly smaller diffraction efficiency (some 20-25%), but for both polarisations [17], so these elements provided higher total efficiency for observations in the non-polarised radiation of the tungsten lamp. From the optical point of view the performance of both elements was practically one and the same.

The experiment consisted of two stages. First we have shown the wide-spectral band correction in one-way imaging scheme. Dashed test-object, positioned in the infinity, was imaged in the light of tungsten lamp by the optical system, containing the distorted primary lens (aperture 15 mm, focal length 230 mm). This lens was distorted by the etched glass plate. In the Fig.2a is shown the interferogram of the "strongest" distorter, diverging the beam up to ~ 0.006 radian (FWHM), i.e. in ~ 70 times more than the diffraction limited divergence. The hologram of these distortions was recorded in OA LC SLM, mounted in the plain, to which the eyepiece was imaging the distorted lens. It was recorded by the coherent radiation from the point source in the vicinity of the imaged object; the spatial carrier of this hologram was equal $95mm^{-1}$. Static holographic grating recombined the spectral components of the image, which was registered at CCD-matrix and processed. In the Fig.2b are shown the dependencies of the image contrast, measured as $K = \{Imax - Imin\} / \{Imax + Imin\}$ (here Imax and Imin correspond to the maximal and minimal exposition in the image) vs. the spatial frequency of dashes in the object. In the same Figure are shown the curves for the diffraction-limited case and for our system without distorter (it was slightly worse due to the aberrations and to the own distortions of the LC SLM element). When the distortions were introduced, but not corrected, even the smallest spatial frequencies of the dashed test object were not resolved. Imaging was made in green, red and white light. One can see from this Figure that in the green range of spectrum (bandwidth ~50 nm) the correction fidelity was practically ideal; for the red radiation it was deteriorated due to the above mentioned chromatic residual error, but yet was pretty good. Imaging in the overall visible spectrum has shown some intermediate results.

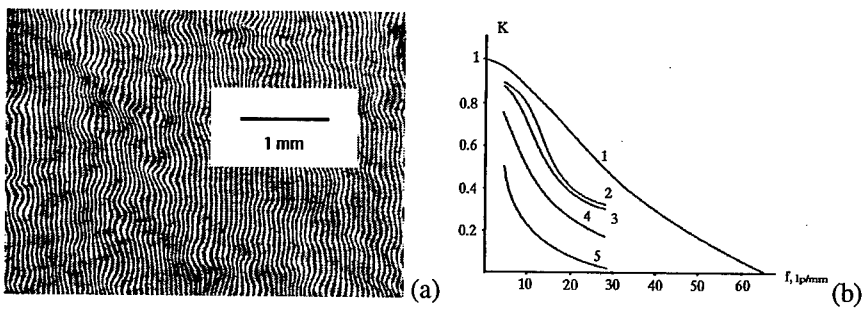

Figure 2. (a) Interferogram of the distorting plate (extra divergence 0.006 rad). (b) Frequency\contrast characteristics, measured for the distorting plate, shown in Fig.2a. 1 – performance of diffraction limited system [24], 2 – performance of the real system without distortions, 3,4,5 – imaging with correction for distortions: 3 – in green light (spectral bandwidth 50 nm, centred at 530 nm), 4 –in natural light of tungsten lamp, 5 –in red light (spectral bandwidth 50 nm, centred at 640 nm)

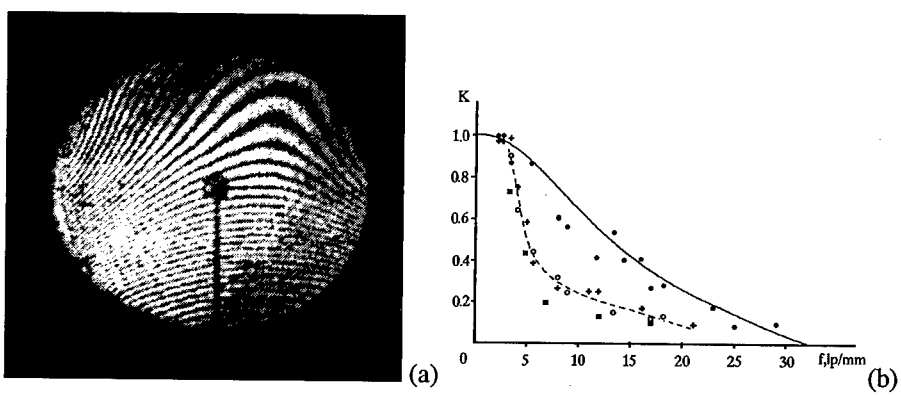

Figure 3. (a) Interferogram of the deformed mirror, recorded at λ=0.54 μm (b) Measured values of frequency\contrast characteristics of telescope with such mirror. Solid line – diffraction limited system, solid dots – zero diffraction order with non-distorted primary; hollow circles – system with "correction" and non-distorted primary, crosses – system with distorted primary and correction (bandwidth 50 nm centred at 540 nm), squares – system with distorted primary and correction (bandwidth 75 nm centred at 565 nm).

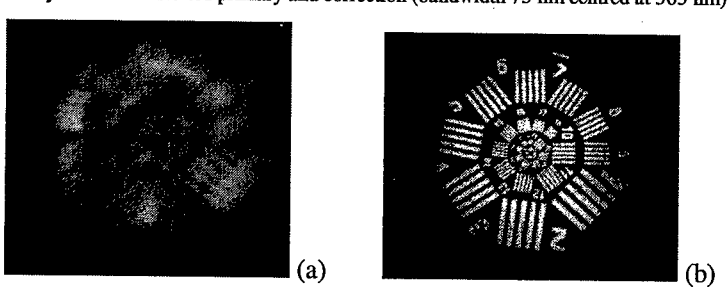

Figure 4. Image of standard test-object without correction of with the distorted primary (a) and with correction (b).

Then similar experiments were carried out in the scheme with proximal beacon. In this case the dynamic holographic correction was applied to the poor-quality primary mirror of model telescope (diameter 300 mm, curvature radius 2400 mm). We have used either the distorted solid mirror (see interferogram in Fig.3a) or the segmented mirror, whose segments had relative tilt and piston shift of ~ 2-3 μm. This telescope has imaged standard dashed test-object, placed at the distance of 17 m. Dynamic hologram of the primary's distortions was recorded from its centre of curvature. The radiation from the focal unit of the telescope passed through this corrector, where phase subtraction of distortions occurred. It was analysed in the same manner as on the first stage. In the Fig.3b is shown the frequency/contrast characteristic, measured in this scheme. Image without correction is shown in the Fig.4a, and that obtained with the correction in the spectral band with the width 50 nm centred nearby the wavelength of the hologram record at 530 nm is shown in the Fig.4b. One can see from the in Fig.3b (see dotted line), that in this case the performance of the system with correction was one and the same when the quality of primary was ideal (hollow circles) and when it was rather bad (crosses; the distortions are shown in the Fig.3a). It was slightly beyond the diffraction limit (solid line) due to the own distortions of the LC SLM substrata and due to the use of complicated optics, combining the channels of hologram record and of the telescope's focal unit. For the radiation with the wider and shifted band (squares) the correction fidelity was slightly deteriorated due to the above-mentioned chromatic effect.

4 Conclusions

We have realised in the experiment the one-way imaging and the proximal beacon schemes with the dynamic correction of distortions in the wide spectral band, using thin dynamic hologram in the optically addressed liquid crystal spatial light modulator. The quality of the image of the standard test-object was evaluated in quantitative terms of the image contrast dependence upon the spatial frequency. In the spectral band nearby the wavelength of the hologram record the fidelity of correction was practically ideal, and the influence of the distortions was eliminated completely. For the radiation with the significantly shifted wavelength and for the white light the fidelity of correction was deteriorated, but yet was pretty good.

5 Acknowledgements

The work was partly funded by the International Science and Technology Centre, grant #929.

References

1. J.Upatnieks, A.VanderLugt, and E.Leith, Appl.Opt. 5 (1966) 589.
2. H.Kogelnik and K.S.Pennington, J.Opt.Soc.Am. 58 (1968) 273.
3. C.B.Burckhart, Bell Syst.Tech.Journ. 45 (1966) 1841.
4. H.Kogelnik, Bell Syst.Tech.Journ.,48 (1966) 2909.
5. M.A.Kramer, C.J.Wetterer, Ty Martinez, Appl.Opt. 30 (1991) 3319.
6. S.Ma, D.Guthals, P.Hu, and B.Campbell, J.Opt.Soc.Amer. A11 (1994) 428.
7. S.A. Dimakov, S.I. Klimentiev, N.A. Sventsitskaya, V.E. Sherstobitov, Opt. Spektrosc. 80 (1996) 699 [Opt. Spektrosc. 80 (1996) 628].
8. Y.Sun, M.G.Moharam, Appl.Opt., 32 (1993) 1954.
9. J.D.Downie, Appl.Optics 33 (1994) 4353.
10. S.H.Chakmakjian, M.T.Gruneisen, K.Koch, M.Kramer, and V.Erch, Appl.Opt. 34 (1995) 1076.
11. A.A.Ageichik, O.G.Kotyayev, A.A.Leshchev et al. Proc.SPIE, 2771(1995)156.
12. M.P.Bogdanov, S.A.Dimakov, A.V.Gorlanov et al. Proc.SPIE, 3263(1998) 29.
13. M.T.Gruneisen, K.W.Peters, J.M.Wilkes, Proc.of SPIE, 3143 (1997) 171.
14. D.M.Guthals, D.Sox, M.D.Joswick, Proc.of SPIE, 3353 (1998) 106.
15. V.A.Berenberg, A.A.Leshchev, P.M.Semenov, M.V.Vasil'ev, V.Yu.Venediktov, Proc.of SPIE, 3353 (1998) 146.
16. C.Warde, A.D.Fisher, Spatial light modulators: applications and functional capabilities. In "Optical Signal Processing", J.L.Homer, ed., Academic Press, NY, 1987, p.477-523.
17. D.V.Wick, Ty Martinez, M.V.Wood, J.M.Wilkes, M.T.Gruneisen, V.A.Berenberg, M.V.Vasil'ev, A.P.Onokhov, Appl.Opt. (to be published).
18. M.A.Groznov, V.S. Myl'nicov, L.N. Soms, A.A. Tarasov, Zh.Tekn.Fiz. 57 (1987) 2041 [Sov.Phys.Tech.Phys. 32 (1987) 1233].
19. L.M.Blinov and V.G.Chigrinov, Electro-Optic Effects in Liquid Crystal Materials, Springer, New York, 1994.
20. L.A. Bereznev, L.M. Blinov, D.I. Dergachev, et al., Pis'ma Zh.Tekn.Fiz. 14 (1988) 260 [Sov.Techn.Fiz.Lett.14 (1988) 116].
21. I.Abdulhalim, G.Moddel, Mol.Cryst.Liq.Cryst. 200 (1991) 79.
22. N.V. Kamanina, L.N. Soms, and A.A. Tarasov, Opt. Spektrosc. 68 (1990) 691 [Opt. Spektrosc. 68 (1990) 403].
23. V.A.Berenberg, N.V.Kamanina, L.N.Soms, Izv.Akad. Nauk SSSR, Ser.Fiz. 55 (1991) 236 (in Russian).
24. M.Born, M.Wolf, Principles of Optics, Pergamon press, New York, 1964.

TWO-WAVELENGTH DYNAMIC HOLOGRAPHY AND ITS APPLICATION IN ADAPTIVE OPTICS

VLADIMIR YU.VENEDIKTOV, VLADIMIR A.BERENBERG,
ALEXEY A.LESHCHEV, MICHAEL V.VASIL'EV

199034, Research Institute for Laser Physics, Birzhevaya, 12, St.-Petersburg, Russia.
Phone: (812) 328-10-93. Fax: (812) 328-58-91. E-mail: vened@ilph.spb.su

MARK GRUNEISEN

Air Force Research Laboratory, AFB Kirtland, Albuquerque, NM, USA,
E-mail: gruneism@plk.af.mil

Two-wavelength holography, when the hologram is recorded at one wavelength and reconstructed at some shifted wavelength, is an efficient tool for many applications. Optically addressed liquid crystal spatial light modulators are very convenient for recording thin dynamic holograms and, in particular, for the purposes of the dynamic two-wavelength holography. On such a basis one can realise the dynamic interferometer, providing the arbitrary scaling of the wave front distortions. Such an interferometer can be of use for solution of some of the tasks of the adaptive optics, namely, for simplification of the procedure of measuring of the robust wavefront distortions, for recording of the dynamic holographic correctors, working in spectral ranges, where the direct holographic record is impossible, in particular, in mid-IR range of spectrum, and for extension of the range of distortions, which can be corrected by means of the phase valve, mounted in the negative optical feedback loop. We report the experimental realisation of such an interferometer.

1 Principles of two-wavelength holography

Two-wavelength holography is based on the following well-known property of hologram. Let the hologram be recorded in some medium as the interference pattern of some probe wave with the distortions $\varphi_1(x,y)$ and the non-distorted reference wave at the wavelength λ_1. Reconstruction of such a hologram by the non-distorted reference wave at the shifted wavelength λ_2 will result in reconstruction of the distorted probe wave, whose distortions will be reproduced in terms of wavelength, i.e. in terms of linear measure they will be scaled as $\varphi_2(x,y)=\lambda_2/\lambda_1\varphi_1(x,y)$. Similarly, reconstruction of the hologram by the probe wave at the shifted wavelength λ_2, bearing the same distortions $\varphi_1(x,y)$ as that of the recording probe wave, will result not in reconstruction of the non-distorted wave, but of the wave with the residual (differential between $\varphi_1(x,y)$ and $\varphi_2(x,y)$) distortions $\varphi'_2(x,y)=(|\lambda_2-\lambda_1|/\lambda_1)\varphi_1(x,y)=k\varphi_1(x,y)$. If $|\lambda_2-\lambda_1|<<\lambda_{1,2}$, then $k<<1$. So in both cases there is realised the scaling of the wavefront distortions, and the hologram serves as the converter of the distortion's magnitude. This effect, in particular, is the main reason, limiting the spectral bandwidth of imaging by the

so-called one-way imaging systems [1,2], where the distortions, introduced by some poor quality system, are subtracted from the image by means of diffraction of the distorted wave on the hologram of these distortions.

However, one can also obtain some positive effect of this scaling. For example, in the holographic interferometery there is widely used the so-called two-wavelength holographic interferometery of the large-scale objects [3,4]. In one and the same holographic plate are recorded two holograms of one and the same object at two wavelengths. Thin (plain) holograms, free of spectral and angular selectivity of the thick (volume, Bragg's) holograms, are especially convenient for these purposes. The spatial beats of these holograms (the moire pattern) are equivalent to the effective hologram of the same object, recorded at the effective wavelength $\Lambda_{eff}=\lambda_1\lambda_2/|\lambda_1-\lambda_2|$ [5,6], which is many times higher than the wavelengths of the recording waves. The spatial frequency of such effective hologram is much smaller than that of usual holograms, recorded in the visible range of spectrum, and thus analysis of the pattern is much simpler.

2 Possible applications of dynamic holographic converter

Recent progress in the field of the optically addressed liquid crystal spatial light modulators (OA LC SLM, [7], these elements comprise the sandwich-like structure, consisting of photoconductor layer, illuminated by some optical pattern and the adjacent layer of liquid crystal, whose optical properties are modified by the charge carriers, photogenerated in photoconductor), has made available the medium for the fast-response record of the efficient thin dynamic holograms [8], which was efficiently used for the dynamic correction purposes [9-13]. So now one has an opportunity to record the two-wavelength dynamic holograms and to use this technique for various purposes, including various tasks of the adaptive optics. At this moment we see at least three different areas of the adaptive optics, where the use of the dynamic holographic converter of the distortions' scale can provide the positive effect, namely:

1. Measuring of the robust wavefront distortions by means of real-time interferometery [14]. Namely, if one has to register (say, at CCD-matrix) the interferogram of large magnitude (many or many dozen wavelengths) distortions, he has to work with a very fine interferogram, i.e. to process a very large amount of information. Reading out of distortions at two wavelengths, and scaling them down to the said differential value makes it possible to get the required information (of course, with the smaller accuracy) from the much smaller number of CCD pixels.
2. Realisation of one-way imaging in mid-IR range of spectrum. Today the OA LC SLM elements can be addressed only by visible light, but the dynamic holograms of such kind can be read out by the mid-IR radiation [15,16]. So

one can record the hologram-corrector by the probe beam of visible light with the differential (scaled down) distortions. Such a hologram will be equivalent to the effective hologram, recorded by radiation with the wavelength Λ_{eff}.

3. Dynamic scaling of distortions makes it possible to solve the so-called 2π-problem of phase reconstruction from intensity distribution, which is, for instance, preventing wide use of negative optical feedback correction technique [17,18]. In this technique phase retardation in corrector is controlled by the interference pattern of non-distorted reference wave, combined co-axially with probe wave, which has collected distortions of the beamlet to be corrected and this corrector. System reaches the stationary state, when the corrector compensates for the distortions at the wavelength of its record. However, if the distortions' magnitude exceeds one wavelength, the corrector aperture splits into separate domains with the relative phase shift of 2π, preventing thus its use at significantly different wavelength. The use for these purposes of the scaled down differential probe wavefront [19,20] makes it possible to cope with much larger distortions with the magnitude of up to Λ_{eff}.

3 Experimental realisation of dynamic holographic converter

We report the experimental realisation of an interferometer with the dynamic holographic converter. The goal of the experiment was to confirm the idea and the feasibility of the method, i.e. the applicability of the beam, reconstructed by the dynamic hologram, recorded in OA LC SLM, for the interferometery applications.

The scheme of the experimental setup is shown in the Fig.1. In this experiment we have tested the holographic scaling of the distortions, imposed by the two-segmented mirror 1 with the relative tilt of its segments. The distortions of this element were read out by the pulsed green radiation of the second harmonics of the Q-switched Nd:YAP laser (λ_1= 0.54μm) 2. Its beam was expanded by the 10x-telescope 3 and split by the mirror 4 into the probe and the reference beams. The probe wave passed through the beam-splitting cube 5 and reflected from the two-segmented mirror 1. The reflected radiation has once passed through the cube 5 and through the 2x-telescope, comprised by lenses 6 and 7. In the plane, to which this telescope imaged the mirror 1, was mounted the OA LC SLM 8. Mirrors 9 and 10 sent the reference wave at the wavelength λ_1 to the same plane. The apertures 11(Ø30 mm) and 12(Ø15 mm), and the 50%-beamsplitters 4 and 5 provided the equality of the probe and the reference waves' intensities in the plane of OA LC SLM 8.

The dynamic hologram, recorded in SLM 8, was reconstructed by the CW radiation of He-Ne laser (λ_2 = 0.63μm) 13. The telescope 14 improved its spatial homogeneity. The mirror 15 splits the beam into the probe beam and the reference

beam. Optical system, comprised by the lenses 16 and 6 and by the folding mirror 17,

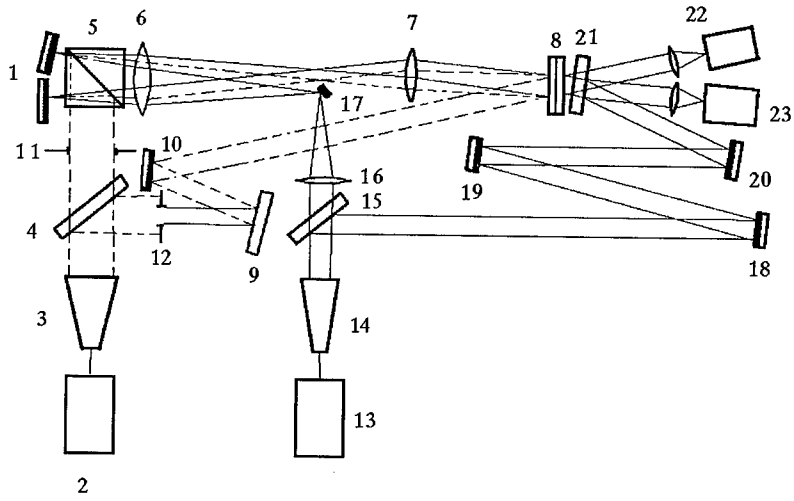

Figure 1. Experimental setup for investigation of dynamic holographic converter of distortions. 1 – two-segmented mirror, 2 – Nd:YAP laser with frequency conversion (λ_1=0.54μm), 3,14 – beam expanders, 4,15,21 – semitransparent mirrors, 5 – beam splitting cube, 6,7,16 – lenses, 8 – optically addressed liquid crystal modulator – dynamic holographic converter, 9,10,17,18,19,20 – mirrors, 11,12 – apertures, 13 – He-Ne laser (λ_2=0.633μm), 22,23 – CCD-cameras.

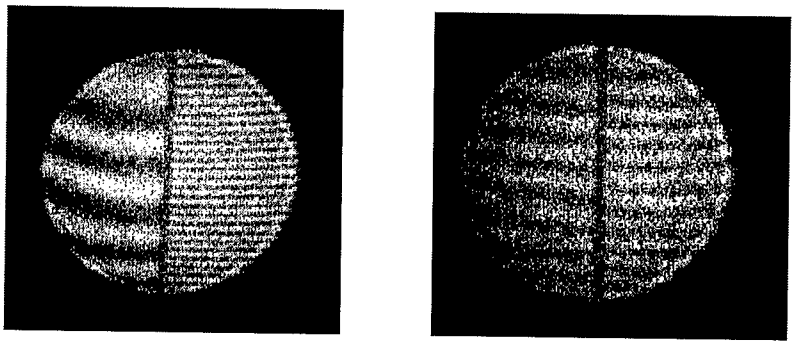

Figure 2. Interferograms of the zero (left) and first (right) orders of He-Ne laser beam diffraction on dynamic converter.

sent the probe beam of red light to the same two-component mirror 1. The angles of the green and the red beams incidence to the mirror 1 were very close (difference of 0.02 rad). So the shapes of the distorted wavefronts was practically the same for both probe beams. Red radiation, reflected by mirror 1, was focused by the lens 6, passed aside the mirror 17 and was collected by the lens 7. So it has reached the dynamic hologram, recorded in the OA LC SLM 8. The photoconductor of the OA LC SLM, used in our experiment, was not sensitive to red light of He-Ne laser, so its radiation has only read out the recorded hologram. The reference beam of He-Ne laser radiation passed through the delay line, comprised by the mirrors 18, 19 and 20. This delay line has equalised the lengths of optical paths of the probe and the reference beams with the accuracy of 1 cm.

The semitransparent mirror 21 reflected the reference beam of He-Ne laser. This mirror and the mirror 20 had two positions, providing registration of the interference pattern of the reference beam either with the beam of the first order of diffraction (CCD-camera 22) or with the beam of the zero order of diffraction (CCD-camera 23). So we had the possibility to register the interferogram of the probe beam, distorted by the mirror 1, and of the beam with scaled down distortions.

In the Fig.2(left) is shown the interferogram of the beam, going to the zero order of diffraction, i.e. just the interferogram of the two-segmented mirror. In the Fig.2(right) is shown the interferogram of the beam, going to the first order of diffraction. One can see the pretty good quality of these interferograms. Both interferograms correspond to the beams with the relative tilt around the horizontal axis. Comparing the right and the left sides of each interferogram, one can evaluate this relative tilt. The processing of two interferograms and comparison of the results has shown that the distortions magnitude was reduced 5.8 times, what well corresponds to the above given relationships.

4 Conclusion

We have realised in the experiment scaling down of distortions of the coherent radiation wavefront. The wave with reduced distortions was obtained by means of reading out by the distorted probe wave of the dynamic hologram in OA LC SLM, recorded at another wavelength by the probe wave with the same distortions. The measured scaling rate well correlates with the theory. The distortions' scaling can be useful for various applications in the adaptive optics, in particular, for:

- recording of the dynamic holographic correctors, working in spectral ranges, where laser sources for holographic record are unavailable, in particular, in mid-IR range of spectrum;
- extension of the range of distortions, which can be corrected by means of the phase valve, mounted in the negative optical feedback loop;

- simplification of the procedure of the measuring of the robust wavefront distortions.

5 Acknowledgements

The work was partly funded by the European Office of Aerospace Research and Development (EOARD), US Air Force.

References

1. J.Upatnieks, A.VanderLugt, and E.Leith. Appl.Opt. **5** (1966) 589.
2. H.Kogelnik and K.S.Pennington. J.Opt.Soc.Am. **58** (1968) 273.
3. K.A.Haines, B.P.Hildebrand. J.Opt.Soc.Am., **57** (1967) 155.
4. F.Weigl. Appl.Opt. **10** (1971) 187.
5. P.de Groot, S.Kishner. Appl.Opt., **30** (1991) 4026.
6. O.Sasaki, H.Sasazaki, T.Suzuki, **30** (1991) 4040.
7. C.Warde, A.D.Fisher, In "Optical Signal Processing", J.L.Homer, ed., Academic Press, NY, 1987, 477.
8. D.V.Wick, Ty Martinez, M.V.Wood, J.M.Wilkes, M.T.Gruneisen, V.A.Berenberg, M.V.Vasil'ev, and A.P.Onokhov, Appl.Opt. (to be published).
9. M.A.Kramer, C.J.Wetterer, Ty Martinez, Appl.Opt. **30** (1991) 3319.
10. S.Ma, D.Guthals, P.Hu, and B.Campbell, J.Opt.Soc.Amer. **A11** (1994) 428.
11. M.T.Gruneisen, K.W.Peters, and J.M.Wilkes, Proc.of SPIE, **3143** (1997) 171.
12. V.A.Berenberg, A.A.Leshchev, M.V.Vasil'ev et al. Proc.of SPIE, **3684** (1998) 1.
13. V.A.Berenberg, A.A.Leshchev, M.V.Vasil'ev, V.Yu.Venediktov. Analogous correction for distortions using dynamic holograms in optically addressed liquid crystal modulators, in this book.
14. M.A.Vorontsov, V.I.Shamlgausen. Principles of adaptive optics. Moscow, "Nauka", 1985 (in Russian).
15. U.Efron, S.T.Wu, J.Grinberg, L.D.Hess. Opt.Eng., **24**, 111 (1985)
16. S.T.Wu, U.Efron, J.Grinberg et al. Proc. of SPIE, **572** (1985).
17. M.A.Vorontzov, V.I.Shmalgauzen. Izvestiya VUZov. Seria Radiofizika, **25**, 1179, in Russian
18. M.A.Vorontzov, M.E.Kirakosyan, A.V.Larichev. Kvantovaya Elektronika, **18** (1991) 117, in Russian
19. V.Yu.Venediktov. Proc. of SPIE, **3219** (1997) 133.
20. V.Yu.Venediktov, V.A.Berenberg, N.A.Bezina et al. Proc.of SPIE, **3684** (1998) 45.

REVIEW OF WAVEFRONT MODULATORS AND SENSORS FOR ADAPTIVE OPTICS

N. COLLINGS

Photonics and Sensors, Dept of Engineering, University of Cambridge, UK

1 Introduction

It seems that inventing new ways of modulating light is one of the favourite pastimes of optical scientists. One reason may be that that it is a fascinating endeavour. There is no standard transducer and the field is wide open, in contrast to the case of sensing where the photodiode is commonplace. Another reason may be that the ideal wavefront modulator has not yet been found. Either the modulation depth is insufficient, or the actuators have hysteresis, or the spatial noise is too severe, or the device is too costly, etc. Moreover, the spatial modulation of the wavefront of a light beam is a critical test of any optoelectronic device. Inserting the device into a beam may degrade rather than improve the quality of the beam in a wavefront correction application. However, the advent of new fabrication technologies (eg MEMS, flat panel displays) has reduced the price of devices, and encouraged research on new applications. A promising application focus stimulates the improvement of devices, which then accelerates the journey to an ideal modulator.

The development of wavefront sensing has been less ambitious in scope but more profound in quality. A wavefront can be measured to a higher precision than the precision with which it can be reliably modulated. There is not much to choose between the precision of the different sensing techniques, and a concentration of products based on one technique (eg Hartmann-Shack sensing), testifies mainly to the facility with which the sensor hardware can be put in place and used, rather than the superiority of the technique.

The main commercial modulating devices and sensing systems will be reviewed in the context of finding a suitable combination which will satisfy the following criteria for a wavefront compensation module: 35 mm beam diameter; wavelength range from the UV to the far infra-red; reflective optics; modulation capability of 100 μm; overall losses less than 1 dB; and that it have no influence on the polarization of the light beam. It is also desirable to make it lightweight.

2 Wavefront modulators (WFMs)

The function of a wavefront modulator is to impart a variable deformation to a propagating wavefront, for example the accommodation produced by the lens of the eye. They act on the phase of the light beam and any amplitude modulation is secondary. Therefore, they are a subset of the class of spatial light modulators which includes amplitude modulating devices, such as displays. Wavefront modulators can be classified as either segmented or continuous, depending on whether the modulation generated by each actuator is local, or extends over neighbouring actuators. The pixellated liquid crystal spatial light modulators made by Meadowlark are examples of the former. The deformable membrane mirror of OKO Technologies is an example of the latter. Segmented devices produce a high frequency fixed pattern noise which is sometimes known as "punch through".

Comp/Uni	Type	N	d (µm)	Lay.	Speed (Hz)	Amp. (µm)	Advant.	Issues
Thermo Trex	SM	76	10000	Squ.	5 k	0.3	Modular	3-axis
Wright AFB[1]	DM	128	203	Squ.		0.3 (14V)	MEMS	Lenslets
Northrop-Grum. [2]	DM	1024	1000	Squ.		1 (40V)	MEMS	Planarity
Meadw[3]	LCD	69	2000	Hex.	26	0.633	Low V	IR abs.
Xinetic[4]	DM	349	7000	Squ.	100	4	Tested	Temp.
Boston Univ.[5]	DM	9	250	Squ.	66 k	0.4 (100V)	MEMS	Hysteres.
OKO Tech.[6]	DM	37	1750	Hex.	500	9	MEMS	Uniform
Cilas[7]	BM	31	15000	Conc.	1 k	15 (400V)	Tested	Hysteres.
Cilas[7]	SAM	185	8000	Squ.	1 k	5 (400V)	Tested	

Table 1.
Legend: Types SM: Segmented Mirror; DM: Deformable Mirror; LCD: Liquid Crystal Device; BM: Bimorph Mirror; SAM: Stacked Actuator Mirror; N: number of pixels; d: actuator separation; Hexagonal, Square, Concentric.

Table 1 shows a broad range of modulators (4 MEMS and 5 large devices) with published performance figures. In a number of cases a company can provide a range

of different product, usually by varying the number of actuators. The highest product in the range has been selected in each case for the Table, except in the case of the Meadowlark LCD where a 127-electrode product exists which has not, however, been characterized in the published literature. Liquid crystal devices work at low voltage, but are polarisation sensitive, absorb in the infrared, and their use is more lossy than mirrors. The MEMS devices have a smaller actuator separation and are cheaper.

It is also important to know what kind of aberrations can be corrected by the device. This can be estimated theoretically by computer modelling (eg finite element analysis) followed by modal decomposition of the influence functions in terms of, for example, Zernike polynomials. In order to measure the performance experimentally, the modulator is used to correct known aberrations, such as turbulence. If we confine the discussion to continuous mirror devices (ie all listed in the Table except for the Thermotrex and Meadowlark devices), there is an ideal rigidity of mirror for a given aberration. Where the aberration is Kolgomorov turbulence, a Gaussian influence function gives the best correction [8]. An example of this is the Itek mirror [9]. All concentric and hexagonal devices correct best the axi-symmetric aberrations, such as defocus and spherical aberration. The other low order aberrations are reasonably well corrected, and there is a gradual fall-off in performance as the order of aberration increases. Tip and tilt can be corrected at the expense of dynamic range for other aberrations. Therefore, they are preferably corrected with a separate tip/tilt mirror.

3 Wavefront sensors (WFSs)

In the laboratory it is usual to measure wavefront deformations with respect to a precisely defined reference wavefront. However, in adaptive optics, the deformed wavefront is measured either with a pre-calibrated instrument, such as the Shack-Hartmann (SH) sensor, or by applying a calibrated extra deformation to it and comparing "before" and "after". Examples of the latter are the shearing interferometer, the curvature sensor, and the phase diversity sensor. The commercial products listed in Table 2 are all SH sensors except for one curvature sensor. They are priced between $25k and $30, and of comparable performance. The SH sensors of Zeiss, Detect 16 marketed by Trioptics, and that of the University of Erlangen, Germany, employ centroiding algorithms with a spot positioning precision of 0.1 μm. The WFS-01 of Adaptive Optics Associates has a large dynamic range due to its capacity to track the focal spot for displacements outside the sub-aperture defined by the microlens.

The speeds of the sensors are not in the product literature for the CLAS-2D (Wavefront Sciences) and the curvature sensor (Laplacian). The WFS-01 has a frame rate of 30 Hz due to high speed acquisition from the CCD camera and effective post-processing algorithms. Extra processing power can be purchased for

the Zeiss SH sensor in order to achieve a speed of 25 Hz. Photonetics have recently announced a 1D SH sensor, the H-line, with a delay of 10 msec.

The curvature sensor measures wavfront curvature from intensity measurements in two planes on either side of the focal plane. In spite of the manufacturer's specifications, which are tighter for the SH sensors than the curvature sensor, theoretical [10] and experimental [11] studies have shown that the performance of SH and curvature sensors is comparable, with a slight advantage for the latter. However, the SH sensor is popular because it is easy to understand and has a lower hardware complexity.

Comp/ Uni	Type	N	Delay	WF slope min	WF slope max	Subap. diam. (μm)
Detect 16	SH	16x16	2 sec	λ/500	14λ	352
Erlangen	SH	24x24	2 sec	λ/500	116 λ	150
WFS-01	SH	72x72	33 ms	λ/100	400 λ	140
CLAS-2D	SH	44x33		λ/55	90λ	144
Laplacian	CS	20x20		λ/5	20 λ	600
H-LINE	1D SH	200	10 ms	λ/70	45 λ	140

Legend: SH: Shack Hartmann; CS: Curvature Sensing. $\lambda = 633$ nm.
N is number of sub-apertures

4 Discussion

None of the WFMs gives the modulation capability specified, although some may be custom engineered to do so. For example, the tension of the membrane in the deformable mirrors can be reduced and the distance to the actuator increased, so that the mirror produces larger deformations at comparable voltages. Although the MEMS devices are lightweight and cheap, there is sometimes a problem scaling them up to useful apertures. With the CCD based WFSs the aperture is also limited by the size of the CCD array.

5 Acknowledgements

I wish to thank Mr. Sigmund Manhart of Dornier Satellite Systems, who encouraged me to consolidate this review, and Professor R. Dandliker of the Institute of Microtechnology (IMT), University of Neuchatel, Switzerland, who assigned this review to me whilst I was working at the IMT.

References

1. Lee M.K. et al., Aberration-correction results from a segmented microelectromechanical deformable mirror and a refractive lenslet array, *Opt. Lett.* **23** (1998) pp. 645-647.
2. Burns B.E. et al., Silicon spatial light modulator fabrication, *Technical Digest of Spatial Light Modulator Conference*, Lake Tahoe (1997) pp. 87-89.
3. Love G.D., Wave-front correction and production of Zernike modes with a liquid-crystal spatial light modulator, *Appl. Opt.* **36** (1997) pp. 1517-1524.
4. Oppenheimer B.R. et al., Investigating a Xinetics Inc. deformable mirror, *Proc SPIE* **3126** (1997) pp. 569-579.
5. Bifano T.G. et al., Continuous-membrane surface-micromachined silicon deformable mirror, *Opt. Eng.* **36** (1997) pp. 1354-1359.
6. Vdovin G., Optimization-based operation of micromachined deformable mirrors, *Proc SPIE* **3353** (1998) pp. 902-909.
7. Product literature from Cilas, Marcoussis, France.
8. Hudgin R., Wave-front compensation error due to finite corrector-element size, *J. Opt. Soc. Am.* **67** (1977) pp. 393-395.
9. Olivier S.S. et al., Performance of adaptive optics at Lick Observatory, *Proc. SPIE* **2201** (1994) pp. 1110-1120.
10. Roddier F., Error propagation in a closed-loop adaptive optics system: a comparison between Shack-Hartmann and curvature sensors, *Opt. Comm.* **113** (1995) pp. 357-359.
11. Rigaut F. et al., Comparison of curvature-based and Shack-Hartmann-based adaptive optics for the Gemini telescope, *Appl.Opt.* **36** (1997) pp.2856-2868.

LIQUID CRYSTAL ACTIVE OPTICS CORRECTION USING EVOLUTIONARY ALGORITHMS

PHILIP BIRCH, CHRIS CHATWIN, RUPERT YOUNG, MARIA FARSARI
School of Engineering, University of Sussex, Brighton, E. Sussex. BN1 9QT UK
E-mail: p.m.birch@sussex.ac.uk

A method of finding a near optimum correction of a phase aberration is demonstrated. A liquid crystal spatial light modulator (SLM) is to be used as the corrective element and the phase screen applied to this is designed by an evolutionary algorithm. Evolutionary algorithms mimic biological evolution, where sets of trail solutions compete to reproduce and form the next generation. Only the best solutions survive. Each generation takes a step closer to a global optimum. This method requires no wavefront sensor, is easy to set up, and has a low cost

1 Introduction

The term "adaptive optics" usually refers to high-speed optical aberration correction (>10Hz) whilst "active optics" is for slower correction (<1Hz). Active optics is often used to correct for slowly varying aberrations caused by mechanical strains upon the optical components and mounting systems. This is commonly used to correct primary mirror distortions in telescopes, but may also be applicable in the lab when mechanical creep in optical mounts is unacceptable. Nematic liquid crystal SLMs potentially provide a low cost, lightweight and compact method of providing correction. In this paper a method of using a corrector such as an SLM with no wavefront sensor except for a Strehl ratio measurement is described. The phase shifts applied to the correcting element are calculated using an evolutionary algorithm.

2 Evolutionary Algorithms

Evolutionary algorithms [1] are a commonly used optimisation technique and can be broken into three main types: genetic algorithms (GA), evolutionary strategies [2] (ES), and evolutionary programming (EP). Genetic algorithms are the most well known out of the three. These algorithms were traditionally designed for binary optimisation, but in this application, we want to use real number values since a nematic liquid crystal SLM is capable of producing analogue phase shifts. The traditional real number problem optimisation algorithm is the evolutionary strategy method and so this technique will be used in this paper.

2.1 *Evolutionary Strategies*

The biological analogy behind an ES is as follows. The population consists of a set of vectors. Each vector represents an individual of the species; the elements of the vectors represent the phenotypic trait of the individuals (not the genes). Each of the individuals competes against each other, and the fittest individuals survive to sexually recombine to produce the next generation.

The basic algorithm for an ES is as follows:

1. Generate a set of μ parent vectors. These are usually taken as random numbers between the range of possible solutions.
2. Recombine the μ parents to produce λ offspring ($\lambda \geq \mu$). In this case two parents were chosen at random and the mean of each vector was used as the offspring. This was repeated until λ offspring were produced.
3. Mutate the offspring. If x_i is the ith element of an offspring vector, the mutated element x_i' is given by

$$\sigma_i' = \sigma_i \exp[\tau' \mathrm{N}(0,1) + \tau \mathrm{N}_i(0,1)] \qquad [1]$$

$$x_i' = x_i + \sigma_i' \mathrm{N}(0,1) \qquad [2]$$

where N(0,1) is a random number with normal distribution, σ_i is the mutation parameter of the previous generation, and

$$\tau = \frac{C}{\sqrt{2\sqrt{n}}} \qquad [3]$$

$$\tau' = \frac{C}{\sqrt{2n}} \qquad [4]$$

n is the number of elements in a vector and C is a constant, usually equal to 1.

4. Select the μ best offspring to be the next generation.
5. Return to step 2 using the new generation as the parents until some stopping criterion is reached.

3 Computer Simulations

The computer simulations of the system were carried out in Matlab™ on a Viglen Pentium II PC. To evaluate the fitness of the phase screens, a circular aperture was placed over them and this data was Fourier transformed to calculate the Strehl ratio.

3.1 *Static Zonal Correction*

The first simulation to be addressed was the static zonal correction. The phase screen and corrector were represented by a 16x16 array. Larger array sizes were also tried but took longer for the ES to run. The initial aberration was one wavelength of defocus aberration. The initial parent vectors were random numbers in the range 0 to 2π. Various values for μ and λ were tried. μ=1 and λ=1 stagnates before the solution is found. μ=5 and λ=25 appeared to produce the fastest correction.

Since the Strehl ratio, S, was used to as the fitness measurement an approximate value for the variance across the aperture can also be calculated. Equation [2] could then be replaced by

$$x_i' = x_i + C\sqrt{-\ln(S)}\,\mathrm{N}(0,1) \qquad [5]$$

This has the advantage over the previously described method in that as the algorithm approaches the best solution, the amount of search space is also decreased. Then when a new aberration is introduced the search space automatically increases. An example of the correction of an aberration is shown in figure 1. The mean line refers to the mean Strehl ratio applied in that generation. The maximum Strehl ratios and the minimum Strehl ratios are also shown.

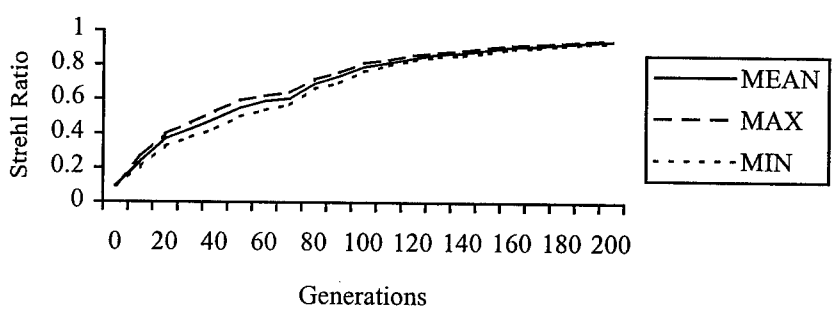

Figure 1. Correction versus generation number for a zonal correction. The mean, maximum, and minimum Strehl ratios applied for each generation are shown.

3.2 *Varying Aberration Zonal Correction*

The real time simulation was carried out by increasing the amount of defocus between each evaluation of the Strehl ratio. Results for a simulation of a linear increase in defocus over time and its correction are shown in figure 2. The aberration rate was 0.007 radians/generation.

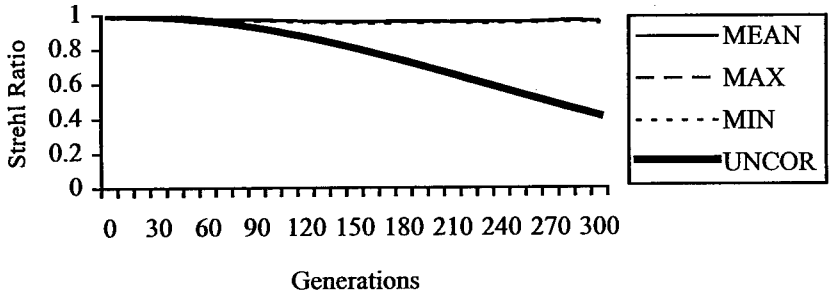

Figure 2. Varying aberration correction provided by the zonal ES method.UNCOR is the uncorrected Strehl ratio.

3.3 Static Modal Correction

Modal correction was achieved by optimising Zernike mode amplitudes that were mapped onto a 64x64 array. Correction for a defocus aberration only is shown in figure 3. Defocus, 2 astigmatisms, 2 comas and spherical correction is shown in figure 4. Tip and tilt were not corrected since these modes can be calculated from the position of the spot in the Fourier plane.

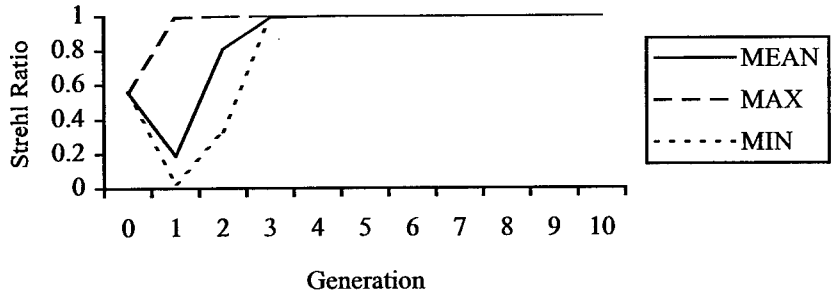

Figure 3. The correction of a defocus aberration over a number of generations. The mean Strehl ratio that is been applied is shown, along with the worst and the best case.

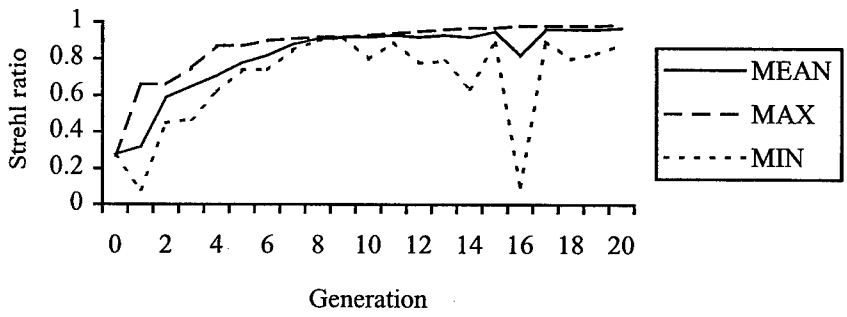

Figure 4 Correction of an aberration using defocus, astigmatism, coma, and spherical Zernike modes. The mean, maximum and minimum applied Strehl ratios are shown.

3.4 Varying Modal Correction

The static correction system was then modified so that defocus was added to the system. After the fourth generation of correction the amount of defocus was increased at a rate of 0.3 radians per generation. To simulate a realistic system this variation needed to be increased after each evaluation of the Strehl ratio, not just between each generation. Results for a typical correction are shown in figure 5. Reducing the aberration rate improves the performance.

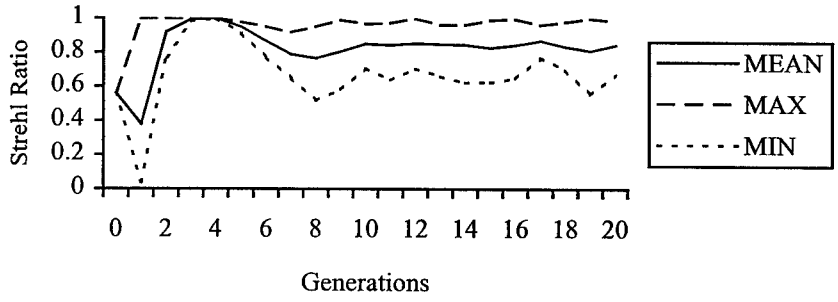

Figure 5. Correction of a time varying defocus aberration. The amplitude of the aberration changes with each measurement of the Strehl ratio.

4 Discussion

Zonal and modal correction based upon a modified ES technique have been demonstrated. Both of these methods provide correction of static and time varying aberrations. The choice of which system to use depends upon the application. The zonal method is much slower but this is due to its larger number of degrees of freedom. For correcting common optical aberration the first few Zernike modes may be adequate, especially if a high speed is required. Say, for example, that the Strehl ratio of a particular phase screen is measured video rate (25Hz). It takes 1 second to assess each generation. So the modal method has a clear time advantage (about 6s compared to 100s for the zonal method to reach a Strehl ratio of 80%).

5 Conclusion

An ES active optics system has been simulated. The potential possibilities of both static and time varying aberration correction have been shown. Both a modal and a zonal system have been shown.

6 Acknowledgements

We thank EPSRC ROPA (grant GR/L71230) for funding this work.

References

1. D. B. Fogel, "An Introduction to Simulated Evolutionary Optimization" IEEE Transactions on Neural Networks. **5** (1) pp3-14 (1994)
2. T. Bäck, F. Hoffmeister, "Basic aspects of evolution strategies." Statistics and Computing. **4** (2) pp 51-63 (1994)

THE ELECTRA ASTRONOMICAL ADAPTIVE OPTICS INSTRUMENT

RICHARD MYERS, JEREMY ALLINGTON-SMITH, DAVID BUSCHER, PAUL CLARK, NIGEL DIPPER, SZILVESZTER JUHOS, COLIN DUNLOP, ROGER HAYNES, GORDON D. LOVE, GRAHAM MURRAY, RAY SHARPLES, ANDREW ZADROZNY

University of Durham Department of Physics, Science Laboratories, South Road, Durham DH1 3LE England
E-mail: R.M.Myers@durham.ac.uk

PETER DOEL

Optical Sciences Laboratories, University College London, Gower Street, London, England

ANDREW LONGMORE, ANDREW VICK

UK Astronomical Technology Centre, Royal Observatory, Blackford Hill, Edinburgh, Scotland

June 1999 on the 4.2m William Herschel Telescope (one of the Isaac Newton Group of telescopes on La Palma in the Canary Islands, Spain) saw two runs with the University of Durham ELECTRA adaptive optics system. The first seven nights were for commissioning various new features and the remainder for 'service mode' AO observing. The new features included the Durham TEIFU integral field unit which can feed WYFFOS with adaptively corrected optical spectra from 500 sky elements simultaneously. This capability will soon be enhanced to 1000 elements (hence TEIFU: Thousand Element Integral Field Unit).

1 ELECTRA

Although these proceedings contain work on non-astronomical adaptive optics, this paper is included here because a tour Durham's Adaptive Optics Laboratories was given at the conference. Adaptive optics (AO) is familiar on 4m class telescopes and it is also now being introduced on larger telescopes such as Keck and Gemini. ELECTRA is quite a high-order system, having 228 degrees-of-freedom altogether and is designed to operate at short wavelengths, with partial correction available in the optical V, R and I bands as well as correction in the near-IR. In June the two modes available were near-IR imaging with the 1-5 micron 256x256 pixel imager WHIRCAM and optical area spectroscopy with TEIFU.

ELECTRA operates at the GHRIL bench at WHT (William Herschel Telescope) Nasmyth as illustrated in figure 1. The optical layout is illustrated schematically in figure 2. ELECTRA's main subsystems are its adaptive mirror, wavefront sensor (WFS), tip-tilt mirror, calibration unit and computer control system.

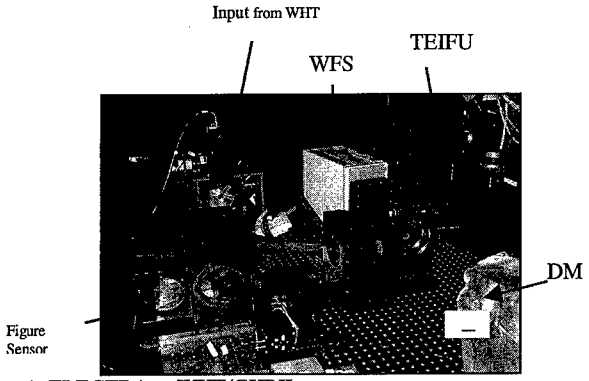

Figure 1: ELECTRA at WHT/GHRIL

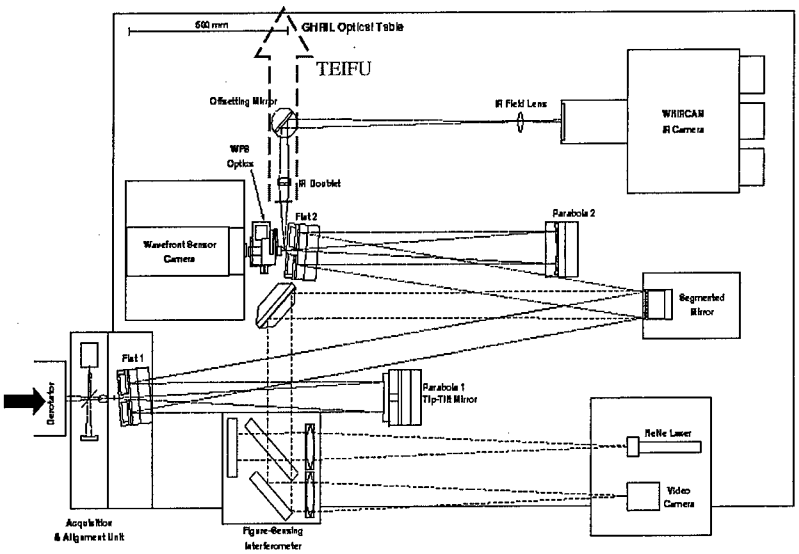

Figure 2. Schematic layout of ELECTRA at WHT/GHRIL

The adaptive mirror was built by TTC in San Diego. It has 76 segments each of which can tip, tilt and piston (hence 228 degrees of freedom) under computer control and is equipped with strain-gauge position feedback which ensures a linear response to wavefront correction commands.

The WFS is a Shack-Hartmann sensor which uses a camera built at Rutherford Appleton Laboratories and based on an 80x80 pixel EEV CCD-39. This camera can read out up to 2 million pixels per second from each of four readout ports. These signals are processed by an array of eight Digital Signal Processors (DSPs)

in order to produce wavefront reconstruction commands which are then passed to an additional bank of eight DSPs. This second back uses digitised feedback from the adaptive mirror strain-gauges to accurately place the required wavefront correcting figure on the mirror.

Near-IR seeing correction with ELECTRA is illustrated in the "before" and "after" correction images of figures 3 and 4. The service mode AO data will be reduced by the requesting observers but an early indication of the subarcsecond detail available is illustrated in the raw image of a planetary nebula in figure 5.

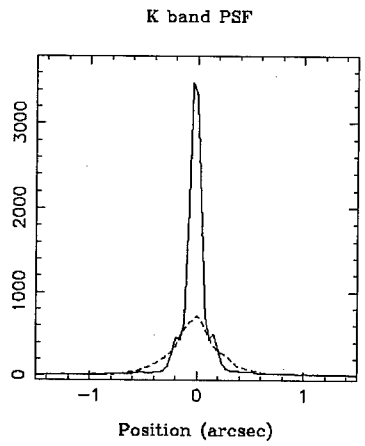

Figure 3: ELECTRA K-band image before and after correction

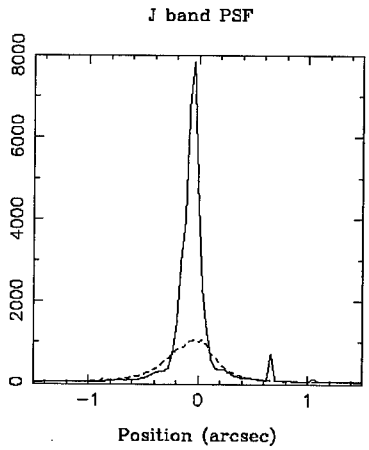

Figure 4: ELECTRA J-band image before and after correction

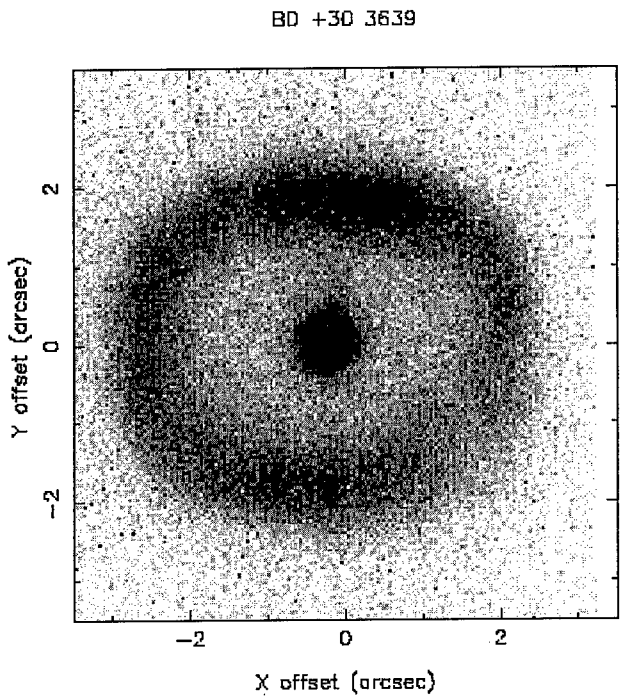

Figure 5: Raw WHIRCAM image of Planetary Nebula taken with ELECTRA AO

2 TEIFU

The TEIFU system will be available for use with ELECTRA. It is a lenslet-fibre areas spectroscopy system with consequently very high spatial fill-factor. A schematic illustrating its mode of operation is given in figure 6. At present it feeds the WYFFOS fibre-input spectrograph in the 300-1000nm wavelength range and has a single field with 28x18 elements each with an angular extent of 0.25 arcseconds. In future it will have two separate fields with 1000 elements in total. These fields will have variable separation for simultaneous object and sky observation and will be available at three different image scales:

Sampling:	0.125	0.25	0.50 *arcsec*
Field:	2x(3.5x2)	2x(7x4)	2x(14x8) *arcsec*^{2}

In future TEIFU will also benefit from a new long camera on WYFFOS giving better sampling. TEIFU will also be adapted for operation in the near-IR.

The characterisation of TEIFU has been very pleasing showing around 50% throughput with an rms fibre-to-fibre uniformity of 6%. An example set of TEIFU spectra from the galaxy 3C327 is shown in figure 7

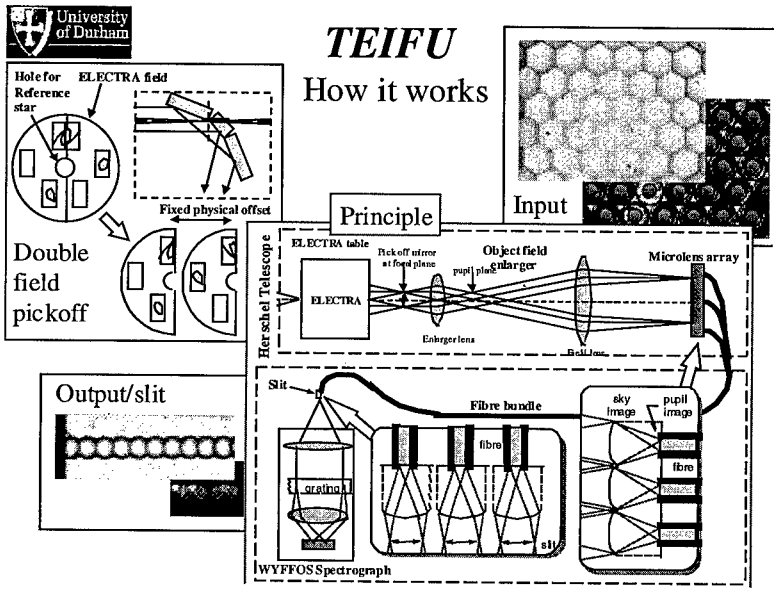

Figure 6: Principles of Operation of TEIFU

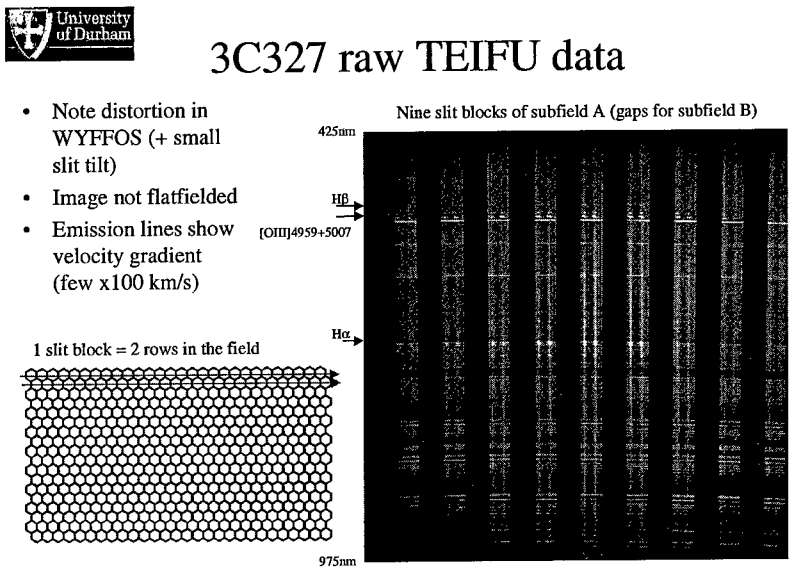

Figure 7: TEIFU raw spectra

3 Acknowledgements

We would like to thank Dr. Nick Waltham's CCD group at RAL for their great work on the WFS, and all ING staff involved in the run for their invaluable help. Funding was kindly provided by PPARC, the Royal Society Paul Instrument Fund (which funded the WFS) and the University of Durham.

BLIND OPTIMIZATION OF OPTICAL POWER INTO A SINGLE MODE OPTICAL FIBER USING A MEMS DEFORMABLE MEMBRANE MIRROR

M.L. PLETT, D.W. RUSH, P.R. BARBIER, and P. POLAK-DINGELS
Laboratory for Physical Sciences and
Electrical and Computer Engineering Department, University of Maryland
8050 Greenmead Drive, College Park, MD 20740, USA
E-mail: plett@lps.umd.edu

In this paper we present the results of a novel compact adaptive optics system for the optimization of optical power into a single mode optical fiber. This system uses a micromachined deformable mirror for aberration correction. The stochastic parallel gradient descent algorithm is used to maximize the coupling efficiency without a direct wavefront measurement.

1 Introduction

The motivation for using an adaptive optics system to couple an aberrated wavefront into an optical fiber comes from optical wireless communications. Optical wireless links provide high bandwidth links across free-space paths where optical fiber is expensive or impossible or to install. These links however require the regeneration of the data before it can be coupled into an optical fiber. An ideal optical wireless link would provide a seamless all-optical link maintaining the continuity of the optical network. An additional advantage of such a link would be the use of erbium doped fiber amplifiers at the receiver. This would greatly increase the overall dynamic range of the free-space optical link.

This paper describes a novel compact adaptive optics system for coupling an aberrated wavefront into a single mode optical fiber. Included in this investigation is the range of correctable aberrations and the maximum coupling coefficient. Having demonstrated the performance of the system, potential techniques to increase the dynamic range and convergence speed are discussed.

2 System Description

The adaptive optics system described in this paper is illustrated in Fig. 1. A collimated beam ($\lambda = 633nm$) is projected onto the deformable mirror. The deformable mirror is a 37 channel micromachined membrane mirror manufactured by OKO Technologies[1]. The beam is then split between a diagnostic wavefront sensor and the fiber coupling optic which focuses the laser onto a

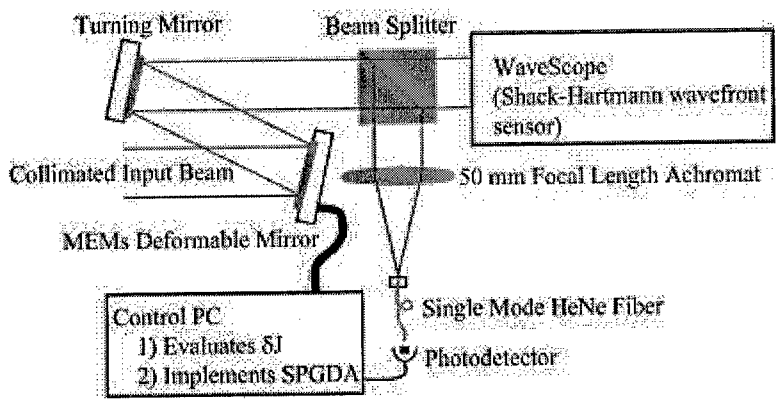

Figure 1: Novel adaptive optics system for the optimization of optical power into a single mode optical fiber.

4 μm core single mode optical fiber. The diagnostic wavefront sensor was *WaveScope* built by Adaptive Optics Associates.[2] The light coupled into the optical fiber is collected on a photodetector and the signal is fed back to the control PC. The stochastic parallel gradient descent algorithm (SPGDA) is then used to adapt the deformable mirror to optimize the optical power coupled into the fiber.

3 Stochastic Parallel Gradient Descent Algorithm

The stochastic parallel gradient descent algorithm enables the control of the deformable mirror from the measurement of a single performance metric. The loop equation for the SPGDA is given by Eq. (1).

$$\vec{\mathbf{U}}_{\mathbf{i+1}} = \vec{\mathbf{U}}_{\mathbf{i}} + \gamma \frac{\delta \mathbf{J}}{\delta \vec{\mathbf{U}}_{\mathbf{i}}} \tag{1}$$

In this experiment, the performance metric ($\mathbf{J}$) was the optical power coupled into the fiber. The algorithm applies a stochastic perturbation $\delta\vec{\mathbf{U}}$ to the mirror control vector $\vec{\mathbf{U}}$. This perturbation is applied simultaneously to all actuators. The change in the performance metric $\delta\mathbf{J}$ is measured, and the next control vector is calculated from this single measurement. This enables all actuators to be updated in parallel. The loop gain is denoted by γ.

The use of this algorithm eliminates direct wavefront sensing from the adaptive optics system. This reduces both the size and complexity of the system.

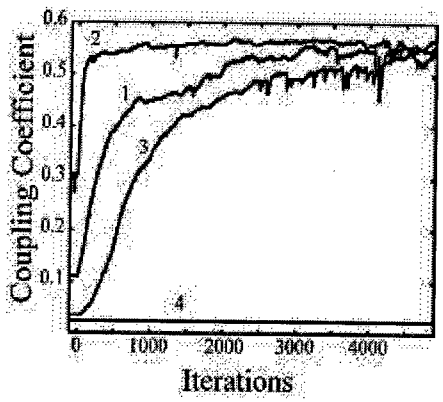

Figure 2: Convergence curves for various initial RMS OPDs: 1)System aberration 0.122 μm 2)Random aberration 0.04 μm 3)Defocus 0.208 μm 4)Defocus 0.35 μm.

4 Optical Path Difference Dynamic Range

In order to demonstrate the dynamic range of aberrations that the system can correct, four initial aberrations were used. These aberrations are the inherent aberration in the optical system, a small random aberration and two large defocus aberrations. The latter three aberrations were generated by changing the control vector to the mirror after it had corrected for the system aberrations. The convergence of the SPGDA for all cases is shown in Fig. 2. Each curve is the average of ten realizations of the algorithm. This average was taken because the algorithm is a stochastic process. The following sections describe the results of each initial condition.

4.1 Self Correction

The first step in demonstrating this adaptive optics system was to demonstrate that the system could compensate for the aberrations inherent in its own optical system. The convergence curve of the SPGDA for this case is shown in Fig. 2 (curve 1). The coupling coefficient was improved from 11% to 55%. The RMS optical path difference (OPD) correction was 0.122 μm. This corrected wavefront was used as the optimal wavefront reference for subsequent tests.

4.2 Small Random Aberration

A random set of voltages was added to the mirror control vector to produce a small random aberration. The convergence curve for this case is shown in

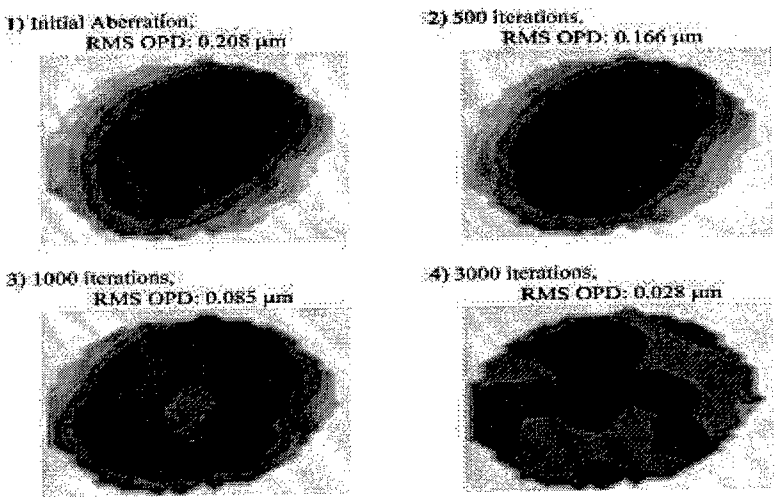

Figure 3: Wavefront measurements taken as the adaptive optics improve the defocus aberration (1) to the corrected wavefront (4).

Fig. 2 (curve 2). The convergence was faster for this initial condition since it began closer to the maximum. The coupling coefficient was increased from 30% to 55%. The initial RMS OPD was 0.04 μm and was corrected to within an RMS OPD of 0.023 μm of the optimal wavefront.

4.3 Large Defocus Aberration

A defocus aberration was added to the converged mirror control vector to demonstrate the correction of a relatively large aberration. The SPGDA improved the coupling coefficient from 3% to 55%. This was the largest improvement in the coupling coefficient. The convergence curve is shown in Fig. 2 (curve 3). Wavefront measurements were taken during this trial to determine that the algorithm was indeed correcting for the defocus aberration. The wavefront correction is shown in Fig. 3. The wavefront began at an RMS OPD of 0.208 μm and improved to an RMS OPD of 0.028 μm after three thousand iterations.

4.4 Larger Defocus Aberration

A larger defocus aberration was then added to the converged mirror control vector to bound the amount of RMS OPD that the system could correct. For

this case, the initial RMS OPD was 0.35 μm. As shown in Fig. 2 (curve 4), the SPGDA could not converge from this initial aberration. In this case there was no power in the optical fiber. The algorithm could not measure a slope in the performance metric and therefore could not optimize the coupling coefficient. For this case, the initial wavefront was never improved.

4.5 Optical Path Difference Dynamic Range Results

The algorithm converged to the same maximum coupling coefficient of 55% for initial conditions that were less than $\lambda/3$ RMS OPD from the optimal wavefront. In this range of initial conditions, the SPGDA consistently converged to the same maximum to within an RMS OPD of $\lambda/25$. The maximum coupling coefficient was less than 100% because of an intensity mode mismatch between the uniform input beam and the approximately Gaussian fiber mode. The achieved maximum of 55% is in agreement with the theoretical maximum coupling coefficient given this mode mismatch.

5 Potential System Improvements

The two main areas for improvement in this adaptive optics system are the correctable OPD dynamic range and the convergence speed. The present system corrects only a small range of OPD and requires a large number of iterations to perform this correction.

5.1 Optical Path Difference Dynamic Range

The OPD dynamic range is limited by the choice of the fiber coupling coefficient for the performance metric. This metric is a sharp function of the wavefront aberration and limits the dynamic range of the system. When there is no power in the optical fiber there is no slope in the performance metric. The SPGDA therefore cannot maximize the coupling coefficient. The choice of another performance metric for large aberrations could increase the OPD dynamic range of the system to take advantage of the full dynamic range of the deformable mirror.[5]

5.2 Convergence Speed

The speed of the convergence is critical to success of this technique in optical wireless communications. Because of the limited bandwidth of the deformable mirror, the algorithm must quickly correct the wavefront changes of the atmosphere with only a few iterations.[5] The reduction of the convergence time for

small aberrations can be seen in Figure 2. This results indicates the potential for this system to quickly track small changes in the wavefront due to atmospheric turbulence. Further research will have to be done to demonstrate the dynamic operation of the system.[6]

The speed of the algorithm could be increased by changing the performance metric[3] and optimizing the SPGDA. A performance metric that tolerates larger aberrations can increase the convergence speed of the algorithm by providing a greater slope to the metric function. The SPGDA could be optimized for speed by adding an active loop gain and the global coupling of the control channels.[4]

6 Conclusions

We have demonstrated a compact adaptive optics system that can increase the coupling into a single mode optical fiber from 3% to 55%. This is the maximum coupling possible with the current mode mismatch. This system has demonstrated correction over a dynamic range of $\lambda/3$ in RMS OPD. Increased dynamic range may be achieved by alternate performance metrics. Additionally, optimization of the control algorithm and performance metric may increase the speed of the system.

References

1. OKO Technologies, Reinier de Graafweg 300, 2625 DJ Delft, The Netherlands, http://www.okotech.com
2. Adaptive Optics Associates, 5400 Cambridgepark Way, Cambridge, MA, USA.
3. M. L. Plett, P. R. Barbier, D. W. Rush, G. W. Carhart, and M. A. Vorontsov, "Compact Adaptive Optics based on a micromachined deformable mirror and a single photodetector," *CLEO Proc. 1999,Adaptive Optics/Compound Semiconductor Devices.*
4. G. W. Carhart, J. C. Ricklin, V. P. Sivokon, and M. A. Vorontsov, "Parallel perturbation gradient descent algorithm for adaptive wavefront correction," *SPIE Proc.* **3126**,*Adaptive Optics and Applications*, pp. 221–2217, 1997.
5. G. Vdovin and P. M. Sarro, "Flexible mirror micromachined in silicon," *Applied Optics* **34**,, No. 16, pp. 2968–2972, 1995.
6. V. I. Polevaev, P. R. Barbier, et. al.,"Adaptive compensation of dynamic wavefront aberrations based on blind metric optimization technique", to be presented at SPIE Proc., Denver,July 1999

HIGH POWER LASER DIODE TO FIBER COUPLING USING A MEMBRANE MIRROR

F. GONTÉ, A. COURTEVILLE, E. ROCHAT, K. HAROUD, N. COLLINGS, R. DÄNDLIKER

Institute of Microtechnology, Neuchatel, Switzerland

G. VDOVIN, S. SAKARYA

University of Delft, Holland

E-mail: frederic.gonte@imt.unine.ch

Side and front coupling of pump laser diodes of 1W emitted power into a double clad doped fiber using a multielectrode deformable mirror is investigated. The shape of the mirror was controlled using a simplex-based algorithm. An increase of the coupling efficiency and the fluorescence output power has been demonstrated in both cases

1 Introduction

A dynamic coupling system for fiber amplifiers has been developed. A micromachined membrane mirror [1] produces the dynamic capability of the system. The mirror has a diameter of 15 mm and 37 computer-controlled electrodes deflect the membrane.

Two coupling systems on the same breadboard have been used. The first system is a traditional coupling, called end-coupling, that has been enhanced with the dynamic mirror. The second is a novel coupling system, called side coupling, and which also uses the dynamic characteristic of the micromachined mirror.

The fiber amplifier used for this demonstration is a double clad fiber [2] with a monomode core and a 125 μm thick outer clad. The fiber is doped with Yb^{3+} and produces a fluorescence output comprised between 960 and 1200nm [3]. This kind of fiber is mainly used with high power pump diode laser at 980 nm. The output beam of these lasers are highly divergent (± 30 degrees for the y axes and ±5 degrees for the x axes) and is therefore difficult to focus onto the fiber. Dynamic coupling is a good way to solve this problem.

First, to analyze the mirror deformation, the breadboard has been set up with an imaging interferometer in order to record the interference pattern produced by the mirror. Afterwards, the imaging interferometer has been replaced by a Shack-Hartmann sensor [4], which is able to retrieve and record the Zernike coefficients of the mirror deformation and to print a picture of the deformation. The mirror has been driven with an algorithm program [5].

2 Coupling of a diode pump laser into a double clad fiber

Double-clad doped-fibers are used as fiber amplifiers and lasers. They have a monomode core that is doped (in our case with Yb^{3+}), where the signal is amplified, and a multimode double clad into which the laser pump is coupled. Figure 1 shows the difference between a monomode fiber and a double-clad fiber. The goal of the experiment is to show the improvement of the pump coupling efficiency and the fluorescence output power accomplished by the adaptive membrane mirror.

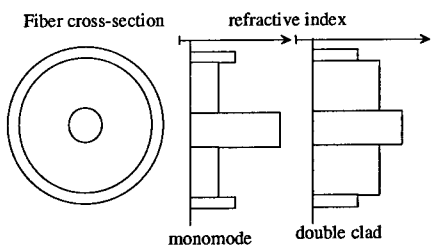

Figure 1. Fiber cross-section

As shown in Fig. 2, the pump is a diode laser with an output power of 1 W at 980 nm and a divergence of 30 degrees in the y-axis and 5 degrees in the x-axis. The pump beam is roughly collimated by a cylindrical and a converging lens which have a focal length of 10 mm and 50 mm, respectively, and is reflected on the membrane mirror before being focused by a 15 mm achromatic lens for the coupling. The set up of the breadboard (Fig. 2) allows two methods of coupling: the first is called front coupling and is traditionally used; the second and more recent method is called side coupling. Side coupling has already been demonstrated [6,7] but not yet with a

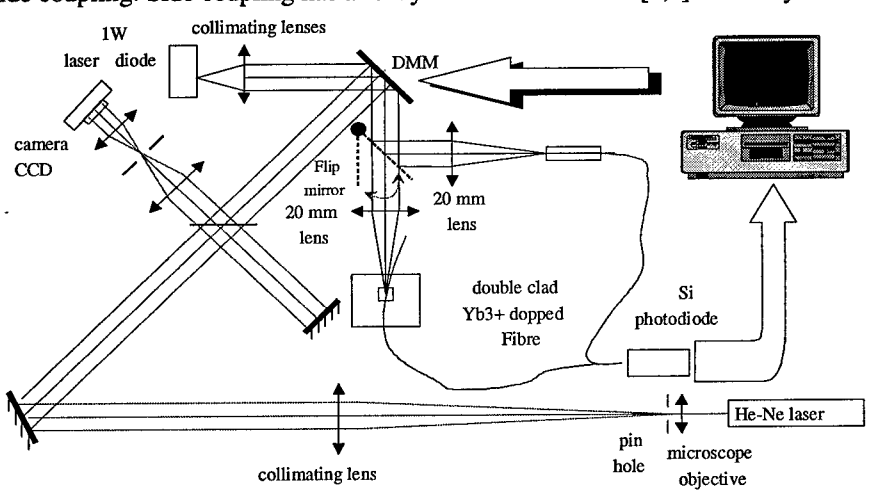

Figure 2. Set up for dynamic fiber coupling experiments

dynamic system. This breadboard has been set up, first, with an interferometer to observe and record the interference pattern due to the deflection of the mirror, and then with a Shack-Hartmann sensor [4] to record the phase change produced by the membrane mirror. Figure 2 shows the schematic set up with the interferometer. The

flip mirror allows to switch between front coupling and end coupling of the two different fibers. Figure 3 is a photograph of the main part of the breadboard. A Si-photodiode detects the light at the fiber ends and is connected to a computer that measures the pump coupling efficiency. The micromachined mirror is driven with a simplex algorithm which works in closed loop with the photodiode [4]. It has to be noticed that the loss in the optical path between the first lens and the entrance of the fiber is about 22%. This loss is due to Fresnel reflection at the focusing lens and to the absorption of the aluminum coated membrane mirror, which is around 10%.

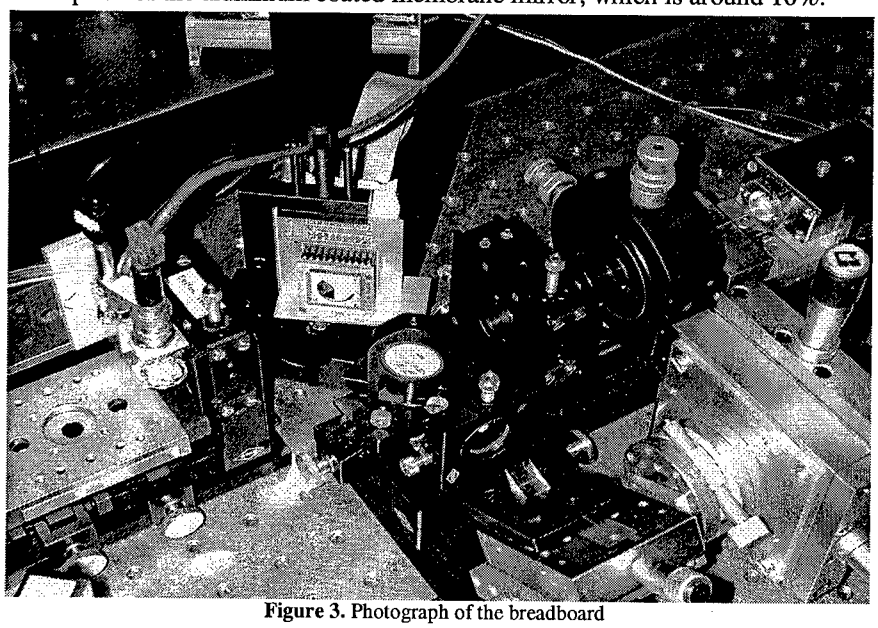

Figure 3. Photograph of the breadboard

The pump coupling efficiency has been measured between the output of the collimating lenses and the output of the concerned fiber. The fibers were 20 cm long.

For the measurement of the fluorescence output power, a monochromator has been used to suppress the pump light and to extract the fluorescence at 1064 nm $\pm$ 3 nm. In this case the fibers were 4 m long to obtain a good fluorescence signal, and a GaAs photodiode was used as detector.

2.1 Side coupling

The signal and the pump are usually coupled through the end of the fiber. In order to free the use of the fiber end for the

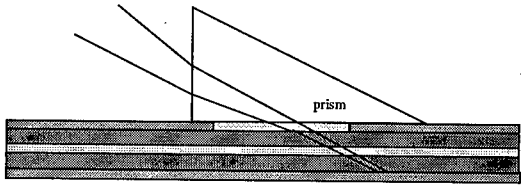

Figure 4. Concept of the side coupling

signal coupling, and to allow multiple coupling points for increased pumping, side-pumping can be performed using a bulk element selective coupler.
A part of the fiber coating is removed a few millimeters long, with the help of a prism (Fig. 4) the laser is coupled into the fiber. An index oil is used to obtain the contact between the double clad fiber and the prism. The membrane mirror is used to adapt the shape of the focal spot and thus increase the efficiency of the coupling. The prism is a right angle silica prism and the laser beam arrives at 24 degrees from its orthogonal axis.
Before the activation of the membrane, the pump coupling efficiency was 12%. This efficiency has been improved to 17% with the help of the adaptive optics, which is a relative improvement of 42%. Figure 5 shows the interferometric pattern due to the particular mirror shape for the improvement. It is close to an astigmatic deformation at an angle of around 20 degrees with respect to the x-axis of the interferometric pattern. No classical optical device can produce such wavefront shape; the adaptive optic mirror is a unique tool to obtain this wavefront.

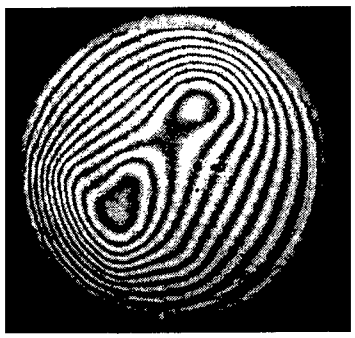

Figure 5. Interference pattern

2.2 *Front coupling*

Front coupling is the traditional way of coupling: the laser pump is focused onto the cleaved part of the fiber, a microscope objective is usually used for this purpose. In our set up a lens with 20 mm focal length has been used.
We first measured the fluorescence output power of a 4m long fiber and the increase using the adaptive optics. An increase of 48% has been obtained. The wavefront

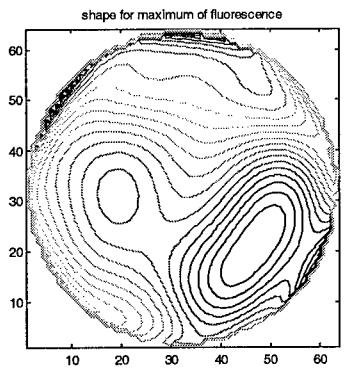

Figure 6. Membrane deflection for maximum fluorescence

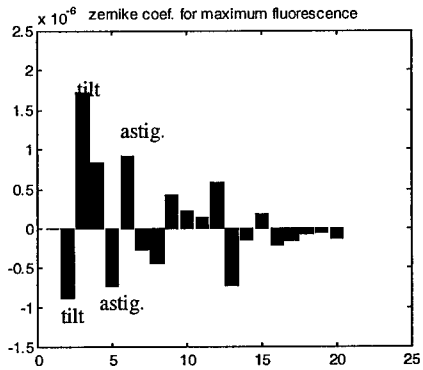

Figure 7. Zernike coefficient for maximum fluorescence

change produced by the deflection of the mirror has been measured with a Shack-Hartmann sensor.

After that the fiber length was reduced to 20 cm for the measurement and the optimization of the pump efficiency The efficiency of the front coupling without the dynamic coupling is 39%, the best pump efficiency obtained with the dynamic coupling is 54%, which means a relative increase of 38%. The corresponding shape of the deflection of the mirror was again measured with the Shack-Hartmann sensor. It is then possible to compare the shapes of the deflection of the mirror for maximum fluorescence and for maximum pump efficiency.

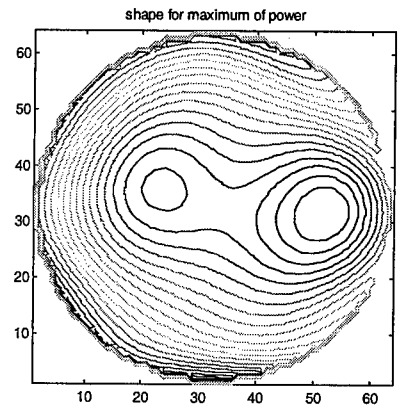

Figure 8. Membrane deflection for best pump coupling

The Shack-Hartmann sensor measures the change of the wavefront shape produced by the deflection of the membrane mirror. The changes are given by the Zernike coefficients and a program uses them to calculate the shape of the deflection of the membrane mirror. The sensor used a pin-hole array instead of a micro-lens array [7].

The Zernike coefficients give an idea of the importance of the aberrations. Comparison of Fig. 7 and 9 shows that the optimum deformations are remarkably different. The difference can be explained by the following considerations. To obtain a maximum of fluorescence the pump needs to cross as often as possible the core of the fiber and the adaptive optic optimize the coupling for this purpose. To obtain maximum t pump efficiency, the pump is coupled in the multimode outer cladding and is optimized for maximum output of pump light.

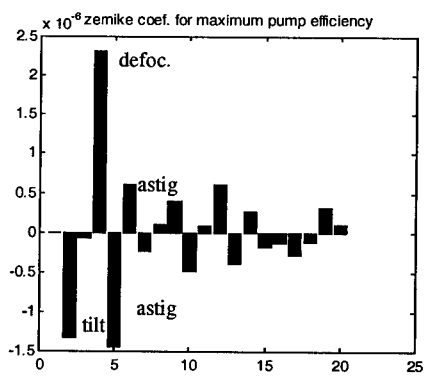

Figure 9. Zernike coefficient for best coupling

3 Conclusion

A dynamic coupling system using a deformable membrane mirror has been demonstrated for the pumping of a double clad doped fiber with a high-power diode laser. Two coupling possibilities have been explored. The first one is the classical

front coupling and the second one is a side coupling. The dynamic capability of the system has been verified for both coupling systems with a relative increase of efficiency of more than 38 % in both cases and with 48% increase of fluorescence in the case of front coupling.
Several improvements could be made on this breadboard to downsize it and to increase the absolute efficiency of the coupling system. The first improvement would be the use of an anamorphic prism pair to reduce the elliptical shape of the laser beam. For the side coupling, a prism with a Brewster angle could be used to reduce the reflection losses on the prism.
The correction of changes during the lifetime of on-board optical systems in space with the membrane mirror is envisaged.
This work is part of the European project MOSIS (ESPRIT 31069).

4 Reference

1. Vdovin G. V. and Saro P. M., Flexible mirror micromachined in Silicon, *Appl. Opt.* **34** (1995) pp. 2968-2972.
2. Rochat E., Haroud K., Dändliker R., High power Nd-doped fiber amplifier for coherent intersatellite links, submitted to *IEEE J. Quantum El.*
3. Pask H. M.et al., Ytterbium-Doped Silica Fiber Lasers: Versatile Sources for the 1-1.2μm Region, *IEEE J. Select. Top. Quantum. El.* **1** (1995) pp.2-12.
4. Vdovin G., Sakarya S., French P., Inexpensive adaptive optical system based on a micromachined deformable mirror, *Semiconductor Advances for Future Electronics Conference,* November 25-27,1998, Mierlo, Netherlands
5. Teukolsky A. et al, Numerical Recipes in C, Cambridge University Press (1988).
6. Luthy W. and Weber H. P., High power monomode fiber lasers, *Opt. Eng.* **34** (1995) pp.2361-2363
7. Goldberg L. et al, V-Groove side-pumped 1.5 μm fiber amplifier, Electron. Lett.**33** (1997) p2127-2129

IMPROVEMENT OF A LASER COMMUNICATION BEAM USING ADAPTIVE OPTICS

P.R. BARBIER, D.W. RUSH, P. POLAK-DINGELS, and M.L. PLETT
Laboratory for Physical Sciences and
Electrical and Computer Engineering Department, University of Maryland
8050 Greenmead Drive, College Park, MD 20740, USA
E-mail: barbier@eng.umd.edu

We present experimental results of the compensation of a laser beam transmitted through static aberrators using a Shack-Hartmann-based adaptive optics system. We investigate system performance as a function of beacon intensity, beacon scintillation, and beacon wavefront.

1 Introduction

Optical wireless communications is emerging as an attractive technology alternative to both fiber and line-of-sight microwave for selected terrestrial scenarios. Commercially available systems employ a variety of techniques to minimize the effects of atmospheric turbulence. These techniques include multiple transmit apertures, large receive apertures, large beam divergences, wavefront scrambling, and reduced link lengths. Compact and affordable adaptive optics systems may provide a powerful tool to improve the performance of these systems by allowing longer link distances, smaller aperture sizes, reduced beam divergence, and increased error-free link availability times. A previous report described initial field tests of an adaptive optics test-bed which has been developed by Adaptive Optics Associates[1]. In this paper, we discuss additional laboratory characterization of the performance of this adaptive optics system.

2 System description

Our experimental system consists of a laser communication transmitter and a receiver. The adaptive optics system, a scoring Hartmann sensor, and a 532 nm communication laser form the communications transmitter. The adaptive optics system includes a 20 cm diameter 2 m focal length telescope, a 37-actuator piezo-electric deformable mirror, a tip-tilt mirror and a 30-subaperture Shack-Hartmann wavefront sensor. The adaptive algorithm performs Karhunen-Loève modal decomposition with a closed-loop bandwidth of 50Hz. The scoring Shack-Hartmann wavefront sensor is used to monitor the corrected wavefront at speeds up to 1000 frames per second. The communication laser is carefully aligned to be counter propagating to the input beacon. The communications

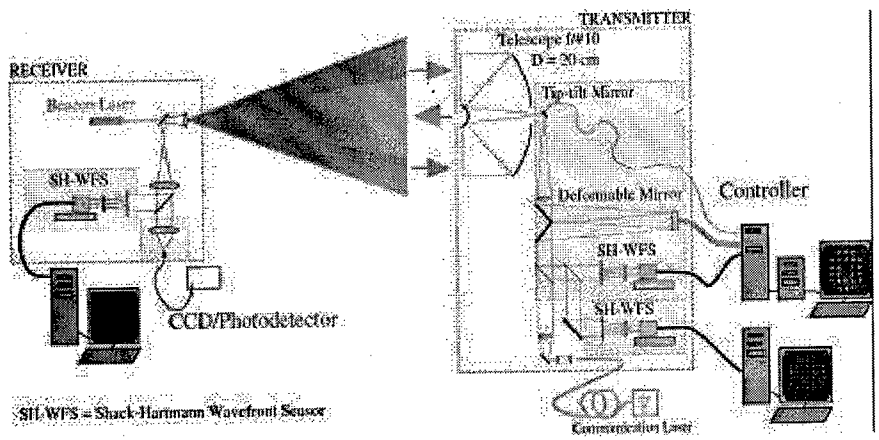

Figure 1: Schematic of optical wireless communication experiment incorporating adaptive optics system.

receiver includes a 20 cm diameter 2 m focal length telescope, a 632.8 nm beacon laser, another fast Shack-Hartmann wavefront sensor,[4] and a communication photodetector. For these experiments, the photodetector was replaced with a video-rate CCD camera. The complete system is shown in Fig. 1 and has been described in detail elsewhere.[1,2].

The purpose of the ideal adaptive system is to focus the communication laser beam onto the receiver by transmitting the phase-conjugate wavefront of the received beacon. In the presence of turbulence we expect the adaptive optics to increase the power collected by the receiver, to improve the wavefront of the communication laser beam at the receiver and, most importantly, to reduce the power fading at the communication photodetector. For the experiments described in this paper, we aligned the transmitter and the receiver in the laboratory over a distance of approximately 5 m. Four measurements were used to evaluate the system performance: 1)the control loop error signals for each Karuhnen-Loève mode of the adaptive optics system 2)beacon laser wavefronts as measured by the fast scoring wavefront sensor data at the transmitter, 3)communication laser wavefronts as measured by the fast wavefront sensor data at the receiver and, 4)the intensity profile of the communications beam as measured by the video-rate CCD camera at the receiver.

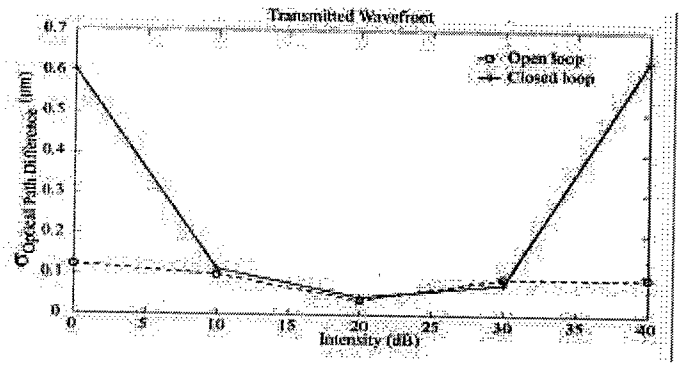

Figure 2: Variance of transmitted wavefront at receiver versus beacon intensity.

3 Experimental results

3.1 Intensity dynamic range

In the first experiment we varied the intensity of the beacon beam that was incident on the control loop wavefront sensor and monitored the wavefront of the communication beam at the receiver. The only aberrations come from the room air flow and were measured to be approximately 0.1 μm_{RMS} over the 20 cm diameter beam. The results are presented in Fig. 2. Because the system was subject to tip-tilt offset caused by the use of neutral-density filters, we plotted the time variance of the RMS optical path difference (OPD). As can be observed in this figure, when the beacon intensity is too weak, the wavefront sensor is CCD-noise limited and the OPD variance increases indicating that the control loop diverges. When the beacon intensity is too high, the control camera saturates, the wavefront sensor spot images smear, the error increases, and the control loop diverges.[3] These results were confirmed from out-of-range error signals. From Fig. 2 we conclude that the intensity dynamic range of our adaptive optics system is approximately 20 to 30 dB corresponding to the dynamic range of the 8-bit control loop camera.

3.2 Partially blocked wavefront sensor

Field-test results have indicated that the wavefront of a 1 km propagated laser beam can be heavily scintillated.[4] Consequently, the propagated beacon beam intensity distribution can fall beyond the dynamic range of our adaptive optics system. In the following experiment, we simulated the effect of heavy scintillation by partially blocking either one half or one quarter of the input aperture

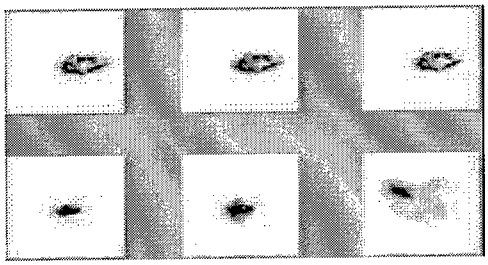

Figure 3: Focal plane image of transmitted beam in (top) open loop and (bottom) closed loop when control wavefront sensor is (left) unblocked, (middle) 25% blocked and (right) 50% locked.

Table 1: Results of partially blocked wavefront sensor experiment.

Fraction Blocked (%)	Error Signal (a.u.) Open Loop/Closed Loop	Transmitted Wavefront (μm_{RMS}) Open Loop/Closed Loop	Beacon Wavefront (μm_{RMS}) Open Loop/Closed Loop
0	2.3/0.06	4.8/0.8	4.8/0.8
25	2.3/0.25	4.8/0.6	4.8/0.6
50	2.3/2.2	4.8/1.4	4.8/1.4
Reference	0.3/0.04	0.1/0.1	0.1/0.1

of the control loop wavefront sensor. The other diagnostic apparatus remained unblocked. In addition, we generate a static aberration by intentionally defocusing the transmit telescope. Focal plane images of the communication beam at the receiver are shown in Fig. 3. The corresponding error signal and wavefront results are summarized in Table 1. Fig. 3 illustrates that the adaptive optics system compensates for static defocus when the wavefront sensor can make an accurate measurement.[1,2] However, when 50 % of the wavefront sensor was blocked the control loop diverged. This conclusion is confirmed by Table 1. We believe that even though the wavefront sensor is capable of making an accurate measurement in the unblocked area, the noise resulting from the blocked area dominates the modal error signals and prevents the control loop from converging.

3.3 Plexiglass aberrators

In this experiment we wanted to test the ability of the system to compensate for high order aberrations. We placed a plexiglass sheet halfway between the transmitter and the receiver. Focal plane images of the transmitted communi-

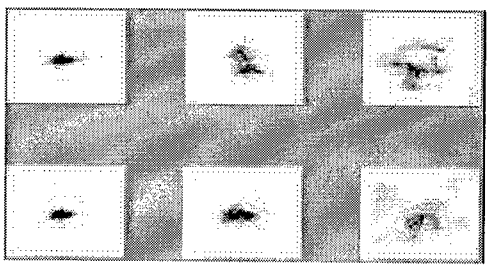

Figure 4: Focal plane image of transmitted beam in (top) open loop and (bottom) closed loop (left) the absence of aberrator, in the presence of (middle) a weak plexiglass aberrator and (right) a stronger plexiglass aberrator.

Table 2: Experimental results of plexiglass aberration compensation.

Plexiglass	Error Signal (a.u.) Open Loop/Closed Loop	Transmitted Wavefront (μm_{RMS}) Open Loop/Closed Loop	Beacon Wavefront (μm_{RMS}) Open Loop/Closed Loop
Sheet 1	2/0.06	1.9/0.7	2.6/2.3
Sheet 2	3.3/2.3	4.0/4.1	4.1/4.0
Reference	0.3/0.04	0.1/0.1	0.1/0.1

cation beam are shown in Fig. 4. The corresponding error signal and wavefront results are summarized in Table 2. These experimental results indicate that the system can compensate for weak *random* aberrations. However, when *random* aberrations are larger, the loop diverges. Note that although the system was able to compensate for 4.8 μm_{RMS} of defocus OPD(see Sec. 3.2), the system is not able to compensate for the 4.0 μm_{RMS} of random OPD.

In Fig. 5 we plotted the error signal for each of the control modes in both open and closed loop for the two plexiglass aberrators. As apparent in the figure, the adaptive optics system compensated each one of the 10 selected modes in the case of the first aberrator. However, in the case of the second aberrator, even though the system compensated for tip and tilt, it did not compensate fully for the higher modes. This result is consistent with those of Table 2 and Fig. 4. Future work will determine whether this limitation results from the wavefront sensor, the deformable mirror or the modal reconstructor.

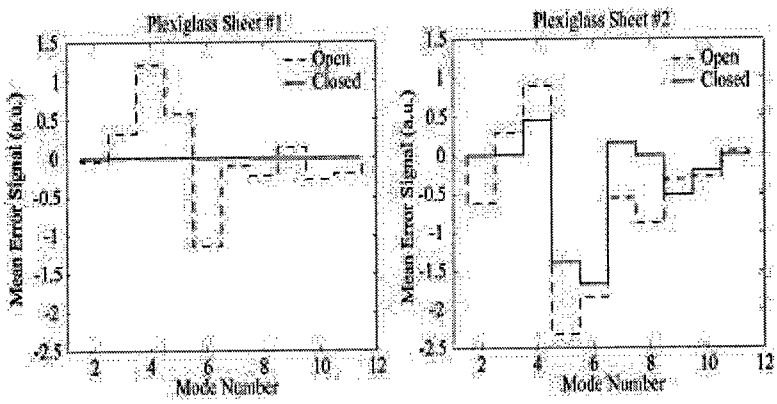

Figure 5: Control open and closed loop error signal for each Karhunen-Loève mode when laser beams were distorted by two different plexiglass sheets.

4 Summary

In summary we have shown that a Shack-Hartmann-based adaptive optics system can provide wavefront correction for a communication beam propagating through static aberrations. However, if the beacon beam is heavily scintillated at the receiver or highly distorted, we have demonstrated that the system may not improve the quality of the communication beam.

References

1. B.M. Levine, A. Wirth, H. DaSilva, F.M. Landers, S. Kahalas, T.L. Bruno, P.R. Barbier, D.W. Rush, P. Polak-Dingels, G.L. Burdge, D.P. Looze, "Active compensation for horizontal line-of-sight turbulence over near-ground paths," *SPIE Proc., Vol. 3233*, pp. 221-232, (1998).
2. B. M. Levine, E. A. Martinsen, A. Wirth, Jankevics, M. Toledo-Quinones, F. Landers, T. L. Bruno, "Horizontal line-of-sight turbulence over near-ground paths and implications for adaptive optics corrections in laser communications," *Applied Optics* **37**, pp. 4553-60 (1998).
3. M. L. Plett, P. R. Barbier, D. W. Rush, P. Polak-Dingels, B. M. Levine, "Measurement error for a Schack-Hartmann wavefront sensor in strong scintillation conditions," *SPIE Proc., Vol. 3433*, pp. 211-20 (1998).
4. P. R. Barbier, P. Polak-Dingels, D. W. Rush, G. L. Burdge, B. M. Levine, E. A. Martinsen, A. Wirth, and A. Jankevics, "Shack-Hartmann wavefront sensing measurements of near-ground propagated laser beams," *SPIE Proc., Vol. 3125*, pp. 284-95 (1997).

PRELIMINARY RESULTS OF HORIZONTAL PATH LENGTH PROPAGATION EXPERIMENTS

G R G ERRY, P HARRISON, P M BLANCHARD, A H GREENAWAY
DERA Malvern, St Andrews Road, Gt Malvern, Worcestershire, WR14 3PS, UK
Email: grgerry@taz.dera.gov.uk
pharrison@taz.dera.gov.uk

The implementation of a wavefront curvature sensor to measure atmospheric turbulence over horizontal paths is described. These measurements are important for defining adaptive optical systems for imaging along such paths. Currently little is known about the expected turbulence structure so the sensor is to be deployed to measure many atmospheric quantities in sufficient detail and over a long period of time so a library can be constructed giving atmospheric conditions for any particular time period. By using this information AO systems can be more accurately defined to cope with horizontal imaging situations. The sensor is a novel device using the intensity transport equation to calculate the wavefronts from information collected using a distorted grating.

1 Introduction

We are interested in imaging along extended path through the earth-atmosphere boundary layer. With the advent of high-resolution imaging most people have been concerned with looking at stars and other celestial bodies, as a consequence there has been a lot of research on the turbulent properties of the atmosphere when viewing vertically. In contrast little work has been done on characterising turbulent properties of the atmosphere when looking in a near horizontal direction. Described is a long-term experiment that will be deployed to measure turbulent properties of the atmosphere in a horizontal direction using a novel wavefront sensor based on finding a solution to the intensity transport equation and using a distorted grating to extract the raw information. By using this sensor, data will be gathered to give a description of the properties of the atmosphere enabling future AO systems to be defined and their performance evaluated more easily.

2 Description of Wavefront Sensor

The wavefront sensor has four distinct components, as seen in Figure 1.

© British Crown Copyright 1999. Published with the permission of the Defence Evaluation and Research Agency on behalf of the Controller of HMSO.

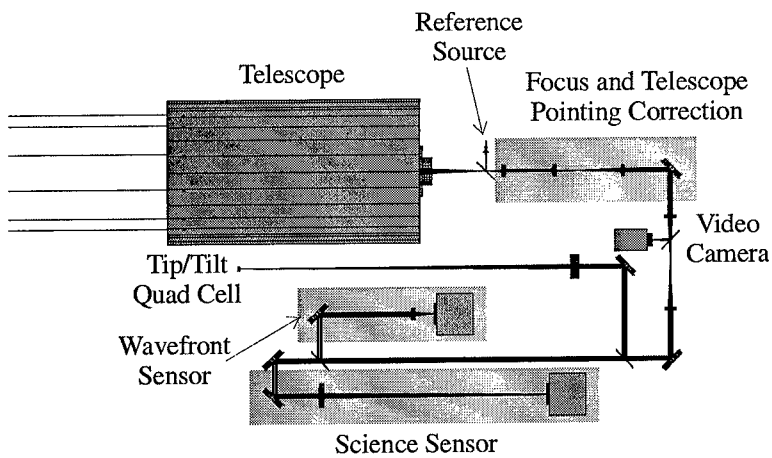

Figure 1. Schematic of the wavefront sensor system.

2.1 The telescope

The telescope is a standard Celestron eleven-inch (280mm) diameter telescope (CG-11), and has a focal ratio of 10. It has not been modified in anyway except for new mounting points on the case enable it to be bolted directly to the optical breadboard. As it is not always practical or desirable to illuminate the telescope using an external source when checking and aligning the optics, a fibre-fed reference source has been used, that is positioned at the same focal position as the telescope and has the same focal ratio. Using the reference enables easy alignment of the optics and gives a consistent source for testing the equipment.

2.2 The focus and the telescope pointing correction

It was initially envisaged that the telescope focus would be adjusted by motorising the focus control on the telescope. After some experimentation it was concluded that due to the image wander that occurs as the focus is moved, it would be unacceptable to use the control in this manner. An alternative was to include a pair of lenses to collimate and then refocus the light, with the former lens mounted on an electrically operated translation stage that enables the focus to be adjusted to fixed pre-calculated positions according to the range of the source being viewed. The second lens then refocuses the light to give a known focal position for the system. The next section in the optical train is the pointing correction system. It is a small tip tilt mirror that was included as the telescope and breadboard are to be mounted on an Andrew Kintec pan and tilt mount, which has a resolution of 0.05°. Due to the small field-of-view of the wavefront sensor it is necessary to correct the pointing. The mount would point at the source, and then the tip/tilt mirror would

make fine corrections to the incoming light to enable it to pass through the centre of the wavefront sensor optics. Inserted at the end of this section is a standard Hitachi CCD video camera that is used to monitor the light entering the system, and provides feedback to the computer to control the focus and tip/tilt sections described previously. By ensuring that the image on this camera is in focus and at the centre gives a reference point for the image, thus ensuring that the entire system is aligned to this point enables easy alignment of the optics.

2.3 Wavefront sensor

Once the light has been corrected for focus and pointing, it is split into two channels feeding the wavefront sensor and the science sensor. The heart of the wavefront sensor is a distorted grating that supplies three images to the camera [1]. The central image is a focused image, the outer two images (the first orders) are images before and after focus. These images are used to calculate the shape of the incoming wavefront [2]. For the expected atmospheric perturbations, it has been estimated that the effective plane separation needed is ±400m either side of the pupil plane. The images are recorded on a Dalsa CA-D1 camera, which has a format of 128x128 pixels.

2.4 The science sensor

The second channel of light is used to form an image on the science camera, which is an identical Dalsa CA-D1 camera. The relay lens has been chosen to give well-sampled images from the telescope given by the Nyquist criterion, so the recorded images will contain diffraction-limited information from the telescope. The two Dalsa CA-D1 cameras are slaved together using a Bitflow Road Runner frame grabber card, and using IO Industries software enables the system to capture data simultaneously from both cameras at a frame rate of 736 frames per second. The data is stored in real-time to a stack of hard disks with a total of 24Gb of storage, enabling data runs in excess of 18 minutes to be taken. This system, provided through Alrad Ltd is now functioning reasonably well, although there remain isolated problems with the data collection from the cameras.

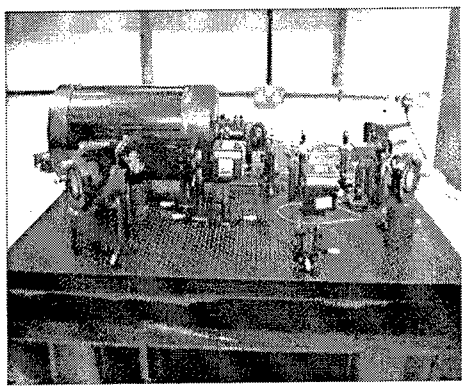

Figure 2. Photograph of the wavefront sensor

2.5 Other equipment issues

The wavefront sensor is intended for deployment at DERA Defford, where it will automatically take data at certain times of the day and night. This requirement means that the entire operation is being geared towards automatic computer control. To enable this, there is a central computer that controls the pan/tilt mount, the focus/tip/tilt system on the sensor, and has a feed from the video camera. It is also connected over a network link to the computer that runs the Dalsa cameras. This central computer will orchestrate all aspects of the system control by either issuing commands itself, or delegating operations to other computers on the network. Another computer is planned that will automatically reduce the data into useable information that can then be downloaded from the system to a remote site, again over the network. The entire breadboard is enclosed in a light aluminium cover to protect the optics from the environment, and thermostatically-controlled heating cables are attached around the breadboard to keep the system at a constant temperature and prevent dew forming on the equipment.

2.6 Light sources

Initially the wavefront sensor will be used for accurate characterisation of the atmosphere so a bright point source is required. Ideally these would be lasers, but due to regulations it is not desirable to have these unsupervised. Additionally due to the coherence of lasers artefacts such as fringe patterns will be imposed on the recorded data due to stray reflections within the optics. To enable 'clean' reconstructions of the wavefront it is imperative that such problems be minimised. At the present time it is thought that for sources close to the system (under 5km) simple light emitting diodes with suitable optics will suffice, however above 5km the power requirements become such that the only viable source may be several laser pig-tailed together to decohere the source.

3 Measurements

Unfortunately due to problems with the camera system and the pan and tilt mount, the wavefront sensor has still to be deployed. It is currently undergoing final construction and testing in the laboratory and deployment is anticipated within the next six weeks. Laboratory validation of the wavefront sensor using a distorted grating is near completion and has been reported elsewhere at this meeting [1]. Initial experiments will involve measuring the wavefronts from a single point-like source at approximately 1km from the sensor. By calculating the wavefronts, and using the science camera to measure the image, the two pieces of information can be checked with each other to ensure that the sensor is functioning correctly. Further an average of many wavefronts can also be used to measure the aberrations present within the system as this has the effect of averaging the atmospheric perturbations, leaving only the static aberrations due to the sensor system. Once the system has been tested, it will then be used to measure the atmospheric perturbations on wavefronts arriving from sources of different ranges, which will enable information to be gathered about the strength of the turbulence for different path lengths. It should be possible with the site chosen for the sensor to measure path lengths in excess of 10km. A further extension is intended to use two or three sources within the field of view of the telescope to try and collect data about the spatial distribution of the turbulence. By using two or three sources it is possible to separate the turbulence into distinct regions where the light from the sources do not overlap, partially overlap and fully overlap.

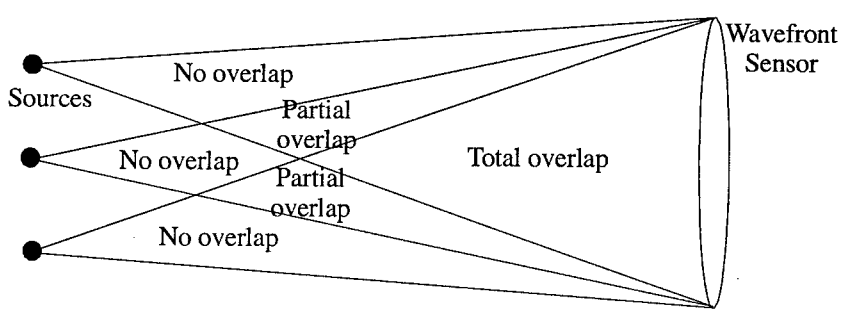

Figure 3. Turbulence measurement with three sources

As the sources are separated spatially, then the data on the wavefront sensor is also separated, so for each source an independent measurement of the wavefront can be calculated. From Figure 3 it is evident that the wavefronts will be correlated in some complex fashion, as the light travels from each source through both the same and different regions of turbulence. By measuring the correlations of the wavefronts in both spatial and temporal domains, it will be possible to extract useful tomographic information from the data in a similar scheme to SCIDAR [3]. In addition to but not simultaneously with the tomography of the turbulence, it is

anticipated that the chromatic properties of the turbulence will be studied. A polychromatic source could be achieved by coupling several lasers together using fibre couplers. It is possible to disperse the light across the sensor, so wavefronts can be constructed for each wavelength used. If three colours are used then it would be possible to measure the turbulence effects at these three wavelengths simultaneously.

4 Future developments

The measurements above describe only the first stage for the wavefront sensor system. Once the sensor has been deployed and is gathering data, then a fast tip/tilt mirror with quad cell will be introduced into the system to stabilise the image. The hardware and software for this section of the AO system is in an advanced stage of development, and is planned to be completed within the next few months. Once these building blocks are in place, then a full AO system will be designed and incorporated onto the breadboard. The wavefront sensor described above will be modified to enable real-time signals to be generated to control a deformable mirror. Depending on the design of the mirror, it may be possible to implement a control scheme with very little processing, as the wavefront sensor detects curvatures and the mirrors are operated on a curvature basis.

5 Conclusion

A complete system for measuring horizontal atmospheric turbulence in the optical region has been described. It uses a novel wavefront sensor based on the intensity transport equation, and uses a distorted grating to gather the necessary information. Two synchronised Dalsa CCD cameras are used to measure the curvature information and the image in real-time over several minutes to enable good statistics to be derived from the data.

6 References

1. Blanchard P M, "Multi-plane imaging with a distorted diffraction grating." This conference
2. Woods S C, "Laser wavefront sensing using the intensity transport equation." This conference
3. Klückers V A et al, "Results from SCIDAR experiments." in "Image Propagation through the Atmosphere." Proc. SPIE **2828**, p234-243.

This research is part of the Technology Groups 8 (Visible and IR Technology) of the MOD Corporate Research Programme.

LOW-ORDER ADAPTIVE OPTICS SYSTEM FOR FREE-SPACE LASERCOM: DESIGN AND PERFORMANCE ANALYSIS

K. H. KUDIELKA, Y. HAYANO, W. KLAUS, K. ARAKI

Communications Research Laboratory, 4-2-1 Nukui-Kitamachi, Koganei, Tokyo 184-8795, Japan

Y. ARIMOTO, J. UCHIDA

National Space Development Agency of Japan, Tsukuba Space Center, 2-1-1 Sengen, Tsukuba, Ibaraki 305-8505, Japan

A laser communications demonstration experiment (LCDE) between the Communications Research Laboratory in Tokyo and the International Space Station is being designed and implemented. To efficiently couple the downlink laser beam into a single-mode Erbium-doped preamplifier and to reduce uplink beam wander and scintillations, we plan to use low-order adaptive optics. The envisaged system dithers the wavefront actuators and evaluates the resulting variations of the received optical power. Simulation shows that, when controlling tilt, focus, and astigmatism, the power penalty due to residual wavefront error amounts to 2.3dB.

1 Introduction

The high bandwidth offered by free-space lightwave communication systems makes them very attractive for future satellite networks requiring intersatellite links of the order of 1Gbit/s. Also, the large amounts of data gathered by Earth-observing satellites or manned spacecraft could be easily downloaded to Earth in a relatively short time.

To demonstrate the advantages of free-space laser communications, the Communications Research Laboratory (CRL) is implementing an experimental link between its optical ground station, situated in a western suburb of Tokyo, and the Japanese Experimental Module (JEM), which is part of the International Space Station.[1] The aims of this project are (1) to realize a compact, light-weight optical terminal, utilizing components and subsystems already developed for terrestrial fiber communications, (2) to demonstrate detection and ranging of space debris, and (3) to demonstrate the feasibility of a space-to-ground link using a ground station equipped with adaptive optics (AO). Table 1 summarizes the key parameters of the communications link. To make maximum use of terrestrial fiber technology, both the uplink and the downlink wavelength have been chosen to lie in the 1.5μm wavelength band. Erbium-doped power- and pre-amplifiers will be employed in both terminals.

Parameter	Downlink	Uplink
Wavelength	1.552μm	1.562μm
Data rate	2.5Gbit/s	1.2Gbit/s
Output power	0.4W	1W
Modulation scheme	intensity modulation	
Transmit telescope diameter	15cm	10cm
Receive telescope diameter	50cm	15cm
Detection scheme	direct detection	
Sensitivity (bit-error rate: 10^{-9})	90photons/bit	

Table 1. Key parameters of the Laser Communications Demonstration Experiment

Also, the modulation scheme is compatible with terrestrial systems.

At the ground station, the optical radiation received from JEM has to be fed to the optical pre-amplifier in a single spatial mode. Hence, diffraction-limited performance of the optical system is required. Measurements of the atmospheric turbulence at $\lambda = 0.8\mu$m revealed Fried's coherence length r_0 to be between 5cm and 9cm.[2] For $\lambda = 1.55\mu$m and a receive telescope diameter of $D_r = 50$cm, one calculates $2.5 \leq D_r/r_0 \leq 4.5$, a range that suggests the use of low-order adaptive optics.

2 Design of adaptive optics system

The block diagram shown in Figure 1 gives an overview of the adaptive optics system to be implemented. The interfaces are CRL's 1.5m telescope on one side and a fiber-coupled transmitter/receiver pair on the other side. Acquisition and coarse pointing will be handled by separate subsystems.

The downlink beam passes through the telescope (used subaperture: 0.5m, magnification: 20) and is reflected by a fast steering mirror and a 13-electrode bimorph mirror (CILAS model BIM-13). A quarter-wave plate converts the circular state of polarization into a linear one. Then the beam passes a polarization splitter, which is used to superimpose the uplink beam. Finally, the beam is truncated to its final diameter (2.5cm) and coupled into a polarization-maintaining single-mode waveguide by a lens.

With the fast steering mirror and the deformable mirror, the adaptive optics system is able to correct five optical aberrations: tilt (2), focus (1), and astigmatism (2). In order to estimate and compensate the current wavefront parameters, we make use of the well-known multidither concept:[3] Each parameter is dithered sinusoidally, and the resulting oscillation of the quantity

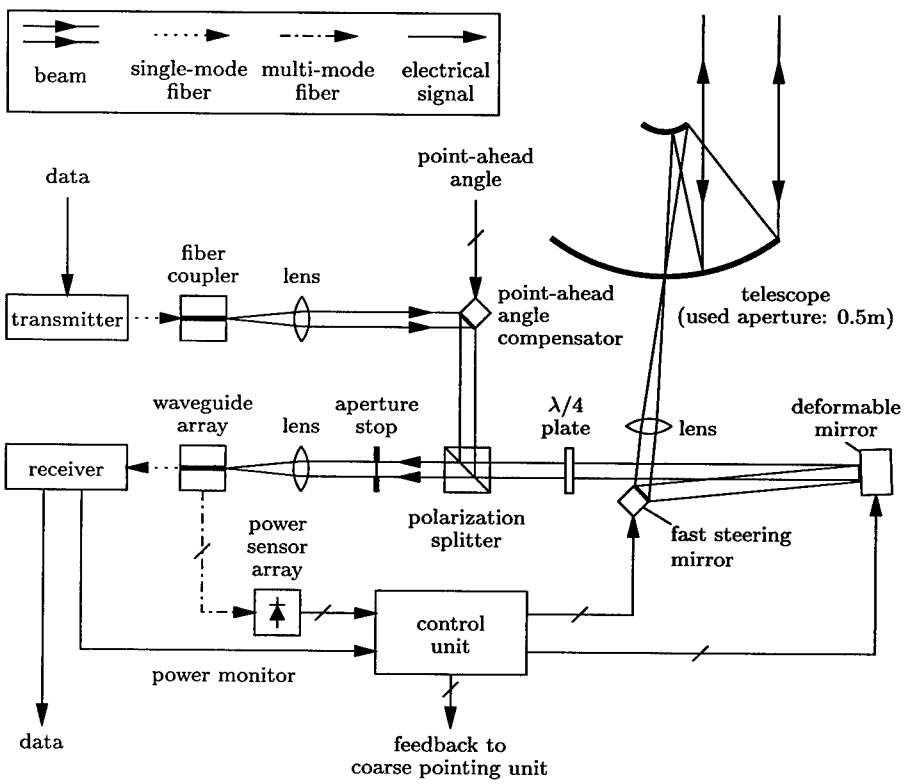

Figure 1. Block diagram of the adaptive optics laser communications system

to be maximized (i.e. the optical power coupled into the receiver) is synchronously demodulated. The such gained error signal is then fed into a loop filter, followed by an integrator. The integrator's output is finally added to the dither signal, and the resulting signal drives the corresponding actuator(s).

For the five control loops to operate independently, the dither signals have to be orthogonal to each other. This is best accomplished by using sine and cosine at three different dither frequencies. Since the bandwidth of the deformable mirror is limited, we plan to assign the highest dither frequency to the fast steering mirror.

For the control loops to lock, the angle of the incident wave has to lie well within the field of view of the telescope, which is about $\lambda/D_r \approx 3.1\mu$rad. Un-

fortunately, the RMS value of the residual error associated with the telescope's coarse pointing unit, is much larger. Hence, a means for angular acquisition needs to be provided separately.

To this end, a novel device, based on multi-layer polymeric optical waveguides, has been developed:[4] Within the focal plane of the receiving lens, the single-mode waveguide, nominally carrying the communication signal, is surrounded by four closely spaced multi-mode waveguides with rectangle-shaped cores. During initial acquisition, the optical powers coupled into those waveguides are measured by optical power sensors and evaluated by the control unit (see Figure 1). This setup functions as a quadrant detector and requires no additional adjustment.

The control unit, which manages acquisition and tracking of the downlink beam, will be implemented by an off-the-shelf DSP system.

The uplink signal, emerging from the end of a polarization-maintaining single-mode fiber, is collimated by a lens and then deflected by a steerable mirror. This mirror is used for setting the point-ahead angle, i.e. the difference between the direction of the transmitted and the received beam, which is necessary to hit the quickly moving target. At the polarization splitter, downlink and uplink beam are finally superimposed.

3 Downlink performance analysis

In the ideal case, an adaptive optics system would completely eliminate stochastic wavefront aberrations, and the optical receiver would be fed with constant optical power. In reality, however, residual aberrations, i.e. aberrations the system doesn't correct *at all* or doesn't correct *perfectly*, cause a reduction of the received optical power. In case of imperfect correction, the variance of each aberration is influenced by the power sensors' noise, the control loops' finite bandwidth, and the dither signals.

To arrive at a meaningful expression for the AO system's performance, we determine the optical transmit power required to achieve a bit-error rate (BER) of 10^{-9} under the presence of turbulence and AO control, and compare it with the power required in a diffraction-limited system. In a Monte-Carlo analysis, 10000 different stripe-shaped phase screens are moved across the receiver's aperture. The phase screens, corresponding to Kolmogorov statistics, are generated using a method proposed by Winick.[5] While moving each phase screen, a complete time-domain simulation of the multidither control algorithm, described in Section 2, is performed, resulting in a trace of received power versus time. From the trace data, the distribution function of the optical power is easily derived. Finally, by applying the BER formula of an

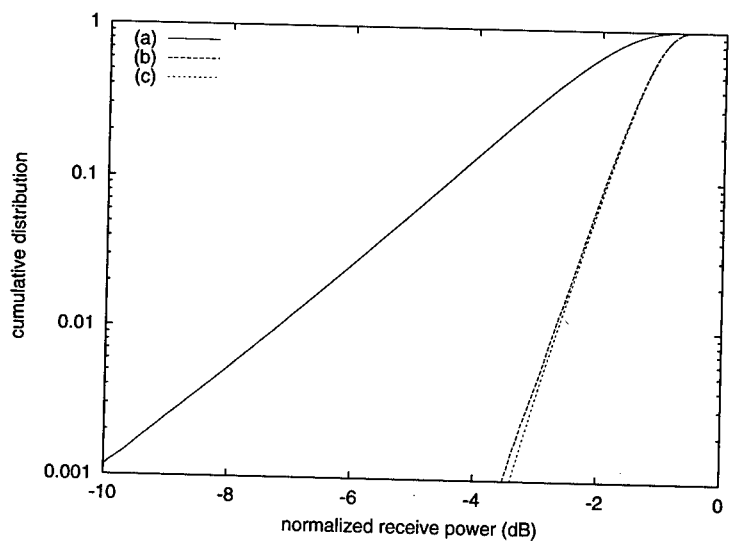

Figure 2. Cumulative distribution of normalized receive power. (a) simple AO system removing only tilt; (b) multidither system; (c) "ideal" second-order AO system

optically pre-amplified direct detection receiver, the mean BER is determined.

In Figs. 2 and 3 we present the results obtained for $D_r/r_0 = 2.5$ and $f_n D_r/v = 4$ (f_n... natural frequency of control loops, v... effective wind speed). The performance of the multidither system is almost identical to that of an "ideal" second-order AO system which *completely* removes tilt, focus, and astigmatism. The probability, that the received power is reduced by more than 3.5dB, is 10^{-3}. To maintain a BER of 10^{-9} under the presence of turbulence, the transmit power has to be increased only by 2.3dB. For comparison, if only wavefront tilt were compensated, the power would have to be increased by 14.7dB.

4 Conclusion

We have presented a preliminary design study which shows that a simple low-order adaptive-optics system, installed in the optical ground station, will significantly improve the link margin of the JEM demonstration experiment. The proposed system uses a multidither algorithm for wavefront tracking and a focal-plane waveguide array for acquisition.

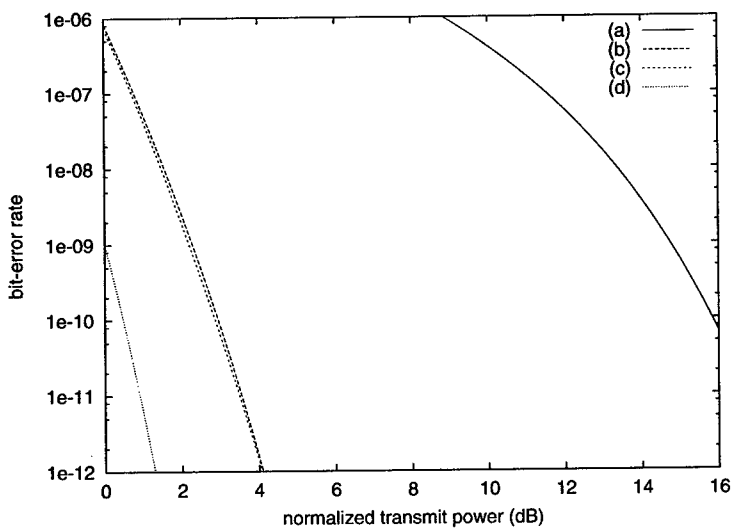

Figure 3. Bit-error rate as a function of normalized transmit power. (a) simple AO system removing only tilt; (b) multidither system; (c) "ideal" second-order AO system; (d) diffraction-limited system

References

1. Y. Arimoto. Study on high-speed space laser communications using adaptive optics and the demonstration experiment on International Space Station. In *Proc. CRL International Symposium on Optical Communications and Sensing toward the next Century*, pages 72–77, March 1999.
2. Y. Hayano et al. Ground-to-satellite laser communication program at CRL using adaptive optics. In *Proc. SPIE*, volume 3126, pages 208–211, 1997.
3. J. E. Pearson et al. Coherent optical adaptive techniques: design and performance of an 18-element visible multidither COAT system. *Appl. Opt.*, 15(3):611–621, 1976.
4. M. Hikita et al. Fabrication of multi-layer polymeric optical waveguides for space laser communication. In *Proc. IEICE General Conference*, March 1999. Paper C-3-95 (in Japanese).
5. K. A. Winick. Atmospheric turbulence-induced signal fades on optical heterodyne communication links. *Appl. Opt.*, 25(11):1817–1825, 1986.

A HIGH PRECISION SYSTEM FOR WAVEFRONT CONTROL

PASCAL JAGOUREL, JEAN-CHRISTOPHE SINQUIN, DAVID WAFLARD
CILAS, Route de Nozay 91460 Marcoussis
FRANCE
E-mail: jagourel@cilas.com

XAVIER LEVECQ, GUILLAUME DOVILLAIRE
Imagine Optic, 2 rue Jean Rostand 91893 Orsay Cedex
FRANCE
E-mail: contact@imagine-optic.com

Wavefront control is a key issue for developing different systems including : lasers (for various applications : isotopic separation, femtosecond solid state lasers, microlithography...), imaging through turbulent media, ophthalmology... For these purposes, we have developed an adaptive optics system that can achieve wavefront very high precision correction.
Subsystems will be described including the Wavefront Sensor (Shack-Hartman type), the Deformable Mirror (Bimorph type) and the Real Time Computer (PC type). Emphasis will be made on results that can be obtained using such a system : ultimate quality of the corrected wavefront, measurement range (important during capture phases)...

1 Introduction

Most previous "traditional" Adaptive Optics applications were aimed to correct for atmospheric turbulence (astronomy, pointing and focusing in military applications, space survey...). Guidelines for the conception of such systems were fast response and no actual need for high precision. In fact, in most cases, these systems are limited, on the one hand, by photon availability for the measurements and, on the other hand, by the speed of the turbulence.

As a result of this situation, conventional Shack-Hartmann wavefront sensors have been designed to make it possible high speed measurements (up to a few kHz sampling frequency). These sensors generally exhibit a precision consistent with these applications (typical : $\lambda/20$ rms).

New requirements have appeared these last years. Concerning wavefront correction of lasers, these requirements can be summarized by the following :

- High precision : typical $\lambda/10$ PV, $\lambda/60$ rms is foreseen in these applications,
- pretty low speed : a sample frequency in the 1 to 20 Hz seems to be enough for the correction of spatial complex shapes that do not move quickly with time as far as they generally result from thermo mechanical effects.

For a Deformable Mirror Manufacturer, it appears that metrology has to be dramatically improved to address the following questions : is a DM, whatever the type, capable of that precision ? If not, what is the limitation and which changes in the design could make it possible to reach the desired quality.

This question is one of the motivations for putting together on a bench a high precision wavefront sensor and state of the art Deformable Mirrors. Nevertheless, as a result of the present work, we are also able to derive a high precision system which can become a commercially available system : the definition of such a system is the second motivation of this work.

2 Presentation of the set-up

The following figure shows the set-up that has been used for closed loop performance measurements :

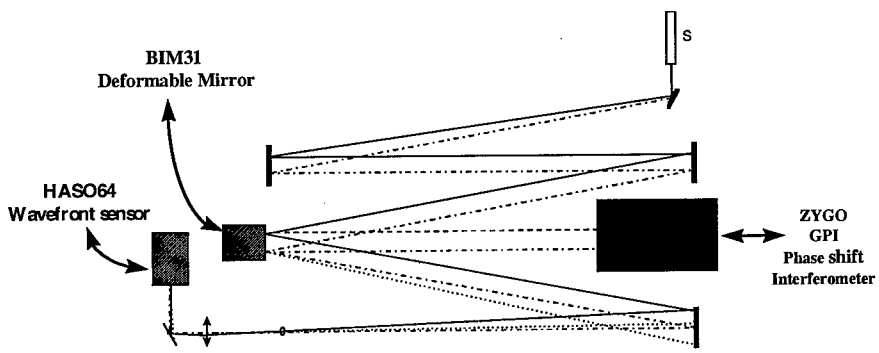

General Presentation of the experimental set-up

One can find following components :

- HASO64 Shack-Hartmann wavefront sensor
offering high spatial resolution (64x64 subapertures)
- BIM31 Deformable Mirror (bimorph technology)
- PC work station to perform closed loop calculations
- ZYGO phase shift interferometer to measure performances

3 The HASO64 WaveFront Sensor

3.1 General description of the HASO 64

One can see on following figure a schematic representation of the HASO 64. This system is based on the Shack Hartmann technology. Moreover, this system is very compact : the distance between the micro lens array and the CCD is less than 10 mm.

There are 64 x 64 sub-apertures (4096 microlenses). The chosen CCD gets 1024 x 1024 pixels.

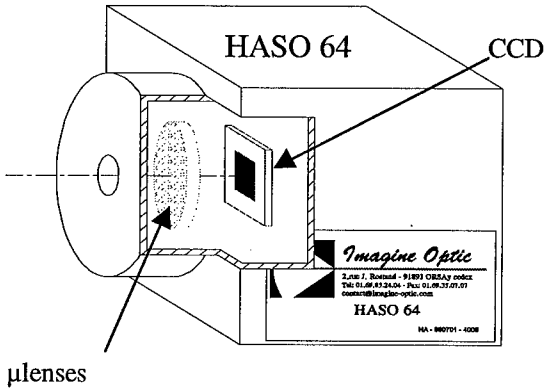

This system is pre-calibrated, that is to say that it can be used to measure "absolute wavefront" : one do not need to have a reference, the HASO 64 measures the absolute shape of the incoming wavefront with an accuracy better then $\lambda/100$ rms.

It can work in a "referenced mode" : in this case, the system computes the difference between the incoming wavefront and a reference measured in the same configuration of tilts and focus. In this mode, the accuracy is better than $\lambda/200$ rms on a 40 λ stroke.

Due to the CCD, the HASO 64 can measure wavefront with a wavelength ranging between 350 nm and 1.1 µm.

The other major characteristics of this system are :

- Local slopes errors lower than 10 µrad rms in absolute mode.
- Local slopes errors lower than 6 µrad rms in referenced mode.
- Huge dynamic : more than 1000 λ.

This stroke allows the system to work with very convergent and divergent beams. Beams can be focalized 40 mm forward or backward the microlens array. So, users can use the HASO 64 to align, characterize and improve lenses and optical bench quality without any need to collimate the beam in front of the sensor.

3.2 HASO 64 specificity for adaptive optics

We have first to notice that deformable mirors can not for correct high spatial frequencies aberrations. This limitation is due to the limited number of actuators. The value of this spatial frequency limitation is theoretically fixed between Shannon frequency and twice Shannon frequency of actuators spatial geometry. The deformable mirror acts like a spatial frequencies filter.

So, if the SH that drives the deformable mirror, introduces errors with spatial frequencies above the Shannon or twice Shannon frequency of the mirror, these errors will not be injected in the correction because the deformable mirror can not fit the corresponding shapes. On the other hand, if the wavefront sensor introduces errors with spatial frequencies below Shannon or twice Shannon frequency of the mirror, all these errors will be directly injected in the correction.

Thanks to their optimized configuration and software, HASO systems are able to reject Shack Hartmann errors at a high spatial frequencies range.

Shack Hartmann errors we are talking about, are "non random" errors on slopes calculations like crosstalk between spots and errors on centroids calculations.

We compare, on the following figure, results of 2 different configurations and software for Shack Hartmann sensors. They have the same number of sub-apertures : 64 x 64. One of them is an HASO 64 with optimized configuration and software (on the left side), the other one has a conventional configuration (like for astronomy) and conventional centroids calculation (on the right side).

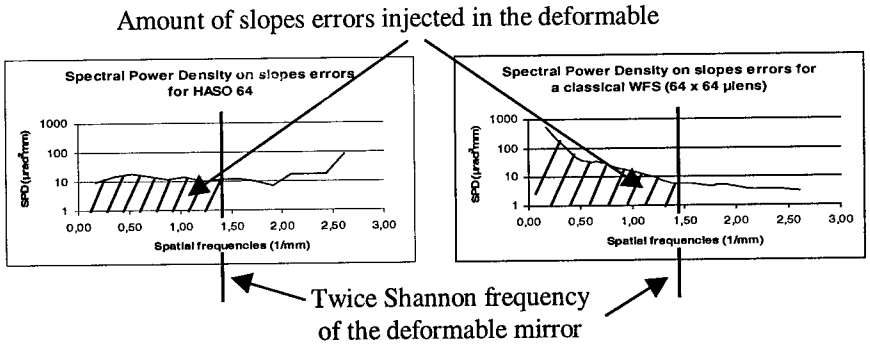

The curves represent slopes errors values versus spatial frequencies. In fact, these curves are the power spectral density of slopes errors, that is to say they are the square module of Fourier Transform of slopes errors.

With the HASO 64 configuration, the lowest slopes errors values are at the lowest spatial frequencies and most of errors are rejected in a high spatial frequency range. On the other hand, most of slopes errors are at a very low spatial frequency range in the case of the conventional configuration. In this example the amount of slope errors injected in the mirror command is 4 times bigger for the conventional configuration than for the HASO configuration.

Thanks to their specific configuration and software, HASO systems can drive deformable mirrors with ultimate accuracy ($\lambda/200$ rms) and actually improve close loop performances.

4 The BIM31 Deformable Mirror

The following figure shows the configuration of the 31 electrode Bimorph deformable mirror that has been used :

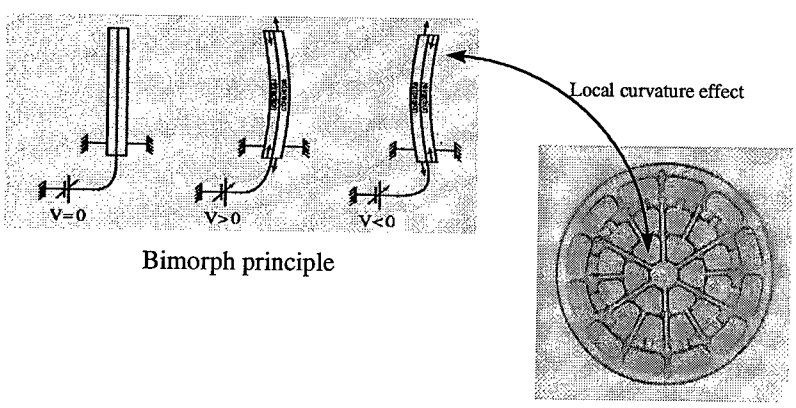

Bimorph principle

BIM31 electrode pattern

19 electrodes act like curvature actuators and are situated inside the clear aperture. The third ring of electrodes is situated outside the pupil and corresponding 12 electrodes are used for boundary conditions at the edge of this pupil. The preceding figure shows how local curvature is generated on such a mirror using differential transverse deformations of 2 piezoelectric plates. The mirror exhibits following characteristics :

<u>Mirror Surface</u>

- Polished glass optical surface onto piezoelectric material
- Protected silver coating (Reflectivity > 97% for $0.6 < \lambda < 10.6$ µm)

- Optical surface roughness < 0.5 nm r.m.s.

Mirror performances
- Full mechanical strokes (@ ± 400 V voltage on electrodes) :
  10 μm peak to valley for low spatial frequencies
  4 μm peak to valley (only one electrode driven)
- Mirror tilt capability : ± 0.2 mrad :
- Hysteresis : < 6% for a ± 400 V cycle
- First resonance frequency : > 2.5 kHz

Concerning mirror flatness, previous closed loop measurements have demonstrated $\lambda/20$ rms quality on the reflected wavefront. Nevertheless, we have to mention that limitation was mainly due to wavefront sensing : for instance rejection of defocus and astigmatism was not perfect although we know from models that bimorph mirror is perfectly adapted for the correction of such modes.

5 The control computer and associated software

Following figure describes the hardware used for the closed loop. It makes use of a standard PC equiped with a wavefront sensor interface board and a digital to analog conversion board.

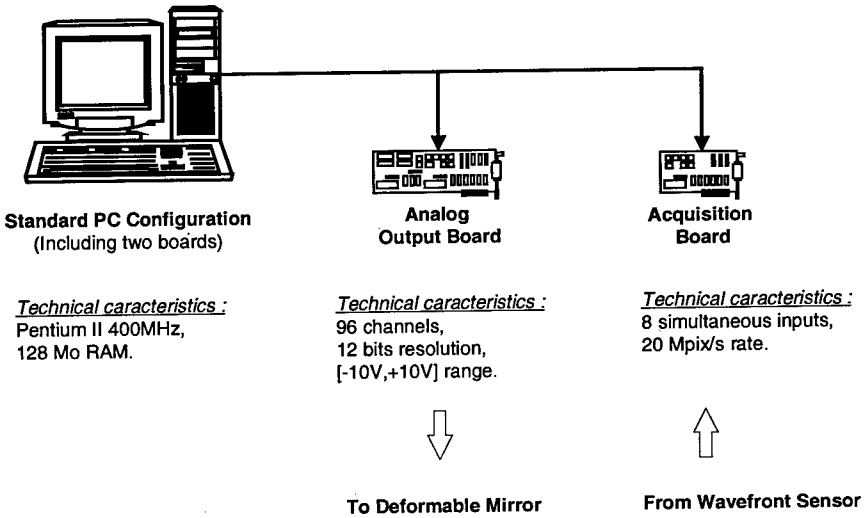

Concerning software, Adaptive Optics Software is a multithread application running under Windows NT4.

AO Software present following Functionalities :

- Mirror Command (voltage outputs in open loop),
- AO System Calibration (reference slopes and interaction matrix),
- AO System Control (mirror command in closed loop).
- AO Graphic User Interface is a multi-windows interface developed with Labviews (National Instruments).

AO Software performance leads to a closed loop refreshment rate of 10 Hz in the BIM31-HASO64 configuration.

6 Experimental results

6.1 Performance of the sensor

The following sequence was used fot the Test of the control loop :
- Drive BIM31 to a random reference shape by applying a set of voltages to the electrodes
- Record corresponding shape *Sh1* with Zygo interferometer
- Record reference slopes ***Sl*** on HASO64 shack-Hartmann wavefront sensor
- Suppress voltages from the BIM31 (mirror is now in rest position)
- Close the loop in order to reach reference slopes ***Sl***
- Record corresponding shape *Sh2* with Zygo interferometer
- Compare *Sh1* and *Sh2*

Clearly, this sequence allows the measurement of the wavefront sensor accuracy. In fact, the only assumption is that the DM can get during closed loop the same shape than during reference measurement.
Quality of 17nm PV, 3nm rms (mechanical shape) was observed during this measurement set which is close to the accuracy of phase shift high quality interferometers.

6.2 Performance of the deformable mirror

The following sequence was used for the Test of the BIM31 Deformable Mirror:
- Replace BIM31 with a flat reference mirror
- Record corresponding shape *Sh1* with Zygo interferometer
- Record reference slopes ***Sl*** on HASO64 wavefront sensor
- Put BIM31 Deformable Mirror back (mirror is in rest position)
- Close the loop in order to reach reference slopes ***Sl***
- Record corresponding shape *Sh2* with Zygo interferometer
- Compare *Sh1* and *Sh2*

Quality of 67nm PV, 10nm rms (DM mechanical shape) was observed during this measurement set. These measurements show that the flatness of a flattened BIM31

is better than λ/30 but it can not allow to conclude on the ultimate quality of such a mirror since this quality is close to the one of the reference mirror.

7 Conclusions

High precision metrology in the *λ/200 rms* range is now available for Adaptive Optics systems thanks to ***Imagine Optic*** design efforts to optimize Shack-Harmann wavefront sensors. Additionnal improvements are to be reached soon by using high precision reference mirrors in the λ/100 rms range : it opens the way to improved **CILAS** Deformable Mirrors since the only precision you can offer is the one you can measure and improvements are possible only if one can analyze the limitations of available techniques.

DEVELOPMENT OF A CURVATURE ADAPTIVE OPTICS SYSTEM FOR A MICHELSON STELLAR INTERFEROMETER

C. VERINAUD, A. BLAZIT, A. DE BONNEVIE

Observatoire de la côte d'Azur, F-06460 Saint-Vallier-de-Thiey, FRANCE

The 'Grand Interféromètre à Deux Télescopes' (GI2T) is a Michelson Stellar Interferometer. The interferometric signal, i.e. the fringe contrast, is directly related to the high spatial frequencies of the object being observed. Because of atmospheric turbulence, the interferogram in the image plane is spread into numerous uncorrelated fringed speckles, thus the dilution of light is decreasing dramatically the Signal-to-Noise Ratio (SNR). We plan to integrate Adaptive Optics (AO) in both interferometric arms. Operating at visible wavelengths, the correction of the atmospheric aberrations, although partial, will concentrate the light in a central core surrounded by a few bright speckles, leading to an enormous increase of the SNR. We describe here the status of the development of the wavefront analysor of the system and some simulation results will show the improvement of the sensitivity of the interferometer equipped with AO. We will also emphasize some problematics concerning the calibration of fringe contrast measured on interferograms corrected by AO.

1 Introduction

The GI2T interferometer is composed of two 1.5 m telescopes which can move on a 65 m long North-South baseline. A complete description of the GI2T and its new focal instrument has been given by D. Mourard [1]. The integration of Adaptive Optics (AO) is an extension of the REGAIN (REcombinateur pour GrAnd INterféromètre) project which aim is the renewal of the whole instrument after the promising astrophysical results obtained in the first operation runs. The design of a novel optical scheme of the Curvature Wavefront Sensor (CWFS) detection module is exposed. Some pictures describe the current status of the construction of the wavefront sensor. Complementary informations especially about the AO optical adaptor for the REGAIN table can be found in [2]. Simulation results stress the tremendous improvement in sensitivity one can get by combining AO and Interferometry. Though, much care has to be taken for the calibration of the fringe contrast measurements as they depend strongly on the residual wavefront errors and on the differential piston between the two corrected beams.

2 Main caracteristics of the GI2T Adaptive Optics System

The GI2T AO system is inspired from F. Roddier's curvature adaptive optics concept [3]. The main specifications of the system are given below:

1. Corrective element: 31 electrodes bimorph deformable mirror.
2. Wavefront sensor: 31 sub-pupils sampled by an array of prisms.
3. Wavefront sensor detectors: Avalanche-Photo-Diodes cooled at –20°C and working in photon counting mode with 40% detection efficiency and about 200 electrons per second of dark current .
4. Sampling frequency: 2.5 kHz.
5. Maximum closed loop control bandwidth : > 200 Hz.
6. Modal control.
7. Maximum Strehl ratio at r_0 = 10 cm and wind speed = 10 m/s (tel. Diam=1.5m): S = 0.35 .

The sensing of the wavefront curvatures and tilts at the edges are performed by measuring the intensity distribution in two out-of-focus images. The detectors used in the few existing curvature systems [4,5] are Avalanche-Photo-Diodes (APD) working in photon counting mode, chosen for their good sensitivity and zero read-out noise. Usually the coupling of the intensity with the detector is ensured by a lens array and optical fibers. For the GI2T CWFS, a novel optical scheme has been chosen. This setup is made of a single optical component that shares the beam and focuses the light coming from each element of the out-of-focus images to the APD's sensitive surface. The alignment is done by the mechanical structure itself, the only degree of freedom beeing the rotation of the mosaic of prisms. A complete description is given in figure 1.

3 Current status of the development of the CWFS

A test bench has been designed to qualify the whole AO system in closed loop operation (fig.2). Now, the wavefront sensing path is being integrated .

The electronic modules of the APDs which were built at OCA by A. Blazit have been successfully tested together with the peltier cooling system. The APDs have reached the specifications and have a linear response up to 5.10^5 photons per second. They can support daylight without any damage and saturate only at more than 3.10^6 photons per second. The figure 3 is a snapshot of the 31 APDs embedded in the cooling device copper structure. The mosaic of prisms has been assembled at Observatoire de Paris. The shape and tolerances of the prisms have been computed by A. De Bonnevie. The figure 4 shows the realization of the mosaic of prisms.

4 Simulations of the improvement of the GI2T sensitivity by adaptive optics

The simulations are based on the AO simulation package of F. Rigaut [6] and the interferograms are obtained by fourier transforming a remapped complex pupil (spatial encoding) [7] containing AO corrected phases of the two telescopes beams.
The figure 5 represents the gain expected in typical atmospheric conditions for a 5th magnitude star. The fringes are recorded on short exposures using speckle interferometry techniques. The SNR have been calculated using the formalism of J.-M. Conan [8].The SNR is **11.2** for the non corrected case and **105** for the corrected one. The gain is really huge in observing time and much fainter objects can thus be observed. Furthermore, if co-phasing the two beams is possible, then the fringes can be recorded directly on long exposures and the SNR will be the largest one can achieve.

5 Problematics about the calibration of fringe contrast on AO corrected interferograms and concluding remarks

Calibration with partial corrected images. In mono-mode fiber-based interferometers, the calibration is done by recording the interferometric intensity together with the intensity in single fibers coming from each telescope; by this way only the coherent core of the images is conserved and the seeing effect is removed. For the GI2T which is a multimode interferometer, an equivalent calibration can be done by recording at the same time the short exposures of the single apertures and the interferograms. F. Roddier demonstrated that a seeing-free visibility estimator can thus be computed [9].

The differential piston due to the deformable mirror. Ideally the correction achieved by the deformable mirror should not introduce any extra optical path between the two beams. In practice it is very difficult to measure the piston term introduced by each influence function of the mirror. A bad calibration can lead to a differential piston with a cut-off frequency much higher than the atmospheric piston cut-off frequency, so that it is difficult to sense it with a fringe tracker designed for atmospheric piston. Figure 6 shows a typical temporal spectrum of the piston introduced by the deformable mirror. In this case we adopted an error of 10% on the estimation of the piston of each influence function, which is approximately an upper limit of the error made on the simulated influence functions. On time scales comparable to the short exposure time, the visibility loss can reach a few percents. Furthermore, this loss depends on r_0 and thus it is difficult to calibrate it. So it is necessarry to measure with high precision the piston influence of the deformable mirror and use a calibration star, unless the fringe

tracker is fast enough to co-phase the two telescopes in presence of fast piston motion [10].

Conclusions. Combining Interferometry and Adaptive Optics will obviously revolutionize the field of high angular resolution (HAR) in astronomy , but much care must be taken for the calibration of fringe visibility. GI2T is now the most advanced interferometer with large apertures and is likely to be a powerful instrument before the VLTI is in operation, and will give a foretaste of the considerable astrophysical results one can get in the future in HAR.

Acknowledgements. We wish to thank the Technology and Research Service of the region Provence-Alpes-Côte d'Azur and the CNRS for supporting this work.

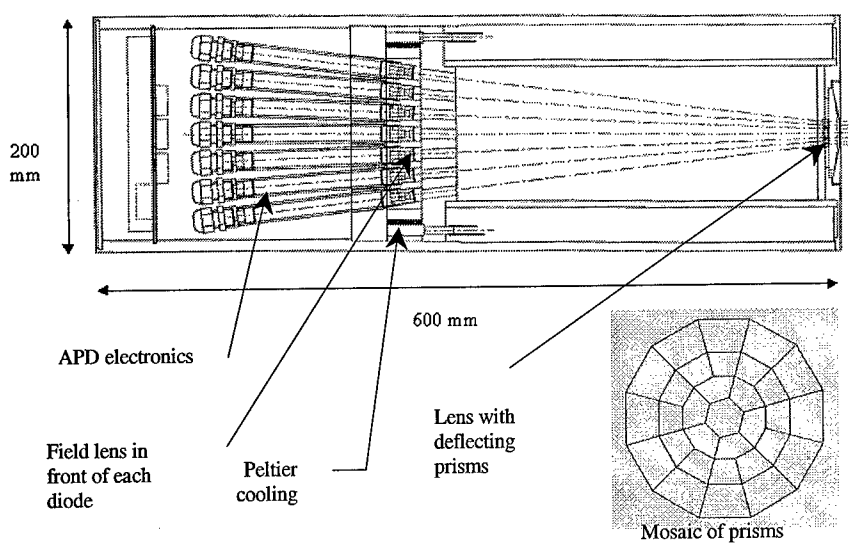

Figure1: Opto-mechanical structure of the CWFS:the sharing and focusing of the beam towards the APDs is ensured by a plano-convex lens with a mosaic of 31 prims stuck on it (bottom right). Each prism deflects the light in one sub-pupil (of the out-of-focus image) to the corresponding APD. A field lens in front of each APD re-images the corresponding prism on the sensitive surface of the diode in order to minimize effects of depointing of the CWFS detection module and diffraction effects.

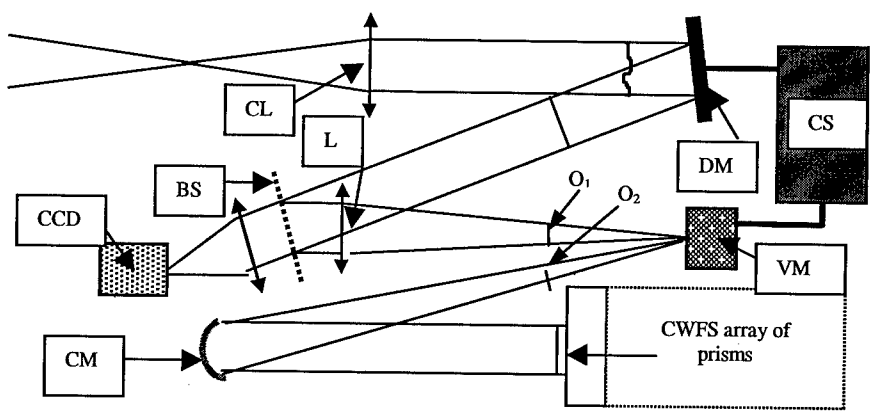

Figure2: Optical scheme of the test bench.. A collimating lens (CL) forms a pupil image onto the deformable mirror (DM). The corrected beam reflected by DM is split into the science beam and the wavefront sensing beam by the beamsplitter BS. The lens L re-images the pupil to infinity and forms a focal point onto a curvature variable membrane mirror (VM) vibrating at 2.5 kHz. When VM is flat the pupil is re-imaged on the array of prisms by a collimating mirror (CM). When VM is concave, respectively convexe, the out-of-focus image O_1, respectively O_2 is re-imaged onto the mosaic of prims. The control system CS performs the calculation of the wavefront and computes the DM commands.

Figure 3 : APD modules and peltier device.

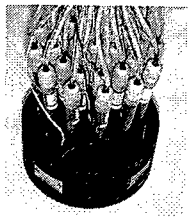

Figure 4 : Mosaic of prisms .

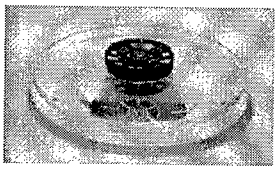

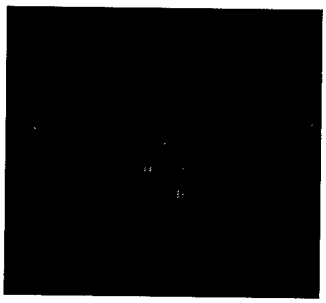

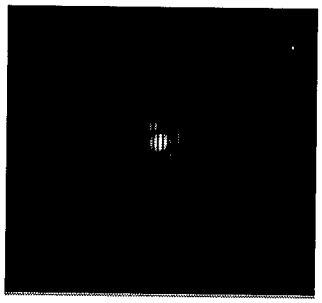

Figure 5. : Interferograms without correction (left) and with correction (right). D/r_0 (0.7 μm) = 12.5 and wind speed = 20 m/s. The strehl is 0.2 in the corrected image. The coherent energy in the central core of the right image is of about 15% of the total intensity. The images are displayed in logarithmic scale.

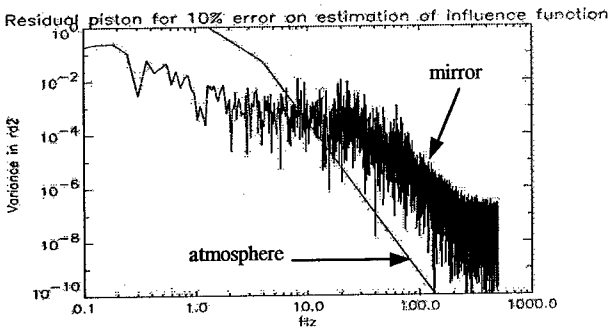

Figure 6: Temporal spectrum of residual piston and theoretical differential piston of atmosphere. r_0 = 8 cm. Wind speed = 20 m/s. The cut-off frequency of the mirror piston is 30 Hz. The cut-off frequency of the atmospheric differential piston is 4 Hz.

References

1. Mourard, D. et al. 1998, *The GI2T/REGAIN Interferometer*, SPIE 3350
2. Verinaud, C. et al. 1998, *Improving the GI2T/REGAIN Interferometer sensitivity using Adaptive Optics* in 'Catching the perfect' wave, ASP conference proceedings, July 98 Albuquerque.
3. Roddier F. et al. 1991, *University of Hawaii adaptive optics system: I General approach*, SPIE 1524
4. Arsenault, R. et al. 1994, *'PUEO ' the Canada-France-Hawaii Telescope adaptive optics bonnette I: System description*, SPIE 2201
5. J. Elon Graves, Malcolm Northcott, Francois Roddier, Claude Roddier & Laird Close 1998 *First light for Hokupa'a: the 36 element curvature AO system at UH.*, Proc. SPIE 3353,
6. Rigaut F. et al. 1994, *The Canada-France-Hawaii Telescope adaptive optics bonnette II : Simulations and control*, SPIE 1524
7. Berio, P. et al 1999, *Spectrally resolved Michelson stellar interferometry. I. Exact formalism in the multispeckle mode*, J. Opt. Soc. Am. A/Vol 16 , N°4
8. Conan, J.-M., 1994 *Correction partielle en Optique Adaptative* ,PhD Thesis
9. Roddier, C. and Roddier, F. 1976 , *Seeing effect removal in a Michelson stellar interferometer,* J. Opt. Soc. Am. A/Vol 66 , N°12
10. Roddier, F. 1999 *Ground-based Interferometry with Adaptive Optics* presented at the Dana Point conference 'Working on the fringes'

BLAZED HOLOGRAPHIC OPTICAL ABERRATION COMPENSATION

ISABELLE PERCHERON
GTC and Boeing North American Inc, PO Box 5670, Albuquerque NM, 871852
USA
E-mail: percheri@flash.net

JEFFREY T. BAKER
Boeing North American Inc, PO Box 5670, Albuquerque NM 87185
USA
E-mail: bakerj@plk.af.mil

MARK GRUNEISEM, TY MARTINEZ, DAVID WICK
USAF Research Labs, AFRL/DEBS, USA.

Conventional deformable mirrors have a limited throw and to compensate the many waves of aberrations of a large aperture membrane mirror we need to use holographic correction. Optically addressed Spatial Light Modulators (SLM) have been used in laboratory demonstrations to remove up to 200 waves dynamic aberrations [1]. The next step is to use a blazed holographic dynamic correctors to more efficiently transform the aberrated beam into a well compensated one, eliminating all the diffractive orders. We are presenting here the results obtained using a combination of an optically addressed, Parallel Aligned Nematic Liquid Crystal SLM and an electrically addressed SLM. Using these SLMs in conjunction with a CCD video camera and a computer we were able to introduce and then correct for first order aberrations (tilt, defocus, astigmatism) with up to 50 waves @543nm, we also used blazed holographic correction techniques to correct for around 20 waves of aberrations on a 2" area of a membrane mirror

1 Introduction

Holographic optical aberration compensation has been demonstrated to be capable of compensating for several waves of aberration. In a basic holographic setup an interferogram of the aberrated beam is generated and written on a diffraction hologram, so the local wavefront is corrected. We used the same technique but blazed the interferogram to put most of the energy in a single diffractive order. We are presenting here the results obtained on highly aberrated inflatable membrane mirror using with this technique.

2 PAL-SLM device and Optical setup

We used a PAL-SLM device from Hamamatsu Corporation, a pattern is written on an electrically addressed SLM (640X480 pixels) using a VGA driver and then

optically written after reimaging on a Parallel Aligned Nematic Liquid Crystal (20x20mm). The phase modulation on the PAL is of more than 2π.
In this setup we simulate a beam coming from a far object, this image is collected by a highly aberrated membrane mirror, an interferogram between a reference laser

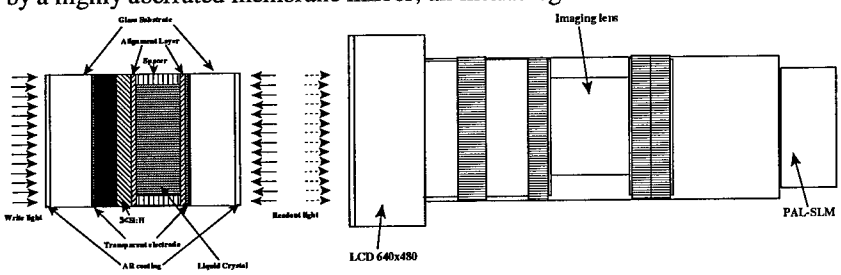

Figure 1. Left: Structure of the PAL SLM,
Right: combination PAL-LCD (PAL SLM X7550 device)

beam and the aberrated beam is recorded on a video camera and digitized, this interferogram is then processed by software and the resulting phase grating used for the correction is applied on the LCD, which is projected on the PAL. The diffractive corrected order of the PAL is also recorded on a video camera to calculate the efficiency of our correction.

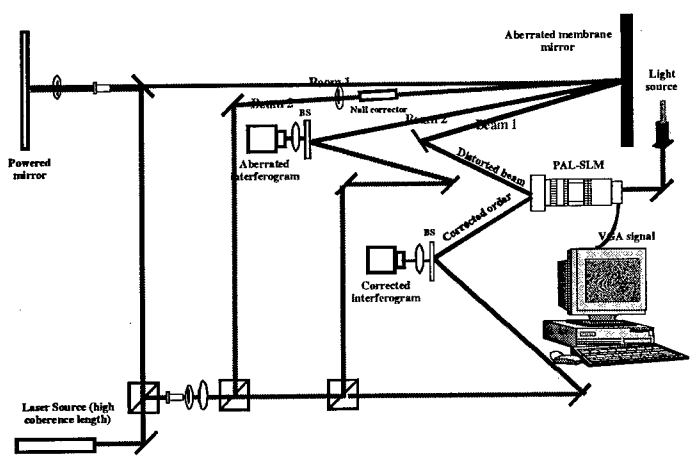

Figure 2. Optical setup: a laser beam is reflected out of a powered mirror to simulate the beam coming from an object (beam 1), the image collected by the membrane mirror is interfered with a reference beam to form the aberrated interferogram. This interferogram is digitized and processed to be blazed and the resulting correction is applied on the LCD-PAL system. The corrected interferogram is displayed on a video camera

3 Diffraction efficiency of the PAL SLM

We measured the diffraction efficiency for different phase gratings, the results are shown in the table 1 and in figure 3. The same measurements have been done by Toyoda et al [2].

Table 1. Diffraction efficiency obtained for different phase gratings

Phase grating	gray level	steps	number of fringes across	diffraction efficiency in different orders			
Binary Grating	0-255	2	5	-1	0	+1	
				38%	1%	26%	
Binary Grating	0-255	2	10	-1	0	+1	
				35%	3.3%	26.5%	
Binary Grating	0-255	2	15	-1	0	+1	
				35.6%	8.6%	26.8%	
Binary Grating	0-255	2	25	-1	0	+1	
				32.3%	7.2%	31%	
Binary Grating	0-255	2	40	-1	0	+1	
				32.8%	5.5%	27.8%	
Sinusoide	0-255			-1	0	+1	+2
				14.1%	47%	11.6%	3%
Blazed Grating	0-255	23	26	-1	+1	+2	
				5.3%	72.2%	4.8%	
Blazed Grating	0-255	53	11	-1	0	+1	+2
				7.8%	7.6%	52.7%	7.7%

Figure 3. Different orders when the PAL is addressed with a blazed grating (20 slopes across, 23 steps per blazed). There is 72% of the diffracted beam in the first order

4 Correction of simulated aberrations

We first simulated the interferograms obtained when one of the two interference beams is aberrated with first order aberrations like tilt, defocus and astigmatism. The results are shown in Table 2

Table 2. Diffraction efficiency obtained for simulated aberrations

Number of Waves of Aberration	Energy in the Corrected Order /Total Energy
45	60
15	30.1
15 (defocus)	78

5 Blazed holographic optical aberration compensations

The aberrated interferogram is recorded and digitized, the inverse cosine function of the aberrated sinusoid (figure 4, left) gives an aberrated triangle function (figure 4, middle), the blazed results is obtained by multiplying this triangle function by the sign of its gradient (figure 4, right).

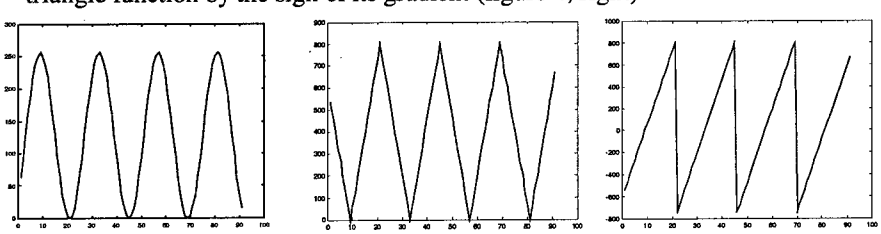

Figure 4. Different steps to blazed the interferogram

We used different different aberarrators including a membrane mirror, the aberrated and blazed interferograms are shown in figure 5 and 6.

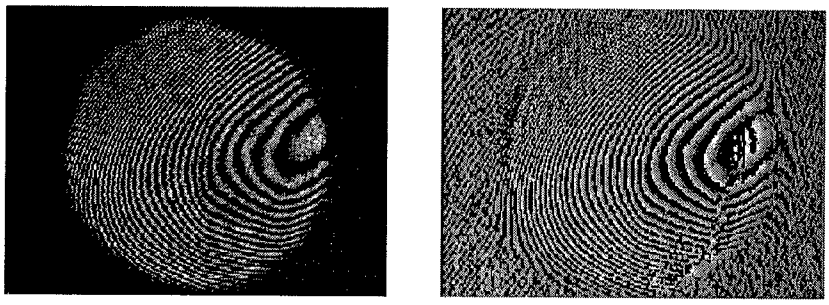

Figure 5. Left: recorded aberrated interferogram, right: blazed results

4

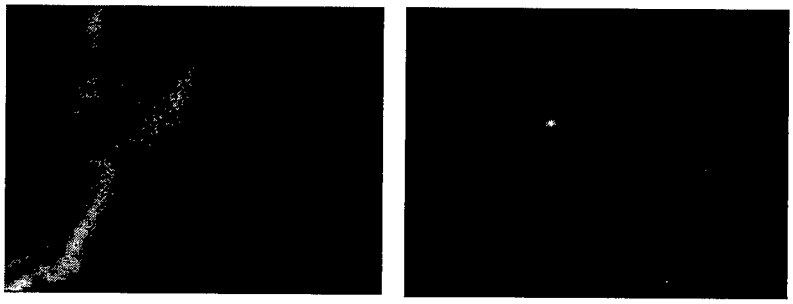

Figure 6. Left: aberrated beam, Right: corrected order

6 Conclusion

We demonstrated by this method that it's possible to correct a highly aberrated inflatable membrane mirror with a higher efficiency that the previously done demonstration [1].

References

1. Gruneisem M., Wick D., Martinez T., Wilkes J., Correction of large dynamic aberration by Real-Time holography using Electro-Optical devices and Non-linear optical media, SPIE Vol 3432, 1998.
2. Toyoda H., Kobayashi Y., Yoshida N, Igasaki Y., Hara T., High efficient electrically addressable spatial light modulator for reconfigurable optical connection, OSA, April 1999.

ADAPTIVE OPTICS IN LASER SCANNING SYSTEMS

E M ELLIS AND J C DAINTY
Blackett Laboratory, Imperial College, London SW7 2BZ, England
E-mail: c.dainty@ic.ac.uk

1 Introduction

Optical scanning systems are encountered in a wide variety of applications from bar-code readers to laser printers. In many cases, diffraction-limited performance is desired but this can be difficult to acheive due to field-dependent aberrations, the simplest of which is defocus. Depth-of-field is an important design consideration, since the object may be tilted or curved. In practice, a trade-off between depth-of-field and tranverse resolution is required.

Adaptive optics offers the possibility of obtaining diffraction-limited scanned imaging of arbitrary objects. The most elementary correction required is for focus, particularly in a post-objective scanner. [1] In this paper we demonstrate that a bimorph mirror can provide focus correction and present a design for the scanning optics of an A4 laser printer using an adaptive mirror.

2 Experimental Demonstration

Figure 1 shows the layout of a breadboard design to demonstrate the operation of a scanned imaging system for a tilted or curved object. The adaptive element is a cooperative bimorph mirror of diameter 50mm fabricated in our laboratory [2]: such mirrors can provide up to 60μm of focus wavefront correction (measured at the edge of the aperture). The curvature of the mirror is sensed by the signal at A, whereas the signal at C is the scanning signal that forms the image: B is a trigger signal. Figure 2 shows the signal at C for a grating like object for different focus settings of the bimorph as recorded by the signal at A. By noting the signal at A that gives the peak modulation of the scanned signal C, we can calibrate the required voltage signals to be imposed on the bimorph during the scan cycle. In practice, these signals would be sent in a step-wise fashion, minimising the bandwidth requirements of the mirror. The calibration procedure has to be repeated for each new curved or tilted object. Clearly more sophisticated calibration (or wavefront sensing) would be required for cases in which every object presented to the scanner had a different tilt or shape.

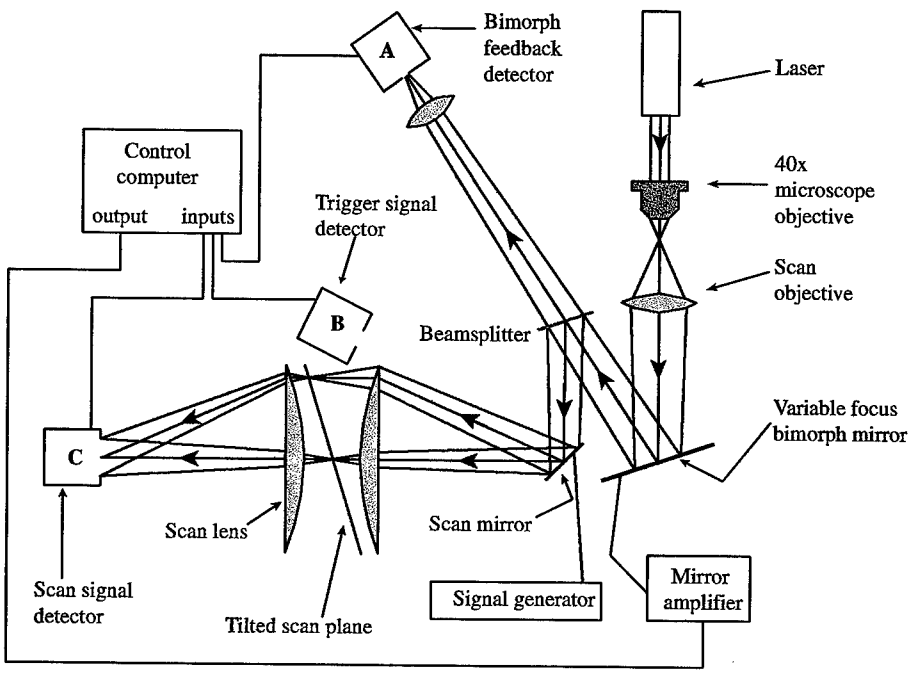

Figure 1. Breadboard optical scanning system for demonstrating the use of adaptive optics

Figure 3 shows a sample result in which the signal at C is plotted as a function of the scan position for a grating-like object without (left) and with (right) operation of the adaptive bimorph mirror. (Note that technical limitations of the A-to-D convertor meant that the signal at C could not be sampled continuously, hence the break-up of the signal.)

It is clear from this simple demonstration that adaptive optics may offer a means of improving the performance of scanned imaging systems.

3 Laser Printer Design

In order to explore further the possible role of adaptive optics in optical scanners, a design study for an A4 600dpi laser printer was carried out. A post-objective scanning system was chosen and the final design shown in Figure 4, based on a low-cost commercially available doublet, has diffraction-limited performance (as in Figure 5). Using current bimorph or membrane mirror

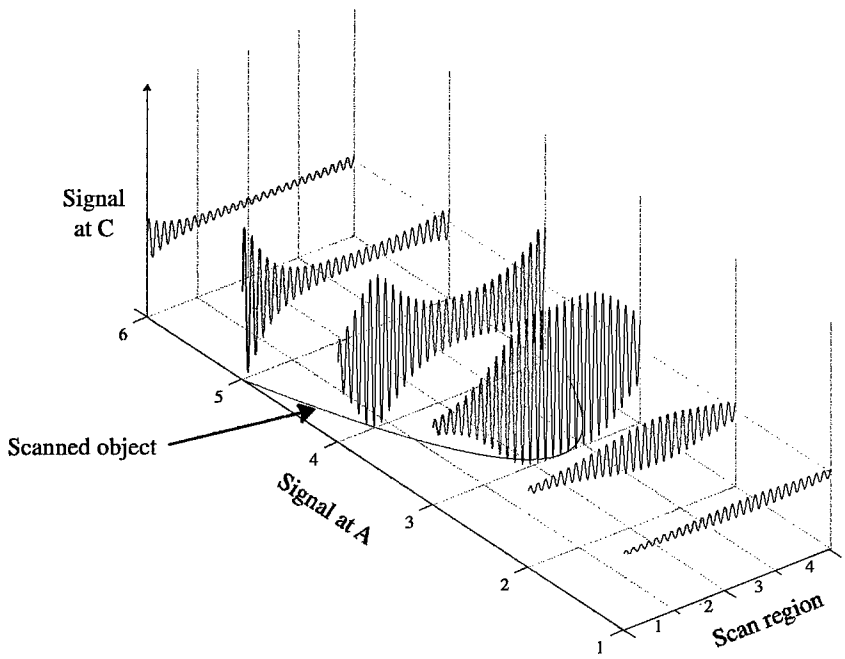

Figure 2. The signal at C for a grating like object for different focus settings of the bimorph as recorded by the signal at A

technology, a print speed on the order of 6 pages per minute would be possible.

In reality, a more realistic target specification might be for an A4 page at 1500 dpi and 20 pages per minute, requiring a much faster adaptive element. Possible options for this include optimised bimorph mirrors, MEMS mirrors or ferroelectric liquid crystal devices.

4 Discussion

We have shown the feasibility of using adaptive optics in laser scanning systems. Although the demonstration was only for the correction of focus, other low order aberrations could be corrected in a straightforward way provided suitable calibration techniques are developed. The main limitation at present

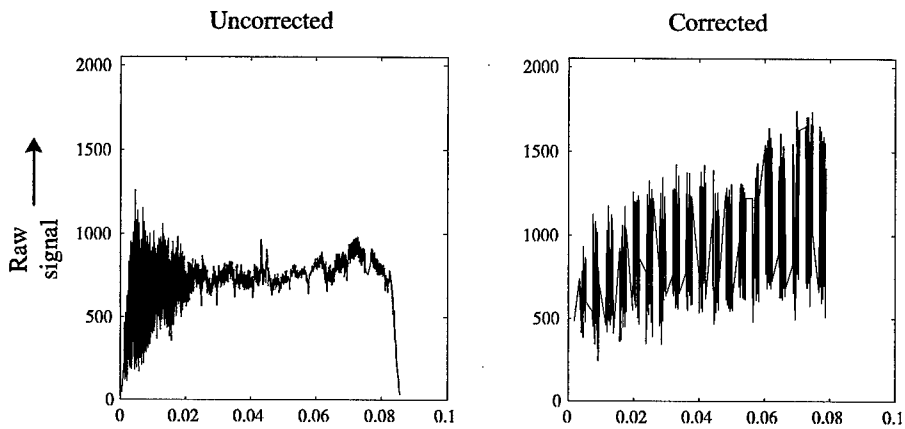

Figure 3. The signal at C is plotted as a function of the scan position for a grating-like object without (left) and with (right) operation of the adaptive bimorph mirror

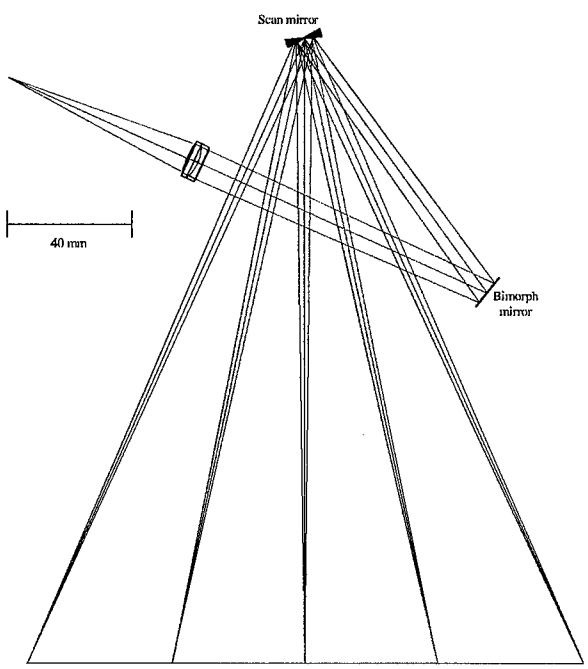

Figure 4. Laser printer optical system using an adaptive mirror for focus correction

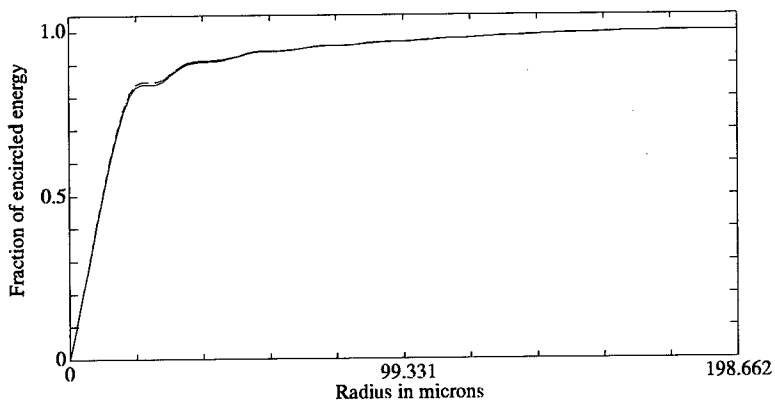

Figure 5. Performance of laser printer optical system

is the speed of response of the adaptive element and, of course, the high cost of present-day adaptive mirrors.

Acknowledgments

This work was supported by the UK Engineering and Physical Sciences Research Council and Pilkington Technology Centre.

References

1. L Beiser, *Laser Scanning Notebook*, (SPIE Optical Engineering Press, 1992).
2. E M Ellis, *Low-cost Bimorph Mirrors in Adaptive Optics*, (PhD Thesis, University of London, 1999).

List of Delegates

Olivier	Albert	University of Michigan	USA
Pablo	Artal	Universidad de Murcia	Spain
Jeffrey	Baker	Boeing North American	USA
Pierre	Barbier	Laboratory for Physical Sciences	USA
Andrew	Barnes	AWE PLC	UK
Tom	Barnes	University of Auckland	New Zealand
Horst	Baumhacker	Max-Planck-Institut für Quantenoptik	Germany
Philip	Birch	University of Sussex	UK
Paul	Blanchard	DERA	UK
Stefan	Borneis	GSI Darmstadt	Germany
Don	Bruns	Trex Enterprises	USA
Samuel	Bucourt	Imagine Optic	France
Arjan	Buist	University of Amsterdam	The Netherlands
David	Buscher	University of Durham	UK
Ivo	Buske	FH-Muenster	Germany
David	Catlin	Imperial College	UK
Mark	Chang	EDS UK Ltd	UK
Rung-Sheng	Chen	Imperial College	UK
Tanya	Cherezova	NICTL	Russia
Joseph	Colineau	Thomson-CSF LCR	France
John	Collier	Rutherford Appleton Laboratory	UK
Neil	Collings	University of Cambridge	UK
Arnaud	Coville	SFIM	France
Michael	Daffner	Universität Stuttgart	Germany
Chris	Dainty	Imperial College	UK
Pamela May	Danforth	Lawrence Livermore National Laboratorv	USA

David William	de Lima Monteiro	TU-Delft	The Netherlands
Luis	Diaz Santano Haro	Imperial College	UK
Peter	Doel	University College London	UK
Harold	Dyson	University of Durham	UK
Gavin	Erry	DERA	UK
Janet	Fender	USAF Research Laboratory	USA
Hubert	Gardette	Laboratorie de Biophysique de la Vision	France
Marie	Glanc	Laboratorie de Biophysique de la Vision	France
Jesper	Gluckstad	Risø National Laboratory	Denmark
Frederic	Gonté	IMT	Switzerland
Thomas	Graf	University of Bern	Switzerland
Alan	Greenaway	DERA	UK
Paul	Harrison	DERA	UK
Robert	Hellwarth	University of Southern California	USA
Ron	Humprheys	University of Durham	UK
Chris	Hooker	Rutherford Appleton Laboratory	UK
Steven	Jackel	Soreq NRC	Israel
Pascal	Jagourel	CILAS	France
Feodor	Kanev	Institute of Atmospheric Optics	Russia
Michael	Kartz	Lawrence Livermore National Laboratory	USA
Thu-Lan	Kelly	University of Durham	UK
Klaus	Kudielka	Communications Research Laboratory	Japan
Alexei	Kudryashov	NICTL	Russia
Nicolas	Kugler	Laser-und Medizin-Technologie GmbH	Germany
Xavier	Levecq	Imagine Optic	France
Martin	Levine	Adaptive Optics Associates	USA
Sacha	Loiseau	Observatoire de Meudon	France
Gary	Loos	USAF Research Labs.	USA
Jean-Louis	Loureau	CILAS	France
Gordon	Love	University of Durham	UK

Pierre-Yves	Madec	ONERA	France
Yanka	Malashko	JSS Central Design Bereau, "Almaz"	Russia
Justin	Mansell	Stanford University	USA
Jon	Maxwell	Imperial College	UK
Wilson	McKellar	Imperial College	UK
Donald	Miller	Indiana University	USA
Paul	Mogensen	Risø National Laboratory	Denmark
Inon	Moshe	Soreq NRC	Israel
Ian	Munro	Imperial College	UK
Richard	Myers	University of Durham	UK
Alexander	Naumov	University of Durham	UK
Daniel	Neal	Wavefront Sciences Inc.	USA
Matthias	Negendanck	ERLAS GmbH	Germany
John	O'Byrne	University of Sydney	Australia
John	Otten	Kestrel Corporation	USA
Carl	Paterson	Imperial College	UK
Deanna	Pennington	Lawrence Livermore National Laboratory	USA
Isabelle	Percheron	Boeing North American	USA
Raphäel	Perdrix	SFIM	France
Mark	Plett	Laboratory for Physical Sciences	USA
Alan	Purvis	University of Durham	UK
Zoran	Popovic	Goteborg University	Sweden
Sergio	Restaino	USAF Research Labs.	USA
Erez	Ribak	Technion	Israel
Vadim V.	Samarkin	Laser Research Center - NICTL	Russia
Bernd	Schäfer	Laser-Laboratorium Göttingen	Germany
Howard	Schlossberg	AFOSR	USA
Reinhard	Schmiedl	Diehl Stiftung & Co.	Germany
Krishna	Seunarine	University of Edinburgh	UK
Ray	Sharples	University of Durham	UK

Victor	Shmalhausen	Moscow State University	Russia
Ian	Smith	AWE PLC	UK
Chris	Stace	British Aerospace	UK
Jorgen	Thaung	Goteborg University	Sweden
Larry	Thibos	Indiana University	USA
Robert	Tyson	University of North Carolina	USA
Argeo	Vazquez	Laser-und Medizin-Technologie GmbH	Germany
Gleb	Vdovin	TU Delft	The Netherlands
Vladimir	Venediktov	Research Institute for Laser Physics	Russia
Christopher	Verinaud	Observatoire de la *Côte* d'Azur	France
Kai	Weidlich	Carl Zeiss	Germany
George	Willliams	Pixelvision Inc	USA
Ulrich	Wittrock	FH-Muenster	Germany
Simon	Woods	DERA	UK
Yudong	Zhang	Institute of Optics & Electronics	China